ОБЩЕСТВО НА ТРИБОЛОЗИТЕ В БЪЛГАРИЯ

SOCIETY OF BULGARIAN TRIBOLOGISTS

ТРИБОЛОГИЧЕН ЖУРНАЛ БУЛТРИБ

TRIBOLOGICAL JOURNAL BULTRIB

Година V, брой 05 (05), 2015
Volume V, Number 05 (05) 2015

Доклади от 11-та международната конференция по трибология

BULTRIB'15, 11-13 септември 2015, Созопол, България

Papers from the 11th International Conference on Tribology

***BULTRIB'15**, 11-13 September, 2015, Sozopol, Bulgaria*

Printing House of the Technical University
Sofia

Трибологичен журнал БУЛТРИБ
Tribological Journal BULTRIB

Доклади от 11-та международната конфереция по трибология
БУЛТРИБ '15, 11-13 септември 2015, Созопол, България
Papers from the 11th International Conference on Tribology
BULTRIB '15, 11-13 September, 2015, Sozopol, Bulgaria

Съставители: доц. д-р Мара Кандева, доц. д-р Емилия Асенова
Compliers: Assoc. Prof. Dr. Mara kandeva, Assoc. Prof. Dr. Emilia Assenova
Sofia, 2015

ISSN: 1313-9878

ОРГАНИЗАТОРИ / ORGANIZERS:

ОБЩЕСТВОТО НА ТРИБОЛОЗИТЕ В БЪЛГАРИЯ

със съдействието на
МТФ на ТЕХНИЧЕСКИЯ УНИВЕРСИТЕТ - София

THE SOCIETY OF BULGARIAN TRIBOLOGISTS

with the assistance of the
FACULTY OF INDUSTRIAL TECHNOLOGY at the TECHNICAL UNIVERSITY OF SOFIA

The Conference BULTRIB'15 is organized together with the International Jubilee Conference "70 years Faculty of Industrial Technology"

Contacts:
Tribology Center, Technical University - Sofia 1756
E-mail: *kandevam@gmail.com* **&** *emiass@abv.bg*
Assoc. Prof. Dr. **Mara Kandeva** (Mob: +359 893341455)
Assoc. Prof. Dr. **Emilia Assenova** (Mob: +359 877438334)
Websites: *http://bultrib.com* & *http://mtf70.tu-sofia.bg*

INTERNATIONAL SCIENTIFIC COMMITTEE

Chairman: Prof. DSc Nyagol Manolov – Bulgaria

Honorary Chairman: Prof. DSc H. Peter Jost – President of the International Tribology Council

Members:

Prof. DSc Slavi Ivanov – Bulgaria
Prof. Dr Ivan Kralov – Bulgaria
Prof. DSc. Jordan Genov– Bulgaria
Prof. Dr Georgi Todorov – Bulgaria
Prof. DSc Jean Frene - France
Prof. DSc Stanislaw Pytko – Poland
Prof. DSc Nikolai Mishkin – Belarus
Prof. DSc Dmitrij Garkunov – Russia
Acad. Prof. DSc Kiril Voinov - Russia
Prof. DSc Wilfried Bartz – Germany
Prof. DSc Gottlieb Polzer – Germany
Prof. DSc Josef Schlattman – Germany
Prof. DSc Friedrich Franek – Austria
Prof. Dr Jeng-Haur Horng - Taiwan
Prof. Dr Gordana Globocki - Bosnia & Herzegovina
Prof. Dr Kresimir Grilec – Croatia
Prof. Dr Zdravko Schauperl – Croatia
Corr. Memb. Dr Petr Kornik - Kazahstan
Prof. DSc K.-D. Bouzakis - Greece
Prof. Dr Atanasios Mihailidis - Greece
Prof. Dr Sevasti Mitsi – Greece
Prof. Dr Niculae N. Antonescu - Romania
Prof. Dr Andrei Tudor - Romania
Prof. Dr Minodora Ripa - Romania
Prof. Dr Alexandru Radulescu - Romania
Prof. Dr Razvan G. Ripeanu - Romania
Prof. Dr Luminita Irimescu - Romania
Prof. Dr Branko Ivkovic - Serbia
Prof. Dr Aleksandar Rac - Serbia
Prof. Dr Miroslav Babic - Serbia
Prof. Dr Aleksandar Vencl – Serbia
Prof. Dr Sloboban Mitrovic – Serbia
Prof. Dr Miroslav Radovanovic – Serbia
Prof. Dr Mehmet Baki Karamis - Turkey
Prof. Dr Hakan Kaleli – Turkey
Prof. Dr Husseyn Cimenoglu – Turkey
Prof. Dr Cem Sinanoglu – Turkey

NATIONAL PROGRAM COMMITTEE

Chairman: Assoc. Prof. Dr Mara Kandeva

Science Secretary: Prof. Dr Viara Pojidaeva

Members:

Prof. Dr Vassil Alexandrov
Prof. Dr Yulika Simeonova
Prof. DSc Georgi Mishev
Prof. Dr Kiril Stanulov
Assoc. Prof. Dr Emilia Assenova
Assoc. Prof. Dr Juliana Javorova
Prof. Dr Georgi Cholakov
Assoc. Prof. Dr Jecho Kalichin
Assoc. Prof. Dr Nina Kostova
Assoc. Prof. DSc Nikolay Nikolov
Assoc. Prof. Dr Nikolay Tonchev

Electronic support: Dr. Temenuga Todorova,
Assoc. Prof. Dr. Aleksandar Tzokev

BULTRIB'15
Sozopol, 11 – 13 September 2015

SUPPORTED BY

Technical University (TU) – Sofia

Society of Bulgarian Tribologists

Balkan Tribological Association

Faculty of Industrial Technology at TU-Sofia

The TIMKEN Company USA

Ravera Ltd. - Burgas
Равера ЕООД, гр. Бургас

ATER Ltd – Shumen
Атер ЕООД, гр Шумен

Venue of the Conference ***BULTRIB'15***
Sozopol Resort House of the Technical University,
Lazuren bryag St. № 7, Sozopol – The New Town, Bulgaria

Sozopol, Black Sea Coast, Bulgaria

Sozòpol (Bulgarian: Созопол, Greek: Sozopolis / Σωζόπολις) is an ancient seaside town located 35 km south of Burgas on the southern Bulgarian Black Sea Coast. Today it is one of the major seaside resorts in the country, known also for the Apollonia art and film festival (which takes place in early September) that is named after one of the town's ancient names.

Hosts

The Technical University of Sofia is the largest educational and scientific complex in Bulgaria in the field of technical and applied science with an institutional accreditation grade of 9.5 (on the scale of 10) for the period 2012 – 2018.

The University structure includes 14 faculties in Sofia, three departments, a Center of Information Resources, a Library and Information Center, a Center for international meetings, a Center for Continuous Education, a Center for Educational and Innovative Projects, a University Science and Research Complex for innovations and knowledge transfer in the field of micro and nano- technologies and materials, energy efficiency and virtual engineering, Post graduate schools, Scientific and Research Sector, small enterprises, a branch in the city of Plovdiv with two faculties, a Faculty of Engineering and Pedagogy and a College in the town of Sliven, a School for power engineering and electronics and two high schools – School of Electronic Systems Technologies in Sofia and a Vocational School for Computer Technologies and Systems in the town of Pravetz.

The Faculty of Industrial Technology (FIT) prepares specialists in the field of engineering and technology. Ever since the first academic year in 1945/1946 the Faculty has trained thousands of engineers and has always been a leading national center in the field of scientific research and applied activities. One of the Laboratories in FIT is the **Scientific & Production Laboratory "Tribology".**

Scientific and Production Laboratory "Tribology" –
40 years National Tribology Centre

The scientific and production **Laboratory "Tribology"** is headed by Assoc. Prof. Dr Mara Kandeva. The **Laboratory "Tribology"** was founded at the **Technical University Sofia** in 1974 by **Prof. DSc Nyagol Manolov**, and acts as National Tribology Centre in Bulgaria. It is the starting place for feeding the National WEB in the tribospace, which is a contact network of researchers/educators, customers and producers, and their achievements in the field of tribology and tribotechnologies. Information about researchers, production companies and consumers of tribological problems, tribomaterials, triboelements and tribotechnologies is rendered systematically, aiming harmonization and improvement of effectiveness of the tribological services. In sight are problems related to the management of friction, wear, lubrication, hermeticity, serviceability and reliability of tribotechnical elements and systems in their operation and maintenance.

The latest tribotechnologies developed in the Laboratory "Tribology" at the Technical University – Sofia are **tribotechnologies for application of wear-resistant gas-flame and ultrasonic powder coatings** in collaboration with the Belgian company "GMA-Technologies. Another tribotechnology actual for Bulgaria and the region is a **tribotechnology for qualification and regeneration of air filters in motorcar and truck transportation**. The method and technology are patent of the Laboratory "Tribology", Sofia.

Lubricants, additives and surface coatings are the thoroughly developed topics of the latest years.

The Laboratory for Tribology, with the support of the Society of Bulgarian Tribologists, organizes the annual International Conferences on Tribology BULTRIB.

CONTENTS

ПРИВЕТСТВИЕ

от доц. д-р Мара Кандева,
Председател на Обществото на триболозите в България и Ръководител на Лабораторията по трибология

Уважаеми колеги и гости, дами и господа,

Лабораторията по трибология като част от Машинно-технологичния факултет, заедно с Обществото на триболозите в България, организират ежегодно международната конференция по трибология БУЛТРИБ.

БУЛТРИБ 2015 е част от юбилейната конференция „70 години МТФ" в знак на дълбокото ни уважение към интердисциплинарния дух и традициите на Факултета. Като ръководител на Лабораторията по трибология и председател на Обществото на триболозите в България имам удоволствието да ви поздравя с „Добре дошли" и да пожелая успешна работа на конференциите.

Изразявам нашата благодарност към основните спонсори на БУЛТРИБ 2015, а именно:

- Техническия университет – София и по-специално Научно-изследователския му сектор и Договор № ДУНК-01/3 "Създаване на Университетски научно-изследователски комплекс (УНИК) за иновации и трансфер на знания в областта на микро/нанотехнологии и материали, енергийната ефективност и виртуалното инженерство";
- Фирмата ТИМКЕН – САЩ;
- Балканската трибологична асоциация и
- Българските фирми РАВЕРА и АТЕР.

Благодаря за вниманието!

OPENING SPEECH

by Assoc. Prof. Dr. Mara Kandeva,
Head of the Tribology Laboratory and Chairman of the Society of Bulgarian Tribologists

Dear colleagues and guests, Ladies and Gentlemen,

Being a part of the faculty of industrial Technology, the Laboratory for Tribology together with the Society of Bulgarian Tribologists organizes the annual International conferences on tribology BULTRIB.

BULTRIB 2015 makes part of the Jubilee Conference "70 Years Faculty of Industrial Technology" emphasizing thus a deep respect to the interdisciplinary sprit and tradition of the Faculty.

As Head of the Tribology Laboratory and Chairman of the Society of Bulgarian Tribologists, I have the pleasure to welcome all of you and to wish successful work to both conferences.

I would like to express gratitude to the main sponsors of BUTRIB 2015, namely:

- The Technical University – Sofia and its Research and Development Sector along with the Project ДУНК-01/3 "University R&D Complex for innovation and transfer of knowledge in micro/nano-technologies andmaterials, energy efficiency and virtual engineering" funded by the Bulgarian Ministry of Education and Science
- The company TIMKEN – USA;
- The Balkan Tribological Association;
- The Bulgarian companies RAVERA and ATER.

Thank you for your attention!

Tribological Journal BULTRIB Vol. 5, 2015
Papers from the International Conference **BULTRIB '15**
September 11-13, 2015, Sozopol, Bulgaria
Society of Bulgarian Tribologists
FIT – Technical University of Sofia

TRIBOLOGY OF METAL MATRIX MICRO- AND NANOCOMPOSITES

Aleksandar VENCL, Ilija BOBIĆ, Mara KANDEVA, Dimitar KARASTOYANOV

Abstract: *This paper presents a short summary of the researches conducted in past few years concerning the metal matrix composites with different matrix material, different reinforcing/alloying elements, and obtained by different processing techniques. The results are classified into three groups according to the matrix material. In the first group are the results for microcomposites with AlSi7Mg matrix alloy obtained by compocasting method. These results cover the influences of amount and size of reinforcement (Al_2O_3), and the influence of type of reinforcement (Al_2O_3, SiC and SiC with graphite addition). In the second group are the results for nanocomposites with ZnAl25Si matrix alloy obtained by casting and compocasting method. These results cover the influences of silicon and strontium addition percentage, and the influences of strontium and/or Al_2O_3 nanoparticles addition. In the third group are the results for micro- and nanocomposites with Cu matrix obtained by powder metallurgy technology (preceded by mechanical alloying and/or internal oxidation). These results cover the influence of size of reinforcement (Al_2O_3) on the macroscale (composite properties), and the same influence on the nanoscale (only the matrix properties).*

Key Words: *composite, A356 alloy, ZA-27 alloy, Cu powder, micro- and nano-sized Al_2O_3 particles, SiC and graphite particles, strontium.*

1. INTRODUCTION

The particulate composites with the aluminium-silicon (Al-Si) alloy matrix are one of the most commonly investigated metal matrix materials. Aluminium base provide these materials low density, good mechanical characteristics and high ductility, as well as excellent casting characteristics and high corrosion resistance. On the other hand, the reinforcements (mainly ceramic) improve the wear resistance of the matrix and the improvers (mainly graphite) reduce the coefficient of friction. The A356 Al-Si alloy (AlSi7Mg) is a casting alloy consisting of aluminium, silicon and magnesium and belongs to a group of hypoeutectic Al-Si alloys. This alloy has been widely applied in the machinery, aircraft and defence industries and particularly in the automotive industry [1].

The zinc-aluminium alloys are well-established zinc alloys with high aluminium content (8 to 28 wt. %). The alloy with 25 to 27 wt. % Al (ZA-27 alloy) is, due to the high strength and good wear resistance, frequently used for making sliding bearings intended for high load/low speed applications [2]. The dimensional stability over a period of time of ZA-27 alloy could be improved by replacing copper in the alloy with silicon (Zn-Al-Si alloys) [3]. By suitable additions of strontium to the Zn-Al-Si alloy (ZnAl25Si) the size of silicon particles can be reduced with its more uniform distribution [4]. The addition of the ceramic nanoparticles to the ZnAl25Si matrix alloy should have the similar role as the strontium addition.

The copper-based composites are used primarily for their excellent electrical and thermal properties, and reinforcements are added for control of thermal expansion or improved wear resistance. The matrix is usually the pure element to retain the excellent thermal or electrical properties [5]. In case when the reinforcement are the non-metallic particles, such as Al_2O_3, added to or formed within the copper matrix, the effectiveness of these oxide particles as strengtheners depends upon particle size (finer is better), particle distribution (well dispersed is better), particle density (more per unit volume is better), and particle spacing (closer is better) [6]. Applying the nanoscale tribological tests, by using an atomic force microscope, to the small and localized area (approx. few μm in diameter), it is possible to distinguish the influence that particles have on wear of the matrix (only the matrix properties) [7].

2. MATERIALS AND TRIBOLOGICAL TEST PROCEDURES

2.1. Microcomposites with AlSi7Mg matrix alloy (group I)

The matrix material was A356 hypoeutectic Al-Si alloy (EN AlSi7Mg0.3) with the following chemical composition (in wt. %): Al-7.2Si-0.02Cu-0.29Mg-0.01Mn-0.18Fe-0.01Zn-0.02Ni-0.11Ti. Composites were produced by applying the compocasting method, where the second phase particles were added into the semi-solid A356 alloy by infiltration and admixing. Experimental procedure and apparatus used for the compocasting processing are described and discussed elsewhere [8].

Composite specimens (Table 1) were subjected to heat treatment with following parameters: solution annealing at 540 °C for 6 h, water quenching and artificial aging at 160 °C for 6 h. The chemical composition

of gray cast iron, chosen as the reference material, fabricated using the sand casting procedure followed with heating at 550 °C, was: Fe-3.18C-2.17Si-0.60Mn-0.7P-0.37Cr.

Table 1. Designation and properties of the tested materials (group I)

Specimen designation	Composition	Particle content, wt. %	Particle size, μm
A0	Gray cast iron (reference material)	–	–
A1	A356 + Al_2O_3	3	12
A2	A356 + Al_2O_3	10	12
A3	A356 + Al_2O_3	10	35
A4	A356 + SiC	10	39
A5	A356 + SiC + Gr (graphite)	10 (SiC); 1 (Gr)	39 (SiC); 35 (Gr)

Microstructures of the tested materials have been presented and discussed elsewhere [1, 8], as well as, the hardness and other mechanical properties [1, 9-12].

Tribological test were conducted in two phases: In the first phase (specimens A0, A1, A2 and A3) influences of amount and size of reinforcement were investigated, and in the second phase (specimens A3, A4 and A5) influences of type of reinforcement and graphite were investigated. Both tests were under dry sliding conditions, in ambient air at room temperature. The phase I tests were carried out on the standard pin-on-disc tribometer with cylindrical pins made of tested materials. Test parameters were as follows: sliding speed: 1 m/s; normal load: 1, 2, 3 and 4 MPa; sliding distance: 5000 m; counter-body: disc (nodular gray cast iron). The phase II tests were carried out on the ball-on-barrel tribometer with linear (reciprocating) movement. Moving body with cylindrical geometry was made of tested materials. Test parameters were as follows: sliding speed: 0.038 m/s (average); normal load: 1 N; sliding distance: 500 m; counter-body: ball (alumina). The values of coefficient of friction were monitored during both tests. Diagrams of the load, sample, counter body and the direction of movement for both tribometers are shown in Fig. 1.

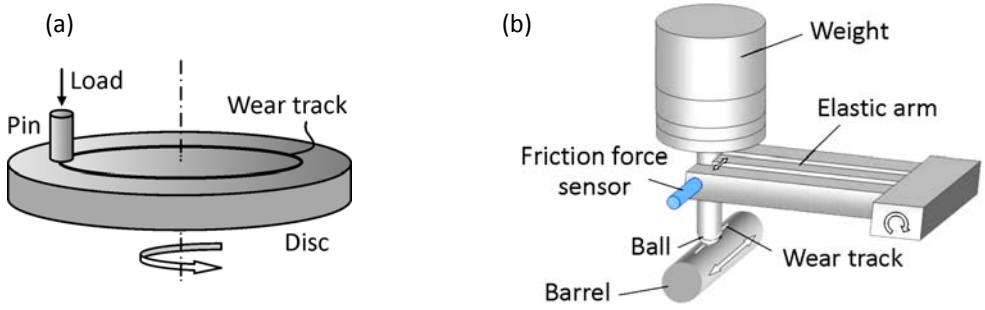

Fig. 1. Schematic drawing of the tribometer used in: (a) phase I and (b) phase II

2.2. Nanocomposites with ZnAl25Si matrix alloy (group II)

Technically pure zinc and aluminium were used to obtain the Zn25AlSi alloys (Table 2), with the addition of master alloys Al7Si and Al18Si for achieving the desired content of silicon. Strontium was added in the alloys using the master alloy Al10Sr. The alloys were melted in the laboratory electric resistance furnace. The molten alloys (570 °C) were poured in the steel moulds preheated to 200 °C. Immediately before pouring the melts were intensively manually stirred. For the purpose of comparison, a commercial ZA-27 alloy [13] was used; with the identical casting procedure as for Zn25AlSi alloys. Microstructures and mechanical properties of these materials have been presented and discussed elsewhere [4].

Table 2. Designation and properties of the tested materials (group II)

Specimen designation	Composition	Particle content, wt. %	Particle size, nm
B0	ZA-27 alloy (reference material)	–	–
B1	Zn25Al-1Si	–	–
B2	Zn25Al-1Si-0.03Sr	–	–
B3	Zn25Al-1Si-0.05Sr	–	–
B4	Zn25Al-3Si	–	–
B5	Zn25Al-3Si-0.03Sr	–	–
B6	Zn25Al-3Si-0.05Sr	–	–
B7	Zn25Al-3Si + Al_2O_3	1	20 – 30
B8	Zn25Al-3Si-0.03Sr + Al_2O_3	1	20 – 30

Nanocomposites (specimens B7 and B8 in Table 2) were produced by applying the compocasting method using Zn25Al-3Si and Zn25Al-3Si-0.03Sr as the matrix alloys, and Al_2O_3 nanoparticles as the reinforcement. The compocasting process was performed in two steps. In the first step each matrix alloy was melted, overheated at 570 °C and then cooled with 5 °C /min cooling rate to 485 °C. After that it was mixed with 50 rpm mixing rate, and continuous cooling (5 °C/min). When the melt reached temperature of 465 °C, the mixing rate was increased to 500 rpm. Mixing of the semisolid melt lasted 5 min, and then the addition of Al_2O_3 nanoparticles was then performed, that lasted 3 min. The addition of nanoparticles was carried out at a reduced mixing rate (250 rpm). After the addition of nanoparticles a short homogenization mixing (at 250 rpm) was carried out at for 3 min, and an intensive mixing (with mixing rate of 500 rpm) for 25 min. Semisolid nanocomposite mixture was poured in the steel moulds preheated at 400 °C, which is the end of the first step of the applied compocasting process. In the second step of the process a hot pressing was performed at the temperature of 350 °C and pressure of 250 MPa.

Tribological test were conducted in two phases: In the first phase (specimens B0, B1, B2, B3, B4, B5 and B6) influences of silicon and strontium addition percentage were investigated, and in the second phase (specimen B7 and B8) influences of strontium and/or Al_2O_3 nanoparticles addition were investigated. Both tests were carried out on the block-on-disc tribometer under lubricated sliding conditions, in ambient air at room temperature. Test parameters were as follows: sliding speed: 0.5 m/s; sliding distance: 1000 m; normal load: 100 N.

A schematic diagram of tribometer is presented in Fig. 2. Rectangular blocks of tested materials were used as wear test samples. Disc (counter-body) was made of steel C60E (46 to 48 HRC). Lubrication was provided by revolving of the disc which was sunk into oil container. Lubricant was mineral engine oil (SAE 15W-40, ACEA E3). Wear scars on blocks were measured in accordance with ASTM G77 with accuracy of 0.05 mm, after each test to calculate the volume loss. The values of oil temperature, coefficient of friction, normal and friction force were monitored during the test.

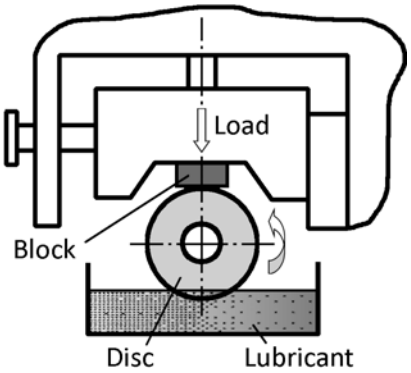

Fig. 2. Schematic drawing of the used tribometer

2.3. Micro- and nanocomposites with Cu matrix (group III)

Both Cu-based composites were produced by powder metallurgy (PM) technology, but the starting components for micro and nano Cu-based composite were different. The microcomposite was produced by PM technology (preceded by mechanical alloying) and contained micro-sized Al_2O_3 particles. Starting components were copper powder and 5 wt. % Al_2O_3 particles. This mixture was mechanically milled and compacted. The nanocomposite was produced by PM technology (preceded by mechanical alloying and internal oxidation) and contained nano-sized Al_2O_3 particles. Starting component was prealloyed copper powder containing 2.5 wt. % Al. This powder was subjected to internal oxidation, i.e. during milling aluminium, dissolved in the copper matrix, oxidizes and forms nano-sized Al_2O_3 particles (approx. 4.7 wt. %). For the purpose of comparison, a copper-based alloy Cu-0.4Cr-0.08Zr produced by casting, followed by heat treatment was used. Designation and properties of tested materials in this group are shown in Table 3. Detailed processing parameters for all materials and other properties are given elsewhere [14].

Table 3. Designation and properties of the tested materials (group III)

Specimen designation	Composition	Particle content, wt. %	Particle size, μm
C0	Cu-0.4Cr-0.08Zr (reference material)	–	–
C1	Cu + Al2O3	5	≈ 750
C2	Cu + Al2O3	4.7	< 100

Tribological test were conducted in two phases: In the first phase (specimens C0, C1 and C2) influences of size of reinforcement (Al_2O_3) on the macroscale (composite properties) were investigated, and in the second phase (specimen C1 and C2) the same influence were investigated on the nanoscale (only the matrix properties). Both tests were under dry sliding conditions, in ambient air at room temperature.

The phase I tests were carried out on the ball-on-disc nanotribometer (Fig. 3a) in rotation sliding mode (Fig 3b). Static body (counter-body) was a steel ball made of 100 Cr6 martensitic bearing steel with 1.5 mm in diameter. Moving body (test sample) was flat circular disc made of the tested materials. Test parameters were as follows: sliding speed: 6, 8 and 10 mm/s; normal load: 1 N; sliding distance: 30 m. Wear volumes of the test samples were calculated after each test, by measuring the wear track width, according to ASTM G99.

The values of coefficients of friction, normal and friction force, steel ball penetration depth were monitored during the test. Used nanotribometer is equipped with optical displacement sensor (fiber optic sensors) for measuring deflection of the cantilever (Fig. 3b), with high sensitivity. Light emitted from the sensor tip is re-

flected from the reflective areas attached to the spring, received by the sensor and converted into electrical signal. The signal is related to the distance between the sensor tip and a reflective area on the cantilever.

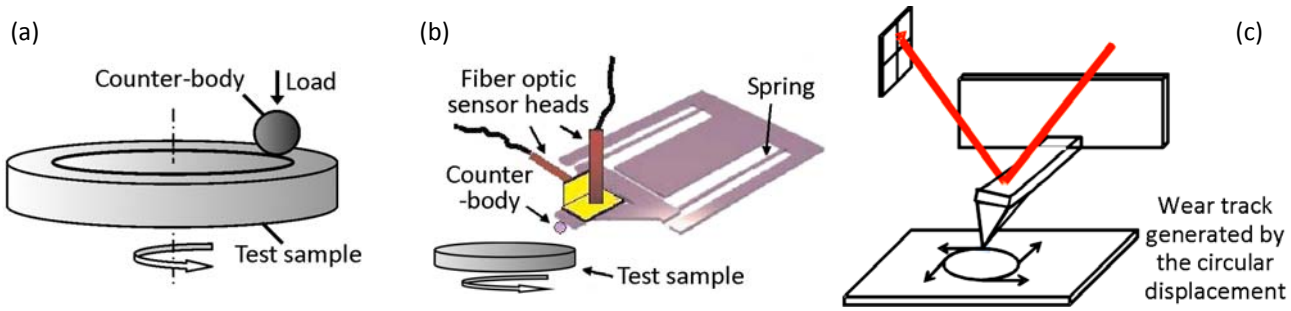

Fig. 3. Schematic drawing of the: (a) and (b) nanotribometer used in phase I (a – contact conditions; b – rotation sliding module) and (c) atomic force microscope used in phase II

The phase II tests were performed with an atomic force microscope (AFM) using the circular mode [15], schematically shown in Fig. 3c. Test parameters were as follows: normal load: 150 nN; sliding distance: ≈ 2.7 m (720.000 cycles of 1.2 μm in diameter). The coefficients of friction were also recorded.

3. RESULTS AND DISCUSSION

3.1. Microcomposites with AlSi7Mg matrix alloy (group I)

Average steady-state values of coefficients of friction, obtained in both phases of the tribological test, are shown in Table 4. All tested materials showed very similar values (0.5 to 0.7), which were in expected range for metals under dry sliding conditions (approximate values for the metals under dry sliding conditions are from 0.3 to 1.5 [17].

In the first phase of the tribological test (specimens A0, A1, A2 and A3), i.e. tests that investigated the influences of amount and size of reinforcement, the coefficient of friction values did not change significantly with the change of specific load, and one mean value per material can be accepted for the whole applied load interval. Both composite materials with 10 wt. % of Al_2O_3 (specimens A2 and A3) had higher values of the coefficient of friction than gray cast iron (specimen A0), principally due to the presence of hard reinforcing particles. Confirmation for this statement is the value of the coefficient of friction obtained with composite containing 3 wt. % of Al_2O_3 (specimen A1). In this case we have the same matrix and the same reinforcement but in lower amount, which induced lower coefficient of friction.

Table 4. The coefficient of friction average values of tested materials (group I) [11, 16]

Specimen designation	Phase I values	Phase II values
A0	0.53	–
A1	0.46	–
A2	0.61	–
A3	0.60	0.73
A4	–	0.71
A5	–	0.65

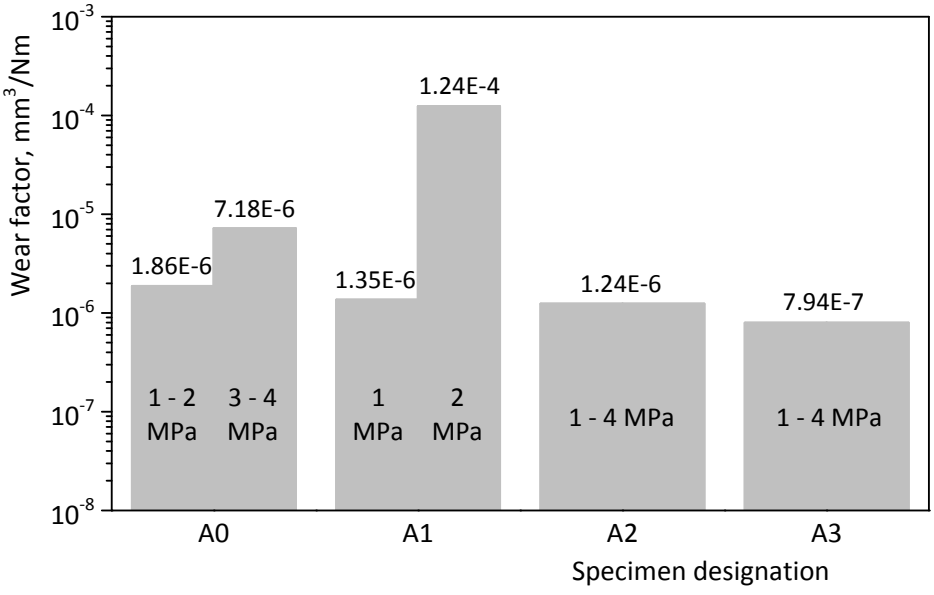

Fig. 4. Wear factors of the tested materials in the first phase (group I) [1, 16]

The wear factors, i.e. specific wear rates of the materials tested in the first phase (calculated for the steady-state period) are presented in Fig. 4. Obtained wear factor values correspond to the literature data for metallic materials in sliding contact (under unlubricated condition, and for adhesive wear, the interval is from 10^{-7} to 10^{-2} mm^3/Nm) [18]. The results show that the increase of the reinforcement amount, as well as, the increase of the reinforcement particle size had beneficial influence on the wear resistance of the composites.

For specimens A0 and A1, the existence of the critical load, at which the wear rate abruptly increases, is noted. This critical load indicates the transition of the wear regime. This transition is confirmed with the scanning electron microscopy (SEM) analysis of the worn surfaces and wear products. Gray cast iron samples (specimen A0) at lower loads (1 and 2 MPa) were not in full contact with the counter-body, and basic lamellar structure of the material could still be clearly noticed (Fig. 5a). At higher loads (3 and 4 MPa) more intensive abrasive wear starts (Fig. 5b). Adhesive wear also occurs due to the presence of high pressures and contact temperatures (Fig. 5c).

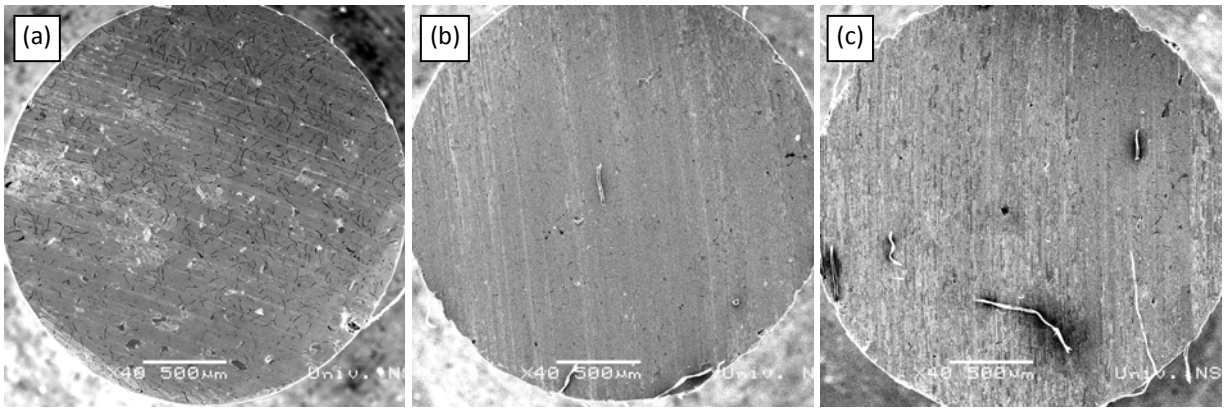

Fig. 5. SEM images of the specimen A0 (gray cast iron) pins worn surfaces, tested at different loads: (a) 2 MPa, (b) 3 MPa and (c) 4 MPa

The transition of the wear regime was especially sudden for the composite containing 3 wt. % of Al_2O_3 (specimen A1), which suggest that relatively small amount of reinforcement (3 wt. %) in this composite was enough just to support loads up to 1 MPa. At higher load (2 MPa) severe wear occur (Fig. 6a). At this load presence of the plastic flow of material on the pin surface was noticed (rounded area in Figure 6a). On the other hand, composites containing 10 wt. % of Al_2O_3 (specimens A2 and A3) at the same load did not show this plastic flow of material (Fig. 6b), and even the presence of transferred counter-body material could be noticed (rounded area in Figure 6b). Severe wear of the composite containing 3 wt. % of Al_2O_3 (specimen A1) at high load is confirmed with the SEM analysis of the wear products, i.e. in presence of the rod-like particles, longer than 50 μm were noticed (Fig. 7), which indicates existence of severe wear [19].

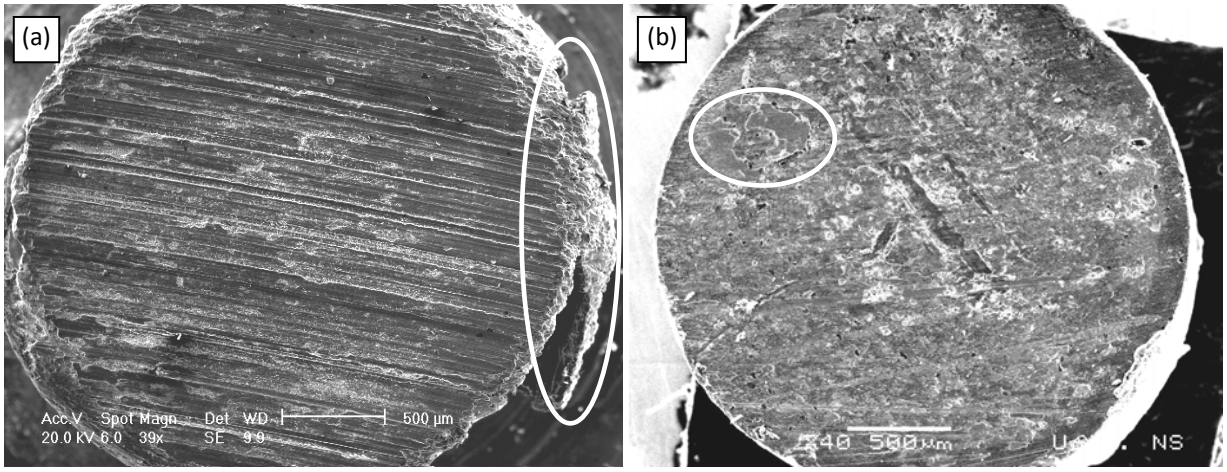

Fig. 6. SEM images of the composite pins worn surfaces at 2 MPa load: (a) specimen A1 (3 wt. % Al_2O_3) and (b) specimen A2 (10 wt. % Al_2O_3)

In the second phase of the tribological test (specimens A3, A4 and A5), i.e. tests that investigated the influences of type of reinforcement and graphite, the obtained wear factor values (Fig. 8) also correspond to the literature data for metallic materials in sliding contact. The results show that composites reinforced with SiC particles (specimens A4 and A5) have higher wear resistance, i.e. that the SiC reinforcement provided better

protection of the matrix than the Al_2O_3 reinforcement, added in the same amount. The simplest explanation is the highest hardness of SiC, but we also found that the SiC particles had more favourable arrangement in the composite matrix, i.e. clusters of type B [11]. Addition of the graphite particles in composite with SiC particles (specimen A5) reduced wear rate and coefficient of friction. The presence of graphite was small (only 1 wt. %) and usually it is not enough to form the lubricant film that could effectively decrease the coefficient of friction and wear [20], so the results should be considered only as a possible trend of behaviour.

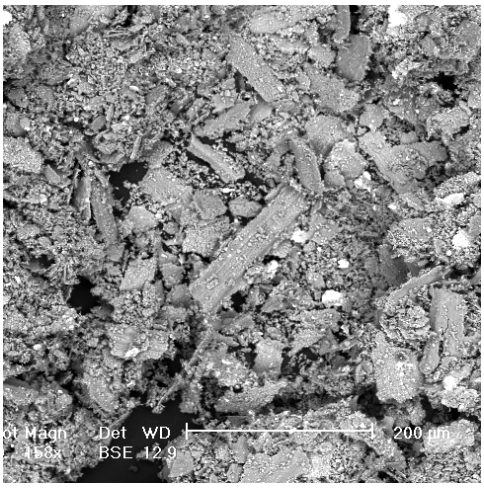

Fig. 7. SEM image of the wear products generated from specimen A1 at 2 MPa load

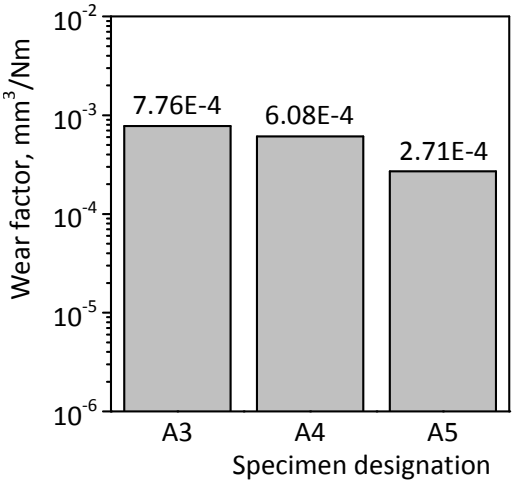

Fig. 8. Wear factors of the tested materials in the second phase (group I) [11]

SEM analysis of worn surfaces confirmed that SiC reinforcing particles were more efficient in protecting the matrix, i.e. while the presence of protruded Al_2O_3 particles on the surface was not noticed (Fig. 9a), protruded SiC particles were obvious (rounded area in Fig. 9b).

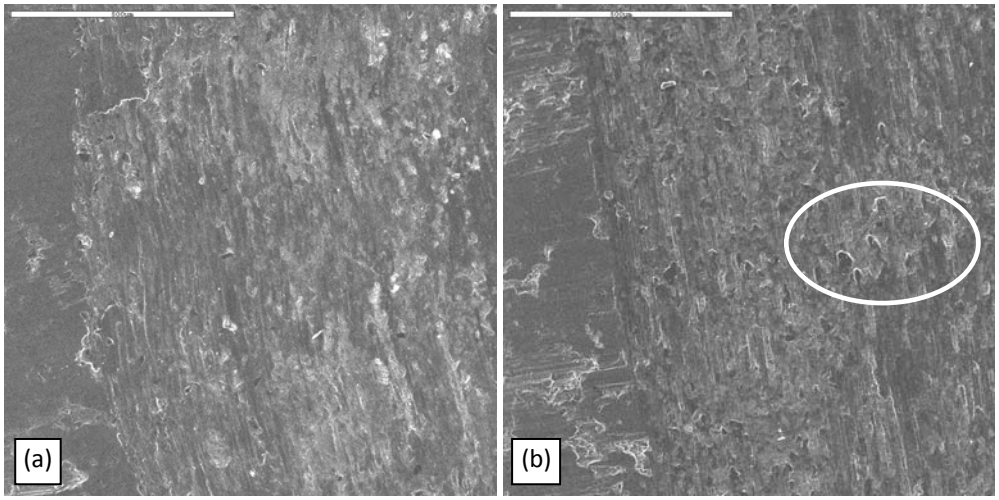

Fig. 9. SEM images of the composite samples worn surfaces: (a) specimen A3 (10 wt. % Al_2O_3) and (b) specimen A4 (10 wt. % SiC)

3.2. Nanocomposites with ZnAl25Si matrix alloy (group II)

Average steady-state values of coefficients of friction, obtained in both phases of the tribological test, are shown in Table 5. The obtained values of the coefficient of friction (0.05 to 0.1) suggest that the tests were performed in boundary lubrication regime (approximate values for the boundary lubrication are from 0.05 to 0.15 [17, 21]).

The replacement of copper with silicon (specimens B1 and B4) lowers the values of the coefficient of friction. On the other hand, addition of strontium (specimens B2, B3, B5 and B6) has negative effect on the coefficient of friction, and with increase of Sr content coefficient of friction increase further. Addition of Al_2O_3 nanoparticles (specimens B7 and B8) also increased the coefficient of friction, principally due to the higher hardness of the nanoparticles comparing to the matrix alloy. During the tests these particles were partially detached causing the three-body abrasion.

The wear factors, i.e. specific wear rates of the materials tested in the first phase are presented in Fig. 10. Wear factor values for the commercial ZA-27 alloy correspond to the literature data for the ZA-27 alloy, obtained via permanent mould casting and tested under similar conditions [22]. The results show that the size of primary silicon particles was reduced in the presence of strontium, with an improvement of their distribution in the alloy base [4, 23].

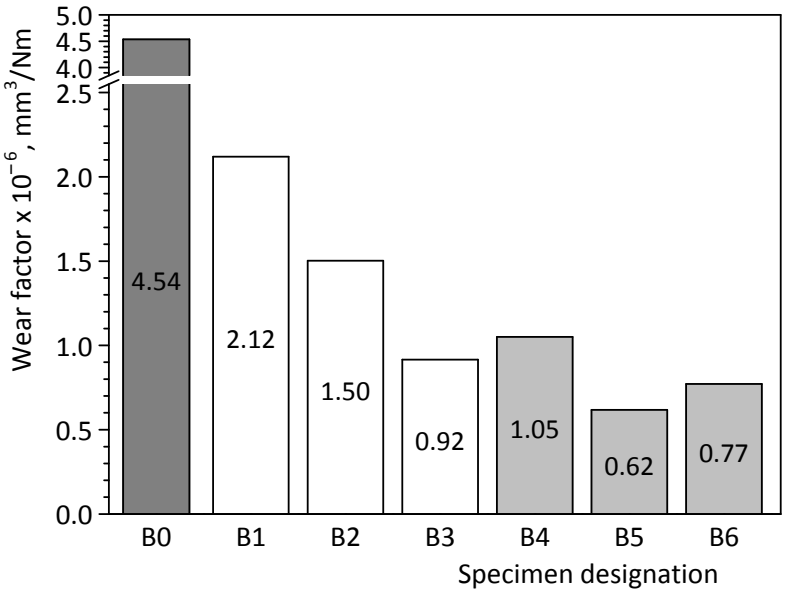

Fig. 10. Wear factors of the tested materials in the first phase (group II) [4]

Table 5. The coefficient of friction average values of tested materials (group II) [4]

Specimen designation	Phase I values	Phase II values
B0	0.069	–
B1	0.047	–
B2	0.059	–
B3	0.065	–
B4	0.061	–
B5	0.073	–
B6	0.079	–
B7	–	0.099
B8	–	0.102

SEM analysis of worn surfaces showed that the strontium modification caused the formation of independent eutectic silicon particles, which was more obvious in the alloys modified with 0.05 wt. % strontium (Fig. 11a). These particles, under the load and sliding, flow across the contact surface causing their better distribution, and thus providing better protection (Fig. 11b).

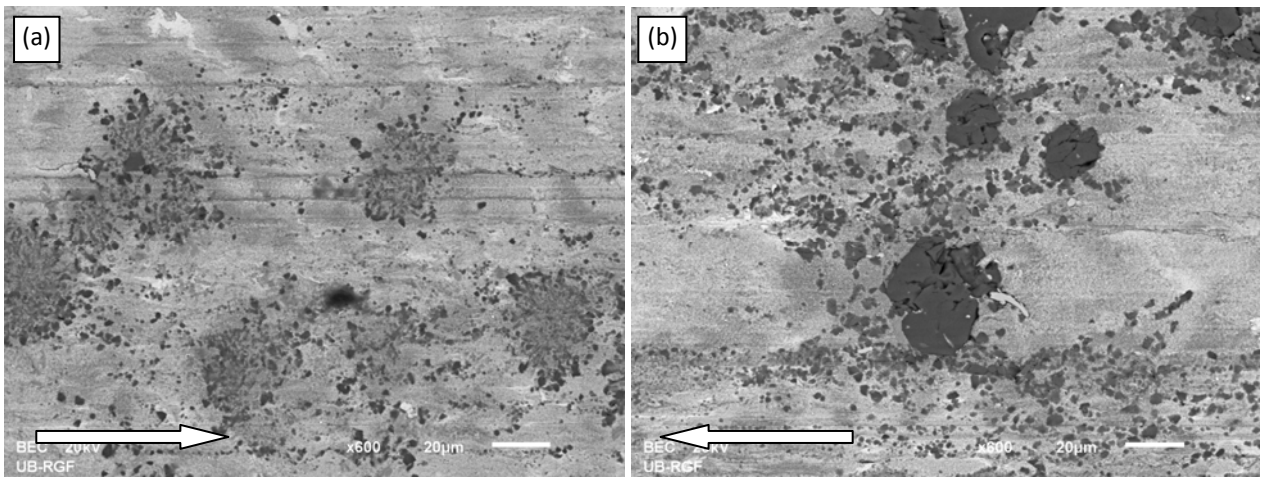

Fig. 11. SEM images of the samples worn surfaces: (a) specimen B6 (3 wt. % Si and 0.05 wt. % Sr) and (b) specimen B3 (1 wt. % Si and 0.05 wt. % Sr); counter-body sliding direction is denoted with arrows

In the case of Zn25Al-3Si alloy (specimen B4), the addition of 0.03 wt. % Sr decreased wear more than addition of 0.05 wt. % Sr, suggesting that over modification with Sr is possible situation [23]. Something similar occurred in the second phase of the tribological test (specimens B7 and B8), i.e. tests that investigated the influences of strontium and/or Al_2O_3 nanoparticles addition (which is not presented in this paper). These tests showed that the wear resistance was improved more in the case when only Al_2O_3 nanoparticles was added to the Zn25Al-3Si alloy (specimen B7) than in the case when both Al_2O_3 nanoparticles and 0.03 wt. % Sr were added to the same alloy (specimen B8).

3.3. Micro- and nanocomposites with Cu matrix (group III)

Average steady-state values of coefficients of friction, obtained in the first phase of the tribological test, are shown in Table 6. The coefficients of friction of specimens C0 (reference material) and C1 (microcomposite) were around 0.5, which is similar with the values obtained by some other researches [24], under similar

sliding speed and load. Coefficient of friction of specimen C2 (nanocomposite) was more than 3 times lower in comparison with other two materials, which is connected with the fact that in this case the adhesion between sliding surfaces was less pronounced – low stick-slip phenomenon [25].

The wear factors, i.e. specific wear rates of the materials tested in the first phase (tests that investigated the influences of size of reinforcement (Al_2O_3) on the macroscale) are presented in Fig. 12. Obtained values of the wear factors are in correlation with the coefficient of friction values and correspond to the literature data for metallic materials in sliding contact [18]. The wear factor for microcomposite (specimen C1) was more than 500 times higher than for nanocomposite (specimen C2). The wt. % of Al_2O_3 particles was similar in micro- and nanocomposite (5 and 4.7 wt. %, respectively), but the size of particles was very different (≈ 750 nm and < 100 nm). It is well-known that the wear resistance increases with the decrease of the particle size for high-load, low-speed conditions (which was our case), whereas for low-load, high-speed conditions the effect is opposite [1]. Smaller particle size enabled better distribution of the nano-sized particles. Favourable distribution of nano-sized Al_2O_3 particles and its effect on slower grain growth (fine-grain structure, i.e. small grain size) reduced the deformation of matrix during sliding.

The micro-sized Al_2O_3 particles did not have the reinforcing role. On contrary, some of these particles were detached from the matrix and acts as a third body, increasing the specimen and counter-body wear. The others were protruded to the surface causing increase of the counter-body wear. For these reasons the wear of the counter-body in contact with microcomposite (specimen C1) was the highest. Detached micro-sized Al_2O_3 particles were mainly located in the worn material accumulated over the wear track (Fig. 13a). This accumulation of the worn material was not noticed at nanocomposite (specimen C2), Fig. 13b. In addition, wear of the counter-body in contact with nanocomposite was the lowest.

Table 6. The coefficient of friction average values of tested materials in the first phase (group III) [14]

Specimen designation	v = 6 mm/s	v = 8 mm/s	v = 10 mm/s
C0	0.43	0.48	0.46
C1	0.47	0.57	0.32
C2	0.13	0.14	0.13

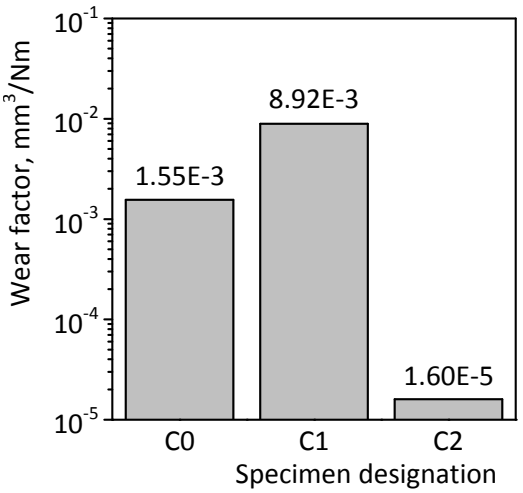

Fig. 12. Wear factors of the tested materials in the first phase (group III) [14]

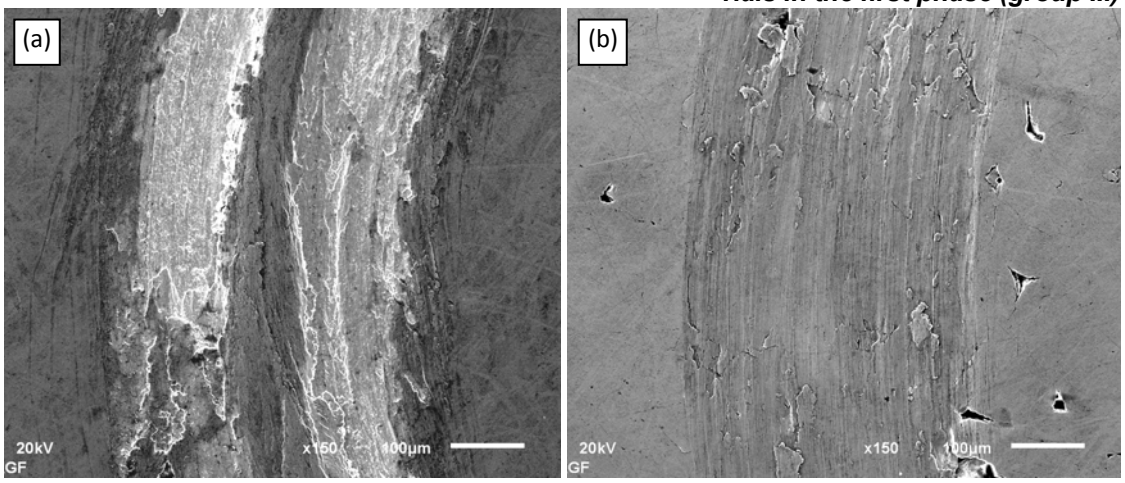

Fig. 13. SEM images of the samples worn surfaces at 8 mm/s: (a) specimen C1 (microcomposite) and (b) specimen C2 (nanocomposite); only part of the wear track is presented in both images

The tribological tests performed in the second phase (tests that investigated the influences of size of reinforcement (Al_2O_3) on the nanoscale) were just an initial one, and some more experiments is planned to completely understand composites tribological behaviour on nanoscale. In this tests only the Cu matrix is tested, since the area without Al_2O_3 particles was chose to test. The values of the coefficient of friction were similar in magnitude for the two composites (specimens C2 and C3) and showed high standard deviation. Nevertheless, the coefficient of friction for the microcomposite (specimen C2) is approximately 15 % higher. The wear rate, as measured by volume of the wear tracks, was found to be typically one order of magnitude higher for the microcomposite. This can be noticed on AFM images (Fig. 14), in which the wear tracks are clearly visible on the microcomposite sample and slightly visible on the nanocomposite sample.

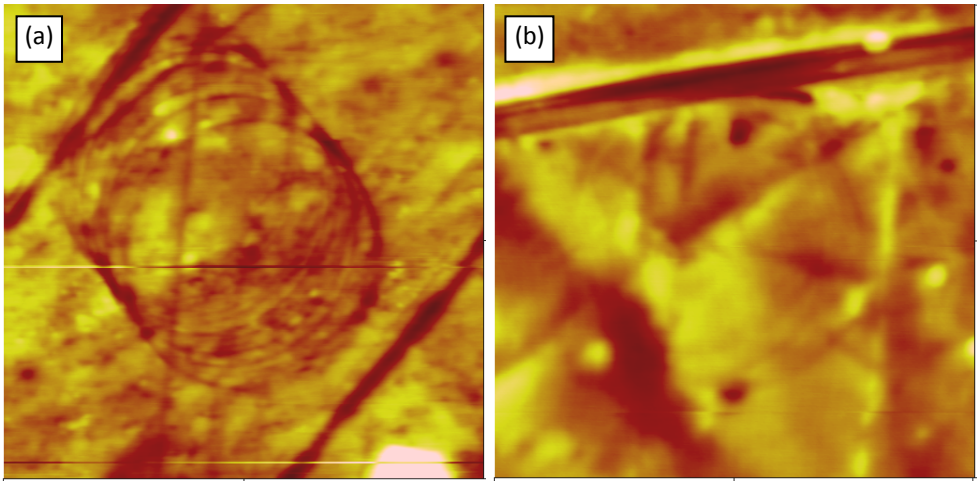

Fig. 14. AFM images (2 x 2 μm) of the samples worn surfaces: (a) specimen C1 (microcomposite) and (b) specimen C2 (nanocomposite); some shifted circular wear tracks are clearly visible on micro-composite and hardly on nanocomposite [7]

4. CONCLUSIONS

The constant development and growing application of various metal matrix composites (MMCs) is based on the fact that relatively small amount of the secondary phase (usually the reinforcing phase) can significantly improve material characteristics. The tribological properties are the most important properties that define possible application of some material in machines where parts are in contact and relative motions. Summarising the results presented in this paper it can be concluded that:

- wear of Al-Si based MMCs decreases with the increase of Al_2O_3 reinforcement amount and size;
- addition of SiC reinforcement reduces wear of Al-Si based composites more than Al_2O_3 reinforcement;
- presence of graphite in Al-Si based composites reduces the wear rate and coefficient of friction;
- replacement of copper with silicon in ZA-27 alloy, as well as, the increase of the silicon content have beneficial influence on the wear resistance;
- addition of optimal amount of strontium and/or Al_2O_3 nanoparticles to the ZnAl25Si alloy increase wear resistance;
- copper-based composites containing Al_2O_3 particles show high dependence on particle size, i.e. the nano-sized particles provide much better wear resistance than the micro-sized particles;
- modified AFM can be used for the tribological tests of small, localized areas;
- addition of the Al_2O_3 nanoparticles improves wear resistance of the Cu matrix itself.

ACKNOWLEDGMENTS

This work has been performed as a part of activities within the following projects: (a) Projects TR 34028 and TR 35021, supported by the Republic of Serbia, Ministry of Education, Science and Technological Development; (b) International Faculty Agreement of Cooperation between the Faculty of Mechanical Engineering at the University of Belgrade and the Faculty of Industrial Technology at the Technical University of Sofia; (c) CEEPUS III Network: CIIIBG0703; (d) COST Action MP1303; (e) FP7-REGPOT project 316087: AComIn (Advanced Computing for Innovation), funded by the FP7 Capacity Programme (Research Potential of Convergence Regions).

REFERENCES

1. VENCL, A., Tribology of the Al-Si alloy based MMCs and their application in automotive industry, in: Magagnin, L. (Ed.), Engineered Metal Matrix Composites: Forming Methods, Material Properties and Industrial Applications, Nova Science Publishers, New York, 2012, pp. 127-166.
2. BABIC, M., NINKOVIC, R., RAC, A., Sliding wear behavior of Zn-Al alloys in conditions of boundary lubrication, The Annals of University "Dunărea de Jos" of Galaţi, Fascicle VIII, Tribology, 2005, 60-64.
3. SAVASKAN, T., MURPHY, S., Mechanical properties and lubricated wear of Zn-25Al based alloys, Wear, 116 (2), 1987, 211-224.
4. VENCL, A., BOBIĆ, I., VUČETIĆ, F., BOBIĆ, B., RUŽIĆ, J., Structural, mechanical and tribological characterization of Zn25Al alloys with Si and Sr addition, Materials & Design, 64, 2014, 381-392.
5. MIRACLE, D.B., DONALDSON, S.L., Introduction to composites, in: ASM Handbook Volume 21, Composites, ASM International, Metals Park, 2001, pp. 3-17.
6. Glidop® Copper Dispersion Strengthened with Aluminum Oxide, SCM Metals Products, Research Triangle Park, 1994.

7. VENCL, A., MAZERAN, P.-E., NOËL, O., Friction and wear of Cu-based micro and nano composite at the macro and nanoscale, in: Proceedings of the International Conference on Understanding and Controlling Nano and Mesoscale Friction, 22-26.06.2015, Istanbul, Turkey, pp. 100.
8. VENCL, A., BOBIĆ, I., JOVANOVIĆ, M.T., BABIĆ, M., MITROVIĆ, S., Microstructural and tribological properties of A356 Al-Si alloy reinforced with Al_2O_3 particles, Tribology Letters, 32 (3), 2008, 159-170.
9. MIŠKOVIĆ, Z., BOBIĆ, I., TRIPKOVIĆ, S., RAC, A., VENCL, A., The structure and mechanical properties of an aluminium A356 alloy base composite with Al_2O_3 particle additions (MMC), Tribology in Industry, 28 (3-4), 2006, 23-27.
10. VENCL, A., BOBIĆ, I., Tribological properties of A356 Al-Si alloy base composite reinforced with Al_2O_3 particles (MMC), in: Proceedings of the 5th Congress of the Metallurgists of Macedonia, 17-20.09.2008, Ohrid, Macedonia, M8–07-E.
11. VENCL, A., BOBIC, I., AROSTEGUI, S., BOBIC, B., MARINKOVIĆ, A., BABIĆ, M., Structural, mechanical and tribological properties of A356 aluminium alloy reinforced with Al_2O_3, SiC and SiC + graphite particles, Journal of Alloys and Compounds, 506 (2), 2010, 631-639.
12. VENCL, A., BOBIC, I., STOJANOVIC, B., Tribological properties of A356 Al-Si alloy composites under dry sliding conditions, Industrial Lubrication and Tribology, 66 (1), 2014, 66-74.
13. EN 12844:1998 Zinc and zinc alloys – Castings – Specifications, 1998.
14. VENCL, A., RAJKOVIC, V., ZIVIC, F., MITROVIĆ, S., CVIJOVIĆ-ALAGIĆ, I., JOVANOVIC, M.T., The effect of processing techniques on microstructural and tribological properties of copper-based alloys, Applied Surface Science, 280, 2013, 646-654.
15. NASRALLAH, H., MAZERAN, P.-E., NOËL, O., Circular mode: A new scanning probe microscopy method for investigating surface properties at constant and continuous scanning velocities, Review of Scientific Instruments, 82 (11), 2011, 113703-1-113703-6.
16. VENCL, A., MMCs based on hypoeutectic Al-Si alloy: Tribological properties in dry sliding conditions, Tribological Journal BULTRIB, 2 (2), 2012, 17-22.
17. RAC, A., Basics of Tribology, Faculty of Mechanical Engineering, University of Belgrade, Belgrade, 1991 (in Serbian).
18. KATO, K., ADACHI, K., Wear mechanisms, in: BHUSHAN, B. (Ed.), Modern Tribology Handbook, CRC Press, Boca Raton, 2001, ch. 7.
19. VAN DRIESSCHE, M., Ferrography, Texaco Technology Ghent, Ghent, 2001.
20. YANG J.B., LIN C.B., WANG T.C., CHU H.Y., The tribological characteristics of A356.2Al alloy/$Gr_{(p)}$ composites, Wear, 257 (9-10), 2004, 941-952.
21. HAMROCK, B.J., SCHMID, S.R., JACOBSON, B.O., Fundamental of Fluid Film Lubrication, Marcel Dekker, New York, 2004.
22. RISDON, T.J., BARNHURST, R.J., MIHAICHUK, W.M., Comparative wear rate evaluation of zinc aluminum (ZA) and bronze alloys through block on ring testing and field application, SAE Technical Paper 860064, 1986.
23. JIAN, L., LAUFER, E.E., MASOUNAVE, J., Wear in Zn-Al-Si alloys, Wear, 165 (1), 1993, 51-56.
24. ZHOU, G., DING, H., ZHANG, Y., HUI, D., LIU, A., Fretting behavior of nano-Al_2O_3 reinforced copper-matrix composites prepared by coprecipitation, Metalurgija – Journal of Metallurgy MJoM, 15 (3), 2009, 169-179.
25. VENCL, A., RAJKOVIC, V., ZIVIC, F., Friction and wear properties of copper-based composites reinforced with micro- and nano-sized Al_2O_3 particles, in: Proceedings of the 8th International Conference on Tribology – BALKANTRIB '14, Sinaia, Romania, 30.10-01.11.2014, pp. 357-364.

CORRESPONDENCE

Aleksandar VENCL
University of Belgrade, Faculty of Mechanical Engineering
Kraljice Marije 16, 11120 Belgrade 35, Serbia
e-mail: avencl@mas.bg.ac.rs

Ilija BOBIĆ
Institute of Nuclear Sciences "Vinca", University of Belgrade
Mike Petrovića Alasa 12-14, 11001 Belgrade, Serbia
e-mail: ilijab@vinca.rs

Mara KANDEVA
Faculty of Industrial Engineering, Technical University – Sofia
Boulevard Kliment Ohridski 8, 1156 Sofia, Bulgaria
e-mail:; kandeva@tu-sofia.bg

Dimitar KARASTOYANOV
Institute for Information and Communication Technologies, Bulgarian Academy of Sciences
Acad. G. Bonchev St., Block 25A, 1113 Sofia, Bulgaria
e-mail: dimikara@abv.bg

Tribological Journal BULTRIB Vol. 5, 2015
Papers from the International Conference **BULTRIB '15**
September 11-13, 2015, Sozopol, Bulgaria
Society of Bulgarian Tribologists
FIT – Technical University of Sofia

OPTICAL - NANOSCOPIC METHODS TO COMPARE LAYER AND ADHESIVE FORCE OF OIL ADDITIVES ON THE RUBBED SURFACES

Hakan KALELİ[1], Doğuş ÖZKAN [2]

[1)] Prof. Dr., Yıldız Technical University, Faculty of Mechanical Engineering, Automotive Division 34349 Beşiktaş-Yıldız-İstanbul / TURKEY, kaleli@yildiz.edu.tr
[2)] Msc. Mechanical Eng, PhD. Student, Yıldız Technical University, Faculty of Mechanical Engineering, Energy Division 34349 Beşiktaş-Yıldız-İstanbul / TURKEY, dogus_ozkan@hotmail.com

Abstract

Aim of this study is to investigate the protective layers formed by lubricant additives on rubbed surfaces for a base-oil and fully formulated oil. Wear tracks were examined using optical microscopy, electron microscopy with X-Ray diffraction analysis and atomic force microscopy (AFM) techniques. Detected wear scars are higher on the pin and plate surfaces which lubricated with base oil than the lubricated with the commercial oil. Adhesive force measurements by AFM showed higher values in pin and plate surface rubbed with commercial oil than those with base oil. There is an increase of adhesion with the speed of friction for the pin and plate tested with commercial oil comparing to the base oil.

Key Words: *Additives and non-additives layer, adhesion force, viscoelasticity, AFM.*

CORRESPONDENCE

Prof.Dr. Hakan KALELİ
Yıldız Technical University,
Faculty of Mechanical Engineering,
Automotive Division,
34349 Beşiktaş-Yıldız-İstanbul / TURKEY,
Mobile: ++90 532 4768608
kaleli@yildiz.edu.tr

Tribological Journal BULTRIB Vol. 5, 2015
Papers from the International Conference **BULTRIB '15**
September 11-13, 2015, Sozopol, Bulgaria
Society of Bulgarian Tribologists
FIT – Technical University of Sofia

CFD MODELING OF ELASTOHYDRODYNAMIC LUBRICATION USING HIGH-PRESSURE RHEOLOGY MODELS

Achim FELDERMANN, M.Sc., Stephan NEUMANN, M.Eng., Prof. Dr.-Ing. Georg JACOBS

Abstract: *Recently, CFD simulations of elastohydrodynamic lubrication (EHL) have been developed to eliminate the traditional limitations of thin film flow. However, those models only employ the Dowson-Higginson equation of state (EOS) and the Roelands viscosity model, which are both not valid for high pressures. Hence, in this work, an empirical fluid model based on high-pressure viscosity measurements is implemented in a CFD model along with the more accurate Tait EOS. This model is then used to analyze the influence of fluid parameters on the film thickness in EHL line contacts.*

Key Words: *CFD, Navier-Stokes, High-Pressure Rheology, Elastohydrodynamic Lubrication*

1. INTRODUCTION

In the last decades, simulations of elastohydrodynamic lubrication (EHL) have been based on the well-known Reynolds equation. In order to derive this equation from the Navier-Stokes equations, inertia and gravity terms are neglected and the velocity gradients along the contact length are assumed to be small compared to the gradients across the lubrication film. Furthermore, pressure gradients across the fluid film are neglected and a constant pressure is assumed in this direction. As a result, the Reynolds equation is only valid for laminar thin film flows. [1]

By using a computational fluid dynamics (CFD) approach, the full Navier-Stokes equations can be solved and the previously mentioned limitations can be eliminated. As a result, the computational domain is no longer restricted to the Hertzian contact zone and both inlet and outlet regions as well as the flow fields within entire machine elements like roller bearings can be investigated. Furthermore, complex rheological models can be implemented very easily, because all fluid parameters are fully resolved within the lubricant.

In the last years, several researchers have already presented CFD simulations of EHL contacts [2, 3, 4]. In their models, the typical Dowson-Higginson equation of state (EOS) together with the commonly used Roelands viscosity model are employed. For high pressures, however, these rheology models are known to be inaccurate [5].

Therefore, in this work, an empirical viscosity model based on high-pressure viscosity measurements is implemented in a CFD model of an EHL line contact along with the more accurate Tait EOS. The results of this model are compared to classical results based on the Dowson-Higginson EOS and the Roelands viscosity model. The Tait parameters as well as the Roelands pressure viscosity coefficient are varied in typical ranges and the influence of these parameters on the film thickness profile is investigated. In the end, an equation is proposed to determine the Roelands pressure viscosity coefficient based on the empirical viscosity model.

2. MODEL

In order to simulate elastohydrodynamic lubrication by means of the full Navier-Stokes equations, the forward iterative solution procedure outlined in Fig. 1 is applied in this work.

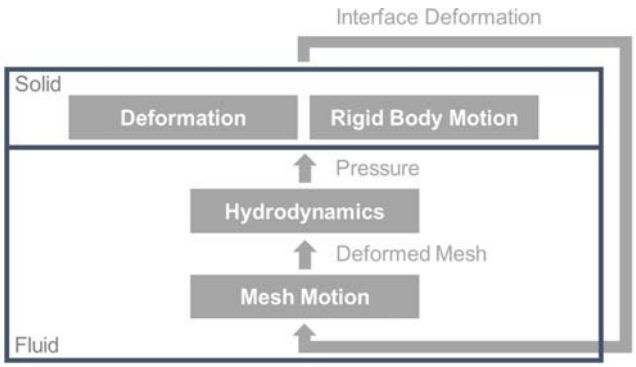

Fig. 1. Solution Prcedure for CFD Simulations of EHL Contacts

The starting point of this procedure is the pressure field of the last iteration. This pressure is used to determine the rigid body motion and the deformation of the solid. As a result, the interface motion of the fluid domain is obtained and used as a boundary condition for the mesh motion solver. This mesh motion solver deforms the entire fluid mesh according to the prescribed interface motion, so that a high mesh quality without significant distortion is maintained. The new mesh is then used in the hydrodynamic solver based on the Navier-Stokes equations and new pressure and velocity fields of the fluid domain are obtained. In the following, the governing equations behind each block are briefly explained.

2.1. Hydrodynamics

The employed hydrodynamics solver is based on the solver CAVITATINGFOAM contained in the freely available package FOAM-EXTEND [6]. This solver employs a homogenous equilibrium model for cavitation, which means that the two phases liquid and vapor are supposed to be in mechanical and thermodynamic equilibrium. Hence, only one set of continuity and momentum equations has to be solved for the liquid-vapor mixture. In this work, the conservation equations are implemented in an Arbitrary-Lagrangian-Eulerian (ALE) formulation [7]. In the original form of CAVITATINGFOAM, a constant compressibility and a constant viscosity for the liquid and vapor phases are assumed. However, for simulations of elastohydrodynamic lubrication problems more complex rheology models with pressure dependent compressibilities and viscosities have to be used. Therefore, in the modified solver, the compressibilities and viscosities are linearized within each iteration step. The overall solution procedure is based on the PISO algorithm [8].

2.2. Solid Deformation and Rigid Body Motion

The solid deformation in this work is based on the elastic half-space approximation of an infinite line contact, given by [1]

$$w(x) = -\frac{1-\upsilon^2}{\pi E_{red}} \int p(\hat{x}) \cdot \ln(|x-\hat{x}|) d\hat{x} \,, \tag{1}$$

with υ as the Poisson's ratio and E_{red} as the reduced elastic modulus of the two contacting solids. The overall deformation of the solid is then described relative to a non-deforming reference point. In order to find the steady state solution for a given external line contact load F_{ext}, the solid has to be moved as a rigid body. Therefore, a simple equation, describing the rigid body motion as a linear function of the relative difference between the external load and the pressure load is used. In order to stabilize the system at the beginning of the simulation, the maximum rigid body velocity is limited by a constant value. Hence, the motion of the fluid-solid interface for each time step is described by the change of the surface deformation relative to the previous time step and the rigid body motion Δh, that is:

$$\Delta s = (w - w_{ref}) - (w - w_{ref})^{t-1} + \Delta h \,. \tag{2}$$

2.3. Mesh Motion

Once the fluid-solid interface motion is obtained, the entire fluid mesh has to deform according to the prescribed motion Δs in order to maintain a good mesh quality without significant distortion. In this work, the resulting mesh deformation is determined by means of a Laplace equation with a constant and uniform diffusivity [9].

3. RHEOLOGY

In the last years, simulations of elastohydrodynamic lubrication problems have nearly exclusively been based on the Dowson-Higginson equation of state, given by

$$\rho_{Liquid} = \rho_0 \frac{2K_0 + (K_0'+1)p}{2K_0 + (K_0'-1)p}, \tag{3}$$

with the commonly used parameters $K_0 = 1.67\,GPa$, $K_0' = 6.67$ and the density ρ_0 at ambient pressure in combination with the Roelands viscosity model, given by

$$\eta_{Roelands} = \eta_0 \exp\left(\left(\ln(\eta_0) + 9.67\right)\left(\left(1 + \frac{p}{p_{ref}}\right)^{Z} - 1\right)\right), \tag{4}$$

where η_0 is the dynamic viscosity at ambient pressure, p_{ref} is the Roelands reference pressure and Z is the pressure viscosity index [5].

Those models, however, are known to be inaccurate for high pressures. The Dowson-Higginson EOS, for instance, has been obtained by curve fitting of only one mineral oil at one temperature for pressures up to about 350 MPa. Moreover, the validity of the Roelands equation is limited to maximum pressures of around 0.15 to 0.5 GPa. [5]

Therefore, more accurate high-pressure rheology models have to be used for simulations of elastohydrodynamic lubrication. In the following, two possible models will be presented.

3.1.1. Density

For the density, the Tait equation of state is applied in this work. This EOS is defined as

$$\rho_{Liquid} = \frac{\rho_0}{1 - \frac{1}{1+K_0^{'}} \ln\left(1 + \frac{p}{K_0}\left(1+K_0^{'}\right)\right)} = \frac{\rho_0}{1 - \frac{1}{1+K_0^{'}} \ln\left(1 + \frac{p}{K_\infty \exp(-\beta T)}\left(1+K_0^{'}\right)\right)}. \tag{5}$$

For simulations of elastohydrodynamic lubrication, a general set of parameters given by $K_0^{'} = 11$, $K_\infty = 9\,GPa$ and $\beta = 6.5e^{-3}\,1/K$ has been proposed by Bair [5]. By using these parameters, the density-pressure relationship, shown in Fig. 2, is obtained for the typical mineral oil FVA 2 at 40°C. For comparison, the results of the Dowson-Higginson EOS are also plotted along with an approximation of density measurements performed by Blume [10]. Clearly visible are the differences between the measured density values and the Dowson-Higginson EOS, while a very good agreement between the Tait EOS and the measurements can be observed.

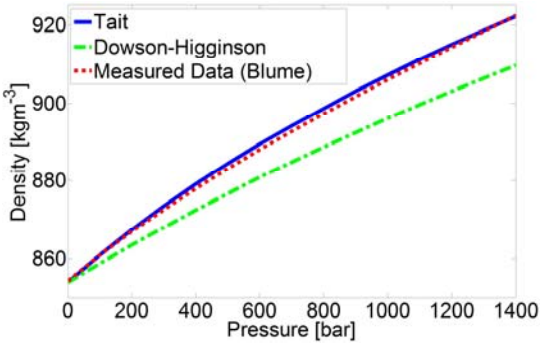

Fig. 2. Comparison of Density Models

3.1.2. Viscosity

For viscosity, an empirical equation based on high-pressure viscosity measurements is employed in this work. The high-pressure test rig, on which the measurements have been performed, is shown in the left part of Fig. 3. It consists of a low pressure chamber (1), a pressure amplifier (2) with a surface ratio of 1:140 and a high pressure piston (3). By lowering the piston, a maximum pressure of 10,000 bar can be build up in the high pressure chamber (5), which consists of a three-part shrinkage assembly (6). The viscometer (4) is placed in the pressurized volume and the pressure is transferred into the measuring sample by bellows.

The right part of Fig. 3 shows the viscometer in detail. The viscometer is based on the falling body viscometer developed by several researchers [10, 11, 12, 13]. In the beginning of a measurement, the falling body (5) is lifted by a lifting coil (4) and held in the upper position by a holding coil (1). As soon as the electromagnetic control system releases the falling body, a time measurement is started and the body begins to fall through the test sample. After a certain time, the falling body reaches the contacting system (8) at the bottom of the viscometer and the time measurement is stopped. Based on the overall falling time, the viscosity can then be determined. More information about the viscometer and the evaluation procedure can be found in [13].

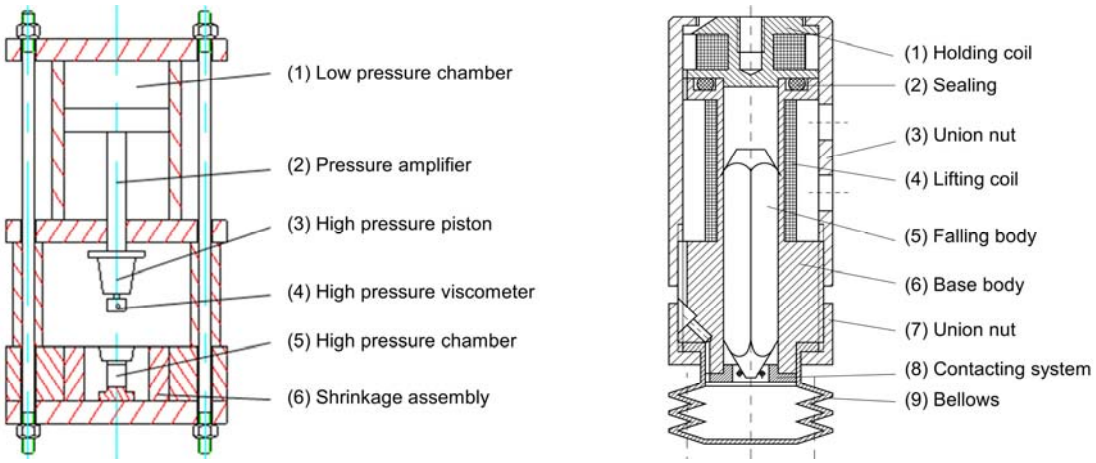

Fig. 3. High-Pressure Test Rig and Falling Body Viscometer

In previous research projects [12, 13, 14], many different mineral oils as well as synthetic oils have been measured and a very good correlation could be observed between the measurements and the modulus equation developed by Dicke [11]. This equation is a further development of the Barus equation [5] in combination with the Vogel equation [5] and reads

$$\eta_{Modulus} = K \exp\left(\frac{B}{\vartheta + C}\right) \exp\left(\frac{p}{a_1 + a_2\vartheta + (b_1 + b_2\vartheta)p}\right) = \eta_0(\vartheta) \exp\left(\alpha_p(p,\vartheta)p\right) \tag{6}$$

with the seven parameters K, B, C, a_1, a_2, b_1, b_2 and the temperature ϑ in degrees Celsius. For this viscosity model, parameter sets for a large number of lubricants are available in the database of the institute. In addition, the Eyring model is applied in this work in order to take non-Newtonian behavior of the liquid into account [5]. The necessary parameters for the Eyring model have been determined for many lubricants based on ball-disc tribometer tests [14].

4. CASE STUDY

After having described the modeling approach, the model is applied to an infinite elastohydrodynamic line contact with a reduced cylinder radius of $R = 10\,mm$. The simulation parameters of the present study are listed in Table 1. The fluid properties are that of a FVA 2 mineral oil at a temperature of 40 °C. The computational domain and the numerical schemes are identical to previous simulations [3, 15].

Table 1. Simulation Parameters

Liquid density	ρ_0	854 kg/m³	Parameter of modulus eq.	a_2	5.39 bar/°C
Liquid viscosity	η_0	0.026 Pas	Parameter of modulus eq.	b_1	4.019e^{-2}
Eyring stress	τ_0	4 MPa	Parameter of modulus eq.	b_2	-1.13e^{-4} 1/°C
Vapor compressibility	ψ_{Vapor}	9.6e^{-5} m²/s²	Sliding wall velocity	u	5 m/s
Vapor viscosity	η_{Vapor}	8.97e^{-6} Pas	Angular velocity cylinder	ω	0 rpm
Saturation pressure	p_{Sat}	5000 Pa	Magnitude of external force	F_{ext}	3e^{5} N/m
Roelands pressure	p_{ref}	1.98e^{8} Pa	Reduced elastic modulus	E_{red}	1e^{11} N/m
Parameter of modulus eq.	a_1	243.1 bar	Poisson‘s ratio	υ	0.3

4.1. Variation of the Density Model

At first, the pressure and film thickness profiles for the Dowson-Higginson EOS and the Tait EOS are compared. In these simulations, the modulus equation has been applied in combination with the Eyring model. The results are shown in the left part of Fig. 4.

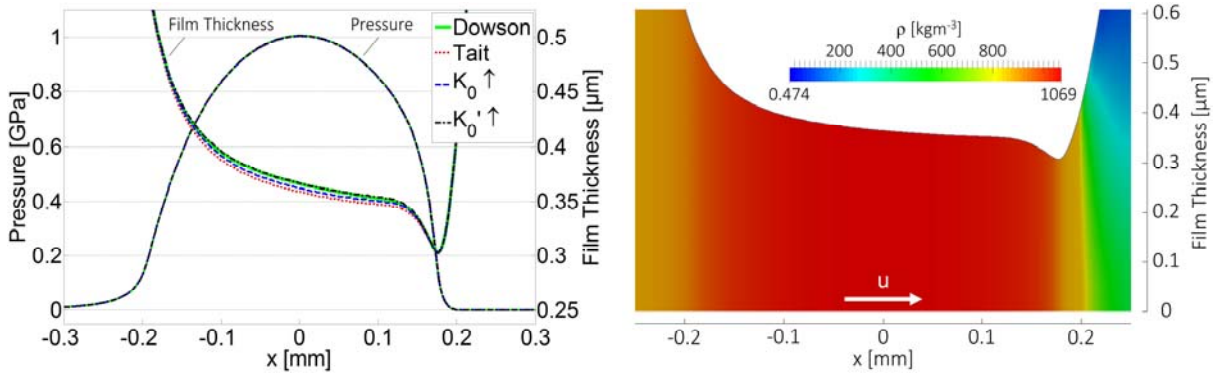

Fig. 4. Comparison of Density Models and Density Distribution

As illustrated, the pressure profile is hardly influenced by the two density models. For the film thickness in the central region of the contact, however, small differences of around 2 % between the two equations of state can be observed. Nevertheless, the changes in the film thickness profiles are negligible and the choice of density model does not influence the minimum film thickness significantly. Even a variation of the two parameters K_0' and K_0 by +20 %, marked by $K_0'\uparrow$ and $K_0\uparrow$, does not influence the film thickness more than 2 %. Hence, the proposed parameter set given above can be regarded as accurate enough for the case investigated.

In the right part of Fig. 4, the density distribution inside the contact region is shown for the Tait EOS. It can be seen, that the density in the high-pressure region is approximately constant across the fluid film. In the outlet region of the contact (right side of the picture), the density decreases due to cavitation and the density varies across the fluid film. This area, however, does not significantly influence the contact region.

4.2. Variation of the Viscosity Model

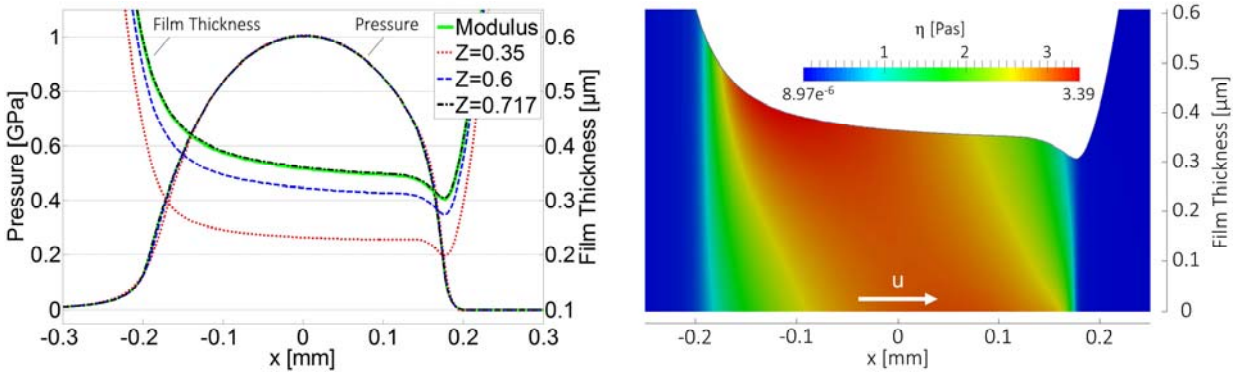

Fig. 5. Comparison of Viscosity Models and Viscosity Distribution

In the left part of Fig. 5, the results of the modulus equation in combination with the Tait EOS are compared to the Roelands viscosity model with three different pressure viscosity coefficients. Those coefficients are usually unknown and an estimation has to be made. Unfortunately, the influence of this parameter on the film thickness profiles is also very significant and no general parameter value can be given. However, assuming identical slopes of the empirical and the Roelands viscosity model at ambient pressure ($p_0 \approx 0\,Pa$), that is

$$\frac{1}{\eta_{Modulus}}\left(\frac{\partial \eta_{Modulus}}{\partial p}\right)_{p_0} = \frac{1}{\eta_{Roelands}}\left(\frac{\partial \eta_{Roelands}}{\partial p}\right)_{p_0} \Rightarrow Z = \frac{p_{ref}}{\ln(\eta_0)+9.67}\frac{1}{a_1+a_2\vartheta}, \tag{7}$$

a good agreement between the pressure and film thickness profiles of the two models can be observed ($Z = 0.717$), although the absolute viscosity values of the two models do not agree and a difference of approximately 30 % is still present in the high-pressure region. Hence, the absolute viscosity values within the pressurized region seem to be less important than the pressure-viscosity gradients at the inlet of the contact. As a result, the large number of parameter sets available for many different lubricants can be used to estimate the Roelands pressure viscosity coefficient for high-pressure simulations of EHL contacts.

In the right part of Fig. 5, the viscosity distribution for the Tait EOS in combination with the modulus

equation is shown. Strong viscosity variations across the lubrication film can be observed, which result from varying shear rates within the contact. Hence, CFD simulations of EHL become necessary, because these gradients could not be captured completely by the Reynolds equation.

5. CONCLUSION

In this contribution, an empirical viscosity model based on high-pressure viscosity measurements has been implemented into a CFD simulation of an infinite elastohydrodynamic line contact along with the more accurate Tait EOS. A comparison between the Dowson-Higginson EOS and the Tait EOS has been made and only small changes in the film thickness profiles of around 2 % could be observed, even for large parameter variations of 20 %. Moreover, the minimum film thickness seems to be unaffected by the choice of the density model.

For viscosity, however, large differences could be observed between the Roelands and the empirical viscosity model depending on the Roelands pressure viscosity coefficient. In general, this parameter is unknown and it has been shown, that the usual assumption of identical slopes of the two viscosity models at ambient pressure can produce a good estimation for the resulting pressure and film thickness profiles, even though the absolute viscosity values in the high-pressure region do not agree between the two models.

A closer look into the contact revealed, that the density is approximately constant across the lubrication film, while the viscosity varies significantly in this direction even for isothermal conditions. This variation results from varying shear rates inside the lubrication film, so that, in order to capture these gradients completely, the full Navier-Stokes equations instead of the Reynolds equation have to be solved.

ACKNOWLEDGMENTS

This research was funded by the Excellence Initiative of the German federal and state governments.

REFERENCES

26. BARTEL, D., Simulation von Tribosystemen. Vieweg+Teubner Verlag 2010.
27. ALMQVIST, T.; ALMQVIST, A.; LARSSON R., A comparison between computational fluid dynamics and Reynolds approaches for simulating transient EHL line contacts. Tribology International, Vol. 37, 2004, 61-69.
28. HARTINGER M., DUMONT, M.-L., IOANNIDES, S., GOSMAN, D., SPIKES, H., CFD Modeling of a Thermal and Shear-Thinning Elastohydrodynamic Line Contact, Journal of Tribology, Vol. 130, 2008, 041503-1-041503-16.
29. HAJISHAFIEE, A, DINI, D., KADIRIC, A., IOANNIDES, S., A fully coupled finite volume solver for elastohydrodynamic lubrication problems with particular application to rolling element bearings. World Tribology Congress, Torino, 2013.
30. BAIR S., High-Pressure Rheology for Quantitative Elastohydrodynamics, Elsevier, 2007.
31. OPENFOAM USER GUIDE, Version 2.4.0., online: http://cfd.direct/openfoam/user-guide/
32. DONEA, J., HUERTA, A., PONTHOT, J.-P., RODRÍGUEZ-FERRAN, A., Arbitrary Lagrangian–Eulerian Methods, Encyclopedia of Computational Mechanics, 2004.
33. ISSA, R. I., Solution of the Implicitly Discretized Fluid Flow Equations by Operator-Splitting. Journal of Computational Physics, Vol. 62, 1985, 40-65.
34. JASAK, H.; TUKOVIC, Z., Automatic mesh motion for the unstructured finite volume method. Transactions of FAMENA, Vol. 30 (2), 2006, 1-20.
35. BLUME, J., Druck- und Temperatureinfluß auf Viskosität und Kompressibilität von flüssigen Schmierstoffen, Dissertation, RWTH Aachen University, 1987.
36. DICKE, H., WELSCH, G., PEEKEN, H., Viscosity-Pressure-Temperature Characteristics of Different Types of Lubricants and their Possible Influence on Fatigue, 3rd World Congress on Gearing and Power Transmission, Paris, 1992, 527-536.
37. GOLD, P. W., SCHMIDT, A., DICKE, H., LOOS, J., ASSMANN, C., Viscosity–pressure–temperature behaviour of mineral and synthetic oils. Journal of Synthetic Lubrication, Vol. 18, 2001, 51–79.
38. GOLD, P. W., WALBECK, T., Einfluss von Grundölart, Additivierung und Gebrauchszustand auf Viskositätsverhalten und Schmierfilmbildung, Final Report FVA 400, Vol. 743, FVA, 2004.
39. JACOBS, G., HENTSCHKE, C., Untersuchung des Schmierfilmaufbaus und der Reibung bei dünnen Schmierfilmen mittels Interferometrie und FE8-Wälzlagerversuchen, Final Report FVA 580, Vol. 1061, FVA, 2013.
40. FELDERMANN, A., NEUMANN, S., JACOBS, G., CFD Modeling of Elastohydrodynamic Lubrication Using Reduced FE-Models, European Conference on Tribology, Lugano, 2015.

CORRESPONDENCE

Achim FELDERMANN, M.Sc.
Institute for Machine Elements and Machine Design, RWTH Aachen University
Schinkelstraße 10, DE-52062 Aachen
feldermann@ime.rwth-aachen.de

Tribological Journal BULTRIB Vol. 5, 2015
Papers from the International Conference **BULTRIB '15**
September 11-13, 2015, Sozopol, Bulgaria
Society of Bulgarian Tribologists
FIT – Technical University of Sofia

CONTINUOUS, ONLINE DETECTION AND CONTROL OF FRICTION LOSS AND WEAR: INNOVATIVE APPROACH WITH THE OIL CONDITION MONITORING SYSTEM WEARSENS®

Dr.-Ing. Manfred MAUNTZ, cmc Instruments GmbH
Prof. Dr.-Ing. Ulrich KUIPERS, South Westphalia University of Applied Sciences
Dr. rer. nat. Jörn PEUSER, cmc Instruments GmbH

Abstract: *A web-based online oil diagnosis system for the early identification of critical operating conditions for premature failures of rolling bearings in industrial and particularly wind energy gearboxes by white etching cracks is presented. The innovative approach utilizes sensor detection of chemical aging of the lubricant and its additives due to critical operation conditions. The online diagnostics system measures components of the specific complex impedance of oils.*

Key Words: *Oil additive degradation, online oil condition monitoring, hydraulic systems, white etching cracks, residual stress*

1. INTRODUCTION

With the WearSens® unit, components of the complex impedances X of oils, in particular the specific electrical conductivity κ and the relative permittivity ε_r as well as the oil temperature T are measured [1-3]. The values ε_r and κ are determined independently of each other. Figure 1 shows the sensor with a 1" connector block ready for robust industrial installation.

Fig. 1. Sensor system with 1" connector block

Oils are electrical non-conductors. The electrical residual conductivity of pure oils lies in the range below 1 pS/m. The conductivity of various materials is illustrated in figure 2. The conductivity range of the presented sensor system is marked in green. It starts below the conductivity of the distilled water. For comparison, the electrical conductivity of the electrical non-conductor distilled water is larger by six orders of magnitude.

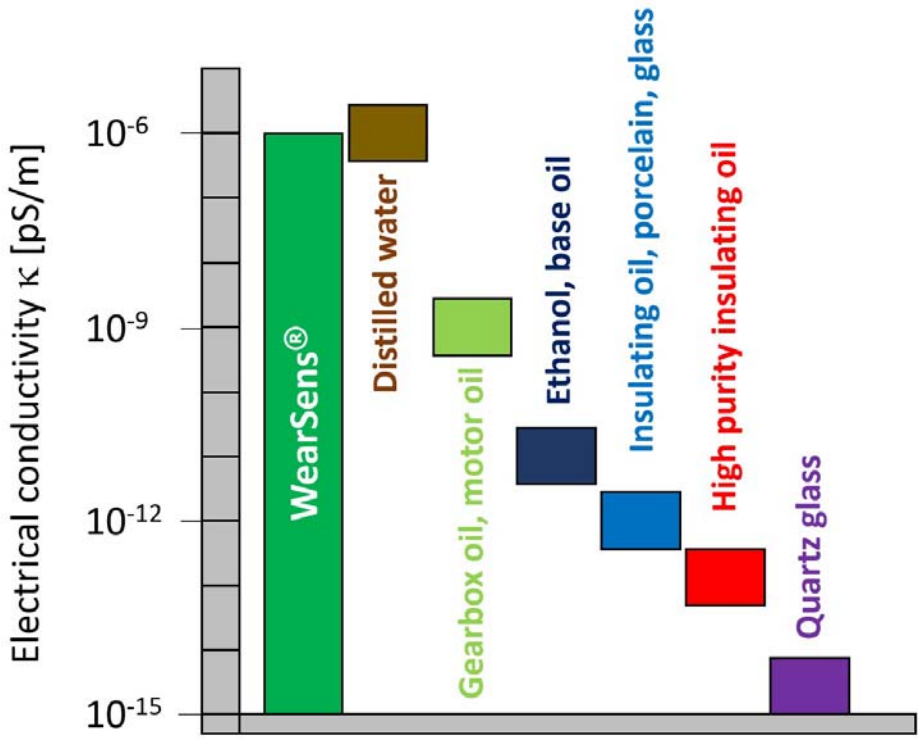

Fig. 2. Conductivities of liquids and solids, measurement range of the presented sensor system is marked in green

Abrasive (metallic) wear, ions, broken oil molecules, acids, oil soaps, etc., cause an increase of the oil conductivity κ. It rises with increasing ion concentration and mobility. The electrical conductivity of almost all impurities is high compared with the extremely low corresponding property of original pure oils. A direct connection between the degree of contamination of oils and the electrical conductivity is found. An increase of the electrical conductivity of the oil in operation can thus be interpreted as increasing wear or contamination of the lubricant. The aging of the oil is also evident in the degradation of additives. The used additives reveal high conductivity compared with the oil.

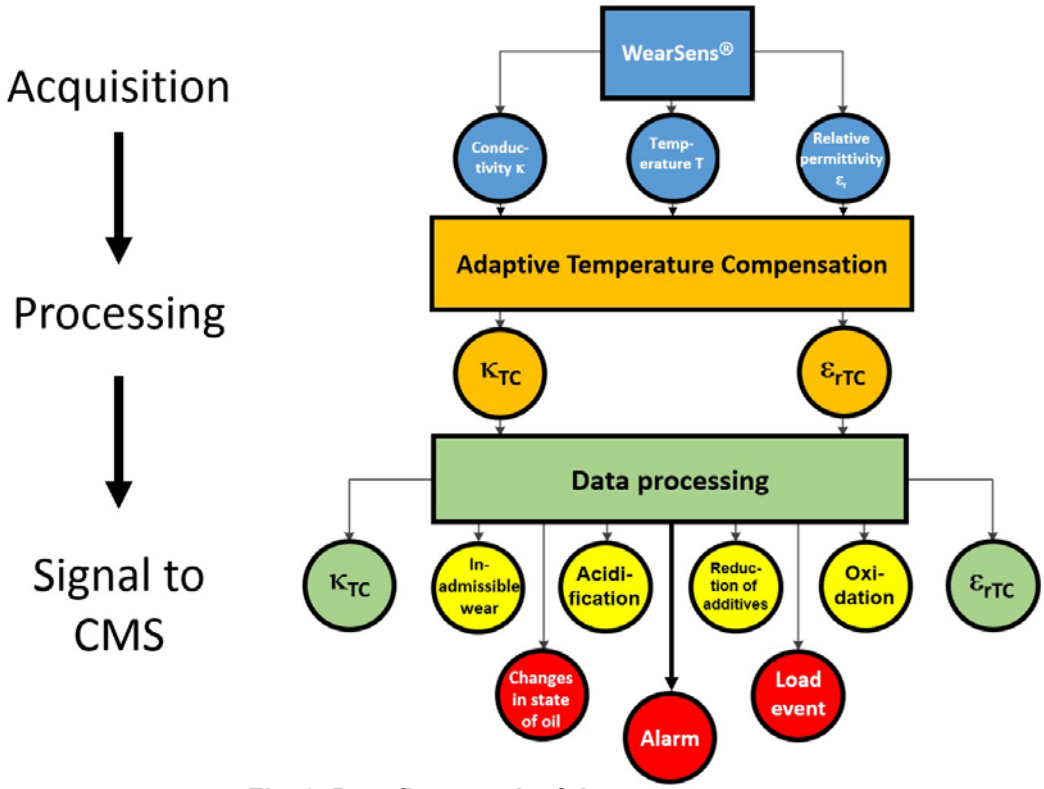

Fig. 3. Data flow graph of the sensor system

In figure 3 the data acquisition and data processing in the sensor system is sketched with the field data acquisition, data processing and signal output. The rectangular boxes represent autonomous functional units with defined responsibilities. They are characterized by inputs and feedback-free outputs. The individual instances communicate with each other via the data spaces shown as circles. Data flow is characterized by means of arrows between data spaces and instances. The instance network allows a static interpretation of the catchment area of the individual functional units.

2. TEMPERATURE COMPENSATION AND MEASUREMENT ACCURACY

Ion mobility and thus, electrical conductivity κ are dependent on the internal friction of the oil and therefore, also on its temperature. The conductivity κ of the oil increases with temperature. The type of contamination and its temperature dependence cannot be assumed to be known. To improve the comparability of measurements, a self-learning adaptive temperature compensation algorithm is necessary. A change of the oil quality can then be assessed by the temperature compensated conductivity value, even though the specific contamination is not determinable. The relative permittivity is measured with the same basic sensor arrangement as used for the determination of the electrical conductivity. Figure 4 shows the effect of temperature compensation.

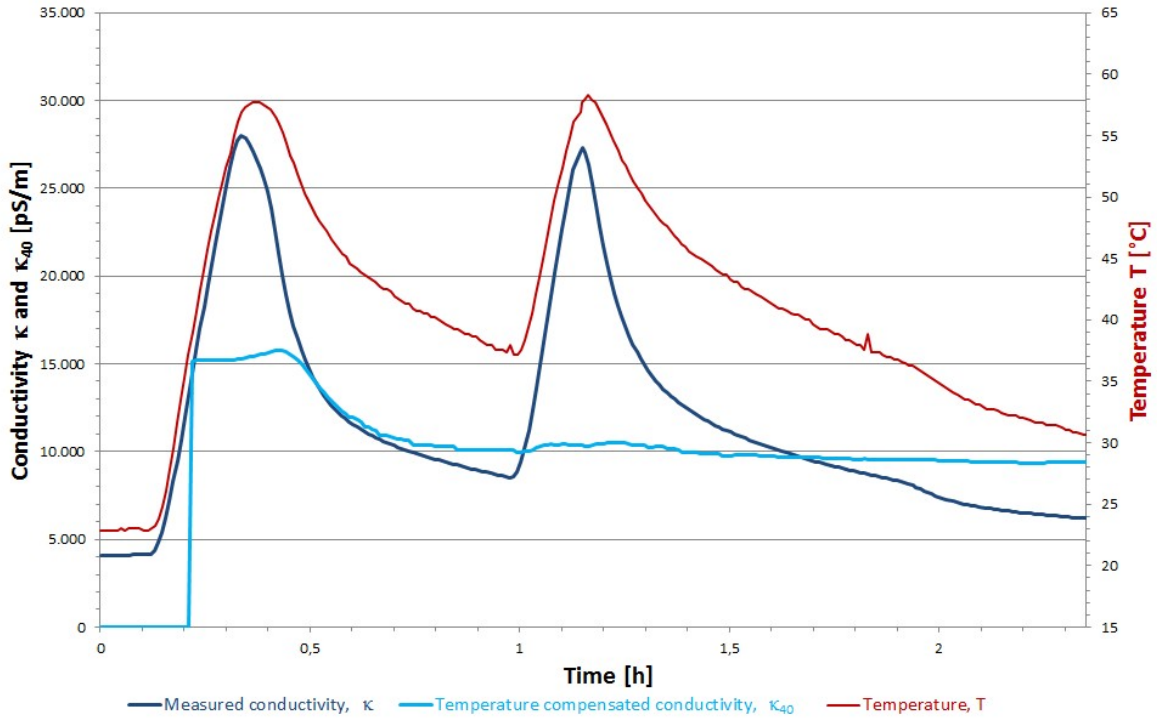

Fig. 4. Effect of the temperature compensation algorithm

While the conductivity κ changes significantly with temperature, the temperature compensated conductivity κ_{40} stays nearly constant.

3. APPROACH FOR CONDITION MONITORING OF ADDITIVATED LUBRICATING OILS

The hypothesis is that the consumption of the additives is reflected in a reduction of the electrical conductivity and permittivity of the oil. The gradient, i.e. the time derivative, of the conductivity or the dielectric constant progression respectively represents a measure of the additive degradation and consumption. The full additive degradation is indicated by the slope of zero (bathtub curve). Then the measurement signal increases further with increasing pollution, water entry, etc.

Fig. 5 schematically shows the temperature compensated time curve of the permittivity of additivated oil continuously contaminated by the addition of wear debris, water or oil acids from chemical aging:

Area A:

Polar additives are combining with impurities, particles, acid and soap products, which reduces the additive content in the lubrication oil and result in a decrease of the relative permittivity ε_{r40}.

Point B:

Full additive degradation.

Area C:

Due to the lack of additive components new generated polar elements can't be chemically neutralized anymore, which leads to an increase of the relative permittivity ε_{r40}.

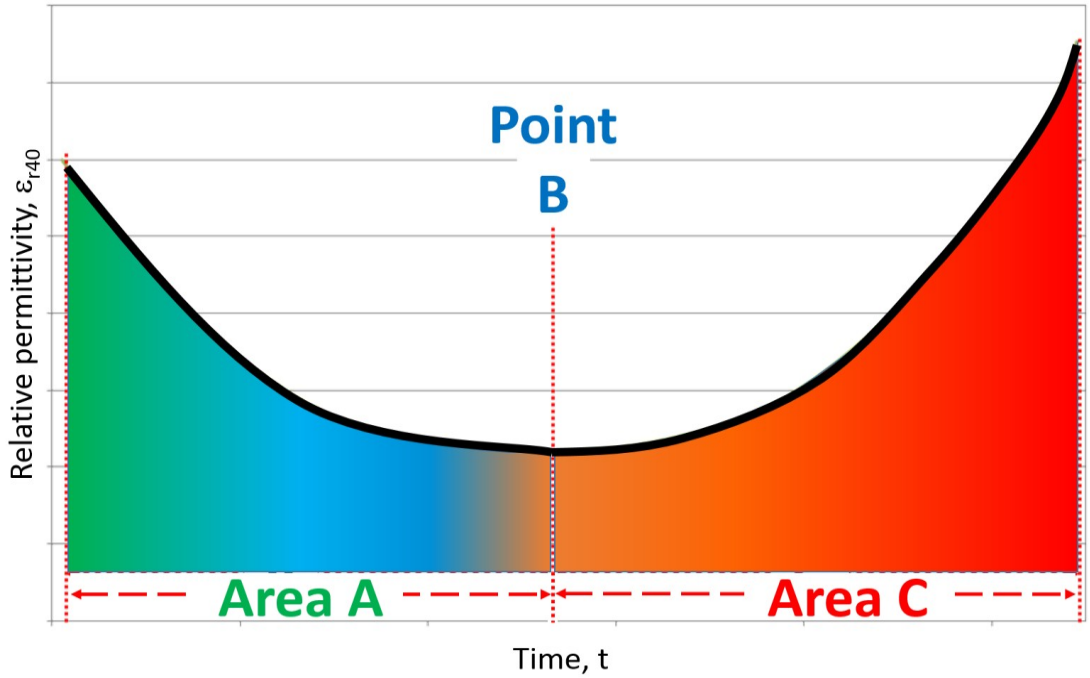

Fig. 5. Model of the temperature compensated permittivity

4. APPLICATION: HYDRAULIC ACTUATOR

This section demonstrates the oil sensor application for the condition monitoring of a hydraulic actuator used for wind turbine testing. The basic setup of this blade fatigue test is depicted in figure 6. During the Ground Resonance Excitation (GREX) the hydraulic actuator applies automated cyclic loading to the blades at its resonant frequency [4].

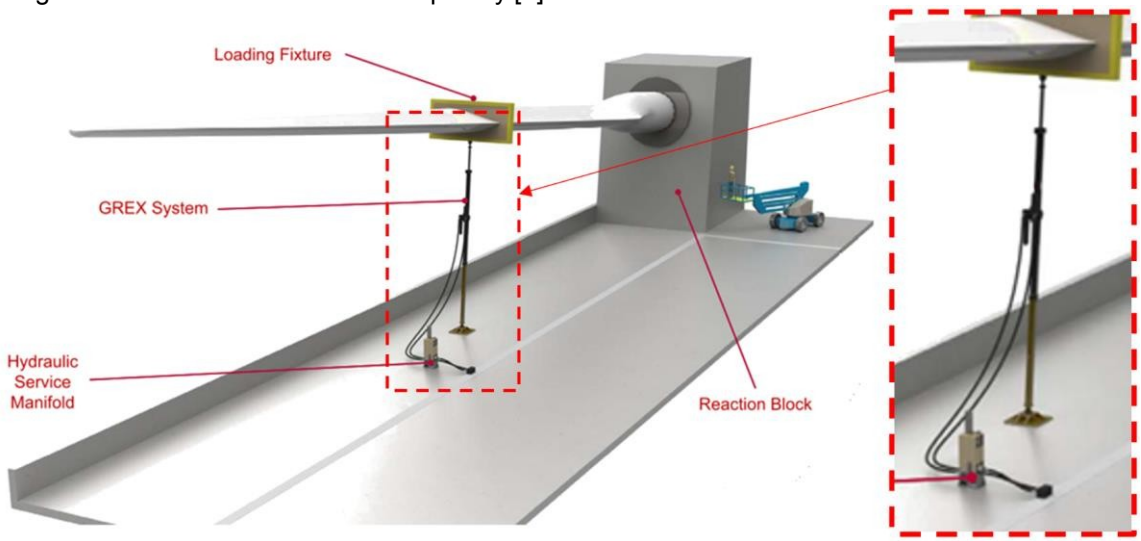

Fig. 6. Rotor blade test stand with GREX [4].

The schematics of the hydraulic oil flow is shown in figure 7. The hydraulic oil tank contains about 1900 Litre; a flow rate of 600 Litre/minute is set between the tank and the hydraulic service manifold (HMS). The HMS regulates the cyclic hydraulic pressure on the actuator, to excite the rotor blade at the resonance frequency. A lower flow rate, 100 ml/minute, is used in the oil cycle with the WearSens sensor. By these flow settings it is assured that there is sufficient oil exchange in each oil cycle via the HPU tank.

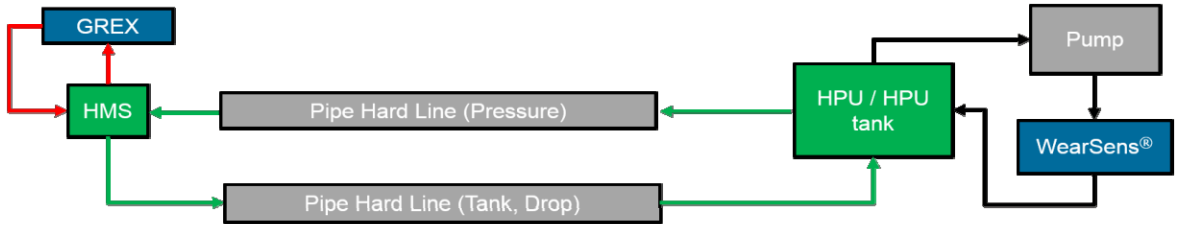

Fig. 7. Scheme of the hydraulic oil cycles at the GREX installation

The presented data in figure 8 and 9 was recorded during a long term rotor blade fatigue test run; the oil sensor system was installed to continuously monitor the hydraulic oil quality, for preventing the actuator from damage.

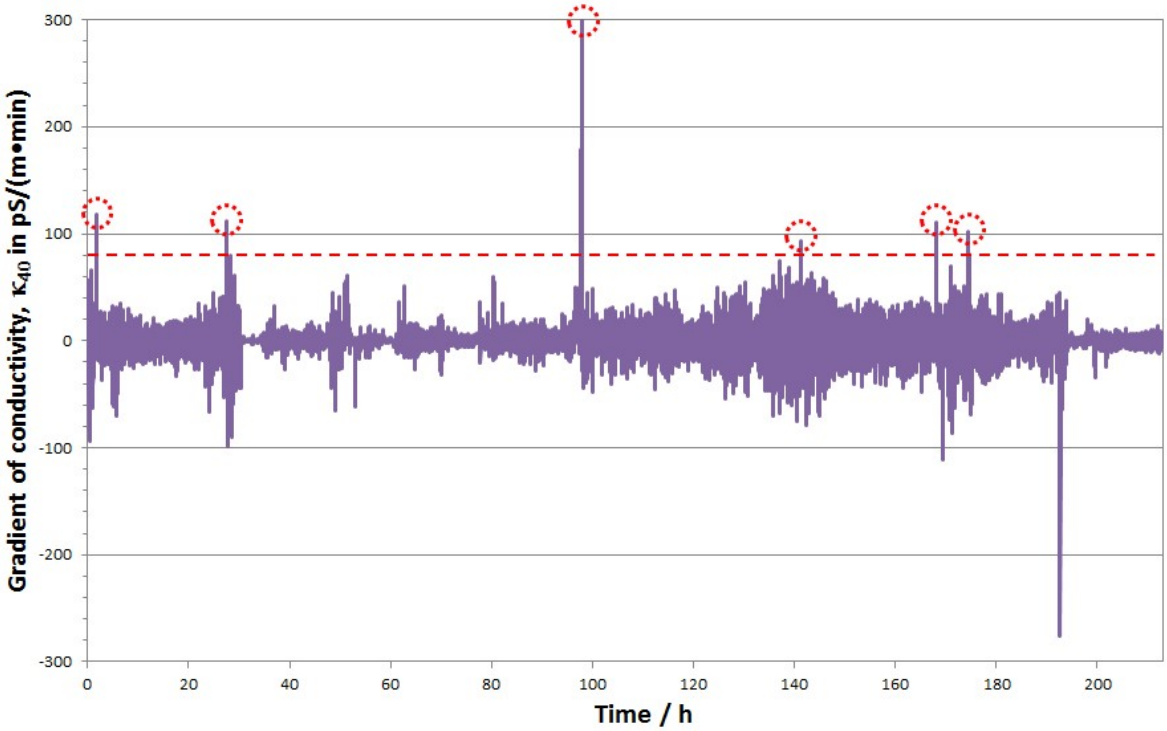

Fig. 8. Gradient of the temperature compensated conductivity over time

The data in figure 8 shows the gradient of the temperature compensated electrical conductivity κ_{40} over time: a continuous increase during normal operation of the hydraulic actuator system has a lower gradient than critical operation conditions, which are visible in sharp peaks, highlighted with red circles. A threshold analysis can be used to minimize the events of critical operation conditions to enable long term stable operation.

The decreasing trend line of the relative permittivity in figure 9 signals the continuous consumption of polar additives in the hydraulic oil due to the actual load over the complete measurement run. Limit settings in the relative permittivity ε_{r40} and the corresponding gradient of ε_{r40} can be used to perform condition based maintenance for adding new additives packages to enable a stable hydraulic oil quality.

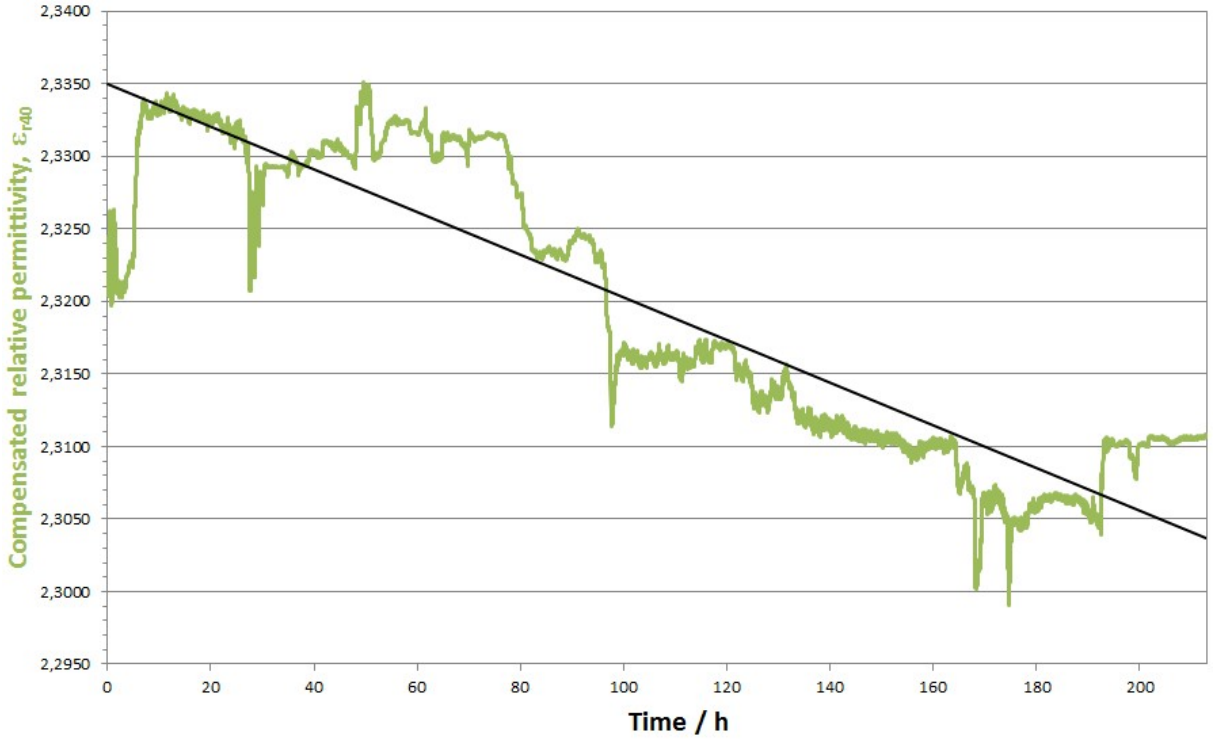

Fig. 9. Temperature compensated relative permittivity over time

5. WEB-BASED DECENTRALIZED LUBRICANT QUALITY MONITORING SYSTEM

The integration into a suitable communication structure and the realization of an online monitoring system offers an interesting practice-oriented utilization of the oil sensor system. This is briefly discussed below.

Preferred areas of application of the sensor system are energy production and automated technical plants that are operated locally, like e.g. wind turbines, generators, hydraulic systems or gearboxes. Plant employers are interested in continuous automated in vivo examination of the oil quality rather than interrupting the operation for regular sampling. Online oil status monitoring significantly improves the economic and ecological efficiency by increasing operating safety, reducing down times or adjusting oil change intervals to actual requirements. Once the oil condition monitoring sensors are installed on the plants, the measuring data can be displayed and evaluated elsewhere. A flexible decentralized monitoring system also enables the analysis of measuring signals and monitoring of the plants by external providers. A user-orientated service ensuring the quantitative evaluation of changes in the oil-machine system, including the recommendation of resulting preventive maintenance measures, relieves plant operators, increases reliability and saves costs.

In a web-based decentralized online oil condition monitoring system, the sensor signals are preferably transferred through the Internet to a database server and recorded on an HTML page as user interface [5].

Following authentication, a simple web browser permits access via the wired or wireless LAN. In case of alarm signals, an immediate automated generation of warning messages, for instance by e-mail or SMS, is possible from any computer with Internet connection. Fig. 10 shows the WearSens® sensor with the triple plate design [6, 7].

Fig. 10. Detail of the triple plate design, WearSens®

6. SUMMARY

The online diagnostics system measures components of the specific complex impedance of oils. For instance, metal abrasion due to bearing wear at the tribological contact, broken oil molecules, acids or oil soap cause an increase in electrical conductivity that directly correlates with the degree of pollution of the oil. The dielectrical properties of the oils are especially determined by the water content, which, in the case of products that are not enriched with additives, becomes accessible by an additional accurate measurement of the dielectric constant. In the case of oils enriched with additives, statements on the degradation of additives can also be deduced from recorded changes in the dielectric constant.

Indication of damage and wear is measured as an integral factor of, e.g., the degree of pollution, oil aging and acidification, water content and the decomposition state of additives or abrasion of the bearings. It provides informative data on lubricant aging and material loading as well as the wear of the bearings and gears for the online operative monitoring of components of machines. Additional loading, for instance, by vibration induced mixed friction in rolling-sliding contact (rolling bearings, gears, cams, etc.) causes faster oil aging. Verified in roller bearing rig tests, the oil suffers from incipient resinification and significant acidification, as proven by infrared spectroscopy of used lubricant.

For an efficient machine utilization and targeted damage prevention, the new WearSens® online condition monitoring system offers the prospect to carry out timely preventative maintenance on demand rather than in rigid inspection intervals. The determination of impurities or reduction in the quality of the lubricants and the quasi continuous evaluation of the bearing and gear wear and oil aging meet the holistic approach of a real-time monitoring of a change in the condition of the oil- machine system.

The measuring signals can be transmitted to a web-based condition monitoring system via LAN, WLAN or serial interfaces of the sensor system. The monitoring of the tribological wear mechanisms during proper operation below the tolerance limits of the components then allows preventive, condition-oriented maintenance to be carried out, if necessary, long before regular overhauling, thus reducing outages caused by wear while simultaneously increasing the overall lifetime of the oil- machine system.

The oil sensor system was installed into an oil circuit of a hydraulic actuator system for ground resonance excitation performing a long term analysis of the hydraulic oil quality. The functionality of the introduced electric online condition monitoring sensor system is tested successfully. The evaluation of the experiment is presented.

ACKNOWLEDGMENTS

The authors wish to thank the technical assistance of Luis Figuerido from CENER, Spain.

REFERENCES

1. GEGNER, J., KUIPERS, U. AND MAUNTZ, M., Ölsensorsystem zur Echtzeit-Zustandsüberwachung von technischen Anlagen und Maschinen, Technisches Messen 77, 2010, pp. 283-292

2. KUIPERS, U., MAUNTZ, M., Ölsensorsystem – Sensorsystem zur Messung von Komponenten der komplexen Impedanz elektrisch gering leitender und nichtleitender Fluide, dessen Realisierung und Anwendung, Patentanmeldung Nr. 10 2008 047 366.9, Anmelder: cmc Instruments GmbH, Deutsches Patentamt, München, Anmeldetag: 15. 9. 2008

3. KUIPERS, U., MAUNTZ, M., Verfahren, Schaltungsanordnung, Sensor zur Messung physikalischer Größen in Fluiden sowie deren Verwendung, Europäische Patentanmeldung Nr. EP 09000244, Europäisches Patentamt, München, 9. 1. 2009

4. MTS, Wind Turbine Testing solutions, Minnesota, 2012

5. GEGNER, J., KUIPERS U. AND MAUNTZ, M., New Electric Online Oil Condition Monitoring Sensor – an Innovation in Early Failure Detection of Industrial Gears, The 4th International Multi-Conference on Engineering and Technological Innovation July 19th – July 22nd, 2011, Orlando, Florida, USA 2011, Proceedings Volume I, International Institute of Informatics and Systemics, Winter Garten, FL, USA, 2011, pp. 238-242

6. GEGNER, J., KUIPERS U. AND MAUNTZ, M., High-precision online sensor condition monitoring of industrial oils in service for the early detection of contamination and chemical aging, Sensor + Test Conferences 7.-9.6.2011, Nürnberg, AMA Service GmbH, Wunstorf, 2011, pp. 702-709

7. GEGNER, J., KLINGAUF, S., KUIPERS, U., MAUNTZ, M., Continuous Wear Measurement in Tribological Systems to Control Operational Wear Damage with a new Online Oil Sensor System, TAE Technische Akademie Esslingen, 19th International Colloquium Tribology, Esslingen, January 21-23, 2014, 23.01.2014

8. MAUNTZ, M., KUIPERS, U., PEUSER, J.: Continuous, online detection of critical operation conditions and wear damage with a new oil condition monitoring system, WearSens®, 14th International Conference on Tribology – SERIATRIB '15 Proceedings, Belgrad, Serbian Tribology Society Kragujevac, University of Belgrade, Faculty of Mechanical Engineering, Belgrade, 13-15 Mai 2015, ISBN: 978-86-7083-857-4, S. 283-288

CORRESPONDENCE

Dr.-Ing. Manfred MAUNTZ
CEO, cmc Instruments GmbH, Hauptstr. 388, 65760 Eschborn, Germany e-mail: mrm@cmc-instruments.de

Tribological Journal BULTRIB Vol. 5, 2015
Papers from the International Conference **BULTRIB '15**
September 11-13, 2015, Sozopol, Bulgaria
Society of Bulgarian Tribologists
FIT – Technical University of Sofia

FRICTION AND WEAR PROCESSES AND PRESSURE DISTRIBUTION IN HELICAL COMPRESSION SPRINGS DEPENDING ON THE SPRING GEOMETRY

Vahan GEVORGYAN; Ulf KLETZIN

Abstract: *Service life and reliability of machines, devices and plants is among other things determined by a secure functioning of the spring components. Tribological loads to helical compression springs lead to wear and can cause malfunction of the components and therefore of the entire unit.*

The goal of the paper is to clarify the influence of the spring geometry on the surface pressure through pressure distribution measurements and contact pressure on wear between end coil and spring plate and/or between end coil and turn over coil and from that resulting fractures at the turn over coils.

Key Words: *Transfer of force in helical compression springs, friction, wear.*

1. INTRODUCTION

Many and diverse forms of Springs are to be found in technical products of the mechanical engineering, precision engineering, electrical engineering, automotive manufacturing industries and in many other technical areas [1]-[11]. The intention of this article is to enable frictional overload to be avoided by analysing the friction system (tribosystem) of springs so that design guidelines can be derived.

Losses in a tribosystem can be quantified in terms of the loss of material (the wear) and the loss of energy (the friction). The calculation of these mechanical and energy losses by wear and friction requires exact knowledge of the contact areas and the microgeometry of the contact surfaces.

A research project in progress includes investigations to find the contact areas in dependence on the configuration of the end coils and transition coils and further to find the influence on friction and wear of shot peening as a surface treatment. The method and initial results are presented here.

Fig. 1 shows the fundamental contact areas within springs and between springs and their surrounding components which are to be considered in the tribosystem. The presentation in this paper is of experiments with helical compression springs with ground coil ends and flat spring discs.The most important contact areas are those at the friction points 1, 2.1 and 2.2 shown in Fig. 1.

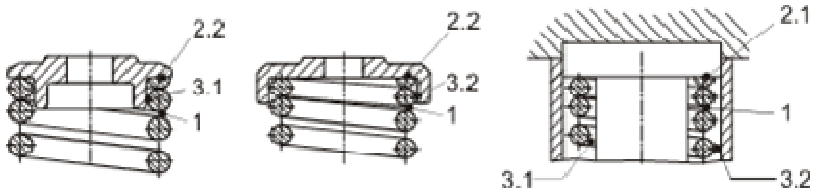

Fig. 1. Friction and wear areas on a helical compression spring between: 1 the coils; 2.1 end coils / housing; 2.2 end coil / spring plate; 3.1 Coil / pivot and/or spring plate; 3.2 Coil / bushing and/or spring plate

Wear leads to changes in the characteristic curve of the spring: $R = \dfrac{G \cdot d^4}{8 \cdot D^3 \cdot n}$ (1)

A decrease in wire diameter because of wear will have an effect on the rate or stiffness of the spring.Wear in the area where the end coils are mounted to their surroundings will result in a change to the effective installed length of the spring and thus a parallel shift in the characteristic curve. These two effects overlap and will result in malfunction if the tolerance limits are exceeded. The malfunction may cause the spring component to fail even before its minimum lifetime has been reached, for example because of cracks in the end and change-over coils.

Wear between helical compression springs and the components surrounding them, also between the coils of springs, will only occur if there is relative movement between these surfaces. Such relative movements are caused by the force components of the spring. In order to clarify the wear activity in the helical

compression spring tribosystem it is necessary to analyse the distribution of the pressure. The pitch design and the surface roughness are of great significance. The pitch design is produced during the coiling procedure.

2. DISTRIBUTION OF PRESSURE AT THE BASE SURFACE OF HELICAL COMPRESSION SPRINGS AND BETWEEN END COIL AND CHANGE-OVER COIL

The contact pressure measurements were carried out on springs of different geometry between the end coil and mounting surface as well as between the end and change-over coil area by means of pressure measuring films, in order to clarify the influence of coil design on the surface pressure and the contact pressure distribution in the tribocontact and the resulting wear as well as the spring fractures caused thereby. Further, a FEA model was created, with which a systematic variation of the spring geometry to investigate the influence of the relevant geometric parameters on the contact pressure is possible. The FEA model was validated through the contact pressure measurements.

When pressure measurement film is used, the pressure is shown by the intensity of discolouration of the film. When applying pressure to the film, its colour turns to red. The colour density varies with the applied pressure level. Pressure was measured between spring and spring disc and also between end coil and change-over coil (see Fig. 2).

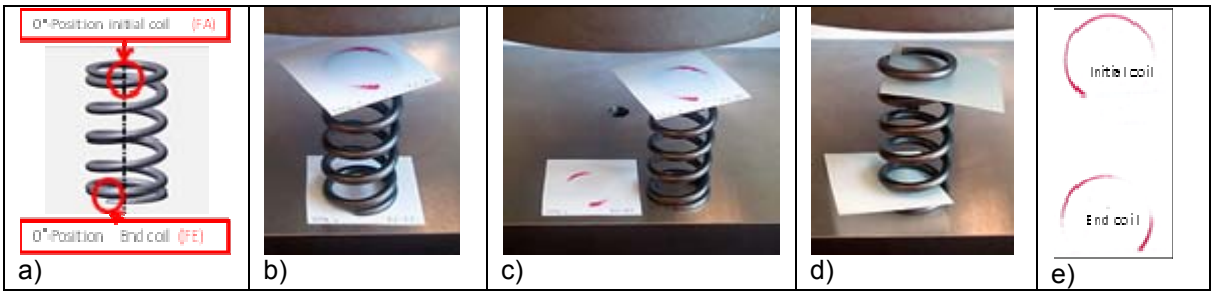

Fig. 2. Visible pressure distribution on pressure measuring films: a) 0 °- position at initial spring and spring end, b) and c) to the contact surfaces d) and e) between spring ends and change-over coils

Sample springs of various shapes (cylindrical helical compression springs with different change-over coils: $n_ü$ = 0,7; 1; 1,3) and with ground ends were tested on a Universal tensile strength Testing Machine at various loads (100 N to 500 N) for these experiments (see Fig. 2).

From the various spring geometries, different spring characteristics result, due to different change-over coils (see Fig. 3).

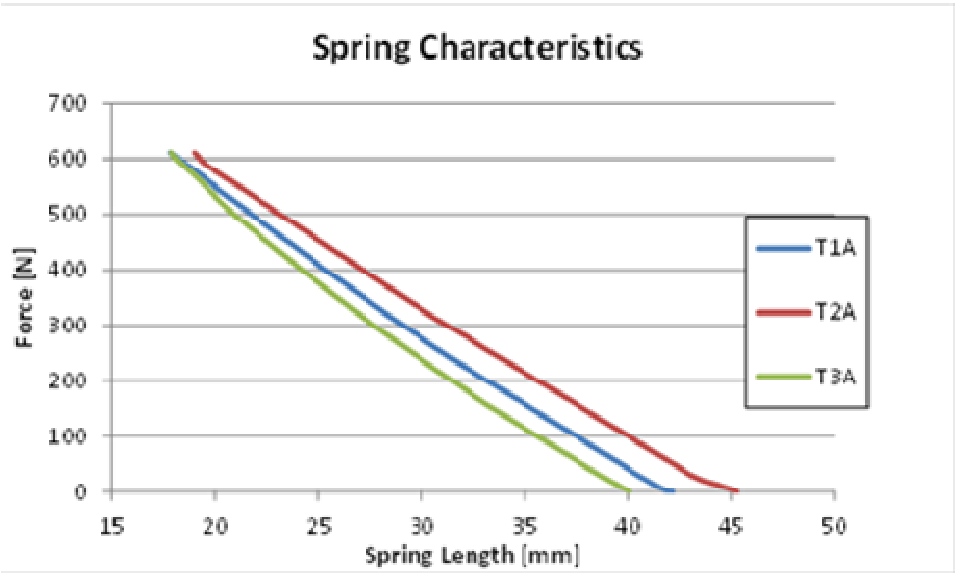

Fig. 3. Spring characteristics of test springs with different geometry: T1A- with n_t=6,0; $n_ü$=1,0; T2A- with n_t=6,0; $n_ü$=0,7 and T3A- with n_t=6,0; $n_ü$=1,3

The investigations proved that the distribution of forces between spring and spring disc is not uniform across the entire spring contact surface but is concentrated at two opposite points of the end coil, namely an average of from 0 ° to 90 ° and from 180 ° to 270 ° (see Fig. 4). The initial spring or spring end was defined as 0 ° (see Fig. 2). The reason is that the force vector changes in its components both longitudinally and transversally to the axis of the spring during compression, both on. the change-over coils and on the spring ends (see Fig. 4).

With the variation of the change-over coils the qualitative pressure distribution hardly changes, so the change-over coil has little influence on the distribution of the surface pressure on the support area (see Fig. 4).

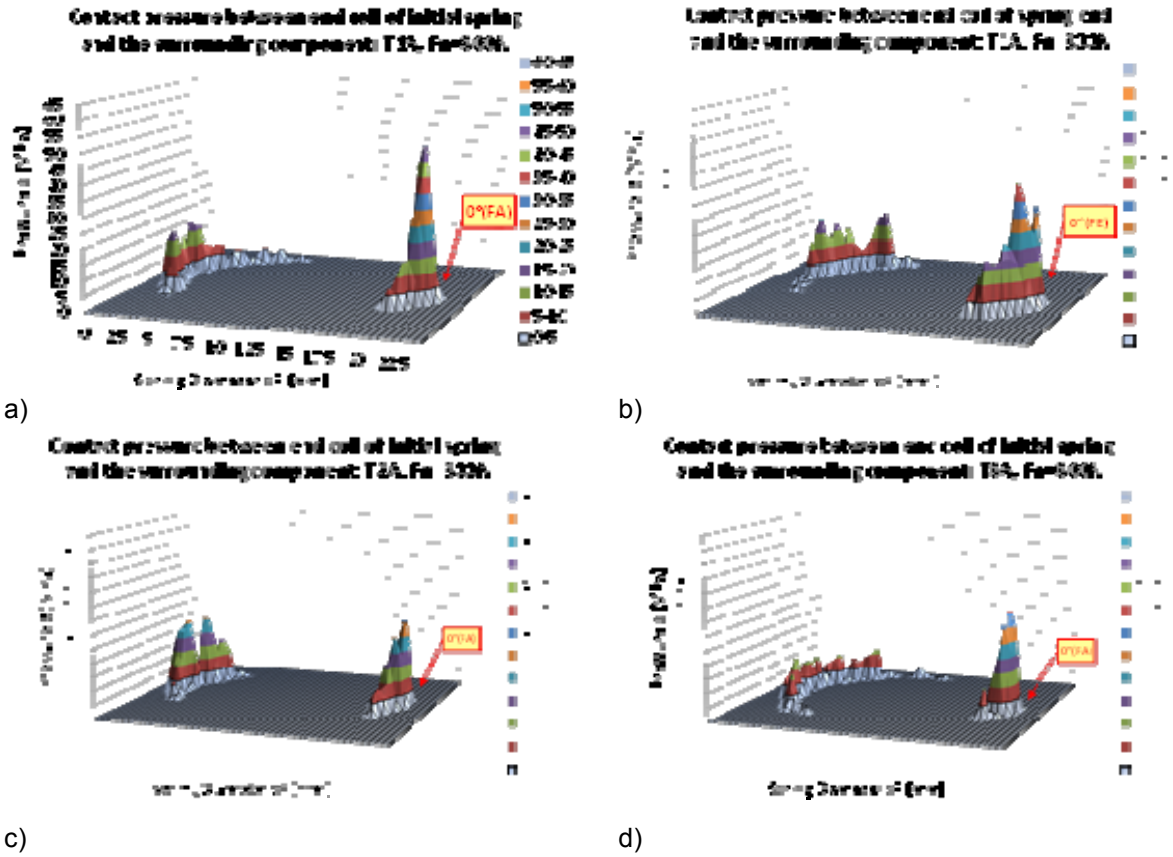

Fig. 4. Pressure distribution on the spring contact surfaces of the spring at 300N: T1A with n_t=6,0; $n_ü$=1,0: a) initial spring and b) spring end; c) T1A with n_t=6,0; $n_ü$=1,0: initial spring; d) T3A with n_t=6,0; $n_ü$=1,3: initial spring

Further pressure measurements were carried out between the end and change-over coils of springs T1A to T3A. After the force distribution measurements between the change-over and end coils a clear difference in force transmission between the beginning and the end of the change-over coil becomes apparent (see Fig. 5 a and b).

If pressure is low there is contact only between the beginning of the change-over coil and the end of the end coil. The higher the pressure, the bigger the contact area. The pressure is greater at the beginning and end of the relevant change-over coil than it is in the turn of the active coil. At higher pressures, the same pressure distribution can be seen as at the spring end (distribution of forces on two sides).

With the variations in the spring geometry the pressure distribution between the end coil and the change-over coil changes (see Fig. 5 a, c and d). The change-over coil has a recognisable impact on the appearance of the surface pressure between the end coil and change-over coil. In the spring T2A with the geometry nü = 0.7 appears a two-sided pressure distribution only at a load of 500N.

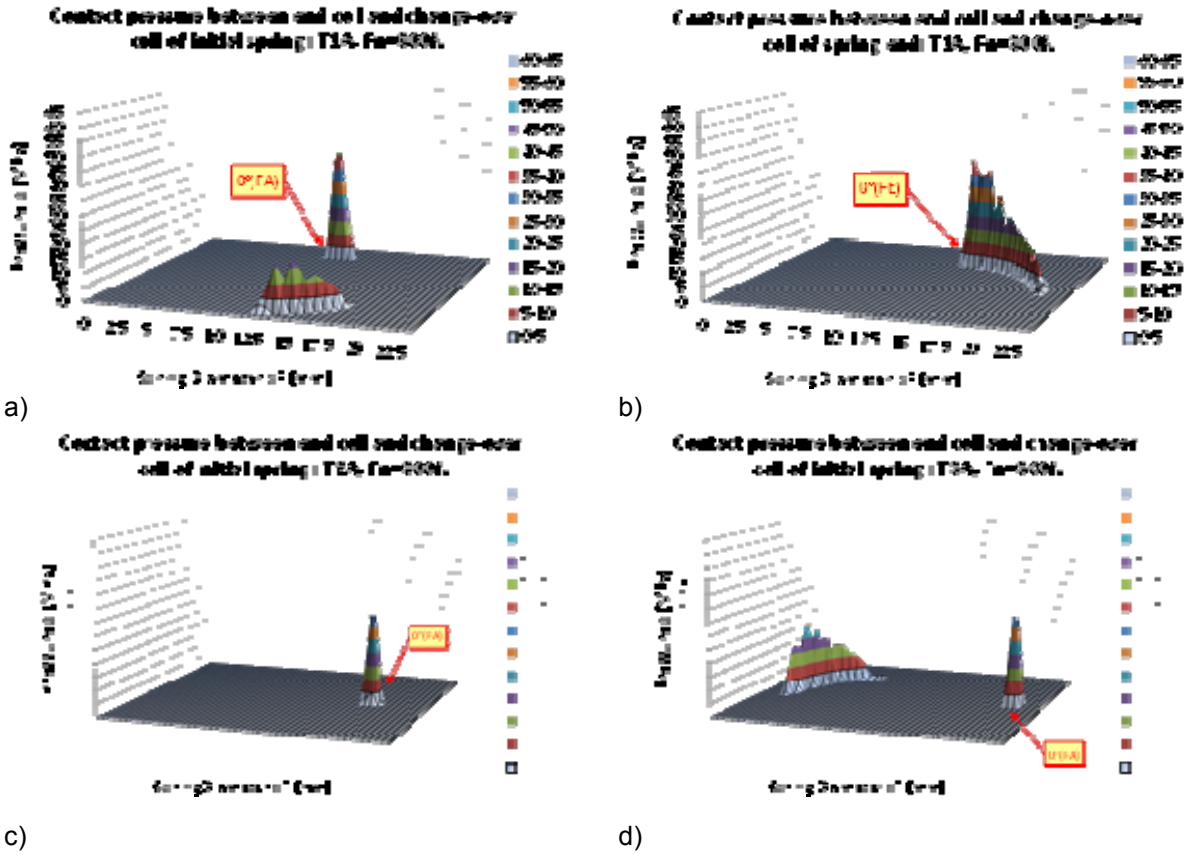

Fig. 5. Pressure distribution between end coil and change-over coil of spring at 300N: T1A with n_t=6,0; $n_ü$=1,0: a) initial spring and b) spring end; c) T1A with n_t=6,0; $n_ü$=1,0: initial spring; d) T3A with n_t=6,0; $n_ü$=1,3: initial spring

The experimental investigations are supported by parameter studies using a FEA model (see Fig. 6). The characteristics were considered initially to validate the FEA model. The paths of the characteristics agree well and have a slight variation of the spring rate of no more than 2.7% to.

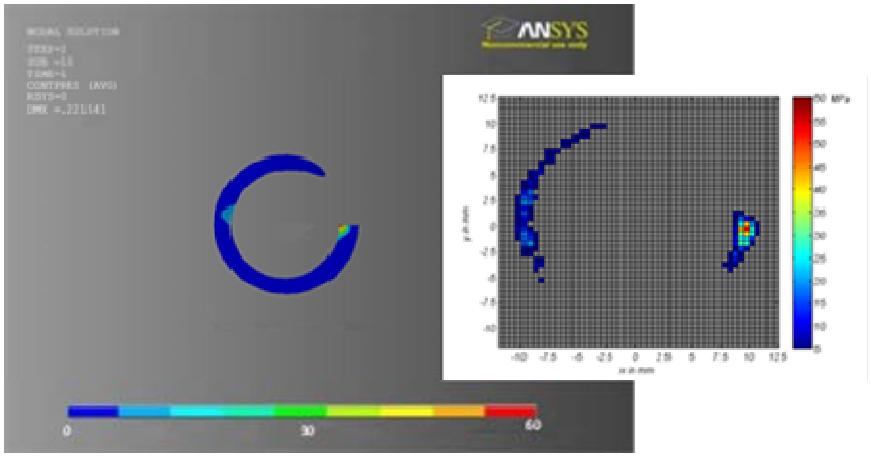

Fig. 6. Pressure distribution at spring contact area (initial spring) of spring T1A with nt = 6.0; nü = 1.0 at 300N: simulated (left) and measured (right)

Fig. 6 shows the pressure distribution of the same spring as was used for the pressure measurements using film shown in Fig. 4. Exact results in the FEA simulation require exact consideration to be given to the geometry of the spring. This was possible by means of image processing test site.

3. WEAR TESTS ON HELICAL COMPRESSION SPRINGS

On springs T1A to T3A, where a different pressure distribution on the contact patch and the change-over coils was determined by measurement and FEA simulation, dynamic fatigue tests were carried out. It should be investigated to what extent different pressure distributions and maximum pressures and thus different distributions of the force into the spring also have significant impact on wear.

The wear tests on the helical compression springs with different geometry showed that the springs T3A show more wear than the springs T1A. Also increased wear occurs at two opposite points.

It is also at these points that more wear is found.As the wear surfaces show, the contact points are at the inside edges of the end coils (see Fig. 7a). This fact is governed by shape and dimension tolerances (DIN 2095).Improvements will be possible in spring manufacture by attending to the configuration of the end and change-over coils, by improving the grinding and by improving the spring disc manufacture.

a) b) c)

Figure 7: Trace of wear: a) at the spring ends, b) on change-over coils and c) fretting corrosion

When wear has taken place between change-over and end coils, the friction surface is enlarged and the pressure is distributed over an even larger area at the same load.Wear then causes the thickness of the wire and the spring rate to change. The Hertzian contact stress becomes surface contact pressure (see Fig. 7b).In addition, the fretting corrosion phenomena due to fretting processes between spring end and change-over coil is visible (see Fig. 7c)

According to the presented investigations the sites of fracture of coil springs mostly occur on the change-over coil at the 0 ° point of the spring contact surface. Heavy dynamically loaded helical compression springs show signs of fatigue at these points in the form of microcracks.

4. SUMMARY

Both pressure measurement and FEA simulations indicated that the contact surfaces with a tribological effect within the spring (between the transition and end coils) and between the spring and the spring seat are dependent on the geometrical shape of the end and transition coils, in particular on the development of the pitch.

Future investigations should focus on full variation of the parameters using the described FEA model using the spring shapes already investigated as a starting point in order to derive design rules for helical compression springs optimised for wear in respect of the contact geometry

Pressure distribution between the change-over coils and the coil ends equals that at the end of the spring, i.e. at two opposite locations where wear occurs. By measuring the wear on helical compression springs, it could be found that there are sites with paused wear in an oscillating field.

REFERENCES

41. MEISSNER, M., SCHORCHT, H-J., Metallfedern. Grundlagen, Werkstoffe, Berechnungen und Gestaltung. Berlin / Heidelberg/ New York: Reihe Konstruktionsbücher, Band 41. Springer-Verlag 1997, 2. Auflage.
42. SCHORCHT, H-J., GEVORGYAN, G., LIEBERMANN, K., Auswirkungen tribologischer Beanspruchungen auf Funktion und Lebensdauer von Schraubendruckfedern. DFG-Abschlussbericht 2007.
43. SCHORCHT, H-J., GEVORGYAN, G., Investigation of the effects of tribological loads on the function and durability of springs. 5th Int. Science. Tribology Conf. Gomel, 2005.
44. GEVORGYAN, G., BARTHOLD, G., Analyse der tribologischen Beanspruchungen von Schraubendruckfedern. 50. Int. Wiss. Kolloquium. Ilmenau 2005. Tagungsband, S. 617-618.
45. GEVORGYAN, G., BARTHOLD, G., Verschleißuntersuchungen an zylindrischen Schraubendruckfedern aus Dauerschwingversuchen. VDI-Tagung Federn - Unverzichtbare Bauteile der Technik. Fulda 2006. VDI-Bericht 1972, S. 293-298.
46. KRIKAU, O., Federbrüche und ihre Beurteilung. Draht 23, 1972, 9; 10.
47. BARTHOLD, G., Spring Failures and Their Causes. Springs, Summer, 1998, p. 21-37.
48. VDI-Richtlinie 3822, Beuth-Verlag, Berlin 1984.
49. HORA, P., Schraubenfederbrüche beurteilen. Materialprüfung 39 (1997) 10, S. 418-422.
50. GEVORGYAN, V., KLETZIN, U., SCHORCHT, H-J., GEVORGYAN, G., Verschleißuntersuchungen an Schraubendruckfedern und Federtellern. Tagung Werkstoffprüfung 2010, Neu-Ulm.
51. KLETZIN, U., GEVORGYAN, V., Untersuchungen zu tribologischen Beanspruchungen von Schraubendruckfedern mit dem Ziel der Optimierung von Reibung und Verschleiß“, DFG-Forschungsantrag, TU Ilmenau 2010.

CORRESPONDENCE

Dipl.-Ing. Vahan GEVORGYAN
Ilmenau University of Technology,
P.O. Box 10 05 65
98684 Ilmenau
e-mail: vahan.gevorgyan@tu-ilmenau.de

Univ.-Prof. Dr.-Ing. Ulf KLETZIN
Ilmenau University of Technology,
P.O. Box 10 05 65
98684 Ilmenau
e-mail: ulf.kletzin@tu-ilmenau.de

Tribological Journal BULTRIB Vol. 5, 2015
Papers from the International Conference **BULTRIB '15**
September 11-13, 2015, Sozopol, Bulgaria
Society of Bulgarian Tribologists
FIT – Technical University of Sofia

TRIBOLOGICAL INFLUENCES ON METALWORKING FLUIDS COMPOSITION

Ljiljana Pedišić*, Bruno Novina

Abstract: *The development trend in metalworking fluids is dependent on three important factors, as follows: human health and environmental protection, improvement of metalworking operation process and permanent customer requirements for cost reduction. The composition of modern metalworking formulations is becoming more and more sophisticated so that a great deal of usual components is changing with new less harmful components. At sophisticated metalworking processes fluids have to fulfill certain requirements such as the heat transport which should be fast enough to prevent formation of cracks while cooling of the basic material, lubricating of the tool in order to reduce wear, and prevent other tribological effects. In this paper are presented new formulations of metalworking fluids based on less harmful components with laboratory screening test results and also application.*

Key Words: *Metalworking fluids, Lubricating additives, Human health and environmental protection, Wear, Application.*

1. INTRODUCTION

At metal working operations, heat is generated between the tool and the workpiece. The cause of heat generation is friction and material resistance to the deformation created in the shear zone. The generated heat usually has a negative impact on the tool and the workpieces and cause numerous tribological effects. High temperature and high pressures on contact surfaces cause unwanted occurrences, such as uncontrolled metal microstructure below the worked area, surface burning, loses in dimension, increased tool wear, etc. [1]. The application of proper metalworking oil considerably reduces friction of contact areas, as well as temperature in the treatment zone, tool wear, energy consumption, and finally overall metalworking costs.

Metalworking fluids contain the oil components and the necessary additives for improving the lubricant's properties. Additives are used in the share ranging from 2-30 %, depending on application requirements. The development of metalworking fluids was very much affected by the abolishment of chlorinated paraffin, widely used in metalworking fluids, through "negative lists" or environmental laws [2]. Reduction or even complete prohibition guidelines are provided through product development and waste oil management. Under boundary lubrication conditions, where chlorinated-paraffin was irreplaceable EP additive for a number of years, a proper substitute is still being sought. Among the possible solutions' are petroleum sulfonates containing earth - alkaline metal salts, nitrated vegetable oils and phosphorus compounds as dialkyl dithiophosphates that are very effective in improving the frictional properties of the lubricant [3, 4, 5].

2. METALWORKING FLUIDS CLASSIFICATION AND FORMULATION

Two world standards classifying metalworking fluids in detail: ISO 6743/7:1986 [6], and DIN 51385:2013-12 [7], while they may generally be classified in two groups. The first group comprises the fluids applied as oil, and the other those applied mixed with water.

International standard ISO 6743/7 Lubricants, industrial oils and related products (Class L) Family M (Metalworking) classified lubricants for metalworking in two main groups. First includes operations primarily needing lubrication-MH symbols, and the second operations primarily needing cooling-MA symbols. According to field of application ISO 6743/7 metalworking products are classified into eight categories: cutting, abrasion, elektrodischarge machining, sheet metal forming, ironing, power spining, wire drawing, forming, stamping and rolling.

DIN 51385:2013-12 select metalworking lubricants based on application in four groups: media for cutting operations (SC), media for forming operations (SF), media for minimal quntity lubrication (MQL) and MFO

multifunctional oils. Further, groups graded based on oil, water solubility: emulsions or solutions, pastes and also particles. Neat oils (SCN and SFN according to DIN or ISO-MH) consist of the basic oil component and additives. In Table 1 are presented main types of additives for metalworking oils and typical compounds. The oil component may be mineral oil, synthetic or natural oil. Additives have the task of improving the properties of the basic oil component [8, 9]. The oil type, composition and viscosity are dependent on application requirements. Viscosity of neat metalworking oils are in ranges from 2 - 100 mm^2/s at 40 ^0C, while 80 % of the application is covered by oils whose viscosity is from 6 - 40 mm^2/s. Water-miscible metalworking fluids are categorized in two considerably different groups: emulsifying fluids containing a part of mineral oil, creating emulsions with water, and, synthetic fluids not containing mineral oil, creating solutions with water. In general products can be classified according to its composition, application or environmental impact like are chlorine free formulations, biodegradable, grinding, drawing products and others.

Table 1. Lubricant additive types and typical compounds used in metalworking oils

ADDITIVE TYPES	TYPICAL COMPOUNDS
Detergents (Metallic Dispersants)	Salicylates, Sulfonates, Phenates, Sulfophenates
Ashless Dispersants**	N-substituted long-chain alkenyl succinimides, High-molecular-weight esters and polyesters, Amine salts of high-molecular-weight organic acids, *Copolymers of methacrylic or acrylic acid derivatives containing polar groups: amines, amides, imines, imides, hydroxyl, ether, etc.
Oxidation and Corrosion Inhibitors	Organic phosphites, Metal dithiocarbamates, Sulfurized olefins, Zinc dithiophosphates
Antioxidants	Phenolic compounds, Aromatic nitrogen compounds, Phosphosulfurized terpenes
AW/ EP Additives ***	Organic phosphates, acid phosphates, Sulfurized olefins, Zinc dithiophosphates, Alkaline compounds as acid neutralizers, Petroleum sulfonates, Chlorinated paraffine
Surface active or polar additives***	Fatty oils and derivatives Synthetic esters

(*Also viscosity modifiers, ** Also emulsifiers, ***Also friction modifiers)

3. METALWORKING FLUID AT GRINDING OPERATION

Grinding is one among the most frequently applied metalworking operations. Requirements for surface quality, stability of forms and dimensions of materials which are difficult to work make the application of metalworking fluids in many cases irreplaceable. Operation of grinding or working by abrasion has specific properties, which requires special attention to be paid to the filtering of the generated tiny particles, heat conductance, and also foaming control, as well as control of mist generation at high cutting speeds. Table 2 showes general recommendations for choosing grinding fluid depending on the grinding process [10].

Table 2. Selection of grinding fluid by process

GRINDING	METALWORKING FLUID			
Type	EMULSION	MICROEMULSION	SOLUTION	OIL
cylindrical	●	●	●	
internal	●	●	●	
internal (enclosed)				●
surface	●	●	●	
centreless				●
thread		●		●
gear				●
creep feed	●	●		
flute				●
honing			●	●

Grinding, abrasion metalworking proces, is a procedure of metal removal in the form of small particles through the activity of blades with undefined geometry i.e. abrasive particles in the tool [11]. The tribological system of operation by grinding consists of workpiece, grinding wheel and the medium within which the process is taking place. Grinding wheel as a grinding tool is multicut, consisting of many mutually connected grinding grains of a natural or artificial grinding agent. The front angle of the grinding wheel cutting surface

blades is mainly negative. The criteria for evaluating the grinding process are the appearances on the ground surface and on the grinding wheel cutting surface [12]. The appearances characteristic of the ground surface are fractures, burns, change of structure, roughness, change of hardness, precise dimensions, and so on.

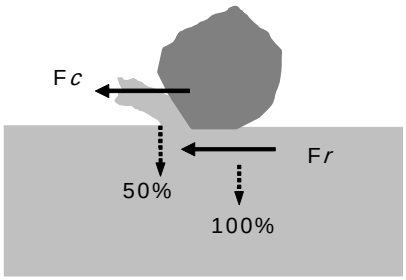

Fig. 1. Schematic presentation of the energy source between grain and material at grinding

At grinding process, the tool grain pushes in front the workpiece metal, thus creating a metal particle. Between them develops a cutting force (F*c*). There is also the friction force (F*r*) appearing between the back grain surface and the worked surface. Both forces develop heat as schematically presented in Fig. 1. Around 50 % of the heat generated by cutting force goes into the workpiece while the rest goes into the metal particle. Nearly all heat of the sliding force, around 100 %, goes into the workpiece. This means that in a typical cylindrical and surface grinding, around 75-90 % of total energy developed at grinding may go directly into the workpiece in the form of heat. Compared to other operations through particle removal, grinding is different in terms of developed heat absorption. In a typical metal removal operations, cutting, 97 % of developed heat goes into the working tool and the environment, and only about 3 % - into the workpiece. Distribution of developed heat at typical working by grinding is 12 % into the grinding wheel, 4 % into the system, and 84 % into the worked surface [13].

Application of grinding fluid promotes the efficiency of the grinding process with three main properties as follows: cooling, lubrication and particle rinsing. Proper cooling conducts the heat away from the system components, thus preventing welding which could damage material structures. This damage is known as material burning. The fluid also takes the heat away from the grinding wheel, thus extending tool service life. Good lubrication helps to reduce friction between grain and workpiece surface. That reduces grinding energy and thus also the volume of heat going to the workpiece. Friction reduction also extends grinding wheel service life and provides better surface quality through improved cutting. The fluid lubricating layer hardness helps to reduce friction, which helps protect the grain in the grinding wheel and reduces tool wear. Particle rinsing or taking particles away from the working zone prevents surface damage by particles, improve heat transport and prevent corrosion.

There is no fluid which can meet all the cooling and lubrication requirements for all grinding operations. The criterion for evaluating individual grinding fluid type is, apart from performances and environmental and health protection requirements, also largely dependent on material workability, compatibility, management, and so on.

4. EXPERIMENTAL

4.1. Objectives

The objective of this work is development of new metalworking oil for severe application at form and thread grinding machines for tools as drilling and milling equipment production processes. New oil should not contain chlorinated compounds as additive. Also need perform high level of performances even higher than commonly used referent oil. Referent oil is low additivated, viscosity grade 40 and phosphorus containing level 0.25 %. So, goal is phosphorus additives use for new neat grinding oil composition.

4.2. Test methods for metalworking fluid examination

Metalworking fluids are tested at the development stage and also during application at metalworking operation. For examination physical and chemical properties of additives and metalworking fluids we used standard methods like DIN, ISO or ASTM [14] and they presented in tables with the specific properties. Lubrication properties or anti wear and extreme pressure properties (AW/EP) of additives and metalworking fluids are tested at three mechanical dynamical test machines as is shown in Table 3.

Table 3. Operating condition of test machines for metalworking oils mechanical dynamical properties evaluation

Test machine	EP-4 BALL	Wear-4 BALL	REICHERT BALANCE
Methods	ASTM D 2783 [14]	ASTM D 4172 [14]	REICHERT
Tribological elemets	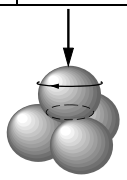		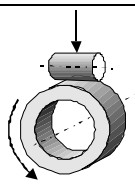
Metal	STEEL AISI-E-52 100		Steel, 100 Cr6
Diameter, mm	12.7 ball's		12.0 roll's
Speed, s^{-1}	Upper ball: 29.5	Upper ball: 20	Ring, 15
Load, N	Up to 8000	400	300
Test temperature, ^0C	20 ± 5	75 ± 1	20 ± 5
Test time	10 ± 0.2 s	1 h	60 s / or 100 m sliding contact
Measured properties	Weld point (WP), N	Wear scar diameter (WSD), mm	Wear scar area (WSA), mm^2

4.3. Tested additives and oil formulations

In accordance to new environmental and safety requirements in laboratory are formulated new metalworking fluids. For formulation we have used paraffinic mineral oils SN 150 and SN 350 in combination with different types of additives from the market: As AW/EP additive we examined calcium overbased sulfonate based on natural raw material and four types of phosphorus additives. The main physical and chemical properties of additives are presented in Table 4.

Table 4. Physical and chemical properties of test additives

ADDITIVE	AD S400	AD P5304	AD P7169	AD P3740	AD P360P
Density, 15^0C, g/ml, ISO 3675	1.22	0.91	1.1	0.97	1.01
Sulphur content, %, X-Ray	1.4	-	-	-	-
Phosphorus content, %, ICP	-	5.25	7.2	9,0	9,5
TBN, mgKOH/g, ISO 3771*	400	-	-	-	-
Viscosity, 100^0C, mm^2s^{-1}, ISO3104	75	5.4	9.8	130	14.3
Composition	Overbased petroleum sulphonate	Alkyl phosphite ashless	Zinc dialkyl dithiophos-phate	Phosphoric acid ester, amine neut-ralized	Alkyl acid phosphate amine neu-tralized

*TBN=total base number

5. RESULTS AND DISCUSSION

Results of laboratory testing of formulations are pesented in Table 5. Test formulations consist of base oils mixture and all additives separately. In comparison to referent oil the most similar properties are obtained with formulation based on additive AD P5304. All formulations are inactive, corrosion grade is 1. After satisfying laboratory test results it can be expected that formulation will have requested application properties. So, that formulation F AD P5304 is examined on field test at two machines on production of drilling and milling tools. In Table 6 are presented metalworking machines, working conditions and some requirements for test fluids' application. Material of taps: steel class M52, M2, M35, M42 according to AISI. Formulation F AD P5304 showed excellent properties at field testing. In comparison to old referent oil (REF) test metalworking formulation F AD P5304 has the same and even better properties. As phosphorus compounds react with metal surfaces under moderate temperatures and pressures, the resulting films provide extreme pressure and anti-wear properties to the lubricant. That results with shine surfaces, without burning spots and achieve precise dimension of workpieces.

Table 5. Examined properties of test oil formulations

Properties	FORMULATION: Base oil + additive					
	AD S400	AD P5304	AD P7169	AD P3740	AD P360P	Ref.oil
Appearance	Clear	Clear	Clear	Clear	Clear	Clear
Weld point, N	2400	1600	2000	2500	2500	1800
Wear scar diameter,mm	0.41	0.40	0.43	0.47	0.56	0.54
Wear scar area, mm^2	6.8	28.7	8.2	8.9	7.0	27.5
Corrosion, Cu, 3h, 100 ^{0}C, ISO 2160	1a					

Table 6. Metalworking machines and working conditions for test fluids' application

Working machine	NORMAC FT 80 Automatic tap straight flute grinding machine	MIKROMAT 3G Rotational form and thread grinding machine
Metalworking operation	Flute grinding	Form and thread grinding
Grinding wheel diameter min./max., mm	150 / 200	200+2x Profilhole /350
Grinding wheel	Tyrolit 85A1001Q5B25, Ø5B25, Ø200X5X76	Universal WA200M7V, Ø450X27X203
Number of flutes	2 ÷ 4	-
Number of runs	4 ÷ 8	2 ÷ 5
Overall flute lenght, mm	70	-
Workpiece diameter	M 10 ÷ M 16	M 16 ÷ M 100
Oil quantity, m^3	1	0.6
Requirements on working fluid	cooling, inhibit local overheating, tool clearing, lubricating, high surface quality, min. 3 months	

Formulation showed excellent grinding power, high surface quality with avoiding formation of burning spots at very severe grinding operations on hard steel such is grinding of drilling and milling equipment. During application samples of working oils are taken from machines and examined according to whole oil monitoring program from viscosity, appearance, particle content and other physical, chemical and mechanical dynamical properties. All examined properties stay constant or with narrow aberrance interval in spite of very high contamination. Measured oil containing element S (sulphur) and P (phosphorus) in oil samples taken from Mikromat G3 machine are presented of Fig. 2. Some of lubrication properties measured in oil samples taken from machine Mikromat G3 are presented on Fig. 3, and from machine Normac FT 80 on Fig. 4. Tested oils satisfy all required properties on both machines and stay in application much longer than planed working life through three months at those severe operations of grinding tools.

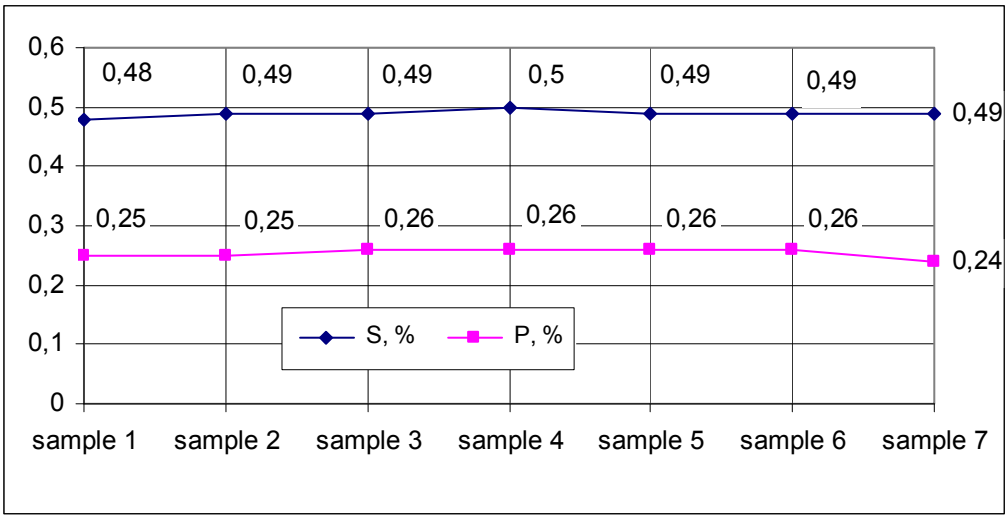

Fig. 2. Results of S and P content determination in tested oil samples from Mikromat 3G

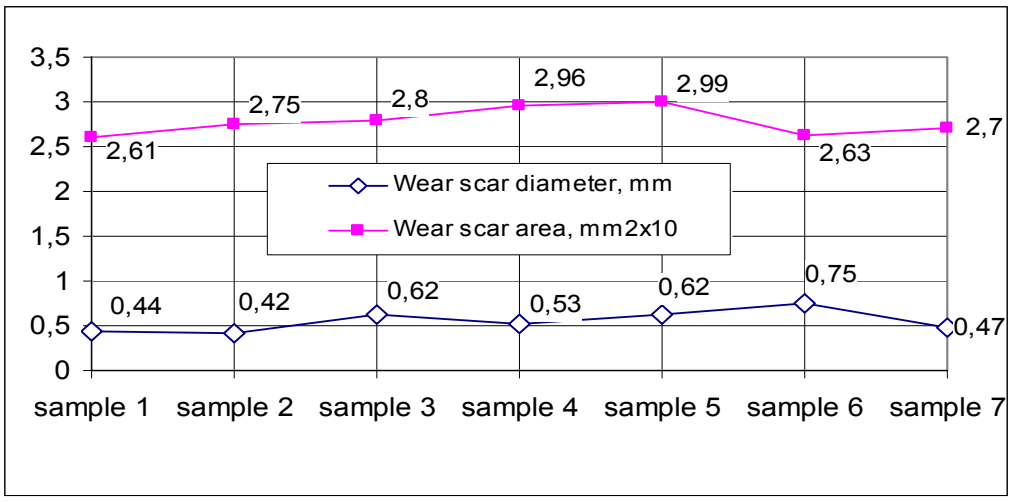

Fig. 3. Results of lubrication properties determination in tested oil samples from Mikromat 3G

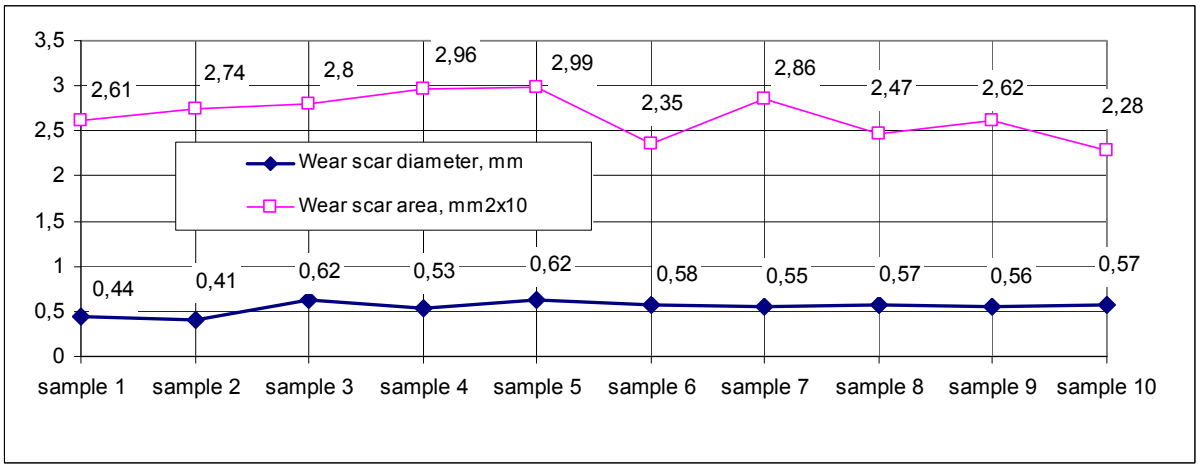

Fig. 4. Results of lubrication properties determination in tested oil samples from Normac FT 80

6. CONCLUSION

In order to improve metalworking grinding process with high concern to protect human health and environment we tested alternative additives for chlorinated paraffin in cutting oils. These are calcium overbased petroleum sulfonates and different types of phosphorus containing additives.

All formulations with tested additives have good properties but formulation F AD P5304, containing phosphorus additive, showed the most similar properties to the referent oil. Because of good laboratory results oil formulation F AD P5304 filled into two grinding machine as cooling and lubricating media at grinding of drilling and milling equipments.

During field test on grinding machines tested oils showed excellent grinding power, high surface quality with avoiding formation of burning spots and also low foaming tendency. At very severe grinding operations on hard steel such is grinding of drilling and milling equipments new metalworking oil showed very stable composition and all examined properties even in presence high quantity of metal and abrasive particles that are characteristic for abrasive operations.

Under both laboratory and field application conditions new formulation of metalworking grinding oil with phosphorus additive has good properties which exceed properties of widely used old formulations and continued working proces after required time of operation.

REFERENCES

1. Trent, E.M., Metal Cutting, Second edition, Butterworth's, 1984.
2. MANG, T., Schmierstoffe und Umwelt - Die Schmierstoffentwicklung im Einfluss der Umweltgesetzgebung, *Mineralöl Technick*, **5-6**,1990.
3. PEDIŠIĆ LJ., ŠVIGLIN MARASOVIĆ M., Development of metalworking oils for application at cold deformation, 15th International colloquium Tribology, Jan 15-17, 2006, Technische Akademie Esslingen, Stuttgart, Deutschland.
4. MINAMI, I., HASEGAWA, T., MEMITA, M., Investigation of Antiwear Additives for synthetic Esters, *Lubrication Engineering*, **58,** 1, 2002.
5. SCHUMACHER, R., ZINKE, H., Tribofragmentation and Antiwear Behaviour of Isogeometric Phosphorus Compounds, *Tribol. Intern*. **30**, 3, 1997.
6. ISO 6743/7:1986, Lubricants, industrial oils and related products (class L) – Classification - Part 7: Family M (Metalworking), International Organization for Standardization, Geneva, Switzerland,1986.
7. DIN 51385:2013-12, Schmierstoffe-Bearbeitungsmedien fur die Umformung und Zerspanung von Werkstoffe- Begriffe, Deutsches Institut fur Normung, 2013.
8. KOTVIS, P. V., Overview of the Chemistry of Extreme - Pressure Additives, *Lubrication Engineering*, **42**, 6, 1986.
9. RUDNIK, L.R., Lubricant Additives Chemistry and Applications, CRC Press, Friction, lubrication and wear technology, pp. 98-118, 2009.
10. SLUHAN, C., Selecting the right cutting and grinding fluids, Tooling & Production, Volume **60**, No. 2, May 1994.
11. IVUŠIĆ, V., Tribologija, Ed. HDMT (Croatian Society for materials and Tribology), Zagreb, Croatia, 2002.
12. CIGLAR, D., CEBALO, R., UDILJAK, T., Influence of grinding productivity on the burn intensity of the ground surface, 6th International Conference on Production Engineering CIM 2000, Proceeding, Ed. Croatian Association of Production Engineering, I-095-106, Zagreb, Croatia, 2000.
13. Grinding manual, http://www.igt.bris.ac.uk/manual/manual4/manual4cont.html
14. Annual book of ASTM Standards 2008, Volume 05.01 & 05.02, Petroleum Products and Lubricants, ISBN 978-0-8031-5774-3, ISSN 0192-2998, ASTM International, Feb. 2008.

CORRESPONDENCE

Ljiljana PEDIŠIĆ, Mag.ing.cheming
INA MAZIVA Ltd, Member of INA Group
Radnička cesta 175, 10000 Zagreb, Croatia
E-mail: ljiljana.pedisic@ina.hr

Tribological Journal BULTRIB Vol. 5, 2015
Papers from the International Conference **BULTRIB '15**
September 11-13, 2015, Sozopol, Bulgaria
Society of Bulgarian Tribologists
FIT – Technical University of Sofia

CONSIDERATION REGARDING THE STRESS AND STRAIN STATUS IN ELASTIC-PLASTIC CONTACT BETWEEN A SPHERE AND A LAYER OF UHMWPE POLYETHYLENE

Alina Magdalena POPESCU, Georgiana Ionela PĂDURARU, Andrei TUDOR and Lucian SEICIU

Abstract: Wear of ultra-high molecular weight polyethylene (UHMWPE) in total knee prostheses is the main cause of limiting the sustainability of these prosthesis. Under action of normal force action and pivoting moment, on the contact area can be observed normal and tangential strains. In this paper we observed two situations on contact surface: total slip (full slip) through pivoting in any location of surface and partial sliping through pivoting and calculate their stress values.

Key Words*:* UHMWPE behavior, knee prosthesis, stress and strain status in elastic plastic contact, deformation of UHMWPE.

INTRODUCTION

Wear of ultra-high molecular weight polyethylene (UHMWPE) in total knee prostheses is the main cause of limiting the sustainability of these prosthesis [1].
Kinematics of motion in the knee prostheses involves the following types of motions: rolling after three directions (internal-external (I-E)), flexion-extension (F-E), valgus - varus (V-V), slip in the anterior-posterior direction (A-P) and pivoting after superior-inferior direction (S-I).
Figure 1 shows schematically these movements.

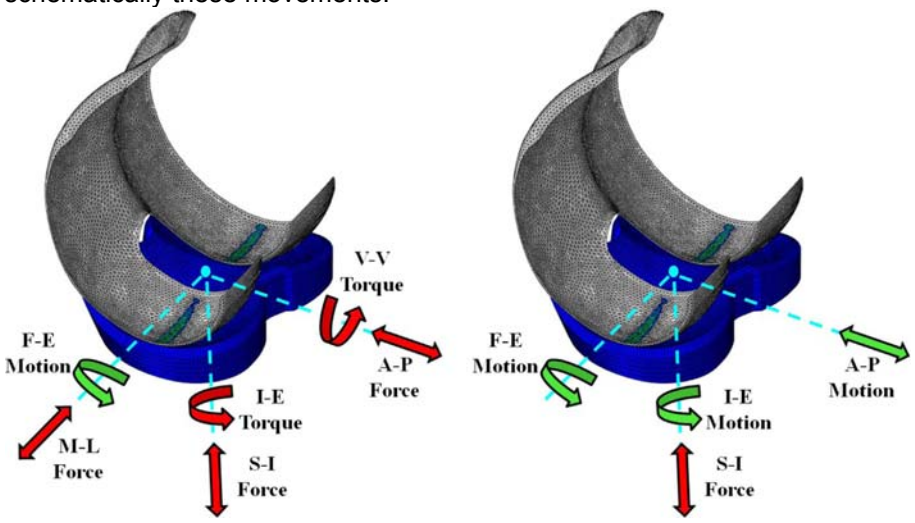

Figure 1. Movements encountered in knee prosthesis

The movements, strain and deformation state define the type of wear and degradation found in prosthesis: the oxidation of support where tibial plateau UHMWPE is, pitting, delamination, adhesion and abrasion. The harmful effects of these degradations wear particles is that they have a high osteolytic potential. Medium particles (0.2 ... 0,8 μm) have the largest share and are the most dangerous „migration" in different parts of the skeletal system [2], [3], [4].
In order to know the mechanism of occurrence of wear debris for different kinematic conditions and to discover the state of shares in tibio-femoral contact area, the current paper aims to analyze the behavior of polyethylene UHMWPE in pivoting. In total knee prosthesis, pivoting occurs during the rotation internal-external motion (I-E), producing a torque (pivoting, twist)($M_{tI\text{-}E}$).
The behavior of polyethylene to pivoting analyze by deducting the maximum stress and strains and by clarifying degradation (wear and creep).

TEORETHICAL MODEL

We consider a sphere or spherical segment manufactured by steel characterized by the radius R_1, the elastic modulus E_1 and Poisson's ratio μ_1 and a support from polyethylene UHMWPE characterized by radius of curvature ($-R_2$ - support concave) or ($+R_2$ - support convex) with elastic modulus E_2 and μ_2 (see figure 2).

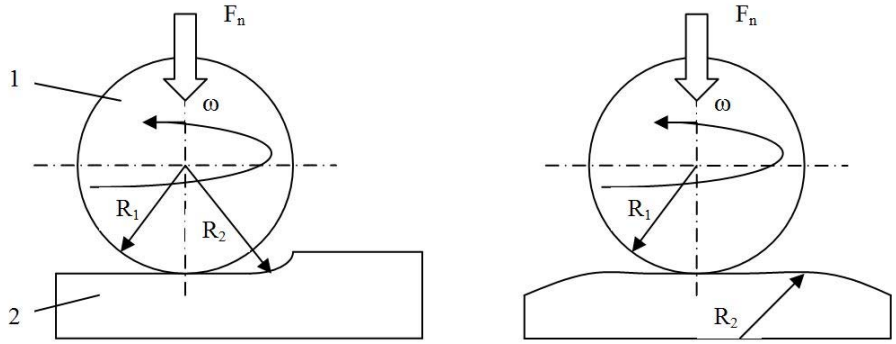

Figure 2. The contact between a steel sphere and a layer of UHMWPE:
a) contact concave; b) contact convex.

The support material is known by the stress-strain diagram determined experimentally (Hooke diagram). To initiate contact with a normal force it is speculated that deformations are perfectly elastic, so it can be applied Hertz relations regarding: circular contact surface radius (a_H), the maximum pressure (p_{oH}) and mutual penetration of spheres (δ_H) [5].

To generalize the results, contact radius is reduced to its dimensionless radius contact ($R_p = \frac{R_1 \cdot R_2}{(R_1 + R_2)}$, $a_a = \frac{a_H}{R_r}$), and tensions become dimensionless towards reduced longitudinal elasticity parameter ($p_{oa} = p_{oH} \cdot \eta$, $\eta = \frac{1-\nu_1^2}{E_1} + \frac{1-\nu_2^2}{E_2}$).

As normal load parameter it is proposed average pressure Stribeck $p_m = \frac{F_n}{(\pi \cdot R_r^2)}$.

So Hertz's relationships become:

$$a_a = \frac{a_H}{R_p} = \frac{1}{R_p} \cdot \left(\frac{3}{2} \cdot \eta \cdot \mathrm{F}_n \cdot R_p \right)^{\frac{1}{3}} \quad (1)$$

$$p_{oa} = p_{oH} \cdot \eta = \left(\frac{3}{2 \cdot \pi^2} \cdot \eta \cdot p_m \right)^{\frac{1}{3}} = \frac{1}{\pi} \cdot a_a \quad (2)$$

$$\delta_a = \frac{\delta}{R_p} = \frac{\pi^2}{2} \cdot \eta^2 \cdot p_o^2 = \frac{\pi^2}{2} \cdot p_{oa}^2 = \frac{1}{2} \cdot a_a^2 \quad (3)$$

After stabilizing elastic contact to a normal load p_m, it is applied a torque (pivot moment) with circular direction perpendicular to the contact surface. This moment induce a tangential stress who separates the circular area in two: one area of stick (bonding, adhesion) in the central part and another of briefs (detachment, sliding) in the peripheral area. To determine the range of separation of the two parts (c), it is assumed the solution given by Hills [6].
Thus, in the contact area corresponding to a point of radius r, deformation (u_θ) and tangential stress ($\tau_{z\theta}$) are given by relationship below (see figure 3):

$$u_\theta = \theta \cdot r \text{ , for } 0 \le r \le c \text{ ;} \tag{4}$$

$$\tau_{\theta z1} = f \cdot p_{oH} \cdot \sqrt{\left(1 - \frac{r}{a_H}\right)^2} \text{ , for c<r<a}_H \tag{5}$$

or in dimensionless coordinates:

$$u_{\theta a} = \frac{u_\theta}{a_H} = \theta \cdot \rho \text{ , for } 0 \le \rho \le k \tag{4´}$$

$$\tau_{\theta z a_1} = \frac{\tau_{\theta z}}{f \cdot p_{oH}} = \sqrt{1 - \rho^2} \text{ , for } k \le \rho \le 1 \tag{5´}$$

where $\rho = \frac{r}{a_H}$ and $k = \frac{c}{a_H}$.

In above relations θ is the angle of rotation (angle of twist) of UHMWPE support, f is the coefficient of sliding friction of a metal sphere on polyethylene support.

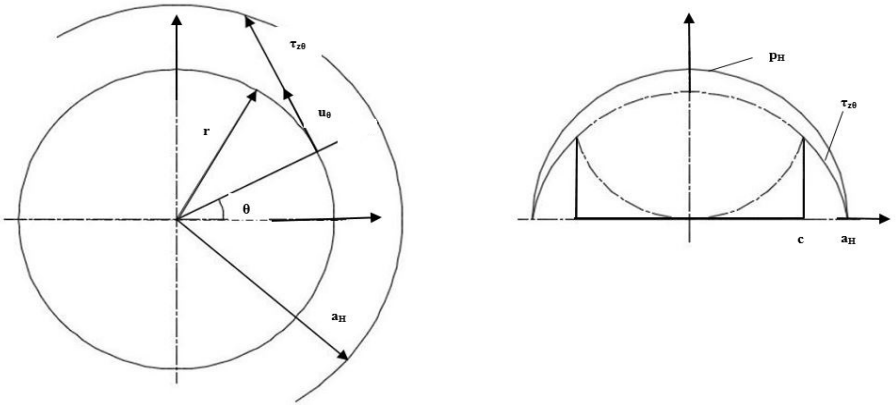

Figure 3. Strains and tensions on the contact surface

The issue of tensions in the contact area is put for the shear stresses ($\tau_{z\theta}(r)$) from the stick area (bonding, adhesion). These tensions together with the slip ones (5) produce a rigid rotation of the UHMWPE support. It is accepted as solution to this problem, the solution given by Hills:

$$\text{for } 0 \le \rho \le k \text{ , } \quad \tau_{az\theta 2} = \sqrt{1-\rho^2} \cdot \left\{1 + \frac{2}{\pi} \cdot \left[k_1^2 \cdot \mathbf{D}(k_1) \cdot \mathbf{F_1}(k,\theta) - \mathbf{K}(k_1) \cdot \mathbf{E_1}(k,\theta)\right]\right\} \tag{6}$$

where $k_1 = \sqrt{1-k^2}$, **F**(x,θ), **E**(x,θ) are the incomplete elliptic functions

$$\mathbf{F_1}(x,\Phi) = \int_0^\Phi \frac{d\alpha}{\sqrt{1 - x^2 \cdot \sin^2 \alpha}} \text{ , } \mathbf{E_1}(x,\Phi) = \int_0^\Phi \sqrt{1 - x^2 \cdot \sin^2 \alpha}\, d\alpha$$

$$\mathbf{D}(x) = \frac{\mathbf{K}(x) - \mathbf{E}(x)}{x^2}$$

respectively the complete elliptic function of order 1 and 2,

$$\mathbf{K}(x) = \int_0^{\frac{\pi}{2}} \frac{d\alpha}{\sqrt{1 - x^2 \cdot \sin^2 \alpha}} \text{ şi } \mathbf{E}(x) = \int_0^{\frac{\pi}{2}} \sqrt{1 - x^2 \cdot \sin^2 \alpha}\, d\alpha$$

θ - angle of rotation (twist),

$$\theta = \arcsin\left(\frac{1}{k}\cdot\sqrt{\frac{k^2-\rho^2}{1-\rho^2}}\right) \qquad (6')$$

Knowing the tangential strain distribution on the two areas of contact surfaces ((5) for slip area and (6) for slick area), it is determined using pivot moment by integrating the strain:

$$M_t = \int_0^{a_H} 2\cdot\pi\cdot r^2\cdot\tau_{\theta z}dr = 2\cdot\pi\cdot f\cdot p_{oH}\cdot a_H^3\cdot\left[\int_0^k \rho^2\cdot\tau_{\theta z a1}d\rho + \int_k^1 \rho^2\cdot\tau_{\theta z a2}d\rho\right] \qquad (7)$$

or $$M_{at} = \frac{M_t}{f\cdot F_n\cdot a_H} = I(k) \qquad (7')$$

where $$I(k) = \int_0^k \rho\cdot\tau_{\theta z a1}d\rho + \int_k^1 \rho^2\cdot\tau_{\theta z a2}d\rho \qquad (8)$$

The integral I(k) has no analytical solution, so we will solve it numerically with the help of MATCHAD2000 utility.

In figure 4 it is exemplified dimensionless radius boundary areas stick and slip (k_e), depending on the dimensionless pivot moment M_{at} considered known.

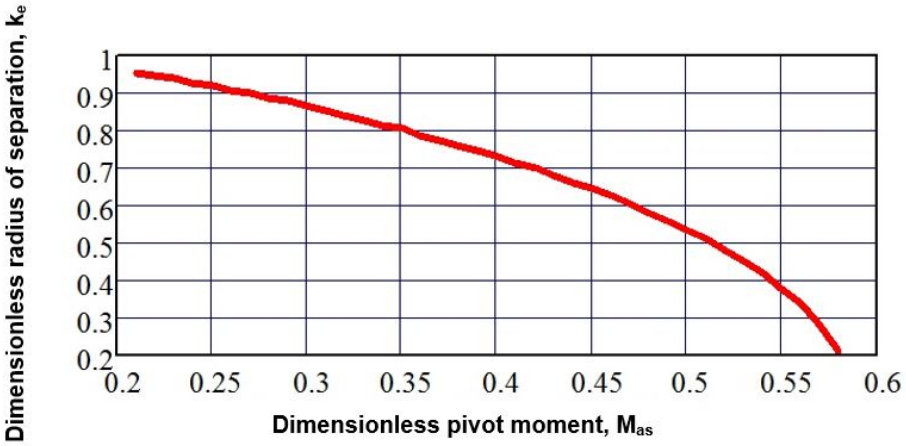

Figure 4. Dimensionless radius of separation (k_e) for stick and slip areas

Thus, it can be determined $\tau_{\theta za}$, the tangential strain from the circular area of contact. In figure 5 is exemplified the tension distribution for different pivot moment M_{at}.

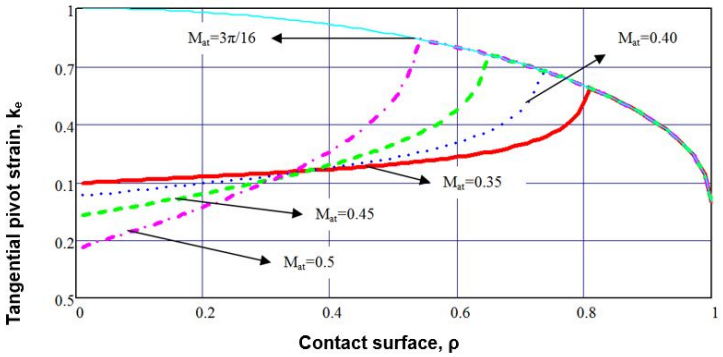

Figure 5. Pivot tangential strain distribution in the contact area

The corresponding angular deflection of the stick area ($0 \le \rho \le k_e(M_{at})$), determined by (6) is show in figure 6.

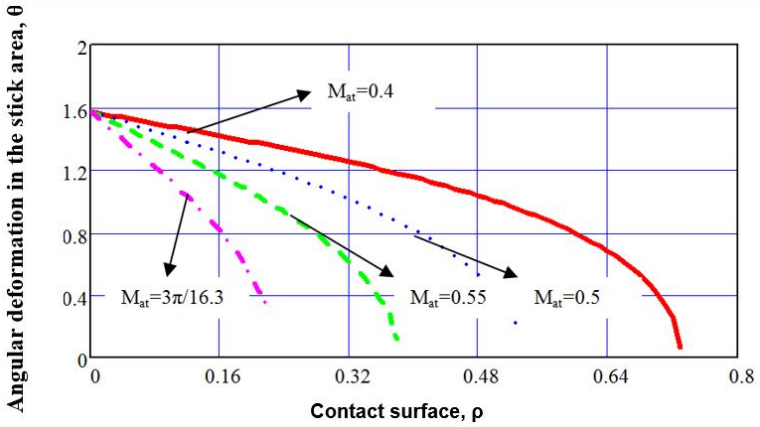

Figure 6. Angular deformation in the stick area

In order to analyze the state of tension and the effects of these strains on prosthesis material, it is assumed to determine the shear stress when pivoting point decreases and increases in a given interval.
For this is considered that pivoting point increase infinitesimal, from value 0 until the value M_s (dimensionless value M_{as}). $T_{\theta za}$ tangential strain can be observed in figure 7, suitable to the moment $M_{as}=M_{at}$.
At this pivoting moment reduces infinitesimal, so tangential strain and angular movement develops in the slip zone and has opposite sign than the adhesion zone (stick).

We will note with b, the ray disc (area) where the tensions change the sign and $b=\frac{b}{a_H}$ is the dimensionless radius of this ring.
To evaluate this radius is considered approximate solution given by Hills:

$$b_a=\frac{1}{\sqrt{3}}\cdot\sqrt{4\cdot\left(1-\frac{3\cdot(M_s-M_t)}{4\cdot f\cdot F_n\cdot a_H}\right)^{1/2}-1}=\frac{1}{\sqrt{3}}\cdot\sqrt{4\cdot\left[1-\frac{3}{4}\cdot(M_{as}-M_{at})\right]^{1/2}-1} \quad (9)$$

Using reasoning tangential strain from the stick and slip areas (relations 4 to 8) shall be deducted:

$$\tau_{az\theta s1}=-\sqrt{1-\rho^2}\text{ , for } b_a<\rho<1 \quad (10.1)$$

$$\tau_{az\theta s2}=-\sqrt{1-\rho^2}\cdot\left[1+\frac{4}{\pi}\cdot(1-b_a^2)\cdot\mathbf{D}(b_a)\cdot\mathbf{F_1}(b_a,\theta_s)-\mathbf{K}\left(\sqrt{1-b_a^2}\right)\cdot\mathbf{E_1}(b_a,\theta_s)\right]\text{, for} \quad (10.2)$$

$k_s\le\rho\le b_a$

$$\tau_{az\theta s3}=-\sqrt{1-\rho^2}\cdot\left[\begin{array}{l}1+\frac{4}{\pi}\cdot(1-b_a^2)\cdot\mathbf{D}(b_a)\cdot\mathbf{F_1}(b_a,\theta_s)-\mathbf{K}\left(\sqrt{1-b_a^2}\right)\cdot\mathbf{E_1}(b_a,\theta_s)-\\-\frac{2}{\pi}\cdot(1-k^2)\cdot\mathbf{D}(k)\cdot\mathbf{F_1}(k,\theta)+\frac{2}{\pi}\cdot\mathbf{K}\left(\sqrt{1-k^2}\right)\cdot\mathbf{E_1}(k,\theta)\end{array}\right]\text{, for} \quad (10.3)$$

$0<\rho<k$

where $\theta_s=\arcsin\left(\frac{1}{b_a}\cdot\sqrt{\frac{b_a^2-\rho^2}{1-\rho^2}}\right)$ (10.4)

Figure 7 presents the evolution of dimensionless tangential strain $\tau_{az\theta s}$ for different pivot moment on loading (M_{at}) and unloading (M_{as}).

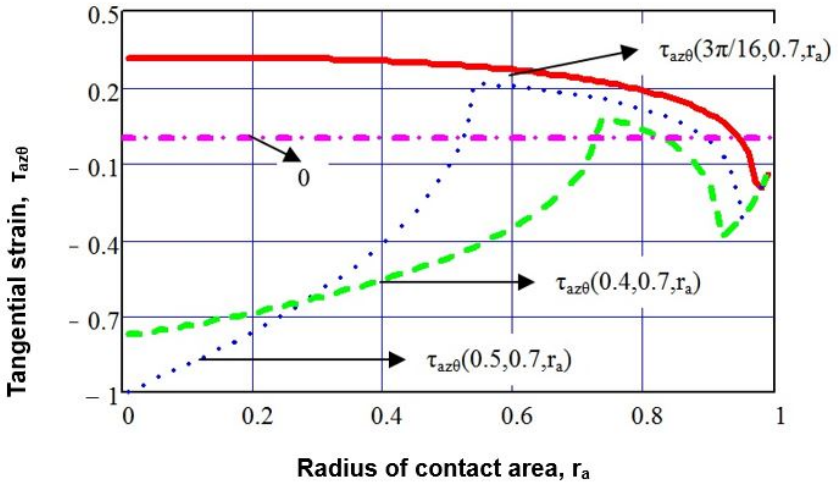

Figure 7. Tangential strain variation on loading and unloading pivoting moment

Applying Deresiewicz's solutions, it can be determined the energy consumed by friction on a cycle, which contributes to the deterioration in wear. So starting with defining the rigid angular deformation as:

$$\theta = \frac{3 \cdot M_t}{16 \cdot G \cdot a_H^3} \tag{11}$$

where G is the transverse modulus of elasticity of UHMWPE, the maximum energy lost per cycle is:

$$E_o = f \cdot F_n \cdot a_H \cdot \theta = \frac{3}{16} \cdot \frac{f^2 \cdot F_n^2}{G \cdot a_H} \tag{12}$$

it can determine the dimensionless energy lost through friction for an oscillating pivot point M_{as} (load-unload) :

$$E_{as} = \frac{E_s}{E_o} = \frac{256}{27} \cdot \left\{ \left[1 - \left(1 - \frac{3}{2} \cdot M_{as} \right)^{3/2} \right] - M_{as} \cdot \left[1 + \left(1 - \frac{3}{2} \cdot M_{as} \right)^{1/2} \right] \right\} \tag{13}$$

In figure 8 it can be observed the variation of the energy lost through friction (E_{as}) as an oscillating pivoting moment function (M_{as}).

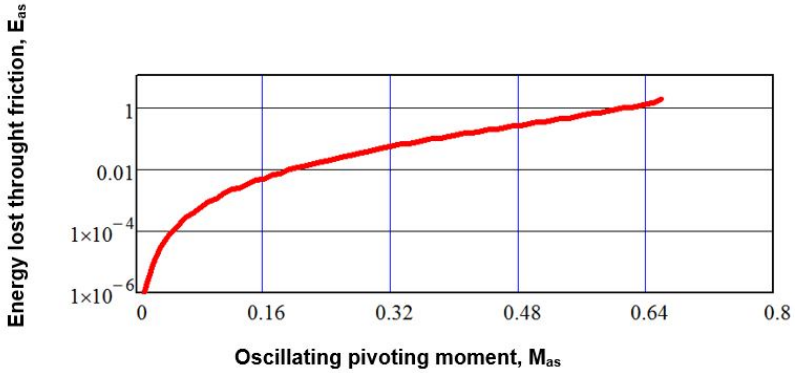

Figure 8. Variation of the energy lost through friction (E_{as}) as an oscillating pivoting moment

Under normal force action F_n and pivoting moment M_t, on the contact area can be observed normal and tangential strains. Depending on the size of pivoting moment, on contact surface can be found one of the two situations:

a) Total slip (full slip) through pivoting in any location of surface
b) Partial sliping through pivoting

Case a – Total slip

For the total slip case, the dimensionless tangential strain on θz direction has the form,

$$\tau_{a\theta z} = \sqrt{1 - \rho^2} \tag{14}$$

For tangential strain on rθ direction, is applied the Barber [6] solution. Abel integral form has the reverse expression of tangential stain:

$$w(\rho) = -\frac{2}{\pi} \cdot \frac{d}{d\rho} \cdot \left[\int_{\rho}^{1} \frac{t \cdot \tau_{\theta z a}(t) dt}{\sqrt{t^2 - \rho^2}} \right] \tag{15}$$

So it can be obtained

$$w(\rho) = \frac{2 \cdot \rho}{\pi} \cdot \left[\mathbf{K}\left(\sqrt{1-\rho^2}\right) - \mathbf{E}\left(\sqrt{1-\rho^2}\right) \right] \tag{16}$$

with complete elliptic integrals of the first (**K**(x)) and second order **E**(x), and x argument.

Tangential strain on rθ ($\tau_{r\theta}$) or dimensionless strain ($\tau_{a\theta r}$) $\tau_{a\theta r} = \frac{\tau_{\theta r}}{f \cdot p_{oH}}$ has as calculation expression:

$$\tau_{a\theta r} = \frac{1}{\rho^2} \cdot \int_{0}^{s} \frac{t \cdot w(t) - t^2 \cdot w'(t)}{\sqrt{\rho^2 - t^2}} dt \,, \tag{17}$$

where the limit integration s=ρ if ρ<1 and s=1 if $\rho \geq 1$, and $\omega'(t) = \frac{dw}{dt}$.
The numeric expression of relation 17 and analytical solution from relation 14 are illustrated in figure 9.

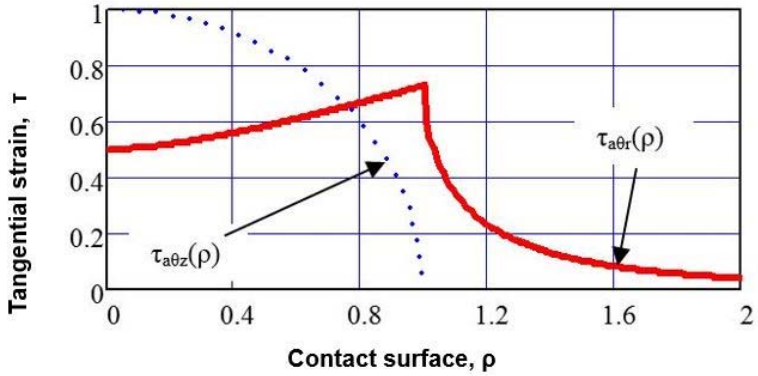

Figure 9. Tangential strain from contact surface in total sliding

Case b - Partial slip through pivoting

Tangential strains after θz direction are described with relations 5´ and 6. Inversing integral Abel to have direct solution 5´and 6 leads to

$$\omega_0(t) = -\frac{2}{\pi} \cdot t \cdot \left[\mathbf{F_1}(\chi_1 t_1) - \mathbf{E_1}(\chi_1 t_1) + \frac{\sqrt{1-k^2}}{k} \cdot \sqrt{k^2 - t^2} \right] \tag{18}$$

and

$$\omega_1(t) = \frac{2}{\pi} \cdot t \cdot \left[\mathbf{K}\left(\sqrt{1-k^2}\right) - \mathbf{E}(\sqrt{1-k^2}) - \mathbf{F_1}(\eta_1 t_1) + \mathbf{E_1}(\eta_1 t_1) \right] \tag{19}$$

in which $\chi = \arcsin\left[\frac{1}{k} \cdot \sqrt{\frac{k^2 - t^2}{1 - t^2}} \right]$ and $\eta = \arcsin \frac{\sqrt{1-k^2}}{t_1}$, with $t_1 = \sqrt{1-t^2}$.

With the help of relations 18 and 19 are deducted the expressions of tangential strains after the two directions θz and θr. So with the help of the following notations

$\rho_z = \left[4 \cdot z^2 \cdot t^2 + \left(\rho^2 + z^2 - t^2 \right)^2 \right]^{\frac{1}{4}}$; $\alpha = arctg\left(\frac{2 \cdot z \cdot t}{\rho^2 + z^2 - t^2} \right)$ results:

$$\tau_{a\theta zto} = \rho \cdot \int_{0}^{1} \frac{\omega_0 \cdot \sin\left(\frac{3 \cdot \alpha}{2} \right)}{\rho_z^{\,3}} dt \tag{20}$$

$$\tau_{ar\theta to} = 2\cdot\int_0^1 \frac{\omega_0\cdot\left(\rho_z\cdot\sin\alpha + z\cdot\sin\frac{\alpha}{2} + t\cdot\cos\frac{\alpha}{2}\right)}{\rho_z\cdot\left[\left(\rho_z\cdot\cos\frac{\alpha}{2}+z\right)^2+\left(\rho\cdot\sin\frac{\alpha}{2}+t\right)^2\right]}dt - \tag{21}$$

$$-\int_0^1 \frac{\omega_0}{\rho_z^{\,3}}\cdot\left(z\cdot\sin\frac{3\cdot\alpha}{2} - t\cdot\cos\frac{3\cdot\alpha}{2}\right)dt$$

$$\tau_{a\theta zt1} = r\cdot\int_0^1 \frac{\omega_1\cdot\sin\left(\frac{3\cdot\alpha}{2}\right)}{\rho_z^{\,3}}dt \tag{22}$$

$$\tau_{ar\theta t1} = 2\cdot\int_0^1 \frac{\omega_1\cdot\left(\rho_z\cdot\sin\alpha + z\cdot\sin\frac{\alpha}{2} + t\cdot\cos\frac{\alpha}{2}\right)}{\rho_z\cdot\left[\left(\rho_z\cdot\cos\frac{\alpha}{2}+z\right)^2+\left(\rho\cdot\sin\frac{\alpha}{2}+t\right)^2\right]}dt - \tag{23}$$

$$-\int_0^1 \frac{\omega_1}{\rho_z^{\,3}}\cdot\left(z\cdot\sin\frac{3\cdot\alpha}{2} - t\cdot\cos\frac{3\cdot\alpha}{2}\right)dt$$

Total tangential strains after θz and rθ directions will result after measuring the strains given by or ω_0 and ω_1:

$$\tau_{a\theta zt} = \tau_{a\theta zt0} + \tau_{a\theta zt1}\ ; \tag{24}$$

$$\tau_{ar\theta t} = \tau_{ar\theta t0} + \tau_{ar\theta t1}\ ; \tag{25}$$

Inside the stick area (0<ρ<k), tangential strains are:

$$\tau_{a\theta zs} = \frac{2}{\pi}\cdot\rho\cdot\sqrt{k^2-\rho^2}\cdot\int_0^{\frac{\pi}{2}} \frac{\left(1-k^2\right)\cdot\frac{\left(\sin^2\alpha\right)}{\left(1-\rho^2\right)}}{\left[1-\left(1-k^2\right)\cdot\frac{\sin^2\alpha}{1-\rho^2}\right]\cdot\sqrt{1-\left(1-k^2\right)\cdot\sin^2\alpha}}d\alpha, \tag{26}$$

for ρ>k,

$$\tau_{ar\theta s} = \frac{2\cdot\sqrt{1-k^2}}{3\cdot\pi\cdot\rho\cdot k}\cdot\left[2\cdot\left(k^2-\rho^2\right)\cdot\mathbf{K}\left(\frac{k}{\rho}\right)+\left(2\cdot\rho^2-k^2\right)\cdot\mathbf{E}\left(\frac{k}{\rho}\right)\right] - \tag{27}$$

$$-\frac{2}{\pi\cdot\rho^2}\cdot\int_0^k \frac{t^2}{\sqrt{\rho^2-t^2}}\cdot\left[\mathbf{E_1}\left(\sqrt{1-t^2},\chi\right)+\mathbf{E_1}\left(\sqrt{1-t^2},\eta\right)\right]dt$$

On the boundary of stick-slip, ρ=k, tangential strain $\tau_{ar\theta sc}$ is:

$$\tau_{ar\theta sc} = \frac{2\cdot\sqrt{1-k^2}}{3\cdot\pi} - \frac{2}{\pi\cdot k^2}\cdot\int_0^k \frac{t^2}{\sqrt{k^2-t^2}}\cdot\left[\mathbf{E_1}\left(\sqrt{1-t^2},\chi\right)+\mathbf{E_1}\left(\sqrt{1-t^2},\eta\right)\right]dt \tag{28}$$

Based on normal hertzian pressure,

$$p_{oa} = \frac{p_o}{p_{oH}} = \sqrt{1-\rho^2}\ , \tag{29}$$

and of tangential strains on rθ and zθ directions for different condition of pivoting it can be obtained the equivalent strain.

The effect of the contact pressure, relation 29, on strains from radial direction (σ_r), tangential (σ_θ) and normal (σ_z) for z=0 is [6]:

$$\sigma_{ar0} = \frac{\sigma_{r0}}{p_{oH}} = \frac{1-2\cdot\nu}{3}\cdot\left(\frac{1}{\rho^2}\right)\cdot\left\{1-\left(1-\rho^2\right)^{\frac{3}{2}}\right\} - \sqrt{1-\rho^2}\,, \tag{30}$$

with limit $\sigma_{ar0} = -\frac{1+2\cdot\nu}{2}$ when ρ→0;

$$\sigma_{a\theta 0} = \frac{\sigma_{\theta 0}}{p_{oH}} = -\frac{1-2\cdot\nu}{3}\cdot\left(\frac{1}{\rho^2}\right)\cdot\left\{1-\left(1-\rho^2\right)^{\frac{3}{2}}\right\} - 2\cdot\nu\cdot\left(1-\rho^2\right)^{\frac{1}{2}}, \tag{31}$$

with limit $\sigma_{a\theta 0} = -\frac{1+2\cdot\nu}{2}$

$$\sigma_{az0} = \frac{\sigma_{z0}}{p_{oH}} = -\sqrt{1-\rho^2}\,, \tag{32}$$

for interior of contact circle $(\rho \le 1)$ and

$$\sigma_{ar0} = -\sigma_{a\theta 0} = -\left(1-2\cdot\nu\right)\cdot\frac{1}{3\cdot\rho^2}, \tag{33}$$

for exterior of contact circle $(\rho > 1)$.

The maximum traction strain (positive strain) appear on the edge of contact circle (ρ=1),

$$\sigma_{ar\max} = \frac{\left(1-2\cdot\nu\right)}{3}, \tag{33´}$$

Strains along the z axis can be determined on the assumption of a concentrated force acting on a ring with radius ρ:

$$\sigma_{ar} = \sigma_{a\theta} = \frac{\sigma_r}{p_{oH}} = \frac{\sigma_\theta}{p_{oH}} = -\left(1+\nu\right)\cdot\left\{1 - z_a\cdot\tan^{-1}\left(\frac{1}{z_a}\right) + \frac{1}{2}\cdot\left(1+z_a{}^2\right)^{-1}\right\}, \tag{34}$$

$$\sigma_{az} = -\left(1+z_a{}^2\right)^{-1}, \tag{35}$$

with $z_a = \frac{z}{a_H}$.

Along the θz axis, strains σ_{ar}, $\sigma_{a\theta}$ and σ_{az} are the main normal strains (σ_1, σ_2, σ_3). Main shear strain

$$\tau_{a1} = \frac{\sigma_1}{p_{oH}} = \frac{1}{2}\cdot\left|\sigma_{ar} - \sigma_{az}\right|, \tag{36}$$

reaches the maximum value in the substrate material, according to Poisson ration (v).

In figure 10 and 11 can be observed normal strains after the radial (σ_{ar}), tangential ($\sigma_{a\theta}$) and axial (σ_{az}), generate by hetzian pressure (relation 29).

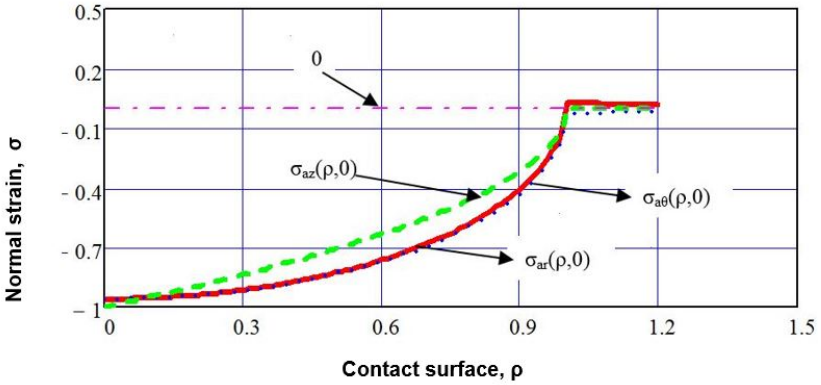

Figure 10. Normal stress distribution on the circular area of contact

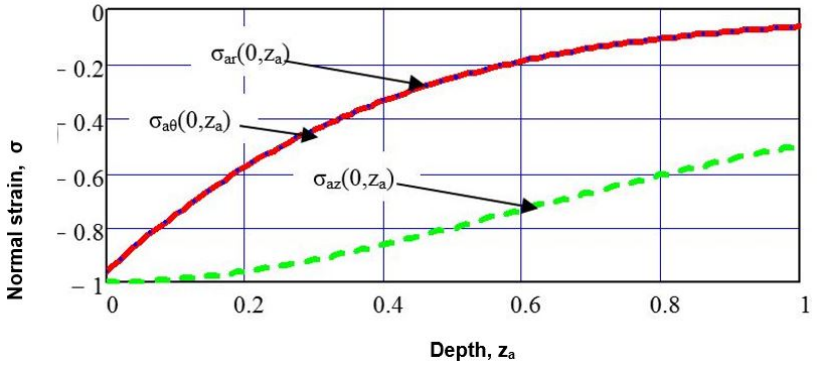

Figure 11. Normal stress distribution on polyethylene

CONCLUSION

From the analysis of the expression of major shear strain and the graph of dependence from dimensionless coordinate z_a (figure 12), it is clear that the deterioration of polyethylene starts from the point within the material situated at $z_a = 0.534 \ \left(z_1 = 0.875 p_{oH}\right)$ where the main tangential shear has maximum value $\tau_{a1} = 0.275 \ \left(z_1 = 0.875 p_{oH}\right)$.

The point with maximum shear strain is obtained provided the derivative putting providing is zero. These equations were solve using program Matchad2000.

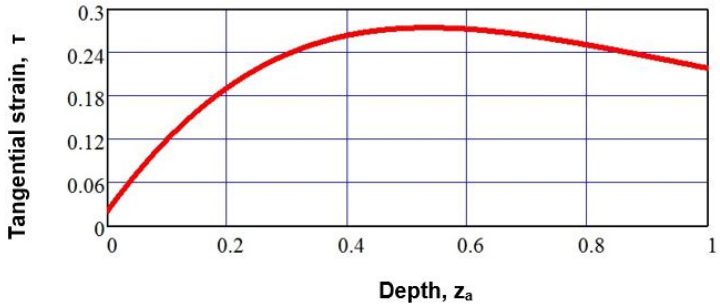

Figure 12. Variation with depth of main tangential shear

ACKNOWLEDGEMENT

The work has been funded by the Sectoral Operational Programme Human Resources Development 2007-2013 of the Ministry of European Funds through the Financial Agreement POSDRU/159/1.5/S/132395.

References

1. P. J. R. Clare K Fitzpatrick, "Estimating total knee replacement joint load ratios from kinematics," *Journal of Biomechanics,* vol. 47, pp. 3003-3011, 2014.
2. S. A. Atwood, John H. Currier, Michael B. Mayor and John P. Colli, "Clinical Wear Measurement on Low Contact Stress," *The Journal of Arthroplasty,* vol. 23, pp. 431-439, 2008.
3. L. A. Knight, Saikat Pal, John C. Coleman and Fred Bronson, "Comparison of long-term numerical and experimental total knee replacement wear during simulated gait loading," *Journal of Biomechanics,* vol. 40, pp. 1550-1558, 2007.
4. F. Jourdan, "Numerical wear modeling in dynamics and large strains: Application to knee joint prostheses," *Wear,* vol. 261, pp. 283-292, 2006.
5. S. Cretu, Contactul concentrat elastic- plastic, Iasi: Politehnium, 2009.
6. L. L. Johnson, Contact mechanics, Great Britain: University Press Cambridge, 1985.

CORRESPONDENCE

Alina Magdalena POPESCU
Department of Machine Elements and Tribology, “POLITEHNICA” University of Bucharest, Splaiul Independentei 313, Sector 6 Bucharest, Romania
e-mail: alinachesnoiu@gmail.com

Tribological Journal BULTRIB Vol. 5, 2015
Papers from the International Conference **BULTRIB '15**
September 11-13, 2015, Sozopol, Bulgaria
Society of Bulgarian Tribologists
FIT – Technical University of Sofia

UHMWPE BEHAVIOUR IN ROLLING WITH APPLICATION AT TOTAL KNEE PROSTHESIS

Alina Magdalena POPESCU, Georgiana Ionela PĂDURARU, Andrei TUDOR, Sorin CANANAU and Lucian SEICIU

Abstract: For total knee replacements, wear of the ultra-high molecular weight polyethylene (UHMWPE) tibial bearing surface is a frequent cause for long term revisions and failure. The purpose of the current study is to observe the way the rolling path is created on the UHMWPE plateau under load and establish the friction coefficient.

Key Words*:* UHMWPE behavior, knee prosthesis, rolling and sliding, wear, friction coefficient

INTRODUCTION

Total knee arthroplasty represents the last phase of treatment for the removal of pain on knee joints to regain mobility, only in the US in 2013 were made about 1 million interventions.

The knee joint is one of the most complex and one of the major joints of the human body, its complexity arises from the interaction of two contradictory concepts at first sight: stability - mobility. This dualism is found in both the normal knee biomechanics and prosthetic mechanics. Mechanical and tribological performance of total joint replacement components has been related to the stress state in ultra-high molecular weight polyethylene (UHMWPE).

Most of knee prostheses used are made from a component of CoCr (femoral component) which is articulated on a part of the UHMWPE (tibial plateau). Unfortunately from worn polyethylene occurs osteolysis leading to loss of mechanical prosthesis [1,2].

Understanding the mechanism of wear of UHMWPE is important to improve its performance in order to reduce the number of design revisions and prosthesis allowing patients return to a normal life.

Depreciation of UHMWPE is a complex process that depends on a number of factors that interact and lead to material degradation; special importance has the kind of movement that supports the polymer and the surface of contact between the femoral component and the tibial plateau [3, 4].

Shear movement in knees appears as a combination of internal-external rotation, flexion-extension, anterior-posterior and medial-lateral slip. All these movements lead to material changes in behavior resulting in increased wear rate of the polymer.

EXPERIMENTAL MODEL

Rolling tests were performed in the Department of Machine Elements and Tribology using tribological test stand Specimen CETR UMT Multi Test System. In the experiment were tested traces of roll on a plate made of UHMWPE for three types of bearings in dry medium and in the presence of saline (sodium chloride 0.9%).

Operating diagram of CETR UMT Multi Specimen Test System is shown in Figure 1. Equipment can execute rotation, translational or reciprocating speeds ranging from 0.1 μm/s to 10 m/s. The force is applied to the sample using the indenter, which may be kept constant or linear range from 0.5 N to maximum 1000 N.

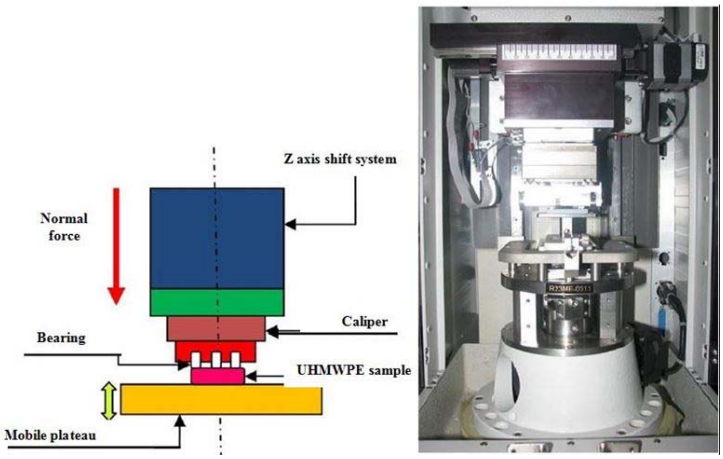

Fig. 1. The CETR Unit testing

Friction force (F_f), the normal force (N), the coefficient of friction (μ) and depth (z) can be recorded by data acquisition system. The experimental results were taken with the acquisition system, which can be viewed processed and interpreted by the control unit.

Polyethylene sheets, used to produce under laboratory conditions encountered in rolling motion of the knee prosthesis, specifically between the femoral head and tibial plateau, were tracked with an optical microscope. Stained rolling experimental tests were tracked using a graphical profiler to realize; their race-way both in the dry and in the lubrication and compare them.

Fig. 2. The profiler and sample UHMWPE

As a means of conducting the experiments for lubricating model: it was brought lubricant (sodium chloride) on the stage of the UHMWPE and turned on the test machine while the support plate made of UHMWPE polyethylene plate forward and backward movement, the bearing was reproducing the rolling movement. After 7200 cycles of rotation the test was stopped and the profiler was mounted on a stand and measured surface roughness and performed the graphics to observe the rolling slide. The experiment was reload for 14 400 cycles of rotation and for 21 600 cycles.

Testing sample of UHMWPE plate was divided into two areas: in the left side were made experiments to the dry environment and in right side were in lubricating environment. With control unit and data collection were recorded values of friction forces and the depth of penetration in UHMWPE testing sample.

In figure 3a) we can observe the evolution of depth in time in dry environment and in 3b) in lubricated environment.

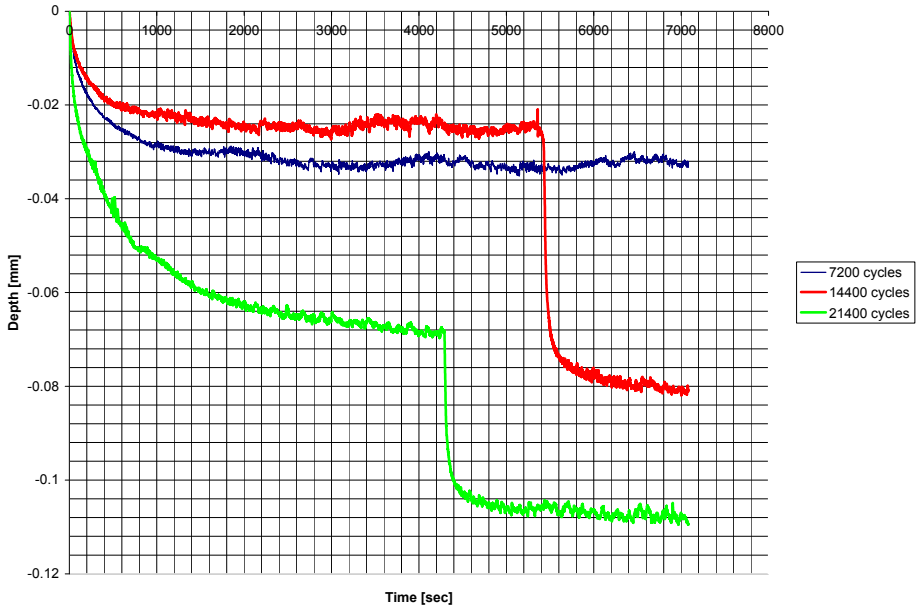

3a)

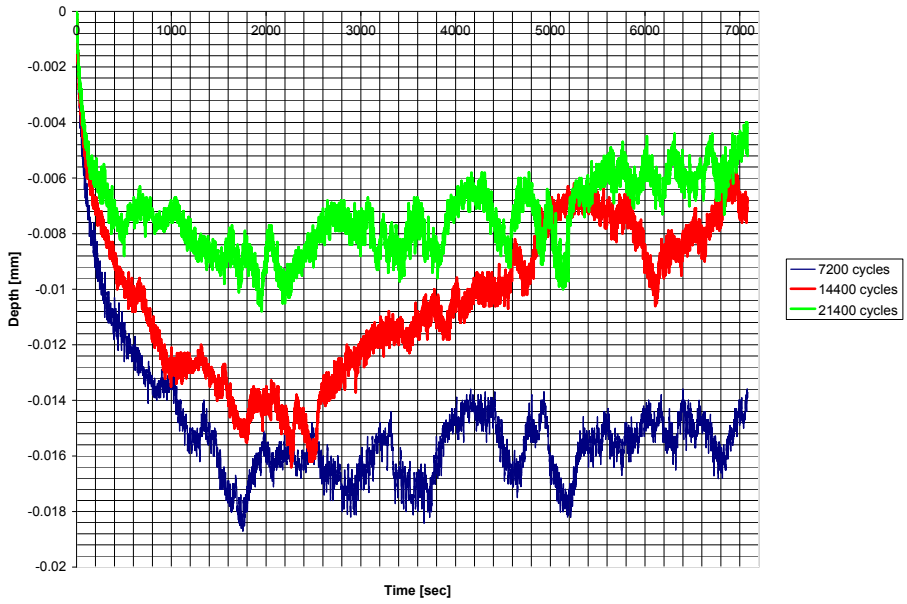

3b)

Fig. 3. Dependence of depth for lubrificated environment on UHMWPE sample

Knowing the friction force, F_f, we can determine the friction coefficient from relation 1:

$$F_f = \mu \cdot N \tag{1}$$

In Table 1 we can see the average for friction coefficients obtained in the two environments (dry and lubricated respectively) for different driving cycle's numbers.

Table 1 Friction coefficient average for the cycles of rolling

μ	7200 cycles	14400 cycles	21400 cycles
Lubricating contact	0.002945	0.002797	0.005658
Dry contact	0.006681	0.007755	0.007277

RESULTS AND CONCLUSIONS

Following the graphics it can be observed that the sample of UHMWPE used in laboratory experiments has a ductile material behavior, with large plastic deformations end effect is clearly laid out even with an open eye. The area is smooth running even glossy but may be seen in some parts of developing potential wear areas, figure 4.

Area	Area 1	Area 2	Area 3
Lubricating contact		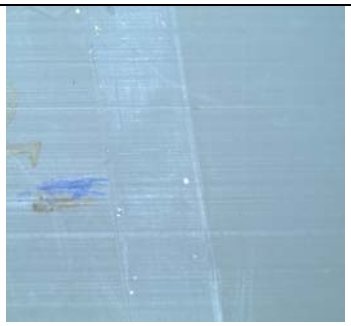	
Dry contact	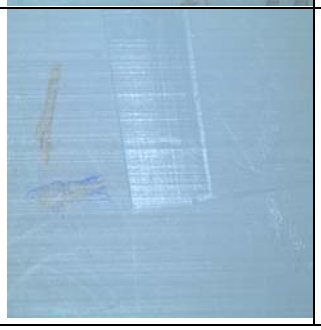		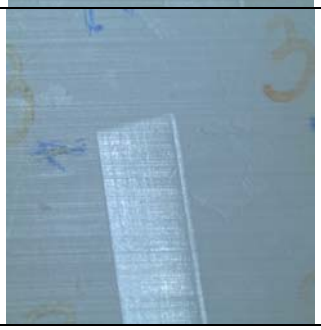

Figure 4. Optical images were can be observed the wear of rolling path

ACKNOWLEDGMENTS

The authors are very grateful to the leading staff of Machine Elements and Tribology Department for continuous support and collaboration to fulfill the experiments presented in this paper and to the leading staff of Centre of Technological Electronics and Interconnection Techniques – CETTI, which offered the supports for the optical measurements of the tested samples.

The work has been funded by the Sectoral Operational Programme Human Resources Development 2007-2013 of the Ministry of European Funds through the Financial Agreement POSDRU/159/1.5/S/132395.

REFERENCES

[1]. Eli W. Patten, Douglas Van Citters, Wear of UHMWPE from sliding, rolling, and rotation in a multidirectional tribo-system, 2013, WEAR, 304, pg. 60-66

[2]. S.M. KURTZ, K.L. ONG, E. LAU, Projection of primary and revisioon hip and knee arthroplasty in the United States fron 2005 to 2030, The Journal of Bone and Joint Surgery, 89, 2007, pg. 780-785.

[3]. S.M. Kurtz, K.L.ONG, J. SCHMIER, F. MOWAT, Futur clinical and economic impact of revision total hip and knee arthroplasty, The Journal of Bone and Joint Surgery, 89, 2007, pg. 144-151.

[4]. D. Y.R.CHONG, Ulrich N. HANSEN, Andrew A. AMIS, Analysis of bone–prosthesis interface micromotion for cementless tibial prosthesis fixation and the influence of loading conditions, Journal of Biomechanics, vol 43, 2010, pg. 1074–1080

[5]. Brandi CARR, Tarun GOSWAMI, Knee implants – Review of models and biomechanics, Materials and Design, vol 30, 2009, pg. 398 – 413

CORRESPONDENCE

Alina Magdalena POPESCU
Department of Machine Elements and Tribology, “POLITEHNICA” University of Bucharest, Splaiul Independentei 313, Sector 6 Bucharest, Romania
e-mail: alinachesnoiu@gmail.com

Tribological Journal BULTRIB Vol. 5, 2015
Papers from the International Conference **BULTRIB '15**
September 11-13, 2015, Sozopol, Bulgaria
Society of Bulgarian Tribologists
FIT – Technical University of Sofia

CONSIDERATIONS REGARDING T HE XC 45 HARD CHROME PLATED MATERIAL IN CONDITIONS OF DRY FRICTION AND HIGH TEMPERATURE

Dr.ing. M.T. POPESCU[1], prof.dr.ing. N. POPA[1], prof.dr.ing. R.N. Dobrescu[1], s.l.dr.ing. C. Onescu [1] , Jean Denape[2]
[1] – Pitesti University, Romania, [2] – ENI Tarbes, France

Abstract: *The XC 45 steel usage in machines construction is frequent. That is the reason we choose to use a chrome coverage treatment of the surface, in order to offer superior mechanical properties in dry friction and high temperature conditions. This paper highlights the results obtained on a disk-pawn tribometer.*

1. INTRODUCTION

Machines construction industry is the most important metallic materials consumer in this economy. According to the functional role and the exploitation specific solicitations, every machines parts or tools category is made from certain metallic materials, which have to maximum satisfy the imposed requirements with a minimum budget cost.

In certain conditions that may appear during a mechanical system activity (for example: poor or zero lubrication), we cannot take into consideration the friction wear resistance characteristics of the metallic materials we use in the present. As result, it is required to cover the surface in friction with certain materials that have superior tribological properties and a good adhesion to the metal support. These materials may be metallic (as chrome) ceramics (carbide, bromide) or composites (NiP + talcum, NiP + SiC etc.)

Many mechanical properties modification modern technologies are used in the industry due to the fact that frequently used traditional materials cannot offer superior mechanical properties. Chrome plating is a pretty heavy coverage and it is applied to a large range of materials, including stainless steel, cast iron, aluminium alloys, titanium, cooper, bronze, nickel. This study is made on high quality carbon steel used at gearbox, in the automobile industry.

The hard chrome plating operation advantages target the following characteristics:

- A higher hardness (~ 1000 HV);
- Very good tribological properties: low friction coefficient, wear resistance (approximatively 200 times) in relation to other hardening treatments, especially in dry friction situations;
- High protection level against corrosion;
- Prolonged exploitation duration and product lifetime extension;
- Cost reduction in relation to other technologies.

2. USED MATERIALS AND APPLIED TECHNOLOGY

XC45 was the material used in the study. The samples on which the hard chrome plating is applied have the geometrical form of a disc with the exterior diameter of ϕ 37mm. There were used 22 samples, 10 for chrome plating at 30 μm thickness and 11 for chrome plating at 50 μm. A blank piece was left for each chromed group.

Before the layer deposition, the support material is heat treated (matertensitic hardening, then high return). No other thermal or thermo-chemic treatments are made after chrome plating.

The chrome plating bath contains trivalent chromic acid. The piece is linked to the cathode and the anode is made of Pb (99% purity). The continuous current density is of 30 A/ dm^2, the chromed plating surface calculated current was set at 48A. The bathroom temperature is 55^0C, the tension is 4 V. The chrome plating speed is 25 μm/h.

The steel chemical composition is the following: 0,46%C; 0,65%Mn; 0,35%Si.

Figure 1 presents hard chrome plating steel sample microstructure XC45 and figure 2 shows the surface image after correction.

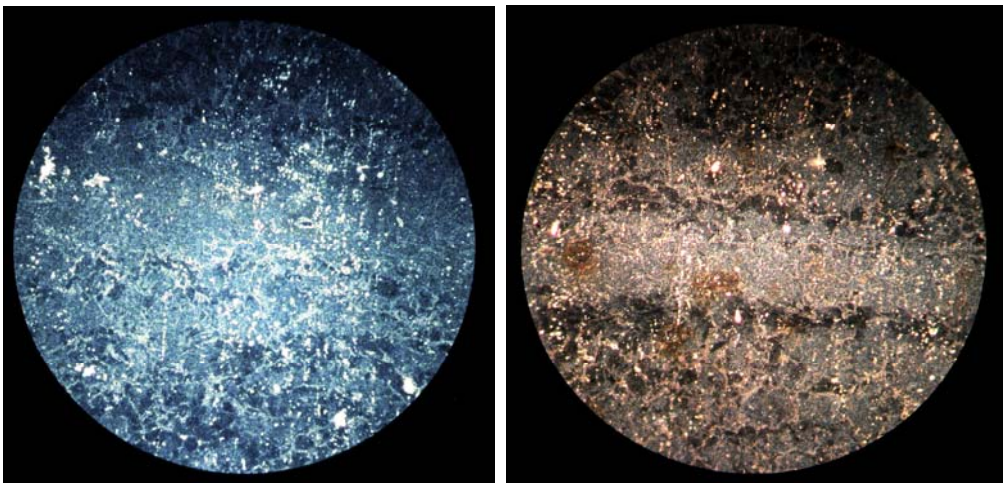

Fig. 1. Steel sample microstructures OLC 45, with hard chrome deposits (transversal sections; attack reactive: nital 2%; increase: 500 ×)

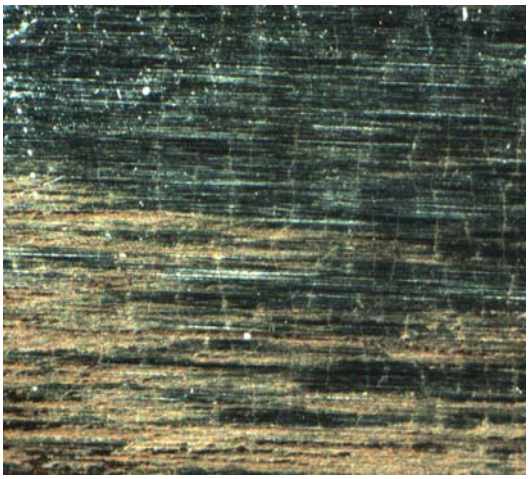

Fig. 2. Hard chrome layer surface image (after correction): remaking traces are observed (horizontal) and the characteristic cracks of the chrome deposits (perpendicular to the remaking traces), under the surface remaking affected layer

At the deposition speed of ***v = 0,25 μm/h,*** in order to deposit a hard chrome layer with thickness ***s*** ≈ 110 μm, the process lasts t = s/v, meaning t = 110/25 = 4,4 h.

The deposition characteristics:

- Chrome layer thickness: 50 μm and 30 μm;
- Hardness: 1000 – 1100 HV100;
- Micro cracks: > 400 micro cracks/cm.

The chrome layer roughness filed on the disk samples, after correction, was measured with the SURTRONIC 4 device. Three samples from the first group were used and the obtained results are written in the table 1.

Table 1. Hard chrome layer roughness after correction

Sample nr	R_a, μm	R_z ISO, μm	Observations
7	3,13	12,85	Reference lenght: 0,8 cm Filter: CR
	2,92	10.87	
9	1,79	7,08	
	2,41	9,74	
10	0,47	2,56	
	0,38	1,86	
	0,43	2,68	

3. TRYING CONDITIONS

One of the mechanical pieces malfunctions comes from the movement surfaces friction. The friction surfaces wear is often produced during the working activity, through rising temperature, geometry change (shape, dimensions), chemical-physical transformations or even material losses.

One of these paper objectives is first to understand the load and speed parameters influence on the steel tribologic behaviour and particularly to study the friction coefficient and wear evolution in time, according to the above mentioned parameters.

The main principle of the tribological wear study devices is to create friction between two pierces, one of them a fixed one. The wear is characterized by the material quantity lost during the friction. The most used method regards a rod called pawn, which rubs a disk (pawn-disk). A determined force is applied to the pawn which usually has a cylindrical surface and rubs the circular movement disk. This is one of the principles used in the wear standard test according to ASTM.

The used tribometer is based on the above mentioned principle.

This was made by Adamou [1] in the tribologic laboratory of ENI Tarbes (fig.3). The contact configuration is pawn-disk type.

It responds to the following technical specifications:

- The adopted contact configuration is fixed plan pawn – turning disk type;
- Vacuum chamber at 10^{-6} mbar, with gas introduction possibility;
- The samples temperature is provided to vary between 20^0 la 900^0 C;
- The normal load is between 1 la 100 N;
- The sliding speed may vary between 0,01 şi 1,5 m/0.

The samples are mounted at two coaxial vertical axles. The cylindrical pawn and the disk have the 6 mm, respectively 37 mm diameters. The contact surface is 28 mm^2 long. The pawn length is 15 mm. The load is made using gravity (marked masses) at the tribometer superior part, at the device exterior. The direct verification is made with a tensile- compression strength captor, located between pawn and disk, in order to standardize the load before the attempts (fig. 4).

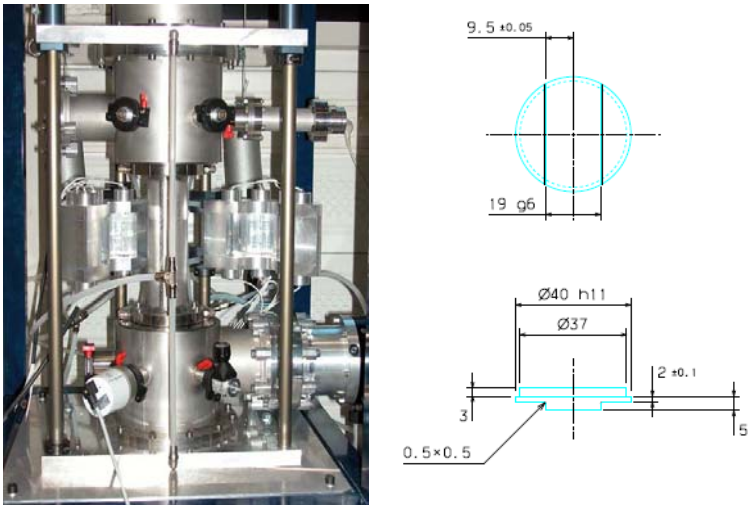

Fig. 3. The attempt device and the samples and pawn device

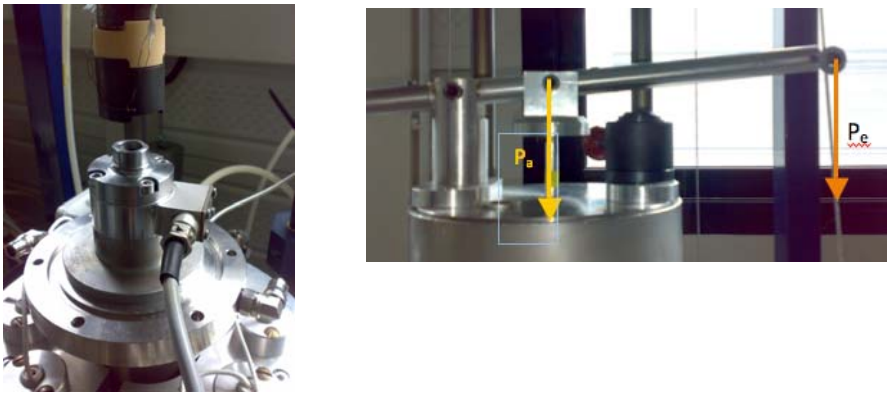

Fig.4 The axial load determination scheme (P_a)

The data acquisition is made continuous with the help of a HBM console, type SPIDER 8, linked to a PC on a parallel post.

The attempts were made in the following conditions:

- First attempt (fig.5);
- Temperature: 300^0 C± 5^0 C;
- Speed: constant of 0,25 m/s;
- Load: cumulative from 2,5 N to 40 N, with levels of 2,5 N, each of them 300 s;
- Total time: 65 minutes;
- The exterior relative humidity: approximately-5 %
- Second attempt (fig.6):

- Temperature: 300^0 C ± 5^0 C;
- Speed: cumulate from 0,1 m/s to 1,5 m/s using layers of 300 s;
- Load: constant of 15 N;
- Total time: 35 min;
- Exterior relative humidity: approximately 65 %

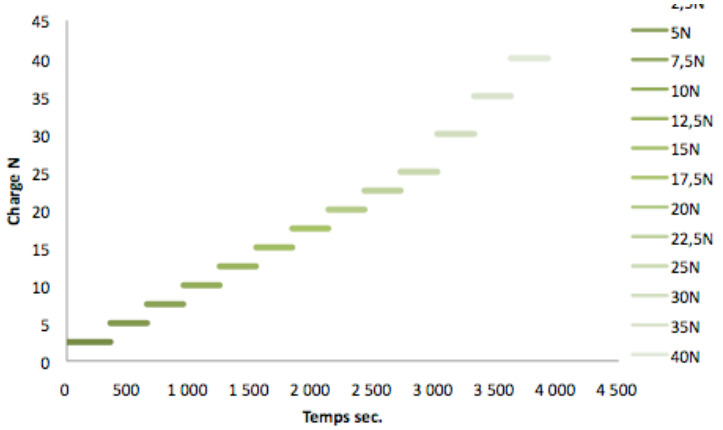

Fig. 5. Constant load attempt

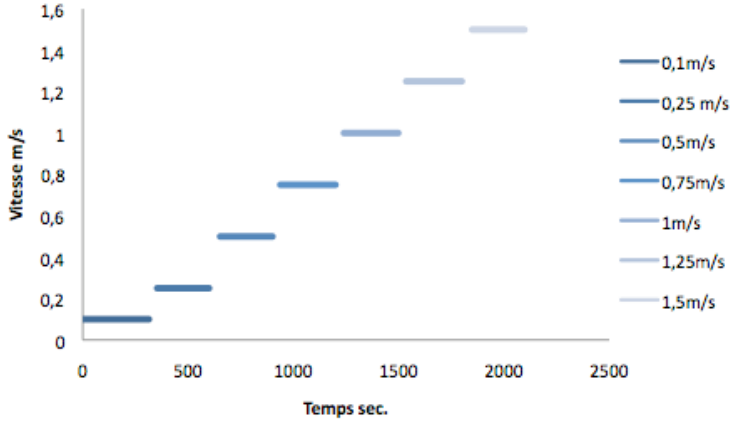

Fig. 6. Cumulate speed attempt

During the attempt, the following parameters were registered, with the captors help:

- The friction coefficient as ratio between tangential force and normal force, in ASCII format under EXCEL;
- Samples vertical movement, represented as material wear
- Friction coefficient evolution in relation to time;
- Contact surface temperature

The plane friction surface pawn is from steel material „Stub" X22CrNi17, hardness 247 HV_{30}.

Samples' heating is made using collar internal surface radiation. The increase of the samples temperature is very fast (in 7 minutes temperature increases from 20 to 900^0 C). Temperature is the same on all the disk surfaces.

The used characterized means are the optical microscope (binocular LEICA), electronic microscope with scanning coupled to X energy dispersion analyser (MEB Philips SEM 515) and the optical profilometer (VEECO NT 1100).

4. RESULTS

Starting from the registered values by the couple captor (Nm) and knowing the average radius of the disk friction track (r = 0,0135 m) and the normal force applied to the pawn, the friction coefficient evolution in time can be followed.

For the steel (pawn) / chrome steel friction couple, the friction coefficient is 0,3 for the first load of 2,5 N. Between 5 N and 40 N, this coefficient has an oscilattory variation from 0,6 and 0,7 (fig. 7)

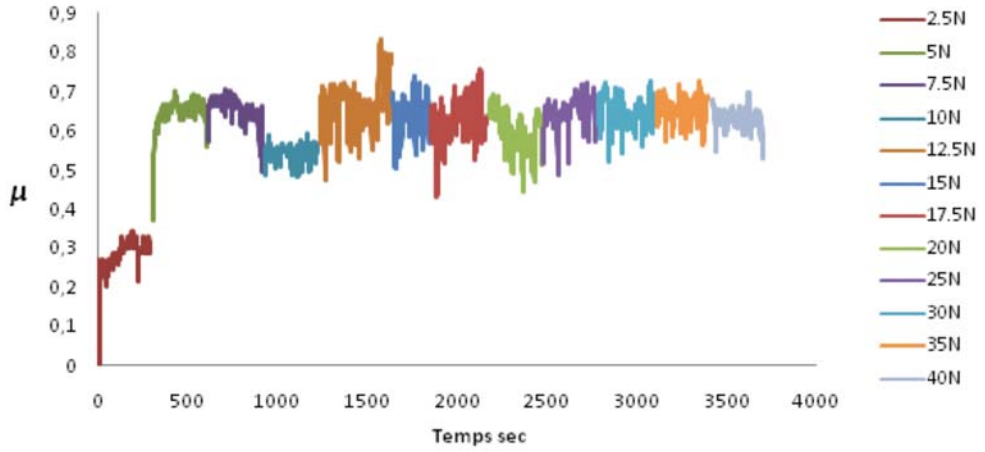

Fig. 7. Chrome steel friction coefficient evolution in time, for a constant speed of 0,25 m/s and a cumulative load at 300^0 C

Figure 8 shows the friction coefficient variation at second attempt.
Figure 9 represents the friction coefficient estimation at constant load and cumulative variable speed.

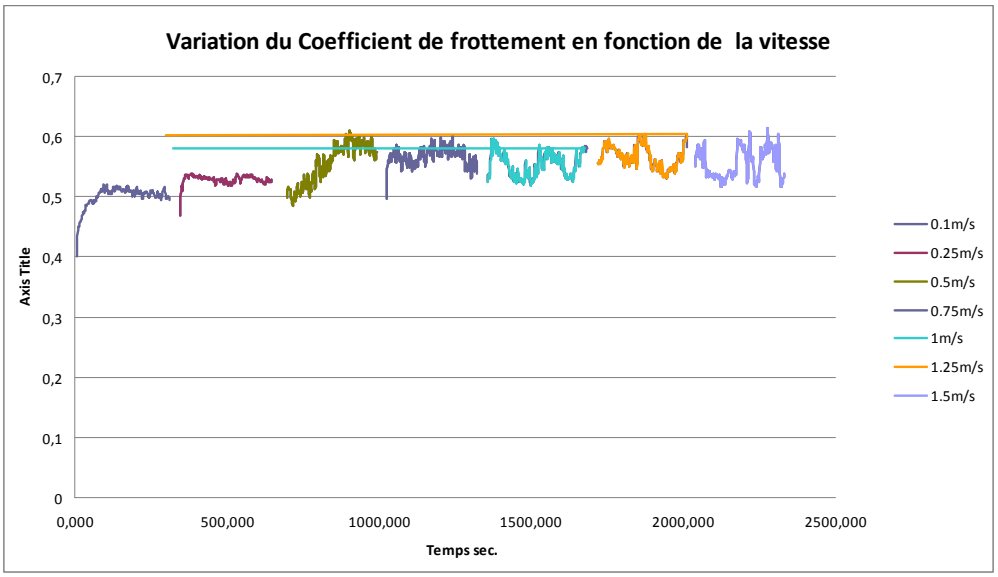

Fig. 8. Friction coefficient evolution at constant load and cumulative speed

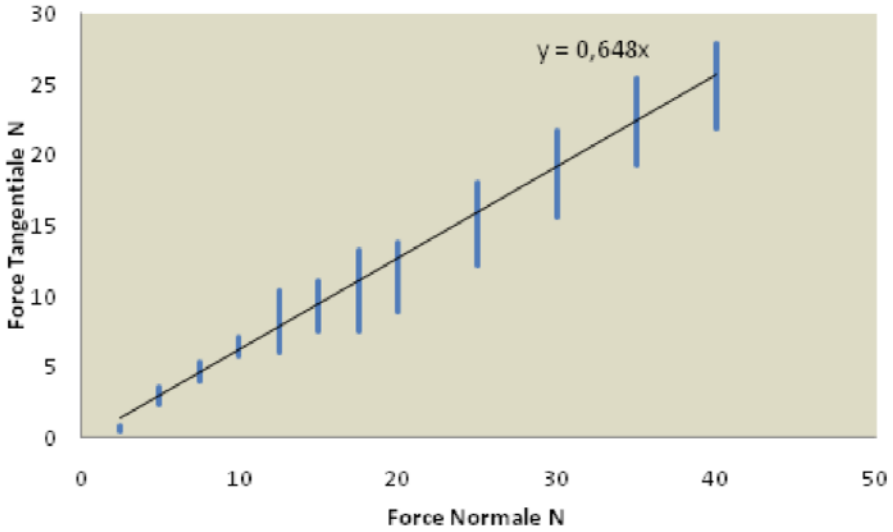

Fig. 9. Average friction coefficient estimation

A global average value is obtained μ = 0,65 (see table 2)

Table 2. Friction coefficient values at load speeds

	Moyenne
m/s	μ
0,1	0,5008363
0,25	0,5287197
0,5	0,5562374
0,75	0,5671996
1	0,5532789
1,25	0,5667199
1,5	0,5554559

5. CONCLUSIONS

This study describes the tribologic behaviour analyse at 400^0 C temperature for XC45 hard chrome material. Its friction coefficient is lower than alloyed steel [4] and also the wear is lower.

From the chrome treatment point of view, the following conclusion is drawn in relation to the advantages mentioned in introduction: it assures a better resistance and it is a future oriented process, combined with an environment advanced technology.

ACKNOWLEDGEMENT

The authors thank the students professionalism shown in the conducting tests.

REFERENCES

1. Adamou, A.S. Thèse dẹ L'Institut National Polytechnique de Toulouse, France, 2005;
2. Dalverny, D. Thèse de l Universitè de Bordeaux, France, 1998;
3. Denape, J. Introduction a la TRIBOLOGIE. Frottement et usure des Materiaux. ENI Tarbes 2008-2009;
4. Popescu, M.T., Alexis, J. Recherches concernant le comportament des aciers revêtus au frottement sec et a haute temperature. Ingineria Automobilului, nr. 14, martie 2010;
5. Popa, N., ş.a. Elemente de Tribologie. Editura Universităţii din Piteşti, 2007.
6. Popescu, M.T. Contribuţii la analiza comparativă a parametrilor tribologici pentru straturi de depunere NIP-talc şi cromare dură pe suport de oţel. Teză de doctorat, Universitatea din Piteşti, 2013.

Tribological Journal BULTRIB Vol. 5, 2015
Papers from the International Conference **BULTRIB '15**
September 11-13, 2015, Sozopol, Bulgaria
Society of Bulgarian Tribologists
FIT – Technical University of Sofia

RESEARCH THE WEAR RESISTANCE OF MULTILAYER COATING Ti/TiN/CrN-ml DEPOSITED ON 1.7034 STEEL

Velko RUPETSOV; Stefan DISHLIEV; Raicho MINCHEV; Georgi MISHEV; Ivan IANCHEV; Milko ANGELOV

Abstract: *Increasing the living resources of the machines and apparatus is of particular importance for the economic performance of companies in the mechanical engineering and food industry. The current work refers to wear resistance investigation of multilayer nanocomposite coating Ti/TiN/CrN-ml, deposited on 1.7034 steel. The proposed methodology for experimental investigation used "Ball on Flat Sliding Wear Test" friction system. The coating Ti/TiN/CrN-ml is applied by PVD method. Experimental studies were conducted to determine the effect of normal load on the wear intensity. On the basis of the results relevant conclusions and recommendations were made.*

Key Words: *Hard coatings, Nanolaminate, Tribology, PVD, Wear intensity.*

ИЗСЛЕДВАНЕ НА ИЗНОСОУСТОЙЧИВОСТТА НА МНОГОСЛОЙНО ПОКРИТИЕ Ti/TiN/CrN-ml ОТЛОЖЕНО ВЪРХУ СТОМАНА 1.7034

Велко Рупецов[1], Стефан Дишлиев[2], Райчо Минчев[1], Георги Мишев[3], Иван Янчев[2], Милко Ангелов[4]

[1]ПУ„Паисий Хилендарски“ Пловдив - Технически колеж Смолян, България
[2]Катедра” Машини и апарати за хранително-вкусовата промишленост” – Университет по хранителни технологии гр. Пловдив, България
[3]Катедра „Машиностроителна техника и технологии“, Технически университет София, Филиал Пловдив, България
[4]“Милко Ангелов Консулт Ко” ЕООД, Пловдив, България

Резюме: *Повишаването на жизнения ресурс на машините и апаратите е от особено значение за икономическите показатели на фирмите от машиностроенето и хранителната промишленост. Настоящата статия се отнася до изследване на износоустойчивостта на многослойно нанопокритие Ti/TiN/CrN-ml, отложено върху конструкционна стомана 1.7034. Предложената методика за експериментално износване се базира на триещата система "Ball on Flat Sliding Wear Test". Нанопокритието Ti/TiN/CrN-ml е нанесено по метода PVD. Проведени са експериментални изследвания за определяне на влиянието на нормалното натоварване върху интензивността на износване. На база на получените резултати са направени съответни изводи и препоръки.*

Ключови думи: *Твърди покрития, Наноламинат, Трибология, PVD метод, Интензивност на износване.*

1. ВЪВЕДЕНИЕ

При експлоатационни условия повърхностните слоеве на триботехническите системи са подложени на уморни, корозионни, топлинни, адхезионни, абразивни и др. въздействия, затова структурата и физико-механичният комплекс от свойства на тънкия повърхностен слой на материала имат важна роля за процеса износване.

Повишаването на износоустойчивостта на триещите се машинни части е един от основните проблеми в практиката за увеличаване живота на машините, а следователно и голям източник за икономия. Този проблем има голямо значение при разработване на нови машини и инструментална екипировка, където се наблюдава постоянна тенденция за повишаване на скоростта, температурата, за увеличаване на механичните напрежения при работа на подвижните съединения, като същевременно се запазва тяхната сигурност и дълготрайност.

Един от най-перспективните методи за повишаване на износоустойчивостта е нанасянето на покрития на работните повърхнини, затова основните усилия са концентрирани преди всичко в развитието на ефективни и функционални съставки на покритията, които да намерят приложение в силно натоварени трибосистеми [10]. Тези покрития гарантират повишаване на скоростта на работа, използване на тежки работни режими (вкл. без охлаждаща течност), по-висока химическа и оксидационна устойчивост, намалено износване и др. [1, 7, 8, 9].

Нитридите на Ti и Cr, комбинирано използвани в подобни покрития, отдавна са доказали своята практическа стойност и са обект на много изследвания [2, 5].

В момента много актуално направление при твърдите покрития е нанасянето на многослойни TiN/CrN покрития с много малък модулационен период (обща дебелина на два различни слоя изграждащи наноламинат) - от порядъка на няколко нанометра [3, 5]. Подобни структури, известни като свръхрешетки или наноламинати, позволяват както умело да се комбинират качествата на отделните слоеве, така и придобиване на нови свойства от цялостното покритие. Например, малкия модулационен период гарантира бързо нарастване на нови кристални структури с различна константа на решетката една върху друга, което силно затруднява развитието на дислокации в цялостното покритие, като така се увеличава твърдостта. Това е една от причините, позволяващи да се достигне твърдост, която може да надмине твърдостта на по-твърдия от изграждащите слоеве. Също така, типичната колонна структура на класическите покрития от твърд разтвор значително понижава оксидационната и химическата устойчивост поради възможността на реагента да се придвижи между колоните до самата подложка. При наноламинатите, поради споменатия по-горе ефект, това се случва много по-трудно. Други предимства са намаленото напрежение в покритието (което частично се разтоварва между отделните слоеве), повишена контактна якост, отлична адхезия и др. Необходимо е да се подчертае, че споменатите наноламинати са качествено по-успешно решение от класическите многослойни покрития, където отделните слоеве са с дебелина от порядъка много над 100 нм, които са вече напълно усвоена и проучена технология.

В настоящата работа се разглежда Ti/TiN/CrN-ml покритие нанесено чрез Physical Vapor Deposition (PVD) върху стомана 1.7034. Тази стомана намира приложение при изработването на оси, валове, зъбни колела, бутала, пръти, колянови валове, пръстени, вретена, дорници, ленти, болтове, втулки и др. елементи с висока якост. Проведени са еднофакторни експериментални изследвания за определяне на влиянието на нормалното натоварване върху интензивността на износване. Износването е определено по обемния метод [4,6].

2. ПОДГОТОВКА НА ОБРАЗЦИТЕ

Опитните образци са изработени от конструкционна стомана 1.7034 (37Cr4) със състав: C – 0,36÷0,44 %; Si – 0.17÷0,37 % ; Mn – 0,5÷0.8 %; Ni до 0,3%; S – до 0,035%; P - до 0,035 %; Cr – 0.8÷1,1 %; Cu до 0,3 %. Образците имат форма на правоъгълен паралелепипед с размери LxBxH, mm = 25x8x5 (виж фиг.1).

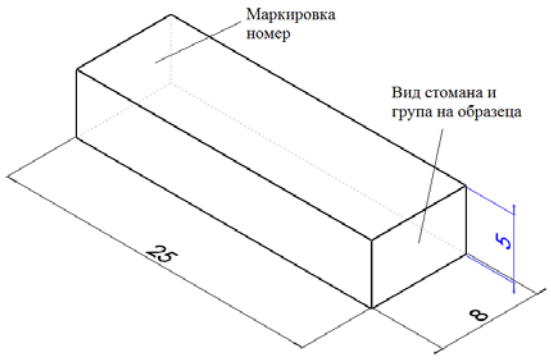

Фиг. 1. Форма, размери и маркировка на опитните образци

Подготвени са три групи образци:

A – Незакалени шлифовани;
B – Закалени шлифовани;
C – Закалени полирани.

Възприето бе следното означение на образците и бе направена маркировка по неработните им повърхнини.

Пример:

1_1.7034_A – образец 1 от стомана 1.7034 – незакален шлифован;
1_1.7034_B – образец 1 от стомана 1.7034 – закален шлифован;
1_1.7034_C – образец 1 от стомана 1.7034 – закален полиран.

Термообработката на образците е извършена в камерни пещи с температури, достигащи до 1100 °C – марка СНОЛ - М, Балчик.

Покритието е отложено чрез Closed Field Unbalanced Magnetron Sputtering (CFUBMS) на индустриална установка HVP100RHD в Нанотех груп ООД – Пловдив. Статичен коефициент на триене – 0,25 ±0,03 (измерен срещу полирана SS 304 L).

Цветът на покритието е златисто жълт. Общата дебелина на слоя е 3,1 μm ±0,05 μm. Първоначално се нанасят градиентни адхезионни слоеве с обща дебелина 0,9 μm: Ti -100 nm/TiN - 250 nm/TiCrN - 550 nm. Следва създаването на наноламинат, съставен от редуващи се слоеве от TiN и CrN с единична дебелина от около 10 ÷ 15 nm (модулационен период от 20 ÷ 30 nm). На края се нанасят градиентни външни слове с обща дебелина 0,5 μm: TiCrN - 350 nm/TiN -150 nm. Поради това, че наноламинатната структура оказва най-голямо влияние върху свойствата на това покритие, се използва обозначението: Ti/TiN/CrN-ml (със съгласието на компанията).

Отлагането се извършва при 170 °C.

Данни за изпитваните образци са посочени в табл.1.

Табл. 1. Изпитвани образци

Образец		**Вид покритие**	**Твърдост преди покритие**	**Грапавост образец *Ra,* μm**	**Грапавост на покрит образец *Ra,* μm**
1.7034_A	незакален, шлифован с покритие	Многослойно покритие (наноламинат) *Ti/TiN/CrN –ml +TiN top*	24 HRC (217HB)	0,120	0,117
1.7034_B	закален, шлифован с покритие		51.5 HRC	0,089	0,086
1.7034_C	закален, полиран с покритие		51.5 HRC	0,026	0,031
E_1.7034_A	незакален, шлифован	без покритие	24 HRC (217HB)	0,120	-
E_1.7034_B	закален, шлифован		51.5 HRC	0,089	-
E_1.7034_C	закален, полиран		51.5 HRC	0,026	-

3. МЕТОДИКА ЗА ЕКСПЕРИМЕНТАЛНО ИЗСЛЕДВАНЕ НА ИЗНОСОУСТОЙЧИВОСТТА ПО ОБЕМНИЯ МЕТОД НА ТЪНКИ, ТВЪРДИ ПОКРИТИЯ

Износоустойчивостта на покритието бе оценена със стенд СИИП-1 [6] в Технически колеж - Смолян.

Експерименталните изследвания са проведени при схема на триене по метод „Ball on Flat Sliding Wear Test“ при хоризонтална ориентация на тестваната повърхност. За контратяло се използва минералокерамична сачма от Al_2O_3 с диаметър d = 3,0 mm, фиксирана в държач. Контратялото се трие по линейно възвратно-постъпателно движещ се образец (Reciprocation drive) без наличие на смазочен материал и работа на въздух при стайна температура. Върху контратяло се прилага натоварване от 1; 2; 3; 4 и 5 N. Ширината на браздите е измерена с микроскоп: безконтактна PC базирана измерителна система TESA VISIO-300 със увеличение x100 (разрешаваща способност 0,001 mm). Определя се средната стойност на широчината $b_{ср}$:

$$b_{cp} = \frac{1}{n}\sum_{i}^{n} b_i \text{ , mm} \quad (1)$$

Интензивността на износване I_w се определя със зависимостта:

$$I_w = \frac{V}{F.L} \text{, mm}^3\text{/N.m} \quad (2)$$

където:

V е обемът на количеството снет материал (следата), mm^3;

F е нормалното натоварване, N;

L е изминатият път или пробег на образеца спрямо контратялото, m.

Обемът на следата се определя по методика описана в [4,6].

4. ИЗСЛЕДВАНЕ ВЛИЯНИЕТО НА НОРМАЛНАТА СИЛА ВЪРХУ ИНТЕНЗИВНОСТТА НА ИЗНОСВАНЕ

Експерименталните изследвания за влиянието на нормалната сила върху интензивността на износване на многослойно нанопокритие Ti/TiN/CrN-ml се проведе при следните постоянни параметри на трибосистемата: средна скорост на плъзгане v_{cp}=10 mm/s; изминат път на плъзгане L =50 m.

Обобщени данни за стойностите на обемите на следите от износването във функция от натоварването $V=f(F)$ при съответните режими са дадени в табл. 2.

Получените експериментални резултати бяха обработени по метода на корелационния анализ за криволинейна корелационна връзка.

Експерименталните и теоретични криви на регресия на обема на износване в зависимост от нормалното натоварване за различните образци са дадени на фиг. 2. На фиг. 3, фиг. 4 и фиг. 5 са дадени графичните зависимости на обема на износване в зависимост от нормалното натоварване за покритите и еталонните образци.

Табл. 2

Обем на следата във функция от натоварването $Iw=f(F)$,v_{cp}=10 mm/s=const, L=50 m=const						
Натоварване F, N	5_1.7034_A	5_1.7034_B	5_1.7034_C	E_1.7034_A	E_1.7034_B	E_1.7034_C
1	435,913	331,115	6,877	2131,127	2652,348	3848,781
2	787,459	531,398	105,861	6059,927	5814,25	4606,87
3	1435,749	1090,168	256,828	17053,99	18065,26	8688,499
4	2030,839	1839,32	485,787	22563,06	22488,53	15852,46
5	4067,01	2574,554	1173,498	25435,97	34217,53	47655,02

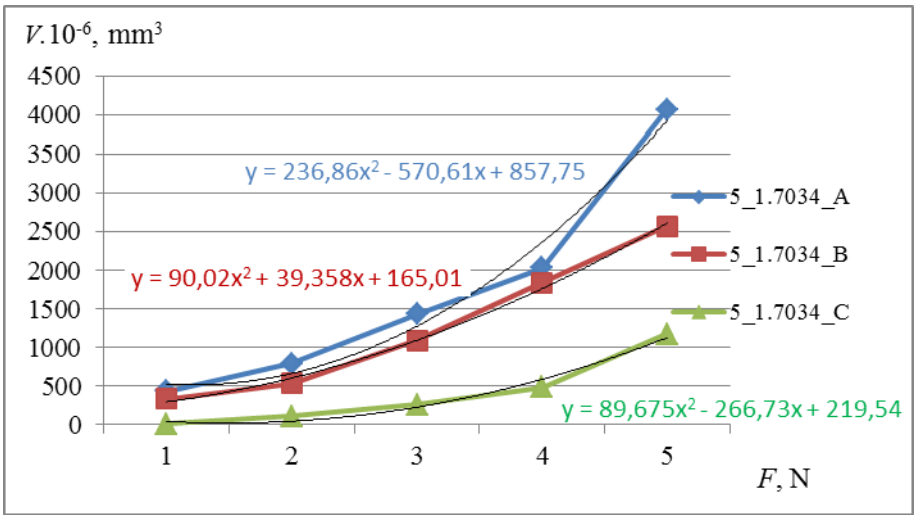

Фиг. 2. Експериментални и теоретични криви на регресия на обемите на износване на покритите образци във функция от натоварването V=f(F)

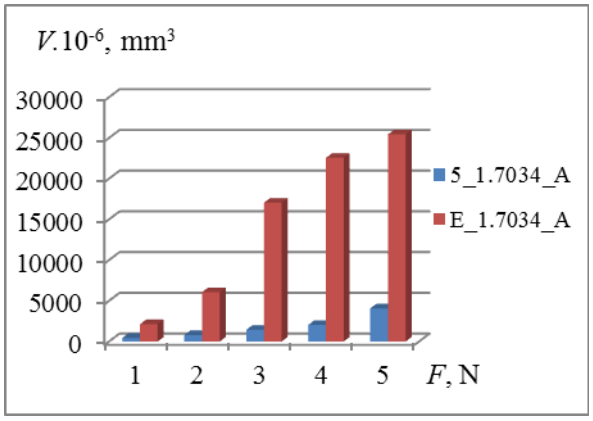

Фиг. 3. Графични зависимости на обемите от износване за покрити и еталонни образци от незакалена шлифована стомана 1.7034 във функция от натоварването V=f(F)

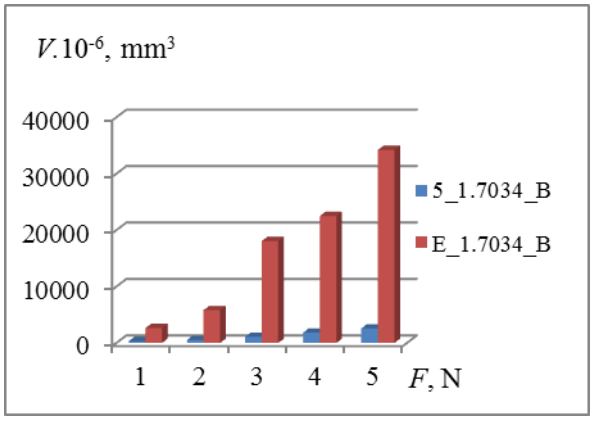

Фиг. 4. Графични зависимости на обемите от изноване за покрити и еталонни образци от закалена шлифована стомана 1.7034 във функция от натоварването V=f(F)

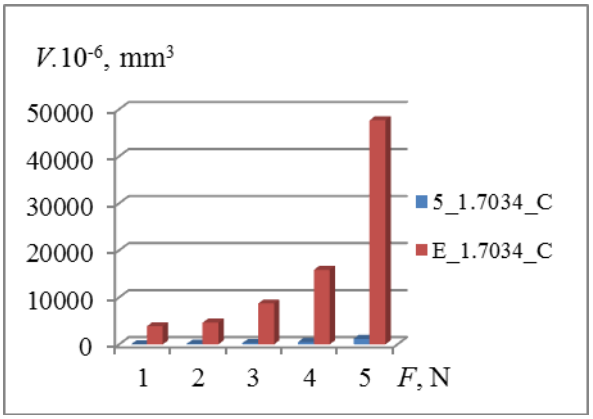

Фиг. 5. Графични зависимости на обемите от износване за покрити и еталонни образци от закалена полирана стомана 1.7034 във функция от натоварването V=f(F)

В табл. 3 са дадени обобщени данни за стойностите на интензивността на износването във функция от натоварването *Iw=f(F)* при съответните режими.

Табл.3

Интензивност на износването във функция от натоварването $I_w=f(F)$, v_{cp}=10 mm/s=const, L=50 m=const						
Натоварване F, N	5_1.7034_A	5_1.7034_B	5_1.7034_C	E_1.7034_A	E_1.7034_B	E_1.7034_C
1	8,718	6,622	0,138	42,623	53,047	76,976
2	7,875	5,314	1,059	60,599	58,143	46,068
3	9,572	7,268	1,712	113,693	120,435	43,442
4	10,155	9,196	2,429	112,815	112,442	105,683
5	16,268	10,298	4,694	101,744	136,87	190,62

Експерименталните и теоретични криви на регресия на интензивността на износване в зависимост от нормалното натоварване за покритите образци са дадени на фиг.6.

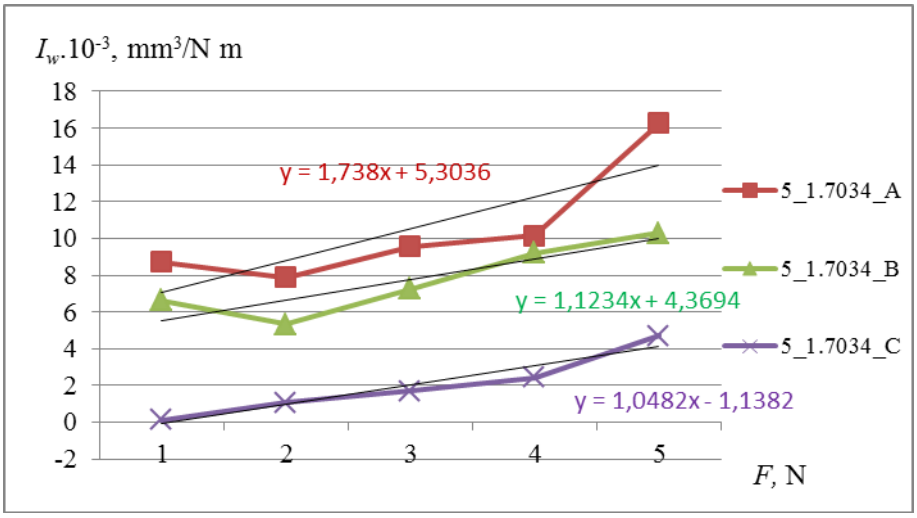

Фиг. 6. Експериментални и теоретични криви на регресия на интензивността на износване на покритите образци във функция от натоварването Iw=f(F)

На фиг.7, фиг.8 и фиг.9 са дадени експериментални и теоретични криви на регресия на интензивността на износване от нормалното натоварване за покрити и еталонни образци.

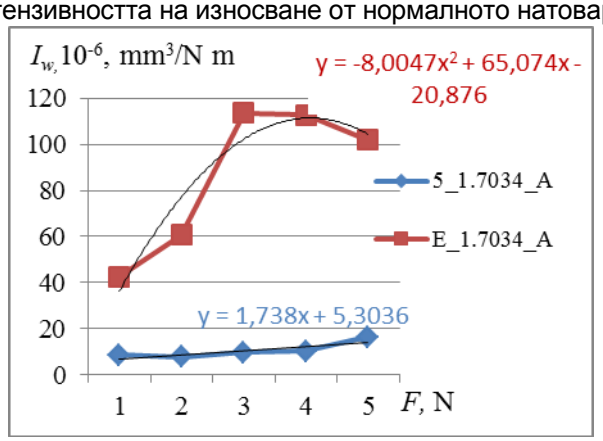

Фиг. 7. Експериментални и теоретични криви на регресия на интензивността на износване за покрити и еталонни образци от незакалена шлифована стомана 1.7034 във функция от натоварването Iw=f(F)

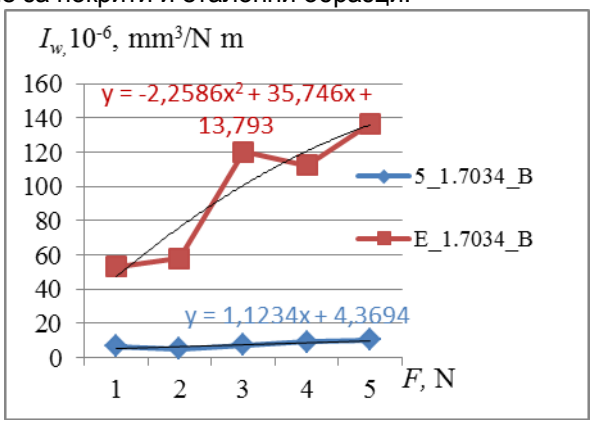

Фиг. 8. Експериментални и теоретични криви на регресия интензивността на износване за покрити и еталонни образци от закалена шлифована стомана 1.7034 във функция от натоварването Iw=f(F)

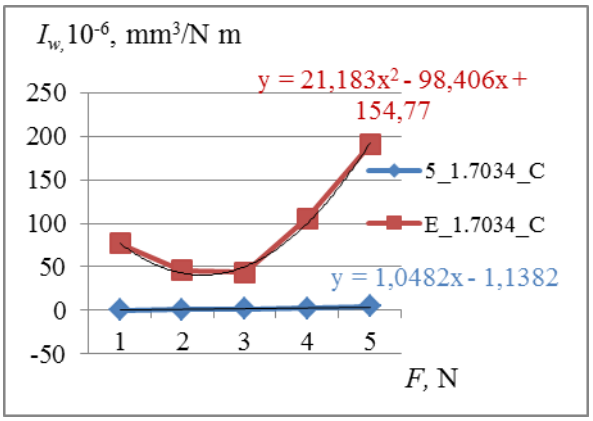

Фиг. 9. Експериментални и теоретични криви на регресия на интензивността на износване за покрити и еталонни образци от закалена полирана стомана 1.7034 във функция от натоварването Iw=f(F)

5. АНАЛИЗ И ИЗВОДИ

Експерименталните резултати показват, че нормалното натоварване влияе съществено върху износването на многослойно покритие (наноламинат) Ti/TiN/CrN-ml. Обемът на износеното покритие се увеличава с увеличаване на нормалното натоварване, докато интензивността на износване се променя слабо. Последното се обяснява с факта, че във формулата за определяне на интензивността на износването (ф-ла 2), обемът V е в числителя, а натоварването F е в знаменателя и тяхното едновременно увеличение донякъде се компенсира. Трябва да се отбележи, че покритието е със сложен вертикален строеж (от повърхността към подложката) и при по-голямо натоварване се преминава през повече негови слоеве, имащи различни механични свойства. Следователно, като пряк критерий за оценка на износването при различните натоварвания се приема изменението на обема V, а интензивността на износване I_w служи като универсална оценка за износването на различни покрития при идентични работни условия.

От получените експериментални резултати могат да се направят следните изводи:

1. Качеството на повърхнините, които се покриват с многослойно покритие (наноламинат) *Ti/TiN/CrN-ml* оказва влияние върху износването на покритието. Най-малък обем на износване има покритието, нанесено върху закалена полирана повърхнина, а най-голям обем на износване – при незакалена шлифована повърхнина. Интензивността на износване на многослойно покритие (наноламинат) *Ti/TiN/CrN-ml* нанесено на закалена полирана повърхнина е средно с 3 пъти по-малка от тази, нанесена върху закалена шлифована повърхнина и средно с 5 пъти по-малка от тази, нанесена върху незакалена шлифована повърхнина. Ето защо се препоръчва най-важните и подложени на интензивно износване елементи да бъдат закалени и полирани, след което да бъде нанесено многослойно покритие (наноламинат) *Ti/TiN/CrN-ml*;
2. Грапавостта на триещите повърхнини оказва влияние както върху коефициента на триене, така и върху интензивността на износване. При нанасянето на многослойно покритие (наноламинат) *Ti/TiN/CrN-ml* по метода на магнетронното разпрашаване (UMS) грапавостта на нанесеното покритие не се различава от тази на подготвената повърхнина за покриване, тъй като при този метод не се получават капки при отлагане на покритието;
3. Интензивността на износване на многослойно покритие (наноламинат) Ti/TiN/CrN-ml нанесено върху незакалена шлифована повърхнина е по-малка средно с 8 пъти от тази без покритие; нанесено върху закалена шлифована повърхнина е по-малка средно с 15 пъти от тази без покритие; нанесено върху закалена полирана повърхнина е по-малка средно с 46 пъти от тази без покритие.

БЛАГОДАРНОСТИ

Настоящите изследвания са резултат от предвидените научни задачи от проект НИ15-КС-016/24.04.2015“ към ПУ „Паисий Хилендарски“ гр. Пловдив.

.

ЛИТЕРАТУРА

1. Ch. Pashinski, R. Kakanakov, L. Kolaklieva, “Superhard nc-(Al1-xTix)N/a-Si3N4 gradient nanocomposite coatings for mashining tools”, Fundamental Sciences and Applications, vol. 19, book 2, 2013, pp. 71-76, ISSN 1310-8271.
2. Kandeva M., B. Ivanova, V. Pozhidaeva, D. Karastoyanov, J. Javorova, Composite coatings to improve durability of the working body of the drill, Proceedings of the 5th World Tribology Congress, September 8–13, Torino, Italy (2013)
3. Miao Q., C.E. Cui, J.D. Pan, CrN–TiN multilayer coating on magnesium alloy AZ91 by arc-glow plasma depositing process, Surface & Coatings Technology 201 (2007), pp. 5077– 5080.
4. Mishev G., Rupetsov V., Dishliev S., Pashinski Ch. Research the wear resistance of multilayer coating TI/TIN/TICrN-ml on 1.2343 steel,The „A“ Coatings, 11th International Conference in Manufacturing Engineering Proceedings, 1-3 October 2014, Thessaloniki, Greece, pp.139-147, ISBN 978-960-98780-8-1.
5. Rupetsov V.S., Kolaklieva L.P., Kopanov V.I. , Chitanov V.A., Pashinski Ch.O., Dishliev S.I. Determination of tribological parameters of Ti/TiN/CrN ml coating applied on 1.2343 steel, Journal of Food and Packaging Science, Technique and Technologies, Year IV, №6 (2015), pp. 91-95, ISSN 1314-7420.
6. Rupetsov V. S., Experimental test stand for the study of coatings resistance, Journal of Food and Packaging Science, Technique and Technologies, vol. 1, iss. 4 (2014), pp. 60-65, ISSN 1314-7773..
7. Sovilj B., J. Javorova, P. Kovac, I. Sovilj-Nikic, Wear of coated profiled tools in production conditions, Proceedings of the XXVI International Science Conference in honour of 65 anniversary of MTF of TU-Sofia and 100 birth anniversary of Acad. Angel Balevski, 13-16 September, Sozopol, Bulgaria (2010), pp. 515-520.
8. Veprek S., M.J.G. Veprek-Heijman, Industrial applications of superhard nanocomposite coatings, Surface & Coatings Technology 202 (2008), pp. 5063–5073
9. Zaharieva V., Deposition and applications of singlelayered and multilayered thin coatings deposited in vacuum, Proceedings of University of Ruse „Angel Kanchev“: Mechanics, Mechanical and Manufacturing Engineering, Vol. 48, book 2 (2009), pp. 17-24 (В. Захариева, Получаване и приложения на едно-, и многослойни тънки

покрития отложени във вакуум).
10. Мишев Г., Хайзел У. Тенденции за подобряване на трибологичните свойства на детайлите и възлите на металорежещите машини; Journal of the Technical University at Plovdiv “Fundamental Sciences and Applications”, Anniversary Scientific Conference, Bulgaria, vol. 13(6) 2006. с. 23-30, ISSN 1310-8271.

КОРЕСПОНДЕНЦИЯ

гл.ас. инж. Велко Рупецов,
ПУ„Паисий Хилендарски“ Пловдив - Технически колеж Смолян
ул. „Д. Петров“ 28
4700 Смолян , България
e-mail: velko_r@abv.bg

Tribological Journal BULTRIB Vol. 5, 2015
Papers from the International Conference **BULTRIB '15**
September 11-13, 2015, Sozopol, Bulgaria
Society of Bulgarian Tribologists
FIT – Technical University of Sofia

ESTIMATION OF WEAR FOR REDUCER TOOTH WHEELS WITH USING THE MODEL OF MECHANICAL (NANO) QUANTUM

Sergey Vasiliy FEDOROV

Department of Theory of Mechanisms and Machines and Machine Parts, Kaliningrad State Technical University, Kaliningrad, Russia
fedorov@klgtu.ru

Abstract: *Friction is examined as transformational, dissipative process. Structural-energetic interpretation of friction as a process of elasto-plastic deformation and fracture contact volumes is proposed. From thermodynamic point of view friction is a competition of two simultaneous, interconnected and opposite tendencies of accumulating latent (potential) energy of various kinds of defects and damages of contact volumes structures and releasing (dissipation) energy due to various relaxation processes. This model of friction presents the structural-energetic interpretation of process and adaptive-dissipative model of friction. The energy interpretation of the coefficient of friction is given. A structural-energy diagram of the rubbing surfaces is proposed. The energy regularities of evolution of tribological contact (elementary tribosystem) are discussed. An idea of the least nano-structural element of dissipative friction structures is discussed. It is standard of wear. Wear calculation for Herzian heavy loaded contact of gear wheels is proposed.*

Key words: *friction, energy, balance, evolution, adaptation, dissipation, nanostructure, wear.*

1. INTRODUCTION

When you create a generalized engineering theory of friction the friction model has an important place. This model should disclose the mechanisms of friction and adequate physical nature of this phenomenon.

We suggest using a generalized model of friction the model of elastic-plastic deformation of the body element, which is located on the surface of the friction pairs. This model is based on our new engineering approach to the problem of friction-triboergodynamics.

Triboergodynamics [1] is an extension (one of its parts) of general Ergodynamics of deformable bodies [2-6]. Ergodynamics is a synthesis to the problem of deformation most general laws of thermodynamics for non-reversable processes, molecular kinetics and dislocation theory in their mutual, dialectical tie on the basis of a most general law of nature – the law of energy conservation at its transformations.

Triboergodynamics is based on modern knowledge of friction too: 1. Friction is a phenomenon of resistance to relative motion between two bodies, originating at their surfaces contact area; 2. Friction is the process of transformation and dissipation of energy of external movement into other kinds of energy; 3. Friction is the process of elasto-plastic deformation localized in thin surface layers of rubbing materials.

Thus, within the framework of triboergodynamics the model of elastic-plastic deformation of contact volumes is examined as a generalized mechanism of transformation and dissipation energy and determines essence of resistance to surfaces displacement.

The major distinction of triboergodynamics from general Ergodynamics of deformed solids is «scale factor» which exhibits itself in existence of critical friction volume. This volume determines the limit friction parameters and separate, in essence, the surface deformation from the traditional volume deformation.

2. SHORT FUNDAMENTALS OF ERGODYNAMIC OF DEFORMED SOLIDS

2.1. Structural model

Deformable body is considered as an open, multicomponent, substantially nonhomo-geneous and nonequilibrium system with hierarchy of different levels (from submicro- to macrolevel) of metastable structural elements (defects and damages) which are statistically uniformly distributed in the volume. Some of these elements are virtual sources and sinks of elementary defects (vacancies, dislocations, etc.), the others are a barrier to their motion.

The structure state is defined by the basic parameters [6]: γ_σ is overstress factor of interatomic bonds which evaluates nonuniformity of external stresses σ distribution in the bonds $\sigma^0\left(\gamma_\sigma = \sigma^0 / \sigma \geq 1\right)$; u_e is the density of latent (free) energy of defects and damages; ν is the coefficient of nonuniformity of latent energy distribution in volume which is equal to ratio between latent energy density in local volume u_e^0 and average value of $u_e\left(\nu = u_e^0 / u_e\right)$. A complex structural parameter $k = \gamma_\sigma / \nu^{0,5} = \sigma_* / S_*$ specifies a relationship between theoretical σ_* and actual S_* strength of a solid body.

2.2. Physical model and structural-energetic interpretation of the process

Macroscopic phenomenon - plastic deformation and fracture of the body element is considered as a cooperation of a huge number of microscopic elementary acts of atomic-molecular regroupings under external force field (mechanical, thermal, electrical, etc.) which are activated by the thermal energy fluctuations. From the thermodynamic point of view, all the mechanisms and structural levels of the process are divided into two most characteristic groups of adaptive and dissipative (relaxation) types. They differ in physical nature and kinetic behavior. The simple acts controlling generation and accumulation of unit defects in deformed body element (damage) are classified as the first group. The specific (referred to unit volume) pumping power of excessive (latent) energy $\dot{u}_e$ is an overall characteristic of the processes rate

$$\dot{u}_e = \frac{du_e}{dt} = A\,sinh\left[\left(\alpha\sigma_i^2 - \nu\,u_e\right) / 2kT\right]. \qquad (1)$$

The mechanisms and simple acts controlling relaxation (dissipative) processes of plastic deformation are classified as the second group. The specific power of thermal effect $\dot{q}$ of plastic deformation is overall characteristic of the processes

$$\dot{q} = \frac{dq}{dt} = B\,sinh\left[\left(\alpha\sigma_i^2 + \nu\,u_e\right) / 2kT\right]. \qquad (2)$$

Here A and B are the kinetic coefficient

$$A = \frac{2kT}{hV_0}\sum_1^n U_i'(\sigma_0, T)\,exp\left[-\frac{U'(\sigma_0, T)_i}{kT}\right], \qquad (3)$$

$$B = \frac{2kT}{hV_0}\sum_1^n U_i''(\sigma_0, T)\,exp\left[-\frac{U''(\sigma_0, T)_i}{kT}\right], \qquad (4)$$

$$U_i'(\sigma_0, T) = U_{0i}' + \Delta U'(T) \pm \beta\sigma_0^2, \qquad U_i''(\sigma_0, T) = U_{0i}'' + \Delta U''(T) \pm \beta\sigma_0^2, \qquad (5)$$

$$\alpha = \frac{\gamma_\sigma^2 V_0}{6G}, \qquad \beta = \frac{\gamma_\sigma^2 V_0}{2K}, \qquad (6)$$

U_{0i}', U_{0i}'' — activation energy of formation and diffusion of the i-th defect; σ_0, σ_i — hydrostatic stress and stress intensity; V_0 — atomic volume; k — Boltzmann constant; h — Planck constant; T — absolute temperature; G, K — shear and bulk modules.

2.3. Thermodynamic analysis of interrelation between deformation and fracture

From thermodynamic point of view, the plastic deformation and the fracture are defined by a competition of two opposite interrelated and simultaneous trends: growth of latent energy density u_e of various defects and damages which are generated and accumulated in the material due to work done by the external forces ω_p and reduction (release) of the density as a result of relaxation processes in deformed body element. The first trend is concerned with strain hardening and damage of material, the second — with dynamic recovery and dissipation of the strain energy which govern the thermal effect of plastic deformation q.

A significant portion of the dissipative energy q is not retained in the deformed element, but passes through it and is dissipated in the environment due to heat exchange $\vec{q}$. Only insignificant portion of the energy q is accumulated in deformed element as a heat component of internal energy $\Delta u_T = q - \vec{q}$ increasing its temperature (self-heating effect).

According to conservation law

$$\omega_p = \Delta u_e + q \quad \text{and} \quad \dot{\omega}_p = \dot{u}_e + \dot{q}. \qquad (7)$$

In mechanics of deformable solids the irreversible work ω_p and power $\dot{\omega}_p$ of deformation are related to stress-strain state of the element by

$$d\omega_p = \sigma_i d\varepsilon_i^p, \qquad \dot{\omega}_p = \sigma_i \dot{\varepsilon}_i^p \tag{8}$$

From (7) and (8) a one-to-one relation follows between stress-strain and thermodynamic states of the element

$$\dot{\varepsilon}_i^p = \frac{\dot{\omega}_p}{\sigma_t} = \frac{1}{\sigma_i}\left(\dot{u}_e + \dot{q}\right) = \dot{\varepsilon}_i^e + \dot{\varepsilon}_i^q . \tag{9}$$

Consequently, from thermodynamic point of view, the total values of work ω_p and irreversible strain ε_i^p as well as their rates ($\dot{\omega}_p, \varepsilon_i^p$) may be presented as a sum of two components related to strain hardening and damage $\left(\varepsilon_i^e = \dot{u}_e / \sigma_i\right)$, and dynamic recovery $\left(\dot{\varepsilon}_i^q = \dot{q} / \sigma_i\right)$ controlling quasi-viscous flow of the body element, respectively.

This deduction is of important value in analyzing interrelation between deformation and fracture processes. Only a portion of plastic (irreversible) strain ε_i^e which is controlled by microscopic processes related to strain hardening and accumulation of latent energy of defects and damages is responsible for damage and fracture of the body element. The significant portion of the irreversible strain ε_i^q controlled by relaxation (dissipative) processes does not effect the damage and fracture of the body element and only causes quasi-viscous flow (steady state creep). The relationship between work and extent of irreversible deformation and their components varies in a very wide range and depends on the structure and deformation conditions of the material [2].

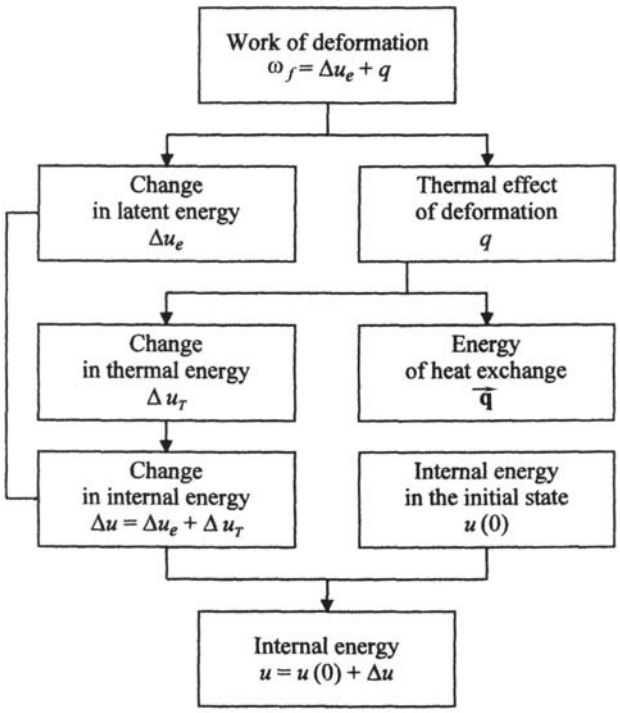

Fig. 1. Scheme of the energy balance for the plastic deformation of a solid body [2-6]

2.4. Thermodynamic condition of local fracture

As a parameter of damage (scattered fracture) we shall take the density of internal energy stored in the deformed volume. The energy is defined as a sum of two components: potential (latent) energy u_e and kinetic (thermal) energy u_T that is,

$$\Delta u = \Delta u_e + \Delta u_T , \qquad \dot{u} = \dot{u}_e + \dot{u}_T . \tag{10}$$

The energy is related to static (Δu_e) and dynamic (Δu_T) damages and distortions of crystal lattice in deformed body. Consequently, it is responsible for scattered fracture (damage).

The body element is looked upon as fractured if at least in one local volume responsible for fracture the internal energy density reaches the critical (ultimate) value u_*. This value corresponds to the loss of stability «in great» by crystal lattice. At this instant the cracks of critical size (after Griffith-Orowan-Irwin) and sharp localization of the process at the crack tip occur in a local volume. The thermodynamic condition of local fracture is written as

$$u(\vec{r}_*, t_*) = u(\vec{r}_*, 0) + \int_0^{t_*} \dot{u}(\vec{r}_*, t)dt = u_* = const\,. \qquad (11)$$

Here $u(\vec{r}_*, 0)$— density of internal energy of the material in initial (before deformation, $t = 0$) state; $\dot{u}(\vec{r}_*, t)$— specific power of internal energy sources in local macrovolume of the material responsible for fracture; $\vec{r}_*$— parameter characterizing coordinates (x_*, y_*, z_*) - of the local volume responsible for fracture.

2.5. Thermodynamic criterion of fracture

According to structural-energetic analogy between mechanical fracture and melting of metals and alloys [7] and experimental data [2], the critical value of internal energy u_* in the local volume responsible for fracture agrees with known thermodynamic characteristic of material ΔH_s (enthalpy of melting)

$$u_* = \Delta H_s = \int_0^{T_s} c_p dT + L_s\,. \qquad (12)$$

Here T_s — melting temperature; c_p - specific heat; L_s - latent melting heat.

2.6. Relationship between force and energy criteria of local fracture

The analysis of kinetic equation of state (damage) (1) indicates that the real solid body approachs the stationary (stable) state under constant action of external fields ($\sigma_0 = const,\ \sigma_i = const,\ T = const$) if

$\Delta u_e = const$ and $\dot{u}_e = 0$. (13)

From the kinetic Equation (1) under condition (13) an important consequence follows

$$\sigma_i = \sigma_s, \quad \sigma_s = \left(\frac{\nu\ u_e}{\alpha}\right)^{1/2} = \frac{1}{K_a}(6Gu_{e^*})^{1/2} \qquad (14)$$

according to which the structure state of material σ_s (α, u_e, ν) adapts (shakes down) in a stable stage to external conditions, which are defined unambiguously by deviatory component of the stress tensor $\sigma_i(\sigma_s = \sigma_i)$. Relationship (14) generalizes the known proposition of dislocation theory on mutual relation between the flow stress σ_s and the density of latent (stored) energy u_e [8] for the case of combined stress state. The material damage u_e in the local volume responsible for fracture becomes critical, therefore, relationship (14) makes it possible to estimate the actual strength of the material S.

$$S = \left(\frac{\nu\ u_{e^*}}{\alpha}\right)^{1/2} = \frac{1}{K_a}(6Gu_{e^*})^{1/2}\,. \qquad (15)$$

Here

$$u_{e^*} = u_e - u_{T_0} = \Delta H_s - \int_0^{T_s} c_p dT\,. \qquad (16)$$

From (15) and (16) under $k_\sigma = 1.0$ and $T = 0$ the theoretical shear strength is:

$$\sigma_* = (6G\Delta H_s)^{1/2} = \left(\frac{3E\Delta H_s}{1+\mu}\right)^{1/2}. \qquad (17)$$

Here E, μ — elasticity modulus and Poisson's ratio.

3. TRIBOERGODYNAMICS METHOD

3.1. Structural-energetic interpretation of friction process

Friction is known to be a product of frictional forces F by friction distance ℓ, that is, the work ω_f, expended on overcoming frictional forces

$\omega_f = F\ell$, (18)

$$\omega_f = \Delta u_e + q\,, \tag{19}$$

or

$$\dot{\omega}_f = \dot{u}_e + \dot{q}\,. \tag{20}$$

Here $\omega_f = d\omega_f / dt$ is a power of friction dissipation of energy; $\dot{u}_e = du_e / dt$ is the rate of storing latent energy in deformed (contact) volumes; $\dot{q} = dq / dt$ the power of thermal effect of plastic deformation (friction).

Since the contact volumes of both materials of the friction pair (Fig. 1) are deformed, Equations (19) and (20) should be rewritten as

$$\omega_f = \Delta u_{e1} + \Delta u_{e2} + q_1 + q_2\,, \tag{21}$$

$$\dot{\omega}_f = \dot{u}_{e1} + \dot{u}_{e2} + \dot{q}_1 + \dot{q}_2\,. \tag{22}$$

These equations show, that from thermodynamic point of view, the work ω_f of friction forces, (friction power $\dot{\omega}_f$) is related to plastic deformation of the contact volumes. The work ω_f may be divided conventionally into two specific parts.

The first part is related to variation of the latent (potential) energy (Δu_{e1} and Δu_{e2}) in deformed (contact) volumes. This is the energy of various simple defects and damages which are generated and accumulated in the bulk. This energy is unique and the total characteristic of submicro- and microstructural variations occurring in plastically deformed volumes [2, 3].This is a measure of strain hardening and damage of material.

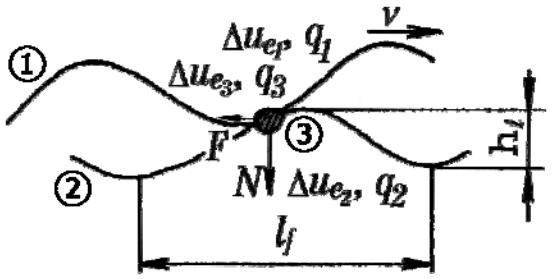

Fig. 2. Schematic view of friction's contact [1]

The second part of the friction work ω_t is related to dynamic recovery which is accompanied by releasing latent energy and thermal effect of friction (q_1, q_2).This energy involves displacement and annihilation of various simple defects of opposite sign terminating at the free surface, healing reversible submicroscopic discontinuities, etc.

The relations between Δu_{e1} and Δu_{e2}, as well as q_1 and q_2 are defined by physico-chemical properties of the materials of the friction pair, their structure and friction conditions.

Since the contact volumes (not unit sizes) of the materials forming a friction couple become strained by friction (Figure 2), equations (1) and (2) can be rewritten in the form

$$W_f = \Delta U_e + Q = \Delta U_{e_1} + \Delta U_{e_2} + Q_1 + Q_2\,, \tag{23}$$

$$\dot{W}_f = \dot{U}_e + \dot{Q} = \dot{U}_{e_1} + \dot{U}_{e_2} + \dot{Q}_1 + \dot{Q}_2\,, \tag{24}$$

where $\Delta U_e = V_f \Delta u_e$; $\dot{U}_e = V_f \dot{u}_e$; V_f - is the deformable (friction) volume.

Solving equations (23) and (24) for the frictional force F, one obtains

$$F_l = \frac{\Delta U_{e_1} + \Delta U_{e_2}}{l} + \frac{Q_1 + Q_2}{l} \tag{25}$$

$$F_v = \frac{\dot{U}_{e_1} + \dot{U}_{e_2}}{v} + \frac{\dot{Q}_1 + \dot{Q}_2}{v}\,, \tag{26}$$

where l and v are the friction path and the slip velocity.

Dividing equations (25) and (26) by the normal force N gives generalized equations for the friction coefficient

$$\mu_l = \frac{\Delta U_{e_1} + \Delta U_{e_2}}{Nl} + \frac{Q_1 + Q_2}{Nl}\,, \tag{27}$$

$$\mu_v = \frac{\dot{U}_{e_1} + \dot{U}_{e_2}}{Nv} + \frac{\dot{Q}_1 + \dot{Q}_2}{Nv}\,. \tag{28}$$

Therefore, the friction is generally described by the energy balance equation and with thermodynamical point of view [1-3] is the process of two interrelated, oppositely directed and concurrent trends operating in a strained contact. According to the energy balance scheme (Figure 1) for plastic deformation and fracture [4] presented above, equations for friction work W_f, frictional force F and friction coefficient μ (without lubrication) has view

$$W_f = \Delta U_e + Q = \Delta U_{e_1} + \Delta U_{e_2} + \Delta U_{T_1} + \Delta U_{T_2} + \vec{Q}_1 + \vec{Q}_2, \quad (29)$$

$$\dot{W}_f = \dot{U}_e + \dot{Q} = \dot{U}_{e_1} + \dot{U}_{e_2} + \dot{U}_{T_1} + \dot{U}_{T_2} + \dot{\vec{Q}}_1 + \dot{\vec{Q}}_2, \quad (30)$$

$$F_l = \frac{\Delta U_e}{l} + \frac{Q}{l} = \frac{\Delta U_{e_1} + \Delta U_{e_2}}{l} + \frac{Q_1 + Q_2}{l}, \quad (31)$$

$$F_v = \frac{\dot{U}_{e_1} + \dot{U}_{e_2}}{v} + \frac{\dot{Q}_1 + \dot{Q}_2}{v} = F_{mechanical} + F_{molecular}, \quad (32)$$

$$\mu_l = \frac{\Delta U_{e_1} + \Delta U_{e_2}}{Nl} + \frac{Q_1 + Q_2}{Nl} = \mu_{adapt} + \mu_{dis} = \mu_{adapt} + \mu_{T(dis)} + \mu_{\vec{Q}(dis)}, \quad (33)$$

$$\mu_v = \frac{\dot{U}_{e_1} + \dot{U}_{e_2}}{Nv} + \frac{\dot{Q}_1 + \dot{Q}_2}{Nv} = \mu_{deformation} + \mu_{adhesion}, \quad (34)$$

where $\Delta U_e = V_f \Delta u_e$; $Q = V_f q$; $\vec{Q} = V_f \vec{q}$; $\dot{U}_e = V_f \dot{u}_e$; $\dot{u}_e = \mathrm{d}\, u_e / \mathrm{d}\, t$ - is the rate of latent energy density change in the contact volumes; V_f - is the deformable (friction) volume; μ - friction coefficient; μ_{adapt} - adaptive friction coefficient; $\mu_{T(dis)}$ and $\mu_{\vec{Q}(dis)}$ - statical and dynamical components of dissipative friction coefficient; ΔU_T - thermal component of internal energy; N - normal load; l - distance of friction; v -sliding velosity. The latent energy density Δu_e is an integral parameter of tribostate and damageability (failure (Δu_e^*)).

Thus, viewed thermodynamically, the work done by friction forces W_f (the friction power $\dot{W}_f$), the friction force F and the friction coefficient μ may be classified conventionally into two specific components with different kinetic behavior [3]. The first component is associated with microscopic mechanisms of adaptive type and relates to the change of latent (potential) energy ($\Delta u_{e_1}, \Delta u_{e_2}$) of various elementary defects and damages that are generated and accumulate in the deformable volumes of materials friction pair (Figure 1). This energy is a unique and integral characteristic of the submicro- and microstructural transformations that occur in plastically strained materials [2-6]. This energy is a measure of strain hardening and damageability of materials. The second component is associated with microscopic mechanisms of dissipative type and relates to dynamic recovery processes in which latent energy is released and heat effect of friction (q_1, q_2) take place. This energy originates in the motion and destruction of various elementary defects of opposite signs, the egress of these defects to the surface, the healing of reversible submicroscopic discontinuities, etc. The ratios of the components Δu_{e_1} and Δu_{e_2} as well as $q_1 q_2$ of the balance vary over a wide range, depending on the physical, chemical, and structural properties of the materials that comprise the friction couple and the friction process conditions.

Thus, the thermodynamic analysis of friction (plastic deformation and fracture) has led to generalized (two-term) relations for the force F and coefficient of friction μ, which agrees with current concepts of the nature of friction – molecular-mechanical theory (32) and deformable-adhesion theory (34). But it is more correct to speak about the adaptive-dissipative nature (model) of friction (33).

Relationships (21)-(28) which generalize the mechanism of energy dissipation at friction allow to classify the tribosystem states. According to ergodynamics of deformed solids (relationships $\Delta u = \Delta u_e + \Delta u_T$ and $q = \Delta u_T + \vec{q}$) and equations (23)-(24) may be transformed to

$$W_f = \Delta U_{e1} + \Delta U_{e2} + \Delta U_{T1} + \Delta U_{T2} + \vec{Q}_1 + \vec{Q}_2, \quad (35)$$

$$\dot{W}_f = \dot{U}_{e1} + \dot{U}_{e2} + \dot{U}_{T1} + \dot{U}_{T2} + \dot{\vec{Q}}_1 + \dot{\vec{Q}}_2. \quad (36)$$

As follows from equations of energy balance (35), (36), all exhibitions of friction and wear may be reduced conventionally at least to two basically different states: the first state defines all types of damage and wear, the second — the so-called "wearless" condition.

The state of damage and wear is characterized by the components of energy balance (35), (36), which are responsible for accumulation of internal energy in deformed volumes $\Delta u = \Delta u_{e1} + \Delta u_{e2} + \Delta u_{T1} + \Delta u_{T2}$, i.e. the process is irreversible. The "wearless" state is characterized by the components responsible for dynamic dissipation (reversibility) of strain energy into elastic and structural dissipated energy of friction contact $\vec{q} = \vec{q}_1 + \vec{q}_2$.

In its turn, the first state may be classified depending on the relation between potential Δu_e and kinetic Δu_T components of internal energy. It is subdivided conventionally into mechanical damage and wear (due to so-called structure activation) and thermal damage and wear (due to thermal activation). For instance, let the thermal component of internal energy Δu_T be equal to zero ($\Delta u_T = 0$) and the internal energy variation at damage and wear be defined only by variation of the potential component $\Delta u_e (\Delta u = \Delta u_e)$. Then, the mechanical damage and wear with brittle fracture of surfaces take place. On the contrary, if we have $\Delta u_e = 0$ ($\Delta u = \Delta u_T$), then the thermal damage and wear with ductile fracture of surfaces take place. All the intermediate values of the components are associated with quasi-brittle or quasi-ductile fracture of solids.

In the most general case, the energy balance at dry friction (23) should be written as

$$W_f = \Delta U_{e1} + \Delta U_{e2} + \Delta U_{e3} + Q_1 + Q_2 + Q_3 \quad . \tag{37}$$

In the special case, where the friction is localized into volume of the "third body" (Fug. 2) equation (37) develops into

$$W_f = \Delta U_{e3} + \vec{Q}_3 . \tag{38}$$

Here $\Delta U_{e3} = V_3 \Delta u_{e3}$.

3.2. Energy interpretation of Leonardo da Vinci (Amonton's) friction coefficient

According to thermodynamic theory of strength [2], the structure parameter should be related to the portion of the accumulated plastic deformation that is responsible for strain hardening. This portion is uniquely and integrally defined by the density of the potential component of internal energy (that is, the latent energy density Δu_e) of various defects and damages that accumulate in a plastically strained material. With this in mind, if we neglect the heat effect Q of friction, one will infer from the thermodynamic analysis of friction of equations (27)-(28) that the Amonton (Leonardo da Vinci) friction coefficient is

$$\mu = \frac{\Delta U_e}{\mu^* N l} = \frac{F}{N}; \qquad F = \frac{\Delta U_e}{l}; \quad Q \cong 0, \quad \mu^* = 1. \tag{39}$$

Consequently, the coefficient of friction has a very deep physical sense. On the one hand, it is the parameter which generally characterizes the resistance of relative displacement (movement) of surfaces, for it reflects the portion of energy, which «is done by friction away» as accumulated latent energy ΔU_e, by relation to parameter of external forces work $\mu^* N l$ (energy of external relative movement). On the other hand, it is the generalized characteristic of damage, for it is defined of the latent energy density Δu_e as integral characteristic of the structure defectiveness measure, because this energy is the generalized parameter of damage. Here too, coefficient of friction generally reflects the structural order (disorder) of deforming contact volume, since the parameter $\Delta U_e = \Delta u_e V_f$ is defined of the energy of defects and damages of different types, that are accumulated into contact volumes V_f solids.

Therefore, coefficient of friction is a true and generalized parameter of tribosystem state. From this conclusion we can say that the analysis of the evolution of the states of a tribosystem is primarily an analysis of the latent deformation energy accumulated within the contact friction volumes.

3.3. Generalized experimental friction curves

The dependences obtained for the friction coefficient μ are in agreement with experimental curves $\mu = \mu(N, v)$ (Fig. 3-5).

A subsequent analyses of modern experimental data using equations (23)-(34) has shown that the experimental friction curves (Fig. 3-5) of type $\mu = \mu(N, v)$ are generalized friction curves that reflect the evolution (the change in the friction coefficient) of tribosystem.

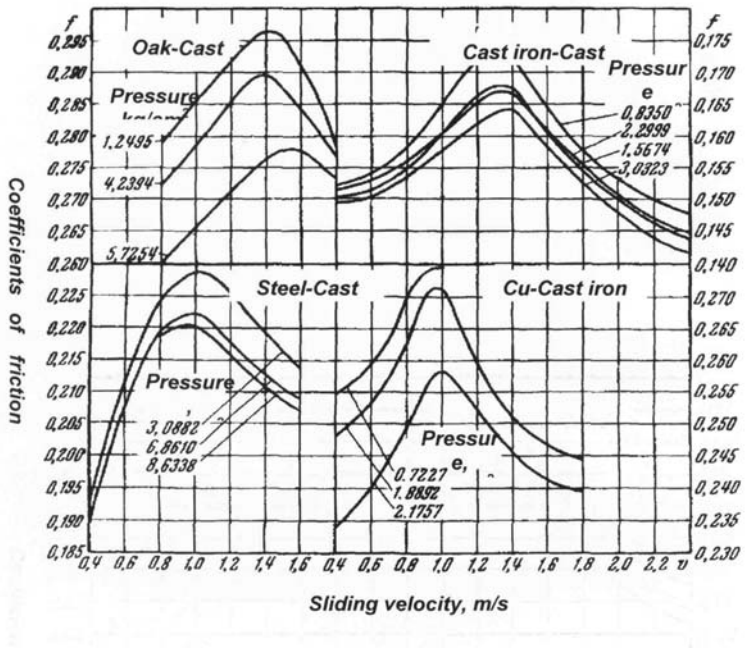

Fig. 3. P.Conti's experimental results [12]

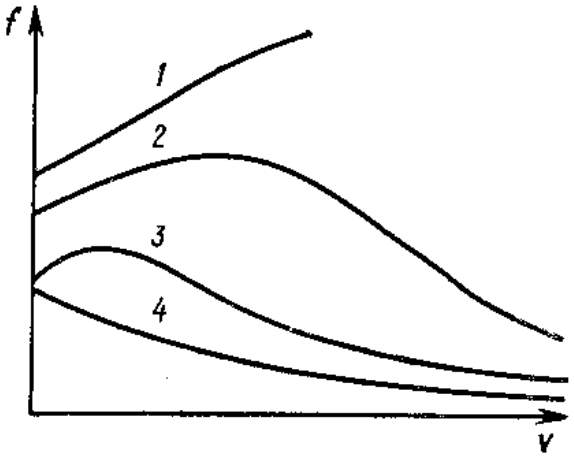

Fig. 4. Generalized friction experiments in Kragelsky's interpretation [12]: v - sliding velocity (load: 1- small; 2 and 3 – medium; 4 - considerable).

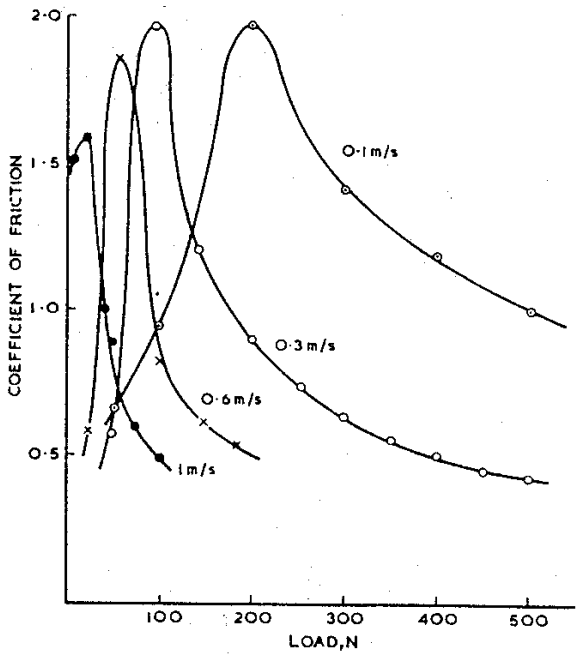

Fig. 5. Watanabe's [13] experimental results of Nylon 6 – Steel pair of friction

3.4. Structural-energy regularities of rubbing surfaces evolution

We propose an energetic interpretation of the experimental friction curves $\mu = \mu(N,v)$ (Fig. 6). According to our concept [1,14], the ascending portion of the friction coefficient curve μ is mainly controlled by processes associated with the accumulation of latent energy ΔU_e in various structural defects and damages. Here the increase in μ is due to the increasing density of latent (potential) energy Δu_e and the increasing adaptive friction volume V_f. The descending portion of the friction curve is mainly controlled by processes associated with the release and dissipation of energy $Q = \Delta U_T + \vec{Q}$. Here the decrease in μ is due to the decrease in latent energy density within the friction volume V_f or (which is virtually the same) to the decrease of the adaptive friction volume V_{adapt} ($u_e = u_e^*$) and to the increase of the dissipative volume V_{dis} ($\vec{q}^{\,*} = u_e^*$).

Evolution of tribosystem, presented as a diagram view (Fig. 6), has an adaptive-dissipative character (29)-(34) and reflects the competitive (dialectical) nature of friction. Evolution curve has the row of principal points (1-5) of transitional tribosystem states, which strictly obeys the balance principle of friction; there are more characteristic areas of tribosystem behavior between these points. These areas reflect the common properties of nonlinear dynamic of evolution.

So, in Figure 6 it is possible to see the following conventionally designated points and stages: 0-1 – a stage of static friction and deformational strengthening; 1 – a point of limit for deformational strengthening; 1-2 – a stage of pumping of excess energy; 2 – a point of gripping (adhesion) and transition of outer friction into internal (critical non-stability): 2-3 – a stage of forming dissipation structures (formation of heat fluctuation in friction volume); 3 – a point of minimum compatibility (maximum frictionness); 1-2-3 - a stage of self-forganization; 3-4 – a stage of compatibility; 4 – a point of wearlessness (anormal-low friction); 5 – a point of thermal adhesion.

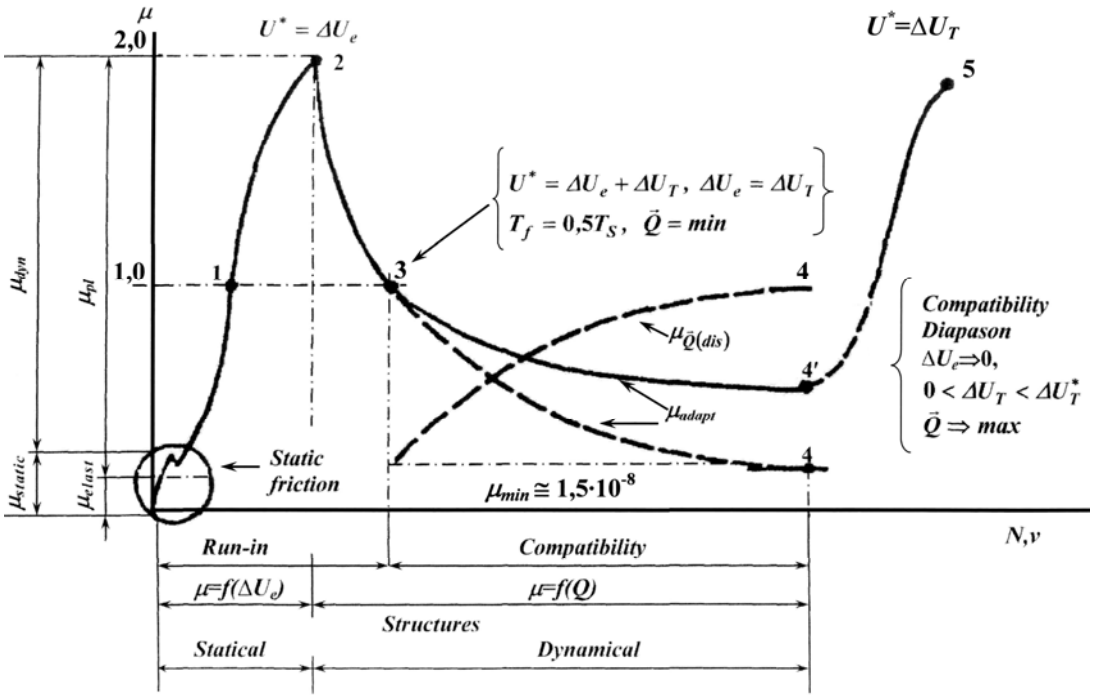

Fig. 6. Structural-energy diagram for evolution of rubbing surfaces [1,14]

An ideal evolution of tribosystem is symmetrical. The process starts and finishes within areas of elastic behavior. A plastic maximum (a superactivated condition) exists between them as a condition of selforganisation and adaptation.

In the most general case evolution (adaptation) regularities of tribosystems may be presented as a 2-stage (Fig. 6). At the first stage (0-2) of adaptation the evolution of friction contact rushes to form some critical volume of friction V_f^* (point 2). It is elementary tribosystem that is the elementary and self-sufficient energy transformer. The first stage - latent energy density growth Δu_e to a limited magnitude Δu_e^* within critical friction volume V_f^*.

This friction volume V_f^* is constant at the second stage of evolution, but here it is evolutionary developed owing to structural transformation; by this one may realize wide spectrum of compatibility friction structures (Fig. 6). The second stage (2-4) – structural transformation of critical friction volume (elementary tribosystem) V_f^* into adaptive V_{adapt} and dissipative V_{dis} volumes (Fig. 7). The limit (point 4) of this stage is characterized by a full transformation of adaptive critical volume V_{adapt}^* into V_{dis}^* dissipative.

The volumes mentioned above characterize different regularities of transforming energy of outer mechanical movement at friction. Adaptive volume V_{adapt} is connected with non-reversible absorption of deformation energy. It is in this volume where latent deformation energy Δu_e accumulates and where the centres of destruction initially emerge (birth). Dissipative volume V_{dis} is capable of reversible transformation (dissipate) of outer movement energy. It doesn't accumulate latent deformation energy owing to reversible elastic-viscous-plastic deformation.

Suggested theoretical and calculation assessments [1, 16-17] showed that dissipative friction volume performs reversible elastic energy transformation of outer mechanical movement with density $\vec{q}^*$ equal to critical density of latent energy u_e^*.

Culmination of tribosystem evolution is its final and limited condition of point 4 – a state of anomalously low friction and wearlessness (maximum efficient).

A schematic evolution of the contact volume of friction in diagram's points 1-5 is presented in Fig. 7.

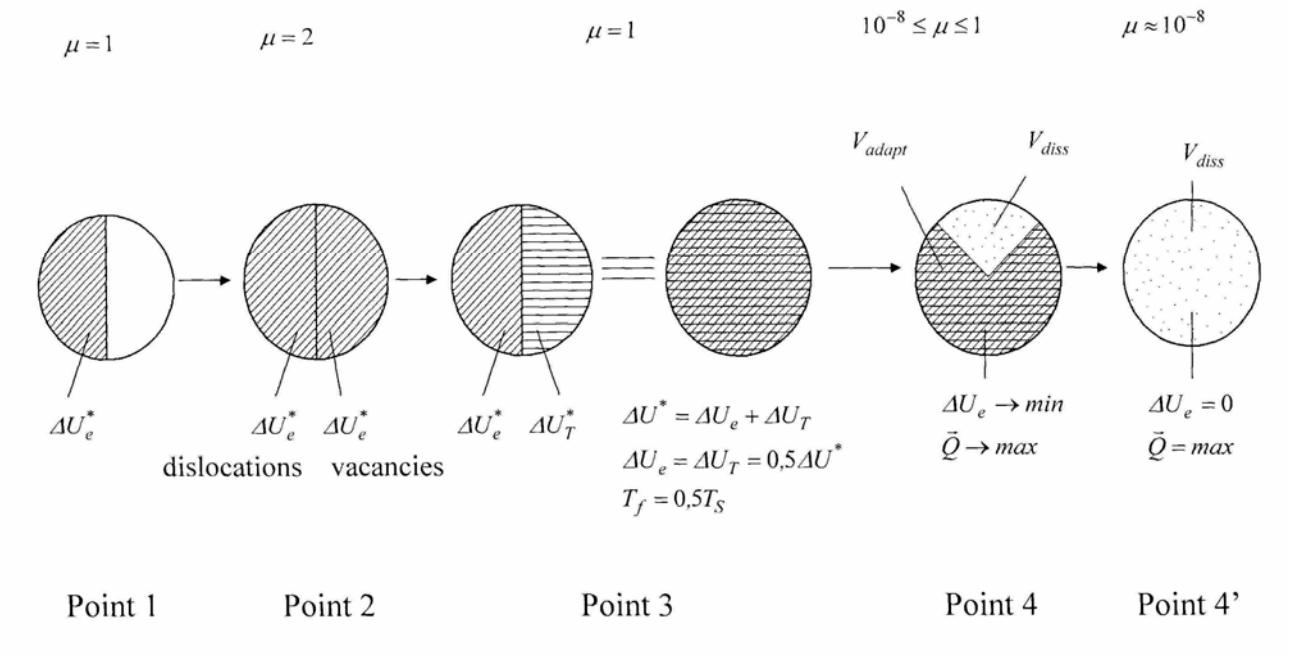

Fig. 7. A schematic evolution of the contact volume of friction in diagram's points 1-5

Calculation show [1] that at an ideal tribosystem evolution an adaptive (Amontons) friction coefficient μ_{adapt} in a point 2 of a diagram falls abruptly down, reaching in a point 4 the value of elastic friction coefficient μ_{elast}. For point 4 of compatibility area 3-4 an equation of energy balance (1) showed be put in the following way:

$$\mu_{adapt} = \mu^* - \mu_{dis} = 1 - \mu_{dis} = \mu_{plast} = 0 = \mu_{elast}; \qquad \mu^* = 1{,}0. \tag{40}$$

Thus, point 4 stands for an ideal evolution of contact friction volume a condition of ideal elastic-viscous-plastic deformation. Equation (40) shows as a matter of fact exactly it, i.e. Amontons friction coefficient μ_{adapt} being in its essence plastic friction coefficient μ_{plast} has a minimum value equal to zero. It follows then, that plastic friction became elastic with friction coefficient μ_{elast}. It means that plastic deformation of contact volume friction is implemented with the maximum dynamic dissipation ($\vec{Q} = max$) of accumulated latent energy. That is why the value of accumulated energy in point 4 is equal to zero ($\Delta U_e = 0$). This fact proves an ideal condition at full evolution of contact volume. From the physics point of view this condition may be explained by the full dissipation of accumulated energy ΔU_e^* in point 2 and by newly emerged structures of point 4 in the form of elastic energy of interaction between them (dynamic dissipation energy $\vec{Q}^*$). Here $\mu_{dis} = 1{,}0$. The structural elements themselves are defectlessness - $\mu_{adapt} = 0$, and friction is elastic - $\mu = \mu_{elast}$.

It has been demonstrated [1] that value of minimum adaptive friction volume V_{adapt}^{min} corresponding to the zero meaning of plastic friction component μ_{adapt} is not equal to zero, but is equal to some minimum structural element of deformed solid body.

3.5. About mechanical (nano) quantum of dissipative friction structures

The result of ideal elementary tribosystem (contact) evolution is forming of unique nanostructure – a mechanical (nano) quantum. Strict notions about mechanical quantum have been obtained [1] considering equation of quasiideal solid body for point 4 of diagram of friction evolution

$$\vec{Q}^* = \vec{S}_Q T = \mu_{dis}^* N I_f = V_f^* u_e^* = V_f^* \vec{q}_*, \tag{41}$$

which is particular case of solving equation of energy friction balance (29) at $\mu_{adapt} = 0$ and $\mu_{dis} = 1 = \mu_{dis}^*$. Here $\vec{S}_Q$ – inertia entropy of compatible friction volume; T - characteristic temperature of contact friction volume; l_f - linear size of elementary contact.

Correspondingly, in conditions of maximum compatibility (point 4) when tribosystem implements full evolution cycle of adaptation with formation of most perfect dissipative structure, the behaviour of structure is subject to equation of quasiideal solid body condition. So, it is to be presumed that, interaction between elements of this structure, are minimized – a condition of ideal elasticity in dynamics. Equation (31) with taking into account Plank-Boltzmann formula $S = k \ln W$ and real number of atoms oscillators N_f in the volume of elementary tribosystem (contact) V_f^* is brought to the form explaining friction regularities from the point of view of system evolution:

$$\mu_{\text{diss}} = \frac{\vec{S}_Q}{Nl_f} = \frac{kTN_f \ln W}{Nl_f}; \tag{42}$$

$$\mu_{adapt} = 1 - \mu_{diss} = 1 - \frac{kTN_f \ln W}{Nl_f} = 1 - \frac{\vec{S}_Q T}{Nl_f} = \frac{S_U T}{Nl_f}; \tag{43}$$

Where k - Boltzmann constant; W - condition probability; S_U - configuration entropy of friction (contact) volume.

Tribosystem always tends to some optimal condition, characterized, i.e. to a most probable condition $W' = N_f \ln W$ for the given friction conditions.

Analysis and solution of these equations [1] allows to demonstrate the principle of constant probability value (parameter of tribosystem condition (order)) W for the whole range of compatible friction precisely $\ln W = 3$ and $W = e^3 = 20{,}08553696\ldots$.

The value of thermodynamic probability W equal to $20{,}08553696\ldots$ was interpreted [1,15-17] as a minimum value of linear, atomic oscillators in one of three directions of minimum adaptive friction volume V_{adapt}^{min} corresponding to condition of practically absolute elastic friction – anomalously-low friction (safe deformation threshold). Then the number of atomic oscillators in this volume equals $V_Q = \left(e^3\right)^3 = (20{,}08553695\ldots)^3 = 8103{,}083969$ atom's oscillators.

It is the universal size (volume) of mechanical quantum [1, 15-17].

On the other hand, adopting the meaning of Boltzmann entropy S, a universal friction constant $R_f = kN_f$ [1,15-17] is obtained, which characterizes in physical meaning «energetical size» of elementary tribosystem (TS), containing in ideal conditions the same number of atomic oscillators N_f (mechanical quanta N_Q):

$$R_f = k \cdot N_f = k \cdot W^3 \cdot N_Q = R_{MQ} \cdot N_Q \qquad \frac{J}{grade \cdot TS}; \tag{44}$$

$$R_{MQ} = k \cdot W^3, \qquad \frac{J}{grade \cdot MQ}, \tag{45}$$

where R_{MQ} - universal constant of deformation at friction.

As it follows from calculations [1] the size of minimum adaptive friction volume V_{adapt}^{min} coincides in its value with the size of submicroscopic area in crevice mouth, which is equal for metals $(4\ldots9)\cdot 10^{-6}$ mm, i.e. of critical volume size responsible to fracture. Thus the size of minimum adaptive friction volume $V_{adapt}^{min} = V_{elast}$, can be presented as the size of some mechanical quantum.

This mechanical quantum constitutes a minimum number of atoms capable to provide such a configurational distribution (structure) which obtains the property of reversibly taking and dissipating (recovering) energy of outer mechanical movement. It also constitutes minimum structure in conditions of plastic deformation and it is formed at tribosystem transition (deformed volume) through an ultimately activated (critical) condition (see Fig. 6) due to development of selforganisational tribosystem adaptation processes. Mutual rotation-oscillation movement of these mechanical quanta in respect of each other within elementary tribosystem (contact) determines condition of most perfect dissipative friction structure. Properly speaking, such condition is described by equation of quasiideal solid body condition (41), a condition when interaction between structural elements (mechanical quanta) is minimized – a condition of ideal elasticity of quasiviscous flow. Calculation friction coefficient between quanta equals about 10^{-8} [1,16-17].

A conclusion that mechanical quantum constitutes a minimum structural form at plastic deformation (friction) is supported by calculation. If values of elasticity modules E correspond to atomic (true) elastisities E_r then values equal to 60 are obtained, where $60 = 3W$ can be interpreted as a characteristic of volume elasticity of one mechanical quantum – minimum adaptive friction volume V_{adapt}^{min}. Calculation assessment of pa-

rameter $W \cong 20 = E / 3E_r$, done for various metals and steels gives an average value 20,77 ((Table)); $\Delta H_S = 3E_r$ - entalpy of melting.

Table. Parameter W for Metals and Steels [1]

Metals and steels	$E \times 10^{-3}$, MPa	$\left(u_e^*\right)\Delta H_S \times 10^{-3}$, MJ/m^3	$E / 3E_r$
Cr	235,4	8,5	27,69
Mg	44,4	1,9	23,37
Ag	79,0	3,7	21,35
Au	78,7	4,0	19,67
Co	200,1	10,6	18,88
Fe	211,4	9,9	21,35
Ta	184,4	10,6	17,39
Ti	105,9	6,7	15,8
Nb	104,0	9,2	11,3
Zr	95,6	5,7	16,77
Mo	316,9	12,0	26,4
W	392,4	14,4	27,25
Ni	201,1	9,4	21,39
Iron	210,9	10,1	20,88
20	200,1	9,5	21,06
1Kh13	206,0	8,9	23,14
3Kh13	218,8	9,2	23,78
Kh18N9T	199,1	9,4	21,19
Kh18M9	199,1	9,6	20,74
30Kh	214,1	10,2	20,99
30N3	207,5	10,3	20,11
40	209,4	9,7	21,58
30G2	207,2	10,0	20,72
30KhGN3	208,0	10,2	20,4
G13	204,0	10,0	20,4
50S2G	196,2	10,3	19,05
U8	198,0	10,3	19,22
U12	198,0	10,4	19,04

$\Delta H_S = 3E_r$, $E / 3E_r = 20{,}77.$

A conclusion is made [1] that the number of atoms (mechanical quantum (MQ)) within volume of one elementary tribosystem (TS) in conditions of ideal tribosystem evolution is a constant value. Thus, it is possible to speak about the quantity of substance equal by mass to one elementary tribosystems and to one mechanic quantum.

3.6. Synergism of tribosystem and optimum states

Mechanical quantum is dynamic oscillator of dissipative friction structure. An ideal quasielastic contact condition at its full evolution constitutes effect of most fully dissipated energy of outer mechanical movement throughout newly formed (by mechanism of selforganization) structural elements –mechanical quantums (dynamic oscillators) which most fully realize their rotationary – oscillatory behavior in relation to each other within elementary tribosystem volume. Their resistance to relative interaction here is minimally elastic and corresponds to elasticity of ideal atomic (thermodynamically balanced) interactions at the level of electron orbits.

Universal constants of mechanical quantum and elementary tribosystem (material point) determine quantum model of surface damping:

$$\mu_{dis} = \frac{3R_{MQ}T_{n_i}}{NI_f} = \frac{U_{1Q^{n_i}}}{U_{1Q^{n_*}}} = \frac{n_i}{n_*} = 1 - \mu_{adapt}; \qquad \mu_{adapt} = 1 - \frac{n_i}{n_*} = \frac{n_{dest}}{n_*}, \tag{46}$$

taking into account destruction quantums n_{dest} (non-reversible process component) and damping quantums n_i (reversible, elastic component – fatigue number), and also probability evolution tribosystem model to a most ordered condition:

$$\mu_{adapt} = 1 - \mu_{dis} = 1 - \frac{R_f T \ln W_i}{N l_f} = 1 - \frac{\ln W_i}{\ln W_*}. \quad (47)$$

where $3R_{MQ}T = U_{1Q}$ - energy of one mechanical quantum; W_i and W_* - current and ultimate probabilities of tribosystems compatibility conditions.

According to a model of quantum surface damping at friction in state of most complete evolution (adaptation) of elementary tribosystem all mechanical quantums with the exeption of one elasticity and reversibly transform energy of outer impact (mechanic movement). One mechanical quantum of radiation ($\cong 8103$ atoms) – is a minimum loss (essence of wearlessness or other wear primary standard).

Linear size of quantum is equal to diameter of spherical ideal crystal with atomic roughness:

$$D_{MQ} = 2 \cdot W \cdot \bar{d}_a \cdot (3/4 \cdot \pi)^{1/3} = 7{,}177 nm. \quad (48)$$

Here $\bar{d}_a$ - mean atomic diameter for metals; $W = e^3$ - parameter of state for mechanical quantum [1].

Mechanical quantum (Figure 4) can be examined as the elementary nanostructure of metal's solid body.

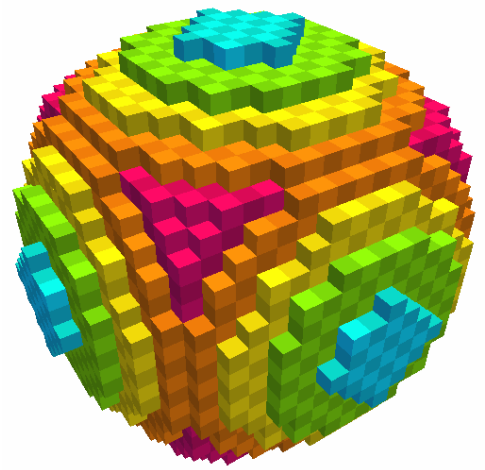

Fig. 8. Model of elementary nanostructure of friction (8103 atomic cubical cells) [1,14-18]

Calculations have shown [1] the number N_Q of such mechanical «quanta» (subtribosystems) within the elementary tribosystem's volume $V_f^* = V_{dis}^*$ to be $0{,}63 \cdot 10^8$, which is close to the safe number n_* of fatigue cycles.

According to the quantum damping model of surfaces under friction, when we have the state of more full evolution of elementary tribosystem, the all mechanical quanta to elastic and reversible transform the energy of external mechanical motion. Only one mechanical quantum (8103 atoms) is the minimum loss (the essence of «wearlessness»).

In these terms (point 4) only one mechanical quantum [1, 18] is the lost – standard wear. The tribosystem (friction contact) has the ideal damping properties – «wearlessness».

The principle of mechanical quantum determines nanoquantum levels of all friction parameters of compatible (optimal) tribosystems and other.

3.6. Gear wear calculation principle

The all parameters of compatibility (optimal) friction have to be in quanta levels - commensurable with the parameters of the one mechanical quantum – standard of wear.

So, all heavy-loaded tribosystems it is necessary to examine with position of tribosystem ideal evolution. This ideal state of tribocontact is true indicator of tribosystem state for practical examples of tribology. It is the standard of maximum tribosystems efficiency - anomalously low friction and wearlessness.

The state of friction contact under its most full evolution is the characteristic with exploitation of hard loaded Hertzian contact, for example, on the surfaces of gear wheels teeth and systems of wheel-rail and other. We can examine the active surface of gear wheel, which consist of equilibrium spherical form asperities after run-in. During one revolution of gear wheel each asperity of gear wheel teeth is loaded one time too. Under it the loss of one friction contact is equal to one mechanical (nano) quantum. Therefore, the whole

contact volume is fatigue failured during about 63 millions cycles. The linear wear h_* of gear wheel is equal to diameter size $Q_{TS} = 2{,}85 \cdot 10^{-6}$ m of an equilibrium friction volume V_f^* (Fig. 9) [19]. It is the physical criterion of wear. One may understood that the constructive (limiting) criterion of gear teeth is equal to the limit clearance between tooth surfaces. For example, it is about $0{,}4$ modulus of gear wheel tooth.

Thus, an elementary nano-structure of deformed solids may examine as the standard of wear and to apply with optimization the life time of real hard pressed Hertzian contact systems.

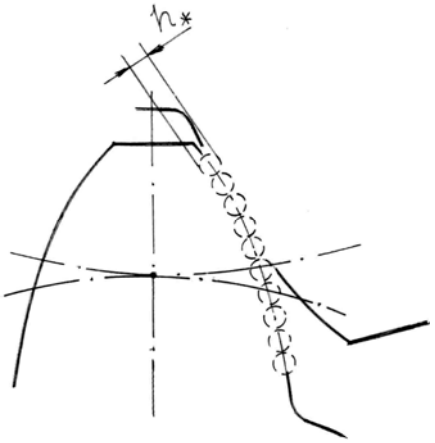

Fig. 9. Model of an active surface of gear wheel with equilibrium spherical form asperities.

4. CONCLUSIONS

4.1. Structural-energy analysis of the friction process allows us to examine the friction process as the evolution process;
4.2. From the energy balance equations of friction follows that the evolution of tribosystem (contact) has an adaptive-dissipative character.
4.3. Experimental friction curves of $\mu = \mu(N, v)$ type may be examined as generalized friction experimental curves;
4.4. The fuller evolution of tribosystem has symmetrical view - the friction process is started and finished within elastic area.
4.5. Under fuller evolution of friction contact (elementary tribosystem) the unique nanostructure is formed; the basis of this structure is the mechanical (nano) quantum and the contact (material point of mechanics) consists of about $0{,}63 \cdot 10^8$ such quantums.
4.6. We can examine the mechanical quantum as the least structural form of solid material body and the standard of wear.
4.7. All parameters of compatibility (optimal) friction have to be in quanta levels - commensurable with the parameters of the one mechanical quantum.
4.8. Interaction between nanoquantums is nature the net elasticity. The value of the coefficient of friction between mechanical quantums has order $\mu_{MQ} = 1{,}587 \cdot 10^{-8}$.
4.9. Exploitation of gear wheels and other heavy-loaded tribosystems (Herzian contact) are subjected to model of nanoquanta damping, when one mechanical quantum is the standard of wear (pitting).

5. REFERENCES

1. S.V.Fedorov, “The Foundations of Triboergodynamics and Physico-Chemical Prerequisits of Compatibility Theory (in Russian)”, Kaliningrad State Technical University Press, Kaliningrad, 2003.
2. V.V. Fedorov, “Thermodynamic Aspects of Strength and Fracture of Solids” (in Russian), Science, Tashkent, 1979.
3. V.V. Fedoro, “Kinetics of Damage and Fracture of Solids” (in Russian), Science, Tashkent. 1985.
4. V.V. Fedorov, “Ergodynamic concept of strength and failure of solids”, in: Proceeding of the VI-th All-Union Congress on Theoretical and Applied Mechanics (in Russian), 1986, Tashkent, USSR, pp. 610-611.
5. V.V. Fedorov, “Ergodynamic and synergetic of deformed solids, Physico-Chemical Mechanics of Materials” (in Russian), No. 1, 1988, pp. 32—36.

6. V.V. Fedorov, “Ergodynamic concept of failure, Strength of Materials” (Translated from Russian), Vol.23, No. 8, 1991, pp. 883-889.
7. V.S. Ivanova, “Fatigue Fracture of Metals” (in Russian), Metallurgy, Moscow, 1963.
8. J. Friedel. Dislocations, Oxford, 1964.
9. I.V. Kragelskii, M.N. Dobychin, and V.S. Kombalov, “Friction and Wear Calculation Methods” (in Russian), Mechanical Engineering, Moscow, 1977.
10. F.P. Bowden, D. Tabor, “The Friction and Lubrication of Solids”, At the Clarendon Press, Oxford, 1964.
11. B.I. Kostetskii, “Friction, Lubrication and Wear in Machines” (in Russian), Technics, Kiev, 1970.
12. I.V. Kragelskii, V.S. Schedrov, “Development of Science of Friction” (in Russian), USSR Academie Science, Moscow, 1956.
13. I.K. Lancaster, “Basic Mechanisms of Friction and Wear of Polimers”, Plastics and Polymers, vol. 41, pp. 296-306, 1973.
14. S.V. Fedorov, “Energy Model of Sliding Friction Coefficient and Generalized Regularities of Tribosystems Evolution”, in: Transactions of the 19th International Colloquium Tribology «Tribology-Industrial and Automotive Lubrication», TAE, 21-23.01.2014, Esslingen, Germany, www.tae.de info@tae.de.
15. S.V. Fedorov, “The mechanical quantum of dissipative friction structures is the elementary tribonanostructure”, IV WTC2009, September 5-11, 2009, Kyoto, p.926.
16. S.V, Fedorov, Some Aspects of the Ergodynamics of Deformed Bodies and Triboergodynamics, Supplement to HANDBOOK. An Engineering Journal. [in Russian], no. 8: 2010.
17. S.V. Fedorov, The Friction Coefficient and its Relation to the Contact Fatigue Characteristics of Materials. Industrial Laboratory. Translated From Zavodskaja Laboratorija. Vol. 61. no. 1: 1995, pp.41-49.
18. S.V. Fedorov, Generalized Energy Model of Sliding Friction Coefficient and Regularities of Tribosystem Evolution. In: Transactions of V World Tribology Congress 2013. Turino, Italy. 2013. ISBN 9788890818509.
19. S.V. Fedorov, Calculation of the true friction volume. Friction & Lubrication in Machines and Mechanisms. No.5 2010, pp. 3-7.

CORRESPONDENCE

Sergey Vasiliy FEDOROV
ESTIMATION of WEAR FOR REDUCER TOOTH WHEELS WITH USING THE MODEL OF MECHANICAL (NANO) QUANTUM
Department of Theory of Mechanisms and Machines and Machine Parts, Kaliningrad State Technical University, Kaliningrad, Russia
e-mail: **fedorov@klgtu.ru**

Tribological Journal BULTRIB Vol. 5, 2015
Papers from the International Conference **BULTRIB '15**
September 11-13, 2015, Sozopol, Bulgaria
Society of Bulgarian Tribologists
FIT – Technical University of Sofia

THEORETICAL STUDY OF THE DAMPING PROPERTIES OF THE NON-NEWTONIAN FLUIDS

Alexandru Valentin RADULESCU, Irina RADULESCU

Abstract: *The paper presents the theoretical analysis of the damping properties of the non-Newtonian fluids for an axial-symmetric flow between two plane circular surfaces. The rheological model of the lubricant is the Herschel-Bulkley model and the flow process is considered isotherm. For this case of flow, the velocity profile in the lubricant film, the shape and the dimensions of the stagnant core, the flow capacity, the pressure distribution and the damping coefficient have been obtained.*

Key Words: *Non-Newtonian fluids, Herschel-Bulkley model, Damping*

1. INTRODUCTION

The paper presents the theoretical analysis of the damping properties of the non-Newtonian fluids for an axial-symmetric flow between two plane circular surfaces.

The damping properties of the Newtonian fluids are well known, taking account of the papers presented by Stefan [8], Brown [1] and Hunt [2]. However, in the meantime, interest has moved to the squeeze film damping of non-Newtonian fluids, specifically grease, because the use of grease as a lubricant for machine parts is receiving increasing attention in a wide field of engineering practice. Very little information is currently available on this aspect of lubricant film dynamics [3], [5].

In order to study the damping characteristics of the non-Newtonian fluids, an elastic system has been considered, composed by a mass M, a vibrator with the rigidity k and a squeeze film damper C (see Fig. 1).

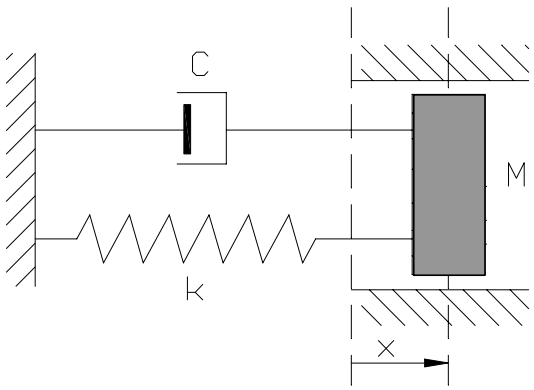

Fig. 1. Dynamic model

The equation of motion is given by:

$$M\ddot{x} + F + kx = 0 \quad (1),$$

where F represents the damping force.

For the Newtonian fluids, this force is proportional with the velocity ($F = c\dot{x}$). In the case of non-Newtonian fluids, the damping force must be calculated for each geometry of the damper.

2. DAMPING FORCE FOR THE NON-NEWTONIAN FLUIDS

The theoretical analysis is based on a generalised model for any incompressible flow, the Herschel-Bulkley model, expressed as:

$$\tau = \tau_0 + m\left(\frac{du}{dy}\right)^n \quad (2),$$

for squeezing flow between two parallel circular plates as shown in Figure 2. Characteristic for this motion is the existence of the stagnant core [4], which move with a constant velocity.

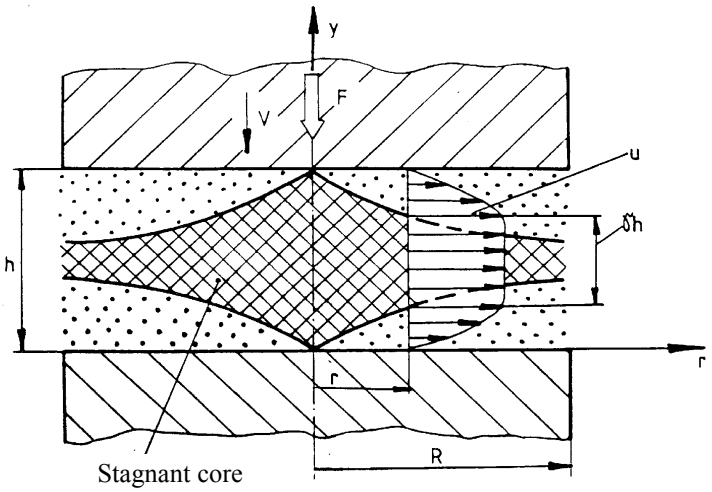

Fig. 2. Fluid flow geometry

Using the Navier-Stokes equations above:

$$\begin{cases} \dfrac{dp}{dx} = m\dfrac{d^2u}{dy^2} & for \quad \tau > \tau_0 \\ \dfrac{d^2u}{dy^2} = 0 & for \quad \tau \le \tau_0 \end{cases} \quad (3)$$

and integrating, the velocity distribution (eq. 4), Reynolds equation (eq. 5) and damping force (see Fig. 3) can be obtained [6].

a) Velocity distribution:

$$u = \begin{cases} \dfrac{n}{n+1}\dfrac{1}{m^{\frac{1}{n}}}\left(-\dfrac{dp}{dr}\right)^{\frac{1}{n}}\left[\left(\dfrac{h-\gamma h}{2}\right)^{\frac{1}{n}+1} - \left(\dfrac{h-\gamma h}{2} - y\right)^{\frac{1}{n}+1}\right] & for\ y \in \left[0; \dfrac{h-\gamma h}{2}\right] \\ \dfrac{n}{n+1}\dfrac{1}{m^{\frac{1}{n}}}\left(-\dfrac{dp}{dr}\right)^{\frac{1}{n}}\left(\dfrac{h-\gamma h}{2}\right)^{\frac{1}{n}+1} & for\ y \in \left[\dfrac{h-\gamma h}{2}; \dfrac{h+\gamma h}{2}\right] \\ \dfrac{n}{n+1}\dfrac{1}{m^{\frac{1}{n}}}\left(-\dfrac{dp}{dr}\right)^{\frac{1}{n}}\left[\left(\dfrac{h-\gamma h}{2}\right)^{\frac{1}{n}+1} - \left(y - \dfrac{h+\gamma h}{2}\right)^{\frac{1}{n}+1}\right] & for\ y \in \left[\dfrac{h+\gamma h}{2}; h\right] \end{cases} \quad (4)$$

b) Reynolds equation:

$$\left(1+\frac{1}{n}\right)\left(-\frac{dp}{dr}\frac{h}{2}-\tau_0\right)^{\frac{1}{n}+2}+\left(2+\frac{1}{n}\right)\left(-\frac{dp}{dr}\frac{h}{2}-\tau_0\right)^{\frac{1}{n}+1}\tau_0-\left(1+\frac{1}{n}\right)\left(2+\frac{1}{n}\right)m^{\frac{1}{n}}\left(\frac{dp}{dr}\right)^2\frac{r}{4}V=0 \qquad (5)$$

c) Damping force:

$$\overline{F}=f(A,n) \qquad (6),$$

where $A=\dfrac{m^{\frac{1}{n}}VR}{\tau_0^{\frac{1}{n}}h^2}$ represent the non-dimensional film coefficient.

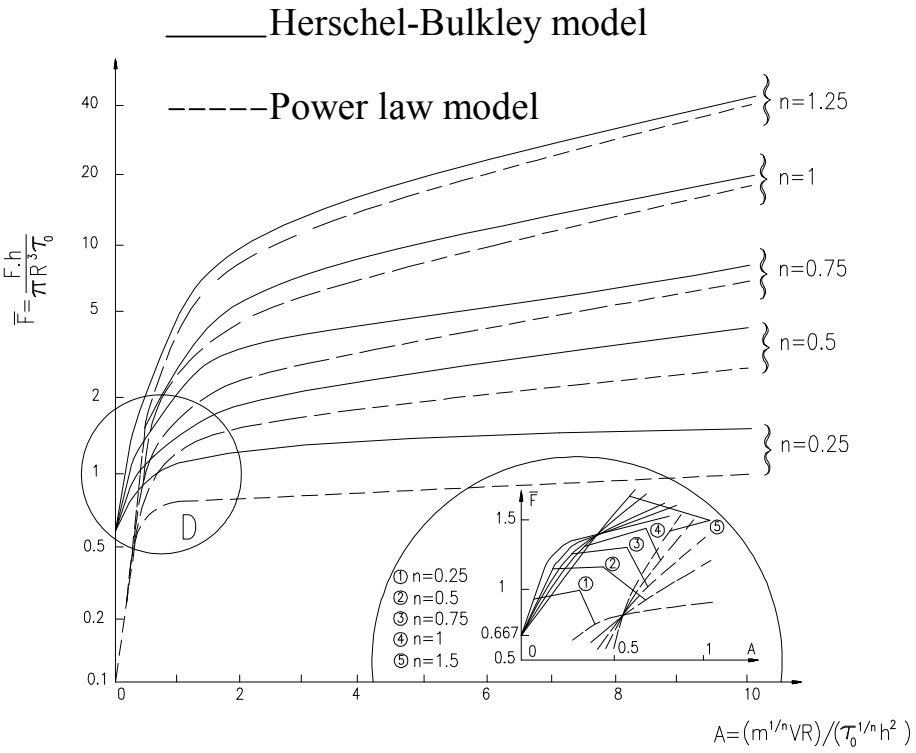

Fig. 3. **Damping force**

As function of the shear yield stress τ_0 and the flow index *n*, the damping force takes different values:

- Newtonian fluid (τ_0 = 0 and *n* = 1): $F=\dfrac{3\pi mR^4}{2h^3}V$ (7)

- Bingham fluid ($\tau_0 \neq 0$ and *n* = 1): $F=f(A,1)\dfrac{\pi R^3\tau_0}{h}$, with $A=\dfrac{mVR}{\tau_0 h^2}$ (8)

- Power law fluid (τ_0 = 0 and $n \neq 1$): $F=\left(\dfrac{2n+1}{n}\right)^n\dfrac{2\pi mR^{n+3}}{(n+3)h^{2n+1}}V^n$ (9)

- Herschel-Bulkley fluid ($\tau_0 \neq 0$ and $n \neq 1$): $F = f(A,n)\frac{\pi R^3 \tau_0}{h}$, with $A = \frac{m^{\frac{1}{n}} VR}{\tau_0^{\frac{1}{n}} h^2}$ (10)

3. RESULTS

The motion equation 1 can be analytically integrated only for the case of the Newtonian damping (eq. 7), obtaining the solution expressed as:

$$x = \sqrt{x_0^2 + \left(\frac{v_0 + \alpha x_0}{\beta}\right)^2}\, e^{-\alpha t} \sin\left(\beta t + arctg \frac{\beta x_0}{v_0 + \alpha x_0}\right) \quad (11),$$

where $\alpha = \frac{3\pi m R^4}{4Mh^3}$, $\omega = \sqrt{\frac{k}{M}}$, $\overline{\alpha} = \frac{\alpha}{\omega}$ and $\beta = \sqrt{\omega^2 - \alpha^2}$ if $\omega > \alpha$

For the case of non-Newtonian damping, the equation 1 is possible to be integrated only numerically. Figures 4a and 4b show the motion diagram and the amplitude for four cases of damping: Newtonian damping (eq.7), Bingham damping (eq.8), pseudo-plastic damping (eq. 10 for n<1) and dilatant damping (eq. 10 for n>1).

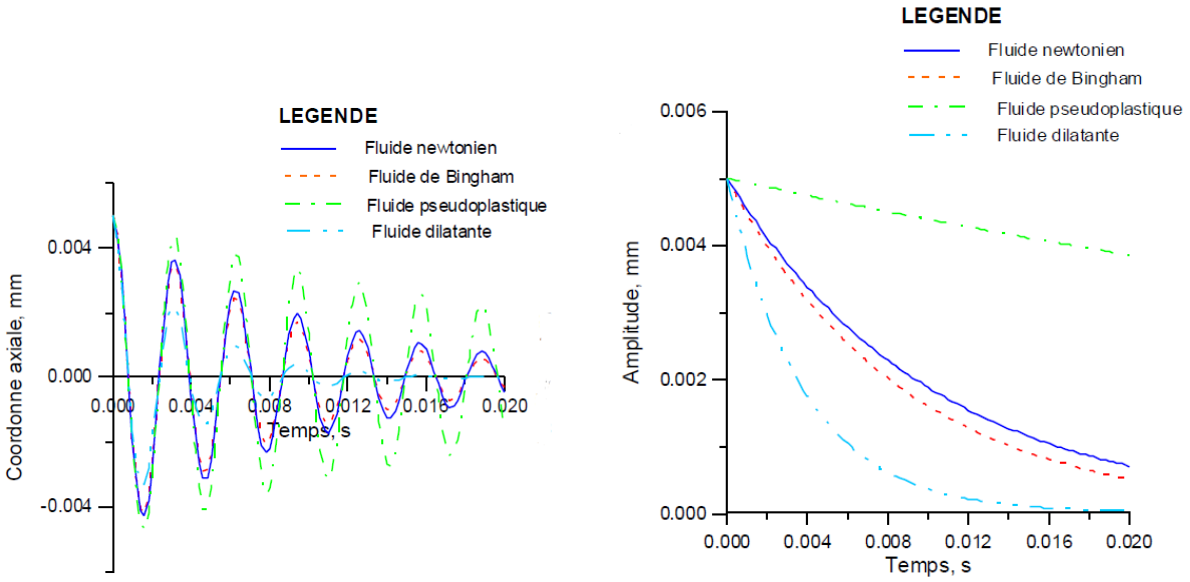

a) Motion diagram b) Amplitude variation

Fig. 4. Vibrating motion (M = 1000 kg, k = 4·10^9 N/m, R = 0,025 m, m = 0,1 Pa·s, h = 0,0001 m, x_0 = 0,005 mm, v_0 = 0 m/s)

Analysing these figures, it can observe that the damping properties of the film fluids depend on the values of the flow index *n*.

In order to obtain more information about the influence of the shear yield stress τ_0 , consistency index *m* and flow index *n*, the variation of the non-dimensional damping ratio $\overline{\alpha}$ have been studied (see Fig. 5a and 5b). Taking account that the greases are the most common non-Newtonian fluids and their behaviour is like a pseudo-plastic fluid, for the flow index only the values $n \leq 1$ have been considered.

Figures 5a and 5b do indicate an increase of the non-dimensional squeeze film damping ratio with increasing of the grease consistency index.

It is also evident from the same figure that the shear yield stress and the flow index have the same influence to the damping ratio as the consistency index.

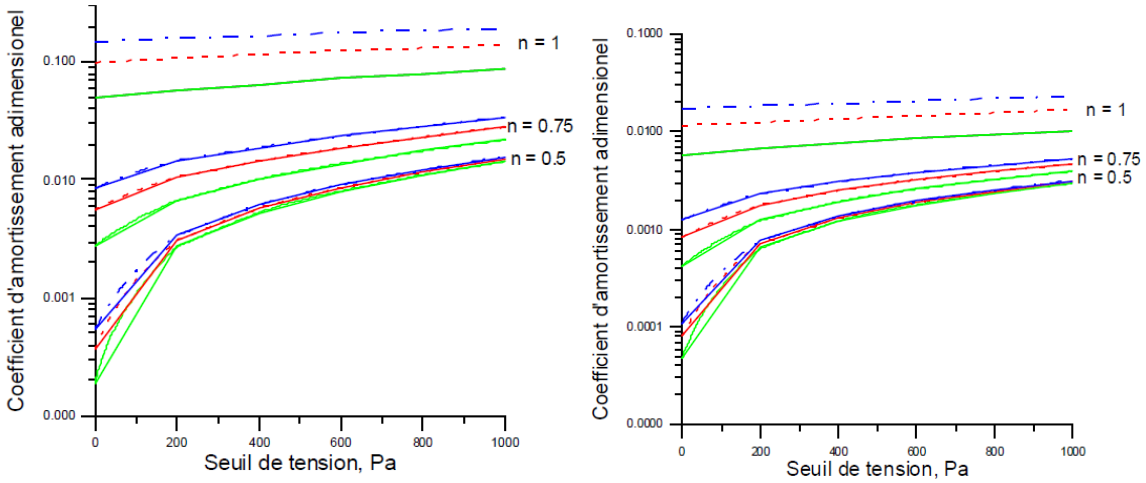

a) h = 0,0001 mm

b) h = 0,0002 mm

Fig. 5. Variation of the non-dimensional damping ratio

4. CONCLUSION

1. The squeeze film damping property of the greases is increasing with the values of the flow index, expressed as:

$$\overline{\alpha}_{pseudo-plastic\ fluids\ (\tau_0\neq 0, n<1)} < \overline{\alpha}_{Newtonian\ fluids\ (\tau_0=0, n=1)} < \overline{\alpha}_{Bingham\ fluids\ (\tau_0\neq 0, n=1)} < \overline{\alpha}_{dilatant\ fluids\ (\tau_0\neq 0, n>1)}$$

2. The squeeze film damping property of the greases bears no relation to the damping property of the base oil. The theoretical results of this paper and also the experimental results presented by Shah [7] have proved that the damping ratio of the greases may be less than that of the base oil by a factor of 7.

3. The damping ratio of the greases is inversely proportional to the cube of the film thickness.

REFERENCES

1. BROWN, G.M. Dynamic Characteristics of Hydrostatic Thrust Bearings, Mac Tool. Des. Res., 1961, No.1, 1-2, pp. 157-163
2. HUNT, J.B. Cavitation in Thin Film of Lubricant, The Engineer, 1965, 219, pp. 1137-1142
3. PASCOVICI, M.D., RADULESCU, A.V. The Grease Squeeze Film, Wear, 1987, 116, pp.261-266
4. PINKUS, O., STERNLICHT, B. Theory of Hydrodynamic Lubrication, Mc Graw Hill, 1961, New York
5. RADOI, M., DECIU, E. Mecanica, Ed. Didactica si pedagogica, 1977, Bucuresti
6. RADULESCU, A.V. An Approximate Global Method for the Determination of the Rheological Properties of the Greases, 11 th International Colloquium, Esslingen, 1998, Vol. III, pp. 2215-2220
7. SHAH, J. HUNT, J.B. Squeeze Film Damping of Non-Newtonian Fluids, Journal of Lubrication Technology, 1979, 101, pp. 516-519
8. STEFAN, J. Versuche über die schienbare Adhäsion, Sitzungsber, D.K. Akad, Wiessenschaften, Wien, 1874, 69, pp. 713-735

CORRESPONDENCE

Alexandru RADULESCU
Organisation: POLITEHNICA University Bucharest, Romania
Address: 313 Spl. Independentei, Sect. 6, 060042, Bucharest, Romania
e-mail: varrav2000@yahoo.com
Irina RADULESCU
Organisation: POLITEHNICA University Bucharest, Romania
Address: 313 Spl. Independentei, Sect. 6, 060042, Bucharest, Romania
e-mail: irena_sandu@yahoo.com

Tribological Journal BULTRIB Vol. 5, 2015
Papers from the International Conference **BULTRIB '15**
September 11-13, 2015, Sozopol, Bulgaria
Society of Bulgarian Tribologists
FIT – Technical University of Sofia

ONE-STEP SYNTHESIS AND CHARACTERIZATION OF NANOMETRIC $Ce_{1-x}Y_xO_{2-\delta}$ SOLID SOLUTIONS

Martin FABIÁN[1*], Nina KOSTOVA[2], Jaroslav BRIANČIN[1], Yordanka KARAKIROVA[2]

[1]Institute of Geotechnics, Slovak Academy of Sciences, Watsonova 45, 04001 Košice, Slovakia
[2]Institute of Catalysis, Bulgarian Academy of Sciences, Acad. G. Bonchev St. 11, Sofia 1113, Bulgaria

Abstract: *The cerium oxide (ceria, CeO_2) and ceria based materials become one of the most interesting ceramics from both fundamental and practical point of view. The nanostructured fluorite-type $Ce_{1-x}Y_xO_{2-d}$ solid solutions with the average crystallite size below 20 nm are produced by high-energy ball milling. Raman spectroscopy indicates an increment in the concentration of intrinsic/extrinsic oxygen vacancies. Broad PL spectra confirm formation of defects. This phenomena is further confirmed by variation in optical properties. The presence of Ce^{3+} cations is confirmed by EPR spectroscopy.*

Key Words: *Ceria, Yttrium, Solid solution, Mechanosynthesis, Optical properties*

1. INTRODUCTION

Numerous studies have shown that materials with a crystal size of less than 100 nm exhibit optical, electrical, catalytic, thermal, and mechanical properties that significantly differ from those observed for their microcrystalline counterparts. Among others, in recent years, cerium dioxide (ceria, CeO_2) and ceria based nanomaterials have attracted much attention becauce they possess many attractive properties which make it highly promising for a wide range of applications such as catalysts, oxygen sensors, SOFC´s etc. (see, e.g., Refs. [1-4] and citations therein). Apart from that, the ceria and ceria based compounds have attracted scientific consideration due to the optical, microelectronic and optoelectronic applications [5]. Contradictory, the valence of Ce is very important for the structure of cerium oxides; while tetravalent Ce forms ceria with cubic fluorite lattice (*Fm3m, S.G.*) the trivalent Ce forms the sesquioxide Ce_2O_3 with hexagonal lattice ($P\bar{3}m1$, *S.G.*). Both oxides possess a high refractive index and a high absorption of Ultra violet (UV) radiation makes it an ideal UV blocker with potential replacement of zinc oxide and titanium dioxide in sunscreens [6,7]. However, Ce^{4+}/Ce^{3+} coexistence in cerium oxides significantly influences the optical properties. As it was reported [8, 9] the fraction of Ce^{3+} localized on surface increase with decreasing crystalline size. The presence of the Ce^{3+} results in the blue shift in nanoparticles because the $Ce^{4+} \rightarrow Ce^{3+}$ reduction increases the charge-transfer gap between O 2p and Ce 4f bands rather than the quantum size effect [10,11].

Many methods have been applied to the preparation of ceria (and ceria based) nanomaterials (see, e.g., Refs. [1,4,12,13]). However, most of these techniques are time/energy consuming, are complex and not environmentally friendly what makes many of them unatractive from the mass production point of view. The one of the cost and time effective methods towards alternative synthesis of plenty of novel (inorganic and organic) nanomaterials, *mechanosynthesis*, and its impact on modified structural, physical and functional properties has been already discussed [14].

Within this study, we provide a comparative investigation of undoped and Y doped CeO_2 nanopowders, synthesized via one-step mechanochemical approach. The stress is forwarded to optical and photoluminescence properties related to microstructural parameters. Hence, the paper brings valuable light inside mechanochemical processing of ceria and ceria based compounds mostly towards their optical applications.

2. EXPERIMENTAL

The solid precursors, cerium oxide (CeO_2, 99.9 % purity; Aldrich) and yttrium oxide (Y_2O_3, 99.99 % purity; Aldrich) were used for the mechanosynthesis of $Ce_{1-x}Y_xO_{2-\delta}$. 5g of the $(1–x)CeO_2 + (x/2)Y_2O_3$ mixtures (x = 0.1 – 0.3) were milled for various times (up to 90 min) in a high-energy planetary ball mill Pulverisette 7 Premium line (Fritsch). A grinding chamber (80 cm^3 in volume) and balls (10 mm in diameter) made of tungsten carbide were used. The ball-to-powder weight ratio was 40:1. Milling experiments were performed in ambient atmosphere at 600 rpm.

XRD patterns were collected using a D8 Advance diffractometer (Brucker) with the CuKα radiation in the Bragg–Brentano configuration. The generator was set up at 40 kV and 40 mA. The divergence and receiving slits were 0.3° and 0.1 mm, respectively. The XRD patterns were recorded in the range of 20–85° 2θ with a step of 0.03° and a measuring time of 20 s.

The ultraviolet-visible-NIR (UV-vis-NIR) diffuse reflectance spectra were performed under ambient conditions using a Thermo Evolution 300 UV-Vis spectrophotometer equipped with a Praying Mantis accessory. The spectra were recorded in the range of 200-1100 nm. The Spectralon (Labsphere, Inc.) as a "white reflectance standard" was used to collect background.

The Raman spectra with excitation laser wavelength 532 nm were performed in back-scattering geometry using a XploRa (Horiba Jobin Yvon) spectrometer. Raman spectra were recorded in the 800-200 cm^{-1} range with the laser power of 10 mW.

The EPR spectra were recorded on JEOL JES-FA 100 EPR spectrometer operating in X-band with standard TE 011 cylindrical resonator at room temperature.

Photoluminescence (PL) measurements were carried out on a luminescence spectrometer PC 1 (ISS) using a Xenon lamp as the excitation source at room temperature. The sample was dispersed in ethanol and the excitation wavelength used in PL measurement was 290 nm.

3. RESULTS AND DISCUSSION

The formation of $Ce_{1-x}Y_xO_{2-\delta}$ (x = 0.1 – 0.35) solid solutions was followed by XRD. As it is shown in Fig. 1 for the case x = 0.35, the XRD pattern of the unmilled mixture is characterized by sharp diffraction peaks corresponding to CeO_2 (JCPDS PDF 28-706) and Y_2O_3 (JCPDS PDF 16-394). After 15 min of intensive ball milling (no presented in figure 1), the Bragg reflections belonging to the Y_2O_3 phase decrease in the intensity, broaden, and merge together with the diffraction peaks of the CeO_2 phase. In the XRD pattern of the sample milled for 90 min, all the diffraction peaks become fully symmetric. The disappearance of the asymmetry of XRD lines and their shift to the higher angular positions indicate the mechanically induced incorporation of yttrium into ceria structure, i.e., the mechanically triggered formation of the $Ce_{0.65}Y_{0.35}O_{2-\delta}$ solid solution (JCPDS PDF 28-811).

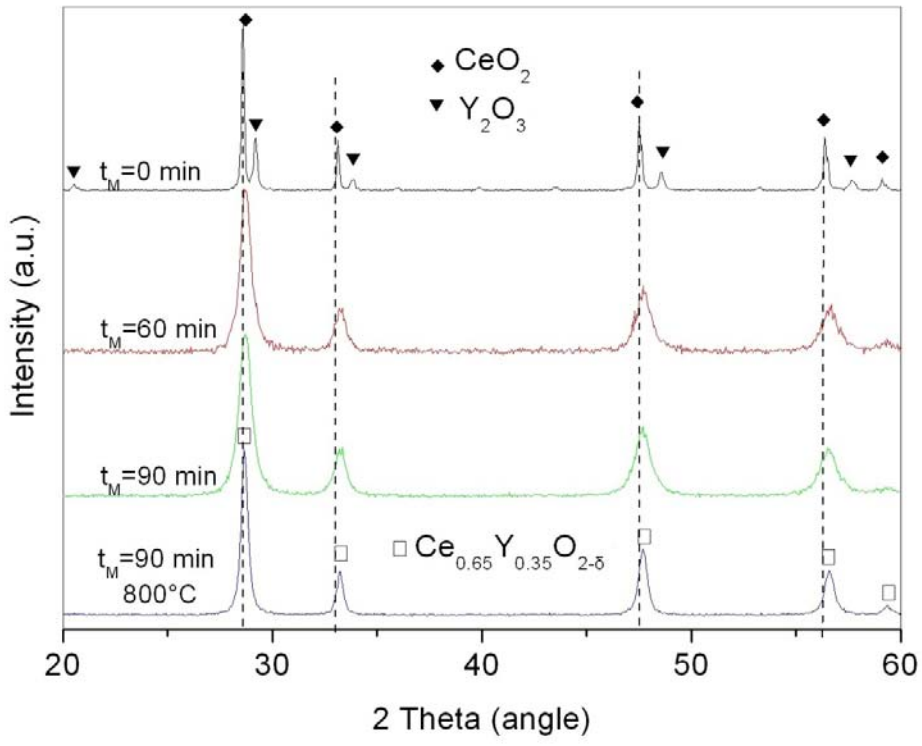

Fig. 1 XRD patterns illustrating the mechanochemical synthesis of the $Ce_{0.65}Y_{0.35}O_{2-\delta}$ solid solution. The milling times (t_M) and calcination temperature are shown in the figure.

Note that for x = 0.4, Rietveld analysis of the XRD data revealed a small amount (~ 3.9 wt%) of unreacted Y_2O_3 residues in the milled mixture. This finding is in agreement with previous work on the thermally induced transformations in the CeO_2–Y_2O_3 system [15]. Fig. 1 (bottom) shows the XRD pattern of the mechanosynthesized $Ce_{0.65}Y_{0.35}O_{2-\delta}$ phase after thermal treatment at 800°C for 4 h in ambient atmosphere. As it is seen, the thermal processing leads to the narrowing of the XRD lines of the $Ce_{0.65}Y_{0.35}O_{2-\delta}$ phase due to its crystallite growth. The XRD patterns of mechanosynthesized $Ce_{1-x}Y_xO_{2-\delta}$ (x = 0.1 – 0.35) solid solutions are

shown in Fig. 2. It is seen that effective incorporation of yttrium into the fluorite-type structure of ceria results in continuous shift of all characteristic XRD reflections to the higher angular positions (lower values of d-spacing), indicating a lattice contraction of $Ce_{1-x}Y_xO_{2-\delta}$ with the Y^{3+} doping.

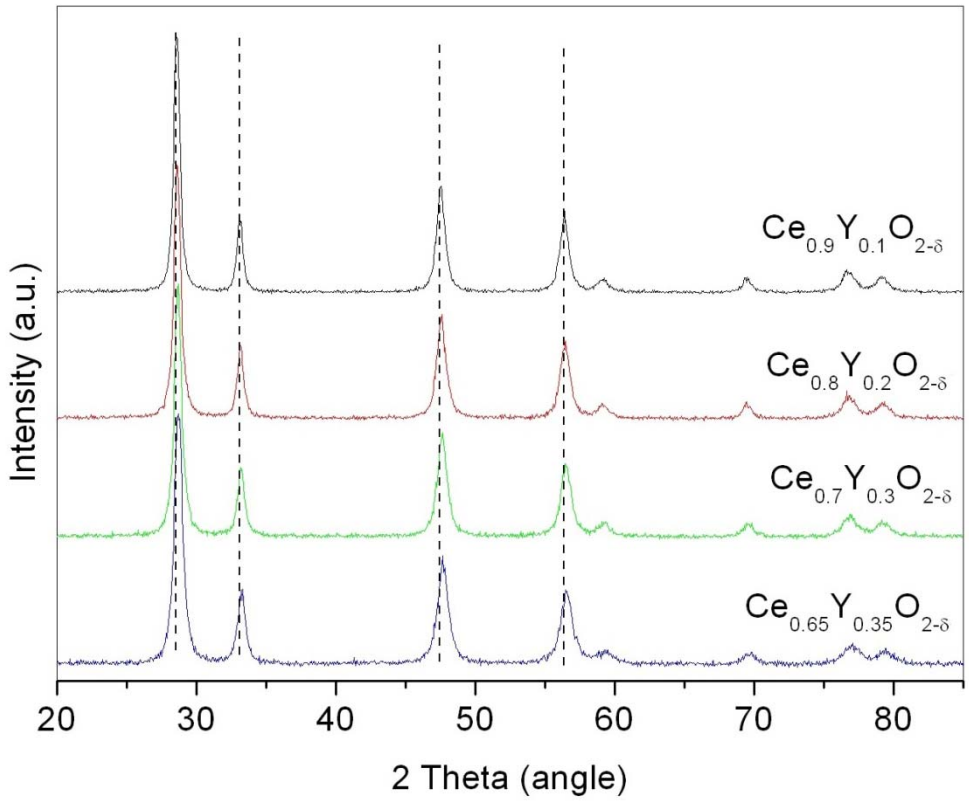

Fig. 2 XRD patterns of mechanosynthesized $Ce_{1-x}Y_xO_{2-\delta}$ (x = 0.1 – 0.35) solid solutions.

Results of Rietveld refinement of XRD data are scrutinizingly described in recent paper of Fabian et al. [16]. It was found that effect of Y^{3+} doping on the long-range structural parameters manifests itself in several aspects, i.e., i) the lattice parameter of the solid solutions decreases linearly with the increase in Y^{3+} content up to x = 0.2; at higher content of Y^{3+} , the nonlinear contraction of lattice is observed; ii) an increase in Y^{3+} concentration induces an increase in microstrains in the host ceria lattice; iii) the lattice contraction of $Ce_{1-x}Y_xO_{2-\delta}$ material with doping is accompanied by a decrease in its interplanar distances.

Fig. 3 presents the normalized room-temperature Raman spectra of $Ce_{1-x}Y_xO_{2-\delta}$ (x = 0 – 0.35) nanopowders. The most intensive peak at 461.4 cm^{-1} corresponds to the triple degenerated F_{2g} Raman active mode characteristic for Ce–O symmetric vibrations in eightfold coordination [17]. With increasing Y^{3+} content, this peak broadened and became asymmetric indicating the formation of solid solution [18]. It has demonstrated that several factors contribute to the changes in both position and broadening of the F_{2g} Raman mode including phonon confinement, strain, non-homogeneity of the size distribution, variations in phonon relaxation with particle size, the presence of oxygen vacancies, defects and changes in lattice parameters [19]. The most interesting features of the Raman spectra of nanocrystalline $Ce_{1-x}Y_xO_{2-\delta}$ solid solutions is the increase of two additional Raman modes centred at ca. 600 cm^{-1} and ca. 550 cm^{-1}. The Raman peak at ca. 600 cm^{-1} is already seen in pure ceria nanopowders [20] and is attributed to the defect spaces which include formation of oxygen vacancies [19]. A new weak shoulder on the high frequency side of the F_{2g} band appears as Y^{3+} ions are incorporated into ceria structure. This feature evolves into a broad peak whose intensity tends to increase with increasing Y content. This mode, centred at ca. 550 cm^{-1} , was first time described in details by Nakajima et al. [17] regarding single crystals of Y-doped CeO_2. They attributed this mode to the defect spaces which include O^{2-} extrinsic vacancies.

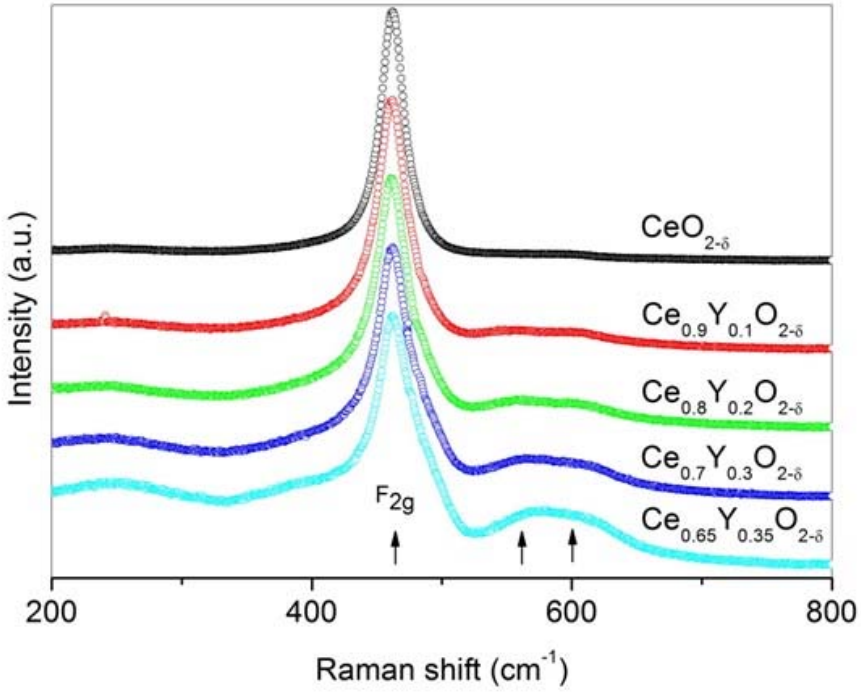

Fig. 3 Raman spectra of the milled ceria and of mechanosynthesized $Ce_{1-x}Y_xO_{2-\delta}$ (x = 0.1 – 0.35) solid solutions. Arrows denote particular vibration modes.

As it is shown in Fig. 4, the UV-vis-NIR diffuse reflectance spectroscopy (UV-vis-NIR DRS) has been utilized to perform information on different oxidation states and surface coordination [21]. The analysis was performed by converting the obtained reflectance spectra (Figure 4, inset) to the Kubelka-Munk absorbance spectra. In the case of CeO_2, band structure calculations show that the valence band (VB) has mainly a 2p(O) character and the conduction band (CB) is essentially 5d(Ce) in character. Following DFT calculations, the gap between those two bands is given to be ~ 5.75 eV [22]. However, the 4f-block band that is empty for Ce^{4+} lies between the VB and CB and then the experimental optical gap, i.e., Eg is attributed to a 2p(O)→4f(Ce) charge transfer [23]. The plot of absorbance against wavelengths in as-prepared nanopowders is aslo shown in Figure 4. As it is clearly seen, all the samples strongly absorb the UV light (below 400 nm) as a consequence of the 2p(O)→4f(Ce) transition. However, the split of the absorption observed at ~256, ~264 and ~330 nm may be attributed to the $O^{2-} \rightarrow Ce^{3+}$ and $O^{2-} \rightarrow Ce^{4+}$ charge transfer (CT) and interband ($4f^1$-$5d^1$) transitions (IBT), respectively [24]. The spectra show that the absorption edge is shifted to longer wavelength upon yttrium incorporation into ceria structure.

Simultaneously, the yttrium loading concentration increases the reflectance in the visible part of the spectrum and in Schuster-Kubelka-Munk absorption. The band gap energies can be determined by fitting the absorption data to the direct/indirect transition equation by extrapolating on the linear portions of the curves to absorption equal to zero according Eq. (1)

$$\alpha h\nu = A(h\nu - E_g)^{\eta} \tag{1}$$

where α is the optical absorption coefficient, $h\nu$ is the photon energy, E_g is optical band gap energy, A is constant and n is a constant with the value ½ for direct allowed transitions and 2 for indirect allowed transitions, respectively [25].

Plotting $(\alpha h\nu)^2$ as a function of photon energy $h\nu$, and extrapolating the linear portion of the curve to the absorption equal zero gives the value of direct band gap of undoped and doped nanocrystalline CeO_2 (Figure 5 (a)). The correlated direct band gap (E_g) for undoped CeO_2 nanoparticles (d_G ~ 21 nm) was found to be 3.55 eV. This vale is within the range characteristic for nanocrystalline CeO_2 (3.31 - 3.7 eV) reported in literature [see e.g. 1 and references therein]. Compared to the bulk CeO_2 (E_g = 3.10 – 3.30 eV) [26] our ball milled CeO_2 samples showed an increase in E_g of ~ 0.2 eV. This blue shifting phenomena of nanocrystalline CeO_2 has been explained in terms of quantum confinement effect and changes in the electronic structure [10].

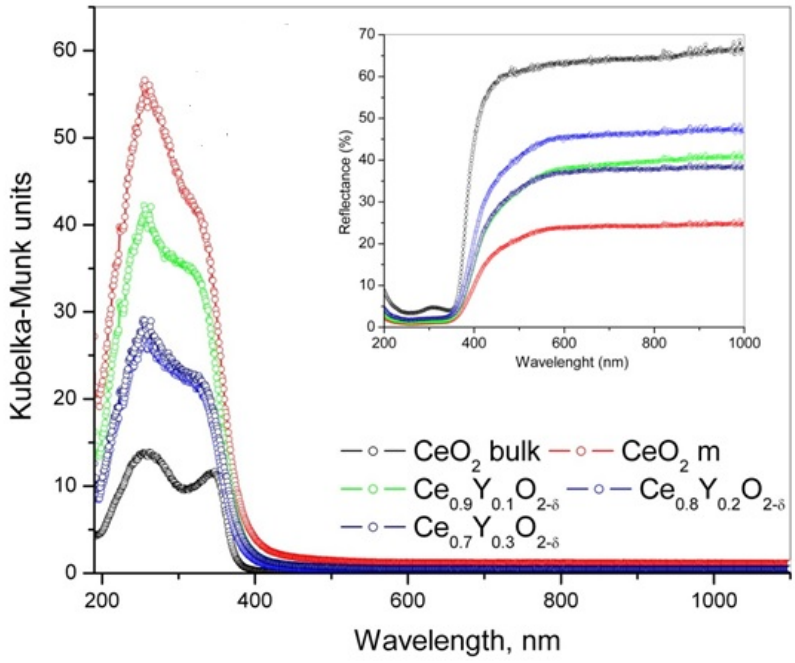

Fig. 4 Absorbance curves in Kubelka –Munk units for $Ce_{1-x}Y_xO_{2-\delta}$ (x = 0.1 – 0.35) solid solutions (inset). Reflectance as a function of wavelenght.

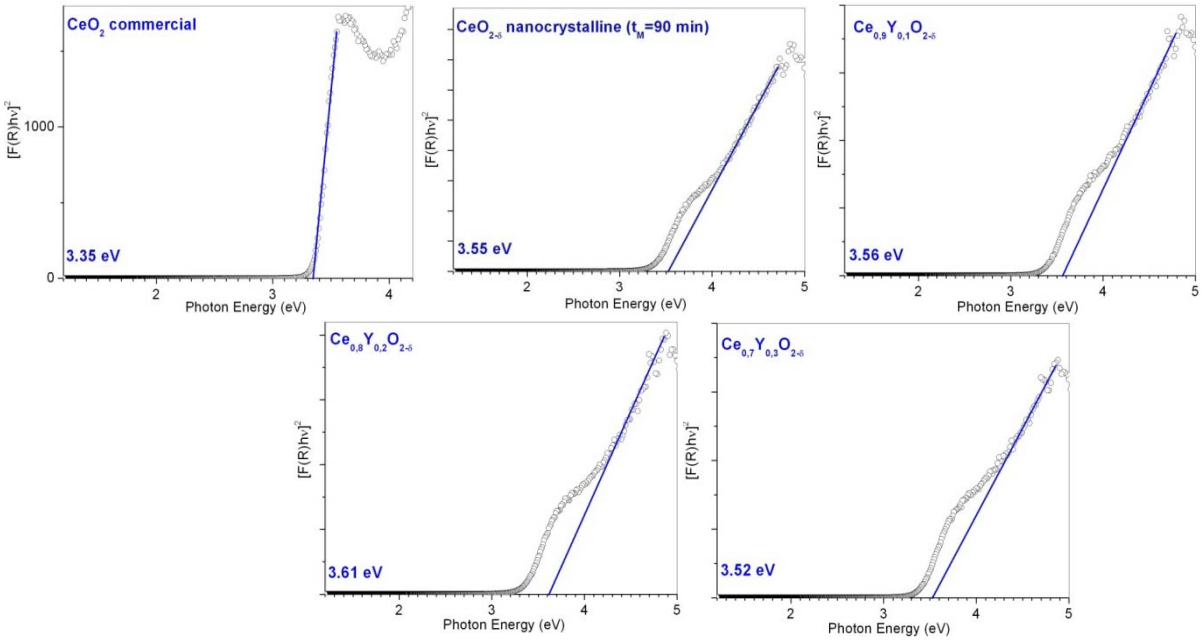

Fig. 5 Tauc plots versus photon energy for direct band gap transitions together with linear fits (solid lines), using the Eq. (1), for $Ce_{1-x}Y_xO_{2-\delta}$ (x = 0.1 – 0.35).

Since the fundamental band gap is mainly deduced by quantum size effect when the particle is between 0 and 3 nm, the quantum size effect in our CeO_2 nanoparticles with particle size of ~ 15-20 nm may be ruled out, and the changes in electronic structure, *i.e.* charge transition of Ce ion (Ce^{3+}–Ce^{4+}) may play an important role in the increase in the band gap of our CeO_2 sample.

Furthermore, it was confirmed that the doping of yttrium may slightly rise the E_g value of CeO_2. As it was interpreted by Liu et al. [27], the further blue shifting is attributed to the creation of new (extrinsic) oxygen vacancies upon doping rather than contribution of 4d (Y) band which is located at higher energies and is not involved in the optical absorption process. Additionally, the 4f (Ce) block band lies in the gap between the valence band and conduction band and its position should not be modified too much along the solid solution. Since the conduction and the valence band are relatively flat according to reported electronic calculations [28], one can assume that the transition involves a direct band gap.

Mixed valence of Ce^{3+}/Ce^{4+} exists in the solid solutions, which is confirmed by the EPR. This technique is efficient in identifying Ce^{3+} in the bulk of ceria-based solid solutions. Ce^{4+} and Y^{3+} are inactive in EPR. As it is seen in Fig. 6 the milled CeO_2 revealed the formation of paramagnetic species of Ce^{3+} which we assigned to signal with $g_{\perp}$ =1.97 and $g_{\parallel}$ =1.94. This result corroborates the assumption of the presence of Ce^{3+} ions and oxygen vacancies in the samples [29].

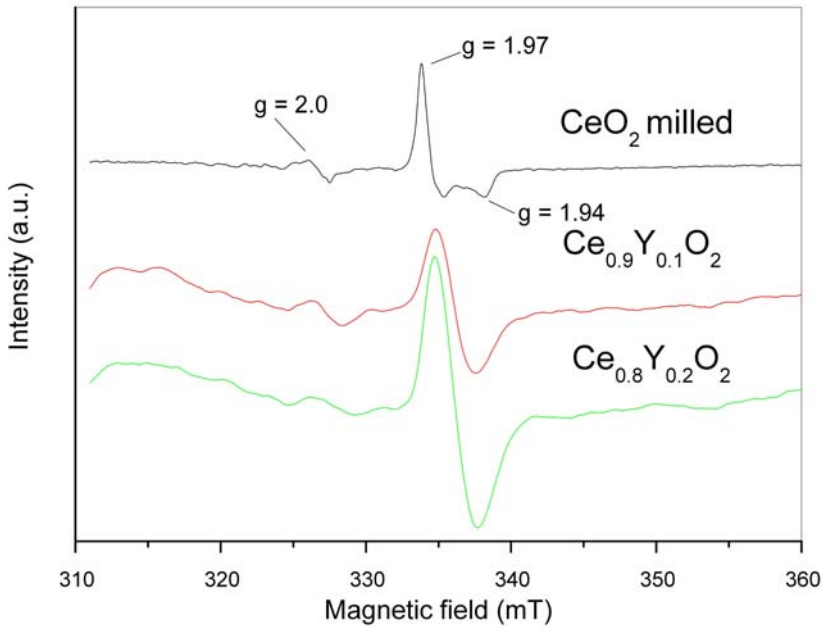

Fig. 6 EPR spectra of the milled ceria and of mechanosynthesized solid solutions

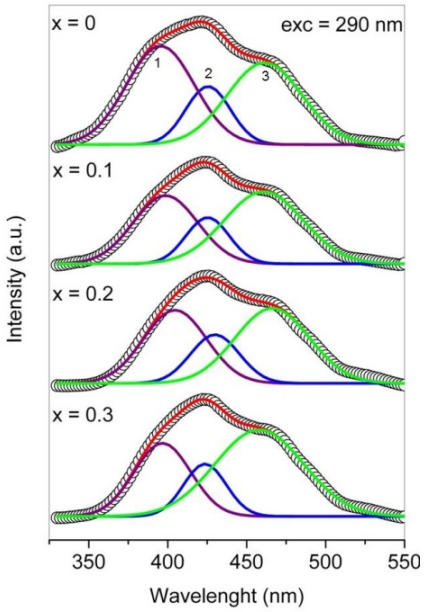

Fig. 7 PL spectra (dots), the corresponding Gaussian fits (thin solid lines) and cumulative curves (red solid lines) of $Ce_{1-x}Y_xO_{2-\delta}$ solid solutions, measured with excitation at 290 nm.

PL spectra of pure nanocrystalline CeO_2 and its solid solutions measured at λ_{ex}=290 nm (Ce^{3+} transition [30]) are shown in Figure 7. Normalized PL spectra were fitted with Gaussian profiles. It is seen that PL spectra are characterized by three main peaks centered at ca. 385 nm (3.22 eV), 425 nm (2.92 eV) and 465 nm (2.67 eV). According Askrabic et al. [31] those energy levels can be ascribed to $4f^0 \rightarrow 4f^1$, $F^{++} \rightarrow 4f^1$ and $F^{+} \rightarrow 4f^1$ transitions, respectively. Intensity ratio of band 2 ($F^{++} \rightarrow 4f^1$, 2.92 eV) and band 3 ($F^{+} \rightarrow 4f^1$, 2.67 eV) to band 1 ($4f^0 \rightarrow 4f^1$, 3.22 eV) increased with increasing Y^{3+} content. This observation could be ascribed to formation of oxygen defects with higher concentration.

4. CONCLUSIONS

One-step mechanosynthesis has been successfully employed to prepare nanocrystalline $Ce_{1-x}Y_xO_{2-\delta}$ (x=0-0.35) solid solutions with average crystallite size below 20 nm. The mechanically triggered yttrium incorporation into the ceria structure was followed by XRD and Raman spectroscopy. It was shown, that formation of oxygen defects and $Ce^{4+} \rightarrow Ce^{3+}$ reduction influence optical properties of as-prepared solid solutions.

ACKNOWLEDGMENTS

The support by the VEGA (2/0097/13), APVV (14-0103) and bilateral project between Slovak Academy of Sciences and Bulgarian Academy of Sciences is gratefully acknowledged.

REFERENCES

1. PHOKA, S., LAOKUL, P., SWATSITANG, G E., PROMARAK, V., SERAPHIN, S., MAENSIRI, IS., Synthesis, structural and optical properties of CeO_2 nanoparticles synthesized by a simple polyvinyl pyrrolidone (PVP) solution route, Materials Chemistry and Physics **115**, 2009, 423-428.

2. GNAMAN, S., RAJENDRAN, V., Synthesis of CeO_2 or α-Mn_2O_3 nanoparticles via sol-gel process and their optical properties, Journal of Sol-Gel Science and Technology **58**, 2011, 62-69.

3. DHANNIA, T., JAYALEKSHMI, S., SANTOSH, KUMAR, M.C., PRASADA RAO, T., CHABDRA BOSE, A., Effect of iron doping and annealing on structural and optical properties of cerium oxide nanocrystals, Journal of Physics and Chemistry of Solids **71**, 2010, 1020-1025.

4. RATH, M.K., ACHARYA, S.K., KIM, B.H., LEE, K.T., AHN, B.G., Photoluminescence properties of sesquioxide doped ceria synthesized by modified sol-gel route, Materials Letters **65,** 2011, 955-958.

5. PATSALAS, P., LOGOTHETIDIS, S., SYGELLOU, L., KENNOU, S., Structure-dependent electronic properties of nanocrystalline cerium oxide films, Physical Review B **68**, 2003, 035104.

6. YABE, S., SATO, T., Cerium oxide for sunscreen cosmetics, Journal of Solid State Chemistry **171**, 2003, 7-11.

7. TRUFFAULT, L., TA M.-T., DEVERS, T., KONSTANTINOV, K., HAREL V., SIMMONARD, C., ANDREAZZA, C., NEVIRKOVETS, I.P., PINEAU, A., VERON, O., BLONDEAU, J.-P., Application of nanostructured Ca doped CeO_2 for ultraviolet filtration, Materials Research Bulletin **45**, 2010, 527-535.

8. WU, L., WIESMANN, H.J., MOODENBAUGH, A.R., KLIE, R.F., ZHU,, Y. WELCH, D.O., SUENAGA, A M., Oxidation state and lattice expansion of CeO_{2-x} nanoparticles as a function of particle size, Physica Review B **69**, 2004, 125415.

9. WANG, Z., QUAN, Z., LIN, J., Remarkable changes in the optical properties of CeO_2 nanocrystals induced by lanthanide ions doping, Inorganic Chemistry **46**, 2007, 5237-5242.

10. TSUNEKAWA, S., FUKUDA, T., KASUYA, A., Blue shift in ultraviolet absorption spectra of monodisperse CeO_{2-x} nanoparticles, Journal of Applied Physics **87**, 2000, 1318-1321.

11. HO, CH., YU, J.C., KWONG, T., MAK, A.C., LAI, S., Morphology-controllable synthesis of mesoporous CeO_2 nano- and microstructures, Chemistry of Materials **17**, 2005, 4514-4522.

12. ANWAR, M.S., KUMAR, S., ARSHI, N., AHMED, F., SEO, Y.J., LEE, C.G., KOO, B.H., Strucutral and optical study of samarium doped cerium oxide thin films prepared by electron beam evaporation, Journal of Alloys and Compounds **509**, 2011, 4525-4529.

13. YUEL,, ZHANG, X.-M., Structural characterization and photocatalytic behaviours of doped CeO_2 nanoparticles, Journal of Alloys and Compounds **475**, 2009, 702-705.

14. ŠEPELAK, V., DEEVAL, A., WILKENING, M., BECKER, K.D., HEITJANS, P., Mechanochemical reactions and syntheses of oxides, Chemical Society Review **42**, 2013, 7507-7520.

15. ANDRIEVSKAYA, E.R., SAMELYUK, A.V., LOPATO, L.M., Reaction of cerium oxide with zirconium and yttrium oxides at 1250°C, Powder Metallurgy and Metal Ceramics **41**, 2002, 63-71.

16. FABIAN, M., ANTIC, B., GIRMAN, V., VUCINIC-VASIC, M., KREMENOVIC, A., SUZUKI, S., HAKN, H., ŠEPELAK, V., Mechanosynthesis and structural characterization of nanocrystalline $Ce_{1-x}Y_xO_{2-\delta}$ (x=0.1-0.35) solid solutions, Journal of Solid State Chemistry **230**, 2015, 42-48.

17. NAKAJIMA, A., YOSHIHARA, A., ISHIGAME, M., Defect-induced Raman spectra in doped CeO_2, Physical Review B **50**, 1994, 13297-13307.

18. DOHCEVIC-MITROVIC, Z.D., GRUJIC-BROJCIN, M., ŠCEPANOVIC, M., POPOVIC, Z.V., BOSKOVIC, S., MATOVIC, B., ZINKEVICH, M., ADLINGER, F., $Ce_{1-x}Y(Nd)_xO_{2-\delta}$ nanopowders: potential materials for intermediate temperature solid oxide fuel cells, Journal of Physics: Condensed Matter **18**, 2006, S2061-S2068.

19. MCBRIDE, J.R., HASS, K.C., POINDEXTER, B.D., WEBER, W.H., Raman and x-ray studies of $Ce_{1-x}RE_xO_{2-y}$, where RE=La, Pr, Nd, Eu, Gd and Tb, Journal of Applied Physics **76**, 1994, 2435-2441.

20. DOHCEVIC-MITROVIC, Z.D., ŠCEPANOVIC, M.J., GRUJIC-BROJCIN, M.U., POPOVIC, Z.V., BOSKOVIC, S.B., MATOVIC, B.M., ZINKEVICH, M.V., The size and strain effects on the Raman spectra of $Ce_{1-x}Nd_xO_{2-\delta}$ ($0 \leq x \leq 0.25$) nanopowders, Solid State Communications **137**, 2006, 387-390.

21. REDDY, B.M., THRIMURTHULU, G., KATTA, L., YAMADA, Y., PARK,-E., Structural characteristics and catalytic activity of nanocrystalline ceria-praseodymia solid solutions, Journal of Physical Chemistry C **113**, 2009, 15882-15890.
22. GOUBIN, F., ROCQUEFELTE, X., WHANGBO, M.H., MONTARDI, Y., BREC, R., JOBIC, S., Experimental and theoretical characterization of the optical properties of CeO_2, $SrCeO_3$, and Sr_2CeO_4 containing Ce^{4+} (f^0) ions, Chemistry of Materials **16**, 2004, 662-669.
23. CHEVIRE, F., MUNOZ, F., BAKER, CH.F., TESSIER, F., LARCHER, O., BOUJDAY, S., COLBEAU-JUSTIN, CH., MARCHAND, R., UV absorption properties of ceria-modified compositions within the fluorite-type solid solution CeO_2-Y_6WO_{12}, Journal of Solid State Chemistry **179**, 2006, 3184-3190.
24. BENSALEM, A., BOZON-VERDURAZ, F., DELAMAR, M., BUGLI, G., Preparation and characterization of highly dispersed silica-supported ceria, Applied Catalysis A 121, 1995, 81-93.
25. SUZULI, S., KASACKI, I., PETROVSKY, V., ANDERSON, H.U., Optical properties of undoped and Gd-doped nanocrystalline thin films, Journal of Applied Physics **91**, 2002, 2308-2314.
26. MEANSIRI, S., MASINGBOON, CH., LAOKUL, P., JAREONBOON, W., PROMARAK, V., ANDERSON, P.L., SERAPHINS, S., Egg white synthesis and photoluminescence of platelike cluters of CeO_2 nanoparticles, Crystal Growth and Design **7,** 2007, 950-955.
27. LIU, K.Q., ZHONG, M.Q., SHI, Y.Q., Synthesis and characterization of stable and crystalline $Ce_{0.6}Y_{0.4}O_{1.8}$ nanoparticle sol, Materials Science and Engineering B **176**, 2011, 157-162.
28. SKORODUMOVA, N.V., AHUJA, A R., SIMAK, S.I., ABRIKOSOV, I.A., JOHANSSON, N B., LUNDQVIST, B.I., Electronic, bonding, and optical properties of CeO_2 and Ce_2O_3 from first principles, Physical Review B **64**, 2001, 115108.
29. SPANIER, J.E., ROBINSON, R.D., ZHANG, F., CHAN, S-W., HERMAN, P.P., Size depent properties of CeO_2-Y nanoparticles, Phys. Rev. B, 64, 2001 245407.
30. MASALOV, A., VIAGIN, N O., MAKSIMCHUK, P., SEMINKO, V., BESPALOVA, I., ASLANOV, A., MALYUKIN, Y., ZORENKO, Y., Formation of luminescent centres in CeO_2 nanocrystals, Journal of Luminescence **145**, 2014, 61-64.
31. ASKRABIC, S., DOHCEVIC-MITROVIC, Z.D., ARAUJO, V.D., IONITA, G., DE LIMA JR. M.M., CANTARERO A., F-centre luminescence in nanocrystalline CeO_2, Journal of Physics D: Applied Physics **46**, 2013, 495306.

CORRESPONDENCE

Dr., Martin FABIÁN
Institute of Geotechnics, Slovak Academy of Sciences
Watsonova 45, 04001, Košice, Slovakia
e-mail: fabianm@saske.sk

Tribological Journal BULTRIB Vol. 5, 2015
Papers from the International Conference **BULTRIB '15**
September 11-13, 2015, Sozopol, Bulgaria
Society of Bulgarian Tribologists
FIT – Technical University of Sofia

INVESTIGATION OF SURFACE ROUGHNESS IN ABRASIVE WATER JET CUTTING USING SHAININ METHOD

Miroslav RADOVANOVIC

Abstract: *Surface roughness in abrasive water jet cutting of carbon steel using Shainin method was investigated. Design of experiment with five factors (material thickness, water pressure, abrasive flow rate, traverse rate and standoff distance) each in two levels is employed to investigate surface roughness. Using Shainin method number of factors is reduced from five to three important and then is employed full factorial design to determine the effect of important factors on surface roughness. Regression analysis was used to find correlation between surface roughness and factors.*

Key Words: *Abrasive water jet cutting, design of experiment, Shainin method*

1. INTRODUCTION

Shainin's approach to experimental design is a powerful tool to determinate the important factors from a large list of factors. It is useful when an experimenter wants to investigate five or more factors (5-20). Shainin method allows for the quick and simple identification of the three major factors that influence the process. Shainin calls important factors as "Red X", "Pink X" and "Pale Pink X". When the number of factors is reduced to three major factors, Shainin recommends detailed investigation using full factorial design [1, 3, 5]. Methodology developed by Shainin is simple, relatively easy to understand and implement, formed by the combination of powerful tools. Shainin methodology uses 12 tools, of which 9 are for problem solving and 3 are for controlling. Problem solving tools are: clue generating (components search, multi-vari chart, paired comparisons, product/process search), design of experiment (variables search, full factorial), validation (B vs C comparison) and optimization (scatter plots, response surface methodology). Variables search is Shainin's answer to fractionated designs and Taguchi's orthogonal arrays. Objective is to pinpoint the important factors, quantify them and their interaction effects, and separate them from the unimportant factors. Variable search is used if there are five or more factors to evaluate. Shainin intention is to reduce the number of factors to three important, from which he performs a full factorial experiment. Full factorial is complete factorial design, and is used if there are four or fewer variables to evaluate. The point of the method is to determine the important factors causing variations and to eliminate unimportant factors. Its strategy is based upon to detection of the three dominant factors by focusing on a problem response. Design of experiment done by Shainin method can result in more than 70% reduction in the variation. Shainin method is a good addition to classical design of experiment and Taguchi method. At Shainin method, the variables were named Green Y, Red X, Pink X and Pale Pink X. Green Y is the response (output variable) which is to be measured in an experiment. Green Y is defined as quality characteristic that is important to customers. Red X, Pink X and Pale Pink X are the factors (input variables) which influence on the response (output variable). Red X, Pink X and Pale Pink X are ranked according to Pareto principle. With Shainin method, the analysis can reduce the variation about 75% to 95% for the causes of the Green Y (Red X, Pink X and Pale Pink X). Designation of variables according to Shainin is shown in Fig.1 [2, 3, 6].

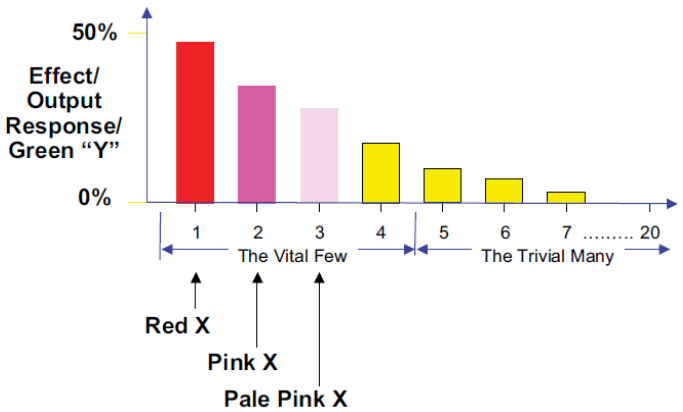

Fig.1. Designation of variables according to Shainin

For identification of important factors Shainin uses tree methods: Multy-Vari Charts, Paired Comparisons and Component Search. The most important prerequisite for the application of Shainin method is the validity of the Pareto principle. This principle states that when there are large numbers of factors, only a few will exert a dominant influence. To reduce the number of factors, Shainin suggests using a screening operation, developed by himself, to identify a smaller number of significant factors from a moderate number (5-20) of factors. When the number of factors is reduced to 3 (maximum 4), Shainin recommends detailed investigation using full factorial design.

The following are the objectives of Shainin method:

1) Separate the important factors from the unimportant in a minimum number of experimental trials.

2) Pinpoint the Red X (first most important factor), Pink X (second most important factor) and Pale Pink X (third most important factor).

3) Determine the optimal settings for the Red X, Pink X and Pale Pink X factors.

2. DESIGN OF EXPERIMENT AND ANALYSIS

Experimental investigation was conducted in order to study the influence of factors on surface roughness in abrasive water jet cutting. Machine tool used for cutting the samples was abrasive water jet machine Hydro Jet Eco 0615, with pump pressure of 150MPa, power of 7.5kW and water flow rate of 2.4lit/min. Cutting head is with orifice diameter of 0.35mm and a focusing tube diameter of 1.02mm. Focusing tube length is 76mm. Abrasive material was Garnet with mesh size of 80. Workpiece material used in experimental tests was carbon steel S235 (EN). Chemical and mechanical properties of S235 are: C 0.13, Si 0.25, Mn 0.58, P 0.013, S 0.008, N 0.01, Cu 0.32, Cr 0.08, Ni 0.10, Mo 0.013, Al 0.033, V 0.001, $R_{p0.2}$=240 N/mm^2, R_m=360-440N/mm^2, A=25%. The Hommel Tester T500 used for measure of surface roughness.

Shainin method of experimental design follows the five phases.

Phase 1: Develop and test a list of input factors. Based on past experience and engineering knowledge of the process or product, list all the variables or factors in descending order of perceived importance, and assign to them a "+1" (high) and "-1" (low) level. Brainstorming and Pareto analysis use for prioritizing the importance of factors to be considered for the experiment. Factors (input variables) analyzed in experiment are: material thickness, water pressure, abrasive flow rate, traverse rate and standoff distance. Table 1 shows the list of factors and their levels [4].

Table 1. List of factors and their levels

Factors		Levels	
		Low (-)	High (+)
A	Material thickness d (mm)	1	6.5
B	Water pressure p (MPa)	100	150
C	Abrasive flow rate m_a(g/min)	300	700
D	Traverse rate v (mm/min)	50	100
E	Standoff distance h (mm)	1	2

Results of two experiments, one with all factors at their "+1" (high) levels and the other with all factors at their "-1" (low) levels are shown in Table 2. These two experiments repeated thrice so there are six runs. Response (output variable) measured in the experiment is arithmetic average roughness (R_a).

Table 2. Experimental phase 1 and results

Run	Factors					Response
	A	B	C	D	E	R_a (μm)
1	+	+	+	+	+	4.215
2	+	+	+	+	+	4.239
3	+	+	+	+	+	4.221
4	-	-	-	-	-	4.471
5	-	-	-	-	-	4.463
6	-	-	-	-	-	4.485

Median response values corresponding to all factors, M_H at "+1" (high) level and M_L at "-1" (low) level, are estimated as:

$$M_H = \frac{1}{3}\left(R_{a1} + R_{a2} + R_{a3}\right) \tag{1}$$

$$M_H = \frac{1}{3}\left(4.215 + 4.239 + 4.221\right) = 4.225$$

$$M_L = \frac{1}{3}\left(R_{a4} + R_{a5} + R_{a6}\right) \quad (2)$$

$$M_L = \frac{1}{3}\left(4.471 + 4.463 + 4.485\right) = 4.473$$

Difference between the median response values D_m is:

$$D_m = M_L - M_H \quad (3)$$

$$D_m = 4.473 - 4.225 = 0.248$$

Range of the response values R_H and R_L are the difference between the maximum and minimum of response value at the "+1" (high) and "-1" (low) level.

$$R_H = R_{aH\max} - R_{aH\min} \quad (4)$$

$$R_H = 4.239 - 4.215 = 0.024$$

$$R_L = R_{aL\max} - R_{aL\min} \quad (5)$$

$$R_L = 4.485 - 4.463 = 0.022$$

Average range R is the mean average of the R_H and R_L values given by equation:

$$R = \frac{R_H + R_L}{2} \quad (6)$$

$$R = \frac{0.024 + 0.022}{2} = 0.023$$

Difference between the medians of the three replications must exceed the average of the two ranges by a factor of at least 1.25. If the ratio $D_m/R \geq 1.25$ than go to Phase 2, If it is not than go back to the beginning and select other factors or levels.

$$\frac{D_m}{R} = \frac{0.248}{0.023} = 10.78 \quad (7)$$

The ratio is $D_m/R = 10.78 > 1.25$. Factors selected in the initial phase were correct and were likely to have sufficient influence on response.

Phase 2: Computation of control limits (CL). Control limits are used to determine whether a factor is important or unimportant and therefore can make a decision for its elimination from further experimentation. If M_H represents the median for an experiment with all factors at high level, the control limits (CL_H) can then be calculated using the equation [2]:

$$CL_H = M_H \pm 2.776\frac{R}{d_2} \quad (8)$$

$$CL_H = 4.208 \pm 2.776\frac{0.023}{1.693} = 4.208 \pm 0.038$$

$$CL_H(4.170 - 4.246)$$

where the constant 2.776 is the value corresponding to a two-tailed t-distribution with 95 percent confidence and 4 degrees of freedom (based on 3+3-2 degrees of freedom) and d_2 is a statistical constant equal to 1.693 (based on a sample size of 3).

Similarly, if M_L represents the median for an experiment with all factors at low level, the control limits (CL_L) can then be calculated using the equation:

$$CL_L = M_L \pm 2.776\frac{R}{d_2} \quad (9)$$

$$CL_L = 4.473 \pm 2.776\frac{0.023}{1.693} = 4.473 \pm 0.038$$

$$CL_L(4.435 - 4.511)$$

Phase 3: Separating the important factors from the not important factors. Using the selected factors determined in Phase 1, an experiment is carried out kept the one factor at "-1" (low) level, while the all other factors kept at "+1" (high) levels. Similarly, another experiment is carried out kept the one factor at "+1" (high) level, while the all other factors kept at "-1" (low) levels. If the result of the experimentation for each factor falls inside the control limits then the factor is said to be not important. If the result of the experimentation falls outside the respective control limits then the factor is said to be important. The same procedure is repeated for all other factors in the experiment. Table 3 shows the separation of factors.

Table 3. Separation of factors

Run	Factors					Response	Control limits	Important factor	
	A	B	C	D	E	R_a (μm)	CL		
7	-	+	+	+	+	4.565	4.170-4.246	A	Yes
8	+	-	-	-	-	4.154	4.435-4.511		Yes
9	+	-	+	+	+	4.140	4.170-4.246	B	Yes
10	-	+	-	-	-	4.594	4.435-4.511		Yes
11	+	+	-	+	+	4.268	4.170-4.246	C	Yes
12	-	-	+	-	-	4.378	4.435-4.511		Yes
13	+	+	+	-	+	4.203	4.170-4.246	D	Not
14	-	-	-	+	-	4.471	4.435-4.511		Not
15	+	+	+	+	-	4.210	4.170-4.246	E	Not
16	-	-	-	-	+	4.491	4.435-4.511		Not

From Table 3, the important factors are A, B and C. Shainin calls important factors as "Red X", "Pink X" and "Pale Pink X". They are responsible for the root causes of any quality related problem.

Phase 4: Capping run. Capping runs conduct to confirm the important factors are correct. This phase is performed to verify whether or not the remaining not important factors in the experiment can be ignored. Two capping runs should be performed. The first capping run is conducted by keeping the important factors (A, B, C) at the "+1" (high) level and the not important factors (D, E) at the "-1" (low) level. The second capping run was conducted by reversing the levels for the factors. The not important factors are verified as being not important if the results of the capping runs lie between the control limits. If the capping runs are not successful, then it means that some important factor are missed in the first phase or must to identify few more important factors from the list of factors in the second phase. The results of the capping runs are shown on Table 4.

Table 4. Capping run results

Run	Factors					Response	Control limits	Important factor	
	A	B	C	D	E	R_a (μm)	CL		
17	+	+	+	-	-	4.195	4.170-4.246	D, E	Not
18	-	-	-	+	+	4.486	4.435-4.511		Not

From Table 4 it is seen that the response values lie between the control limits. Thus indicating the factors D and E have not important effect on surface roughness. This verifies the important factors identified in Phase 3 of the experiment.

Phase 5: Factorial analysis. Factorial analysis is performed to determine the main effects of factors and to identify significant interactions. Three factors are arranged in full factorial design. Table 5 shows factorial design and results.

Table 5. Factorial design and results

Run	Factors			Response
	A	B	C	R_a (μm)
1	-1	-1	-1	4.471, 4.463, 4.485, 4.471, 4.491, 4.486
2	1	-1	1	4.140
3	-1	-1	1	4.378
4	1	1	1	4.215, 4.239, 4.221, 4.203, 4.210, 4.195
5	1	1	-1	4.268
6	-1	1	-1	4.594
7	-1	1	1	4.565
8	1	-1	-1	4.154

Normal plot, Pareto chart, Main effect plot and Interaction plot were generated. In Fig.2 is shown Normal plot of the standardized effects and in Fig.3 is shown Pareto chart. From Fig.2 and Fig.3 it is seen effect type of factors and interactions (significant or not significant). Factor A (material thickness), factor B (water pressure) and factor C (abrasive flow rate) are significant factors on surface roughness. 2-Way interactions AB (material thickness-water pressure), AC (material thickness-abrasive flow rate) and BC (water pressure-abrasive flow rate), and 3-Way interaction ABC (material thickness-water pressure-abrasive flow rate) are significant on surface roughness.

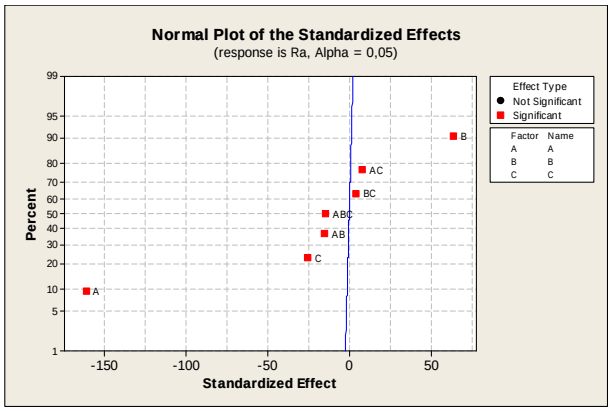

Fig.2. Normal plot of the standardized effects

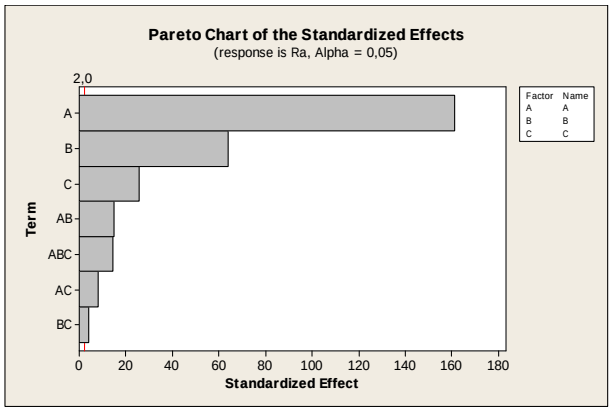

Fig.3. Pareto chart of the standardized effects

Main effects plot for surface roughness (Ra) is presented in Fig. 4. The verticality of the line indicates the effect of factors. Factor A (material thickness) is more significant factor as the slope gradient is big. From Fig. 4 it is seen that as the material thickness and abrasive flow rate increase the surface roughness decreases, as the water pressure increases the surface roughness increases. Shainin promotes the use of Interaction plots as a quick and effective method to see possible interaction effects. In Fig. 5 is shown Interaction plot for surface roughness.

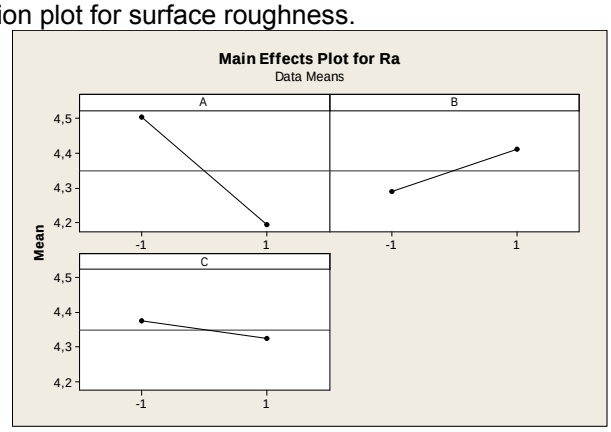

Fig.4. Main effects plot for surface roughness

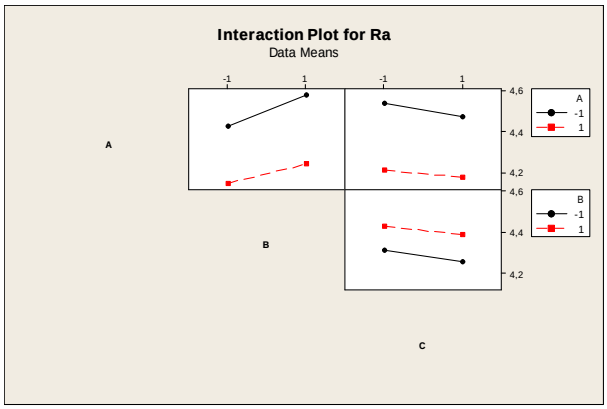

Fig.5. Interaction plot for surface roughness

Analysis of variance (ANOVA) was carried out to find the relative effect of factors and interactions on surface roughness. Fisher's ratio (F) is used to determine whether the factor or interaction has a significant effect on response by comparing the F table value at the α significance level. Greater the F-ratio more significant is the factor or interaction. Analysis of variance for surface roughness (Ra) is shown in Table 6.

Table 6. Analysis of variance for Ra

Source	DF	SS	MS	F	p	%
A	1	1.15134	1.15134	25906.79	0.000	83.08
B	1	0.18081	0.18081	4068.50	0.000	13.05
C	1	0.02911	0.02911	654.94	0.000	2.10
AB	1	0.00998	0.00998	224.48	0.000	0.72
AC	1	0.00276	0.00276	62.11	0.000	0.20
BC	1	0.00071	0.00071	15.87	0.000	0.05
ABC	1	0.00924	0.00924	207.93	0.000	0.67
Error	40	0.00178	0.00004	-	-	0.13
Total	47	1.38572	-	-	-	100

DF-degree of freedom, SS-sum of square, MS-mean square, F-ratio, p–value, %-percent contribution

F table value at α=0.05 is $F_{0.05,1,40}$=4.08. From Table 6, it is seen that factors: A (material thickness), B (water pressure) and C (abrasive flow rate) have strong (clearly statistically significant) effect on the surface roughness. Factor A (material thickness) is the most significant factor affecting the surface roughness with contribution of 83.08%. Factor B (water pressure) affecting the surface roughness with contribution of 13.05%, and factor C (abrasive flow rate) affecting the surface roughness with contribution of 2.10%. From Table 6 it is seen that the interactions have significant effect on surface roughness. Interaction AB (material thickness-water pressure) affects on the surface roughness with contribution of 0.72%. Interaction AC (material thickness-abrasive flow rate) affects on the surface roughness with contribution of 0.20%. Interaction BC

(water pressure-abrasive flow rate) affects on the surface roughness with contribution of 0.05%. From Fig. 3 and Table 6, factors A, B and C being identified as Red X, Pink X and Pale pink X respectively.

Regression analysis was used to find correlation between response and factors. Quasi-linear regression equation representing the surface roughness (R_a) can be expressed as a function of material thickness (d), water pressure (p) and abrasive flow rate (m_a). The following regression equation, with coefficient of determination of R^2=99.82%, was obtained:

$$R_a = 4.52669 - 0.100068d + 0.000965985p - 0.000743674m_a + 0.000294848dp + 0.000139924dm_a + 0.000004551pm_a - 0.000001009dpm_a \quad (10)$$

Selection of the optimal factor settings is obtained by analyzing the Main effects plot for surface roughness (Ra) presented in Fig. 4. The selection of optimal factor level is obtained by identifying the level with lowest response value for each factor. Shainin method does not assign a factor level for the not important factors and, therefore, these factors can theoretically be set at either level. The levels of not important factors are marked with () to show their ability to be moved from high to low settings to suit the conditions. The surface roughness has a minimal value of $R_{a,min}$=4.14 μm for combination of factor levels A(+1)B(-1)C(+1)D()E(), i.e. for material thickness of 6.5 mm, water pressure of 100 MPa, abrasive flow rate of 700 g/min, traverse rate of 50-100 mm/min and standoff distance of 1-2 mm.

3. CONCLUSION

Presented experimental investigation of surface roughness in abrasive water jet cutting using Shainin method has shown efficiency of this method. From five factors at the starting of the experiment, three major factors are identified. Using full factorial design for three factors, detailed investigation was realized and optimal factor settings are obtained. For design of experiment with five factors on two levels, full factorial design needs 32 tests, Taguchi method needs 25 tests, and Shainin method needs 18 tests.

ACKNOWLEDGMENT

The paper is a result of the technological project TR35034 which is supported by the Ministry of Education, Science and Technological Development of the Republic of Serbia.

REFERENCES

1. AKSU, B., BAYNAL, K., Shainin and Taguchi Methods and Their Comparison on an Application, 1st International Symposium in Computing inScience & Engineering, June 3-5, Kusadasi, Aydin, Turkey, 2010, 801-808
2. ANTONY, J., CHENG, A., Training for Shainin's approach to experimental design using a catapult, Journal of European Industrial Training, Vol.27, No.8, 2008, 405-412
3. BHOTE, K., BHOTE, A., World class quality, Using design of experiments to make it happen, American Management Association AMACOM, 2000
4. HERGHELEGIU, E., Contributions to the optimization of the water jet working parameters, Dissertation, University ″Vasile Alecsandri″ of Bacau, Industrial Engineering, Bacau, Romania, 2011
5. RADOVANOVIC, M., Shainin's approach to experimental design, International Scientific Conference UNITECH 2013, November 22-23, Gabrovo, Bulgaria, 2013, Vol.3, 227-232
6. STEINER, S., MACKAY, J. RAMBERG, J., An Overview of the Shainin System TM for Quality Improvement, Quality Engineering, No.20, 2008, 6–19

CORRESPONDENCE

Miroslav RADOVANOVIC
University of Nis, Faculty of Mechanical Engineering, A. Medvedeva 14, 18000 Nis, Serbia
E-mail: mirado@masfak.ni.ac.rs

Tribological Journal BULTRIB Vol. 5, 2015
Papers from the International Conference **BULTRIB '15**
September11-13, 2015, Sozopol, Bulgaria
Society of Bulgarian Tribologists
FIT – Technical University of Sofia

HIGH PRESSURE JET ASSISTED MACHINING - APPLICATION IN TURNING

Gordana Globočki Lakić, Branislav Sredanović

Abstract: *High Pressure Jet Assisted Machining (HPJAM) in turning is a hybrid machining method where jet of cooling and lubrication fluid, under high pressure (50 MPa), leads to the zone between the cutting tool edge and workpiece. An experimental study has been performed to investigate the capabilities of high pressure jet assisted turning of different steels, i.e., construction carbon steel C45E (hardness 45 HRc) and hardened bearing steel 100Cr6 (62 HRc) using carbide tools. Experimental measurements were performed for different input process parameters. Process of cutting tool wear is analyzed by monitoring of width of flank wear on carbide tool inserts. Results of experimental research shows that the application of HPJAM offers great advantages in regarding of tool life, tool wear and chip breakability.*

Key words: *tool wear, modelling, cooling and lubrication, HPJAM*

1. INTODUCTION

The requirements of modern production going to the way of increasing the productivity, surface quality and accuracy of machining parts, while reducing processing costs. Increase in productivity and efficiency of the process can be achieved by the optimization cutting tool geometry and its design, optimization of the machining operation and the optimal selection of cutting parameters. Modern machining technology combines the advantages of high material removal rates in roughing and high speed machining for finishing by using medium cutting speeds and high feeds. Also, the tendencies in modern manufacturing going to the way of used a hibrid machining method (HPJAM) to achieve numerous requirements.

Machining process for workpiece materials that are hardened above 45 HRc and up to 65 HRc is a hard turning. This process used as a replacement for the traditional method of machining the hardened materials - rough turning,heat treatment and grinding process. This method required new cutting tool materials such as cubic boron nitride (CBN), PCD and ceramics. Hard turning has some advantages compared to the traditional method of machining the hardened materials: increased efficiency and productivity, increased tool life, reduction of cutting temperature and tool wear, improvement of chip breakability, reduced power consumption. The costs of the cutting tools employed for turning of hardened steels are very high. One of possible way to reduce of high tool costs are to investigate the possibility of using other cutting tool materials that are economical and which can effectively utilize the hard turning process. In hard cutting, tool wear is a fundamental issue.It is known that in hard turning, cutting edge of a tool is subject to high temperatures and stresses which cause intensive wear of carbide tools. One possibility of reducing tool wear is the use of modern technique of cooling and lubricating-high pressure cooling (HPC), where cutting fluid acts simultaneously as coolants and as lubricants.In this paper are presented possibility of use inexpensive coated carbide tools in hard turning of two steels: construction carbon steel C45E (hardness 45 HRc) and hardened bearing steel 100Cr6 (62 HRc).

Economical production requires reducing of tool wear to minimize interruption in the manufacturing process and tool cost. Hard cutting using coated carbide tools, with conventional turning parameters and conventional cooling, usually follows severe adhesion wear mechanisms and forming extremely long chips that causes problems in machining. By applying HPJAM at reduced cutting fluids flow rates, the friction and the heat on tool-chip contact can be reduced.Compared with conventional flooding, using the HPJAM technology, the cost related to the usage of cutting fluids can be reduced. Further, those principles can contribute to environment concerns.From the structure of the cost of machined part, it can be concluded that the cost of CLF participate 15%, costs of tools 10% and costs of energy consumption 4% of total costs.

The largest influence on the chip formation in the cutting process has heat and friction generated in the contact zone between the rake face of the tool and the machined surface. Conventional flooding is not efficient enough in this case. Many authors have investigated the possibility of using HPJAM- Pigott, Ma-

zurkievicz, Yankoff, Kaminski, Kramar and many others [1 - 6]. From the analysis of papers that deal with HP technology, it can be noticed that the liquid jet of high pressure can lead in the cutting zone in 2 ways:

1. With an external nozzle: the jet is injected directly in between the rake face and the chip or can be directed to the gap between the flank face and the workpiece.
2. Through internal channels: the cutting fluid is injected through the tool using small holes in the insert

In this investigation, the jet that is directly injected between the rake face and the chip, has been used (see Fig.1). High pressure jet is applied on the rake face through an external nozzle that can provide higher machining performances and is easier to set on the conventional lathe.

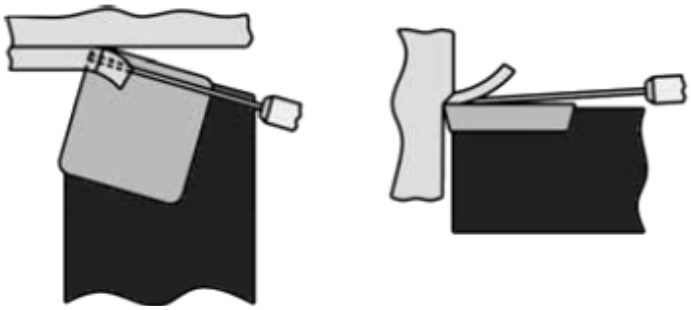

Fig. 1.The jet injected directly between the rake face and the chip [5, 7]

Since the HPJAM applied in highly productive processes of chip removal - roughing and semi-machining, investigations in this paper were focused on analyzing of tool wear and chip forming. Experiments were performed on construction carbon steel C45E with hardness 45 HRc and hardened bearing steel 100Cr6 (62 HRc) using carbide tools. Process of cutting tool wear is analyzed by monitoring of width of flank wear on carbide tool inserts.

2. EXPERIMENTAL SETUP AND EQUIPEMENT

Workpiece materials used in experimental research were:

- the carbon steel C45E with hardness 45 HRc and
- alloyed steel 100Cr6 which is used to make bearings because it has a high resistance to wear. This steel is a heat treated - hardened.

Experimental research was performed on conventional lathe with maximum spindle speed n_{max}= 2240 *rev/min*, and feed f_{max}= 1.6 *mm/rev*.In HPJAM [7, 8] the jet is normally directed to the cutting edge at a low angle directly between the rake face and the chip. For this application, conventional universal lathe was fitted with high pressure plunger pump (see Fig. 2). Pressure was set at50 *MPa* and flow rate at 2.0 $l \cdot min^{-1}$. Standard sapphire nozzle with diameter 0.4 *mm* commonly used in water jet cutting applications was installed on the distance of 30 *mm* from tool cutting edge in order to assure its use in the jet core zone, and avoid variations in the jet diameter and radial distribution of the pressure [9]. The jet was directed normal to the cutting edge and 30° from clearance face at a low angle 5° with the tool rake face (see Fig. 3).Monitoring and measurement of tool wear was performed using a tool microscope TM-MITOTOYO 510 equipped with high-resolution camera. Surface roughness was measured using a mobile measuring device MITOTOYO SURFTEST SJ-301. During the experiments a chip formation process was monitored as well.

In practice, the most common measured and analyzed parameter is flank tool wear (*VB*), which is manifested by a series of furrows on the flank surface of the tool. The measurement of the selected parameter of tool wear during cutting enables the formation of the experimental curves of wear [10]. By defining the wear resistance of tools for a given criterion VBk, can be determined the tool life T. According to ISO 3685, the tool life is defined as the time when the size of width trace of wear achieves a value of 0.3 mm.For describes the tool wear with a high degree of correlation, approximate models can be found in the literature, as polynomial function of the third degree:

$$VB = C_1 T + C_2 T^2 + C_3 T^3 \quad (1)$$

where C_1 and C_3 are constant with positive and C_2 are constant with negative value.

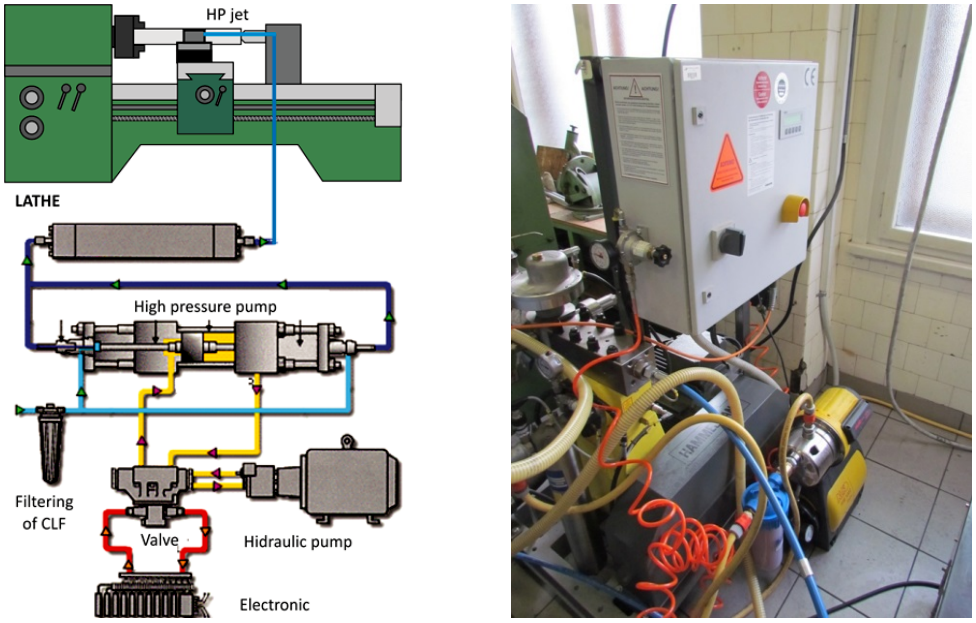

Fig. 2. Scheme (left) and installation of HPJAM (right)

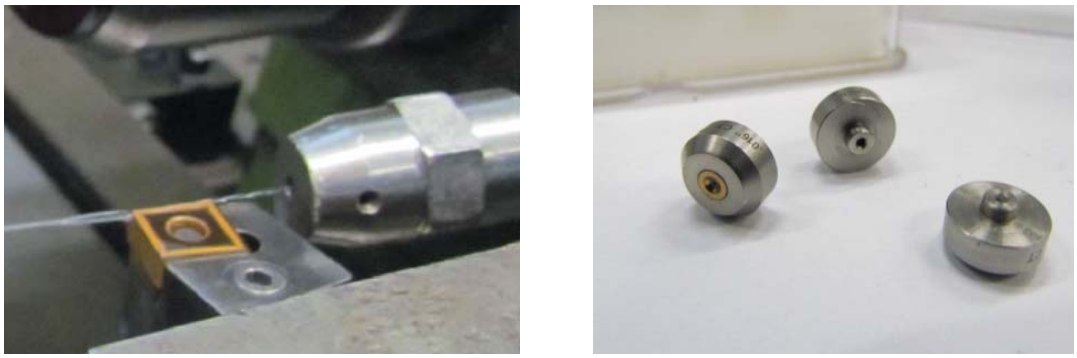

Figure 3.Initial jet of CLF in HPJAM(left) and sapphire nozzle (right)

3. RESULTS AND EVALUATION

3.1. Experimental work with steel C45E (45 HRc)

Workpiece material was C45E carbon steel, tensile straight is 820 N/mm², and hardness 45 HRc. Cutting tool was carbide cutting tool SNMG 1204 08 NMX for semi-turning was recommended cutting tool by manufactures. Tool holder was PSDN 2525 M12, with inclination angle 45°. Cutting fluid was 3% emulsion of vegetable oil. As CLF technique, HPJAM with pressure set at 50 MPa and flow rate at 2.0 $l \cdot min^{-1}$ was used.

Input parameter levels and value: Cutting speed vcon 3 levels (210, 310 and 400 m/min), feed fon four levels (0,224; 0,280; 0,355 and 0,400 mm/rev) and cutting depth ap on three levels (1,5; 2,0 and 2,5 mm). Measured parameters of wear: flank tool wear (VB) and the wear on minor flank face ($VB_{'}$). As a criterion of wear was adopted value VB_k = 0.3 mm, at which evaluates the tool life (T). Measured parameters of surface roughness: mean height of surfaces roughness (Ra) and maximum height of surfaces roughness (Ry). All parameters are monitored depending on the processing time.

In Table 1 are presented photography of tool wear SNMG 1204 08 NMX by applying HPJAM technique of CLF. The distribution of the wear along the flank face was quite uniform, due to the reduced influence of the heat generated. Crater wear was also present on the rake face. These can be seen on photography in Table 1. In addition, there was no a sudden dismissal of tools, which is the case for conventional flooding. Figure 4shows the tool flank wear trend in HPJAM. For the selected criteria VB = 0.3 mm, tool life in the case of HPJAM was about 26 minutes, which is approximately 3-4 times longer than in the case of conventional flooding. Further, the consumption of cutting fluid in the case of HPJAM is a few times lower as compared with conventional flooding.

Table 1. Photography of tool wear for HPJAM (machining of steel C45E)

Time T [min]	0,75	2,85	4,05	7,18	8,52
Wear on rake face	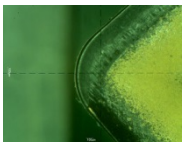	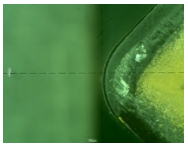	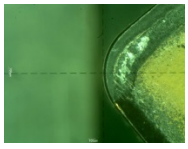	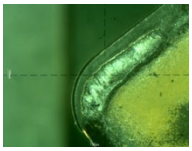	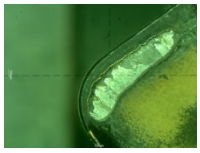
Wear on flank face	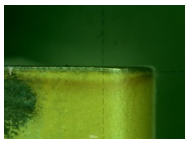	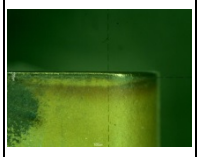	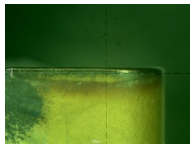	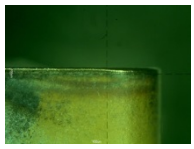	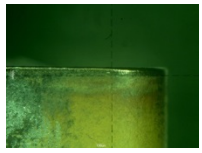
Wear on minor flank face	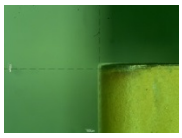	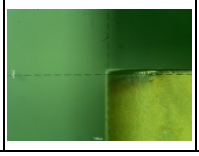	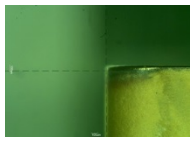	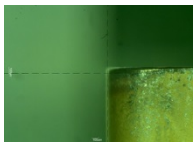	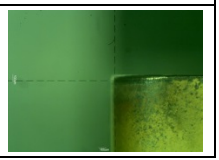

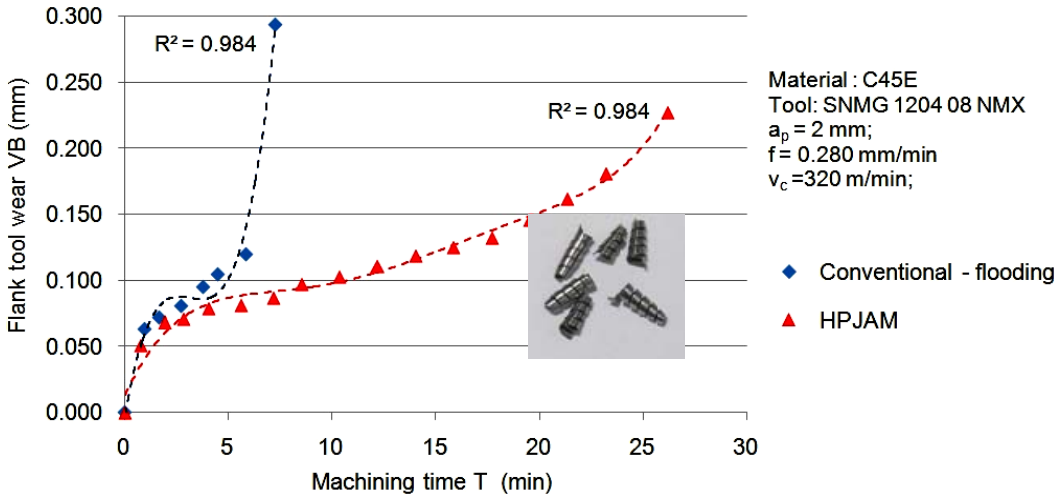

Fig. 4. Tool flank wear of steel C45E using HPJAM and flooding for the same conditions [11].

The form of the generated chips for all combinations of input parameters of processing was analyzed (see Table 2). Chip shape is very significant indirect parameter of metal cutting process. In this paper the standard classification and acceptable estimating for chip shape was used. Based on chip shapes the following features can be determined: tool wear, surface roughness, the amount of generated heat and related phenomena. By applying the HPJAM achieved favourable chip shapes for all combinations of cutting regimes. Chips are brighter - better conducted heat. A chip shape tends improvements with increase feed and cutting speed.

Table 2. Chip shapes during the machining of steel C45E using the HPJAM

Depth of cut a_p[mm]	Cutting speed v_c[m/min]	Feed f [mm/rev]			
		0,224	0,280	0,355	0,400
2,5	210			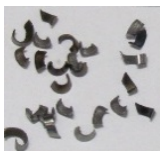	
	400				

The changes in roughness were noticed as a consequence of the increasing tool wear. Compared to conventional technique (flooding) can be noticed that the surface roughness the slightly higher in HPJA techniques due to action of high pressure jet to the surface (see Fig. 5).

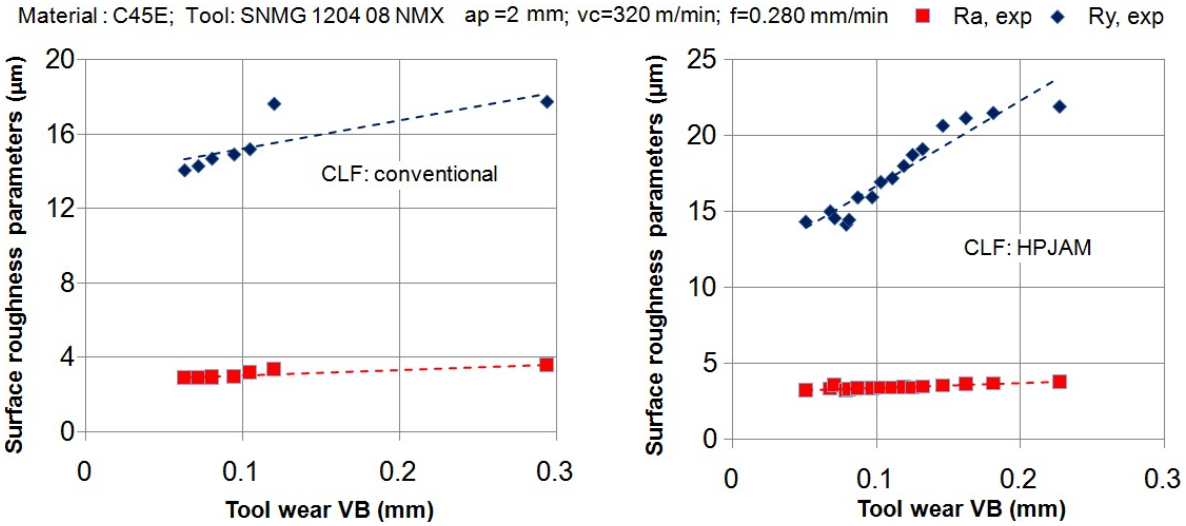

Fig. 5. Parameters Ra and Ry, depending on the tool wear for HPJAM and conventional

Table 3. Models of wear and surface roughness in machining of steel C45E using the HPJAM

Material: Ck45E (45 HRc); Tool: SNMG 1204 08 NXM; CLF: HPJAM a_p=2,0 [mm] f=0,280 [mm/rev]v_c=320 [m/min]	
Flank tool wear VB [mm] as a function of machining time	$VB = 0.001T^2 + 0.015T + 0,026$
Flank tool wear VB [mm] as a function of the traversed path	$VB = 9 \cdot 10^{-9} \cdot L_c^2 + 5 \cdot 10^{-5} \cdot L_c + 0.026$
Surface rough.parameter Ra as a function of machining time	$R_a = 0.016 \cdot T + 3.260$
Surface roughness parameter Ra as a function of tool wear	$R_a = 3.097 \cdot h + 3.105$
Surface roughness parameter Ry as a function of machining time	$Ry = 0.334 \cdot T + (s2 \cdot 103/ (8 \cdot r))$
Surface roughness parameter Ry as a function of tool wear	$R_y = 56.02 \cdot h + (s^2 \cdot 10^3/ (8 \cdot r))$

3.2. Experimental work with bearing steel 100Cr6 (62 HRc)

Tool wear in turning of 100Cr6 steel with HPJAM and carbide tool is analyzed. Main target was capabilities of hardened steel processing analysis with carbide tool insert, because mentioned material are processed dominantly with CBN tool inserts, which are much more expensive than the carbide tool inserts. In this paper, the possibility of hard turning with inexpensive coated carbide tools was examined. Workpiece material was alloy bearing steel 100Cr6, tensile strength is 1100 MPa, hardness of 62 HRC. This steel is very difficult to machined. Cutting tool was carbide insert with nano-coating CNMG 1204 08 MF5, SECO producer, internal designation TH1000 inserted on tool holder: PCBNR 2525 M12. Cutting fluid was 3% emulsion of vegetable oil. CLF technique was HPJAM, pressure was set at 50 MPa and flow rate at 2.0 $l \cdot min^{-1}$.

Input parameter levels and value was combined as follow cutting speed v_c on 4 levels (65, 85, 100, 120 m/min), feed f on four levels (0,08; 0,125; 0,16 and 0,2 mm/rev) and cutting depth in this case was constant, a_p =0,5 mm.

Experiments have been conducted for a specific set of cutting conditions until the flank wear reaches approximately 0.25 mm or if an interval of time of cutting reaches value of 20 min. In Table 4 are presented photography of tool wear CNMG 1204 08 MF5 by applying HPJAM technique of CLF in next cutting conditions: a_p =0,5mm, f=0,125 mm/rev and v_c=85 m/min. Fig. 6 shows the curve of flank of tool wear and shapes of the chip. Based on results in Table 4 and Figure 6 it can be concluded that the shape of chip changed during the machining due the tool wear. As seen from Figure 6, it is clear that tool wear has a significant effect on chip forming behaviour. Also, on Figure 6 it can see that the unfavourable shape of chip appeared before the dismissal tool.

Table 4. Photography of tool wear for HPJAM (machining steel 100Cr6)

a_p =0,5mm f=0,125 mm/rev v_c=85 m/min	Time T [min]	2,6	6,2	13,2
	Wear on rake face	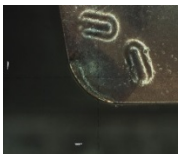		
	Wear on flank face			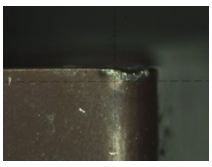

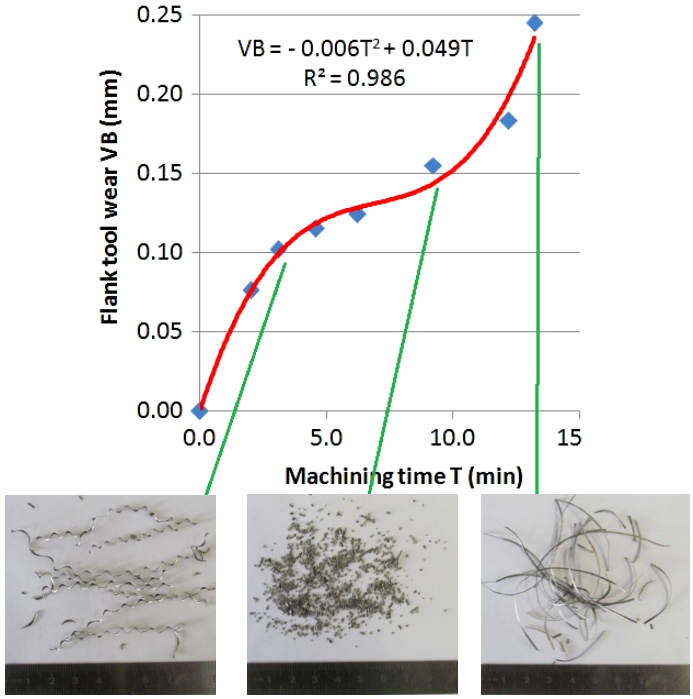

Fig. 6. Curve of tool wear in machining of steel 100Cr6 with HPJAM and shapes of chip

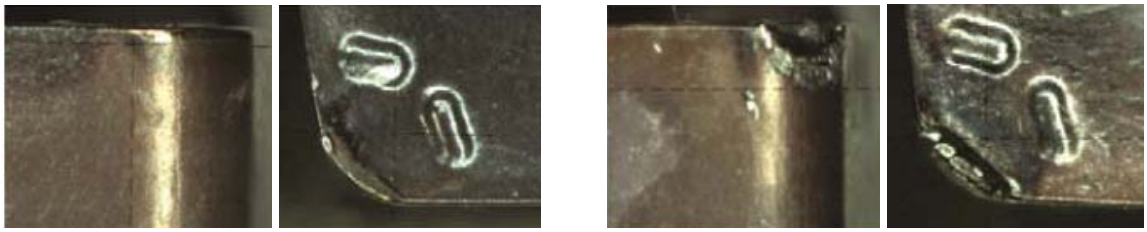

a) ***b)***

Fig. 7. Tool wear at the end of cutting process for cutting speed 85 m/min and feed 0.08 mm/rev (a) and for cutting speed 120 m/min and feed 0.125 mm/rev (b)

Table 5.shows experimental values of tool wear and surface roughness for tested conditions. Based on analyzing of results in Table 5 it can be concluded: tool wear depend of feed and cutting speed, but the influence of cutting speed is the higher expressed in percentages. Intense tool wear is a consequence of high contact pressure on the cutting tool edge area in the machining and intense heat generation during turning of hard-to-machining steels. Minimal tool wear was obtained when using cutting speed 85 m/min and feed 0.08 mm/rev, but high intensity of tool wear was obtained during cutting speed 120 m/min and feed 0.125 mm/rev (see Fig. 7), [12].

Table 5. Experimental values of tool wear and surface roughness for tested conditions

No	Feed [mm/rev]	Cutting speed [m/min]	Time [min]	Exp. tool wear [mm]	Exp. surface roughness [µm]
1	0.08	85	3.3	0.056	0.36
2	0.08	85	7.7	0.078	0.39
3	0.08	85	14.8	0.094	0.49
4	0.16	85	1.1	0.092	0.85
5	0.16	85	2.8	0.126	0.83
6	0.16	85	3.8	0.199	0.93
7	0.18	85	1.4	0.123	0.87
8	0.18	85	2.3	0.189	0.91
9	0.18	85	3.1	0.252	0.95
10	0.2	85	1.1	0.091	0.59
11	0.2	85	2.4	0.143	0.95
12	0.2	85	3.7	0.194	2.51
13	0.125	65	2.2	0.065	0.68
14	0.125	65	6	0.087	0.63
15	0.125	65	13.4	0.106	0.61
16	0.125	85	2.6	0.09	0.56
17	0.125	85	6.2	0.124	0.49
18	0.125	85	13.2	0.245	0.49
19	0.125	100	2.4	0.085	0.54
20	0.125	100	4.2	0.167	0.55
21	0.125	100	5.1	0.245	0.58
22	0.125	120	2.7	0.103	0.53
23	0.125	120	3.5	0.178	0.55
24	0.125	120	4	0.213	0.57

On the other hand, results on Table 5 show that feed has a great impact on surface quality, where the increase in cutting speed reduces the average roughness under the same feed.

In practice, this steel is usually processed with CBN tools, which are expensive. Presented results in this paper show that the steel 100Cr6 can be machined with cheaper carbide tool using HPJAM. The analysis in terms of the of removed material volume (MRV) showed, that with increasing MRV, significantly increase the wear of the tool, [13]. The greatest wear but also the highest material removal rates (MRR) is happening when machining with a cutting speed of 120 m/min and feed 0.125 mm/rev. When cutting speed 85 m / min and feed 0.08 mm / rev is happening a minimal tool wear. This case indicates that, in terms of productivity, this is the most favourable case of application HPJAM for machining steel 100Cr6 using carbide tool (see Fig. 8).

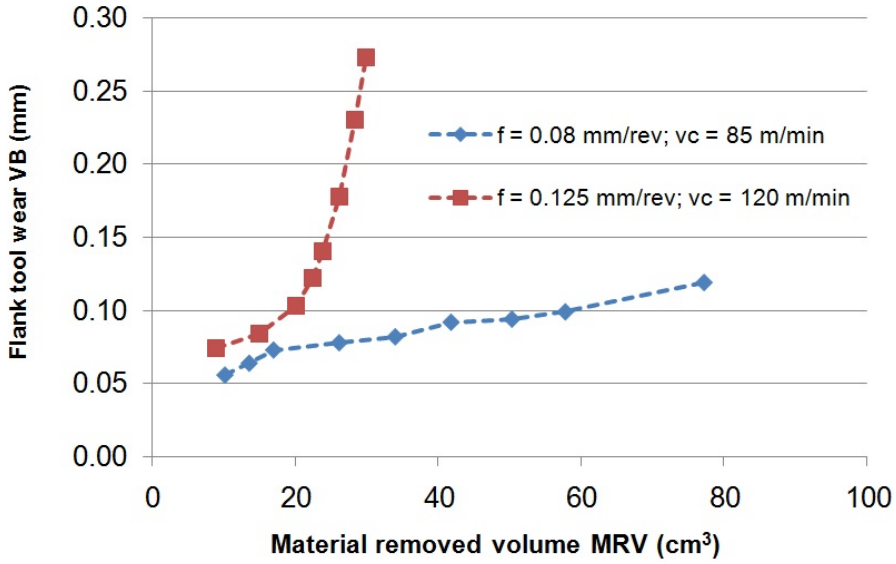

Fig. 8. Tool wear depending on material removed volume (MRV)

CONCLUSION

This paper presented results of experimental investigation of new CLF technique such as HPJAM in turning on two different steels C45E with hardness 45HRc and alloyed steel 100Cr6 with hardness 62 HRc with coated carbide tool. Results of examination on the steel C45E (hardness HRC 45) have shown a number of advantages HPJAM in compared to conventional process, especially from the point of chip breaking and tool wear. Results of experimental investigations indicate that, at low values of cutting conditions, HPJAM techniques can be successfully used for hard turning of steel 100Cr6 (hardness 62 HRc). Using HPJAM was achieved by significant increase in chip breakability. Also, observed the significant is the volume of material removed, which gives good grades for this technique in terms of productivity. It should be noticed that is significantly reducing the consumption of cutting fluid in comparison to conventional machining.

Further investigations will go in the direction of extending the area of cutting conditions and test the application of different pressures and flow fluid. It is necessary to examine and compare of the costs machining using HPJAM with carbide tools and the usual machining with CBN tools. In this comparison should look for a compromise between productivity, quality and tool costs.

ACKNOWLEDGMENTS

This research is part of the research on bilateral project BI-BA/14-15-001 between Laboratory for Cutting from FME in Ljubljana and Laboratory for cutting technologies and machining systems from FME in Banja Luka.

REFERENCES

1. PIGOTT, R.J.S., Method of applying cutting liquids, US patent 2,653,517.
2. MAZURKIEVICZ, M., A manufacturing tool for a new century, Journal of Materials Processing Technology, 2000, Vol.106, No 1-3, pp. 112-118.
3. KAMINSKI,J., LJUNGKRONA, O., CRAFOORD, R., LAGERBERG, S., Control of chip flow direction in high pressure water jet assisted orthogonal tube turning, Proc. Instn. Mech. Engrs., Part B, Journal of Engineering Manufacture, 2000, Vol.214, No. B7, pp.529-534.
4. YANKOFF, G.K., Method and apparatus for machining, US Patent 4,621,547.
5. KRAMAR, D., KRAJNIK P., KOPAČ J., High pressure jet assisted turning of surface hardened piston rods, Int. J. Materials and Product Technology, 2010, Vol. 38, No. 4, pp.399-417
6. DENIZ, A.E., MICARONI, R., Influence of the Direction and Flow Rate of the Cutting Fluid on Tool Life in Turning Process of AISI 1045 Steel, International Journal of Machine Tools & Manufacture, 2007, Vol. 47, No. 2, pp. 247-254.
7. SREDANOVIC, B., GLOBOČKI LAKIĆ, G, ČIČA, D., KRAMAR, D. Influence of Different Cooling and Lubrication Techniques on Material Machinability in Machining, Strojniški vestnik - Journal of Mechanical Engineering,2013. Vol. 59, No. 12, pp. 748-754.
8. COURBON, C., KRAMAR, D., KRAJNIK, P., PUSAVEC, F., RECH, J., KOPAC, J., : Investigation of machining performance in high-pressure jet assisted turning of Inconel 718: an experimental study. International Journal of Machine Tools & Manufacture, 2009, Vol. 49, No. 14, pp. 1114-1125
9. SREDANOVIC, B., GLOBOČKI LAKIĆ, G., KRAMAR, D., KOPAČ, J. New trends in cutting technologies: application of high pressure jet assisted machining, 14th International conference on tribology, Belgrade, Serbia, May 2015
10. GLOBOČKI-LAKIĆ,G., KRAMAR, D., KOPAČ, J. Metal cutting-theory and applications. Faculty of Mechanical Engineering, Banja Luka and Ljubljana, 2014
11. SREDANOVIC, B., *Development of universal machinability model based on cutting process parameters*, MSc thesis (in Serbian), Faculty of Mechanical Engineering Banja Luka, University of Banjaluka, Banja Luka, 2012.
12. SREDANOVIC, B., GLOBOČKI LAKIĆ, G., KRAMAR, D., KOPAČ, J. Modelling of tool wear in turning of bearing steel using carbide tool and HPJAM technique, 12. International Conference on Accomplishments in Electrical and Mechanical Engineering and Information Technology, Banja Luka, BiH, May 2015.
13. CICA, D., SREDANOVIC, B., KRAMAR, D. Modelling of tool life and surface roughness in hard turning using soft computing techniques: A comparative study, *International Journal of Materials and Product Technology*, 2015, Vol. 50, No.1, pp. 49 - 64.

CORRESPONDENCE

GORDANA GLOBOČKI LAKIĆ
High pressure jet assisted machining - application in turning, University in Banja Luka, Faculty of Mechanical Engineering
e-mail:gordana.globocki@gmail.com

Tribological Journal BULTRIB Vol. 5, 2015
Papers from the International Conference **BULTRIB '15**
September 11-13, 2015, Sozopol, Bulgaria
Society of Bulgarian Tribologists
FIT – Technical University of Sofia

ABRASIVE WEAR OF SALTS DOPED EPOXY COMPOSITES

Mihai BOȚAN, Ioan BOSOANCĂ, Radu BOSOANCĂ, Iulia GRAUR, Ionuț MIHALACHE, Marius BODOR, Adrian CÎRCIUMARU

Abstract: *The study was carried out in order to complete the characterization of ionic substances doped epoxy resin. Two types of ionic substances had been used namely Potassium dichromate and Sodium dichromate while the epoxy system was WWA and WWB from Resoltech. The doping method had been developed as part as research activity under the Project POSCCE 12P01.024/CD111 and was meant as an ease method to increase the electrical conductivity of polymers. The abrasive wear analysis had been performed on the pin-on-disk geometry with composite pin and with the steel disk covered with abrasive paper.*

Key Words: *abrasive wear, polymer composites, epoxy resin, salts*

1. INTRODUCTION

Polymer composites are the most used materials in nowadays industry due to their low price and their excellent properties. The low specific weight of these materials is recommending them for use in aero and spatial industry and in the automotive industry, in this last case especially for car body parts, but not only. Since the future seems to belong to the electrical vehicles a new way to interpret and design these materials is required. Basically, designing a composite means to find a balanced fibers/matrix ratio and an appropriate distribution of fibers to be placed into a polymer matrix such as, at the end, the formed material, to fulfill intended mechanical tasks. It is well known the forming techniques for thermoset matrix polymer are ease and unpretentious allowing obtaining these materials, practically, in every laboratory or workshop. Generally a thermoset polymer is obtained by mixing together two liquid components (the resin and the hardener) and that is why such materials are the most susceptible of modification by adding various agents.

The agents – carbon nanotubes, ferrites, fullerenes, various ceramic nano-structures – are used to modify the physical properties of polymers and, generally, their use is leading to decreases in mechanical performance of materials. One very important issue when the named compounds are used as agents is their aggregation because their clusters act as efforts concentrators for the matrix [1-4]. That is why one capital issue of thermoset matrix composite forming (as well as for all the composites) is to ensure a high quality interphase between immersed phases and the matrix [5-9]. Using large concentrations of particulate agents the polymer composite becomes brittle and its application is no longer reliable even if the physical properties are more valuable [10-13]. The problem of more than two phase composite design is complex and difficult. For instance, in the case of a fiber reinforced composites with modified polymer matrix even the behavior of two phase composites are known (reinforced polymer and modified polymer) it is difficult to predict the behavior of three phase composite [14]. There are also important effects of reinforcements or modifying agents on the tribological and wear properties of composites [15-18].

The polymers are electric insulators and the efforts are directed towards changing their electromagnetic properties especially the electric conductivity (and as consequence other transport phenomena). The use of particulate agents, as it was said, reduces the mechanical resistance of materials depending on particles dimensions. A solution for this problem is to diminish the particles dimensions and transferring the problem form physics to mezzo- or even nano-physics but the problem of uniform dispersion of these particles will remain. Another solution is to produce the small particles directly into the polymer matrix while another one is to change the polymer properties using appropriate soluble substances. In the last case the solvent has to not interact with the matrix and it has to be volatile in order to be removed from mixture – this technique might be appropriate to obtain salts modified resins or polymers mixtures with special properties. Of course such modified polymers might be used as matrix to form reinforced composites with different reinforcement distributions or with different matrix distribution as an attempt to control the final properties of formed hybrid composite materials.

2. MATERIALS

The epoxy system WWA-WWB from *Resoltech* had been used as matrix. The two components of the system are liquid and that is favouring intervention on the final properties even in this stage or in the pre-polymer stage. As test modifiers Potassium dichromate and Sodium dichromate had been selected due to the similar properties of alkaline ions and to orange colour that can be used as an indicator. Both salts were dehydrated by thermal cure to avoid the placement of water molecules into the polymer. As solvent a commercial use nitro diluent named D209 had been used it consists of a mixture of toluene, acetone, butyl acetate and butanol. The resin contains 75-78% bisfenol A according to the specification and the materials had been formed based on the lowest value such as at a given number of bisfenol A molecules to correspond an alkaline ion.

The two salts were solubilized into the solvent and the solution was mixed with the main component of epoxy system. When the dispersion was uniform the conditions for solvent vaporization were set as follows: mechanical stirring at 200rot/min, temperature 70^{o}C and continuous ventilation above the pot. The duration for solvent removal is about 150 minutes. The amounts of salts had been computed such as the doping levels to be of 1 alkaline ion at 5000 bisfenol A molecules and with decrements of 1000 up until 1 alkaline ion to 1000 bisfenol A molecules and with decrements of 100 from 1/500 to 1/100 alkaline ion/bisfenol A molecules. After the solvent is removed the alkaline and dichromate ions are remaining into the polymer.

The resin-ions mixture was mixed with the required amount of hardener and samples were formed into cylindrical moulds of 11 mm diameter and 200 mm height. For each material six samples were formed. As reference materials epoxy resin and diluted resin had been formed. The diluted resin is the epoxy resin in which the solvent was mixed and then removed. To avoid the gaseous intrusions all the cylindrical moulds were vibrated on a granular media with vibrations generated by ultrasounds. For each material ultrasonic exposure during the pre-polymer phase was considered for duration from one to five minutes (one minute increment) to increase the homogeneity of dispersions. The ultrasonic exposure was realized during the gel time of the pre-polymer while the vibrations were applied after moulding.

After polymerization (24 hours) the samples were thermally cured to get the best properties of the epoxy system and the samples were removed from the moulds.

3. MEASUREMENTS AND RESULTS

The main goal of the test is to identify the effect of slats presence into the matrix on the basic properties of epoxy resin. The second aim is to identify the effect of ultrasonic exposure on the properties of ions doped polymer. All the materials were thermally analysed to determine the specific heat but the results are far away from the value of specific heat of epoxy resin meaning that mixing rule is not giving, in this case, a valid approximation. In order to investigate probable formation of new chemical structures (for example by chelation of dichromate ions) Raman analysis was performed but, as it can be seen in fig. 1-4, there are not important modifications. The salt concentration, even for the highest levels of doping, is extremely low, less than 1% weight ratio and in such conditions the mixing rule is not sensitive enough to give some decidable results. Remarkable is the fact that for both salts at a doping level of one alkaline ion at 400 molecules of bisphenol A the composites are showing high density and high value of specific heat independently on the time of ultrasonic exposure.

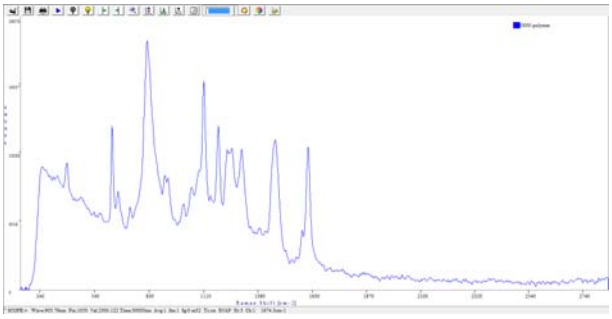

Fig. 1. Raman spectrum of epoxy resin

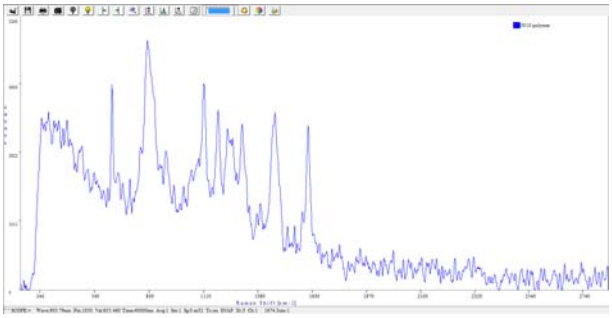

Fig. 2. Raman spectrum of diluted epoxy resin

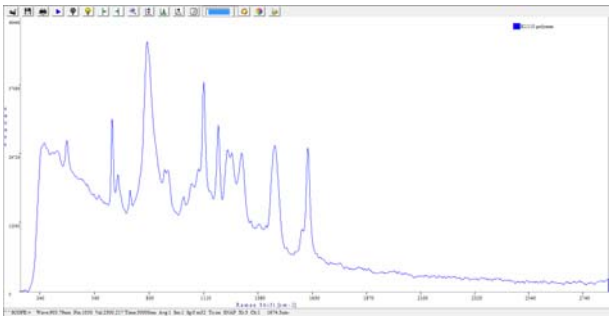

Fig. 3. Raman spectrum of highest level of doping 1 Potassium ion at 100 bisfenol A molecules

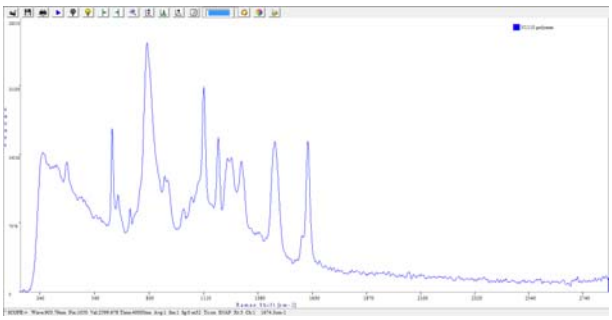

Fig. 4. Raman spectrum of highest level of doping 1 Sodium ion at 100 bisfenol A molecules

The abrasive tests were performed on a Universal Testing Machine on the pin on disk geometry with the pin made of composite and the steel disk covered with abrasive paper P150. Three regimes were set and the sliding distance was of 100m. The three regimes were set such as such as the product sliding speed normal force to be constant and the values are given in the graphs below. The reference materials are labelled 000x – epoxy resin and 001x – diluted epoxy resin where x denotes number of minutes of ultrasonic exposure (0 to 5). The doped materials are labelled with four digits first of them identifying the salt (N for sodium dichromate and K for potassium dichromate), the last digit marks the number of minutes of ultrasonic exposure. The second digit is corresponding to the salts concentration – 1 for one alkaline ion at 5000 molecules of bisphenol A, 5 for one alkaline ion at 1000 molecules of bisphenol A, 6 for one alkaline ion at 500 bisphenol A molecules, 9 for one alkaline ion at 200 bisphenol molecules. With five digits are labelled the materials with the highest salts concentration the second and third digits are 11 and corresponds to the doping level of one alkaline ion at 100 bisphenol A molecules.

According to [19] the wear rate is computed with Z=V/Fd where is the lost volume, F is the normal load and d is the sliding distance. The wear resistance is 1/Z and this is the parameter that had been studied. The specific weight of each material was determined by the classical method measuring the volume and the weight of each sample and these results were used to determine the wear rate and the wear resistance. As it was mentioned before the highest values of specific weight were obtained for the materials with one alkaline ion at 400 bisphenol A molecules and the wear resistance of the two materials (K71, N71) is presented together with the wear resistance of epoxy resin and diluted epoxy resin. Also to point the doping effect on the wear resistance the wear resistance of the materials with the lowest (K11, N11) and the highest (K111, N111) levels of doping are also presented (fig. 5-8).

It is noticeable that the materials labelled K11 and N11 (fig. 6) shows almost the same behaviour as the epoxy resin and the diluted epoxy resin (fig. 5). As expected, all the presented materials show high wear resistance during the low speed regime and lowered wear resistance for the other two regimes. In fig. 5 one may notice that the abrasive wear resistance of diluted epoxy resin is higher than the same parameter for epoxy resin but is decreasing with the duration of ultrasonic exposure while the abrasive wear resistance of

epoxy resin is increasing with the duration of ultra-sonication. The same behaviour is observable for materials in fig. 6 and fig. 7.

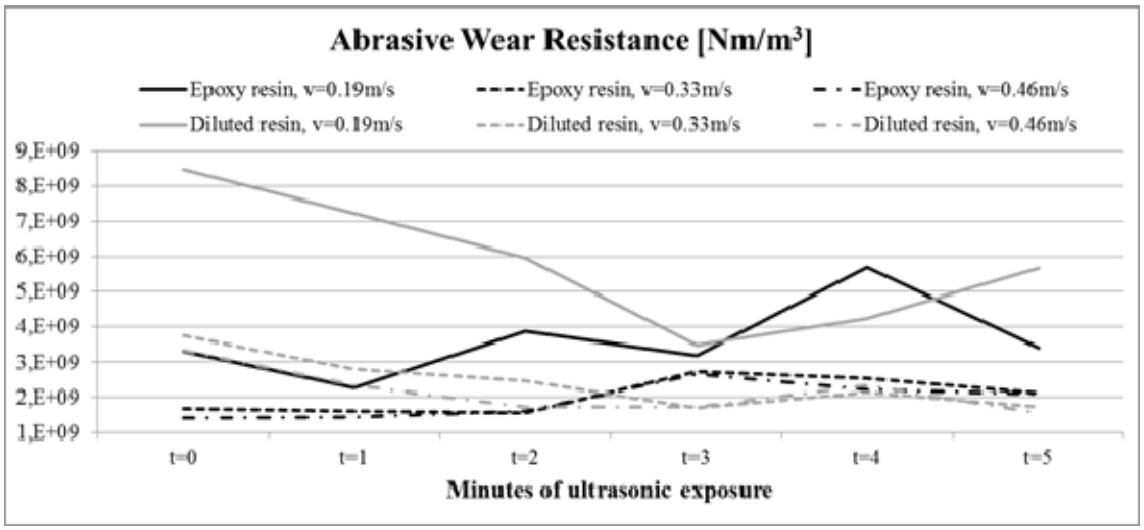

Fig. 5. Abrasive wear resistance of epoxy and diluted epoxy

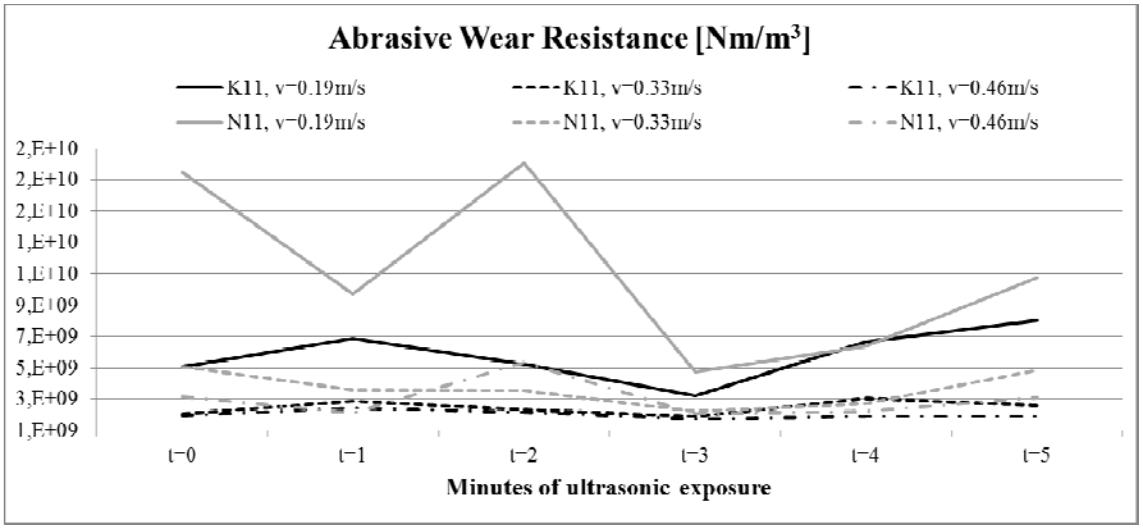

Fig. 6. Abrasive wear resistance of materials with lowest doping level

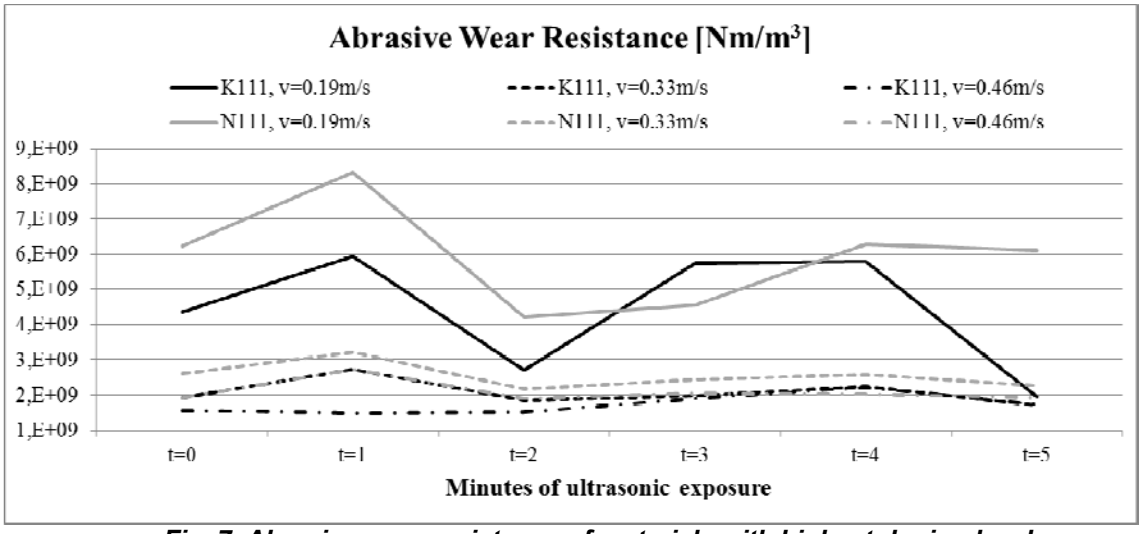

Fig. 7. Abrasive wear resistance of materials with highest doping level

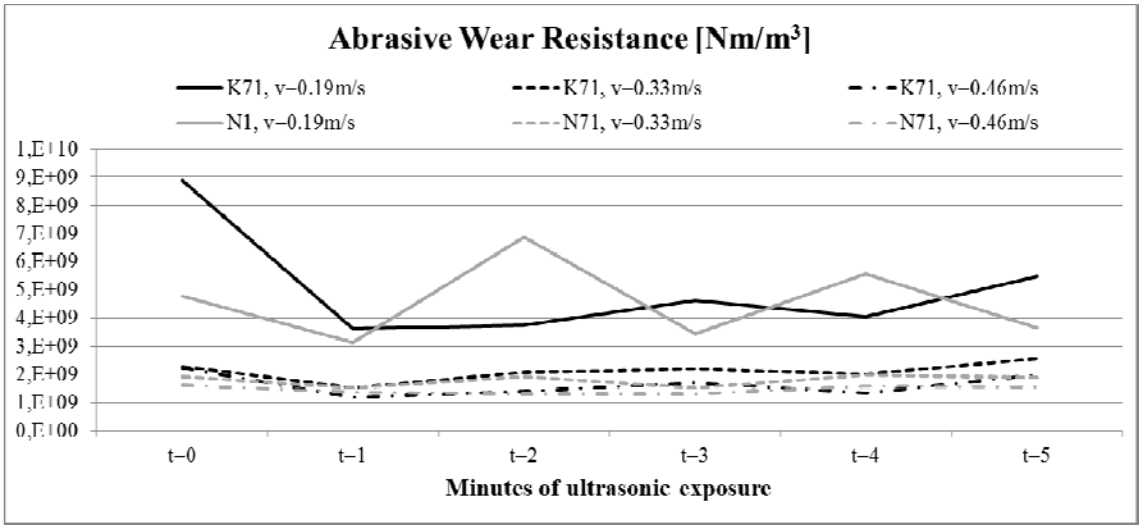

Fig. 8. Abrasive wear resistance of materials with one alkaline ion at 400 bisphenol A molecules

4. CONCLUSION

A method of doping the epoxy resin with metallic ions had been tested and obtained materials had been studied to identify the modifications determined by the presence of metallic ions. The doping method consists of mixing the resin with a solution of an inorganic salt followed by the removal of solvent. In such condition the behaviour of solvent modified resin is important to separate its effect from the effect of metallic ions. The solvent modified resin – called diluted resin – is obtained by mixing the resin with an amount of solvent and removal of solvent.

The diluted resin shows, generally, higher values of abrasive wear resistance, comparing with the epoxy resin, but these values are decreasing with the increase of ultrasonic exposure duration. In the case of doped materials the Sodium dichromate doped materials seem to have higher values of abrasive wear resistance than the values showed by the Potassium dichromate doped materials at the same doping level and for the first regime of speed and loading (low speed, high load) and all the materials are showing same values of abrasive wear resistance for the other two regimes.

The materials with one alkaline ion at 400 bisphenol A molecules are showing the same abrasive behaviour independent on the type of alkaline ion and this result together with the fact that these materials are showing the highest values of specific weight leads to the conclusion that it is possible to appear some chemical structures determined by the presence of alkaline ions. These structures cannot be identified by means of Raman spectrophotometry because they are packed in polymer and their signal is very low due to the low concentration of alkaline ions relative to the amount of resin.

ACKNOWLEDGMENTS

This work had been supported by the Project 12P01 024 21(C11)/31.08.2012 (code SMIS 50414).

REFERENCES

1. BIE, B.X., HAN, J.N., LU, L., ZHOU, X.M., QI, M.L., ZHANG, Z., LUO, S.N., Dynamic fracture of carbon nanotube/epoxy composites under high strain-rate loading, Composites. Part A, **Vol. 68**, 2015, 282–288.
2. LI, Q., ZAISER, M., JANE, BLACKFORD, R., JEFFREE, C., HE, Y., KOUTSOS, V., Mechanical properties and microstructure of single-wall carbon nanotube/elastomeric epoxy composites with block copolymers, Materials Letters, **Vol. 125**, 2014, 116–119.
3. CHANDRASEKARAN, S., SEIDEL, C., SCHULTE, K., Preparation and characterization of graphite nano-platelet (GNP)/epoxy nano-composite: Mechanical, electrical and thermal properties, European Polymer Journal, **Vol. 49**, 2013, 3878–3888.
4. TSUDA, T., OGASAWARA, T., MOON, S.-Y., NAKAMOTO, K., TAKEDA, N., SHIMAMURA, Y., INOUE, Y., Three dimensional orientation angle distribution counting and calculation for the mechanical properties of aligned carbon nanotube/epoxy composites, Composites: Part A, **Vol. 65**, 2014, 1–9.
5. MECKLENBURG, M.,MIZUSHIMA, D., OHTAKE, N., BAUHOFER, W.,FIEDLER, B., SCHULTE, K., On the manufacturing and electrical and mechanical properties of ultra-high wt.% fraction aligned MWCNT and randomly oriented CNT epoxy composites, Carbon, 2015, doi: http://dx.doi.org/10.1016/j.carbon. 2015.04.085.

6. WEI, X.,XING, R., ZHANG, B., ZHANG, Q., BULIN, C., Preparation and dielectric properties of PATP-coated nano-$BaTiO_3$/epoxy resin composites, Ceramics International, 2015, http://dx.doi.org/ 10.1016/j.ceramint.2015.03.121.
7. TRIHOTRI, MANINDRA, DWIVEDI, U. K., KHAN, Fozia H., MALIK, M. M., QURESHI, M. S., Efect of curing on activation energy and dielectric properties of carbon blak-epoxy composites at different temperatures, Journal of Non-Crystalline Solids, **Vol. 421**, 2015, 1 – 13.
8. GHOSH, P. K., KUMAR, KAUSHAL, CHAUDHARY, NAYAN, Influence of ultrasonic dual mixing on thermal and tensile properties of MWCNTs-epoxy composite, Composites: Part B, **Vol. 77**, 2015, 139 – 144.
9. FIORE, V., SCALICI, T., VITALE, G., VALENZA, A., Static and dynamic mechanical properties of *Arundo Donax* fillers-epoxy composites, Materials and Design, **Vol. 57**, 2014, 456 – 464.
10. CHOI, S, YANG, J., KIM, Y., NAM, J., KIM, K., SHIM, S. E., Microwave-accelerated synthesis of silica nanoparticles-coated graphite nanoplatelets and properties of their epoxy composites, Composites Science and Technology, **Vol. 103**, 2014, 8 – 15.
11. WAN, Y.-J., TANG, L.-C., GONG, L.-X., YAN, D., LI, Y.-B., WU, L.-B., JIANG, J.-X., LAI, G.-Q., Grafting of epoxy chains onto grapheme oxide for epoxy composites with improved mechanical and thermal properties, Carbon, **Vol. 69**, 2014, 467 – 480.
12. GAO, Z., ZHAO, L., Effect of nano-fillers on thermal conductivity of epoxy composites with micro-Al_2O_3 particles, Materials and Design, **Vol. 66**, 2015, 176 – 182.
13. ZAINUDDIN, S., FAHIM, A., ARIFIN, T., HOSUR, M. V., RAHMAN, M.M., TYSON, J.D., JEELANI, S., Optimization of mechanical and thermo-mechanical properties of epoxy and E-glass/epoxy composites using NH2-MWCNYs, acetone solvent and combined dispersion methods, Composite Structures, **Vol. 110**, 2014, 39 – 50.
14. RAHMANIAN, S., SURAYA, A.R., SHAZED, M.A., ZAHARI, R., ZAINUDIN, E.S., Mechanical characterization of epoxy composite with multiscale reinforcements: Carbon nanotubes and short carbon fibers, Materials and Design, **Vol. 60**, 2014, 34 – 40.
15. CAMPO, M., JIMENEZ-SUAREZ, A., URENA, A., Effect of type, percentage and dispersion method of multi-walled carbon nanotubes on tribological properties of epoxy composites, Wear, **Vol. 324-325**, 2015, 100 – 108.
16. SHEN, J.T., TOP, M., PEI, Y.T., HOSSON, J.Th.M. de, Wear and friction performance of PTFE filled epoxy composites with a high concentration of SiO_2 particles, Wear, **Vol. 322-323**, 2015, 171 – 180.
17. HAN, J.-H., ZHANG, H., CHU, P.-F., IMANI, A., ZHANG, Z., Friction and wear of high electrical conductive carbon nanotube buckypaper/epoxy composites, Composites Science and Technology, **Vol. 114**, 2015, 1 – 10.
18. RAMESH, B. N., SURESHA, B., Optimization of tribological parameters in abrasive wear mode of carbon-epoxy hybrid composites, Materials and Design, **Vol. 59**, 2014, 38 – 49.
19. OLEA-MEJIA, O., BROSTOW, W., BUCHMAN, E., Wear Resistance and Wear Mechanisms in Polymer + Metal Composites, Journal of Nanoscience and Nanotechnology, **Vol. 10**, 2010, 3524 – 3530.

CORRESPONDENCE

Adrian CÎRCIUMARU
Doctor, Diagnose and Measurement Group, 41st Roșiori Str., Galați 800008, România
e-mail: acirciumaru@ugal.ro

Tribological Journal BULTRIB Vol. 5, 2015
Papers from the International Conference **BULTRIB '15**
September 11-13, 2015, Sozopol, Bulgaria
Society of Bulgarian Tribologists
FIT – Technical University of Sofia

ANALYTICAL AND EXPERIMENTAL MODEL FOR TRIBOLOGICAL BEHAVIOUR OF THIN COPPER LAYERS SUBJECTED TO PUNCTUAL STRESS

Georgiana Ionela PĂDURARU, Alina Maria PETRESCU,
Nicolae Alexandru STOICA and Andrei TUDOR

Abstract: *The paper presents theoretical and experimental aspects about the study of tribological behavior of thin cooper layer deposit on printed circuit boards. The analytical model is based on contact of a rigid sphere of given radius with a rigid or free layer on a rigid support that is characterized by the contact radius and penetration. For the experiment we used CSM Calowear stand and the tested materials were FR4, FR2 and CEM. At the same time were determined the thickness and the abrasive wear of copper layer deposit on printed circuit boards.*

Key Words: *copper layer, abrasive wear, printed circuit boards, punctual stress.*

1. MOTIVATION

The solder joint functionality (electrical, mechanical and thermal) is determine in principal by their micro-structure which is the result of the soldering Process temperature gradient action over the trinomial solder alloy/Paste, electronic components terminals/Pin and PCBs Pads finishes, according to 4P Soldering Model, concept [1, 2].

Is known that the resistance and mechanical integrity of the electronic assembly (composed from: printed circuit boards (PCB), devices/ electronic components and electronic component installation on printed circuit boards), is provided by the mechanical function [3].

Tendency to decrease the production cost has led to a decreased quality of electronic assemblies, therefore the novelty of this paper is given by the fact that we used new method to characterize the printed circuit board (PCB) substrate.

The analytical model describes the contact of a rigid sphere with thin copper layer and the effect of punctual stress on the mechanical integrity of the rigid support - cooper layer assembly. We used Hertz theory to deduce the radius of contact circle, penetration and hertz pressure. From the point of view of cooper layer fixing on rigid support there were defined two cases, the layer is not fixed on the support and the layer is completely fixed on the rigid support. For both cases were determined axial tensions, pressure distribution, contact radius, deformation and other parameters.

The tribological tests were made with CSEM Calowear stand that reproduces the abrasive wear test in small-scale. The equipment allows the evaluation of the inherent wear coefficient for bulk materials and for both the substrate and the coating in a coated sample from their combined wear data. Tested printed circuit boards (PCB's) are FR2 (synthetic resin bonded paper), FR4 (woven glass fabric with epoxy resin system) and CEM (Composite epoxy material).

The measurement principle is based on a lightly loaded ball coated with an aqueous suspension of a small abrasive (SiC - silicon carbide) that is rotated against the sample by mean of rectangular cut shaft. The result of the sphere rotation on the material surface is a wear crater (abrasion cap). The size of the resulting wear crater is determined with optical equipment.

After the experiment the wear gap dimension was determinate with the help of optical equipment. The wear volume both for the coating and substrate material were determinate by using the experimental data. Also the thickness of the coating was determinate.

2. ANALYTICAL MODEL

The contact between solids of which at least one of the surfaces is coated with a layer with different elastic properties that the rigid support represent a problem of tribological interest. The pressure distribution in the contact area is essentially different. [4]

We consider the case of a sphere of radius R that is in contact with a rigid layer or free layer (with thickness "b", elastic modulus "E" and Poisson's ratio (ν)) on a rigid support (Fig.1). The contact is characterized by the contact radius (a) and penetration (δ), when the sphere is loaded with normal force F_n and tangential force Q applied to the contact zone.

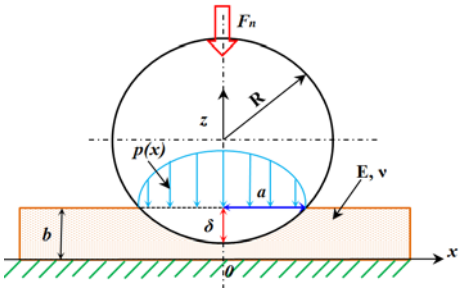

Fig. 1 The contact of a rigid sphere with a deformable layer

From the point of view of thickness(b) an elastic layer it is considered to be thin when its thickness is approximately equal to half the width of the contact area (b≈a). When b<<a the layer is considered to be very thin.

The radius of the contact circle is determined in the assumptions that the layer is thin and it constitutes an infinite semi-space. Using Hertz theory it will be determinate:

The contact circle radius:

$$a_H = \left(\frac{3 \cdot F_n \cdot R}{4 \cdot E^*}\right)^{\frac{1}{3}} \quad with\ E^* = \frac{E}{(1-\nu^2)} \tag{1}$$

Penetration:

$$\delta_H = \frac{a_H^2}{R} \tag{2}$$

Maximum pressure:

$$p_{0H} = \frac{3 \cdot F_n}{2 \cdot \pi \cdot a_H^2} \tag{3}$$

Hertz pressure:

$$p = p_{0H} \cdot \sqrt{1-\rho^2} \ \ cu\ \rho = \frac{r}{a} \tag{4}$$

When the thickness of the layer b<<a_H, the layer is considered thin. In this case the Hertz's theory cannot be applied, changing the pressure distribution on the contact surface. In the three-dimensional axes system (x, y ,z) with origin in point 0 (Fig.2), the generalized Hertz's law for the tensions (σ_x; σ_y σ_z; γ_{xy}; γ_{yz} ; γ_{yz}) from the elastic layer has the form:

$$\begin{aligned} \varepsilon_x &= \frac{1}{E} \cdot [\sigma_x - \nu(\sigma_y + \sigma_z)]; \quad \gamma_{xy} = \frac{1}{G} \cdot \tau_{xy} \\ \varepsilon_y &= \frac{1}{E} \cdot [\sigma_y - \nu(\sigma_z + \sigma_x)]; \quad \gamma_{yz} = \frac{1}{G} \cdot \tau_{yz} \\ \varepsilon_z &= \frac{1}{E} \cdot [\sigma_z - \nu(\sigma_x + \sigma_y)]; \quad \gamma_{zx} = \frac{1}{G} \cdot \tau_{zx} \end{aligned} \tag{5}$$

with:

E - Layer logitudinal elastic modulus

G - Layer transversal elastic modulus

$$G = \frac{E}{2 \cdot (1 + \nu)} \tag{6}$$

From the elastic layer fixing on the rigid support, there can be distinguished tow cases: the layer is free on the rigid support and the layer is completely fixed on the rigid support.

For the first case (layer free on the rigid support) the tensions $\sigma_x = 0; \sigma_y = 0$ in consequence from equation 5 results:

$$\varepsilon_x = -\nu \cdot \sigma_z = \varepsilon_y \tag{7}$$

$$\varepsilon_z = \frac{1}{E} \cdot \sigma_z = -\frac{1}{E} \cdot p(x) \tag{8}$$

Accepting that the sphere is a rigid:

$$\varepsilon_z = -\frac{\delta_z}{b} = -\frac{\delta - \frac{x^2}{R}}{b} = \frac{\left(\frac{a^2}{2 \cdot R} - \frac{x^2}{2 \cdot R}\right)}{b} = -\frac{a^2}{2 \cdot R \cdot b} \cdot (1 - \rho^2) \tag{9}$$

$$\rho = \frac{x}{a}$$

The pressure distribution on sphere at the contact with an elastic layer will be:

$$p(x) = E \cdot \frac{a^2}{2 \cdot R \cdot b} \cdot (1 - \rho^2) = p_0 \cdot (1 - \rho^2) \tag{10}$$

With the maximum pressure in the initial contact point:

$$p_0 = E \cdot \frac{a^2}{2 \cdot R \cdot b} \tag{11}$$

The maximum pressure is determinate from mechanical equilibrium condition:

$$F_n = \int_0^a 2 \cdot \pi \cdot r \cdot p_0 (1 - \rho^2)\, dr = 2 \cdot \pi \cdot p_0 \cdot a \cdot \int_0^1 \rho (1 - \rho^2)\, d\rho = \frac{\pi}{2} \cdot a^2 \cdot p_0 \tag{12}$$

With:

$$p_0 = \frac{2 \cdot F_n}{\pi \cdot a^2} \tag{13}$$

From equation 11 and 13 is determined the contact radius a, when is known the loading F_n, the geometry of the rigid sphere (R), the geometry of the layer b and the layer elasticity

$$a = \left(\frac{4 \cdot F_n \cdot R \cdot b}{\pi \cdot E}\right)^{\frac{1}{4}} \text{ sau } a_a = \frac{a}{R} = (4 \cdot p_{case} \cdot b_r)^{\frac{1}{4}} \tag{14}$$

With

$$b_R = \frac{b}{R}$$

For the second case (layer fixed on the rigid support) the functional condition is:

$$\varepsilon_x = 0; \sigma_x = \sigma_y$$

From Hooke generalized law (Ec. 5) it results:

$$\sigma_x = \frac{-\nu}{1-\nu} \cdot \sigma_z = \frac{\nu}{1-\nu} \cdot p(x) \tag{15}$$

The deformation on z direction is known geometrically (Ec. 9):

$$\varepsilon_z = \frac{1}{E} \cdot \left[-p(x) - \frac{2 \cdot \nu^2}{1-\nu} \cdot p(x) \right] = -\frac{a^2}{2 \cdot R \cdot b} \cdot (1 - \rho^2)$$

Results the pressure distribution on the sphere:

$$p(x) = \frac{(1-\nu) \cdot E}{1-\nu+2 \cdot \nu^2} \cdot \frac{a^2}{2 \cdot R \cdot b} \cdot (1 - \rho^2) = p_0 \cdot (1 - \rho^2) \tag{16}$$

with

$$p_0 = \frac{(1-\nu) \cdot E}{1-\nu+2 \cdot \nu^2} \cdot \frac{a^2}{2 \cdot R \cdot b} \tag{17}$$

or

$$p_{0e} = \frac{p_0}{E} = \frac{1-\nu}{1-\nu+2 \cdot \nu^2} \cdot \frac{a^2}{2 \cdot R \cdot b}$$

From mechanical equilibrium condition **Error! Reference source not found.**) și (), it results the contact radius for fixed layer case.

$$a = \left[\frac{2 \cdot F_n \cdot R \cdot b \cdot (1-\nu+2 \cdot \nu^2)}{(1-\nu) \cdot E} \right]^{\frac{1}{4}} \tag{18}$$

or

$$a_a = \frac{a}{R} = \left[\frac{2 \cdot \pi \cdot (1-\nu+2 \cdot \nu^2)}{1-\nu} \cdot p_{0se} \cdot b_R \right]^{\frac{1}{4}}$$

In [5] is exemplified, comparatively, the dependence of dimensionless contact radius (a_a) on Striebeck pressure (p_{ase}) for Hertz contact (a_{aH}) and for the specific contact of thin layer fixed (a_{a2}) and free (a_a) on the rigid support.

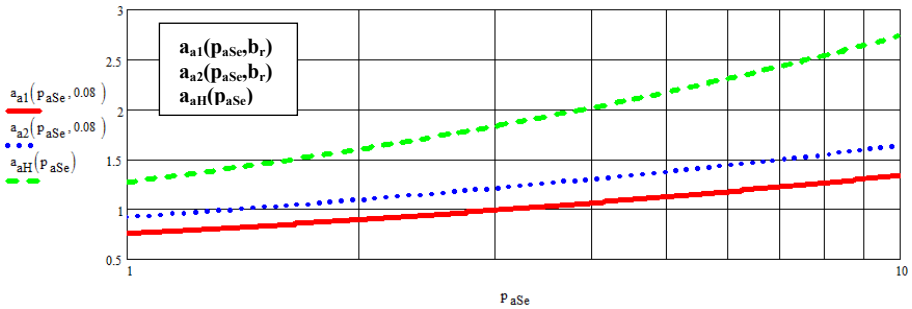

Fig. 2 Dependence of dimensionless contact radius on Striebeck pressure for hertz contact and for thin layer free and fixed on rigid support

In Fig. 3 is exemplified the dependence of maxim dimensionless contact pressure for three cases: Hertz pressure (p_{0eH}), pressure on thin layer free on rigid support(p_{01e}), and pressure on thin layer fixed on rigid support (p_{02e}).

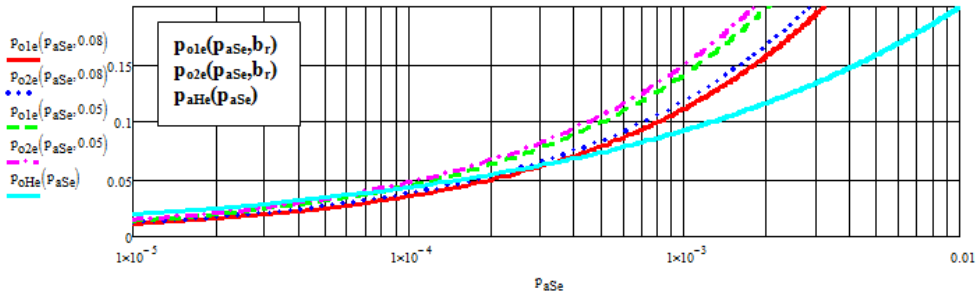

Fig. 3 The dependence of dimensionless pressure contact for Hertz contact, thin layer fixed on rigid support and thin layer free on rigid support

3. EXPERIMENTAL MODEL

The purpose of the present experiment was to determine the thickness of the cooper layer deposit on the surface of printed circuit boards and determination of the abrasive wear resistance. For the experiment we used CSM Calowear stand and the tested materials were FR4, FR2 and CEM

The wear volume both for the coating and substrate material were determinate by using the experimental data. Also the thickness of the coating was determinate with the help of Equation 19, [4,5]

$$h = \frac{x \cdot y}{d} \tag{19}$$

were the distance x and y are inspected by an optical microscope and d represents the alumina sphere diameter.

In the case of the coated materials Archard equation was expanded for combined wear of both materials (coating and substrate), each having a different coefficient of wear. [4]

For bulk materials the Archard equation is:

$$L \cdot F_n = \frac{v}{k} \tag{20}$$

if: $b \ll d$

$$L \cdot F_n \approx \frac{1}{k} \cdot \left(\frac{\pi \cdot b^4}{32 \cdot d_s} \right) \tag{21}$$

were:

L	Sliding lenght
F_n	Normal force
v	Wear volume
k	Wear coefficient
b	Diameter of the wear gap on sample surface
d_s	Sphere diameter

In Figure 4 are presented the two diameters used in the Equation 2 and 3.

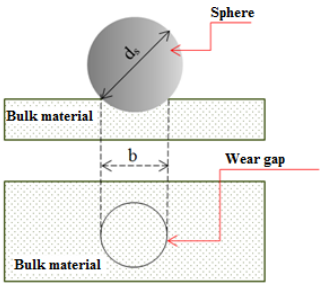

Fig. 4 Calowear principle for wear coefficient evaluation (in the case of bulk materials)

By reordering equation 2 the wear coefficient can be determined by:

$$k = \frac{\pi \cdot b^4}{32 \cdot L \cdot F_n \cdot d} \tag{22}$$

In this case

$$k = 2{,}5 \cdot 10^{-8} \frac{b^4}{L \cdot F_n}$$

For covered materials the equation 4 becomes:

$$L \cdot F_n = \left(\frac{v_a}{k_a} + \frac{v_s}{k_s}\right) \tag{23}$$

were"a" and "s" coefficients refers to the coating and substrate.
According to Hutchings Equation 23 can be expressed as a function of total wear volume "v" and of layer wear volume "v_s".[4]

$$L \cdot F_n = \frac{v_a \cdot k_a + (v - v_a) \cdot k_a}{k_a \cdot k_s} \tag{24}$$

Both volumes can be determined with the help of wear gap total diameter "b" and layer thickness "h".
Therefor:

$$\frac{L \cdot F_n}{b^4} - \left(\frac{k_s - k_a}{k_s \cdot k_a}\right) \cdot \left(\frac{\pi \cdot h}{4 \cdot b^2} - \frac{\pi \cdot d \cdot h^2}{2 \cdot b^4}\right) + \left(\frac{1}{k_s}\right) \cdot \left(\frac{\pi}{32 \cdot d}\right) \tag{25}$$

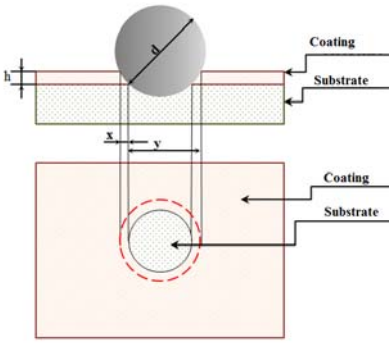

Fig. 5 Calowear principle for wear coefficient evaluation (in the case of covered materials)

The sliding length can be calculated using Equation 26:

$$L = \frac{\pi \cdot R'' \cdot n'' \cdot d}{\sqrt{\left(\frac{d^2}{4} - 25\right)}} \tag{26}$$

were:

d	Sphera diameter
L	Sliding lenght
L'	Virtual sliding lenght for R'
L''	Sliding lenght of drive shaft
n	Sphera number of revolutions
n'	Virtual circle number of revolutions
n''	Drive shaft number of revolutions
R'	Virtual circle radius (contact radius between drive shaft and sphera)
R''	Drive shaft radius

In this case:

$$L = \frac{\pi \cdot 6{,}5 \cdot n'' \cdot 42}{\sqrt{\left(\frac{42^2}{4} - 25\right)}} \Rightarrow L = 42{,}04 \cdot n'' \quad (27)$$

4. RESULTS AND CONCLUSIONS

For tribological characterization of test samples was used an alumina sphere with a diameter (d) of 42 mm and mass (m) of 135.88 g. During the experiment the normal force value was registered at every 10 seconds. Before starting the test the samples were cleaned with isopropyl alcohol to remove the copper layer deposited oxides.

In order to determine the thickness of the copper layer deposited on the surface of the circuit boards measurements were performed with help of an optical microscope. The wear gap dimensions were measured on both principal diameters and the thickness was determined using a medium diameter

Table 1 Cooper layer thickness

FR 2	
	
Medium diameter of wear gap on copper layer	Medium diameter of wear gap on rigid support
$D_m = \frac{D_1 + D_2}{2} = 2,266\ mm$	$d_m = \frac{d_1 + d_2}{2} = 0,433\ mm$
Necessary dimensions to determine the thickness of the copper	
$x = \frac{D_m - d_m}{2} = 0,916$	$y = d_m = 0,433$
Cooper layer thickness: $h_{FR2} = \frac{x \cdot y}{d} = 0,00944\ mm \approx 9,4\ \mu m$	
FR 4	
	
Medium diameter of wear gap on copper layer	Medium diameter of wear gap on rigid support
$D_m = 3,333\ mm$	$d_m = 1,083\ mm$
Necessary dimensions to determine the thickness of the copper	
$x = 1,125$	$y = d_m = 1,083$
Cooper layer thickness: $h_{FR4} = \frac{x \cdot y}{d} = 0,029\ mm \approx 29\ \mu m$	
CEM	
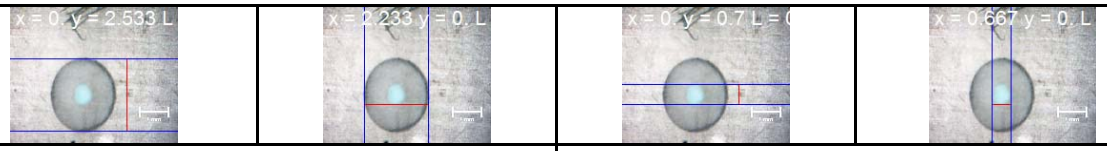	
Medium diameter of wear gap on copper layer	Medium diameter of wear gap on rigid support
$D_m = 2,383\ mm$	$d_m = 0,683\ mm$
Necessary dimensions to determine the thickness of the copper	
$x = 0,85\ mm$	$y = d_m = 0,683\ mm$
Cooper layer thickness: $h_{CEM} = \frac{x \cdot y}{d} = 0,0138\ mm \approx 13,8\ \mu m$	

The wear coefficient and volume were also determined.

Table 2 Values for wear coefficient and wear volume determined for tested samples

Sample	T[s]	Sliding Lenght [mm]	Abrasion gap medium diameter *„b”* [mm]		Wear coefficient *„k”*		Wear volume *„v”[mm^3]*	
FR2	900	225.942	Cu	2.464	Cu	$2.5 \cdot 10^{-4}$	Cu	0.0402
			FR2	0.875	FR2	$4 \cdot 10^{-6}$	FR2	$1.37 \cdot 10^{-3}$
FR4	900	226,315	Cu	1.937	Cu	$2.4 \cdot 10^{-4}$	Cu	0.0399
			FR4	-	FR4	-	FR4	-
			CEM	-	CEM	-	CEM	-
CEM	900	225,995	Cu	2.542	Cu	$6.9 \cdot 10^{-4}$	Cu	0.976
			CEM	1.515	CEM	$8.7 \cdot 10^{-5}$	CEM	0.123

From the analytical model we can illustrate, comparatively, the dependence of dimensionless contact radius on Striebeck dimensionless pressure for hertz contact and for both studied cases (the layer is not fixed on the support and the layer is completely fixed on the rigid support). We determined the variation of the normal and radial displacing for hertz contact, for fixed and no fixed layer.

After interpreting the results obtained from the experimental model we can say that the experiment does not confirm the manufacturer prescription regarding the cooper layer thickness, according to manufacturer's specifications in all three cases the copper layer has a thickness of 35 microns after the experiment we can see that the cooper layer thickness is different all three cases. (See table 2).

ACKNOWLEDGMENTS

The authors are very grateful to the leading staff of Machine Elements and Tribology Department for continuous support and collaboration to fulfil the experiments presented in the paper and to the leading staff of Centre of Technological Electronics and Interconnection Techniques – CETTI, which offered the rigid supports for experiments and assured the optical measurements of the tested boards.

This work was partially supported by the strategic grant POSDRU/159/1.5/S/137070 (2014) of the Ministry of National Education, Romania, co-financed by the European Social Fund – Investing in People, within the Sectoral Operational Programme Human Resources Development 2007-2013.

The work has been founded by the Sectoral Operational Programme Human Resources Development 2007-2013 of the Ministry of European Funds trough the Financial Agreement POSDRU 187/1.5/S/155536.

REFERENCES

20. JEONG-WON YOON A, BO-IN NOH A, YOUNG-HO LEE B, HYO-SOO LEE C, SEUNG-BOO JUN, Effects of isothermal aging andtemperature–humidity treatment of substrate on joint reliability of Sn–3.0Ag–0.5Cu / OSP-finished Cu CSP solder joint, ELSEVIER, Microelectronics Reliability 48 1864–1874, 2008

21. I. PLOTOG, G. DUMITRU, ET.AL., Microstructure Comparative Analysis of the Solder Joints Based on SAC/SN100 Soldering Alloy Type Depending on the Cooling Rate, 18th International Symposium for Design and Technology in Electronic Packaging (SIITME), 978-1-4673-4760-0, 167-172, 2012

22. CUCU, T.C. ; PLOTOG, I.; BRANZEI, M., “Mechanical tests regarding low-temperature lead-free solder pastes application in automotive electronics”, Published in 2014 IEEE 20th International Symposium for Design and Technology in Electronic Packaging, SIITME 2014, pages 63-68, 23-26 Oct. 2014, Bucharest, Romania

23. J.F. ARCHARD: Contact and rubbing of flat surfaces, Journal of Applied Physics (1953), 24:981-988

24. K.L. RUTHERFORD AND I.M. HUTCHINGS, ”Surface Coating Technology”, Thinning Films and Tribological Interfaces, Proceedings of the 26th Leeds-Lyon Symposium, ISBN: 978-0-444-50531-6, Elsevier, 1999

CORRESPONDENCE

Georgiana Ionela PĂDURARU
Department of Machine Elements and Tribology, “POLITEHNICA” University of Bucharest, Splaiul Independentei 313, Sector 6 Bucharest, Romania
e-mail: gi.dumitru@gmail.com

Tribological Journal BULTRIB Vol. 5, 2015
Papers from the International Conference **BULTRIB '15**
September 11-13, 2015, Sozopol, Bulgaria
Society of Bulgarian Tribologists
FIT – Technical University of Sofia

EXPERIMENTAL STUDY OF BEARING BOXES FRICTION

Radu VELICU, Mihai LATEȘ, Silviu POPA

Abstract: *The subjects of this paper are the bearing boxes of a testing rig for chain drives. Friction in transmission without bearings is calculated by subtracting the bearing friction from the global friction. This is why it is of maximal importance in the correct evaluation of experimental measurements on the rig to have accurate data on the friction on bearings. Bearing boxes friction is measured depending on rotational speed, load and lubricating oil temperature.*

Key Words: *Bearing box, friction torque, friction loss.*

1. INTRODUCTION

This paper deals with the first stage of research on chain drive friction: evaluation of bearing friction of a basic chain drive system with transmission ratio equal to 1. The final goal of the research is the evaluation of friction losses in chain drives.

Very few experimental results on chain friction have been published. A technique for measuring sliding loss in the timing chain and the loss in the guides of an engine, using equipment developed on a full engine is presented in [1]. The results are separate timing chain system losses into components, for given constant speed and temperature.

The current research is looking to evaluate chain friction depending on the tensioning force, speed, temperature and quality of lubrication. The basic procedure of our research on chain friction is presented in [2]. It uses the chain rig presented in Fig. 1, together with a functional diagram. The driving sprocket (1) is mounted on the input shaft, which is part of the lower bearing box (2). The driven sprocket (3) is mounted on the output shaft, which is part of the upper bearing box (4). The upper bearing box is fixed on a sliding carriage (5) which allows vertical adjustment of the driven sprocket, also creating the tensioning force by a screw-nut mechanism. The screw (6) is connected to the upper bearing box sliding carriage by a force sensor (7), measuring the tensioning force. Specific sensors and devices measure the input shaft speed and input torque (determined by the frictions in chain and bearing boxes), the chain tensioning force, the temperature and pressure of the oil for the bearing boxes lubrication and for the chain lubrication. Testing rig devices control the input shaft rotational speed, tensioning force and temperature of the lubrication oil.

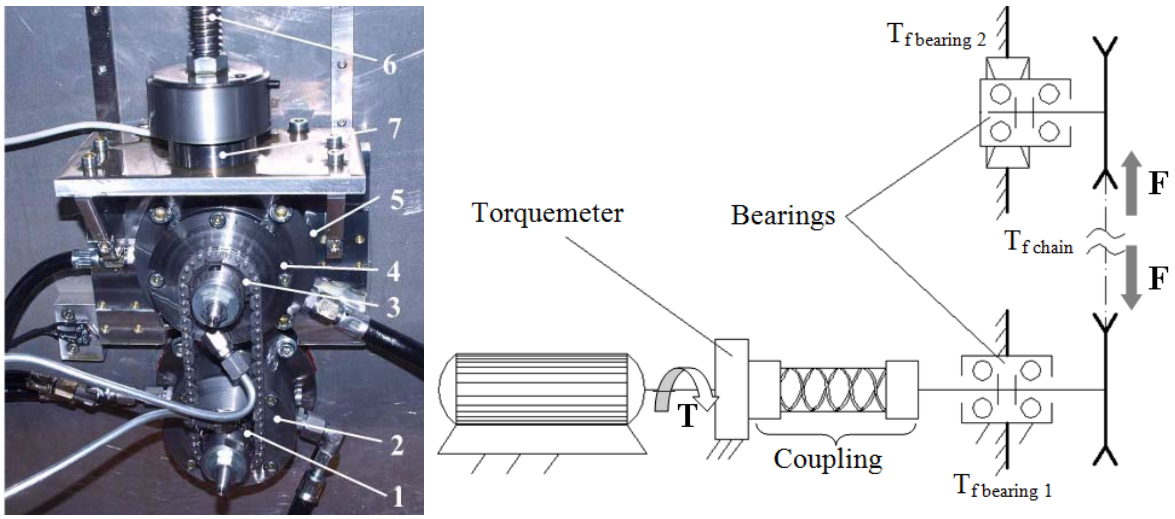

a b

Fig. 1. Chain friction rig: a) front view; b) functional diagram

The measured input torque is a sum of all the frictional torques in the transmission: from the bearing boxes and from the chain transmission. Friction in chain transmission without bearings is calculated by subtracting the bearing boxes friction (sum of friction in the two bearing boxes) from the global friction. It is of maximal importance in the correct evaluation of experimental measurements on the rig to have accurate data on the bearing boxes friction.

The subject of this paper is the evaluation of friction in the bearing boxes of previously presented testing chain friction rig. As a first stage of the research on chain friction, this paper presents the measured friction torque in bearing boxes, depending on rotational speed, load and lubricating oil temperature.

The global friction on these bearing boxes is a sum of friction in bearings and sealing elements, with important influence of the lubricating circuit. It is difficult to separate and identify with accuracy each friction and evaluate all the influences [3]. As presented in the calculus model of bearing friction of the producer [3], the global friction depends on rotational speed, radial load (there is no axial load in this case), bearings and sealing types (construction, dimensions, clearances, lubrication and materials), temperature, pressure and type of oil. Calculus relations show that the friction torque in a bearing increases with increase of applied load, increase of rotational speed and increase of lubricant viscosity. An analyse of these influences on bearing boxes friction is presented in [4]. Even if the theoretical models of individual bearing friction calculus are comprehensive, based on years of experiments and can be applied to bearing boxes, they cannot be considered as highly accurate. Author's opinion is that only experimental measurements of bearing boxes friction, copying exactly the conditions of functioning give accuracy of results. Several aspects like deformations, time depending parameters, measurement conditions and strictly following procedures have maximal importance.

2. BEARING BOXES DESCRIPTION

The chain rig uses two bearing boxes. Figure 2 presents the assembling of bearings and chain drive. Figure 3 presents the lower bearing box. The upper bearing box is similar but not identical. Both bearing boxes are consisted of: one deep grove ball bearing 6206 (1 – see Fig. 3), which takes radial force and possible axial forces on both directions; one single row cylindrical roller bearing with two shoulders NU 2305 (2), taking the most important radial force; sealing rings (3) at both ends; lubrication with low pressure oil circuit.

Both bearing boxes are radial loaded with force F positioned as in the chain transmission tensioning situation. Radial loads on bearings depend on position of force F.

There is no influence on the bearing friction from the torque used for mounting or demounting the sprockets.

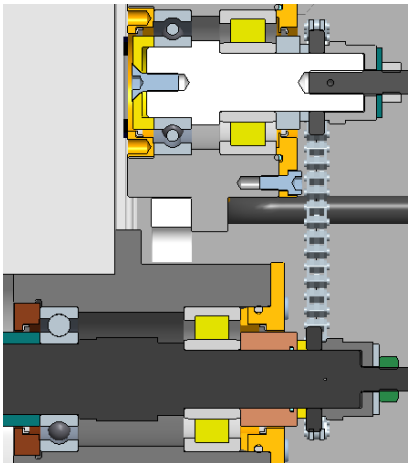

Fig. 2. Bearings and chain drive

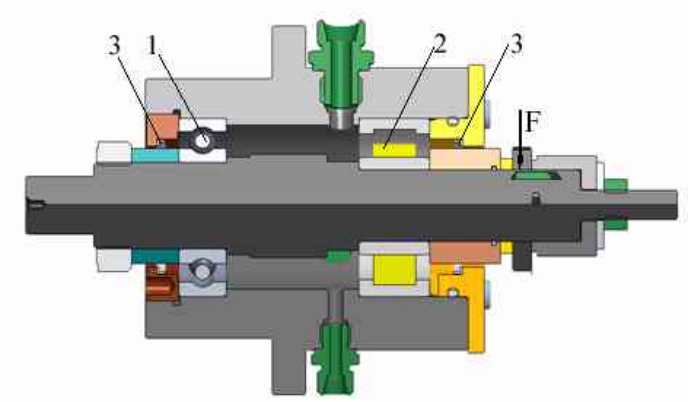

Fig. 3. Lower bearing box

3. EQUIPMENT AND TESTING PROCEDURE

The measurement device is adapted on the chain rig presented in Fig. 1. Fig. 4 shows an image of the device together with a functional diagram. The upper and lower bearing boxes are coaxially mounted, head to head, connected through a mobile coupling [5]. The connection must assure that the torque is transmitted between the two shafts but also that the reduced load on shafts end is only radial forces and not bending.

Both bearing boxes are radial loaded with force F positioned as in the chain transmission tensioning situation. The load is applied through the tensioning system of the testing rig and a rigid element, mounted between the sliding carriage and the upper bearing box. The constructive solution gives the possibility of adjustment of the coaxially position of the two shafts. With this device, the measurement of bearing friction is performed in the same conditions of running as in the case of testing the chain drive. The same tensioning device, lubrication and drive systems and their instruments of measurement are used (see Fig. 1.).

The testing procedure and preparation of the rig are presented in detail in [6].

The testing program is consisted in steps of constant controlled parameters (rotational speed, tensioning force and oil temperature). The first step is usually longer since it must check and adjust the oil temperature and also stabilize the temperature distribution on all the elements of the rig. The time for each step is minimum 250 seconds. The role of these steps is to stabilize the system and create the steady state conditions where the measurements are made. There is a general trend of stabilizing by decreasing the value of the friction torque in time. This stabilizing is faster for lower speeds.

The readings that count in evaluation of bearing friction are only the one of the steady state period. In this experimental research the measurements of friction torque considered in steady state is an average of the last quarter of each step of constant rotational speed.

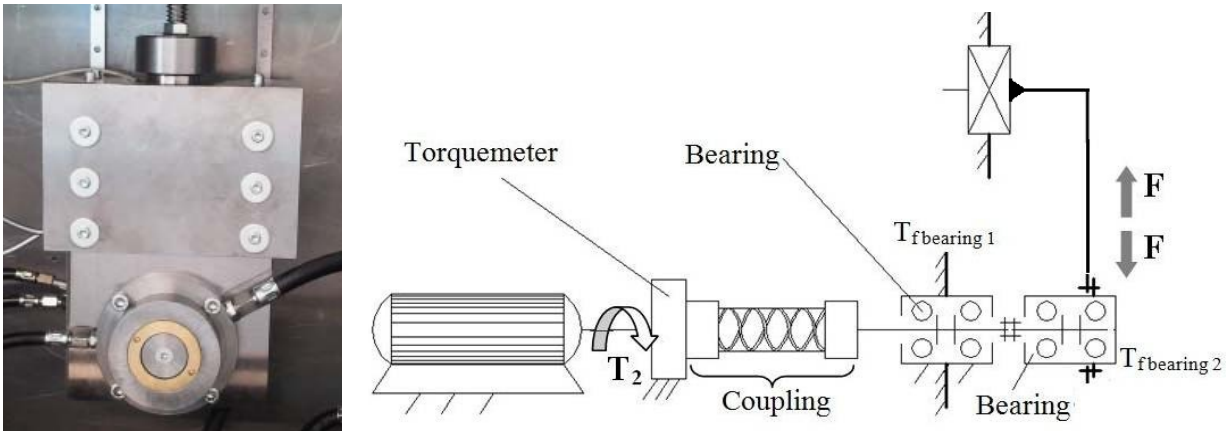

a b

Fig. 4. Bearing friction measurement device: a) front view; b) functional diagram

Bearing friction torque (T_b) has been measured for:

- Rotational speed, n: 500, 1000 1800, 3000, 5000 rpm;
- Tensioning force, F: 0.5, 1, 2, 3 kN;
- Oil temperature for bearings lubrication, t: 35, 50, 60 °C.

The tests have been repeated 3 times and an average of the results has been considered.

The oil used in bearing lubrication is Castrol Edge 5W30 and the measured viscosity depending on temperature is presented in Fig. 5.

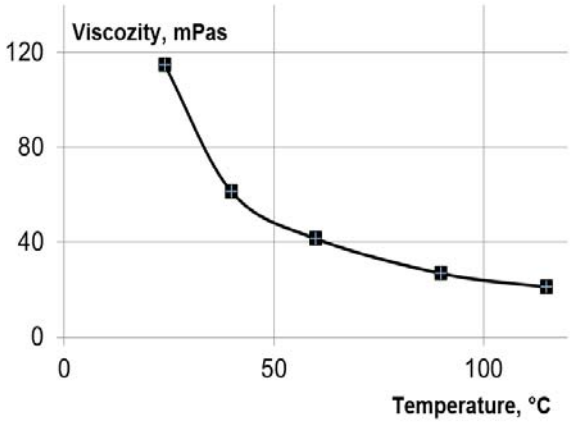

Fig. 5. Viscosity versus temperature

4. EXPERIMENTAL RESULTS

Figure 6 presents the diagrams for bearing boxes friction torque depending on rotational speed and tensioning force, for three steps of temperature for lubricating oil.

Figure 7 presents the diagrams for bearing boxes friction torque depending on oil temperature and tensioning force, for four steps of rotational speed.

Figure 8 presents the diagrams for bearing boxes friction torque depending on tensioning force and oil temperature, for four steps of rotational speed.

Figure 9 presents the diagrams for bearing boxes friction torque depending on oil temperature and rotational speed for four steps of tensioning force.

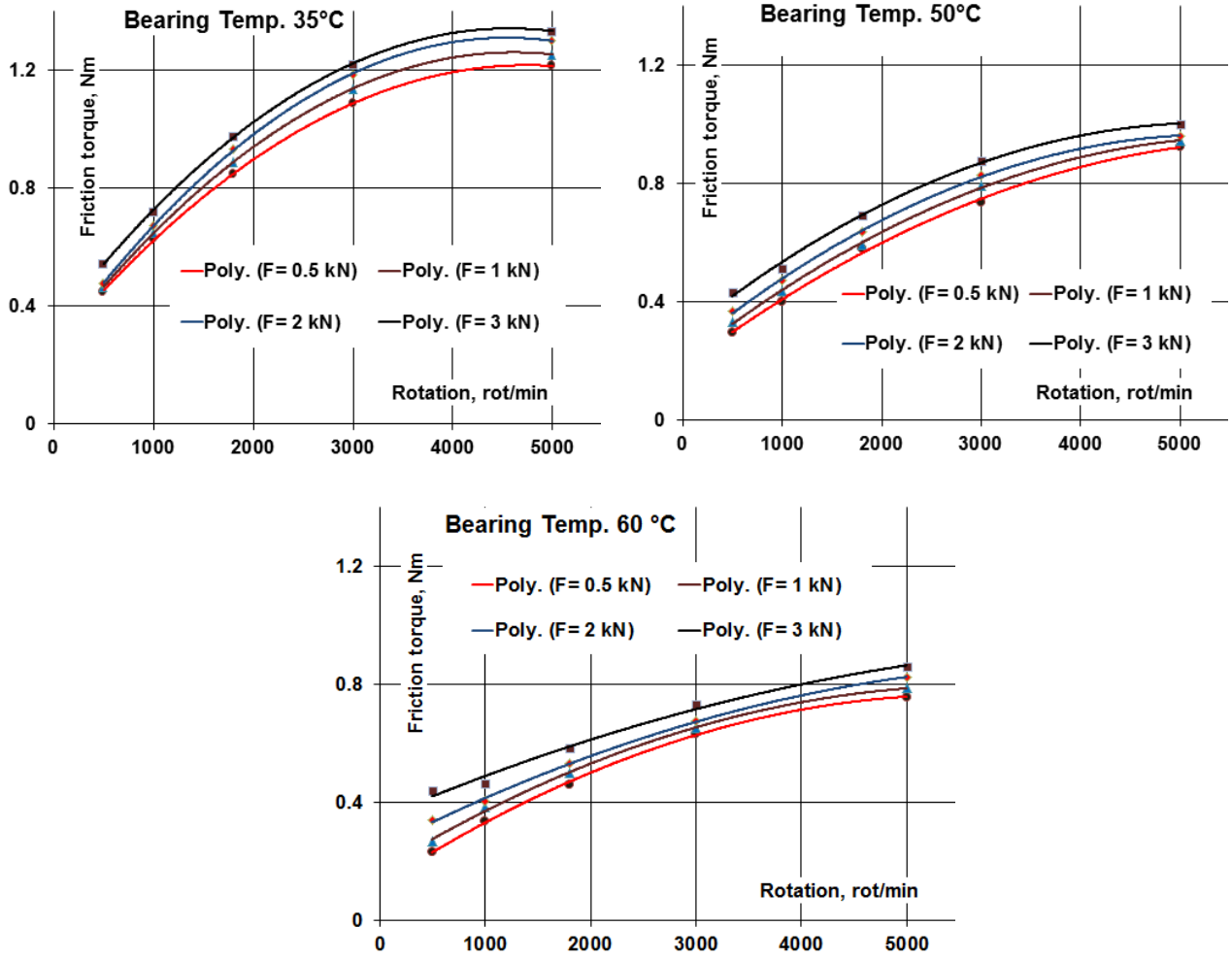

Fig. 6. T_b (n, F)

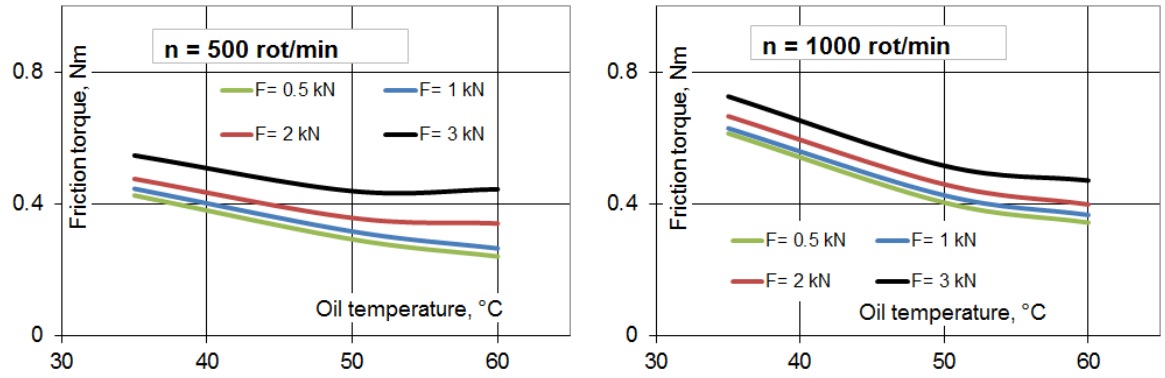

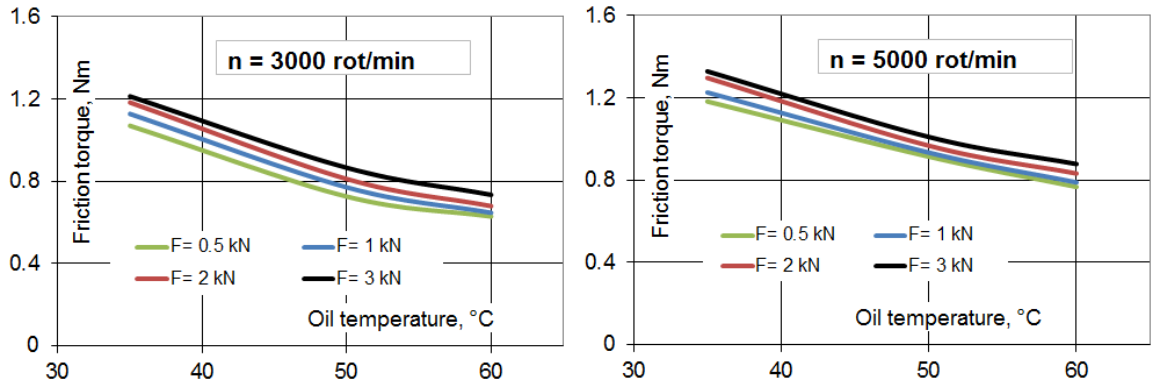

Fig. 7. T_b (t, F)

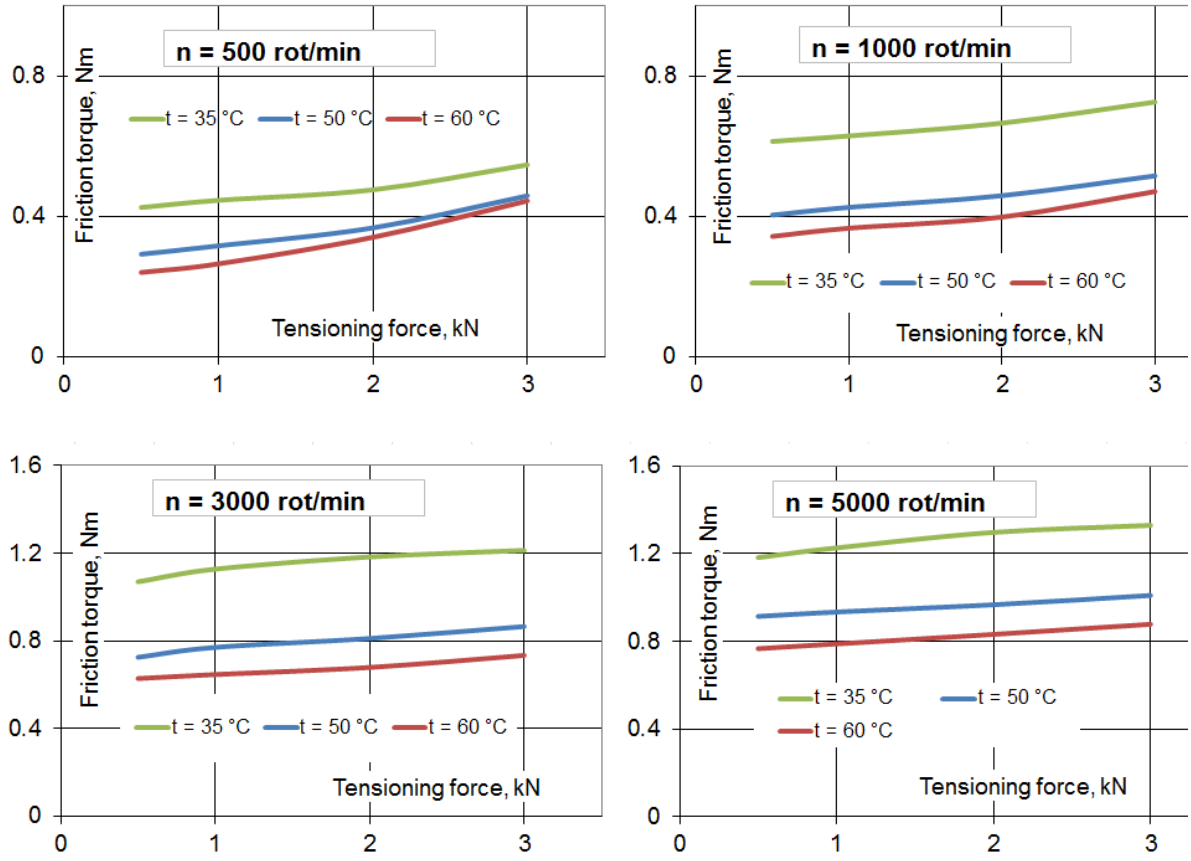

Fig. 8. T_b (F, t)

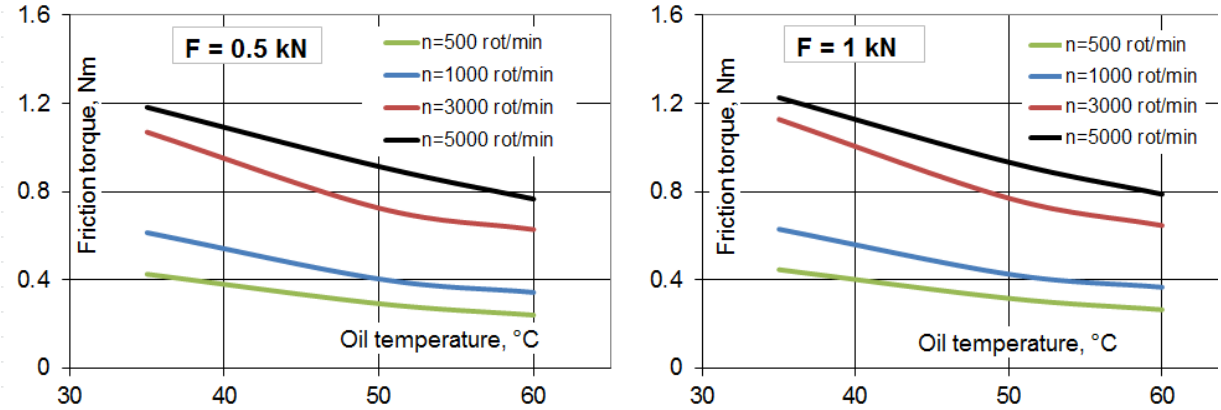

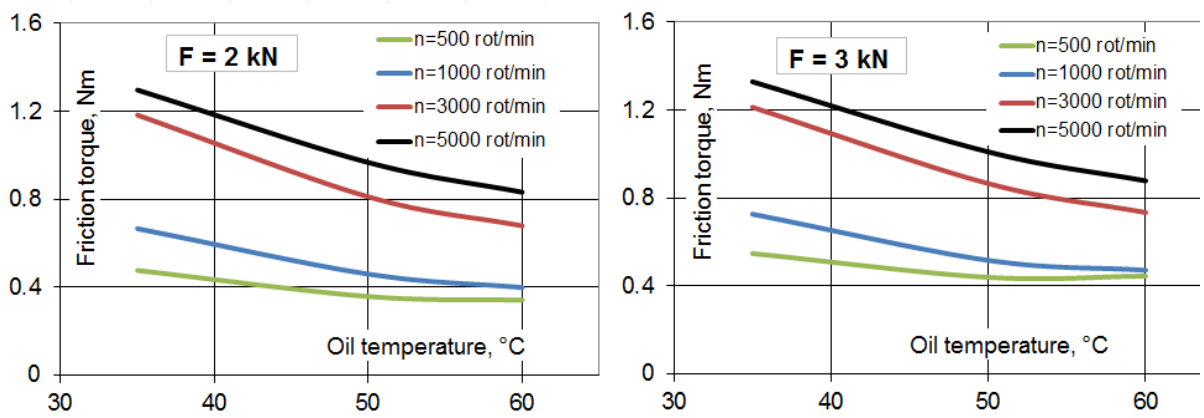

Fig. 9. T_b (t, n)

5. CONCLUSION

The results show the increase of bearing friction with rotational speed and load and also with decrease of oil temperature (increase of viscosity). The trends are according to the theoretical models from [3], analysed in [4].

There are some trends that have to be pointed as influences on bearing friction torque:

- Load influence (see Fig. 7): a 6 times increase of the load (0.5 to 3 kN) only generates an increase with 20-40% of the friction torque, the bigger influence is in the case of low rotation and higher oil temperatures (low viscosity);
- Speed influence (see Fig. 6 and Fig. 9): a 10 times increase of the rotational speed (500 to 5000 rot/min) generates an approx. 3 times increase of the friction torque. Speed influence is bigger for lower speed than for higher speed (convex shape of the T_b (n) curves – Fig. 6); Speed influence is bigger for temperatures between 35 and 50°C (higher viscosity) than for temperatures between 50 and 60°C (lower viscosity) – Fig. 7; The curves T_b (n) – Fig. 6 tend to be linear in case of high loads and high temperatures (low viscosity);
- Temperature influence: (see Fig. 8): an increase of temperature from 35 to 60°C (3 times decrease of viscosity) generates a maximum 50% decrease of the friction torque; The influence is smaller in the case of high loads and small rotational speed.

Since these bearing boxes are used for long periods of testing (around 1000 hours at this moment), next aspect that will be studied is the running time influence on friction losses.

REFERENCES

1. HYAKUTAKE T., INAGAKI M., MATSUDA M., HAKAMADA N., TERAMACHI Y., Measurement of friction in timing chain, JSAE Review 22:5, 2001.
2. TODI-EFTIMIE, A.L., VELICU, R., SAULESCU, R., JALIU, C., Bearing friction vs. chain friction for chain drives, Advanced Materials Research, Vol.753-755, 2013, 1110–1113.
3. INA FAG Walzlager, Schaeffler Gruppe Industrie, 2006.
4. TODI-EFTIMIE, A., VELICU, R., BRANDS, C., SCHLEREGE, F., LATES, M., Friction in Bearings of Parallel Axes Transmissions, Applied Mechanics and Materials 658, 2014, 371-376.
5. GAVRILA, C. C., A Transversal Coupling 3D Modeling, Annals of the Oradea University, Fascicle of Management and Technological Engineering, vol. 12, (22) no. 1, 2013, 133–137.
6. VELICU, R., LATES, M., On the measurement procedure for testing friction in bearing boxes, Annals of the Oradea University, Fascicle of Management and Technological Engineering, vol. 14, (24), 2015, no. 1, 59–64.

CORRESPONDENCE

Prof.dr.ing. Radu VELICU
Transilvania University of Brasov, Department of Product Design Mechatronics and Environment, Eroilor 29, 500036 Brasov, Romania
e-mail: rvelicu@unitbv.ro

Tribological Journal BULTRIB Vol. 5, 2015
Papers from the International Conference **BULTRIB '15**
September 11-13, 2015, Sozopol, Bulgaria
Society of Bulgarian Tribologists
FIT – Technical University of Sofia

EFFICIENCY ANALYSIS OF LIQUID PISTON ENGINE SYSTEM

Ranjeet Rana, Aman Gupta, Sunny Narayan

Abstract: *Stirling engines have several advantages as compared with conventional internal combustion engines. However poor heat transfer rate and sealing problems due to high pressure of gases are major issues . Liquid piston engines have been proposed as an alternative solution to these engines. The irregular shape of piston volume helps in better heat transfer thus helping in isothermal operation and eliminating need for external heat exchangers. Cooling of compression side of engine helps to improve thermal efficiency of engine. Stirling engine pumps need further research as they have potential application in various tasks.*

Key Words: Heat engines, Liquid piston fluidynes

1. INTRODUCTION

There are several power supply machines which are important sources of power .These include internal combustion engine driven by a hydraulic pump. How ever these machines include complex operations of kinematic connections ,piston pump, engine valves, piston connecting rod, crankshaft and cylinder block. All these operations are complexity and expensive and also result in energy losses. Previous works have studied use of free-piston internal combustion engines[1–3]. Other works include monopropellant driven free-piston hydraulic pumps [4].

Most commonly used engines use spark and the diesel engines cycle both having efficiencies of 35% and 40%, respectively [5]. The short combustion. An alternative is use of the Stirling engine which have higher efficiency than that of the Carnot cycle. This engine consists of following four phases: isothermal expansion, isochoric cooling, isothermal compression, and isochoric heating. The Stirling cycle engine has several advantages over other cycles. Continuous combustion of wide range of fuel is reason for higher efficiency and lesser emissions as comparison to conventional engines. Solar energy can also be used to operate this machine with high efficiency of 31% [6].Work at NASA has resulted in a hydraulic output free-piston Stirling engine [7,8].Another design of Stirling engine pump has been shown in [9–11]. Here a U shaped wobbling fluid column was used to pump water working on basis of pressure oscillations in fluid column. Stirling engines have many drawbacks due to lesser power and efficiency. Sealing of hydrogen and helium at high pressure is a big challenge[12].

2. EXPERIMENTAL SETUP

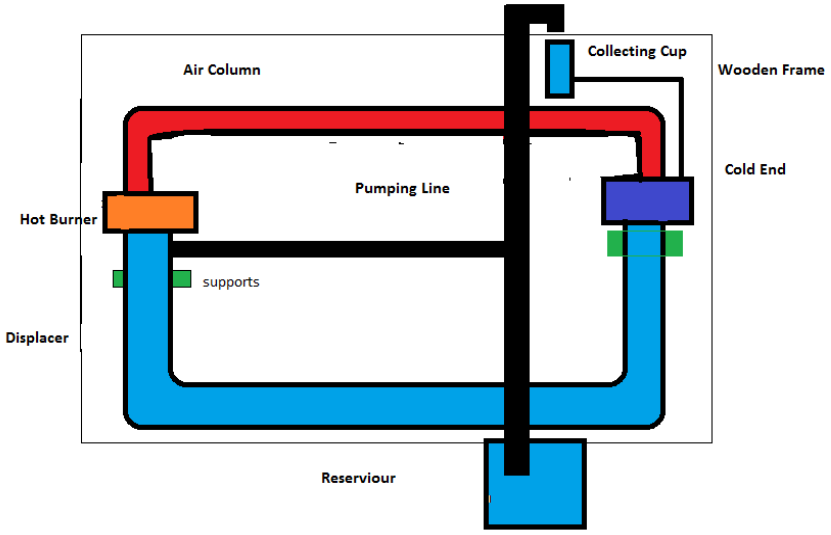

Figure 1: Layout of set up

A liquid piston system was designed as shown in figure no1.Various important parts of system are as following:

1) Displacer Piston-Plastic tube is ideal for this case being cheap and readily available.
2) Wooden base for support and robustness.
3) Fuel -methylated spirit and cotton for use in burner due to ease of use.
4) Choice of material for pumping line, burner, air column, cold end: Copper and Brass were the choices available. Thermal conductivity of copper is 401W/m K, whereas for Brass it is 109W/m K Using copper can cause more heat losses to the ambient atmosphere. Also Copper is more prone to corrosion. Brass is an alloy of copper and zinc having better corrosion resistance than Copper. Hence it is more suitable for use. The system consists of following major parts:

a) Plastic tube for displacer column of radius pipe 0.63cm and length 30cm.It Consists of a hot chamber and a cold chamber.
b) Pumping Column- Brass column of radius 0.39cm and height 15cm.
c) Burner for providing the heat.
d) Collecting cup.
e) Connecting arm of length 6 cm and diameter 3mm.
f) Air column of 5 mm diameter and length 18cm.
g) Supporting wooden base.
h) Two balls of mild steel of diameter 5mm which act as one way valves.
i) Brass couple at cold end holding the collecting cup, other end of air column and water returning tube.
j) Plastic supports at hot and cold ends.
k) 2 Hose clips for effective sealing at hot and cold ends.

3. RESULTS AND DISCUSSIONS

Variations in Pressure and temperature of air column with time were recorded with thermocouple and manometer as depicted in figure no 2.

Figure 2 : Experimental setup for finding pressure and temperature

Table 1: Variation of pressure and temperature of air with time

Reading in mm of Hg	Pressure in Bar	Temperature (K)	Time in seconds
730	0.96	296	0
988	1.3	298	300
912	1.2	300	320
1216	1.6	305	340
912	1.2	306	360
1368	1.8	308	380
760	1	310	400
1444	1.9	311	420
745	0.98	312	440

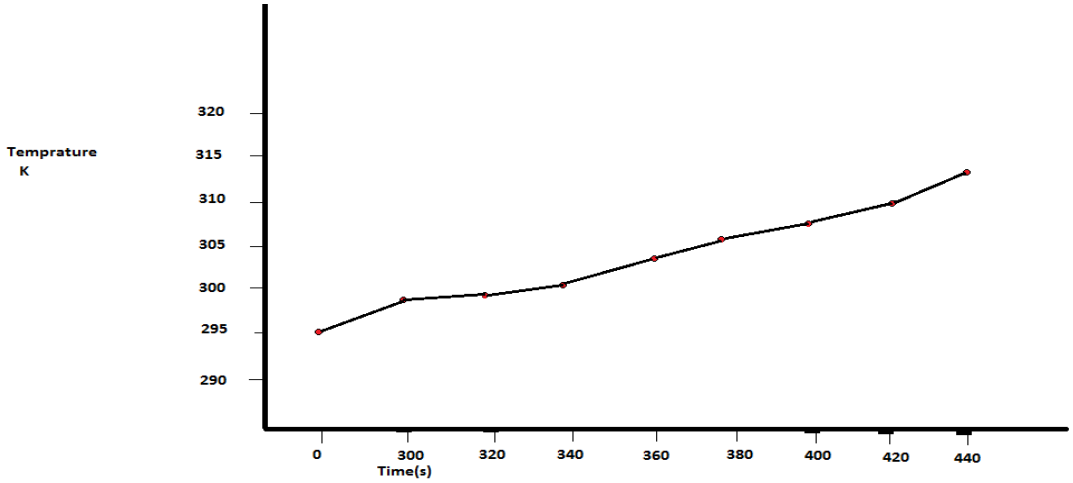

Figure 3: Variation of temperature with time

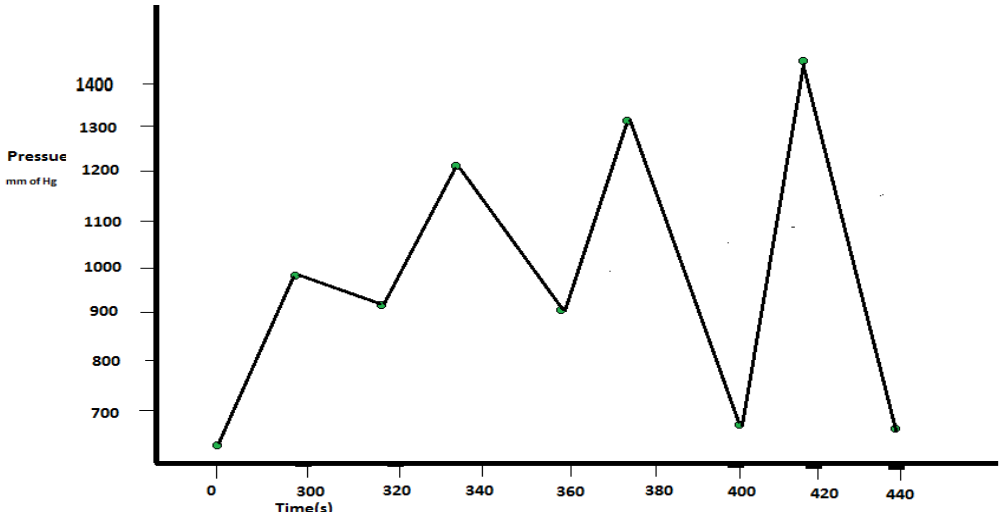

Figure 4: Variation of pressure with time

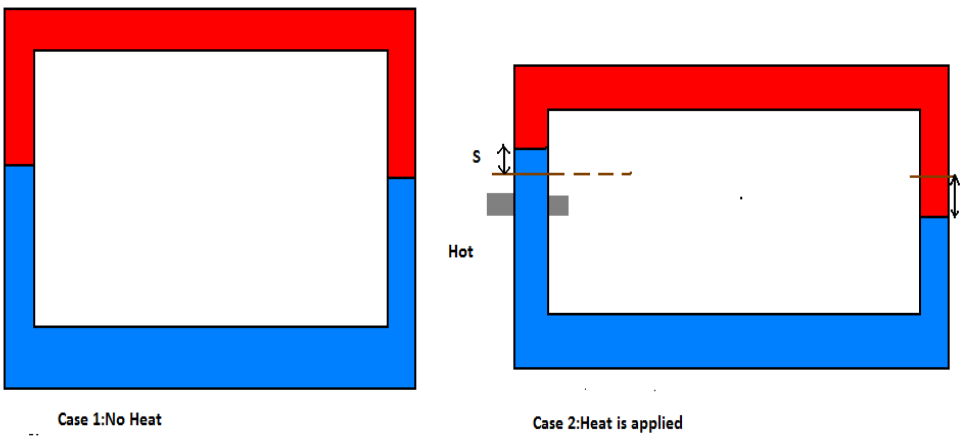

Figure 5: Calculation of length of stroke

Calculation of stroke of water column was difficult due to quick oscillations, however it was theoretically found using ideal gas laws and observing temperature and pressure at certain time intervals using manometer, stop watch and thermocouple.
According to gas law-

$$\frac{P_1V_1}{T_1} = \frac{P_2V_2}{T_2}$$

$$Vd = V_1 - V_2 = 2(\pi \frac{D^2 S}{4})$$

Where S is length of stroke

Table 2: Variation of stroke length with time

P_1 mm of Hg	V_1 (Cm^3)	T_1(K)	P_2 mm of Hg	T_2(K)	V_2 (Cm^3)	V_1-V_2 (Cm^3)	S(cm) In cm	Time (s) sec
733	22.6	296	988	298	16.8	5.8	2.56	300
988	16.8	298	912	300	18.32	1.52	0.67	320
912	18.32	300	1216	305	13.96	4.36	1.9	340
1216	13.96	305	912	306	18.68	4.72	2.085	360
912	18.68	306	1368	308	12.53	6.15	2.7	380
1368	12.53	308	760	310	22.7	10.17	4.5	400
760	22.7	310	1444	311	11.99	10.71	4.7	420
1444	11.99	311	745	312	23.31	11.32	4.98	440

Power output (W), can be expressed in terms of product of Beals number(B_n),displaced volume(V_t), and Pressure(P), as-

$W = B_n X P_f X V_t$

$$= 0.015 \times 1.57 \times Vt \times P$$

$$= 0.023 \times Vt \times P$$

Table 3: Variation of efficiency of pumping column with time.

Pressure (Bar)	V_d (cm^3)	V_t (cm^3)	Power (W)	η of pump	Time in seconds
0.96	5.8	8.2	0.185	6.4%	300
1.3	1.52	2.14	0.069	2.2%	320
1.6	4.36	6.16	0.22	5.4%	340
1.8	4.72	6.6	0.27	4.3%	360
1.9	6.15	8.69	0.37	3.15%	380
1.7	10.17	14.38	0.56	2.13%	400
1.2	10.71	15.14	0.41	2.8%	420

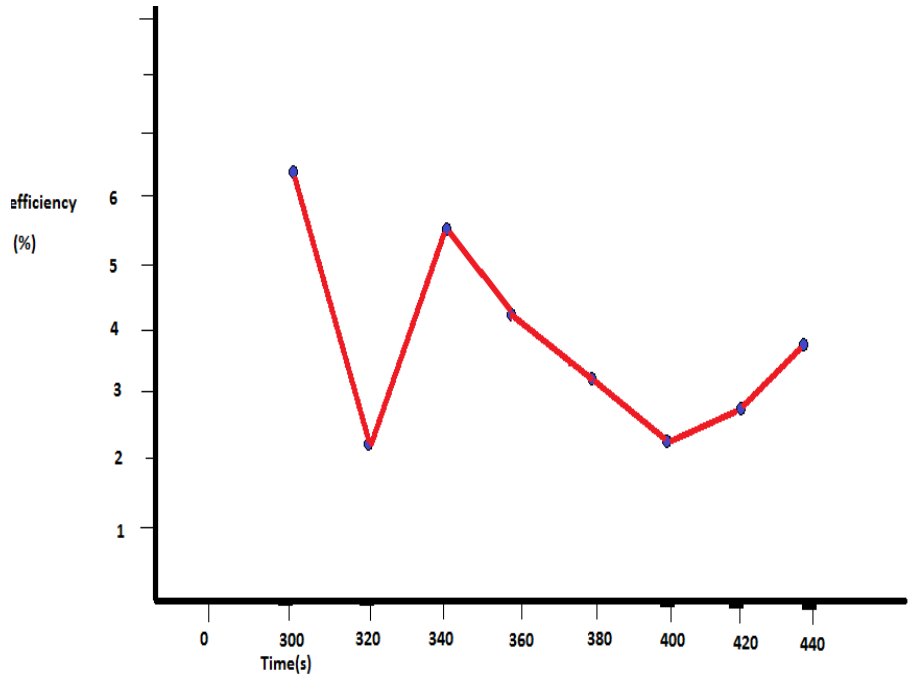

Figure 6 : Variation of efficiency of pumping column with time

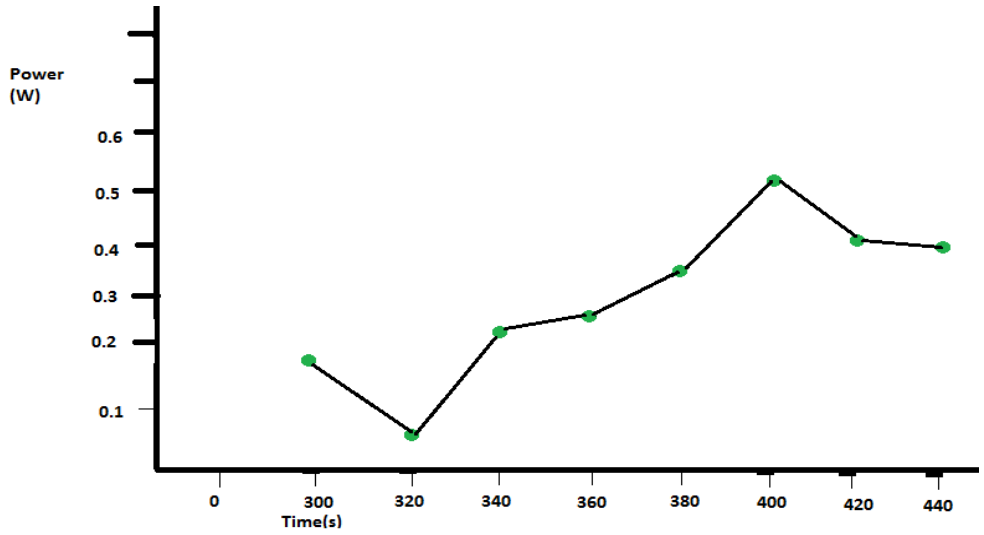

Figure 7: Variation of power output with time

4.CONCLUSION

The efficiency of device was found to be in order of 2-6% which is very low due to various poor heat transfer ,leakage ,viscous and frictional losses.

REFERENCES

1. Beachley NH, Fronczak FJ. Design of a free-piston engine-pump, International off-highway and power-plant congress and exposition, SAE, Milwaukee, WI;1992, p. 921740.
2. Hibi A, Ito T. Fundamental test results of a hydraulic free piston internal combustion engine. Journal of Automobile Engineering 2004;218(10):1149–57.
3. Tikkanen S, Vilenius M. Control of dual hydraulic free piston engine. International Journal of Vehicle Autonomous Systems 2006;4(1):3–23.
4. McGee TG, Raade JW, Kazerooni H. Monopropellant-driven free piston hydraulic pump for mobile robotic systems. Journal of Dynamic Systems, Measurement and Control 2004;126(1):75–81.
5. Heywood JB. Internal combustion engine fundamentals. New York: McGraw-Hill, Inc.; 1988.

6. Washom B. Parabolic dish Stirling module development and test results, Intersociety Energy Conversion Engineering Conference, American Nuclear Society, vol 3, San Francisco, CA; 1984, pp. 1686–94.
7. Schreiber JG, Geng SM. Re-1000 free-piston Stirling engine hydraulic output system description, Intersociety Energy Conversion Engineering Conference, ACS, San Diego, CA; 1986, pp. 484–49.
8. Schreiber JG, Geng SM. Re-1000 free-piston Stirling engine hydraulic output system description. NASA Technical Memorandum 100185, Lewis Reseach Center, Cleveland, OH; 1987.
9. De Klerk GB, Rallis CJ. A solar powered, back-to-back, liquid piston Stirling engine for water pumping. Journal of Energy in Southern Africa 2002;13(2):36–42.
10. Kluppel RP, Gurgel JM. Thermodynamic cycle of a liquid piston pump. Renewable Energy 1998;13(2):261–8.
11. West CD. Liquid piston Stirling engines. NewYork: Van Nostrand Reinhold; 1983.
12. Conde R, Faroughy D. Fluidic-piston engine.United States Patent 6,568,169; 2003.

CORRESPONDENCE

Sunny Narayan, Assistant professor, Indus International University
Address -VPO Bathu, Una, Himachal Pradesh,India-174301
e-mail:rarekv@gmail.com

Tribological Journal BULTRIB Vol. 5, 2015
Papers from the International Conference **BULTRIB '15**
September 11-13, 2015, Sozopol, Bulgaria
Society of Bulgarian Tribologists
FIT – Technical University of Sofia

REVIEW OF STIRLING ENGINE SYSTEM

Ranjeet Rana, Aman Gupta, Sunny Narayan

Abstract: *A model for working of striling engines has been analysed considering effects of regenerator system. The working fluid motion in a liquid piston engine which is a practical form striling engine has been analysed and scope of future improvement in current engine design has been discussed.*

Key Words: Heat engines ,Liquid piston fluidynes

1. INTRODUCTION

In a Stirling engine the fluid is contained in a confined space, hence there are no problems of contamination. In order to reduce the heat losses, the mass flow rate must be low which can be maintained by low viscosity fluid or high working pressures. These engines are 30 to 40% efficient in a temperature range of 923K–1073 K[1].

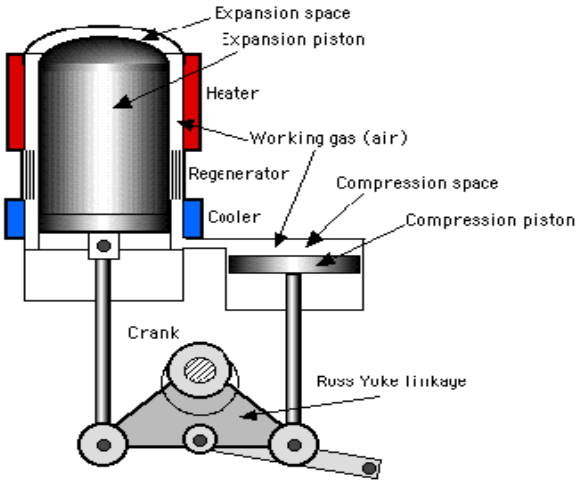

Figure 1: Stirling engine Model

A Stirling engine consists of following components as seen in figure no 1[2]:
1. **Heat source**-as fuel does not come in direct contact with the working fluid ,Stirling engines can work on fluids which may damage parts of a conventional engine.
2. **Regenerator**-the function of regenerator is to use the waste heat from being lost to environment by storing it temporarily, thus helping to achieve high efficiencies close to an ideal Carnot cycle. A simple configuration consists of fine mesh of metallic wires. In an ideal Stirling cycle, the connecting space between hot and cold ends acts as regenerator.
3. **Heat sink**-typically the ambient environment acts as an ideal heat sink, otherwise the cold side can be maintained by iced water or cold fluids like liquid nitrogen.
4. **Displacer piston**-it causes the displacement of working gas between hot and cold regions so that expansion and contraction occurs alternatively for operation of engine.
5. **Power piston**- transmits the pressure to crankshaft.

2. WORKING OF A STIRLING ENGINE

In a Stirling engine ,hot air expands when heated and contracts when cooled. This principle of operation was most properly understood by Irish scientist Robert Boyle from his results on experiments on air trapped in a J shaped glass tube. Boyle stated that pressure of a gas is inversely proportional to its volume and product of pressure and volume occupied is a constant depending on temperature of gas[3].

Hence PV=NRT

Various assumptions are made in this cycle are:
1) Working fluid is an ideal gas.
2) Conduction and flow resistance is negligible.
3) Frictional losses are neglected.
4) Iso-thermal expansion and contraction.

This cycle can be described by following stages from figure no 2[4]:
1) Phase C-D: Iso thermal expansion-the working fluid undergoes an iso-thermal expansion absorbing the heat from source. The power piston moves out, hence increasing the volume and reducing the pressure. The work done in expansion of gas is given by:

$$We = RTln\left[\frac{V_D}{V_C}\right] = \int pdv = nR\ Tc\ ln\left[\frac{V_D}{V_C}\right] \quad \textbf{- 1}$$

2) Phase D-A: Power piston now reaches the outermost position and stays there so that volume is constant. The working fluid is passed through the regenerator where it gives up heat for use in next cycle. Hence its temperature and pressure falls. No work is done during this phase.

3) Phase A-B: The power piston stats moving inwards, reducing its volume and increasing its pressure the working fluid gives up heat to cold sink. The work done in compressing the gas is given by:

$$Wc = RTln\left[\frac{V_B}{V_A}\right] = \int pdv = nRTh\ ln\left[\frac{V_B}{V_A}\right] \quad \textbf{-2}$$

4) Phase 2-3: The power piston is at its most inwards point and stays there to keep volume constant. Working fluid passes again through the regenerator, recovering the heat lost in 2nd phase, hence its pressure and temperature goes up.

$$Wnet = We - Wc$$
$$= nR[Th - Tc]\left[\frac{Vmax}{Vmin}\right] \quad \textbf{-3}$$

But

$$V_B = V_C \ \&\ V_A = V_D$$

$$efficiency\ of\ engine = \eta = \frac{Wnet}{Qe} = \frac{n\ R\ (Th - Tc)\ ln\left[\frac{Vmax}{Vmin}\right]}{n\ R\ Th\ \ ln\left[\frac{Vmax}{Vmin}\right]}$$

$$\eta = \frac{Th - Tc}{Th} \quad \textbf{-4}$$

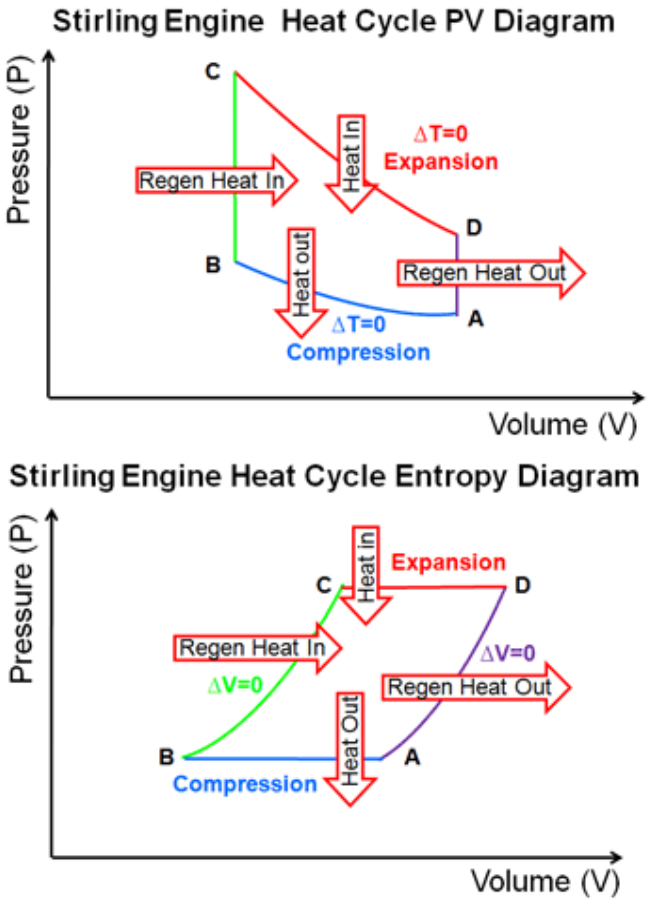

Figure 2: P-V & T-S plot of a Stirling cycle

In Stirling cycle, two Isochoric processes replace the two Iso-entropic processes s in an ideal Carnot cycle[5].Hence more work is available than a Carnot cycle as net area under P-V curve is more. Thus there is no need for high pressures or swept volumes. This can be seen in the figure no 3 presented below.

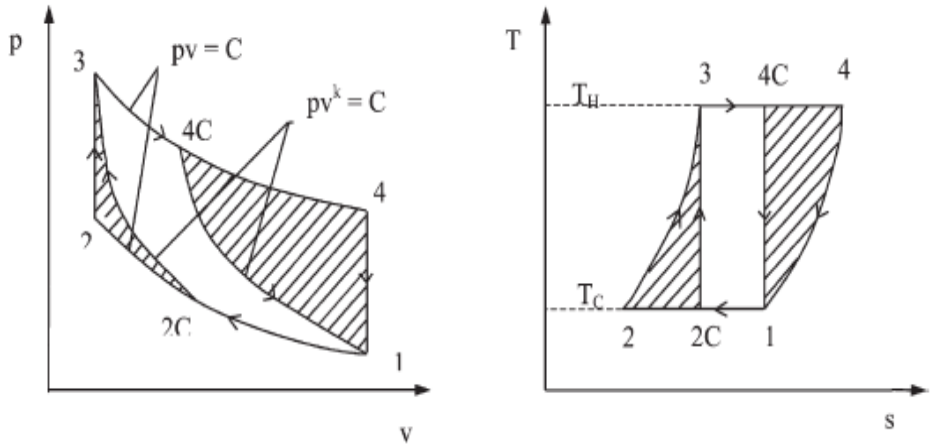

Figure 3: Comparison of Stirling cycle and Carnot cycle

3. LIQUID PISTON STIRLING ENGINE

The basic principle of a fluidyne is similar to a Stirling engine. A gas when heated expands and if its expansion is confined, its temperature rises. This can be understood more easily by following operations[2]:

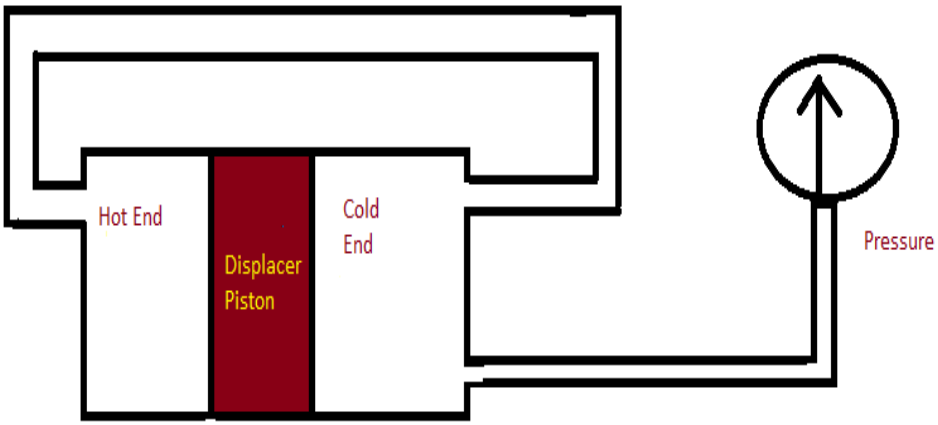

Figure 4: Motion of a displacer piston in cylinder

Initially the displacer piston is at centre, with half of the gas in hot side and other half of gas in cold side of cylinder. The pressure gauge is neutral as depicted in figure no 4.

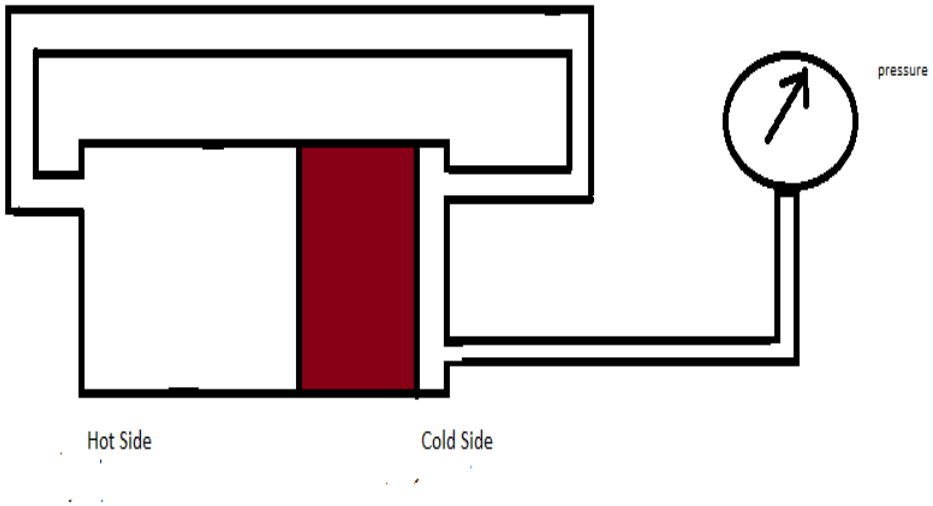

Figure 5: Motion of displacer piston towards cold side

As the displacer piston moves towards the cold end ,the gas is displaced towards the hot end by the connecting tube, its temperature and hence pressure goes up as indicated by the gauge in figure no 5.

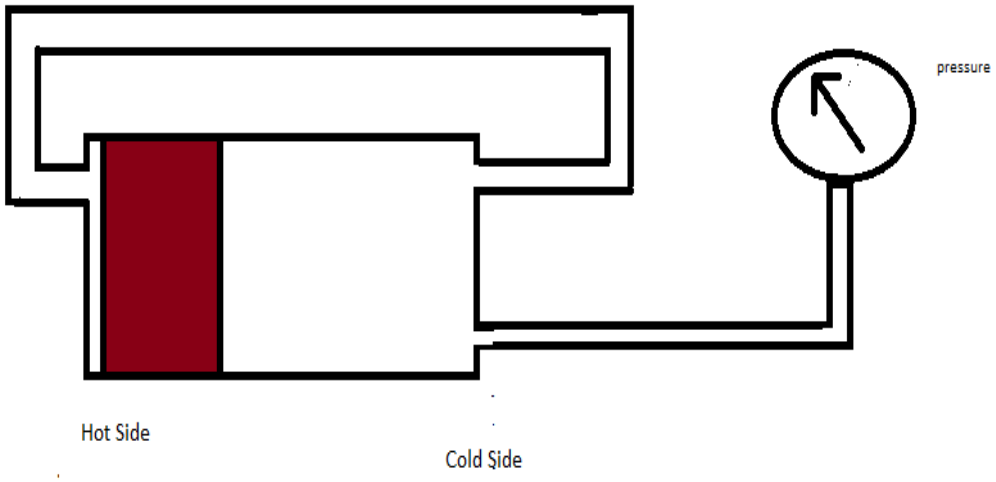

Figure6: Motion of displacer piston towards hot side

As the piston moves towards the hot side, the gas is displaced towards the cold end, its temperature and hence pressure falls as seen in figure no 6. The changes in the displacer pressure can be used to drive another piston known as the power piston. When the gas pressure is high, the power piston moves towards the open end of cylinder, hence doing some work which can be used to pump water or rotate a crankshaft.

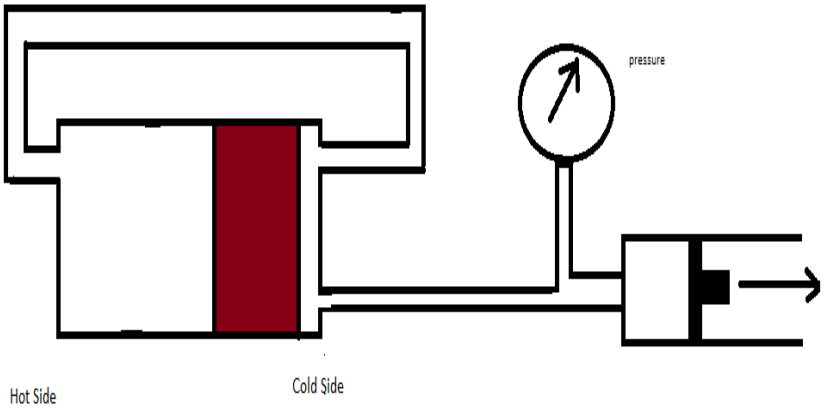

Figure 7: Motion of displacer piston and power piston

But when the gas pressure is low, the power piston returns towards its original position for which work is needed which is lesser than the work available from the previous stroke as lesser force is acting on the piston due to low gas pressure. Hence there is an excess of energy that can be used for pumping operation or other tasks.

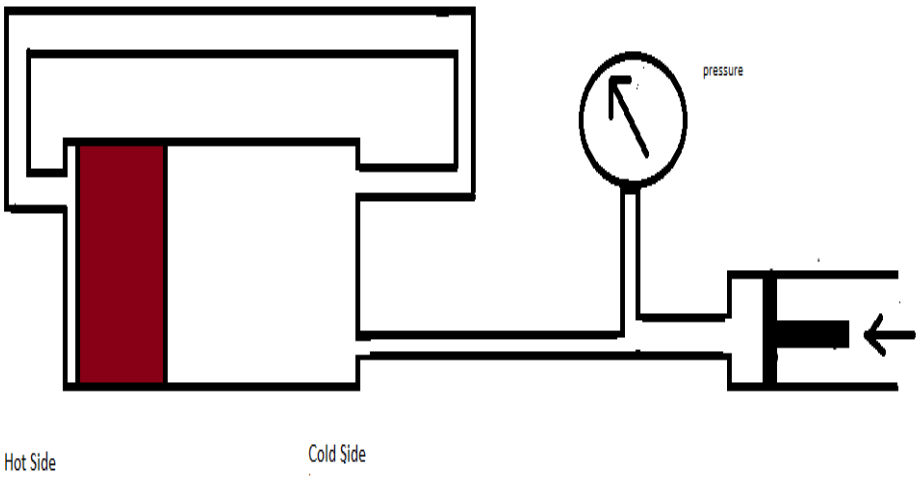

Figure 8: Motion of displacer piston and power piston

By clever and innovative engineering, some of the power available from the power piston can be used to drive the displacer piston, and so to create a variable pressure heat engine.

4. ROLE OF REGENERATOR

Though this does not constitute a mandatory part of engine, use of regenerator is beneficial .With the use of regenerator, there is a steady state fall in temperature as the gas gives up heat to the regenerator .Hence by the time the gas goes into the cold chamber it has already been cooled .as the gas moves into hot chamber ,it picks up the heat from regenerator ,thus the regenerator acts as a buffer of heat and increases the efficiency of cycle. There are several ways to design this heat exchanger. one of the common ways is to increase the heat exchanging are keeping the resistance to flow minimum. This material of regenerator can be honey comb, wire meshes or metallic strips made of high capacity heat absorbing materials.

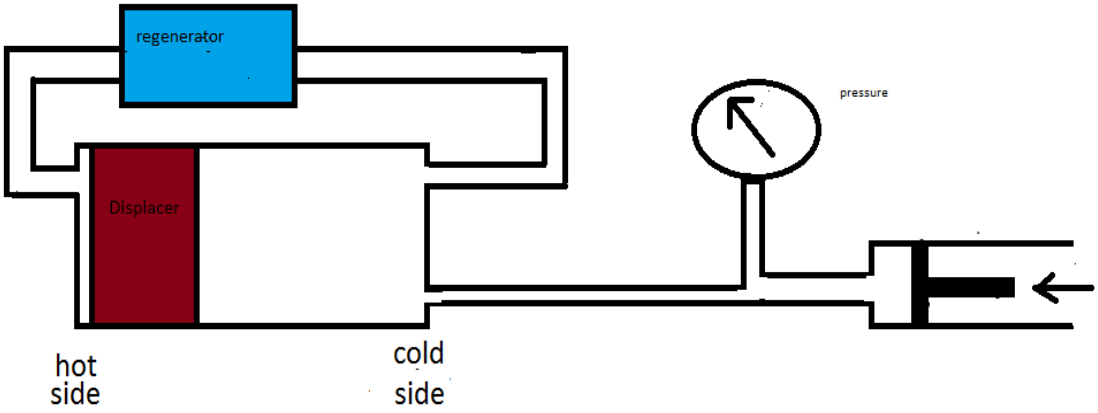

Figure 9: Regenerator

The action of a regenerator and properties of some materials suitable for use in regenerator can be seen in figure no 9,10.

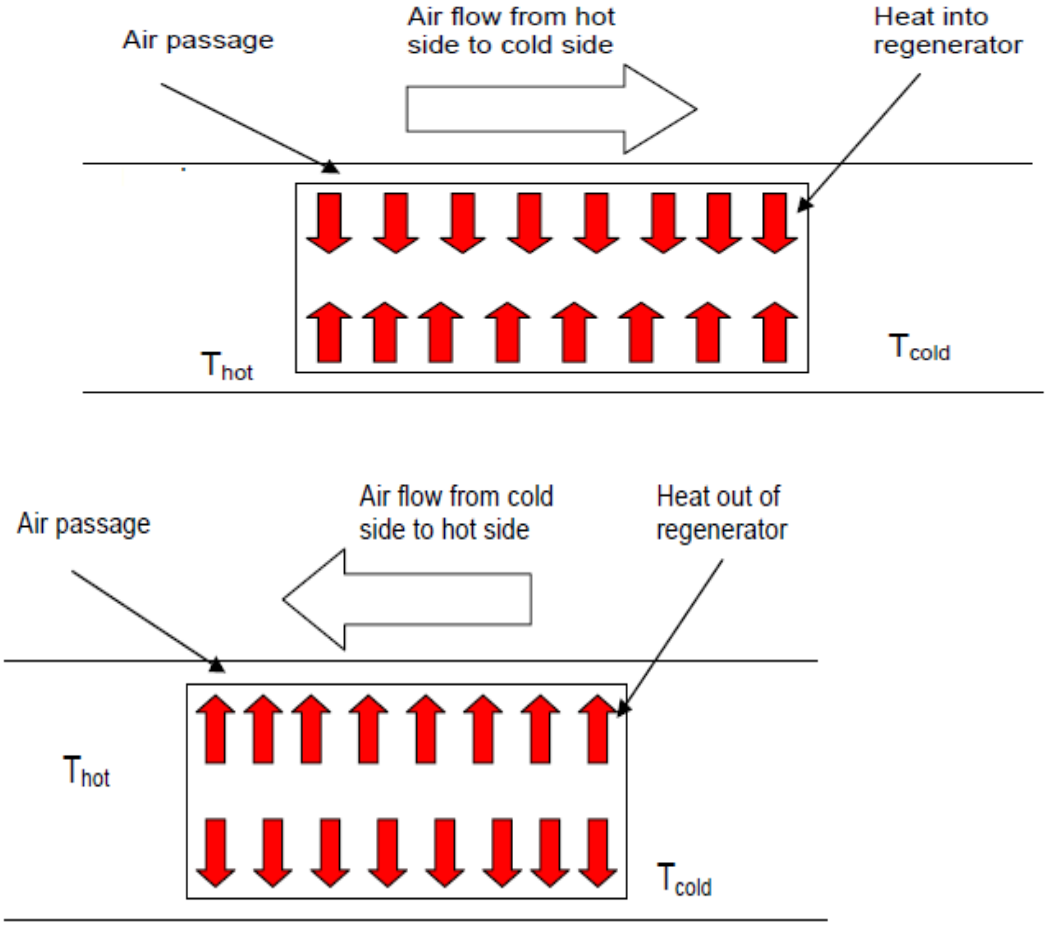

Figure 10:Regenerator Action

5. CONCLUSION

This work considers the effects of regenerator on a liquid piston engine. To increase the engine efficiency some of following improvements can be made in the current design[6-9]:

1) Use of bigger diameter displacer tubes-it ensures the greater amount of air flowing between cold and hot side. This can lead to larger amplitude of oscillations due to higher pressure, but smaller compression ratio whereas smaller tubing results in a larger compression ratio.

2) Use of regenerator
The regenerator acts as a thermal sink, releasing and absorbing heat at various stages hence increasing the efficiency of engine. Most common method of heat storage is to obstruct the flow of working fluid by use of metallic mesh, porous material, array of tubes, but this may cause flow losses.

3)Better heat exchange-in order to enhance the heat exchange at the hot end, resistance heating can be used instead of burning fuel along with fins for greater heat transfer

REFERENCES

1. http://www.engin.swarthmore.edu/academics/courses/e90/2005_6/e90reports/fk_ao_final.pdf
2. C. D. West, Liquid Piston Engines, Van Nostrand Reinhold, New York, 1983.
3. Watanabe, H., Fujisawa, Y, Yoshida, M., Moriya, S. et al., "A study on temperature distribution of stirling engine regenerator," SAE technical paper 1999-01-2506, 1999, doi:10.4271/1999-01-2506.
4. Smook, W. and Naude, A., "Using a Stirling Engine Simulation Program as a Regenerator Design Aid," SAE Technical Paper 950097, 1995, doi:10.4271/950097.
5. Chan., Kaviany.,Evaporation-Combustion Affected by In-Cylinder, Reciprocating Porous Regenerator ,*J. Heat Transfer* 124(1), 184-194 (May 20, 2001) (11 pages)doi:10.1115/1.1418368.
6. Patton, R. and Bennett, G., "High Efficiency Internal Combustion Stirling Engine Development," SAE Technical Paper 2011-01-0410, 2011, doi:10.4271/2011-01-0410.
7. Ruiz, F., "Analysis of the 3rd Generation IC-Stirling Engine," SAE Technical Paper 2005-01-3462, 2005, doi:10.4271/2005-01-3462.
8. http://www.engin.swarthmore.edu/academics/courses/e90/2005_6/E90Reports/FK_AO_Final.pdf
9. Asnaghi et. al., Thermodynamic Performance Analysis of Solar Stirling Engine, 2 May 2012, REDEER center,Tehran, Iran.

CORRESPONDENCE

Sunny Narayan, Assistant professor, Indus International University
Address -VPO Bathu, Una, Himachal Pradesh,India-174301
e-mail:rarekv@gmail.com

Tribological Journal BULTRIB Vol. 5, 2015
Papers from the International Conference **BULTRIB '15**
September 11-13, 2015, Sozopol, Bulgaria
Society of Bulgarian Tribologists
FIT – Technical University of Sofia

DESIGN OF LIQUID PISTON ENGINE SYSTEM

Ranjeet Rana, Aman Gupta, Sunny Narayan

Abstract: *A working model of liquid piston fluidyne system has been designed in which water has been taken as a working fluid. Motion of liquid was analysed and future recommendations were made to improve the current design.*

Key Words: Heat engines ,Liquid piston fluidynes

4. INTRODUCTION

The basic principle of a fluidyne is similar to a Stirling engine [1]. A gas when heated expands and if its expansion is confined, its temperature rises[2,3,4]. This can be understood more easily by following operations as seen in figures 1-5:
a) **Stage 1**-initially levels of liquid in columns is equal when no heat is applied.

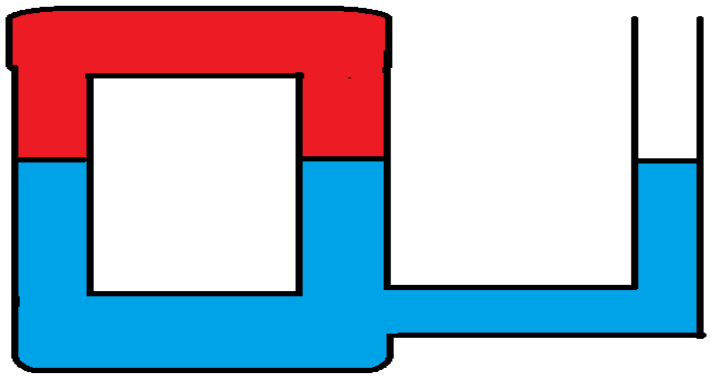

Figure 1: Stages of operation of a fluidyne

b) **Stage 2**- as heat is applied at the hot end, the air at that end is heated up and expands moving towards the cold end through the connecting arm. This pushes the fluid to TDC at the hot end and BDC at the cold end and the fluid out of the output column.

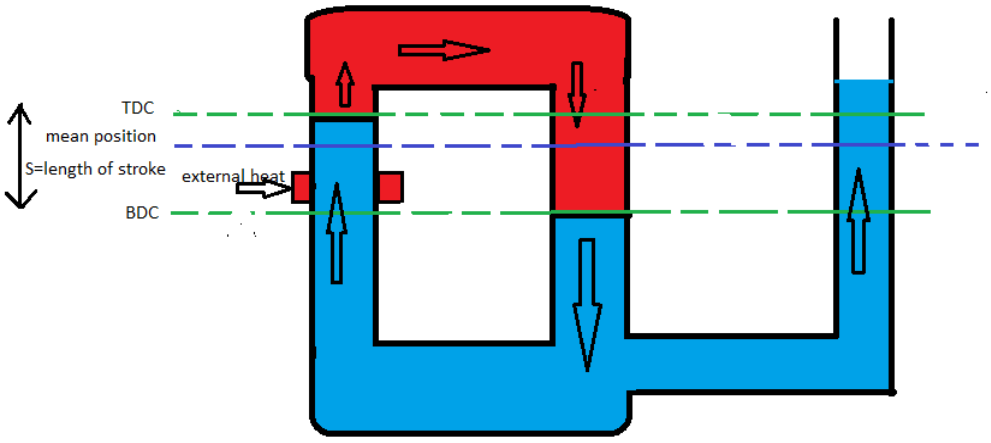

Figure 2: Stages of operation of a fluidyne

c) **Stage 3**-the air comes in contact with fluid at cold end, cools down and contracts. Once the fluid has reached its extreme positions at both columns of the U tube, at the hot side, the inertia of weight of extra risen fluid column tries to bring down the raised level of fluid to its mean position

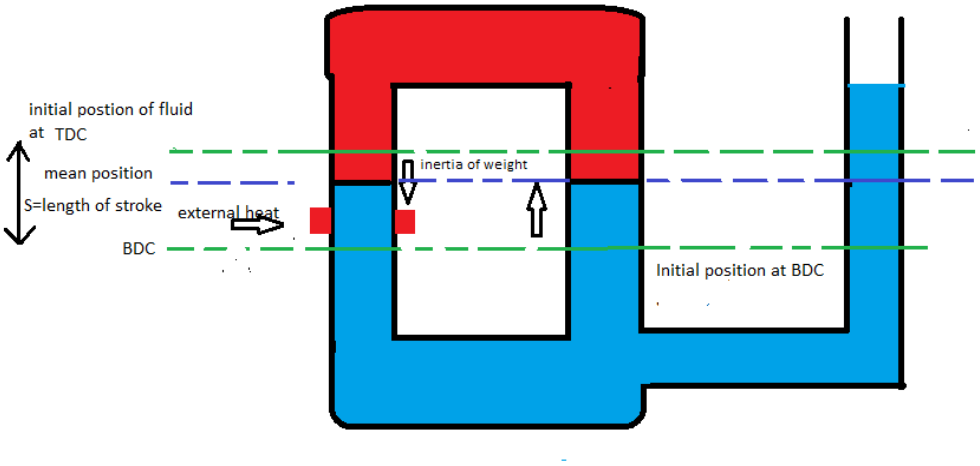

Figure 3: Stages of operation of a fluidyne

d) **Stage 4**-as this happens, the air is again transferred from cold end to hot end through the connecting space, so that level of fluid overshoots mean at hot side and reaches BDC whereas at cold end it reaches the TDC & the fluid is again sucked back in the output column.

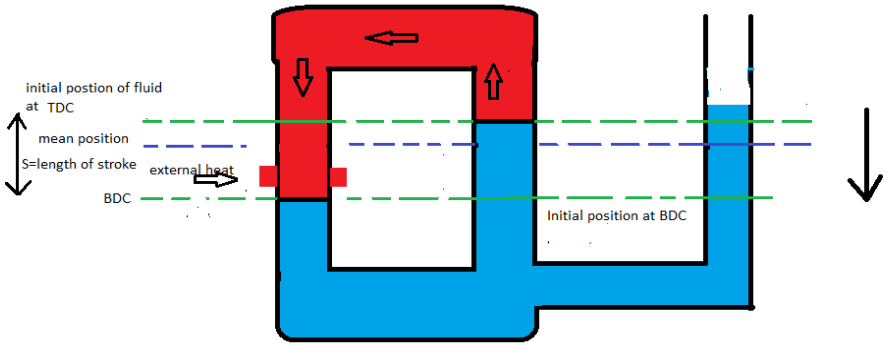

Figure 4: Stages of operation of a fluidyne

e) **Stage 5**-inertia of weight tries again to restore the levels of fluids equal at both ends, so that cycle starts again.

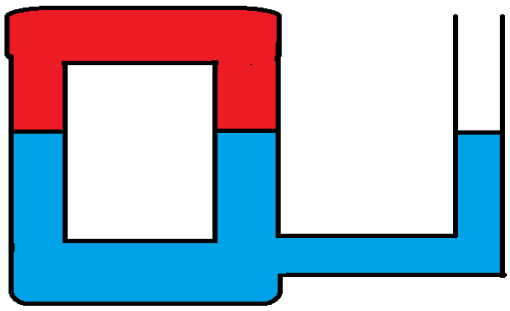

Figure 5: Stages of operation of a fluidyne

5. EXPERIMENTAL SETUP

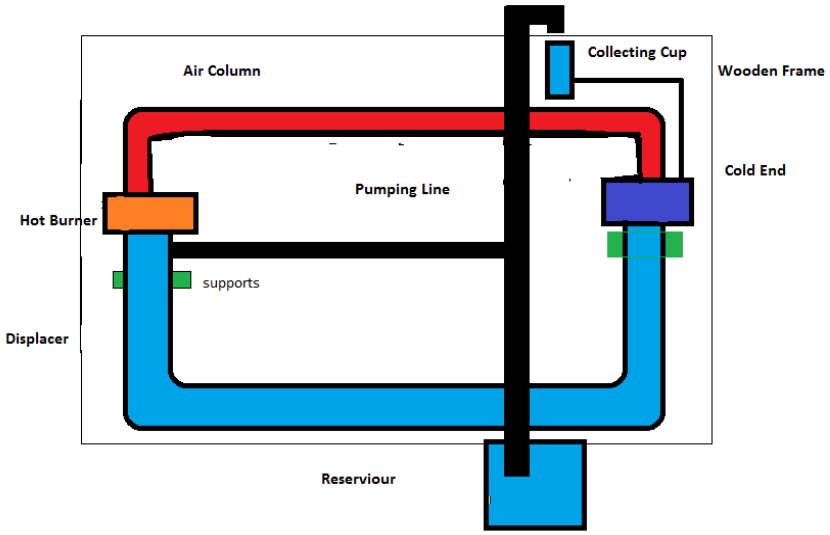

Figure 6: Layout of set up

In this section various factors taken into considerations while designing the set up have been discussed .An experimental setup was designed to analyze liquid piston fluidyne systems a seen in figure no 6.
The chosen design has following characteristics:
1) Easy to assemble.
2) Easy to transport due to small size.
3) Relative low cost.
4) Provision of cheap and ready to use fuel.

The tables shown in following sections give an idea about choice of various design ideas which were evaluated on basis of various parameters. Red color indicates the most preferred idea, yellow one represents a reasonable one whereas the green color denotes the most preferred choice.

The aim of this design was to pump water upto a certain height using liquid piston engine. Initially hair dryer was chosen as a source of heat with copper tubes and elbow joints as material for displacer.

Displacer Column Material	Cost	Availability	Ease of working
Glass			
Plastic			
Copper tube			

Heat source	Availability	Cost	Required Tempera-ture attained
Alcohol			
Hair dryer			

Other parts	Heat transfer	Corrosion rate
Copper		
Brass		
Plastic		

Table 1: Comparison of various design choices

Based on above criteria final selection was made for various design parameters as following:

1) Displacer Piston-material must be cheap and corrosion resistant and provide ease of assembly. Plastic tube is ideal for this case being cheap and readily available.
2) Wooden base for support and robustness.
3) Fuel -methylated spirit and cotton for use in burner due to ease of use.
4) Choice of material for pumping line, burner, air column, cold end: Copper and Brass were the choices available. Thermal conductivity of copper is 401W/m K, whereas for Brass it is 109W/m K Using copper can cause more heat losses to the ambient atmosphere. Also Copper is more prone to corrosion. Brass is an alloy of copper and zinc having better corrosion resistance than Copper. Hence it is more suitable for use. The designed system consists of following major parts:

a) Plastic tube for displacer column of radius pipe 0.63cm and length 30cm.It Consists of a hot chamber and a cold chamber.
b) Pumping Column- Brass column of radius 0.39cm and height 15cm.
c) Burner for providing the heat.
d) Collecting cup.
e) Connecting arm of length 6 cm and diameter 3mm.
f) Air column of 5 mm diameter and length 18cm.
g) Supporting wooden base.
h) Two balls of mild steel of diameter 5mm which act as one way valves.
i) Brass couple at cold end holding the collecting cup, other end of air column and water returning tube.
j) Plastic supports at hot and cold ends.
k) 2 Hose clips for effective sealing at hot and cold ends.

6. RESULTS AND DISCUSSIONS

Frequency of fluid oscillations is given by *f*

Hence

$$f = \frac{\frac{\sqrt{2g}}{l}}{2\pi} = 1.57\mathbf{Hz}$$

Time period=1/f=0.63sec

Pumping rate = $Q = A \times \sqrt{2\mathbf{gH}}$ =8.19cm^3/s =8.19×10^{-6}m^3/s

Power needed to pump water =ρ×*Q*×*g*×*H*
=1000 ×8.19×10^{-6}×9.8 ×0.15
=0.012 W

4.CONCLUSION

A proto type of liquid piston fluidyne engine was fabricated using common material available. Furthur variations of Temperature and pressures of air in the engine can be recorded using thermocouple and manometers which can be used to calculate stroke length of fluid. In order to reduce heat losses the connecting column can be covered with an insulation covering of poly tetra flouro ethylene tape. Further in order to improve the heat transfer rate, bigger connections can be used so that more mass of air is able to gain heat from the burning fuel.

REFERENCES

1. C.W. Stammers, The operation of the Fluidyne heat engine at low differential temperatures, *Journal of Sound and Vibration, Volume 63, Issue 4, 22 April 1979, Pages 507-516*
2. Jackson W. Mason, James W. Stevens,Characterization of a solar-powered fluidyne test bedSustainable Energy Technologies and Assessments, December 2014, Pages 1–8.
3. Yu, L., Fauvel, R., Reader, G., and Walker, G., "Application of the fluidyne in developing countries," SAE technical paper 929389, 1992, doi:10.4271/929389
4. http://www.engin.swarthmore.edu/academics/courses/e90/2005_6/e90reports/fk_ao_final.pdf
5. C. D. West, Liquid Piston Engines, Van Nostrand Reinhold, New York, 1983.

NOMENCLATURE

ρ Density of pumping fluid

H Pumping height

A Area of pumping column

Q Flow rate of fluid

CORRESPONDENCE

Sunny Narayan, Assistant professor, Indus International University
Address -VPO Bathu, Una, Himachal Pradesh,India-174301
e-mail:rarekv@gmail.com

Tribological Journal BULTRIB Vol. 5, 2015
Papers from the International Conference **BULTRIB '15**
September 11-13, 2015, Sozopol, Bulgaria
Society of Bulgarian Tribologists
FIT – Technical University of Sofia

REVIEW ON VISCOSITY EFFECTS OF HYDRODYNAMIC LUBRICATION IN TUBE SPINNING PROCESS

Ismail NAWI

Abstract: *This research aims to analyze the influence of lubricants viscosity to the tube spinning process. A theoretical analysis based on the two dimensional isothermal Reynolds equation was developed for the hydrodynamic lubrication. Experimental has been done on a lathe machine where the metal spinning was performed. The results show that viscosity, linear velocity of the forming tool and rotational velocity of the mandrel both influence the establishment of a hydrodynamic lubricant film thickness at the inlet zone . Formation of a hydrodynamic lubricant film thickness at the outside of the tube is ruled by the eccentricity of the mandrel and tube. Theoretical and experimental estimate the values film thickness of the outside wall .The comparison illustrates that they are related on various lubricant viscosity.*

Key Words: *Hydrodynamic Lubrication; Metal Forming; Tube Spinning*

1. INTRODUCTION

Metal spinning is a kind of forming process which is used to form pre-formed blanks either to be stretched further or modify shapes. The pre-formed tube shape product is placed over the mandrel and held firmly to the mandrel. In forming process, the mandrel with the pre-formed tube rotates and the forming tool, with one or two small rollers used to apply localized pressure, and moves forward over the mandrel length with steady velocity. This movement stretches the tube in axial direction and decreases its thickness. The presence of an effective lubricant film between contact surfaces in tube spinning process will increase the reduction in thickness, reduce tool wear, prevent cracking and wave forming build-up, and effect the surface roughness of the product.

Researches and studies in metal forming with hydrodynamic lubrication have been conducted by many researchers. Scaraggi, M. [1], studied the friction properties of lubricant and analyzed the texture surfaces, where the experimental is based on boundary to hydrodynamic lubrication. Alshamma, F. [2] performed a research of a combined effect of hydrodynamic lubrication in cold rolling.

Previously, the results and analyses of plasto-hydrodynamic lubrication in other metal forming processes such as in extrusion process by Wilson [3], wire drawing given by Dowson, Parson and Lidgitt [4], and deep drawing by Mahdavian and Shao [5]. However, they have not be either to implement or modified for the spinning process to estimate the lubricant film thickness. The major difficulty in using these models is the additional relative movement between the tool and work-piece in the spinning process which makes it different from the other processes.

In this paper, researcher concerns with the development, using the two dimensional Reynolds equation, of a realistic steady hydrodynamic lubrication model for the metal tube spinning process. This analysis includes both the tool and mandrel velocities. The analysis produces an estimate of the lubricant film thicknesses between the outside and outside surfaces of the work-piece, mandrel, and forming tool.

2. PROCESS ANALYSIS

Process of tube spinning with lubrication of work-piece and tooling surfaces is shown in Fig.1. The tube is clamped to the mandrel and is rotating with the same speed with the mandrel. The forming roller, while free to rotate, is also advancing forward, parallel to the mandrel axis towards the trailing edge of the tube. The lubricant is drawn between the outside surface of the tube and the roller into the converging wedge spaces between these surfaces. The following table is the type of lubricant applied to the outside surface of tube during the experiments.

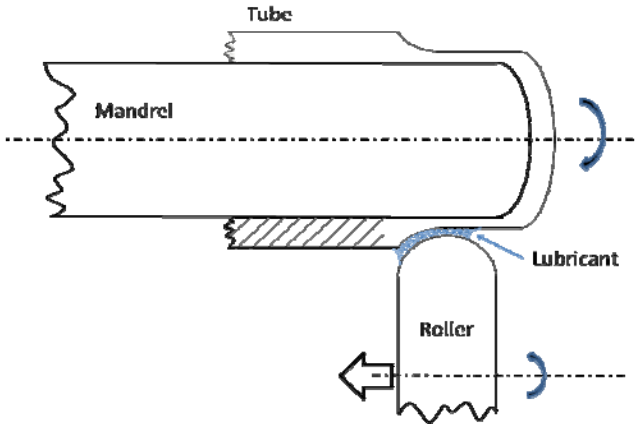

Fig. 1. Tube Spinning Process

Table 1. Type of Lubricants Application

Type of Lubricant	Viscosity at Room Temperature (Pa.s)	Remark
Castor Vegetable natural Oil	0.082	-
Impregno Drawing Oil	0.164	Chlorinated long chain paraffin & fatty acid extract
DK 1172 Oil Drawing Oil	1.472	Chlorinated paraffin & petroleum suffonate
PTFE Spray Oil	-	Colloidal dispersed type

The lubricant film between the mandrel and the outside tube surface, is formed due to both stretching of the tube wall in the feed direction over the surface of mandrel and also by squeezing the lubricant between the outside tube and mandrel surfaces. It is essential to notice that the spinning action, which is caused by continuous changes in the clearance between the tube and mandrel, is due to the eccentricity of the mandrel while rotating against the roller.

3. TUBE - ROLLER OUTSIDE LUBRICANT FILM ANALYSIS

In order to model the lubrication process, the deformation of the tube by the roller is divided into zones as follows:

1. Inlet Zone is the zone where the lubricant enters between the roller and tube wall. In this area the tube wall is rigid.
2. Work Zone is the zone where plastic deformation of the tube wall occurs and it is perfectly plastic deformation.
3. Outlet Zone is the zone where the film thickness is assumed to be constant and the workpiece is rigid.

In the inlet zone, both the workpiece and mandrel surfaces remain rigid. Once the hydrodynamic lubricant film is created due to the inlet wedge action the interfaces between the workpiece and roller are completely separated. The boundaries of this zone are the points A and B which are located at distances of Xa and L on the x axis which is a small portion of the roller width. The roller diameter is much greater than the width of the roller.

At the inlet zone the lubricant is subjected to two surface velocities. The relative rotation of the mandrel and roller is the surface velocity in y direction, and the roller movement in the direction of feed rate is the other surface velocity in x direction. The lubricant pressure is increased from ambient pressure to the level where the tube starts to yield at the boundary of the inlet and work zones.

In the work zone the plastic deformation of the tube proceeds from its inlet zone boundary with the constant flow stress over the work zone until it is completed at the boundary between the work and outlet zones. The local lubricant film varies in this zone and is influenced by the inlet film thickness. The lubricant pressure gradient in this zone is insignificant . The boundaries of the work zone are points B and C. In the outlet zone both the work piece and roller surfaces are rigid and separated by a constant film thickness.

The analysis of this zone is similar to the other forming process such as extrusion and wire drawing which have already been carried out by numerous researches and does not significantly effect the estimating of the lubricant film thickness.

3.1. The Inlet Zone

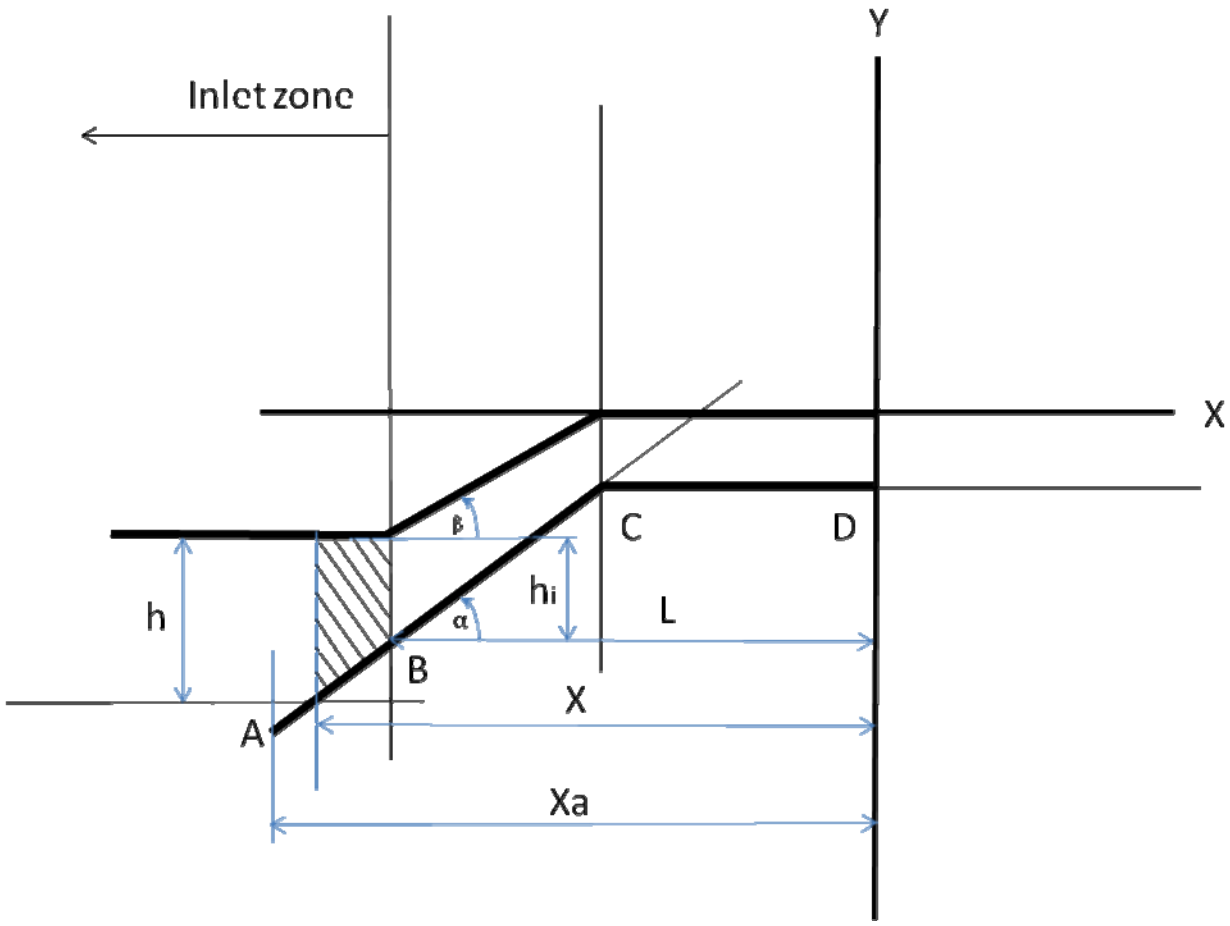

Fig. 2. Inlet Zone of Film Thickness on the x-y Plane

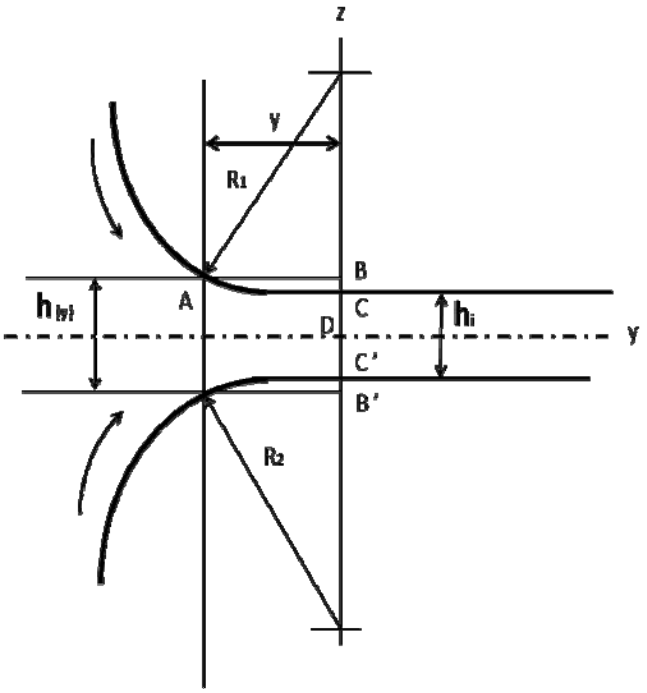

Fig. 3. Inlet Zone Film Thickness on the y-z Plane

The geometry in Fig.2 shows that the film thickness in the inlet zone along the axis x in the plane x- z is given by:

$h(x) = h_i + (x-L) \tan \alpha$
(1)

The film thickness h(y) in the plane y-z is a function of y which can be found from the geometry of disc to disc system as shown in Fig.3.

Introducing $1/R = 1/R1 + 1/R2$ (2)

$h(y) = h_i (1 + y^2/2Rh_i)$ (3)

The general form of the inlet film thickness h in direction of z axis as a function of x and y from the geometry of the tube and roller is:

$h(x,y) = h_i + (y^2/2R) + (x-L) \tan \alpha$ (4)

where Eqs (1, 3) are special cases of the Eq. (4).
The pressure gradient in the x direction is much greater than the pressure gradient in the y direction. This is justified through comparison of the pressure variations across the small length of inlet zone with the large radius of the roller. This means the steady Reynolds equation for the inlet zone for steady state becomes,

$\partial/\partial x(h^3 \partial p/\partial x)= 6\eta (U\partial h/\partial x + V \partial h/\partial y)$ (5)

Introducing, $U_1 + U_2 = - U$ and $V_1 + V_2 = -V$ in Eq. (5) then integration gives,

$h^3 (dp/dx) = - 6\eta (Uh + V x \partial h/\partial y) + C1$ (6)

Substitute for $\partial h/\partial y$ and $h(x,y)$ in Eq. 6 gives,

$dp/dx = - [(6\eta U)/ \{h_i + (y^2/2R) + (x-L) \tan \alpha\}2] - [(6\eta Vxy)/R\{h_i + (y^2/2R) + (x-L)\tan \alpha\}^3] +$

$$+ [C1 / \{h_i + (y^2/2R) + (x-L) \tan\}^3] \quad (7)$$

For boundary conditions,

$dp/dx = 0$ at $x = L$ and let $y = \delta$ where δ is very small so, $y^2/2R \approx 0$

Hence Eq. (7) becomes,

$$C1 = 6\eta (Uh_i + V L\delta/R) \quad (8)$$

Substitute C1 from Eq. (8) in to Eq. (7) then after integrating yields,

$$p = [(6\eta U)/\tan\alpha\{h_i + (y^2/2R) + (x-L) \tan \alpha\}] + [(6\eta Vy)/R \tan^2\alpha\{h_i + (y^2/2R)+ (x-L)\tan \alpha\}] +$$

$$[(6\eta Vy)(L\tan\alpha - h_i - y^2/2R)/2R \tan^2\alpha\{h_i + (y^2/2R)+ (x-L) \tan \alpha\}^2] - [(6\eta Uh_i + 6\eta V\delta L/R)/ 2$$

$$\tan\alpha \{h_i + (y^2/2R)+ (x-L) \tan \alpha\}^2] + C2 \quad (9)$$

Calculating the constant C2 from the boundary conditions, $p = 0$ at $x = \infty$ and $y = \infty$, substituting in Eq. (9) gives $C2 = 0$.

Assume that the material starts to yield at value of $p = \sigma_y$ (yield stress) at $x = L$ and,

substitute, $y = \delta$ for contact width from the following Eq. (10).

δ is estimated from the half width of Hertz contact . In a real situation the contact between the roller and work piece is a Hertz contact. It is assumed that the pressure is maximum at the edge of the contact and remains constant to the position of $y = 0$

$$\sigma_y = (6\eta U/h_i \tan\alpha) + (6\eta V\delta/h_i R\tan^2\alpha) + (3\eta V\delta(L \tan\alpha - h_i)/h_i^2 R\tan^2\alpha) - ((3\eta Uh_i + 3\eta V \delta L/R)/$$

$$h_i^2 \tan\alpha) \quad (10)$$

Simplifying the above equation , the inlet film thickness becomes,

$$h_i = (3\eta V)(U/V \tan\alpha + \delta/R) / \sigma_y \tan^2\alpha$$
(11)

For the case $\delta = 0$ Eq. (11) becomes ,

$$h_i = 3\eta U/ \sigma_y R \tan\alpha$$
(12)

Eq. (12) which becomes independent of velocity V, is similar to the analysis of the inlet zone of extrusion given by Wilson [5].

Introducing the nondimensional parameters:

for $H_i = h_i/L$ $U_i = U/V$ $d_i = \delta/R$ $Fi = 3\eta V /\sigma L$

Eq. (12) becomes,

$$H_i = F_i (Ui \tan\alpha + d_i) / \tan^2\alpha$$
(13)

The effect of the angle α to the lubricant film thickness for the various of non dimensional is half width of the Hertzian contact d_i. The film thickness decreases as the roller angle is increased. Non dimensional value of di effects the film thickness. A high value of di generates a higher film thickness than a low value

of d_i . Wilson's analysis of the extrusion process may be considered as a special case of the two dimensional analysis where di is equal to zero. In another words in the extrusion process the die is not rotating in y axis direction hence V1 and V2 are zero and the influence of di is diminished. The surface velocity of mandrel (mandrel rotation) causes to drag more viscous fluid between the diverging surfaces. This will change the pressure distribution and increase the inlet film thickness. The importance of the term (V. δ) in increasing the inlet film thickness is noticeable in the inlet film thickness equation. The mandrel rotation influences the establishment of hydrodynamic lubricant film even a small contact area (fraction of square millimeters) is recognized between the roller and the tube surfaces.

Any increase in the feed rate velocity increases the film thickness. In addition, it shows that if the feed rate velocity is increased, the film thickness also increases particularly at the value of α smaller than aproximately 30^o. The rotational motion of the workpiece in addition to its linear motion assists the wedge action to enhance the formation of a thick lubricant film thickness.

3.2. The Work Zone Analysis

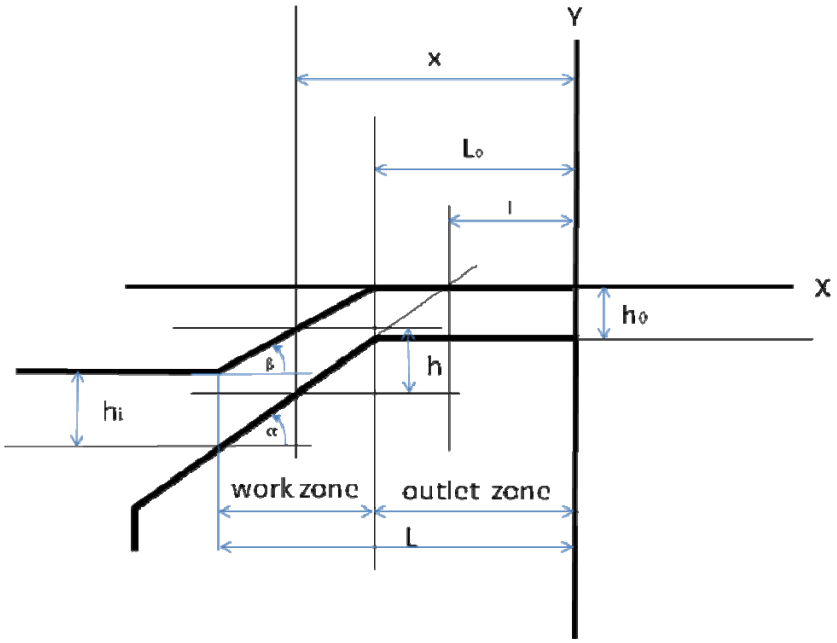

Fig.4. Work Zone FilmTicknes on x-y Plane

In the work zone, where the tube material is deformed at the constant pressure p , hence there is no rate of change of the pressure either with x or y so $\partial p/\partial x = 0$ and $\partial p/\partial y = 0$. Therefore, because dh/dt is also zero, the Reynolds equation may be written as,

$$U\,\partial h/\partial x + V\,\partial h/\partial y = 0 \quad \text{or} \quad \partial h/\partial x + (V/U)\,\partial h/\partial y = 0 \qquad (14)$$

This equation can be solved by Langrange decomposition follows.
The differential equation of the family of characteristic is,

$$dx = dy / (V/U) \quad \text{or} \quad dy/dx = V/U \qquad (15)$$

From the geometry of the work zone in Fig. 4, the initial conditions of the film thickness h can be found as,

$$h(x) = \{x\,(h_i - (Lo - lh)\tan\beta) + L\,(Lo - lh)\tan\beta - h_i\,lh\}/(L - lh) \qquad (16)$$

where,

$$lh = \{L\tan\alpha - h_i - L\tan\beta + lo\tan\beta\}/\tan\alpha \qquad (17)$$

Hence the initial condition of the case of characteristic equation is,

$x > L$ $\quad h(x) = h_i + (x-L) \tan \alpha$

$Lo \leq x \leq L$ $\quad h(x) = (x (h_i - (Lo - lh) \tan \beta) + L (Lo - l) \tan \beta - h_i lh) / (L - lh)$

If $h(x, 0)$ is $f(x)$ then the solution along this characteristic is $h(x,y) = f(xR) = f(x - Uy/V)$.

hence, the solution along this characteristic is,

$$h(x,y) = (x - Uy/V)(h_i - (Lo - lh) \tan \beta) + L (Lo - lh) \tan \beta - h_i lh)/(L - lh) \quad (18)$$

Eq. (18), may be written in nondimensianal form,

$$H_w = \{(X_w - U_w d_w R_w)(H_i - (Lo_w - l_w)\tan \beta) + (Lo_w - l_w)\tan \beta - H_i lw\}/(lh - l_w) \quad (19)$$

Where,

$\delta^* = y$ $\quad d_w = \delta^*/R$ $\quad H_w = h/L$ $\quad U_w = U/V$ $\quad H_i = h_i/L$

. $\quad l_w = lh/L$ $\quad Lo_w = Lo/L$ $\quad R_w = R/L$ $\quad X_w = x/L$ $\quad (20)$

and, Hi is the nondimensional inlet film thickness.

The non dimensional work zone film thickness is plotted against the non dimensional feed rate U_i for various value of β. The high feed rate increases the film thickness at the work zone as at the inlet zone. Large value of the angle β also contribute to the high value of lubricant film in this zone. This case is applied for $\alpha = 45$ degree, and if $\alpha = \beta$, the film thickness at the work zone is equal to the film thickness at the inlet zone.

4. COMPARISON BETWEEN THEORITICAL AND EXPERIMENTS

Comparison between theory and the experimental results is shown in Fig 5. Lubricant film thickness between the work-piece - mandrel theoretically and practically produce similar trend as indicated significantly The experimental results are higher than the theoretical results beyond the viscosity of drawing oil which is 0.164 Pa.s. This is because of the factors or variables that have not been considered in the formulation of the equation such as the influence of temperature and pressure changes in viscosity. Another factor that can be influenced to this phenomena is the estimation of the eccentricity between the mandrel and the tube. Since the eccentricity can affect the speed of the lubricant on Z direction, the eccentricity has to be estimated accurately.

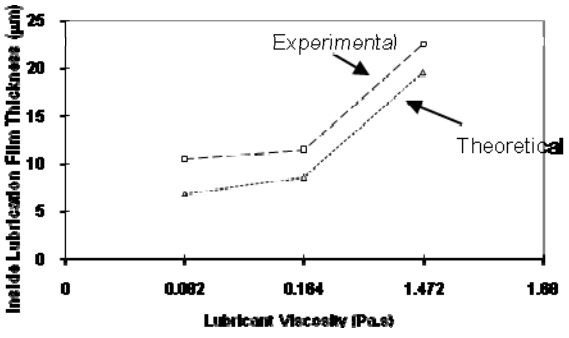

Fig.5. Comparison of the Film Thickness Between Experimental and Theoretical Results

5. CONCLUSIONS

In this research the theoretical analysis for the film thickness in tube spinning was derived by using the Reynolds equation (1). Theoretical models were developed for the inlet zone of the work-piece. The film thickness at the outside of the wall, between the work-piece and mandrel, was analyzed. The result of the theoretical model for the inlet zone film thickness was obtained in a closed form equation (2). The variation of film thickness was plotted for the various viscosities and it was concluded that the formation of high lubricant thickness is only achieved under certain conditions. It was also shown that the angle of attack α influences the magnitude of the film thickness. Increasing the feed rate and mandrel rotation results in a higher film thickness. The comparison between theoretical and experimental film thickness indicated that the outside film thickness from theory was higher than the experimental measurement.

REFERENCES

1. MICHELE SCARAGGI, FRANCESCO P. MEZZAPESA, GIUSEPPE CARBONE, ANTONIO ANCONA, LUIGI TRICARICO., Friction Properties of Lubricant Laser-Micro Texture-Surfaces: an Experimental Study From Boundary To Hydrodynamic Lubrication, Tribology Letter, **Vol. 49**, pp117-125, 2013.
2. ALSHAMMA, F., A Combined Effect of Hydrodynamic Lubrication In Cold Rolling", Global Journal of Research In Engineering Mechanical And Mechanics Engineering, **Vol.11**, Issue 7, December 2011.
3. MAHDAVIAN, S.M., S, Z.M., Iso-Viscous Hydrodynamic Lubrication of Deep Drawing and It Is Comparison With Experiment", Asme, Journal of Tribology, **Vol.115**, January, pp 111-118, 1993.
4. DOWSON, D., PARSON, B., LIDGITT, P. J., An Elastoplastohydrodynamic Lubrication Analysis of Wire Drawing Process, Elastohydodynamic Lubrication Symposium, Inst. Mech. Eng., pp. 97, 1972.
5. WILSON, W. R. D., The Temporary Breakdown of Hydrodynamic Lubrication During The Initiation of Extrusion", Int. J. Mech. Sci., **Vol.13**, pp 17-28, 1971

CORRESPONDENCE

Ismail NAWI
DR,

Universiti Tun Hussein Onn Malaysia (UTHM)
Batu-Pahat, Johor, Malaysia 86400

e-mail: ismailn@uthm.edu.my

Tribological Journal BULTRIB Vol. 5, 2015
Papers from the International Conference **BULTRIB '15**
September 11-13, 2015, Sozopol, Bulgaria
Society of Bulgarian Tribologists
FIT – Technical University of Sofia

STUDY ON STABILITY AND WEAR IN TOTAL HIP PROSTHESES

Virgil FLORESCU, Lucian CAPITANU

Abstract: *The objectives are to study the mechanisms of achieving stability of acetabular prosthetic components and the influence of some characteristic parameters, to evaluate the effect of femoral stem fixation modality on the stability of components and to predict long-term behavior, to analyze a critical phenomena which influence the loading transfer mechanism through artificial joints and could lead to aseptic loosening – the wear of joint frictional surfaces.*

Key Words: *THA, acetabular stability, FEM simulation, stresses and displacements, wear tests, wear simulation.*

1. INTRODUCTION

Total hip arthroplasty – meaning the total replacement of hip joint wihh an artificial one. The implant used for this procedure has generally two main components: the acetabular part (inserted in the iliac bone), and the femoral part (inserted in the femur). Fixation methods used today in clinical practice are two: fixation using an acrylic cement – which has good results on short and medium-term, but lead to late failure especially for young patients – and press-fitted fixation which allows, for a satisfactory post-surgical fixation, better results on long-term stability (this kind of fixation lead to stimulation and not inhibition of bone remodeling process in the area where the implant is located). The problematic of Total Hip Arthroplasty and other related phenomena is a large one with focusing on both the acteabular prosthetic components as well as on femoral components [1].

Looking back, from the beginning of arthroplasty until today, we will see that the design of a prosthesis was strongly influenced by a demand - after rehabilitation program, the patient was able to use the artificial joint in almost the same way as the natural one.

The attention of the specialists was moved forward to the problematic induced by slow phenomena as wearing, that are found to limit the durability of a prosthesis, and subsequently the lifetime of it [2 - 4]. The researchers were focusing on two directions – estimation of the load transfer mechanism by explicating the frictional contact parameters, and estimation of the correlation between those parameters and the wearing of the components involved in contact. In the first part of the tribological study, the authors shows that there is a strong correlations between the contact pressure and the wear rate (see also, Capitanu et al, 2005 [5]). It means that different activities – that will induce different contact pressures – will conduct to different level of wearing. More than that, for the same activity, the contact pressure will vary during different stances of the activity. So, the wearing phenomena will be not a constant rate phenomena, neither for the same activity nor across activities. The issue is even more difficult considering that different activities have different frequencies.

The problem is how to quantify for the same activity or across activities the parameters that influence the wearing phenomena. The authors tried in this study to offer a reliable method for a critical parameter as the contact pressure. Clinical experience shows that, in the case the revision replacement of the cup due to wearing, that the profile of the contact surface was spherical no more, some areas being more damaged than others. It was obvious that this phenomenon is caused by the unequal distribution of load over the contact surface. Previous studies establish the location of the maximal pressure point on the acetabulum, revealing the dependence to the magnitude of the contact force. Others studies focus on the evolution (location, direction and magnitude) of the contact force determined by experimental methods on a prosthetic femoral head (Taylor et al [2], Bergmann et al [3], Miyanaga et al, 1984 [6] and Davy et al [7]). Unfortunately, this contact force could not offer a good image of the wearing phenomenon. Instead of that, by transferring, by intermediate of the contact mechanism, the contact force from the femoral head to the acetabular cup, one could obtain a good estimation of the distribution of the contact pressure, over the entire interface. A good method to do that is performing by FEM a non-linear, dynamic analysis of the contact couple behavior under the loading produced by a specific activity.

2. METHODS

We assumed for the beginning a simplified axisymmetric finite element model with material inhomogeneity - a large volume of trabecular bone enclosed by a thin layer of cortical bone. In studying the mechanical behavior of the human body in contact with prosthetic parts there are some uncertainties which regard in the same time the elastic behavior but also the frictional characteristics. It is very important to establish some general or standard results, which is almost impossible considering that the parameters values are quite different among individuals. So, we consider only some significant values for three parameters: the Young modulus of spongy bone, the interference width (half the difference between the diameter of the cup and the diameter of reamed acetabulum), and the frictional coefficient. One could notice that we examine the variation of the elastic parameters, variation of geometry, but also the variation of dissipative term of the equation of motion. By introducing the cup with constant velocity we nullify the inertial term in the same equation.

The elastic support for the press-fitting mechanism is the spongy (trabecular) bone. It resulted that the elastic characteristics of the bone in the area of the acetabulum will influence the general behavior and of course the efficiency of the press-fitting fixation which means – for the immediate period after the surgical act – the primary stability of the cup. The spongy bone Young modulus varies between 0.1 and 2 GPa (Dalstra et al, 1993 [8]). The value reported by Spears et al, 2000 [1] – and used by us in all analyses - for the Young modulus of the cortical bone is 15.6 GPa.

The press-fitting fixation implies using a cup with a diameter larger than the reamed acetabullum. There is no doubt that larger the diameter, larger the interference width will be, and that means an enlarged interference area. But, on the other hand, it will need to increase the insertion force magnitude. Some studies report that there is a limit value for insertion force, above that the spongy bone is suffering permanent modifications (Adler et al, 1992 [9]). The cups are chosen so that the difference between their diameter and the diameter of the acetabulum lies between 0.2 and 1 mm.

A great importance in the primary stability of the implant has the frictional mechanism that accompanies the contact. By variation of the values of this parameter we covered not only the large variety of the prostheses used today but also the possible values of the roughness of the acetabulum surface after reaming operation (Shirazi-Adl et al, 1993 [10]). The values for the frictional coefficient are till 0.1 untill 0.5.

3. RESULTS AND DISCUSSION

3.1. Study on the acetabular cup stability

We used in our evaluation an inhomogeneous simplified finite element model which comprises the both types of bone encountered in the real situation. It was an axisymmetric model with three components: the spongy bone for what we used plane solid elements, the cortical bone (a very thin layer at the outer surface of the iliac bone) and the cup modeled by plane elements which are more rigid than the spongy bone (~ 200 - 1000 times) or the cortical one (~10 times). The simplified axisymmetric model considers only a part of the iliac bone (the acetabulum zone) as could be seen in Figure 1.

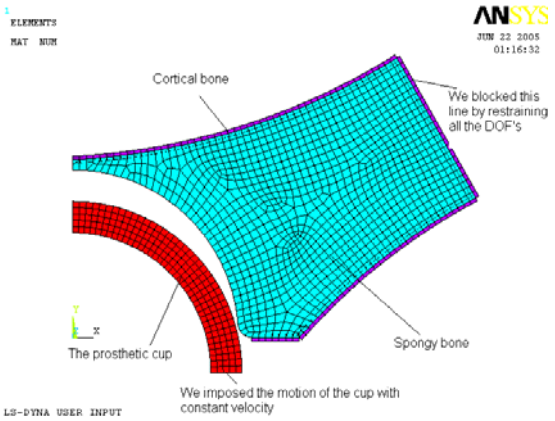

Fig. 1. The finite element axisymmetric model

One could see also the boundaries where the restraints are imposed (the line where all the DOF's are blocked). We consider that the rigid cup has an imposed displacement and is moving with a constant velocity. We tried to evaluate the contribution of some important parameters for the variation of the force needed to be applied in order to obtain the desired kinematics (the insertion force), for the maximum value of stress in the contact area and finally for the pull-out force needed to extract the cup from acetabulum which is also

the resistance of the cup against undesirable motions. The analytic expression for the insertion force is listed bellow:

$$F_i = \int_{A_c} \sigma_n \left(\mu \cos\alpha + \sin\alpha\right) dA \tag{1}$$

where σ_n is the normal stress to the contact area A_c, α is the angular coordinate of the contact surface and μ is the friction coefficient.

One could see that the insertion force must counter-balance the elastic forces and the friction. For the pull-out force one could notice that in this case the elastic force due to the press-fitting contribute to the migration of cup. Considering this we have for the pull-out force the following expression:

$$F_e = \int_{A_c} \sigma_n \left(\mu \cos\alpha - \sin\alpha\right) dA \tag{2}$$

where A_f is the final interference area.

The studied cases are listed in Table 1. The standard values listed there for the parameters are used when other parameters are varied.

Table 1 Values used for parameters analysis

Parameters	Young's modulus for spongy bone (GPa)	Interference width (mm)	Friction coefficient
Standard value	0.1	1.0	0.25
Variation of the parameter	0.1	0.2	0.10
	0.2	0.4	0.20
	0.5	0.6	0.30
	1.0	0.8	0.40
	2.0	1.0	0.50

In Figure 2 one could see the stress distribution and the displacements in the spongy bone for the following parameters combination: E_{spongy} = 0.1 GPa; Interference = 1 mm; μ = 0.25.

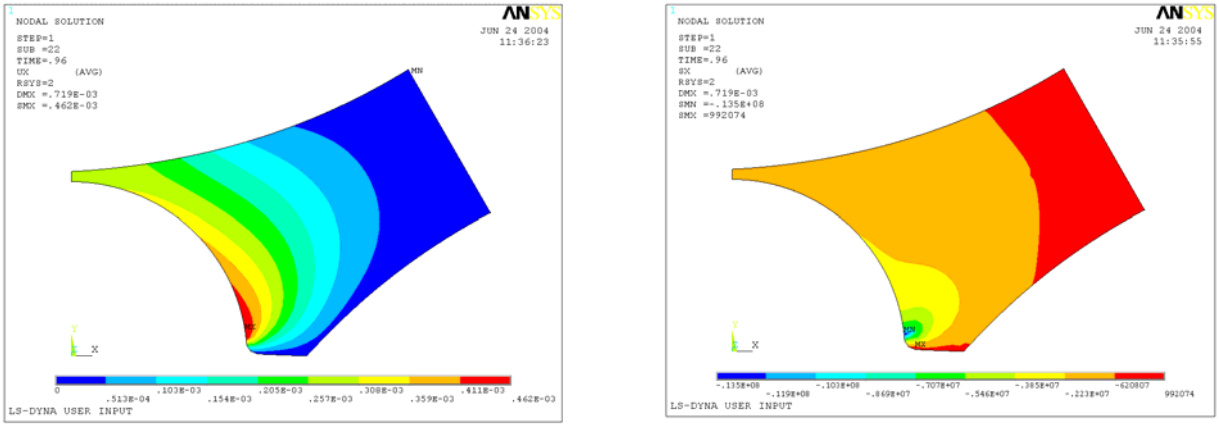

(a) (b)

Fig. 2. Periacetabular deformations (a) and normal stresses (b)

Of course, from all cases studied we choose only one to show here, the distributions of displacements and stresses for the rest of them having similar aspect but different values.

In Figures 3 one could see the variation of the insertion force for different values of elastic and frictional parameters. One could notice that the variation of Young modulus of spongy bone and the interference width (Figures 3a and.3b) has a greater impact on the insertion force than the variation of frictional coefficient (Figure 3c); the contribution of the first two parameters is – as one could see in Eq. (1) – in both terms of the sum under integral.

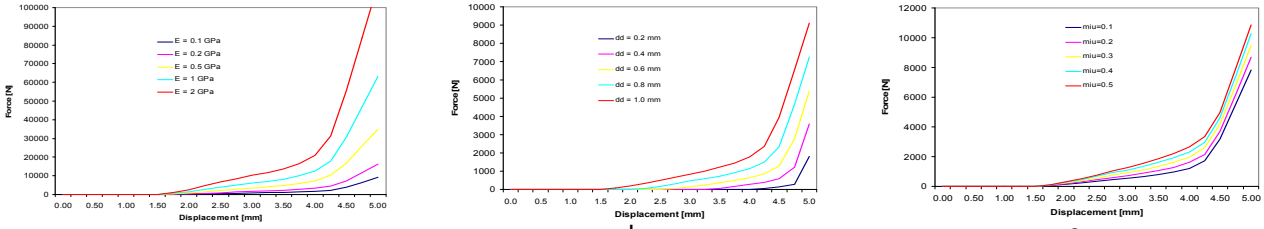

a b c

Fig. 3. The influence of bone elasticity (a), interference (b), and friction ceofficient (c) on insertion needed force

Also, one could notice that there are two important stages in the press-fitting procedure. First, we have a linear increase of the insertion force which covers almost the entire motion of the cup. During this stage the spongy bone in the acetabulum area has important radial deformation. In the last sequences this radial deformation is accompanied with an elastic bending deformation of the entire spongy bone which increases the needed insertion force almost exponentially.

In Figure 4, the circumferential distribution of radial stress (at the fixation position) and the evolution of maximal von Mises stresses are plotted. The observation made before remains still available.

The pull-out force could be computed via Eq. (2) integrating over the entire contact area.

For example, varying the Young modulus of the elastic support for contact (the spongy bone) between 0.1 and 2 GPa one could obtain the pull-out force values between 130 and 1270 N. A negative value of this pull-out force means that the cup will not remain in the acetabulum after the load will be removed (the cup will be rejected by the elastic forces stored in the iliac bone by the press-fitting). Due to the anisotropic mechanical behavior and to its complex geometry, a 3D model of iliac bone is not easy to achieve. An important part of recent studies are concerning on the possibility to obtain viable finite element models based on detailed investigation methods as Computed Tomography (CT-scanning). In this part of the paper we use a finite element model of the iliac bone created under an EU Project namely “Virtual Animation of the Kinematics of the Human” (VAKHUM, 1999). This model is generated from CT-scans, mapping the elastic properties (evaluated by specific tomodensitometry relations) on a 3D mesh, obtained by approximating the real geometry of the bone (see Figure 5).

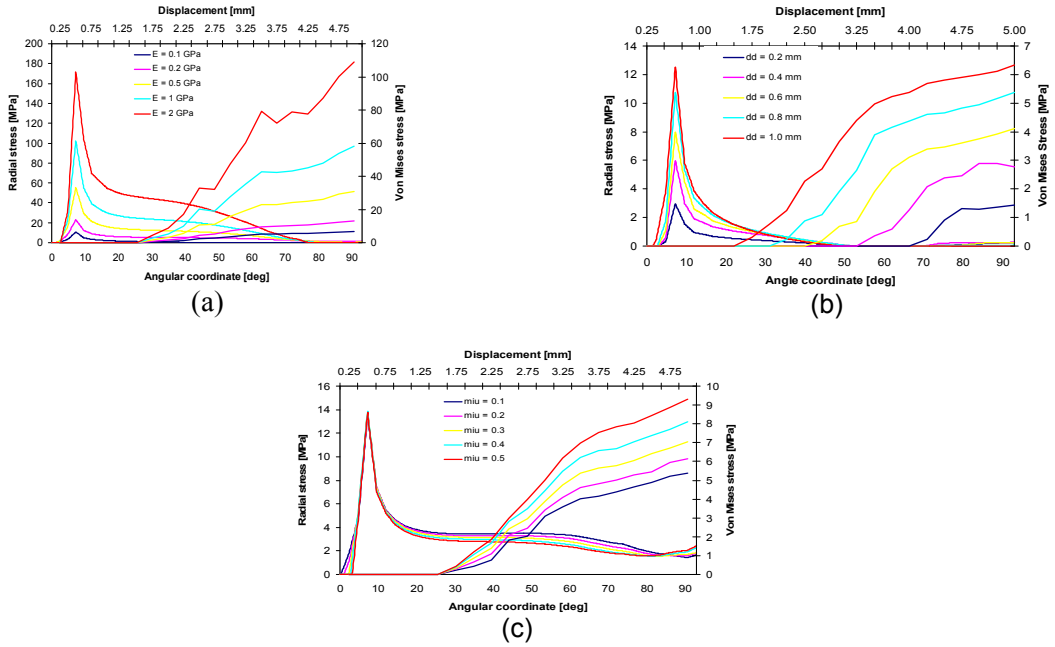

Fig. 4. The influence of bone elasticity (a), interference (b), and friction ceofficient (c) on the periactebular stress distribution

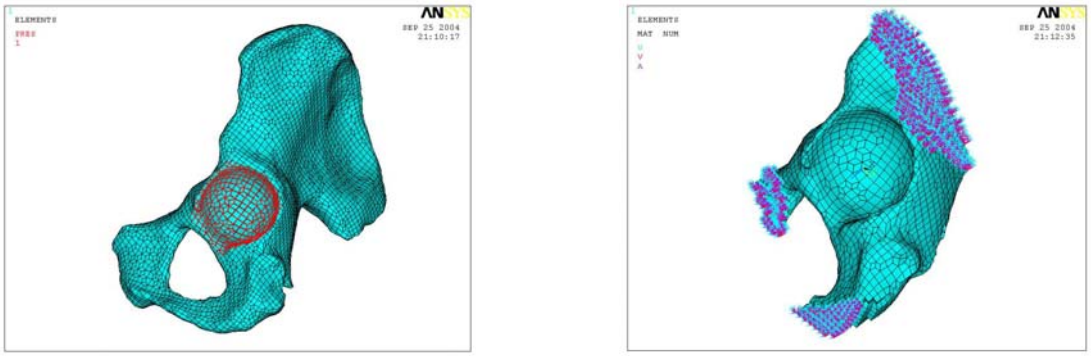

(a) (b)

Fig. 5. The iliac bone model with reamed acetabulum (a) and the reduced model (b)

In order to avoid excessive distortion of the elements, special methods, like relaxation and laplacian smoothing are used. By these procedures the entire bone anisotropic elasticity is replaced by a heterogeneous set of isotropic elements. A good image of the complexity of the model could be offered by the fact that it contains almost 15000 nodes and 13000 elements. The material characteristics are situated between 0.741 and 1.823 g/cm^3 for density, and 1531 to 22849 N/mm^2 for Young modulus. The interior surface of acetabulum was considered reamed, with the subcondhral bone totally removed, considering that the contact was established between the exterior surface of the cup and the spongy bone (see Figure 5a). In the analysis we used a reduced model like that in the Figure 5b.

One could consider the initial position of the cup, like in figure 6a, where R is the external radius of the cup, and r the radius of the reamed acetabulum. It follows that the distance between the pole of the cup and the pole of the acetabulum (the gap d), can be computed by:

$$d = \sqrt{R^2 - r^2} + r - R. \tag{3}$$

We consider that the insertion force is applied on the cup, via impact, like in the surgical procedure (see Figure 6b, with f – the value of pulse force, $3t$ **–** duration of one pulse of force, and n **–** the numbers of the pulses).

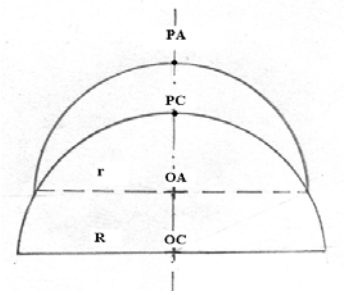

(a)

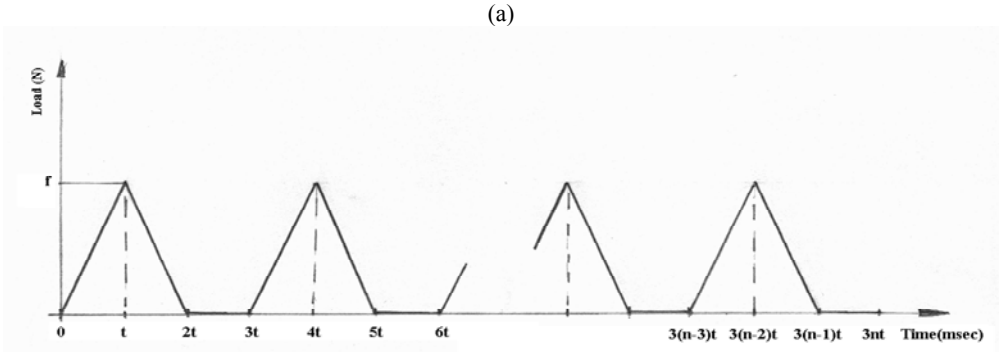

(b)

Fig. 6. The initial position of the cup in the acetabulum (a), and the insertion impact force (b)

By varying the numerical values of the parameters (f, t, n) one could obtain a suitable loading in order to achieve a desirable displacement of the cup. The FE analyses were made for the following values, of the input parameters: f = 170 N; t = 0.5 msec; n = 10; R = 24.5 mm; r = 24 mm. The initial and the final positions of the inserted cup, are presented in Figure 7.

(a) (b)

Fig. 7. The inserted cup in the initial (a) and final (b) position

The diagram, obtained for the external mechanical work, is plotted in the Figure 8a, and the von Mises stress evolution corresponding to three key stages of the loading, are shown in Figures 8b – 8d, respectively. As we stated before, by THA the hip joint is completely replaced by an artificial joint. This requires some modification of the acetabular part of the joint. Practically, the surface of the acetabulum is no longer an active surface instead of that becoming a seating surface for a cup that is part of the artificial joint.

The connection between the acetabulum and the cup could be cemented or press-fitted. In the last case, an oversized metallic cup is introduced in the acetabulum by some pulse forces induced by a surgical mallet. In this way the metallic cup is press-fitted in the acetabulum.

Subsequently this cup will contain an UHMWPE (Ultra-High Molecular Weight Polyethylene) hollow hemisphere which concave surface will be active tribological surface being in contact with the ball that replaces the femoral head (Capitanu et al, 2004 [11]).

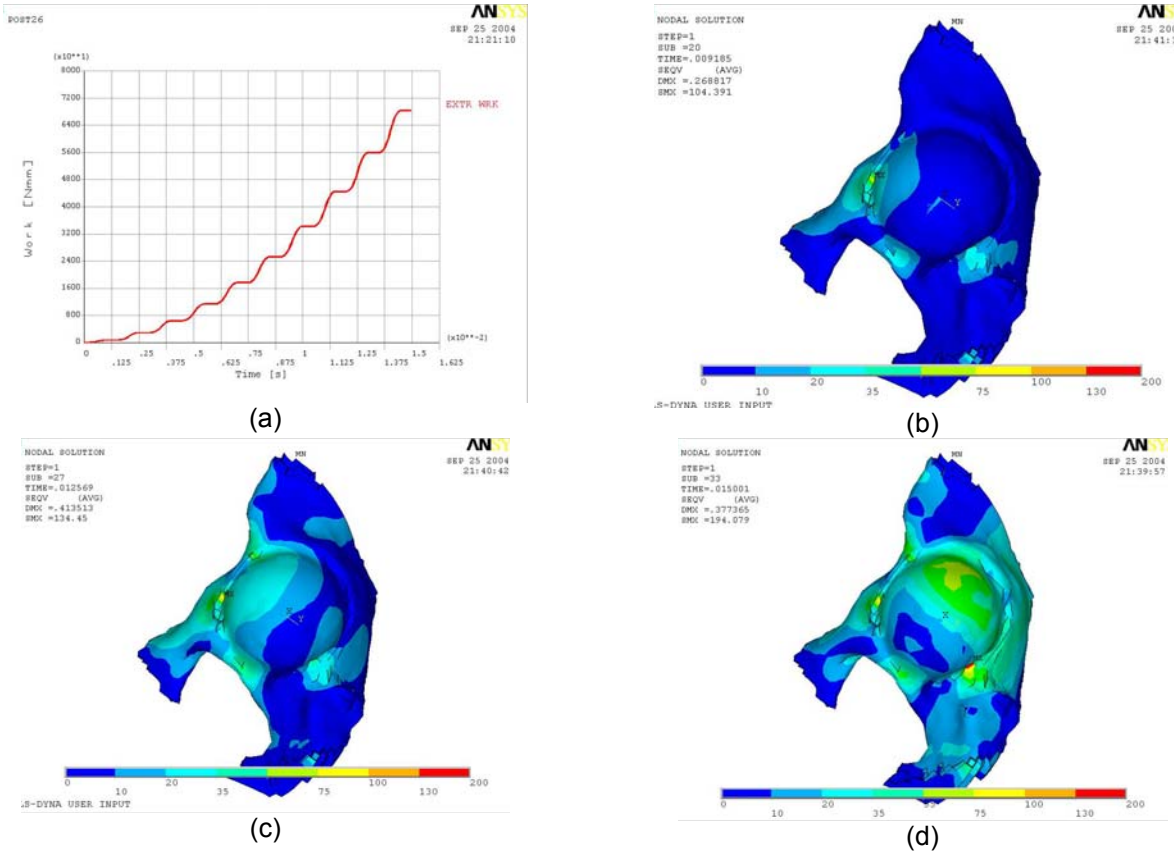

(a) (b) (c) (d)

Fig. 8. The external mechanical work (a) and Von Mises stresses at initial (b), intermediary (c), and finaly (d) stages of insertion

As a conclusion we could state that using even simplified models, for computing the force needed for insertion and the level of fixation given by the pull-out force value, FEM could be a suitable method for such sensitivity analyses and could provide a good way for quantitatively describing the phenomena that were evaluated before.

3.2. Study on the wear of total hip prostheses

For the experimental study of the frictional and wearing processes of the total hip prostheses, a simulator of 2D movement was used, using an electrical engine of 5.5 kW having variable speed between 0 and 3000 r.p.m.

The friction couple is made from a femoral head of a modulated Johnson & Johnson prosthesis (Stellite 21), who rotates under load, in the cavity of UHMWPE acetabular cup. The femoral head has a diameter of 28 mm and executes an oscillation of ± 30^0, corresponding to a stroke of 22 mm driving rod. Table 2 show the friction coefficient values for dry and lubricated friction conditions (physiological serum).

Table 2. Friction coefficients measured in dry and lubricated conditions

p (MPa)	v (cm/min)	F_n (N)	F_f (N)	μ	F_f (N)	μ
			Dry conditions		Phisiological serum	
0.7	527	500	14.25	0.285	1.75	0.035
1.4	527	1000	32.00	0.320	4.90	0.073
2.1	527	1500	51.30	0.342	9.75	0.090
0.7	1055	500	14.00	0.280	1.60	0.280
1.4	1055	1000	29.50	0.295	4.10	0.295
2.1	1055	1500	45.00	0.300	6.75	0.300

The experimental conditions as well as the values of friction force and frictional coefficients at the interface between the femoral head and the acetabular cup are listed in Table 2 for dry friction as for physiological serum lubrication.

The dependence of the frictional coefficients by the contact pressure is plotted in Figure 9.

This couple is doubled by a witness identical couple (Stellite 21/UHMWPE) under same loads but without movement. The both couples are mounted on a tensometric device, on which the variable, non-continuous working loads are applied. The witness couple is needed in order to determinate the lubricant absorption by the acetabular cups, knowing that the UHMWPE has hygroscopic behavior. The loads are applied by means of a calibrated spring.

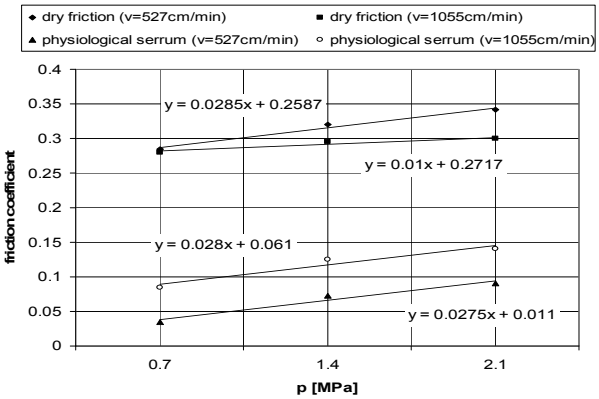

Fig. 9. Friction coefficient vs contact pressure in dry and lubricated friction conditions

The experimental setup contains a strain gauge bridge with two measurement channels, one for normal force F_N and the other one for friction F_f, the values being registered by a plotter. For tests only the 60 and 120 rpm frequencies are used (corresponding to a normal respectively accelerated walk). These correspond to some relative speeds of 527 and 1055 cm/min. The duration of tests was $3 \cdot 10^6$ cycles, it means 834 hours (approximately 35 days). So, the total travel length was 44.106 respectively 88.106 mm (depends of the two relative speeds). The measurement of the normal force and friction yields to the evaluation of the frictional coefficient, based on Coulomb Law.

The wear of the UHMWPE acetabular cups was established by gravimetric measurements as being the difference in weight before and after the $3 \cdot 10^6$ cycles of loading, considering also the hygroscopic effect (measured as the difference on the witness specimen due to the lubricant absorption by the polyethylene) [12].

The results of the experimental tests of wear of the acetabular cups, in the same loading conditions, based on gravimetric measurements are listed in Table 3 and plotted in Figure 10.

Table 3. Wear rate

p (MPa)	v (cm/min)	L_f (10^6 mm)	Wear rate (10^{-7} mm^3/mm)	
			Dry friction	Phisiological serum
0.7	527	22.02	18.955	9.579
1.4	527	22.02	47.914	26.088
2.1	527	22.02	128.334	48.126
0.7	1055	44.04	10.072	2.344
1.4	1055	44.04	37.264	6.384
2.1	1055	44.04	90.030	9.579

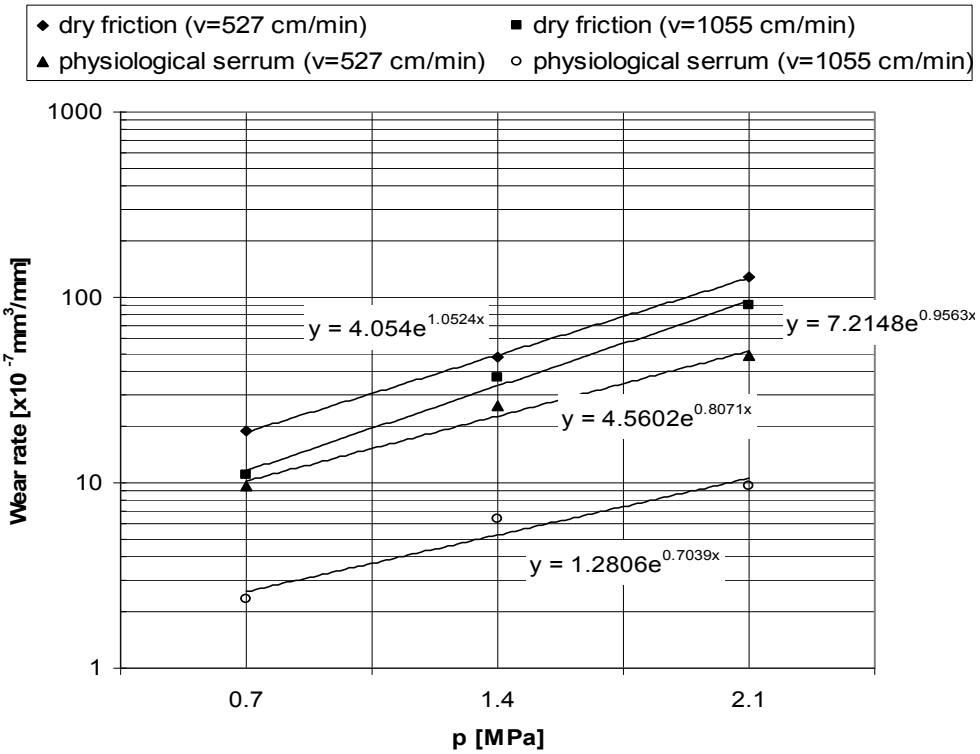

Fig. 10. The wear of the acetabular cups in dry and lubricated conditions

The analyses cover all three load cases (F = 500 N, F = 1000 N, and F = 1500 N) corresponding to normal walk (at a speed of 527 cm/min) for which we have determined the wear rate and the frictional coefficient. The speed being held constant it is assumed that no inertial effects occur.

The model used for all analyses [13] is presented in Figure 11. The model comprises a large part of UHMWPE (having circular form) in contact with the head of a femoral prosthesis made from Stellite21. The UHMWPE part is considered restrained on its exterior circumference located far enough in order to not interfere with the stresses at the contact interface. The loads are applied in the centre of femoral head, the direction of these loads varying by an angle of 30^0 against the vertical axis.

The elastic properties of the two components are for UHMWPE part E = 980 N/mm^2 and v = 0.36 and for femoral head (Stellite 21), $E = 2 \cdot 10^5$ N/mm^2 and v = 0.28 [13].

Only dry friction conditions are analysed.

To give an explicit description of the results, we choose three position of the femoral cup as being important (the femoral cup at 0^0 - corresponding to the start position, the femoral cup at 15^0 - corresponding to an intermediate position, and the femoral cup at 30^0 - corresponding to the large amplitude position). The angles are measured from vertical axis the positive direction being toward the X axis. The results for all these three positions are given in a polar coordinate system located on the centre of femoral head. The extreme values are listed in Table 4.

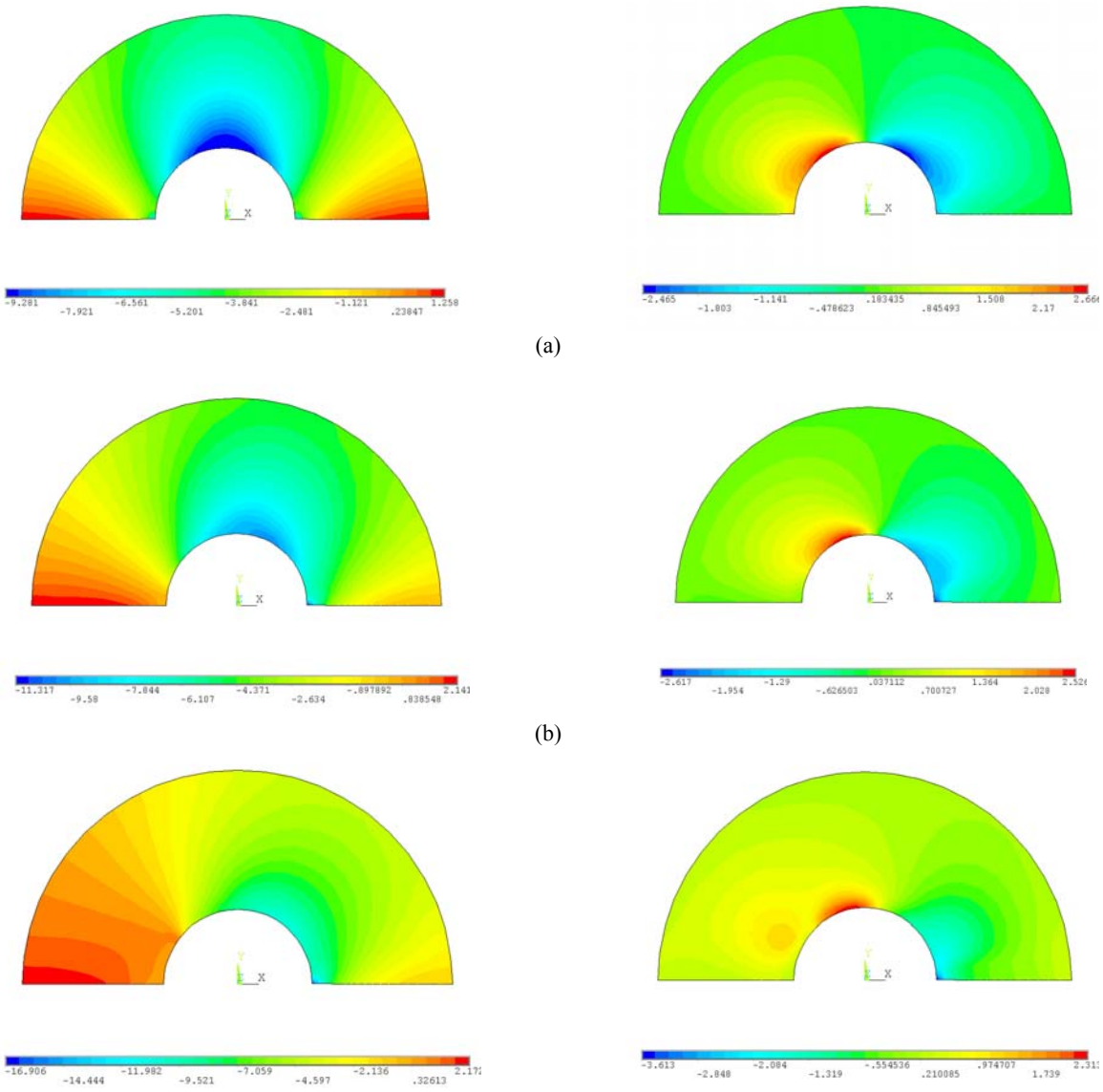

Fig. 11 Radial (left) and tangential (right) stresses for three different positions of femoral head - 0^0 (a), 15^0 (b) and 30^0 (c)

Table 4. Minimum / maximum stresses at contact interface

Case no.	Force (N)	Radial stress (MPa)			Shear stress (MPa)		
		0^0	15^0	30^0	0^0	15^0	30^0
1	500	- 3.203	- 3.496	-3.767	- 0.881	- 0.702	- 0.403
					0.912	0.837	0.777
2	1000	- 6.403	- 6.990	- 7.535	- 1.762	- 1.406	- 1.075
					1.823	1.686	1.560
3	1500	- 9.621	- 10.510	- 10.918	- 2.630	- 2.088	- 1.637
					2.650	2.526	2.313

The stress state in the polyethylene part was described here by the radial stress σ_{rr} interpreted as a measure of the kinematics of the contact surface and by the shear stress $\sigma_{r\theta}$ characterizing the frictional phenomena at the contact interface. The plots presented in Figure 12 shows the distribution of the radial and shear stress for all the three positions of the femoral head considered (0^0, 15^0 and 30^0).

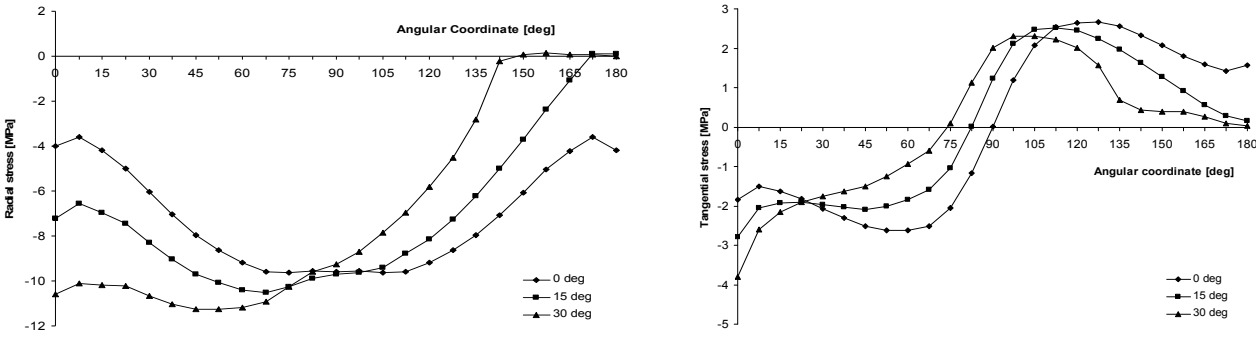

(a) (b)

Fig. 12. Evolution of radial (a) and shear (b) stress during flexion

The maximum radial stress is located around the point of intersection between the direction of load and the internal circumference of the polyethylene part. For shear stresses we have two maximum zones (corresponding of two different orientation of the friction) disposed anti-symmetric for initial position. This characteristic was removed as the femoral head approach to the maximum amplitude position. If for radial stresses we could notice an increase of a maximum value as the amplitude of femoral head was increased in the case of the shear stress we notice the opposite. The two local extreme values of the shear stress are decreasing (for large amplitude loosing even the character of local extreme).

The profiles of the radial stresses plotted versus the angular coordinate in Figure 13a reveals the fact that closer to the maximum amplitude position the distribution of the radial stress have an unsymmetrical aspect. Also, we could notice that the stresses are increasing when the amplitude was increased and the contact gap is opening on that part far away from the centre of the maximum stress area (closer to the higher values of angular coordinates). The distributions of the shear stress versus the angular coordinate for all the three positions of the femoral head considered were plotted in Figure 13b.

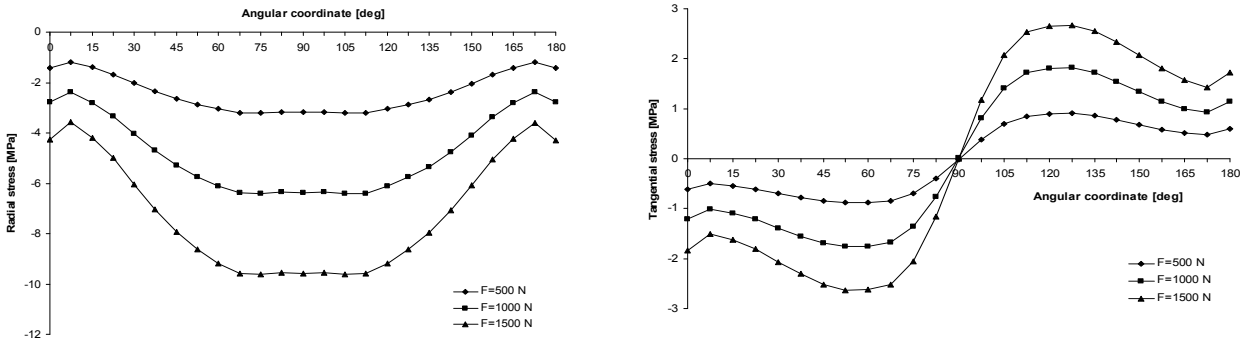

(a) (b)

Fig. 13. Radial and tangential stress for three positions of the femoral head (0^0, 15^0 and 30^0)

The evaluation of the wearing phenomena that occurs in a tribological couple often used in the hip replacement (Stellite21/UHMWPE) has a critical importance for the functionality of the prosthesis. The lifetime of a THP is highly connected to the contact mechanism.

The hardness measurements and profilometric qualitative and quantitative evaluations of the elements of the couples presented in some replaced prostheses (after revision surgical procedure) shows non-uniform tarnishing of the femoral head, local surface hardening of it and local melting of the polyethylene cups due to the increased temperature that occurs due to higher loads.

Using an experimental setup special designed for this purpose we evaluated the behaviour of the frictional couple provided by a Johnson & Johnson total hip prosthesis during an oscillatory movement of the femoral head ($\pm 30^0$) with two different frequencies (60 and 120 rpm) corresponding to the normal and accelerated walking.

The results show a linear dependence between the frictional coefficient and the contact pressure. Also this coefficient decrease when the speed is increasing.

The measurements of gravimetric and volumetric wear rate reveal an exponential variation of that measure with the variation of the contact pressure. Also, the absence of lubricant (physiological serum) doubles the wear rate. Some Finite Element analyses reveal the non-uniform distribution of stresses that could cause the non-uniform wear of the polyethylene cup. Also, analyzing the values of stresses determined we could conclude that the tribological experiments described in the first part of this paper covers (by the three cases analysed) all the contact situations encountered during normal walking.

Following the experimental study, the authors used a simple FE model of the artificial joint (see Figure 14) trying to simulate the contact dynamics at the interface between a rigid sphere representing the femoral head and a deformable hollow hemisphere representing the UHMWPE acetabular cup [12].

The mechanical behavior of the polyethylene part was assumed as linear elastic. The physical properties used in analyses are those from Table 5.

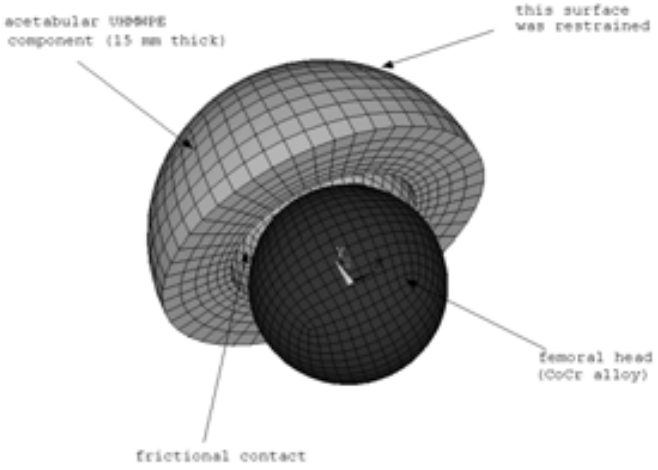

Fig. 14. The FF model used in analysis

Table 5. Material properties of modeled proshetic components

Material	Young Modulus (N/mm^2)	Poisson ratio, *v*	Reference
UHMWPE	981	0.36	ISO 5832-4
CoCr alloy	200,000	0.3	Lewis, 2001, [13]

The assumed hypothesis of the rigid-deformable contact was verified by computing the contact stiffness for each parts of the artificial joint based on following formula:

$$\gamma = \frac{E}{4\left(1-\nu^2\right)} \tag{4}$$

It results a ratio for the metallic femoral head stiffness to polyethylene acetabular cup of $\gamma_{femoral\ head}$ / $\gamma_{acetabular\ cup}$ ~ 200, large enough to validate our assumption. The loading conditions considered in the analyses (the joint contact forces) are those provided by Bergmann et al. in [3].

In Figure 15, the authors reproduced the joint loading history for most common activities. For the analyses, three cases, considered dominant, are selected: the normal walking, stair ascending and stair descending active cycles.

The main objective of simulations was to evaluate the dynamics of contact pressure distribution on the frictional interface for every activities considered. If one consider the contact deformable surface S and the duration of active loading cycle T one could formulate the contact pressure as a position and time function. For each instance of time one could define the instantaneous maximum pressure as given by:

$$p_m(t) = \max\left[p(t,x); x \in S.\right]; \quad t \in \left[0,T\right]; \tag{5}$$

Also, one could evaluate the maximum pressure:

$$p_M = \max\left\{p(t,x); x \in S, t \in [0,T]\right\} \tag{6}$$

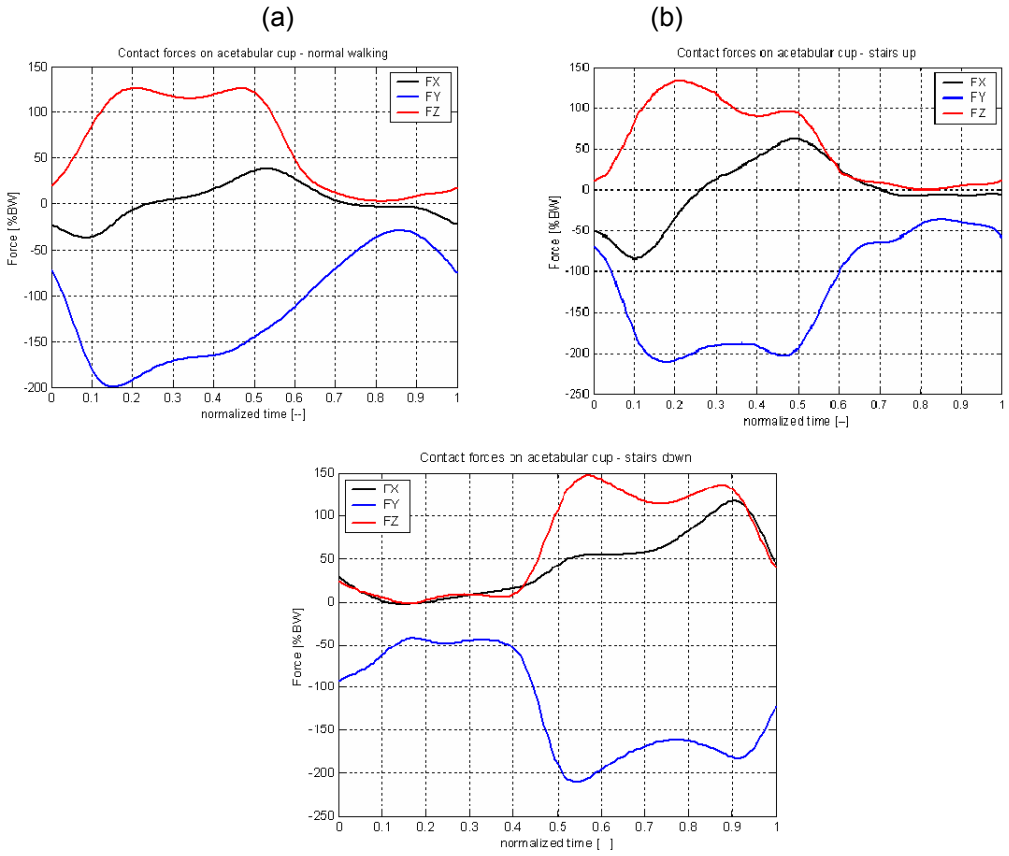

(c)

Fig. 15. Loading time histories for every activity considered in the analyses

Based on previously defined functions we could evaluate the proximity degree of some point on the contact surface to the contact pole (which is the point where the maximum contact pressure could be located) by intermediate of some instantaneous pressure index, given by:

$$\tilde{p}(t,x)=\frac{p(t,x)}{p_m(t)} \tag{7}$$

Also, for each instance of time one could evaluate the level of loading at the frictional interface by intermediate of:

$$\lambda(t)=\frac{p_m(t)}{p_M} \tag{8}$$

One could consider that the wear obey the Archard law [14], the weared volume being given by:

$$V=kPL=\int_0^T k(t)P(t)vdt \tag{9}$$

for a dependency between the wear rate and the interfacial level of loading (given by instantaneous maximum pressure p_m) conforming with that proposed by Wang et al., 2001 [15]:

$$k(t)=Cp_m^n \qquad C=7.99\cdot10^{-6} \qquad n=-0.653 \tag{10}$$

In formula (9) L represents the length of the wearing path corresponding to an active loading cycle, and v is the speed of the relative movement between the frictional parts supposed to be constant and equal with *L* / *T*. The compressive loading between joint contact surfaces is given by:

$$P(t)=\int_S p(t,x)dA \tag{11}$$

It results that, for every activity *i*, the weared volume would be given by:

$$V_i = n_i C \frac{L_i}{T} p_{M,i}^{n+1} \int_0^T \int_S \left(\frac{p_m(t)}{p_{M,i}} \right)^{n+1} \left(\frac{p(x,t)}{p_m(t)} \right) dA dt = \\ = n_i C p_{M,i}^{n+1} L_i \int_S \frac{1}{T} \int_0^T \lambda^{n+1} \cdot \tilde{p}(t,x)\, dt dA = n_i C p_{M,i}^{n+1} L_i \int_S \psi_i(x)\, dA \tag{12}$$

where $\Psi_i(x)$ is a point measure characteristic for each activity.

Practically, one could distinguish three measures of the wear tendency of some interfacial region for a specific activity: the maximum contact pressure, $p_{M,i}$, the length of the wear trace L_i and this measure $\Psi_i(x)$ defined above which also includes the effect of the wear rate dependency on the joint contact level of loading. Obviously, when considering a large spectrum of activities, the total worn volume will be given cumulating the worn volumes specific for each activity considered:

$$V_{total} = \sum_i V_i = \sum_i \left(n_i C p_{M,i}^{n+1} L_i \int_S \psi_i dA \right) = \int_S \left(\sum_i n_i C p_{M,i}^{n+1} L_i \cdot \psi_i \right) dA = \int_S \phi dA \tag{13}$$

where:

$$\phi = \sum_i n_i C p_M^{n+1} L \cdot \frac{1}{T} \int_0^T \lambda^{n+1} \cdot \tilde{p}(t,x)\, dt \tag{14}$$

has the significance of an wearing flux through the joint contact surface corresponding to a spectrum of activities which are defined by their frequency and by the dynamics of loads transfer through the joint (namely, the dynamics of the contact pressure during the relative movement between the joint surfaces). The distribution of Ψ_i on the contact surface for every activity are plotted in Figure 16.

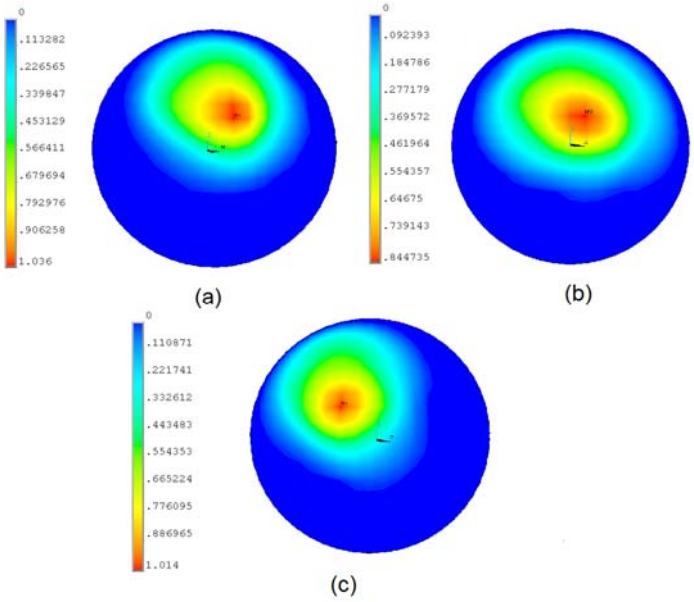

***Fig. 16.* Ψ_i distribution for every analyzed activity: (a) normal walking, (b) stair ascending and (c) stair descending**

One could see that, for normal walking the maximum of this measure of wearing tendency is maximum in the superior-posterior part of the acetabulum, but for stair descending this maximum could be located in the superior-anterior region of the joint surface. Also, for stair ascending, the maxima (with a value lower than for the two activities mentioned above) is located in the neighboring region of the central part of the surface. Anyway, plots of this measure distribution could be useful in determining those regions of the joint surfaces that are likely to be worn during some specific activity. Also, by integrating over entire joint surface one could evaluate the worn volume. Using a special summation technique, we could also delimitate the regions likely to be worn when considering a spectrum of activities. For example, in Figure 17, there are plotted the maps of the wearing fluxes through artificial joint frictional surface considering the summation of all three activities

analyzed also in an unbalanced frequency of occurrence for those activities (as for the real loading pattern for a year, i.e. 2,000,000 cycles for normal walking and 42,000 for stair ascending as for stair descending – see Morlock et al, 2001 [16]) and for a balanced activity regime (an ideal situation when all three activities have the same frequency of 42,000 cycles).

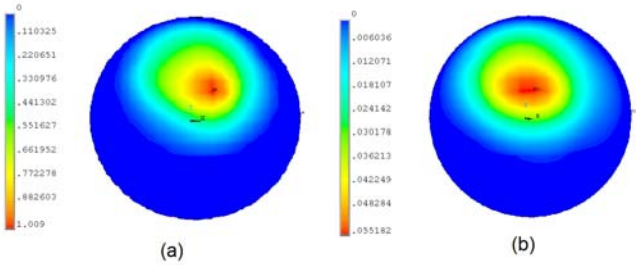

Fig. 17. The wearing flux through the frictional surface (a) for real activity pattern (with an unbalanced frequencies distribution), and (b) an ideal pattern when all activities has the same frequency

Analyzing Figure 16c, one could notice that the regions where the wearing flux is maximum are practically coincident (due to strong disproportion between the frequencies of the activities) with those areas where $\psi_{normalwalking}$ is maxim, the normal walking being the dominant activity. So, the area where the wear is likely to occur is the superior-posterior part of the polyethylene acetabular cup. Even for this kind of activity pattern the method would not be so useful for a more equilibrated activity regime the worn areas could be accurately determined this target being difficult to achieve otherwise.

The results of the predictive study for the real activity pattern are listed in Table 6.

There, for every activity are presented the characteristic parameters (frequency of occurrence, n_i, the length of wear trace L_i, the maximum contact pressure $p_{M,i}$) and the worn volume (per year as well as per megacycle) resulting from integration of the wearing flux over the entire frictional surface is listed. We obtain a predicted wear rate, for the combination of considered activities, of approximately 81 mm^3/Mcycles. This value is bounded by the values obtained experimentally (Table 5.2) i.e. ~ 77.094 mm^3/Mcycle for a normal walking speed on a medium pressure of 1.4 MPa and 142.22 mm^3/Mcycle as corresponding to a medium pressure of 2.1 MPa (the values of pressure bounding the load in the joint). Anyway, the predicted value is higher than experimental wear rates reported by Saikko, 2005 [17] ~ 16.67 mm^3/Mcycle, and Barbour, 1999 [18] ~ 47 $\pm$ 4 mm^3/Mcycle, wear rates obtained on hip joint simulators.

Table 6 Predictive results

Activity (frecvency, n_i)	Wear trace length, L_f (mm)	Maximum contact pressure, $p_{M,i}$ (N/mm^2)	Wear rate
Normal walking (2 Mcyce/year)	28.776	7.925	~ 169 mm^3/year or ~ 81 mm^3/Mcycle
Stair ascending (42 kcyce/year)	33.095	8.670	
Stair desscending (42 kcyce/year)	33.381	9.918	

Based on the results obtained from experimental and numerical previous studies, the authors try to evaluate the wear evolution in the components of a THP, during the service period. Topographic investigations of polyethylene cup and femoral head surfaces, of a modular total hip prosthesis, retrieved after 10 years service period, are made. The aim of this study is to identify the damaging mechanism of a femoral head and his influence on the UHMWPE acetabular cup wear. For this purpose one analyses: the state of surfaces (roughness, micro hardness), surfaces wear type, localization and microscopic investigation of damages, wear mechanism.

4. CONCLUSION

In our paper, we tried to establish a criterion for the success of the acetabular cup fixation by evaluating the short-term stability. The influence of the contact parameters established between the cup and peripheral zone of the acetabulum was investigated. These parameters depend on the intra-operative procedures: the reaming and the fixation. The reaming is considered with no residual stresses but the acetabulum was remodeled (a sphere was fitted by an optimization algorithm). The non-cemented fixation (press-fitting) implies a series of load pulses applied to the cup simulating the impact blows via the surgeon's mallet. As result of FEM simulation analysis and used a model of pelvis based on CT it is obtained a post-operative residual

state of stress. The evaluation of this state of stress conduct to a good estimation of the short-term stability. The maximum stresses in the acetabulum could be used for estimating the bone remodelling around the titanium cup. This is an important phenomenon that could drive to the osteointegration of the implant or to the loosening of it. The value of this stresses is greater than that obtained for a cemented prosthesis.

We identified the path by which the efforts generated in the acetabulum area are transmitted to the neighbouring parts of human skeleton. This path is the line that connects the upper point of pubian symphysis and the lower point of the connection between the iliac bone and the sacrum. The evolution of the iliac bone by in-growth and internal distribution of the material (for trabecular bone) depends on this preferential direction giving to the bone its helical aspect.

To improve the performance of the implant, we use FEM to evaluate the changes induced in the mechanical behavior of the femur by the presence of prosthetic stems implanted by two different methods (cementation and press-fitting).The differences between the two kinds of fixation are revealed by the load transfer pattern between the implant and the bone.

The authors proposed an accurate method for evaluating the osseointegration process following implantation based on some FE analyses of an anisotropic model of bone-implant assembly under a large spectrum of loading generated by most common activities. Evaluating the stress state at the interface between the bone and the implant, one could see that the bone is maximum loaded during stair ascending, followed by stair descending and normal walking (these three activities being considered as dominant). Also, the results reveals that all stress maxima are located at the distal end of the implanted area, for normal walking being laterally, and for stair activities being medially. A good estimator for the osseointegration process was considered the strain energy density (which is also maxim in the distal area, being strongly localized for stair descending activity).

The lifetime of a total hip prosthesis is highly connected to the contact mechanism that occurs in the frictional couple. Using an experimental setup special designed for this purpose we evaluated the behaviour of the frictional couple during an oscillatory movement of the femoral head with two different frequencies corresponding to the normal and accelerated walking. The results show a linear dependence between the frictional coefficient and the contact pressure. Also this coefficient decrease when the speed is increasing. The measurements of gravimetric and volumetric wear rate reveal an exponential variation of that measure with the variation of the contact pressure. Also, the absence of lubricant (physiological serum) doubles the wear rate.

Following the experimental study, a predictive methodology for evaluating the wear of artificial joints due to a large spectrum of activities are presented. The method consists in determining the distribution of some point function considered characteristic for cumulative effect of wear due to different activities. After a theoretical background an application is made considering only three activities: normal walking, stair ascending and stair descending. For each activity, this function is maximized in a different locations: if for normal walking the maxima is in the superior-posterior part of the acetabular cup, for stair descending this maxim value could be located rather in the superior-anterior part, for stair ascending being even closer to the central area of the cup.

Considering the cumulative effect of all activities, one could notice that for an unbalanced pattern of loading (where normal walking has almost 2,000,000 cycles/year, and stair ascending and stair descending only 42,000 cycles/year) that the more frequent activity will dominate the wearing phenomena, the cumulative estimator map being close to that generated by that activity. But, for an equilibrated pattern of activities, a prediction of areas where the wear is likely to occur is hardly possible without the presented methodology.

Finally, based on simple loading characteristics (maximum contact pressure, length of the wear trace due to each activity loading cycle), the worn volume for a year and the wear rate was evaluated by integrating the proposed estimator over the frictional joint surface. The computed value is similar with those obtained experimentally but higher than reported values obtained using hip joint simulators.

ACKNOWLEDGMENTS

The authors would like to thank their colleagues from the Institute of Solid Mechanics of the Romanian Academy and University of Civil Engineering for your material and logistic support.

REFERENCES

1. SPEARS, I.R., PFEIDERER M., SCHNEIDER, E., HILLE, E., MORLOCK, M.M., The influence of friction and interference on the seating of a hemispherical press-fit cup: a finite element investigation. J. Biomech. 1999 Nov, 32(11):1183-9
2. TAYLOR, S.G.J., PERRY, J.S., MESWANIA, J.M., DONALDSON, N., WALKER, P.S., CANNON S.R., "Telemetry of forces from proximal femoral replacements and relevance to fixation", J Biomech, 30, 3, 225-234, 1997.
3. BERGMANN G., DEURETZBRACHER, G., HELLER, M., ROHLMANN, F., STRAUSS, J., DUDA, G.N., Hip contact forces and gait pattern from routine activities, J Biomech, 34, 7, 859-871, 2001.
4. HUISKES, R., WEINANS, H., GROOTENBOER, H.J., DALSTRA, M., FUDALA, B., SLOOFF,T.J., Adaptive bone-remodeling theory applied to prosthetic-design analysis, J Biomech, 20, 12, 1135-1150, 1987.
5. CAPITANU, L., IAROVICI, A., ONISORU, J., POPESCU, M., Tribological behavior of a Total Hip Prosthesis during normal walking active cycle, Proceedings of Balkantrib 05, Kragujevac, Serbia, 317 - 323, 2005.
6. MIYANAGA, Y., FUKUBAYASHI, T., HUROSAWA, H., Contact Study of the Hip Joint: Load Deformation Pattern, contact area, and contact pressure, Arch Orth Trauma Surgery, 103, 13-17, 1984.
7. DAVY, D.T., KOTZAR, G.M., BROWN, R.H., HEIPLE, K.G., GOLDBERG, V.M., BERILLA, J., BURNSTEIN, A.H., Telemetric force measurements across the hip after Total Arthroplasty, *Journal of Bone and Joint Surgery*, 70, 45–50, 1988.
8. DALSTRA, M., HUISKES, R., ODGAAD, A., VAN EARING, L., Mechanical and textural properties of pelvic trabecular bone", J Biomech, 26, 4-5, 523-535, 1993
9. ADLER, E., STUCHIN, S.A., KLUMMER, F.J., Stability of press-fit acetabular cups, J Arthroplasty, 7, 3, 295-301, 1992.
10. SHIRAZI, A., DAMMAK, M., PAIEMENT, G., Experimental determination of friction characteristics at the trabecular bone/porous coated metal interface in cementless implants, J Biomed Mater Res, 27, 2, 167-175, 1993.
11. CAPITANU, L.., The orthopaedical endoprostheses durability, BREN Publishing, Bucharest, 2004, (in Romanian).
12. ONISORU, J., CAPITANU, L., IAROVICI, A., POPESCU, M., A method for predicting the wear of the artificial joints", *J Biomech*, 39, Suppl 1, S141, 2006.
13. LEWIS, G., Properties of cross-linked ultra-high-molecular-weight polyethylene", Biomat., 22, 4, 371 - 401, 2001.
14. ARCHARD,J.F., Contact and rubbing of flat surfaces, J Appl Phys, 24, 438-455, 1953.
15. WANG, A., ESSNER, R., KLEIN, R. Klein., Effect of contact stress on friction and wear of ultra high molecular weight polyethylene in total hip replacement", *Proc Inst Mech Eng (H)*, 215, 133-139, 2001.
16. MORLOCK M., SCHNEIDER, E., BLUHM, A., VOLLMER, M., BERGMANN, G., MÜLLER, V., HONI, M., Duration and frequnecies of everyday activities in total hip patients, J Biomech, 34, 7, 873-881, 2001
17. SAIKKO, V., A 12-station anatomic hip joint simulator", Proc Inst Mech Eng (H), 219, 437-448, 2005.
18. BARBOUR, P.S., STONE, M.H., FISHER, J., A hip joint simulator study using simplified loading and motion cycles generating physiological wear paths and rates", *Proc Inst Mech Eng (H)*, 213, 455-467, 1999.

CORRESPONDENCE

Lucian CAPITANU
Prof., Institute of Solid Mechanics of the Romanian Academy, Bucharest, Romania
e-mail: lucian.capitanu@yahoo.com

Tribological Journal BULTRIB Vol. 5, 2015
Papers from the International Conference **BULTRIB '15**
September 11-13, 2015, Sozopol, Bulgaria
Society of Bulgarian Tribologists
FIT – Technical University of Sofia

ON THE POLISHED STEEL SURFACES WEAR IN LINEAR DRY SLIDING FRICTION CONTACT ON POLYMER COMPOSITES WITH SGF

[1]Lucian CAPITANU
[1]Institute of Solid Mechanics of Romanian Academy, Bucharest, Romania
luciancapitanu@yahoo.com

[2]Virgil Florescu
[2]Technical University of Civil Engineering Bucharest, Romania
florescuvirgil@yahoo.com

Abstract: *It is generally known that the friction and wear between polymers and polished steel surfaces has a special character, the behaviour to friction and wear of a certain polymer might not be valid for a different polymer, moreover in dry friction conditions. In this paper, we study the reaction to wear of certain polymers with short glass fibers (polyamides having 20% and respectively 30% glass fibers and polycarbonate with 30% glass fibers) on different steel surfaces, considering the linear friction contact, observing the friction influence over the metallic surfaces wear. The paper includes also its analysis over the steel's wear from different points of view: the reinforcement content influence and tribological parameters (load, contact pressure, relative slip speed, contact temperature, etc.). Thus, we present our findings related to the fact that the abrasive component of friction force's is superior to the adhesion component, which generally is specific to the polymers' friction. Our detections also state that, in the case of the polyamide with 30% glass fibers, the steel surface linear wear rate ordinal are of 10^{-4} mm/h, respectively the ordinal of volumetric wear rate is of 10^{-6} cm^3 /h. The resulting volumetric wear coefficients are of ordinal (10^{-11} – 10^{-12}) cm^3/cm and respectively linear wear coefficients of 10^{-9} mm/cm*

Key Words: *friction, wear, composite thermoplastics, comparative wearing coefficient*

1. INTRODUCTION

The polymers' behaviour has distinctive characteristics, some of them being described by Bowden and Tabor [1]. The main concept related to the polymers' tribology is composed of three basic elements involved in friction: (i) junctions adhesion, their type and resistance; (ii) materials' shearing and fracture through friction during the contact; and (iii) the real contact area.

Friction's straining component results from the polymer's resistance to "ploughing" made by the asperities existing on the harder counter-face. The polymer's surface asperities bears elastic, plastic and viscous-elastic strains, according to the material's properties. Friction adhesion component comes out of the adhesion junctions formed on the real contact spots between the paired surfaces. Friction adhesion component in what the polymers are concerned is considered to overpass by far the straining component. Special attention should be granted to the transfer films, these transfer films being the key factors determining the tribological behaviour of polymers and polymeric composites. In what the glass fibers reinforced polymer is concerned, we also encounter a strong abrasive component [2].

Several models were developed to describe the contact adhesion. The Johnson-Kendall-Robers (JKR) model, mentioned sometimes as the contact mechanics model [3-4] and the Derjaguin-Muller-Toporov (DMT) model [5] are the best known. The models' comparative analysis [6] shows that the JKR model is applied to bodies with micrometric dimensions and larger than that, with polymer properties, whilst the DMT model is valid for bodies with nanometer dimensions, with metal properties. Accordingly, we will further briefly discuss the JKR model.

The JKR model is based on the hypothesis of an infinite small radius in what the surface forces effect is concerned, that supposed that the interactions take place only in the contact area. The elastic contact between a sphere with an *R* radius and a half of space is analysed by taking into consideration the van der Waals forces, which compresses the bodies paired together, in addition to the applied load. The molecular interaction energy is $W_m = -\pi a^2 \gamma$. The contact rigidity resists to the forces' action. By using the energetic

balance equations, the contact main parameters are being derived, based upon a combination between the hertzian pressure distribution (load) and the Boussinesq distribution. Such a combination produces compression in the middle of the contact and an infinite traction at its edges.

Adhesion's contact *a* radius calculus formula is:

$$a^3 = \frac{R}{K}\left(P + 3\pi R\gamma + \sqrt{6\pi RP\gamma + (3\pi R\gamma)^2} \right) \tag{1}$$

where $K = \frac{4}{3}\frac{1-\nu^2}{E}$ is the elastic constant, *E* is Young's module, and *P* is normal load.

Consequently, it is obvious that, without adhesion (γ = 0) we obtain the Hertz equation, whilst if $\gamma > 0$, the contact area always surpasses the hertzian contact area under the same normal load *P*. We noticed that when the contact is completely discharged (*P* = 0) the adhesion doesn't disappear, but it registers a finite radius:

$$a = \left(6\pi R^2\gamma / K\right)^{1/3} \tag{2}$$

Tis radius may be reduced only by applying a traction load (negative), and then, the contacting surfaces separate at the smallest load corresponding to the radius conversion from equation (4) to zero:

$$P_{pull-off} = -\frac{3}{2}\pi R\gamma \tag{3}$$

This circumstance represents the specific characteristic of JKR model.

Derjaguin was the first (1934) who formulated and almost solved the issue of adhesion contact's elastic strain effect. Subsequently to Derjaguin, Muller and Toporov developed this issue in their researches, resulting in the creation of DMT model which describes the elastic contact of a sphere with a rigid semi-space. This model is based upon the following two postulates: surface forces do not change the strained profile of the sphere and it stays Hertzian; the attraction force acts outside the contact circle pressing the bodies one against the other, the contact area being under compression through the distributed efforts, according to Hertz.

The balance is reached when there is enough strain to have an elastic response (the sphere's elastic annealing force) $F_{e,}$ to counterbalance the effect of the external load *P* applied to the articulation and of the molecular attraction forces F_s:

$$F_e = P + F_s \tag{4}$$

Let's suppose that the attraction is represented by the Lennard-Jones potential. As we known, the profile of the sphere strained outside the contact area for a given r radius is described by the equation:

$$z(r,a) = \frac{1}{\pi R}\left[a\left(r^2 - a^2\right)^{1/2} - \left(2a^2 - r^2\right)\arctan\left(r^2/a^2 - 1\right)^{1/2} \right] \tag{5}$$

to which we add the balance state z_0 (the tolerance within the contact). Then, we calculate molecular attraction force through direct integration:

$$F_s = 2\pi\int_a^\infty p(z + z_0)rdr.$$

Is quite difficult to calculate this integral, but in order to facilitate the use of the respective model there are a series of approximate published formulae. More specifically, there is a simple relation Maugis established between load and approach, obtained for the DMT model conditions [7]:

$$\frac{P}{P_c} = \frac{1}{\sqrt{3}}\left(\frac{\delta}{\delta_c}\right)^{3/2} - \frac{4}{3}, \tag{6}$$

where δ is the elastic shift, $P_c = \frac{3}{2}\pi\gamma R$, $\delta_c = \left(\frac{P_c^2}{3K^2R}\right)^{1/3}$.

The analysis shows that each of these models is valid for certain combinations of bodies' physico-mechanical and geometrical properties. The DMT theory is applicable to those materials which have the point with the coordinates (*K, y*) below the line corresponding to the asperity's (roughness) peak's constant radius representation. In this case *K* represents the reduced materials' rigidity, while in contact, and *y* represents the interface's energy.

Several authors [8, 9-17] studied the polymers' friction on hard surfaces. By using the method of contact's conformity [18] they obtain the hardness, the deformability value (index) (which describes the coarse surfaces' deformation properties), as well as the elasticity module for organic polymers polymethylmethacrylate – PMMA; polystyrene – PS; polycarbonate – PC, ultra high molecular weight polyethylene – UHMWPE. We also describe the dependence of the imposed penetration depth, the maximum load and the straining speed, the hardness and the elastic modulus [19-22]. The typical penetrating depths are included within the approximate 10 nm to 10 μm range, whilst the applied loads are smaller than 300 mN.

We can observe the fact that almost without exception, the ploughing is accompanied by adhesion and in certain conditions it may lead to micro-cutting, which represents a supplementary adding to increase the friction force.

There are other mechanisms to dissipate the energy while straining. For instance, whenever a polymer with viscous-elastic reaction slides on a hard surface, the energy dissipation is caused by the high losses through hysteresis. This straining component is known under the name of friction due to elastic hysteresis [1]. The energy can, as well, be transported further, for instance through elastic waves generated at the interface and coming out at infinit, as, a nucleation and micro-cracks development within the material, consequence [20].

The mechanic component consists in the resistance of the softer material to harder asperities' ploughing. The adhesion component comes of the adhesion links formed between the surfaces during the friction contact. We believe that for polymers the adhesion molecular component exceeds by far the mechanical one [20], and we can explain it through the generated films' transfer on the metal counter-face. We pay special attention to the transfer films, as a key factor determining the polymeric materials' tribological reaction. The following factors considerably affect the friction force: the contact load, sliding speed and temperature. Effects are not independent. For instance, according to the contact load and contact speed, the temperature may considerably vary, changing the friction mode [21].

2. MATERIALS AND METHODS

In order to study the metallic counter-part's wear in dry contact with glass fibeers reinforced plastic materials we use Timken type friction couples (with linear contact), cylinder on plan, which allows us to attain high contact pressures, hence high contact temperatures. In this manner we notice, whether and in which conditions the plastic material transfer on the metallic surface appears, as well as the influence of the glass fibres filling during this phenomenon, and its effect on the surface's wear. As we do not follow the polymer's wear, but only the polymer's friction influence, over the samples' metallic surfaces wear, we use the unidirectional sliding movement.

We perform the tests using experimental equipment containing a Timken type linear contact friction couple, continuously controlling the normal load, friction and contact temperature. The unidirectional movement and the linear contact allow us to attain very high contact pressures and temperatures. We build the friction couple out of a plastic cylinder Nylonplast AVE PA + 30% fiberglass, which rotates at different speeds against the polished surface of a steel plan disc. The cylinder has an outer diameter of 22.5 mm and 10 mm height.

We choose as sample steel disks with 18.2 mm diameter and 3 mm height. We polish the disks' surfaces successively using sandpaper of different granulations (200, 400, 600 and 800) and, finally, we polish them on the felt with diamond paste. We obtain mirror polished surfaces, with roughness R_a of 0.05 μm. This metal surfaces quality allows us to eliminate the influence of the metallic surfaces' state on the friction's coefficient and visualization evolution, to make measurements using optical microscopy and to accurately record the wear traces appeared on the metallic surfaces.

Fig. 1 shows the friction couple and the diagram of the experimental equipement.

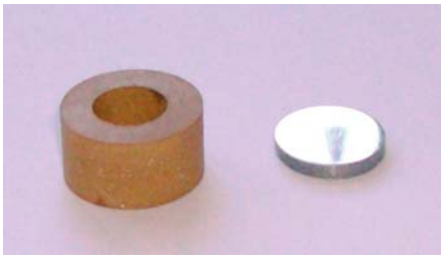

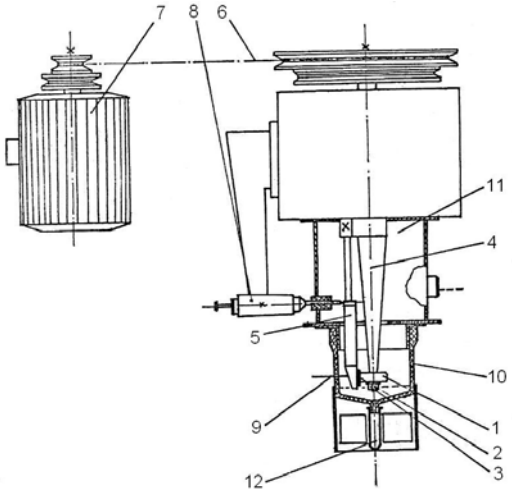

Fig. 1. Friction couple (left) and the experimental equipment (right).

The friction couple is build out of a cylindrical bushing (1) and a plane disk type sample (2). The bushing is fixed with the help of a nut (3) on the driving shaft (4), and the disk sample is placed in a special hole made within the elastic bar (5). We build the sample disk base in such a manner so that the base allows the pastille to make small rotations around the edge of a knife fixed perpendicularly on the driving arbour. In this way we ensure a uniform repartition of the load on the entire bushing width, even if there are small building or assembling imperfections. An electric engine (7) puts the rod (4) into a rotation movement using trapezoidal transmission belts (6). The installation allows us to simultaneously measure the normal and tangential (friction) efforts through resistive converter strain-gauges, assembled on the elastic blade (5). The use of a pair of converters strain-gauges connected within the circuits of two strain-gauges bridges, offers us the possibility to make simultaneous measurements, while separately, gives us the possibility to measure the normal and friction forces. We apply the normal load to the elastic blade (5), through a calibrated arc system (8). The installation allows us to register the friction force on an *X*-*Y* recorder. We control the tests' duration through an alarm clock and we measure the contact temperature with the help of a miniature thermocouple (9), connected to a millivotmeter calibrated in ^{0}C. The installation offers the possibility to study the reaction to wear by using also several other radiometers technics. For this purpose, the installation includes a tank (10) assembled on a base (11) and a tube collecting the wear particles (12). I used the uni-directional testing because the purpose of investigations was the study of metallic surface wear. We perform the tests, based on Hooke's law, at normal loadings of 10; 20; 30; 40 and 50 N, loadings which are adequate to some contact pressures all calculated considering the elastic contact hypothesis, that is: 16.62; 23.51; 28.95; 33.25 and 37.18 MPa (for Nylonplast AVE polyamide with 30% SGF) respectively, we use relative sliding speeds, adequate to the diameter of the plastic composite sample, which are: 0.1856; 0.2785; 0.3713; 0.4641; 0.5570; 1.114 and 1.5357 m/s, and which resulted as a consequence of the band pulleys' primitive diameters.

As we known [21], we may characterise a material's wearing coefficient (percentage) by wearing factor *k*. Archard's relation defines this factor:

$$V_u = kNvt \tag{7}$$

where: *Vu* – the wear's material volume (cm^3); *N* - the test load; *v* - the relative sliding speed; *t* - the test period; *k* – volumetric wearing factor.

By dividing both of this relation's terms (1) by nominal contact area *A*, we obtain:

$$V_u / A = kNvt / A \tag{8}$$

Which means that:

$$h_u = k^* pvt \tag{9}$$

where: h_u - wear's material depth; *p* - the pressure on the nominal contact area and k^* is the linear wearing factor. Relation (9) expresses a general law of the wear as function of the contact pressure *p* and the length of the wearing path, so that $L_f = vt.$

Friction and wear processes were analyzed for a relatively wide range of tribological parameter values that affect it (load, relative speed, contact temperature). Range of values used for the parameters mentioned include both values commonly encountered in industrial applications, as well as some extreme values, less common, but that are of interest from the point of view of the friction and wear mechanism. Thus, although the values of the stresses and the speeds some parts made of thermoplastic materials usually work are between 0.2 – 1 MPa and respectively 1 – 500 cm/s, attempts were made at speeds and loads greater than or less than the ranges mentioned.

The two elements of friction couples (cylindrical liner and flat sample) were made of plastic material and metal, respectively.

The metallic elements of the examined couples were made of steels of different qualities and with different surface states. Of tested steels only a few qualities widely used in industrial practice have been selected for presentation.

For friction and wear tests polyamides and polycarbonates were selected from the wide range of thermoplastic materials processed in industry, in view of their increased reinforcing possibilities with glass fibers, and high density polyethylene because of its use as a replacement of metals in some practical applications. Experimental tests have been conducted using polyamides and polycarbonates reinforced with 20% and 30% of glass fibers.

We tried to present in this paper a global tribological aproach of friction dry contact polymer with SGF on steel, in terms of consequences on metallic surface condition (comparative wear coefficients of steel surfaces).

To illustrate the method of working, in Table 1 is the representation of the experimental tests results, testing two friction couples, for one of the 8 different relative sliding speeds used.

Table 1. The results of the experimental tests performed in order to determine the wear rate of metallic surface. Friction couple: Nylonplast Polyamide + 30% SGF / C120; v = 18,56 cm/s; t = 1 hour.

N (N)	Width of wear imprint l (mm)			l_1^2 (mm^2)	l_2^2 (mm^2)	l_3^2 (mm^2)	Mean wear rate	
	l_1 (mm)	l_2 (mm)	l_3 (mm)				h_{mu} (10^{-4} mm/h)	V_{mu} (10^{-6} cm^3/h)
10	0.208	0.304	0.307	0.090	0.9316	1.365		
10	0.307	0.204	0.318	0.096	0.9982	1,410	0.9649	0.1387
20	0.472	0.489	0.484	0.232	2.4409	4.386		
20	0.478	0.489	0.491	0.239	2.5187	4.423	2.4798	0.4404
30	0.592	0.641	0.703	0.418	4.4392	8.804		
30	0.658	0.595	0.497	0.345	3.6281	7.958	4.0336	0.8381
40	0.662	0.736	0.701	0.490	5.1708	12.743		
40	0.658	0.785	0.770	0.547	5.8041	13.432	5.4874	1.3086
50	0.851	0.757	0.877	0.689	7.3135	18.844		
50	0.788	0.789	0.854	0.662	7.0135	18.502	7.1635	1.8667

Table 1 shows the results of the tribological experimental tests, e.g. the mean values of the wear imprint depth h_u (10^{-4} mm), and the average values of the worn material volume V_u (10^{-6} cm^3). The average width lm represents the arithmetical average calculated based upon 3 measured values of the wear trace's width. By dividing h_u and V_u to the duration of experimental test, the values of the wear rate in terms of mean depth h_{mu} (10^{-4} mm/h) and volume V_{mu} (10^{-6} cm^3/h) are obtained.

Increasing the friction coefficient increases the wear rate, but no one managed to establish a mathematical relation between the two quantities, although this is widely recognized. In the following we shall give some suggestive graphical representations that make a qualitative correlation between the two quantities, and tying them to the contact temperature.

The influence of load on the friction coefficient of the Nylonplast AVE PA + 30% glass fibers/ C120 steel couple is shown in Figures 1 and 2, for Timken type couples (with linear contact), at the sliding speed of 18.56 cm/ s.

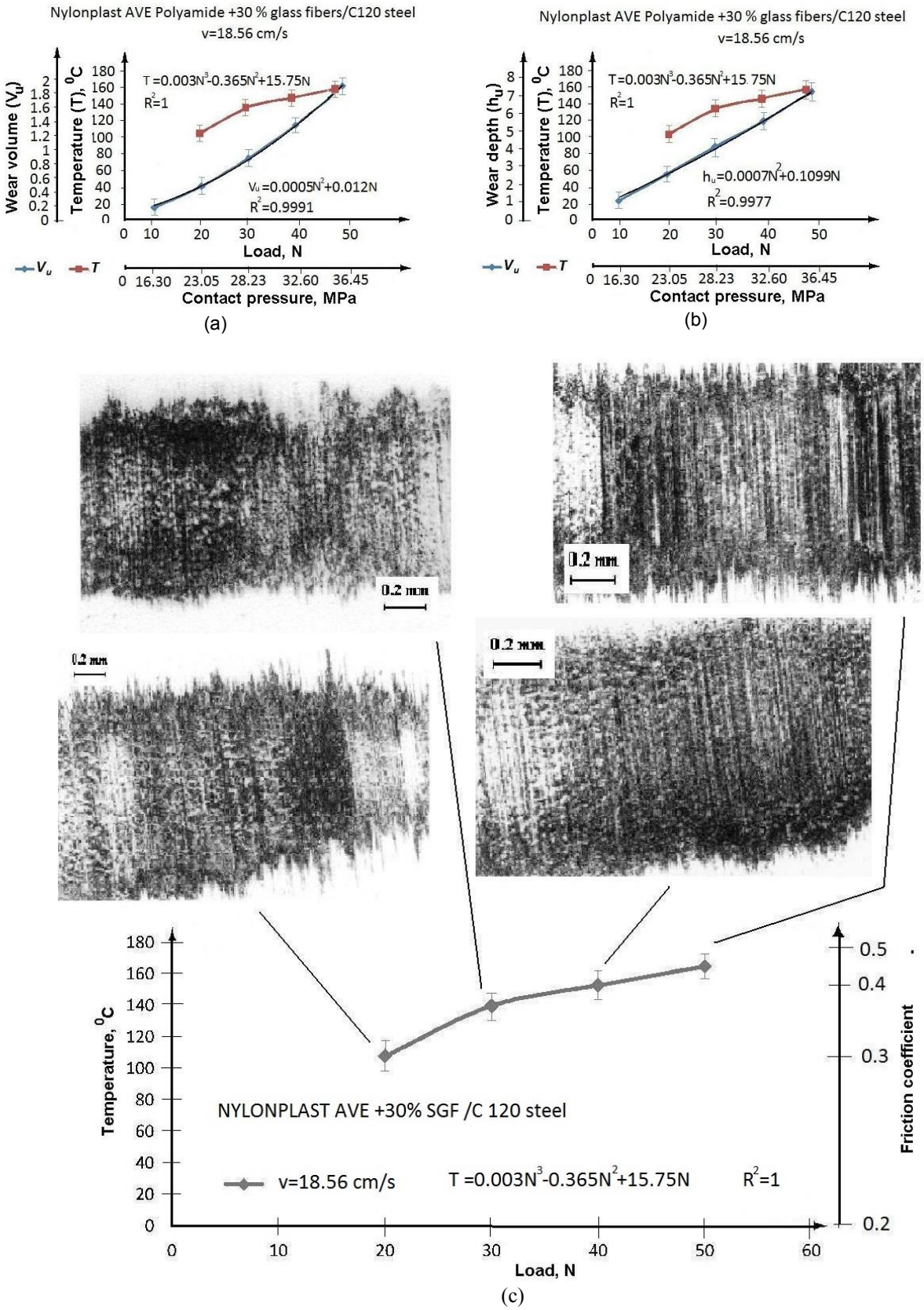

Figure 1. Wear evolution as scar wear volume (a) and depth (b) function of the normal load and contact temperature and variation of contact temperature (c) function of the normal load and friction coefficient at the sliding speed of 18.56 cm/s for Nylonplast AVE Polyamide + 30% SGF / C120 steel

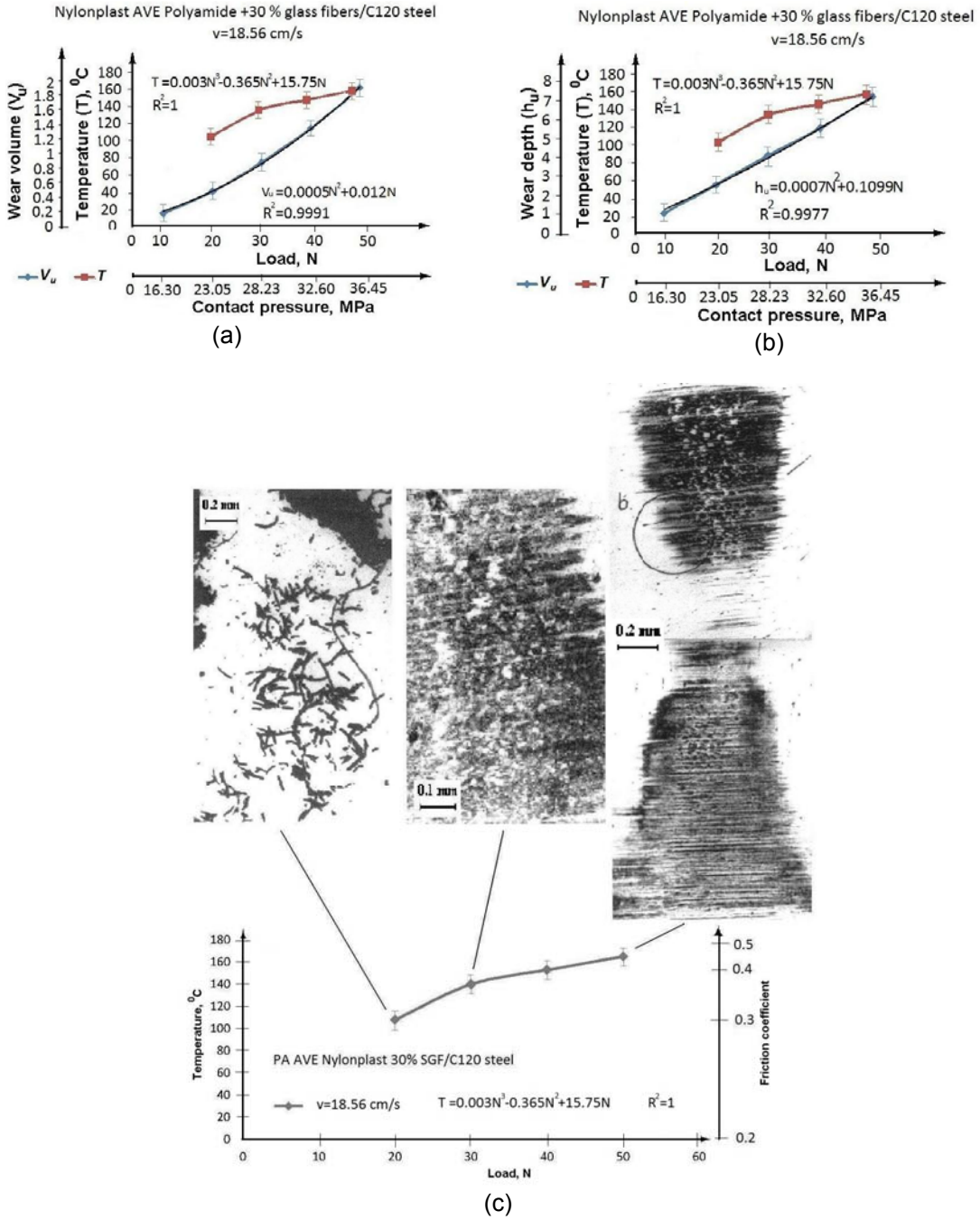

Figure 2. Wear evolution as scar wear volume (a) and depth (b) function of the normal load and contact temperature and variation of wear mode (c) depending of the contact temperature and normal load, at sliding speed of 18.56 cm/s for Nylonplast AVE Polyamide + 30% SGF / C120 steel

All presented tests lasted 1 hour, so all wear data represent the wear rate, expressed in cm^3/h and mm/h. Quantitative data regarding the wear rates have been presented in detail elsewhere [22].

We chose to present two figures in order to illustrate suggestive qualitative aspects regarding the pulling of fiberglass filler from the plastic material matrix, of the beginning of plastic material transfer, initially on the boundary of the wear defect and then within it. The curves in figures (a) and (b) show, as expected, the increase of the wear rate both as volume and depth, at the increase of the normal load (contact pressure), concomitant with the increase of the contact temperature. The increase of the contact temperature occurs as a result of the increase of the friction coefficient.

In this paper are presented only the variation curves of the wear rates (wear volume and wear depth) in parallel with the contact temperature variation measured during the tests - diagrams marked with (a) and (b) from the top of the figures, depending on normal load and contact pressure, respectively. For a complete image of the wear process, on the bottom of the figures, denoted by (c), are the variation curves of contact temperature and friction coefficient function of the normal load, indicating by optical micrographs some

characteristic images of the wear defects. We have adopted this quantitative - qualitative manner of presentation to highlight the complexity of friction - wear process and its evolution over time.

At this sliding speed the dry friction coefficient on C120 steel has values between 0.27 and 0.37, the contact temperature ranging between 108 ^{0}C and 165 ^{0}C. In the case of friction on C120 steel, dry friction coefficient values (Figure 2) are between 0.25 and 0.38, the contact temperature ranging between 78 ^{0}C and 155 ^{0}C. It should be noted both the polynomial variation of the friction coefficient, and of the wear rate (both in volume and depth), depending on load (contact pressure).

At the onset of friction process (temperature around 100 ^{0}C) glass fibers are ripped from the array of plastic and expelled on the surface of steel with plastified polymer (left). Around the contact temperature of 140 ^{0}C the transfer of the polymer occurs on the output of all of the wear (center), at a temperature of 160 ^{0}C to protect the cross-bridges of polymer (right) that interrupt the direct contact of the composite sample with a metallic surface.

At same slidind speed, in the case of friction on steel Rp3, dry friction coefficient values (Figure 3) are ranging between 0.25 and 0.38 and contact temperature ranging between 81 ^{0}C and 155 ^{0}C.

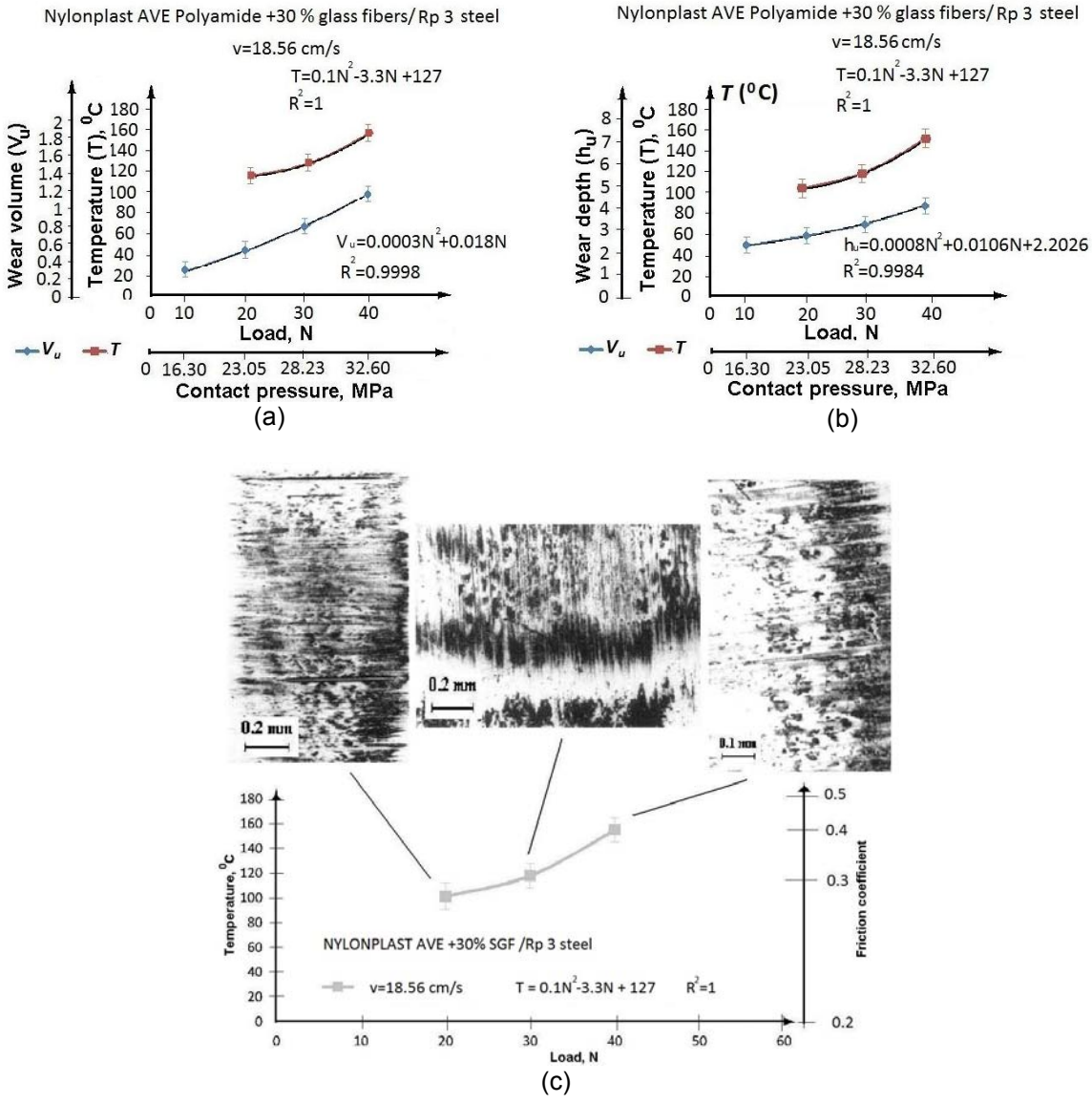

Figure 3. Wear evolution as scar wear volume (a) and depth (b) function of the normal load and contact temperature and variation of contact temperature (c) function of the normal load and friction coefficient at the sliding speed of 18.56 cm/s for Nylonplast AVE Polyamide + 30% SGF / Rp3 steel

It is remarked the same polynomial increase of the friction coefficient, of the wear speed, and of the contact temperature with the normal load, but the wear rate increases from $0.2136 \cdot 10^{-6}$ cm^3/h to $1.1247 \cdot 10^{-6}$ cm^3/h and from $2.3815 \cdot 10^{-4}$ mm/h, to $3.9708 \cdot 10^{-4}$ mm/h, respectively, at the increase of

the normal load from10 N to 40 N.

Increasing of the wear rate is lower than in the case of contact against C120 steel, this probably due to higher hardness of Rp3 steel.

Also, in Figure 3 (c) it can be seen the corrosion wear (top left), the transfer of the plastic material encompassing glass fibers removed from the matrix (top center) and adhesion traces on the wear defect (top right).

From Eq. 8 it could be written:

$$k = V_u / Nvt = V_u / NL_f \tag{10}$$

and from Eq. 8 it could be written:

$$k = V_u / Nvt = V_u / NL_f \tag{12}$$

Considering the large area of the load (*N*) or pressure (*p*) and the relative speed values used during tests in order to evaluate the wear reaction of the metallic counter-pieces of the frictional couples, are used comparative wear coefficients *K* (volumetric) and *K** (linear), defined by:

$$K = V_u / L_f = kN \ (\mathrm{cm}^3 / \mathrm{cm}), \tag{13}$$

and

$$K^* = h_u / L_f \ (\mathrm{cm} / \mathrm{cm}). \tag{11}$$

These wear coefficients are considered with respect to the duration in which the frictional couple functions at different sliding speeds, under certain loading conditions (contact pressure).

The main objectives of these tests are the determination of the volume of material removed by wear, the mean depth of the worn layers, the frictional factors and coefficients, for different loading conditions.

Coefficients *k* and *k** are coefficients of the wear process, while the comparative factors *K* and *K** are coefficients of this process's consequences, that is, the amount of resulted wear and reported to the length of the friction pathway.

They can be qualitatively expressed in units of wear volume on a measure of the length of the friction pathway (cm^3 / cm), as wear's depth on a measure of the length of the friction pathway (cm / cm) or as wear's weight on a measure of the length of the sliding friction pathway (mg / cm). Coefficients *K* and *K** have no mathematical implication (can not simplify).

Based on the results of experimental tests have been traced the curves of variation of comparative wear coefficients. In Figure 4 are presented the variation curves for comparative wear coefficient for polyamide Nylonplast AVE with 30% SGF in dry friction on the C120 and Rp3 steels, depending on the sliding speed.

In Figure 5 are presented the variation curves for comparative wear coefficients *K* and *K** for polyamide Nylonplast AVE with 30% SGF in dry friction on the C120 and Rp3 steels, depending on the sliding speed.

For an overview of comparative wear coefficients, in Table 2 we summarized the equations of the variation curve of comparative wear coefficient for all tested friction couples

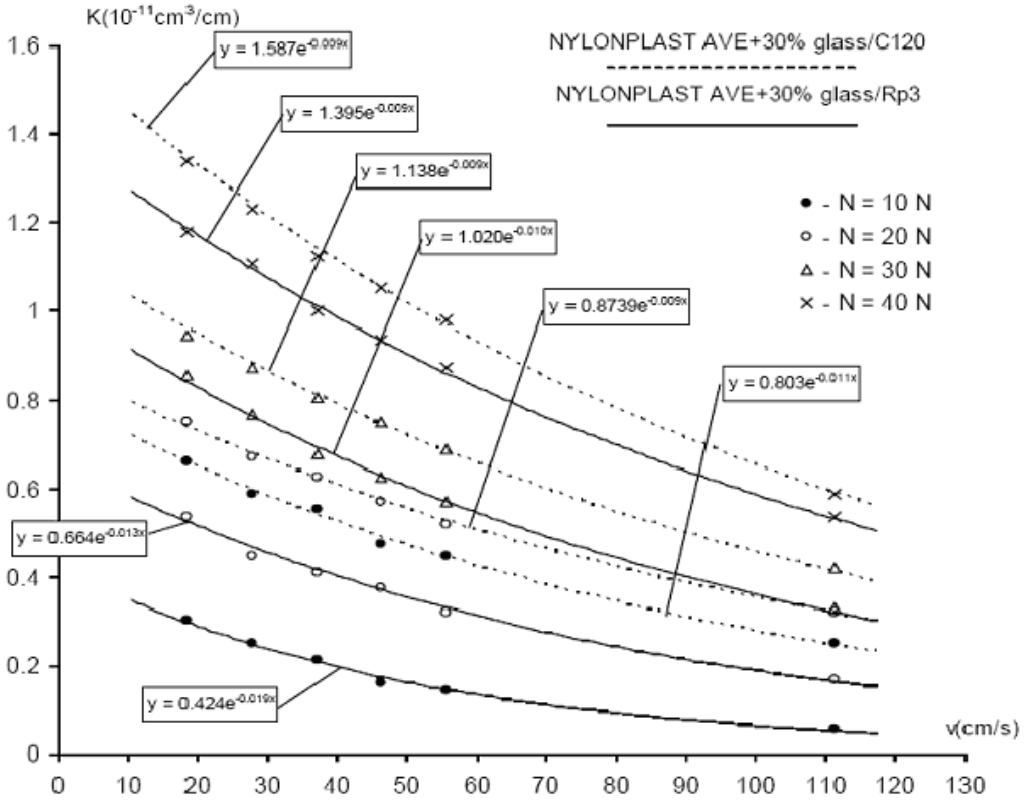

Fig. 4. The variation curves of the volumetric comparative wear coefficients K (cm^3/cm) vs. sliding speed to friction couples Nylonplast AVE + 30% SGF on C120 and Rp3 steels

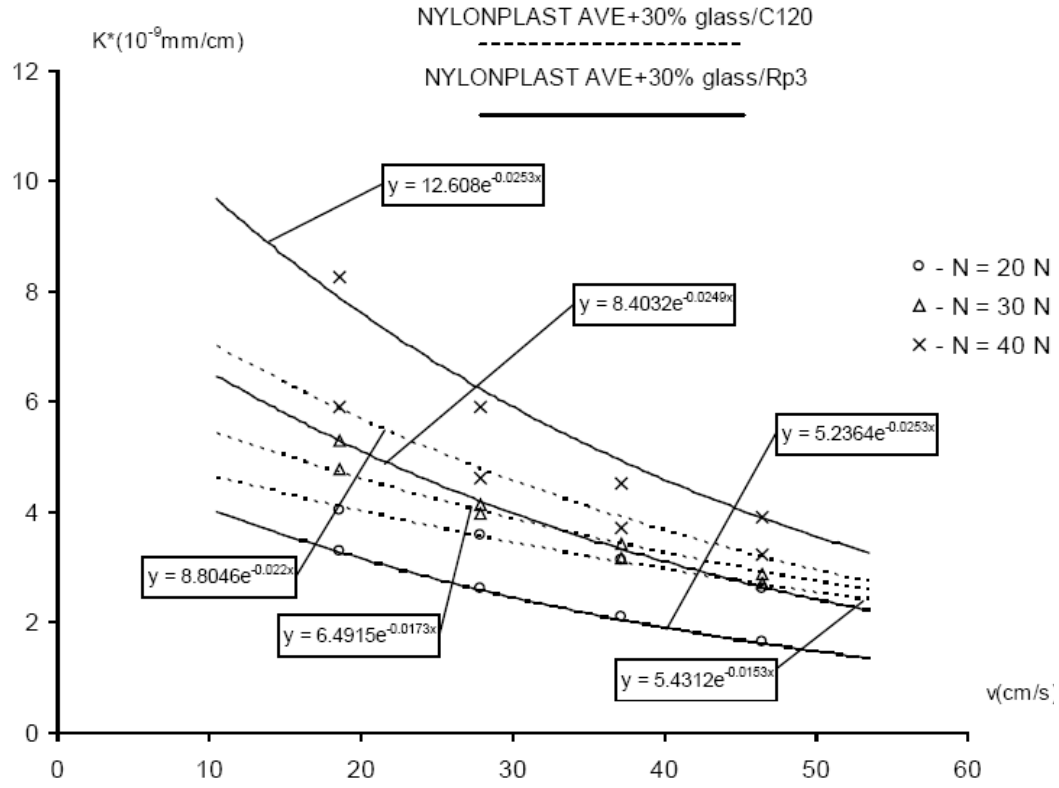

Fig. 5. The variation curves of the linear comparative wear coefficients K* (mm/cm) vs. sliding sped to friction couples Nylonplast AVE + 30% SGF on C120 and Rp3 steels.

Table 1. The variation curve of comparative wear coefficient for all tested friction couples

Friction couple	Load (N)	Comparative wear coefficients equatios	
		K	K^*
Nylonplast AVE polyamide + 30% SGF on C120 steel	10	$K = 0.8030\ e^{-0.0110\ v}$	
	20	$K = 0.8739\ e^{-0.090\ v}$	$K^* = 5.4312\ e^{-0.0153\ v}$
	30	$K = 1.1380\ e^{-0.090\ v}$	$K^* = 6.4915\ e^{-0.0173\ v}$
	40	$K = 1.1380\ e^{-0.0190\ v}$	$K^* = 8.8046\ e^{-0.0070\ v}$
Nylonplast AVE polyamide + 30% SGF on Rp3 steel	10	$K = 0.4240\ e^{-0.0190\ v}$	
	20	$K = 0.6540\ e^{-0.0130\ v}$	$K^* = 5.2346\ e^{-0.0053\ v}$
	30	$K = 1.0200\ e^{-0.0100\ v}$	$K^* = 8{,}4032\ e^{-0.0049\ v}$
	40	$K = 1.3950\ e^{-0.0090\ v}$	$K^* = 12.6080\ e^{-0.0053\ v}$
Noryl polyamide + 20% SGF on C120 steel	10	$K = 1.5024\ e^{-0.0012\ v}$	$K^* = 3.8934\ e^{-0.0097\ v}$
Noryl polyamide + 20% SGF on Rp3 steel	10	$K = 1.7070\ e^{-0.0120\ v}$	$K^* = 4.4259\ e^{-00980\ v}$
Lexan polycarbonate + 20% SGF on C120	10	$K = 0.4455\ e^{-0.0250\ v}$	$K^* = 6.3660\ e^{-0.0018\ v}$
	20	$K = 0.9988\ e^{-0.0247\ v}$	$K^* = 7.1108\ e^{-0.0030\ v}$
	30	$K = 1.4396\ e^{-0.0211\ v}$	$K^* = 6.8809\ e^{-0.0065\ v}$
	40	$K = 2.2425\ e^{-0.0244\ v}$	$K^* = 7.2365\ e^{-0.0044\ v}$
	50	$K = 3.0600\ e^{-0.0256\ v}$	$K^* = 7.0065\ e^{-0/0004\ v}$

3. CONCLUSION

The diagrams' analysis plotted in Figs. 4 and 5 allows to establish the variation equations for the comparative volumetric wear coefficient K and for the comparative depth wear coefficient K^*, for steel in linear contact, while in friction with glass reinforced thermoplastics.

The equations listed in Table 1 for the comparative wear coefficients (the volumetric and the depth ones) show that the variation is not a linear one, these coefficients evolving exponentially.

The decrease of the K^* coefficient with the increase of relative speed is faster than the decrease of the K coefficient. It is considered that this effect is due to the fact that the thermoplastic material deforms under load which means that for Timken type couples the increase of the wear imprint width is more effective than that of the depth of the wear imprint.

From the diagrams plotted here, one can notice that the values of wear coefficients for the metallic component of the couple glass reinforced thermoplastic/steel are in the domain $(10^{-11} \div 10^{-12})$ cm^3/cm and respectively 10^{-9} mm/cm.

The comparative wear coefficients and their master - curves vs. relative speed have a special importance from the practical point of view. Based on these findings we can establish an optimal couple of materials from the design phase.

ACKNOWLEDGMENTS

The authors would like to thank the Institute of Solid Mechanics of the Romanian Academy and Civil Engineering University, for its material and technical support offered in order to achieve these researches

REFERENCES

1. BOWDEN F.P., TABOR D. *The Friction and Lubrication of Solids*, part I-II, Clarendon Press,Oxford,1964.. B. J. Briscoe, in: *Friction and Wear of Polymer Composites*, Ed. F. Klaus (Elsevier, Amsterdam, 1986), p. 25.
2. BRISCOE, B. J. in: *Friction and Wear of Polymer Composites*, Ed. F. Klaus (Elsevier, Amsterdam, 1986), p. 25.
3. JOHNSON, K. L., KENDALL, K., ROBERTS A. D. Surface Energy and the Contact of Elastic Solids. Proc. Roy. Soc. A324, 301 (1971).
4. JOHNSON, K. L., *Contacts Mechanics,* (Cambridge University Press, Cambridge, 1987).
5. DERYAGIN, B. V., MULLER, M., TOPOROV, Yu. P. Adhesive Contact Deformation of a Single Microelastic Sphere. *J. Colloid Interface Sci.*, **53**, 314 (1975).
6. JOHNSON, K. L., GREENWOOD, J. A. An Adhesion Map for the Contact of Elastic Spheres *J. Colloid Interf. Sci.*, **192**, 326 (1997).
7. MAUGIS, D., Adhesion of spheres: The JKR – DMT transition using a Dugdale model. *J. Colloid Interf. Sci.*, **150**, 243 (1992).

8. KRAGELSKII, I. V. *Friction and Wear* (Pergamon Press, Elmsford, 1982).
9. MYSHIN, N. K., KOVALEV, A. V. Adhesion and Friction of Polymers, in *PolymerTribology*. Imperial College Press, London, 2009.
10. STARZHYNSKY, V. E., FARBEROV, A. M., PESETSKII, S., OSPIENKO, S. A., BRAGINSKY, V. *Precision Plastic Parts and Their Production Technology*, (Nauka I Tekhnika, Minsk, 1992) (in Russian).
11. BRISCOE B. J. Wear of polymers: an essay on fundamental aspects. *Tribology Int.,* **14**, 231, (1998).
12. JINTANG, G. Tribochemical effects in formation of polymer transfer film. *Wear*, **245**, 100 (2000).
13. UNAL H., SEN, U., MIMAROGLU A. Friction and wear behavior of unfilled engineering thermoplastics. 183–187. *Tribol. Int.*, **37**, 727 (2004).
14. UNAL, H., MIMAROGLU A. Sliding friction and wear behaviour of polytetrafluoroethylene and its composites under dry conditions. Mater. Des., 24 (2003), 239–245*Mater. Des.*, **24**, 183 (2003).
15. CHEN, Y. K., MODI, O. P., MHAY A. S., CHRYSANTHOU, A., O'SULLIVAN/ The effect of different metallic counterface materials and different surface treatments on the wear and friction of polyamide 66 and its composite in rolling–sliding contact. *Wear*, **255**, 714 (2003).
16. SCHWARTZ, C. J., BAHADUR, S. The role of filler deformability, filler–polymer bonding, and counterface material on the tribological behavior of polyphenylene sulfide (PPS). *Wear*, **251**, 1532 (2001).
17. XU, Y., XU, M., MELLOR, B.G. The effect of fillers on the wear resistance of thermoplastic polymeric coatings. *Wear*, **251**, 1522 (2001).
18. BRISCOE, B. J., FIORI, L., PELILLO. Nano-indentation of polymeric Surfaces. *J. Phys. D: Appl. Phys.*, **31**, 2395 (1998).
19. SHULGA, H., KOVALEV, A., MYSHKIN, N., TSUKRUK, V. V. Some aspects of AFM nanomechanical probing of surface polymer films. *European Polymer Journal*, **40**, 949 (2004).
20. KOVALEV, A., SHULGA, H., LEMIEUX, M., MYSHKIN, N., and TSUKRUK, V. V. Nano-mechanical probing of layered nanoscale polymer films with atomic force microscopy. *J. Mater. Res.*, **19**, 716 (2004).
21. BARTENEV, G. M., LAVRENTIEV, V. V. *Friction and Wear of Polymers*, (Elsevier, Amsterdam, 1981).
22. CAPITANU, L. Capitanu, IAROVICI, A., ONISORU, J. *On polyamide and polycarbonate materials behaviour under dry friction*, The Annals of University "Dunarea de jos" Galati, fascicle **VIII**, Tribology, 2003, ISSN 1221-4590

CORRESPONDENCE

Lucian CAPITANU
Institute of Solid Mechanics of Romanian Academy, 15 Constantin Mille, Bucharest, Romania
e-mail: lucian.capitahu@yahoo.com

Tribological Journal BULTRIB Vol. 5, 2015
Papers from the International Conference **BULTRIB '15**
October 29-31, 2015, Sofia
Society of Bulgarian Tribologists
FIT – Technical University of Sofia

ASPECTS OF LOOSENING DYNAMICS OF TOTAL HIP PROSTHESIS

[1]Lucian CAPITANU
[1]Institute of Solid Mechanics of Romanian Academy, Bucharest, Romania
luciancapitanu@yahoo.com

[2]Virgil Florescu
[2]Technical University of Civil Engineering Bucharest, Romania
florescuvirgil@yahoo.com

Abstract: *We report on scratch resistance of femoral heads made of Co-Cr-Mo and Ti-6Al-4V alloys retrived during the revision surgery and the evolution of the surface state influence on the acetabular cups wear. This work points out that TiN protective coatings deposited by PLD technique with 20,000 pulses can represent an alternative technology to ensure adhesion and scratch resistance of TiN coatings. The success condition for such coating is to provide an optimal surface roughness of femoral head that serves as substrate for TiN coating.*

Key Words: *total hip prosthesis, femoral head wear, surface coatings, TiN, PLD.*

1. INTRODUCTION

Total hip prosthesis (THP) is the most success of the 20th century in orthopaedic biomedical engineering. If the insurance process of primary and secondary mechanical stability of THP takes less, stability loss of THP is a dynamic process that takes place throughout the life of the prosthesis. It depends on mechanical stress, movements and heat [1] that support artificial hip joint, bone-cement and cement-stem interfaces strength for cemented stems [2], on the growth of bone inside for uncemented stems [3], porous coatings efficiency of femoral stems [4] and acetabular shells, and on the resistance to wear of femoral stems, acetabular cups and femoral heads of THP [5]. The most successful orthopaedic device proves to be a progressive bio-tribo-system due to request bills action and hostile environment specific to the human body. Co-Cr-Mo and Ti-6Al-4V alloys are the most used materials for femoral heads. With all the technological advances (coatings with mono or multi-thin films) femoral head damage remains a major problem in the THP.

This paper refers to the wear and scratching resistance of the femoral heads. Taking into account only the matting areas without deep scratches, R_a values 3 - 4 times higher were recorded. This increase in average roughness value leads to scratching of the inner surface UHMWPE of the acetabular liner, which adhere on the protective titanium nitride (TiN) coatings of Ti-6A-4V femoral heads. Hostile environment from the human body makes every crack on the TiN coating surface to become a focal point for development of tribo-corrosion, which finally leads to spalling of thin coatings areas and, in this way, to the formation of many particles that become embedded in the inner surface of the acetabular cup. In this way, the lubrication, supposed boundary or mixed, from the femoral head and acetabular cup is compromised. Ti and its alloys are resistant to corrosion [6] and represent biocompatible materials widely used in orthopaedic implants because of their light weight and low elastic modulus [7]. However, the use of these materials in joint implants is limited by their high coefficient of friction and poor wear resistance. In order to improve their tribological properties, these materials have been submitted to surface modification treatments. Since TiN are hard biocompatible materials [7, 8, 9] of excellent abrasion resistance, many advanced processing methods have been developed aiming the production of a nitrided layer on the materials surface. In plasma nitriding [10], nitrogen atoms diffuse into the Ti matrix thus forming a top layer of TiN and Ti_2N compounds followed by a deeper diffusion layer. This layered structure produces a continuous hardness profile thus providing an adequate support of the protective layer [8, 11]. The physical properties of the treated surface, however, depend strongly on the plasma technique and processing parameters. The excellent corrosion resistance of the Ti alloys results from the formation of a very stable protective oxide film strongly adhered to the metal surfaces [12]. The wear and corrosion resistance of TiN, on the other hand, may be affected by its structural defects (pinholes, pores and small cracks) [10]. In fact, Meletis et al [13] showed that an adequately defect-free and

dense structure of the TiN film can improve considerably the wear and corrosion resistance. The present work contributes to the investigation of how plasma nitriding affects the wear, scratching and corrosion behaviour of the Ti-6Al-4V alloy. The main differences to previous studies on this subject concern the nitriding and scratch resistance testing conditions.

In present work we report on the synthesis of thin films on steel substrates by pulsed laser deposition (PLD) method for improving the general performances and in particular the mechanical characteristics of the structures. The films were grown in reactive atmosphere using a TiN target. The substrate temperature during depositions was kept at 500 ^{0}C. Our samples were nitrided in a pulsed plasma reactor containing a gaseous nitrogen and wear and adhesion resistance of the coating on the sublayer was evaluated by scratching tests accompanied by Fourier Transform Infrared (FTIR) Spectroscopy, X-ray Diffraction (XRD), Optical Microscopy (OM), Scanning Electron Microscopy (SEM), Atomic Force Microscopy (AFM) and scratch tests.

FTIR investigations proved the stoichiometric transfer of the material. XRD diffractograms showed that TiN coatings were polycrystalline, exhibiting reflections assigned to B1 cubic structure of TiN. We measured for the best TiN films by f(ψ) method high values (-10 to -13 GPa) of residual compressive stress. Using AFM, surface tribological parameters, such as maximum and minimum height, average roughness, surface skewness, were inferred. Graphic variation curves of scratch depths, depending on the applied normal loads were drawn. The surface of the sublayer did not present dislocations or other major structural defects. The increase of the surface hardness of the deposited TiN layer in respect with the thickness is discussed.

2. MATERIALS AND METHODS

2.1. PLD experiments

PLD experiments were conducted inside a stainless steel deposition chamber using a KrF* excimer source (λ = 248 nm, $\tau_{FWHM} \approx$ 25 ns, ν = 10 Hz). Cylindrical samples (22.5 mm in diameter and 10 mm in height), made of 316L stainless steel, with hardness of 150 HV_{30} were used as substrates. Depositions were made into deposition chambers (Fig. 1), with Stainless steel reaction chamber (Fig. 2) to 5000, 10000 and 20000. The laser fluence was ~ 5 J/cm^2, at an energy of 500 mJ. The target-substrate separation distance was of 5 cm. The TiN target was ablated in a dynamic flux of N_2 constantly controlled using an MKS 400 mass flow controller. The pressure inside the deposition chamber was ~ 2x10^{-3} Torr. In order to eliminate the micro-impurities, the steel substrates were cleaned using a laboratory procedure previously described. During the deposition, the substrates were heated and maintained at 500 ^{0}C. In Fig. 1 is represented the PLD experimental set-up.

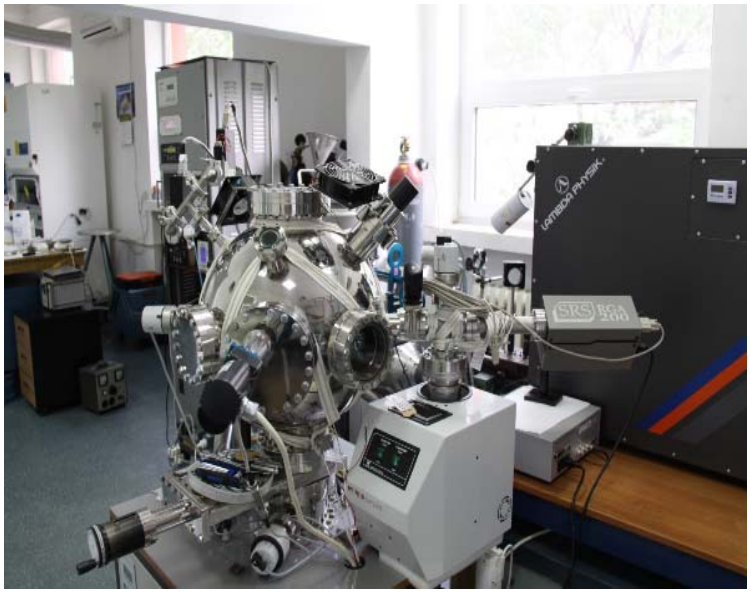

Fig. 1. Deposition Chambers

Fig. 2. Stainless steel reaction chamber

2.2. Characterisation of deposited thin films

Microstructure of TiN layers deposited by PLD was investigated using Grazing Incidence X - rays diffraction (GIXRD) technique.

Using a small incidence angle, this technique allows obtaining information from a small volume adjacent to the sample surface, the analyzed layer diffraction intensity being higher than that of conventional techniques. Therefore, the influence of substrate is reduced. Also, very important when analyzing films tension is the fact that the investigated depth remains relatively constant throughout the analysis interval.

Diffraction measurements were performed with Cu Kα radiation on Rigaku Ultima IV apparatus, equipped with parallel optics and vertical θ-θ goniometer. Divergence angle of the beam emitted by means of the multilayer mirror is about 0.05^0. This type of optics is suitable for thin films analysis, especially for measurements of residual stresses, due to strong beam's intensity and significantly reduction of the instrumental errors (position of diffraction lines is out of phase, shape and width of diffraction lines profiles are retained even at large angles of inclination) [15]. The diffractograms were purchased at a fixed angle of incidence $\alpha = 1^0$, in the angular range 2θ of 34^0 - 105^0, with step acquisition of 0.02^0 and counting time per step of 10s.

To determine the instrumental contribution, required for Rietveld analysis, it was used the standard material NIST SRM 660a - LaB_6. Diffractogram of standard material was acquired under the same conditions as the samples analyzed.

Microstructural analysis was performed with the help of FullProf specialized software developed by Juan Rodríguez-Carvajal that allows Rietveld analysis of the entire spectrum of diffraction. For modeling physical profile, pseudo-Voigt TCH function was used [16] which include Finger correction of axial divergence [17]. Determination of residual stresses was made using GIXRD. Assuming that the sample is subjected to biaxial tension with rotational symmetry ($\sigma_{11} = \sigma_{22} = \sigma_{\parallel}$, without dependance of φ, $(\sigma_{\perp} = 0)$, without shear stresses), condition usually satisfied in the case of thin films, dependence of the elastic deformation of the crystal lattice on the angle ψ can be expressed by the law $\sin^2\psi$ [18]:

$$\varepsilon_{\psi}^{hkl} = \left(2S_1^{hkl} + \frac{1}{2}S_2^{hkl}\sin^2\psi\right)\sigma_{\parallel} \tag{1}$$

where S_1^{hkl} şi S_2^{hkl} are elastic constants of the material. In this study, these were calculated starting from single crystal elastic constants [19] and using the elastic interaction model of Reuss crystallites.

In the case of residual stresses analysis at grazing incidence, there are measured absolute positions of all diffraction lines *hkl*, corresponding to the respective phase, presented in diffractogram.

The angle of inclination ψ for crystalline planes *hkl* is given by:

$$\psi = \theta^{hkl} - \alpha \tag{2}$$

where θ^{hkl} is Bragg angle, and α is the constant angle of incidence. For $f(\psi)$ method [20], elastic constants are included directly in construction of stress dependence on elastic deformation of crystalline lattice:

$$\varepsilon_{\psi}^{hkl} = f(\psi, hkl)\cdot\sigma_{II} \tag{3}$$

by

$$f(\psi, hkl) = 2S_1^{hkl} + 1/2S_2^{hkl}\sin^2\psi \tag{4}$$

For materials with cubic structure, equation (3) can be reformulated in terms of network parameter *a*:

$$a_{\psi}^{hkl} = a_0\cdot f(\psi)\cdot\sigma_{II} + a_0 \tag{5}$$

where a_0 is the unstressed network parameter. Gravity centers of the diffraction lines used in stresses analysis were determined by their filtering with split - Pearson VII functions. Using Bragg's law and the calculation relationship for the cubic structure, a_{ψ}^{hkl} network parameters were calculated.

Fourier Transform Infrared (FTIR) Spectroscopy investigations were performed on a Shimadzu 8400S device (Fig. 3) equipped with a Shimadzu AIM - 8800 infrared microscope (Fig. 4), in a single optical phase, in a wavenumber range of (7800-350) cm^{-1}.

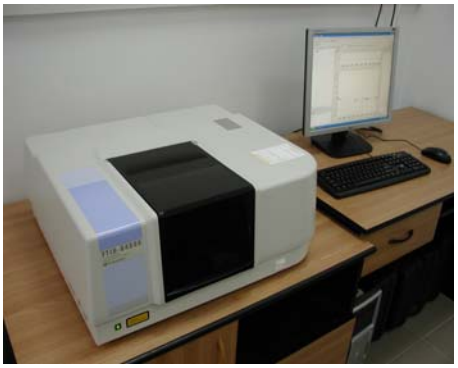

Fig. 3. Shimadzu 8400S FTIR apparatus

Fig. 4. Shimadzu AIM - 8800 infrared microscope

Optical microscopy (OM) and Atomic Force Microscopy (AFM) were carried on an optical microscope Epiquant, Carl Zeiss Jena GmbH, Germany and on an NTEGRA Probe NanoLaboratory NT - MDT, Moscow, Russia, respectively. Scanning electron microscopy (SEM) images were acquired with a FEI Microscope, up to a voltage of 20 kV at an inclination angle of 0°.

The adhesion resistance of the deposited layers was analyzed by scratch testing, with a tester Fig. 5(a), having a diamond tip. The applied loads were in the range of (2.5 – 125) N. The use of a friction pair that involves natural diamond against the material to be investigated, allows considerable simplification of the test devices. The movement is, in this case, pure sliding, common in many tribometers with continuous or alternate motion and the tested body is a small circular plate. Fig. 5(b) presents a schema of a new scratching and fatigue wear tester. The plate (2), made of the investigated material, has an unidirectional motion (for scratching tests), or oscillatory motion (for fatigue tests), respectively. The plate is loaded against a diamond spherical segment with a radius of 2 mm (1). The diamond can also be easily adapted to any wear-testing device with continuous or oscillatory moment. The plate is covered during the test with a thin layer (3) of lubricant (bovine serum).

(a)

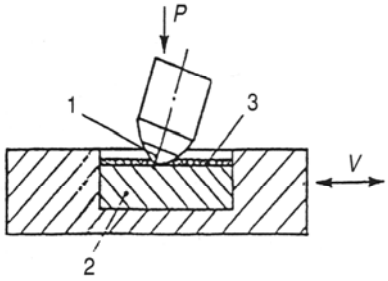

(b)

Fig. 5. Scratching tester with a diamond spherical segment. (a) General view; (b) 1 - natural diamond spherical segment; 2 - sample of tested material; 3 – lubricant (bovine serum). The plate has an oscillatory movement.

Each Scratch was analysed by optical microscopy, AFM and SEM. Width and depth of the scratches were measured and graphic variation curves of scratch depth depending on the applied normal load were drawn.

3. RESULTS

The hardness of 316L stainless steel samples before coating and microhardness of deposited TiN layers were determined. These hardness values were:

- TIN/316L sample; 5000p: Basic material's hardness: 277; 299; 286 *HV* 5 kgf, HV_5; Medium hardness 287 HV_5; Layer's microhardness: 352; 345 *HV* 50 grf; Medium microhardness: 348,5 HV_{50}.

- TIN/316L sample; 10000p: Basic material's hardness: 407; 429; 423 HV 5 kgf; Medium hardness 420 HV_5; Layer's microhardness: 532; 545 *HV* 50 grf.; Medium microhardness: 539 HV_{50}.
- TIN/316L sample; 20000p: Basic material's hardness: 453;473;466 HV 5 kgf; Medium hardness 466 HV_5; Layer's microhardness: 748; 727 *HV* 50 grf.; Medium microhardness: 728 HV_{50}

Average thickness of the coating, measured with optical microscopy was 0.0179 μm for 5000 pls., 0.219 μm for 10000 pls. and for 20000 pls. was 0.032 μm.

Average thickness determined by AFM was 17.4 nm for 5000 pls., 21.4 nm for 10000 pls. and 27 nm for 20000 pls.

Average thickness determined by SEM was 0.8 - 1 μm for 5000 pls., 1.2 μm -1.4 for 10000 pls. and 1.5 - 1.6 μm for 20000 pls.

To investigate the microstructure of TiN layers deposited by PLD, were used X-ray diffraction techniques (XRD - GIXRD). Diffractograms with X rays were purchased at a fixed angle of incidence $\alpha = 1^0$, in the angular range 2θ of 34^0 - 105^0, with step acquisition of 0.02^0 and counting time per step of 10s.

To determine the instrumental contribution, required for Rietveld analysis, it was used the standard material NIST SRM 660a - LaB_6. Diffractogram of standard material was acquired under the same conditions as the samples analyzed.

Characteristics of the analyzed samples are presented in Table 1.

Table 1. Characteristics of the analyzed samples.

Cod sample	Target	Substr.	*d* (cm)	Energy (mJ)	Fluence (J/cm^2)	Frecvency (Hz)	Pressure (Torr N_2)	*T* (^0C)	No of Pulses
5k	TiN	SS 316L	5	500	4,8	10	1.3×10^{-3}	500	5000
10k	TiN	SS 316L	5	500	4,8	10	1.3×10^{-3}	500	10000
15k	TiN	SS 316L	5	500	4,8	10	1.3×10^{-3}	500	15000
20k	TiN	SS 316L	5	500	4,8	10	1.3×10^{-3}	500	20000

3.1. Results of phase analysis

The micro-structural parameters obtained from Rietveld analysis are centralized in Table 2, and the recorded diffractograms in the analysis phase with X rays, at a fixed incidence angle α = 1º, are presented in Fig. 6 (a-d).

Table 2. Main parameters obtained from Rietveld analysis

Sample code	The average size of crystallites (Å)	Maximum mediated microdeformation (%)
5k	143.04	84.1698
10k	195.19	80.1921
15k	344.92	79.1179
20k	107.12	102.9714

3.2. Determination of residual stresses

Analysis of residual stresses of TiN layer for 5K sample was not possible because of strong overlapping diffraction lines corresponding to the two polycrystalline phases - TiN and Fe_3O_4. In Table 3 are presented the values of residual stresses and un-stresses network parameter, obtained using $f(\psi)$ method, and Fig. 7 (a – c) shows the linear dependencies of network parameters according to $f(\psi)$.

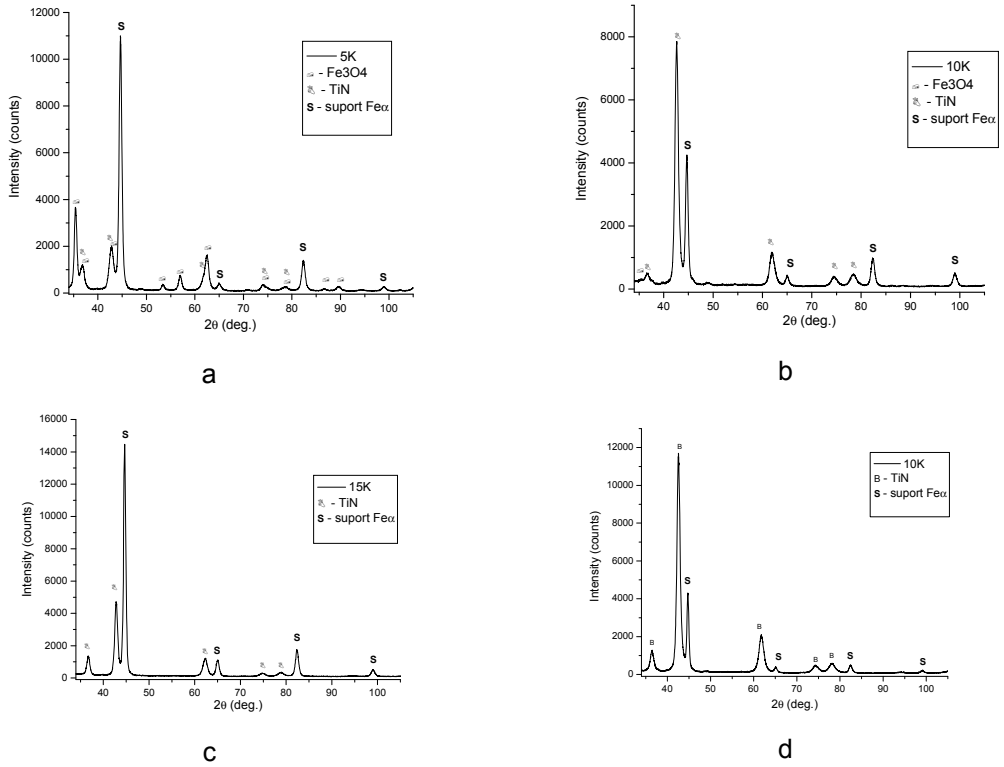

Fig. 6. Phase analysis. X-ray diffraction pattern of (a) 5k, (b) 10 k, (c) 15 k, and respectively (d) 20 k TiN thin films.

Table 3. Values of residual stresses and un-stresse network parameter obtained using $f(\psi)$ method

Sample code	σ_{II} (GPa)	a_0 (Å)
10k	-12.95	4.2155
15k	-10.06	4.2016
20k	-10.40	4.2299

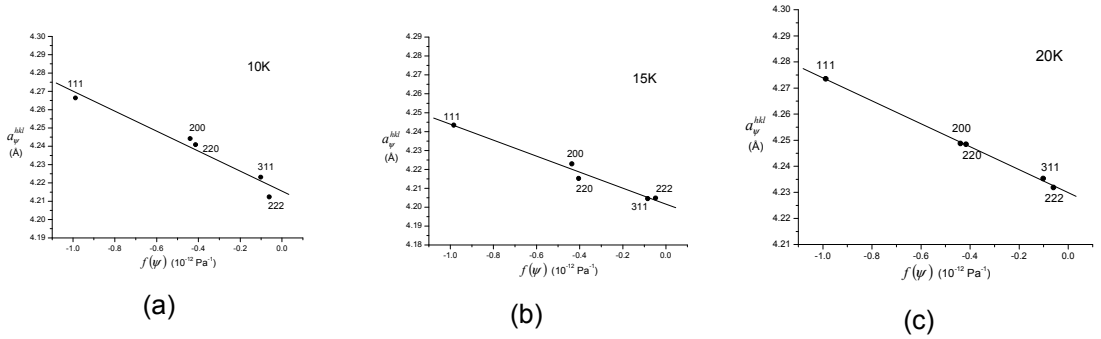

Fig. 7. Representation a_ψ^{hkl} vs. $f(\psi)$ for elastic interaction model of Reuss crystallites, for (a) 5k sample, (b) 10k sample and (c) 20k sample.

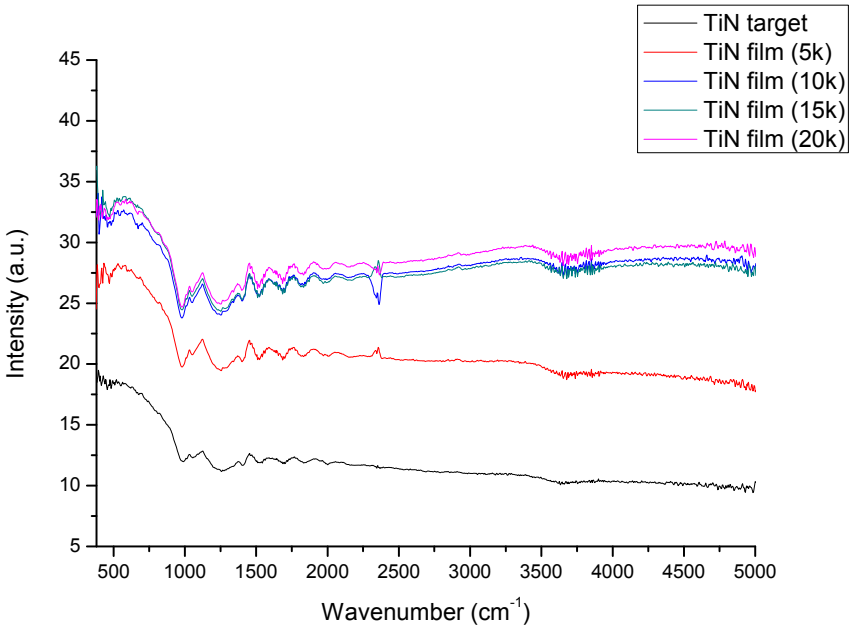

Fig. 8. FTIR of TiN target and deposited thin films (80 SPEC)

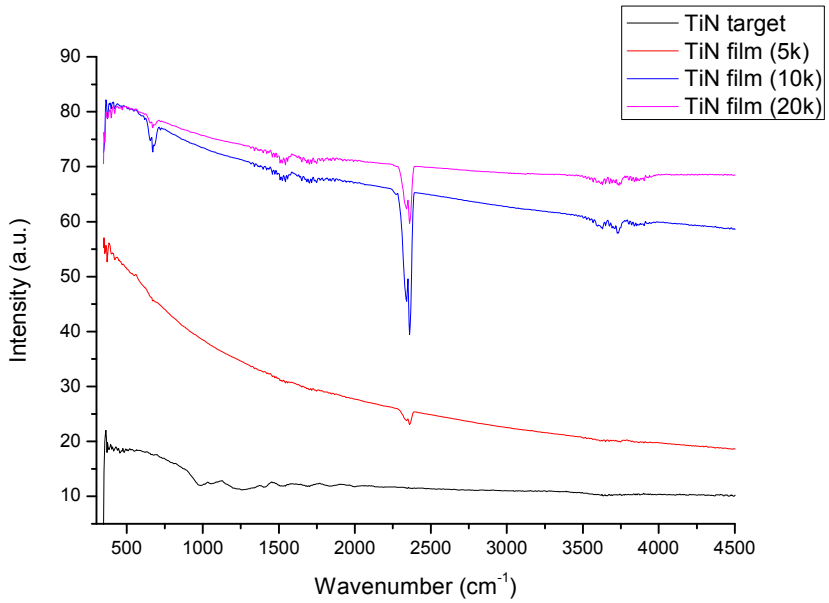

Fig. 9. FTIR of TiN target and deposited thin films (10 SPEC)

FTIR has been used in order to determine the molecular vibrational modes belonging to the main functional groups or to determine the nature. Spectrum matches identify constituent(s) in the sample. Generally, absorption bands in the range of 4000 – 1500 wavenumbers are typically due to functional groups (e.g. – OH, C = O, N – H, CH_3, etc.). The absorption bands in the region 1500 – 400 wavenumbers are generally due to inter-molecular phenomena and are highly specific to each material.

3.4. Thickness of the deposited layers

By optical microscopy (OM) - Fig. 10 and SEM (Fig. 11) were measured widths of scratch traces and their depths were calculated and by calculation their depths. In order to determine the thickness of the deposited layers, OM, AFM and SEM investigations were performed on polished cross sections of specimens tested for scratch.

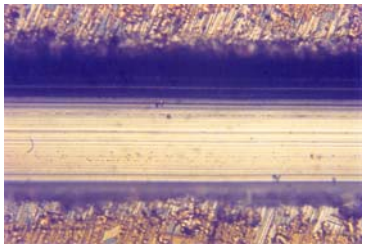

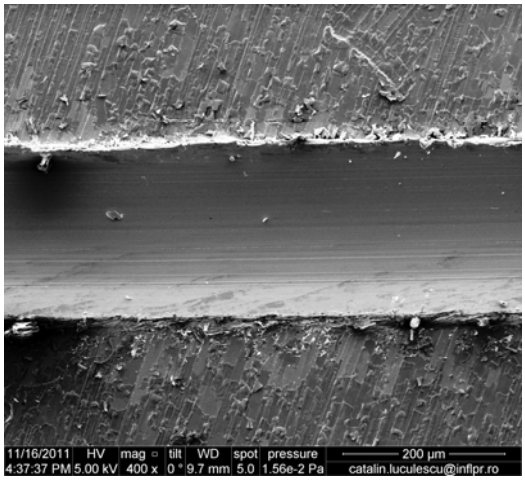

Fig. 10. Optical microscopy image: 5000 pls; 40 N; x 200.

Fig. 11. SEM image: 5000 pls; 40 N: x 400.

On the OM images were measured in ten places scratch traces widths, then were calculated their depths *h* based on a simplified relationship (indent method), which takes into account the radius of diamond tip *(r)* and the medium value of measured widths of the indent *(l)*: $h = l/8r$. Variation of scratching depth function of applied normal load is presented in Fig. 12. These curves show some "indenter drops" due to indentation on voids or other defects of coatings.

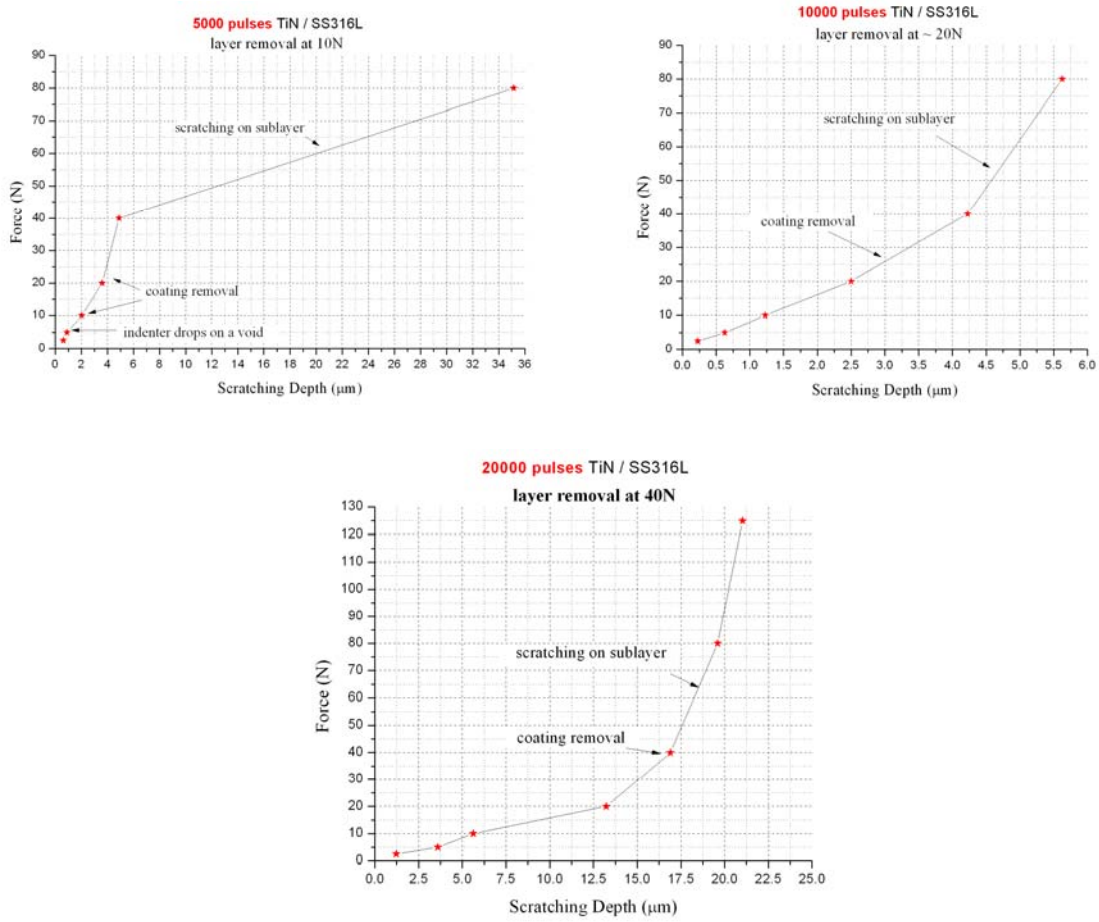

Fig. 12. Variation of scratching depth (µm) function of normal load applied over the indenter (N), on steel SS316L samples, coated with TiN by PLD, at 5000 pulses, 10000 pulses and 20000 pulses.

After OM investigations, the samples were cross-sectioned and after that polished with 400 and 600 grit sandpaper, and then inspected by AFM (Fig. 13).

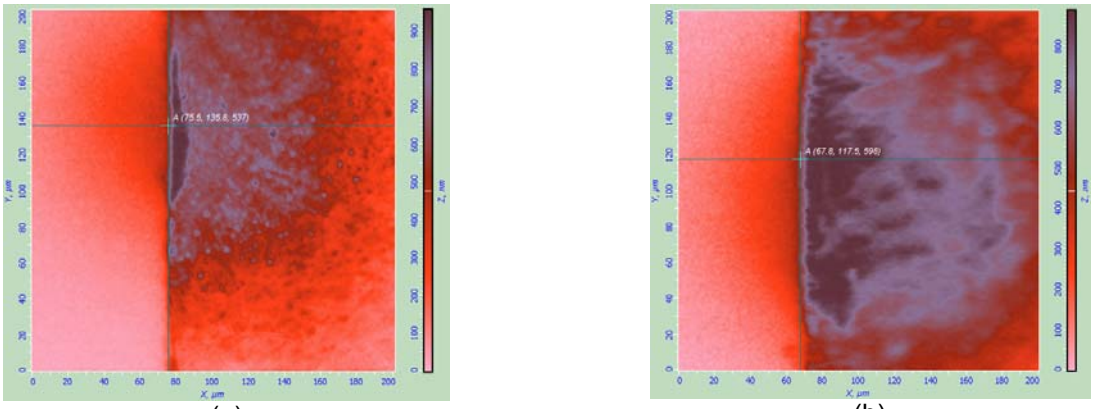

(a) (b)

Figure 13. AFM images of cross sections of SS316L steel samples coated with (a) 5000 and (b) 20000 pulses

The average depths of the layer resulted for 5k sample were of 13.25 μm (12 μm global and 12; 13; 14; 14 individual) and for 20k sample, of 65.1 μm (78 μm global and 58; 56; 65; 75 individual), respectively. For comparison, measurements of thickness were also realized by SEM, at different magnifications (250X, 1000X and 2000X). The 250X magnification was considered optimal allowing an accurate view of the section of deposited layer.

In Fig. 14 are presented for comparison, the SEM images of TiN coatings thickness for 5k, 10k and 20k samples. All images were acquired up to a voltage of 20 kV at an inclination angle of 0^0.

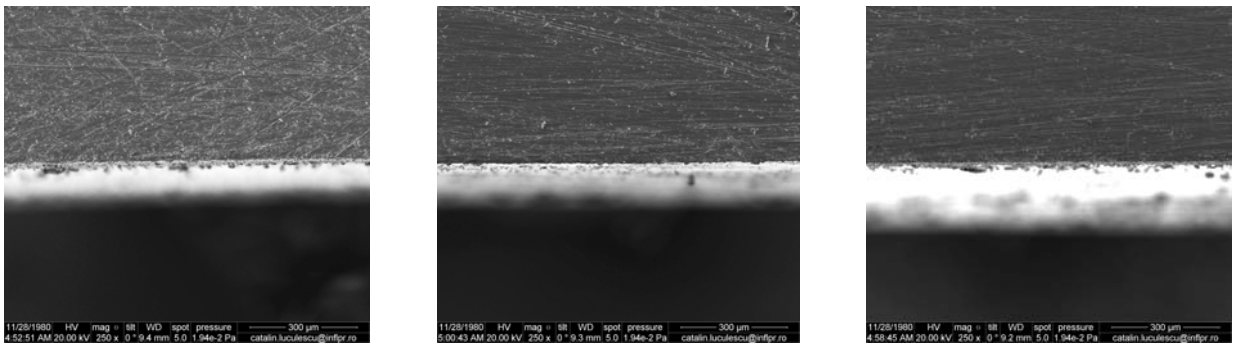

Fig. 14. SEM images of TiN coatings thickness for 5k, 10k and 20k samples.

From the SEM images presented in Fig. 14, one can calculate the thicknesses for 5k sample (~0.8-1 μm), 10k sample (~1.2-1.4 μm) and 20k sample (1.5-1.6 μm).

Before testing at relatively low voltages (10 kV) were recorded with images secondary electrons (SE) of surface topography (Fig 15) and of nitrated samples sections to minimize the edge effects in image formation of the free samples surfaces.

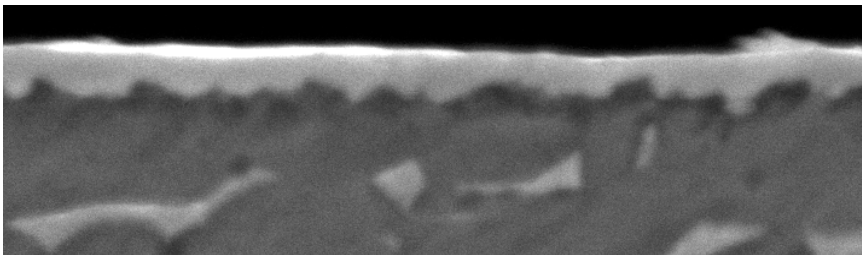

Fig. 15. SEM image of a cross section of Ti-6Al-4V plasma nitrided at 1048 K for 2h. Overall width of the image corresponds to 10μm. (0,5 cm = 1 μm)

SEM controlled characteristics, i.e. voltage, beam's diameter, scan time, amplification, remaining deviation and increasing were set to the same values in all images of morphologies of surfaces sections. One can clearly see irregular distribution of the input material on an enough large depth in the substrate material.

4. DISCUSSIONS AND CONCLUSION

The recorded GIXRD patterns for TiN thin films, presented in Figs. 6 (a-d), shown that TiN coatings were polycrystalline, exhibiting reflections related to B1 cubic structure. Reflections corresponding to the substrate (Fe_α phase) were detected in all the X-ray diffraction patterns. In addition, in the 5k and 10k samples, Fe_3O_4 polycrystalline phase was present.

Phase qualitative analysis of TiN coatings showed the presence of three polycrystalline phases in samples analyzed:

- In 5k and 10k samples: TiN (B1 cubic structure), Fe_α (cubic structure) and Fe_3O_4 (cubic structure);
- In 15k and 20k samples (B1 cubic structure) and Fe_α (cubic structure).

Analyzing the residual stresses of the TiN deposited layers, presented in Table 3, it results that all the analyzed samples are subjected to high compressive stresses. It can also be observed a tendency to relax as the layer grows.

The paper points out that TiN protective coatings deposited by PLD technique with 20000 pulses can be an alternative technology to ensure adhesion and scratch resistance of TiN coatings of Ti-6Al-4V femoral heads. The condition for the success of such coating is to provide an optimal surface roughness of femoral head that serves as substrate for TiN coating.

Analyzing the overall experimental results it can be concluded that although the 20000 pulses layer is promising as alternative technology, further studies are necessary to determine the optimal roughness of the basic layer and fit it with the hardness and elasticity modulus of the coating. Perhaps that will be also necessary to realize biocompatibility studies of TiN layer.

ACKNOWLEDGMENTS

The authors would like to thank the Institute of Solid Mechanics of the Romanian Academy and Civil Engineering University, for its material and technical support offered in order to achieve these researches.

REFERENCES

1. BERGMANN, G., DEURETZBRACHER, M., HELLER, F.. GRAICHEN, A., RONLMANN, J., STRAUSS, G.. DUDA, N. Wear of Orthopaedic Implants and Artificial Joints. J. Biomechanics, 34:859-71, 2001.
2. PÉREZ, M.A., GARCÍA – AZNAR, J. M., DOBLARÉ, M., SERAL. A comparative FEA of the debonding process in different concepts of cemented hip implants. J Biomech, 39:1859-72, 2006.
3. ABDUL-KADIR M. R., HANSEN, U., KLABUNDE, R., LUCAS, E., AMIS, A. Finite element modelling of primary hip stem stability. J. Biomechanics 41 (2008) 587-594.
4. ORLIK, J, ZHUKOV, A., MIDDLEON, J. On the secondary stability of coated cementless hip replacement: parameters that affected interface strength. Med. Eng. Phis 25:825-31, 2003.
5. NAJJAR, D. BIGERELLE M.,MIGAUD, H., IOST., A. Iost. Identification of scratch mechanisms on a retrieved metallic femoral head. Wear, 258:240-50, 2005.
6. JAVORSKY, C.S., BORGES DA COSTA, J.A.T., MÜLLER, STROHAECHER, R., ENGLERT,G.E. Corrosion Resistance of Plasma Nitrided Ti-6Al-4V Alloy in Hank's Solution. Anais do Congresso NACE-Brasil Corrosão'99, Vol.1, pp.433-440. (São Paulo, SP, NACE-Brasil, 1999) ISBN 85-86686-08-
7. COLL, B., et al. Metallurgical and Tribological Modification of Titanium and Titanium Based Alloys for Medical Devices by Plasma Assisted Techniques. In Technical Bulletin from Multi-Arc Scientific Coatings/Innovatique S.A. 1998.
8. RIE, K. et al. Plasma Surface Treatment and PACVD coatings on Ti alloys for Surgical Implants. Surface and Coatings. Technology. 74-75 (1995): p. 973.
9. PELLMAN, M., *PVD Coatings for Medical Device Applications*. In Technical Bulletin from Multi-Arc Scientific Coatings/Innovatique S.A. 1998.
10. YLBAS, B.S. et al. *A Study of the Corrosion Properties f TiN coated and nitrided Ti-6Al-4V*. Corrosion. Science, v. 37, p.1627- , oct.1995.
11. BEKIR, S. et al. *Plasma Nitriding of Ti6Al4V alloy to improve some tribological properties*. Surface. and Coatings. Technology. v. 80,p.287-292, 1996.
12. SCHUTZ, R.W., THOMAS,D.E.,*Corrosion of titanium and titanium alloys*, Corrosion-Metals Handbook, 9. Ed.United States, ASM,1987.p.669-705.
13. MELETIS, E.I. et al. *Ion Plating and Implantation Applications to Materials*. In American Society for Metals, (Metals Park, OH ,1986): p.173.
14. SOCOL, G et al. Tailoring Of Optical, Compositional And Electrical Properties Of The $In_xZn_{1-x}O$ Thin Films Obtained By Combinatorial Pulsed Laser Deposition.Digest Journal of Nanomaterials and Biostructures, 6 (1), pp. 107 – 115, 2011

15. KUMAR A., U. Welzel and E.J. Mittemeijer: Diffraction Stress Analysis of Strongly Fibre-Textured Gold Layers. Zeitschrift für Kristallographie Suppl. **23**, 55-60 (2006).
16. THOMPSON, D., COX, D.E., HASTINGS J. B. Rietveld refinement of Debye-Scherrer synchrotron X-ray from Al_2O_3. J. Appl. Cryst. **20**, 79 (1987). P. *Thompson*, D. E. *Cox*, J. B. *Hastings*, *Rietveld Refinement* of *Debye-Scherrer Synchrotron X-ray* Data from *Al2O3*, *J*. *Appl*. *Cryst*. *20* (*1987*) *79*.
17. FINGER, L.W. Rietveld refinement of Debye-Scherrer synchrotron X-ray data from Al_2O_3. J. Appl. Cryst. **31**, 111 (1998).
18. NOYAN, I.C., COHEN, J.B. Residual stress – measurement by diffraction and interpretation. Springer Series on Materials Research and Engineering, edited by B. Ilschner and N. J. Grant. Springer-Verlag, New York-Berlin-Heidelberg-London-Paris-Tokyo 1987.
19. NAGAO, S., NORDLUND, K., NONAK, R. Anisotropic effect of piezoelectric polarization on Schottky barrier height in elastically deformed bulk GaN crystal. Phys. Rev., **B 73** (2006) 144113.
20. WELTZEL U., LIGOT, J., LAMPARTER P. VARMEULEN, A. C., MITTEMEIJER E. J. Stress analysis of polycrystalline thin films and surface regions by X-ray diffraction. J. Appl. Cryst. (2005). **38**, 1–29.

CORRESPONDENCE

Lucian CAPITANU
Institute of Solid Mechanics of Romanian Academy, Bucharest, Romania
lucian.capitanu@yahoo.com

Tribological Journal BULTRIB Vol. 5, 2015
Papers from the International Conference **BULTRIB '15**
September 11-13, 2015, Sozopol, Bulgaria
Society of Bulgarian Tribologists
FIT – Technical University of Sofia

TRIBOLOGICAL PROPERTIES OF SPRAYED TiO_2 AND TiO_2/ZnO COATINGS

Mara KANDEVA[1], Vladimir BLASKOV[2], Nina KOSTOVA[3], Irina STAMBOLOVA[2], Konstantin BALASHEV[4], Silviya SIMEONOVA[4], Sasho VASSILEV[5], Alexander ELIYAS[3]
[1]Technical University-Sofia, , Tribology Center, 8, Blvd Kl. Ohridski, 1156 Sofia, Bulgaria
[2]Institute of General and Inorganic Chemistry, BAS, Acad. G. Bonchev St., Bl 11, 1113 Sofia, Bulgaria
[3]Institute of Catalysis, BAS, Acad. G. Bonchev St., Bl 11, 1113 Sofia, Bulgaria
[4]Sofia University, Faculty of Chemistry and Pharmacy, 1 James Bouchier Blvd, 1164 Sofia, Bulgaria
[5]Institute of Electrochemistry and Energy Systems, BAS, Acad. G. Bonchev, bl. 10, 1113 Sofia, Bulgaria

Abstract: *The effects of ZnO underlayer and titanium precursor on the wear resistance of the TiO_2 sprayed coatings were investigated. All samples revealed anatase crystallographic phase. No characteristic peaks of zinc oxide phases were detected in TiO_2/ZnO coatings.The composite coatings have lower wear resistance than pure TiO_2. Due to mismatch of the unit cells of the crystalline lattices of ZnO and TiO_2 there exists a greater strain in the TiO_2 lattice and therefore greater external tension is required to be applied in order to move the dislocation. TiO_2 coatings from titanium chloride exhibit higher wear resistance than those obtained from titanium isopropoxide due to the lower roughness and smaller crystallites sizes.*
Key Words: *wear resistance, titania coatings, AFM, roughness, tribology*

1. INTRODUCTION

Since 1988 the term 'lubricious oxides' was introduced to tribology and numerous tribological studies have been carried out on bulk (mostly sintered or hot-pressed) materials or coatings [1] with low coefficients of friction (COF) and high wear resistances. Titanium oxide coatings have a great potential for tribological and biomedical applications thanks to a good biocompatibility and good wear resistance [2]. Various methods have been suggested to prepare TiO_2 and other ceramic wear resistance coatings i.e plasma spray technique [3], sputter deposition [4] atomic layer deposition [5]. Among the chemical methods the sol-gel method is widely used for deposition of wear resistant titania coatings [6].

Thermal spray processes represent an important and rapidly growing group of surface modification technologies, having a particularly high importance for wear resistant coatings [7]. Recently our group has prepared TiO_2 sprayed coatings on Al foil and has investigated their wear resistance [8]. Very recently, Wun-Kai Wang et al. [5] have investigated the tribological and microstructural behaviors of the bilayer TiO_2/ZnO films and revealed that the samples exhibited higher scratch resistance and friction, indicating that the wear volume is reduced with increased annealing temperature. These results have motivated us to obtain TiO_2/ZnO coatings by spray pyrolysis and to investigate the effect of deposition parameters of ZnO underlayer on their wear resistance. We have also studied the influence of titanium precursor (titanium chloride - $TiCl_4$ and titanium isopropoxide $Ti(OPr)_4$) on the surface features and on the tribogical properties of the TiO_2 coatings.

2. EXPERIMENTAL PART

Aluminium foil plates with thickness of 0.3 mm were used as substrates. Titanium chloride and. titanium isopropoxide, dissolved in isopropanol were applied as inorganic and organic source of titanium,respectively. To obtain TiO_2/ZnO coating we have deposited ZnO coatings by spraying of zinc acetate dissolved in mixture of water and ethanol (1:3) onto heated substrate. To obtain different thickness of ZnO coatings, 6 ml of the initial solution were diluted with different solvent volume (Table 1). In order to prevent hydrolysis several drops of nitric acid were added. The titanium dioxide coatings were sprayed onto ZnO film. The deposition conditions of the samples are presented in Table 1. The precursor solution was sprayed onto substrate heated at 270-300^{o}C. The deposits were finally treated at 400^{o}C for 1 hour.

The mean crystallite sizes of the samples have been estimated using Scherrer's formula. The phase composition of the samples was studied by X-ray diffraction (XRD) with CuK_α-radiation (Philips PW 1050). The crystallites sizes were estimated based on XRD patterns.

Table 1: Deposition conditions of the coatings

Sample code	Titanium precursor	Molarity of solution	Zn acetate solution ml	Solvent ml	Volume of spray Zn solution, (ml)	Volume of spray Ti solution, (ml)
1	$TiCl_4$	0,1	-	-	-	22
2	$Ti(OPr)_4$	0,1	-	-	-	22
3	$TiCl_4$ $Zn(CH_3COOH).2H_2O$	0,1 0,4	6	-	6	22
4	$TiCl_4$ $Zn(CH_3COOH).2H_2O$	0,1 0,4	6	3	6	22
5	$TiCl_4$ $Zn(CH_3COOH).2H_2O$	0,1 0,4	6	6	6	22
6	$TiCl_4$ $Zn(CH_3COOH).2H_2O$	0,1 0,4	6	9	6	22

The surface analyses of the coatings were carried out by X-ray photoelectron spectroscopy (XPS). The measurements were performed in VG ESCALAB II electron spectrometer using AlK_α radiation with energy of 1486.6.eV. The binding energies were determined with an accuracy of ±0.1 eV. The chemical composition of the films was investigated on the basis of areas and binding energies of O1s and Ti2p photoelectron peaks (after linear subtraction of the background and Scofield's photoionization cross-sections).

The surface topography was studied by means of Atomic Force microscope (AFM) (NanoScopeV system, Bruker Inc.) operating in tapping mode in air at room temperature. The silicon cantilevers (Tap 300 Al-G, Budget Sensors, Innovative solutions Ltd, Bulgaria) were used with 30 nm thick aluminum reflex coating. The reported by the producer cantilever spring constant was in the range of 1.5–15 N/m, the resonance frequency was 150 ± 75 kHz and the tip radius was less than 10 nm. The scan rate was set at 1 Hz and the images were captured in the height mode with 512 512 pixelsSubsequently, all the images were flattened by means of the Nanoscope software.

The obtained samples were subjected to wear resistance tests. The experimental runs of abrasive wearing resistance of the coatings were realized by means of the test rig TABER ABRASER according to the kinematical scheme „disk-on-disk" [9]. The device used for this test is shown on Figure 1**.**

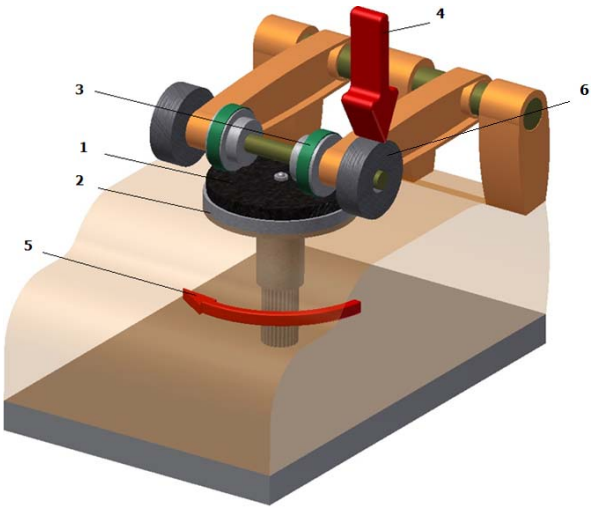

Fig. 1. 3D model of the apparatus for abrasive friction under dry wear conditions

Specimen (1) is mounted on a horizontal bearing plate (2), which is driven by an electric motor at a constant angular velocity (5) of 60 [rpm]. Abrasive roller (antibody) (3), made of plastic abrasive material CS 10, is mounted on a horizontal axis in the device. Thus the specimen (1) and the roller (3) are located in two orthogonal directions and at a constant angular velocity (5) of the specimen (1) and permanent normal loading, the friction in the contact area maintains a constant speed of rotation of the roller (3). The contact normal loading is transmitted by weights (6) through the axis of the roll; in this case there is one weight with a mass of 1,250 kg, i.e. the load (4) is 1,250 kg.

The procedure of the experimental study on abrasive wearing off is realized in the following sequence of operation steps:

- Cleaning of lubricants and drying of the identical specimens. The specimens represent disks of diameter 100 mm and thickness of 3 mm of the deposited coatings;
- Measuring of roughness of the contact surfaces of the specimens before and after the wear test
- Measuring of specimens mass m_o before and its mass m_i after a given friction path L by electronic balance WPS 180/C/2 of accuracy 0.1 mg. Before every measurement the specimens are cleaned with appropriate solution against static electricity;
- The specimen 1 is fixed on the carrying horizontal disk 3; then the normal load *P* is set. The friction path L is determined by the number of cycles read by the revolution counter 8.

Abrasive wearing off for all coatings is obtained by fixed identical operating conditions – nominal contact pressure given with the normal load *P*, average sliding speed *V* and parameters of the abrasive surface.

The experiment data are listed in Table 2.

Table 2. Parameters of wear resistance experiments

Apparent contact area	A_a = 0.26 cm^2
Normal contact pressure	P_a = 17.3 N/cm^2
Average sliding speed	V = 17.9 cm/s

The following parameters of mass wearing off are studied:

- Absolute mass *m* worn off;
- Average rate of mass *dm/dt*, [mg/min] wearing off;
- Absolute intensity of mass wearing off i, $[mg/m]$:

$$i = m/S \tag{1}$$

- The friction distance *S* is calculated by the corresponding number of cycles *N* and the distance *R* between the axis of rotation and the mass center of the nominal contact site by the formulae:

$$S = 2\pi RN \tag{2}$$

- Absolute wear resistance by mass I, $[m/mg]$:

$$I = 1/i = S/m \tag{3}$$

3. RESULTS AND DISCUSSION

The X-ray diffraction method was used to investigate the phase structure and crystallite size of the titania coatings. All the diffraction peaks match well with those of standard XRD patterns of anatase, represented by (101) peak only (Figure 2). It should be pointed out that no characteristic peaks of zinc oxide phases were detected, which indicates that the oxide coating is very thin or is in amorphous state. Similar results we were obtained for mixed TiO_2-ZnO films (25 mol% ZnO) XRD pattern of these films reveals the existence of well crystallized anatase phase, while ZnO is in amorphous state [10]. The XRD of the sample 2 proved that the film is in amorphous state, because anatase peaks is not detected. It has also been found out that the position of (101) anatase peak is preserved after 400 cycles of friction. The X- ray diffraction patterns also revealed that the increase of concentration of sprayed ZnO underlayer results in enhanced crystallization of samples with double coatings (Figure 3). This phenomena is in accordance with studies of ref. [11] and ref. [12]. It should be noted that the crystallites sizes of the samples with ZnO undercoating (samples 5 and 6) are larger than those for samples 1 and 2 (17 nm *vs* 37-46 nm).

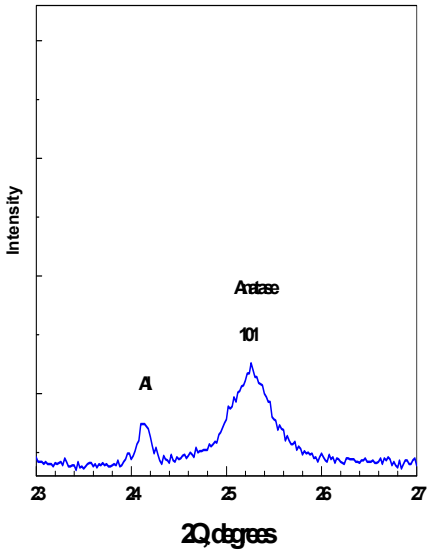

Fig. 2 XRD patterns of TiO_2 coatings, obtained from $TiCl_4$

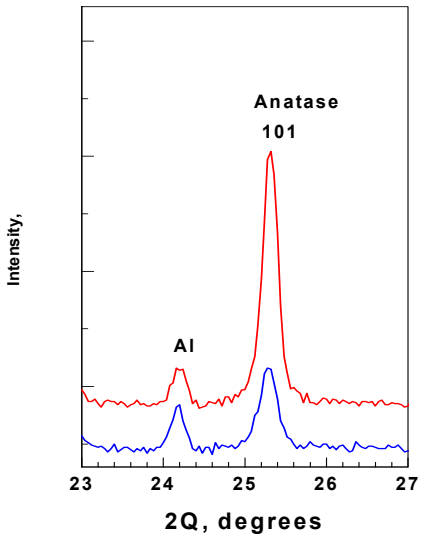

Fig. 3. XRD patterns of TiO_2/ZnO coatings

The surface composition and chemical state of the films are investigated by XPS analyses. Fig.4 shows the O1s, Ti2p and Zn2p photoelectron spectra of the films. The peaks observed at around 529.9 and 530.1 eV were assigned to O^{2-} ions in TiO_2, for samples 3 and 5, respectively. The peak position of O1s is confirming that the main chemical states of oxygen in the samples was −2 valence. The higher binding energy peak centered at around 532.5 eV relates to the OH^- group on the surface. The Ti $2p_{3/2}$ peaks of the films, are located at 458.6 eV and 458.7 for samples 3 and 5, respectively. The binding energy and the shape of the Ti2p peak are characteristic of Ti^{4+} oxidation state. The Zn $2p_3/_2$ peaks of the both samples are similar and have a maximum at 1021.7 eV, typical of ZnO. Based on the XPS spectra the actual surface concentrations of the elements in the final TiO_2 coatings were evaluated and the results are represented in Table 3.

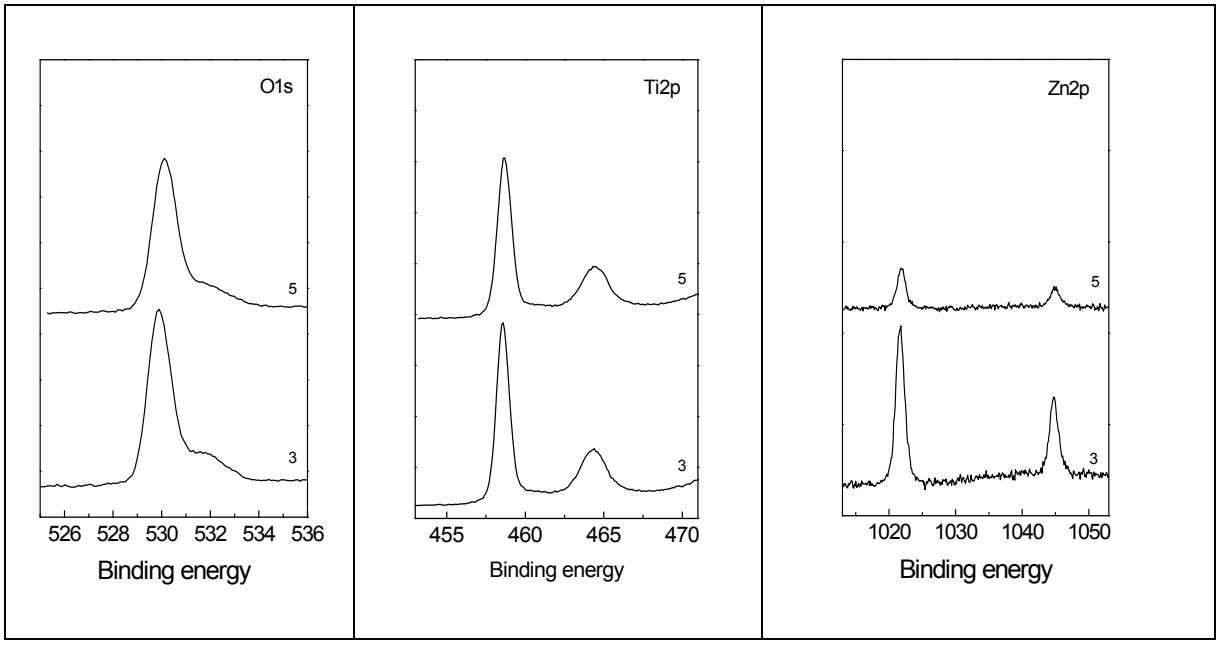

Fig. 4. XPS spectra for O1s, Ti2p and Zn2p photoelectron spectra of the samples 3 and 5

The XPS analyses of the surface composition indicate that some zinc atoms from ZnO underlayer diffuse into the TiO_2 coating. With the increasing of the ZnO thickness, the surface zinc concentration is increasing too (Table 3).

Table 3: Chemical composition of the coatings, evaluated by XPS

Sample code	O (at%)	Ti (at%)	Zn (at%)
3	65.4	25.8	8.8
5	68.5	28.9	2.6

The surface morphology of the TiO_2 coatings before and after 400 abrasive cycles was investigated by Atomic Force Microscopy (AFM). Typical topographical images of the surface of non-modified TiO_2 coatings before and after 400 abrasive cycles are shown in Figures 5a and 5b, respectively. The AFM images are presented in 2D and 3D format and they are also accompanied by sections across the sample surface.

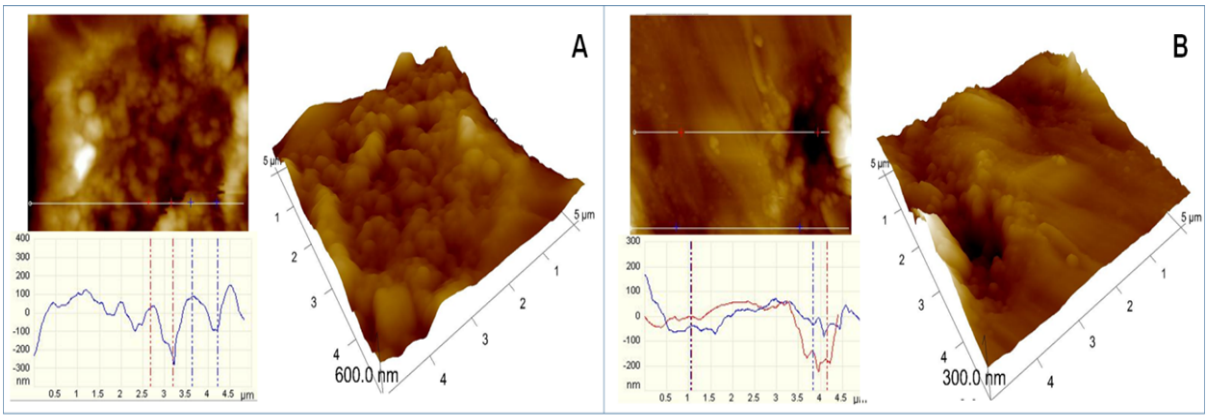

Fig. 5. AFM topographical images presented in 2D and 3D format, together with the spots on the surface of TiO_2 coating of sample 1 before (A) and after 400 abrasive cycles (B),

The comparison of the AFM images of TiO_2 coatings (sample 1) clearly demonstrates that after 400 abrasive cycles the coating's surface becomes considerably smoother. The performed degree of roughness analysis shows a profound difference in the surface structure of the samples before and after the abrasive cycles test. It gives the mean roughness Ra and values of about 41 nm for the sample, while after performing the test this value drops down about 7 times.

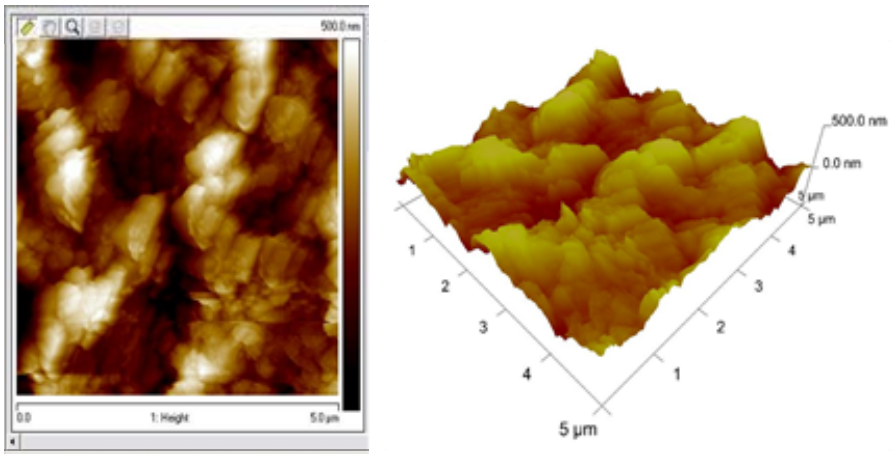

Fig. 6. AFM topographical images presented in 2D and 3D format, together with the spots on the surface of TiO_2 coating of sample 2 before test

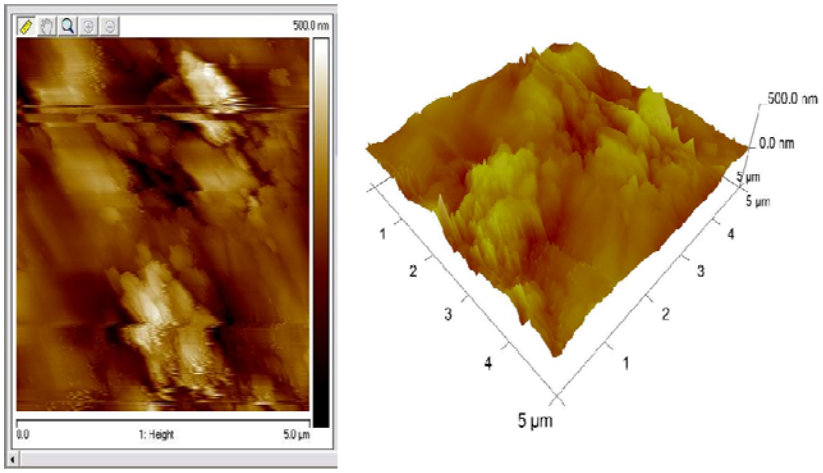

Fig. 7. AFM topographical images presented in 2D and 3D format, together with the spots on the surface of TiO_2 coating of sample 2 after 400 abrasive cycles

After the abrasive tests the coatings' roughness significantly lowers due to plastic deformation, as it is evidenced by the AFM image. For the sample, obtained from $Ti(OC_3H_7)_4$ the calculated values for the surface degree of roughness Ra is about 142-116 nm before and 65-96 nm after the test (Fig.6 and Fig. 7).

The TiO_2 and TiO_2/ZnO coatings increase the wear resistance of the aluminum substrate. The presence of ZnO underlayer were found out to result in decreasing of wear resistance (Figure 8).

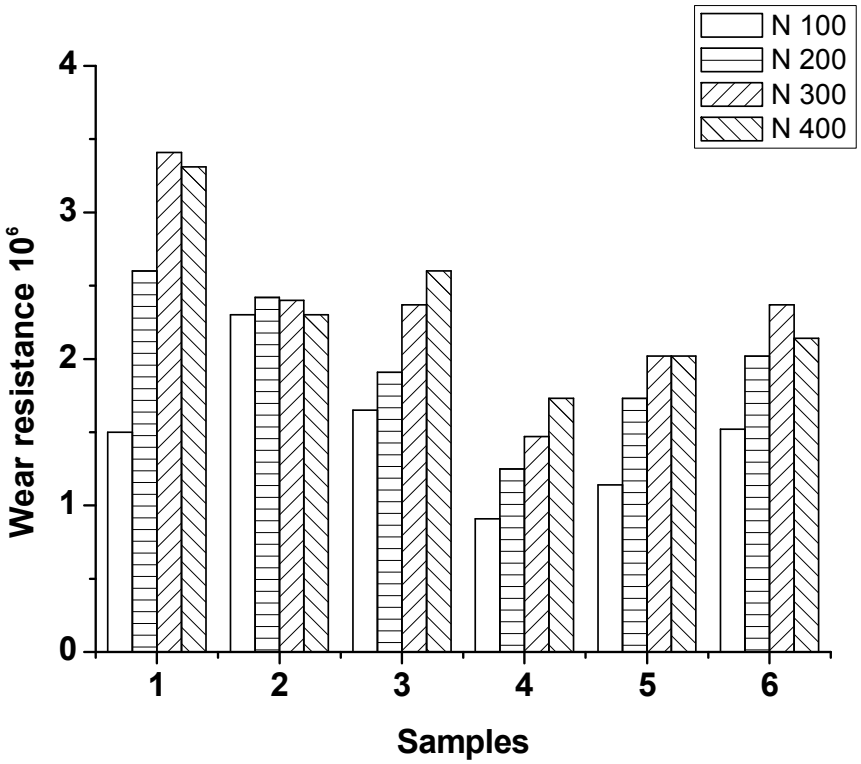

Fig. 8 Wear resistances of samples (see Table 1) after 100, 200, 300 and 400 abrasive cycles

This behavior of TiO_2/ZnO coatings could be explained with several factors:

(i) Increased crystallites size of the titania coatings, which results in higher roughness.

(ii) theTiO_2 lattice in interface was pressed by stress due to the bigger lattice mismatch between TiO_2 and ZnO crystal lattices. Zhao L. et al. [12] have found for TiO_2 nanorods on ZnO seed layer that the c-axis lattice constant of TiO_2 is bigger than that of the standard sample. The plastic deformation is caused by movement of the dislocations. External strain is necessary to be applied to transfer the dislocation to a definite distance. Due to mismatch of the unit cells of the crystalline

lattices of ZnO and TiO_2 there exists a greater strain in the TiO_2 lattice and therefore greater external tension is required to be applied in order to move the dislocation [13].

(iii) probably the ZnO underlayer has influence on the TiO_2 particle morphology. Similar results were obtained in [14] for TiO_2/ZnO nanocomposite, which have proved that morphology and size distribution of the TiO_2 was affected by the addition of ZnO.

The improved wear resistance of TiO_2 coatings, obtained from inorganic precursor ($TiCl_4$) can probably be attributed to the smaller crystallites size (17nm) and lower surface roughness, as it is evidenced by the XRD and AFM analyses. The AFM analyses revealed also that after the abrasive cycles the surface of these samples became considerably smoother with visible signs of plastic deformations. This explanation is in accordance with the observations for TiO_2 sol-gel coatings on glass substrate by Zhang et al. [6]. The authors stated that such signs of plastic deformation indicate that the TiO_2 film has very good toughness or even super plasticity, which is consistent with the plastic deformation behavior. The different behavoiur of the sample 2, obtained from titanium isopropoxide (compared to the sample 1), could be a result of the presence of various crystalline defects in the crystal lattice . Our previous results based on XPS analyses of the surface have shown that inorganic TiO_2 contain the chlor [15]. According to Xu et al. Cl^- doping of TiO_2 created surface defect [16, 17].

4. CONCLUSIONS

TiO_2 and TiO_2/ZnO coatings have been deposited on aluminium foil by spray pyrolysis method. According to the XRD analyses no characteristic peaks of zinc oxide phases were detected, which indicates that this oxide coating is either very thin or it is in amorphous state. The crystallites sizes of the samples with ZnO undercoating are larger than those for standart samples. The presence of ZnO underlayer was found out to result in decreasing of wear resistance of the titania coatings due to the increased crystallites size and existance of bigger stress for TiO_2 lattice. The improved wear resistance of TiO_2 coatings obtained from inorganic precursor can probably be attributed to the smaller crystallites size (17nm) and lower surface roughness. The AFM analyses revealed that after 400 abrasive cycles their surface became considerably smoother with visible signs of plastic deformations.

5. ACKNOWLEDGMENTS

The authors gratefully acknowledge the financial support by the National Science Fund under Contract DFNI T 02/16.

REFERENCES

1. GARDOS, M.N., The effect of anion vacancies on the tribological properties of rutile (TiO_{2-x}), Tribol. Trans. **31**, (4), 1988, 427–436.
2. SIVA RAMA KRISHNA, D., Y. SUN, Thermally oxidized rutile-TiO_2 coating on stainless steel for tribological properties and corrosion resistance enhancement, Appl. Surf. Sci., **252,** 2005 1107.
3. SATHISH, S., M. GEETHA, S.T. ARUNA, N. BALAJI , K.S. RAJAM, R. ASOKAMANI, Sliding wear behavior of plasma sprayed nanoceramic coatings for biomedical applications, Wear, **271**, 2011, 934– 941.
4. SUN, Y., Tribological rutile-TiO_2 coating on allumium alloys, Appl. Surf. Sci., **233**, 2004, 328-335.
5. WUN-KAI WANG, HUA-CHIANG WEN, CHUN-HU CHENG, CHING-HUA HUNG, WU-CHING CHOU, WEI-HUNG YAU, PING-FENG YANG, YI-SHAO LAI, Nanotribological properties of ALD-processed bilayer TiO_2/ZnO films, Microelectronics Reliability, **54**, 2014, 2754–2759.
6. ZHANG, W., W LIU, C WANG, Tribological behaviour of sol gel TiO_2 films on glass, Wear, **253,** 2002, 377-384.
7. BERGER, M., C.C. STAHR, S. SAARO, S. THIELE, M. WOYDT, N. KELLING, Dry sliding up to 7.5 m/s and 800◦C of thermally sprayed coatings of the TiO_2–Cr_2O_3 system and (Ti,Mo)(C,N)–Ni(Co), Wear, **267,** 2009, 954–964.
8. KANDEVA M., V. BLASKOV, I. STAMBOLOVA, N.G. KOSTOVA, AL. ELIYAS, S. VASSILEV, “Study of wear resistance of TiO_2 sprayed coatings. Correlation between deposition parameters and wear properties” Proceedings of 11th International conference “THE A Coatings”, Editors: K.-D. Bouzakis, K. Bobzin, B. Denkena, M. Merklein, October 1-3, 2014, Thessaloniki, Greece, pp. 203-210.
9. KANDEVA M., D. KARASTOYANOV, A. ANDONOVA., Wear and tribothermal effects of nanostructured nickel chemical coatings, Applied Mechanics Materials, **157-158**, 2012, 960-963

10. STAMBOLOVA I., V. BLASKOV, N. KANEVA, M. SHIPOCHKA, S VASSILEV, O DIMITROV, A ELIYAS, Effect of titanium dopant on the surface features and on the photocatalytic characteristics of ZnO films, Materials Science Semiconductors Proc., **25,** 2014, 244-250.
11.ZHANG Z., Y. YUAN, Y. FANG, l. LIANG, H. DING, l. JIN,Preparation and photocatalytic nano-ZnO/TiO_2 film and application for determination of chemical oxygen demand, Talanta, **73**, 2007, 523-527.
12. ZHAO L, M. XIA, Y. LIU,B.ZHENG, Q. JIANG, J.LIAN, Micro-twins TiO_2 nanorods grown on seeded ZnO film, Journal of Crystal Growth, **344**, 2012, 1–5.
13. Physical Metallurgy, Ed R. W. Cahn, North-Holland Publ. Company ,Amsterdam, 1965.
14. MORADI S., P. ABEROOMAND-AZAR, S. RAEIS-FARSHID, S. ABEDINI-KHORRAMI, M. HADI GIVIANRAD S.MORADI , P. ABEROOMAND-AZAR, S. RAEIS-FARSHID,S. ABEDINI-KHORRAMI, M. HADI GIVIANRAD, The effect of different molar ratios of ZnO on characterization and photocatalytic activity of TiO_2/ZnO nanocomposite, J. Saudi Chem. Soc., *In Press,* 2012
15. BLASKOV V., M. SHIPOCHKA, I. STAMBOLOVA, S. VASSILEV, A. ELIYAS, P. STEFANOV, A. LOUKANOV, Influence of titanium precursor on the photocatalytic properties of TiO_2 sprayed films under visible light Journal of Physics: Conference Series, IOP science, **398,** 2012, 012021 17.
16. BLASKOV V., M. SHIPOCHKA, I. STAMBOLOVA, S. VASSILEV, A ELIYAS, P. STEFANOV, unpublished results.
17. XU H., ZHENG Z.,ZHANG L.Z., ZHANG H.L., DENG F., Hierarchical chlorine-doped rutile TiO_2 spherical clusters of nanorods: Large-scale synthesis and high photocatalytic activity, J. Solid State Chem., **181,** 2008, 2516-2522.

CORRESPONDENCE

STAMBOLOVA IRINA
Assoc Prof Dr., Institute of General and Inorganic Chemistry, BAS, Acad G. Bonchev St. bl 11,
Sofia 1113, Bulgaria
e-mail: stambolova@yahoo.com

Tribological Journal BULTRIB Vol. 5, 2015
Papers from the International Conference **BULTRIB '15**
September 11-13, 2015, Sozopol, Bulgaria
Society of Bulgarian Tribologists
FIT – Technical University of Sofia

MECHANOCHEMICAL SYNTHESIS OF CdS/TiO_2 COMPOSITES FOR VISIBLE LIGHT PHOTOCATALYTIC DECONTAMINATION OF WASTEWATERS

Nina G. KOSTOVA*[1], Erika DUTKOVÁ[2], Alexander ELIYAS[1], Martin FABIÁN[2], Peter BALÁŽ[2]

[1]*Institute of Catalysis, Bulgarian Academy of Sciences, 1113, Sofia, Bulgaria*
[2]*Institute of Geotechnics, Slovak Academy of Sciences, 04001 Košice, Slovakia*
e-mail: nkostova@ic.bas.bg; Tel: (+359 2) 979 25 03; Fax: (+359 2) 971 29 67

Abstract: *Nanosized composite materials CdS/TiO_2 have been prepared by the method of mechanochemical synthesis. The samples have been characterized by means of XRD and DRS analyses. The specific surface area of the sample CdS/TiO_2, obtained by single–step mechanochemical synthesis exceeds with some 50% that of the commercially available reference photocatalyst TiO_2 P25 Degussa. The properties of the two composite materials are compared with those of the pure CdS, prepared by us, as well as with the standard reference TiO_2 photocatalyst. The properties of samples have been studied in regard to the degree of Methyl Orange dye degradation under UV-light and visible light irradiation. It has been found out that the mechanochemically synthesized samples manifest good photocatalytic activity under visible light irradiation in contrast to pure TiO_2, which is inactive under these conditions.*

Key Words: *mechanochemistry, photocatalysis, titania, CdS, Methyl Orange dye*

1. INTRODUCTION

One of the contemporary global problems is the industrial contamination of the waterways in addition to household wastewaters. The photocatalytic degradation of the wastewater contaminants appears to be a promising approach to solve this problem. Titanium dioxide is the most widely applied photocatalyst, due to its good chemical stability and photo-corrosion resistance as well as its low price [1]. The commercially available powder-form TiO_2 P25 Degussa is prepared by hydrolysis of $TiCl_4$ at high temperature or by gas-phase synthesis in a flame reactor. However, in spite of its high photonic efficiency with respect to UV-light, its wide band gap (3.2 eV for the anatase phase and 3.0 eV for the rutile phase) is limiting the absorbance of light only to the UV-region at wavelengths smaller than 390 nm. Different strategies have been put forward aimed at improving its photocatalytic activity. A series of different additives of nanosized semiconductor particles have often been used having a narrower band gap [2]. A number of methods exist for the preparation of nanometer size materials such as co-precipitation in aqueous medium, hydrothermal synthesis, the sol-gel method and others [3-4]. During the last years special attention is paid to the mechanochemical approach for the synthesis of nanomaterials, whereupon the number of research papers on this topic (i.e. mechanochemistry) is growing up considerably [5-6]. One of the advantages of the mechanochemical approach is the option to obtain a wide variety of nanosized materials by means of carrying out solid-state reactions between two or more components without any heating - at room temperature [7]. The mechanochemical synthesis has also found application in the preparation of series of catalysts [8, 9]. In the present work we report details on the direct mechanochemical synthesis of CdS/TiO_2 composite material. In parallel to this synthesis mechanical activation was carried out on a mixture of cadmium sulfide, synthesized by us in advance, and titanium dioxide P25. The properties of the synthesized composites have been studied as well as the option to use them in the process of photocatalytic degradation of the textile azo dye Methyl Orange.

6. EXPERIMENTAL

The mechano-chemical synthesis of the samples was carried out in a Pulverisette 6 planetary ball mill (Fritsch, Germany) under the following conditions: the ball mill was charged with 50 balls of diameter 10 mm having weight of 360 grams, made of tungsten carbide. The rate of rotation of the planetary carrier was 500 rpm. The experimental runs were conducted in inert atmosphere of argon at room temperature.

Pure cadmium sulfide was prepared mechanochemically in the Department of Mechanochemistry at the Institute of Geotechnics of the Slovak Academy of Sciences. A stoichiometric mixture of cadmium acetate

and sodium sulfide was milled in the course of 30 minutes in a high-energy ball mill and the reaction is described by the equation (1):

$$(CH_3COO)_2Cd.2H_2O + Na_2S.9H_2O \rightarrow CdS + 2CH_3COONa + 11\ H_2O \quad (1)$$

The CdS phase, being formed during the milling, was filtered off and washed with the aim to remove all the soluble side products of the reaction.

The first sample was denoted as CdS/TiO_2-1 and it was synthesized by milling in a planetary ball mill using the pure cadmium sulfide, prepared by us, and the commercially available TiO_2 at a ratio 1:4. The milling time interval was 30 minutes.

For the second mechanochemically synthesized composite sample CdS/TiO_2-2 a mixture of cadmium acetate, sodium sulfide and TiO_2 P25 Degussa was used. The synthesis was carried out in the planetary ball mill in inert atmosphere under the same conditions as described above.

The X-ray diffraction patterns were obtained using a D8 Advance diffractometer (Brucker, Germany) based on the Bragg—Brentano geometry, working with a CuKα radiation and a scintillation detector. Then data were collected over the angular range 15°<2 theta< 150° with steps of 0.02 and a measurement step time of 6s. For the data treatment, the commercial Bruker processing tools have been used. Specifically, for phase identification the Diffrac^{plus} Eva and the ICDD PDF2 database has been used.

The values of specific surface area (S_A) were obtained by the low-temperature nitrogen adsorption method using a Gemini 2360 sorption apparatus (Micromeritics, USA.

The diffuse reflectance UV–vis spectra were measured with a Thermo Evolution 300 UV-Vis Spectrophotometer equipped with a Praying Mantis device with Spectralon as the reference. Spectralon is a fluoropolymer, which has the highest diffuse reflectance of any known material or coating over the ultraviolet, visible, and near-infrared regions of the spectrum. Kubelka-Munk's relationships were used to transform the reflectance data into absorption spectra.

The photocatalytic experiments were carried out in a semi-batch photoreactor equipped with a magnetic stirrer, similarly as in the case of our previous work [10]. The suspension was prepared by adding CdS/TiO_2 sample (100 mg) to 100 mL of Methyl Orange (MO) solution with a concentration 1.10^{-5} M. MO degree of decolorization can be easily monitored by optical absorption spectroscopy. Prior to deposition, the suspension of MO with CdS/TiO_2 was sonificated for 5 min using UP200S ultrasound processor (Hielscher, Germany) at 24 Hz in a pulse mode. The suspension was magnetically stirred in the dark for 30 min to ensure an adsorption-desorption equilibrium. Then the light was turned on and this was considered to be the initial moment (t = 0 s) of the photocatalytic reaction. The suspension was irradiated by Philips TUV lamp (4 W). UV-C monochromatic radiation is λ=254 nm. All experiments were performed at constant stirring rate 400 rpm at a room temperature. The concentration of MO during the photocatalytic reaction was determined by monitoring the changes of the main absorbance peak at λ=463 nm. The course of MO decolorization reaction was monitored after aliquot sampling at regular time intervals. Each aliquot sample was returned to the reaction mixture immediately after the spectrophotometric measurement (operation under constant volume) and the illumination was switched on again.

7. RESULTS AND DISCUSSION

The XRD measurements were carried out to study the phase structure of the obtained samples. Figure 1 represents the XRD patterns of the two mechanochemically synthesized CdS/TiO_2 nano-composite materials. The diffractograms of the cadmium sulfide and of the commercial product TiO_2 P25 Degussa are also given for comparison in the figure. Some diffraction lines are observable in the XRD pattern of the CdS, synthesized by us, which indicate the cubic structure of hawleyite CdS (JCPDS 00-010-044). All the diffraction lines are wide, which gives evidence for the formation of fine-sized nanocrystals [11], as well as for structural disorder, which is appearing in the cadmium sulfide during the process of milling [12].

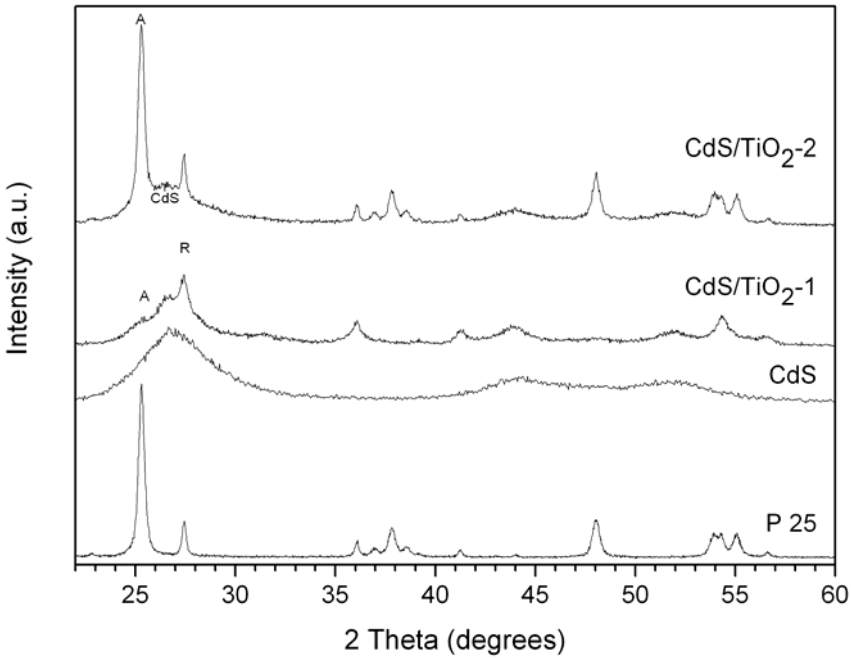

Fig. 1. X-ray diffraction patterns of the initial TiO_2 P25 Degussa and of the mechanochemically synthesized samples CdS, CdS/TiO_2-1 and CdS/TiO_2-2.

The X-ray diffraction pattern of TiO_2 P25 Degussa shows that it is composed of crystallites of anatase and rutile in a ratio 80:20. The content of the anatase phase was determined based on the formula:

$$\text{Anatase (\%)} = [0.79I_A/I_R + 0.79I_A)] \times 100 \quad (2),$$

where I_A and I_R are the intensities of the peaks respectively of (101) for the anatase and of (110) for the rutile [13].

Substantial changes were registered in the XRD pattern of the sample CdS/TiO_2-1. The XRD pattern of the sample CdS/TiO_2-1, obtained by means of mechanochemical synthesis of the mixture of cadmium sulfide and P 25 in the ball mill shows that there is substantial decrease in the intensity of the peak at $2\theta=25.2^{o}$, related to the plane (101) of the anatase. A considerable decrease in the size of the crystallites was registered in this sample. A significant widening is observed for all the registered diffraction lines. Some lines of CdS are also present. The rutile is the prevailing phase in this sample. The wide diffraction lines of the mechanochemically synthesized CdS clearly prove the nanosized nature of the sample [14]. The impact of the energy during the milling is manifested in the form of phase transformation [15]. When the powder samples are crushed between two balls during the mechanochemical synthesis or between a ball and the wall of the mill their particles are undergoing plastic deformation. These collisions, acting upon the powder particles, are leading to disruption of the crystallographic bonding and formation of a new surface. The continuing mechanical deformation could result in reduction of the size of the particles and to growth of the energy on the surface of the milled material. This is manifested through appearance of various defects, such as dislocations, vacancies, deformed or even disrupted chemical bonds, as well as increase in the number newly appearing boundary surface of the grain. The energy, supplied by the high-energy ball mill, can be controlled by varying the time interval of milling treatment, as well as by changing the velocity of rotation of the mill. Preliminary experiments were made in order to determine the optimal conditions of milling process. The milling of the material in the ball mill renders the crystal lattice of the material to be unstable and distorted, which means that a phase transformation is being induced during the milling process. This is evidenced by the XRD pattern of the sample CdS/TiO_2-1.

All the lines of TiO_2 P 25 are present, as well as those of CdS having cubic structure of hawleyite, in the diffraction diagram of the sample CdS/TiO_2-2, which was prepared by direct mechanochemical synthesis of CdS from cadmium acetate and sodium sulfide, on the surface of TiO_2 P 25. No phase transformation of anatase into rutile was registered. In this case the high-energy milling was accompanied by the generation of

fresh surface, which is displayed in a considerable growing of the specific surface area of the sample CdS/TiO_2-2 (72 m^2g^{-1}) in comparison to that of P 25 (50 m^2g^{-1}). The specific surface area of the sample CdS/TiO_2-1 was measured to be 19 m^2g^{-1}. The values of the specific surface areas of the samples are one of the most important characteristics of the milled samples [12]. The high values of the specific surface areas of the mechanochemically synthesized samples suppose their effective application in processes, depending on the surface area such as sorption, heterogeneous catalysis and others. The sample CdS/TiO_2-1 represents a soft, more plastic and less crystalline material, while the sample CdS/TiO_2-2 is less plastic and more crystalline material (Figure 1).

The diffuse-reflectance spectra in the ultra-violet and in the visible range were recorded aiming at the investigation of the optical absorbance properties of the synthesized samples. The diffuse-reflectance spectra of the samples were transformed into absorbance spectra by means of the equation of Kubelka-Munk [16].

$$F(R)=(1-R)^2/2R = \alpha/S$$

where α is the absorbance coefficient, while S is the scattering coefficient and R is the reflection of the sample.

Figure 2 represents the spectra of the initial TiO_2 P25 Degussa sample and the CdS/TiO_2-2, synthesized by us.

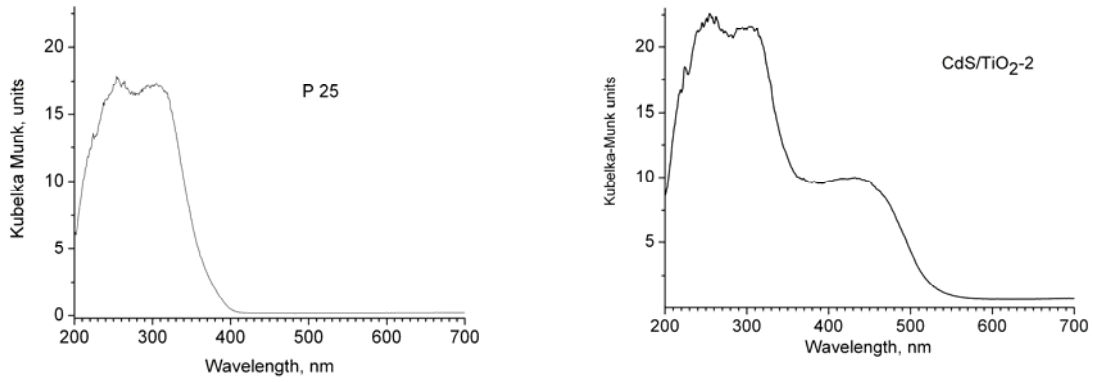

Fig. 2 UV-vis DRS spectra of TiO_2 P25 and mechanochemically synthesized sample CdS/TiO_2-2.

The absorbance spectrum of TiO_2 P25 consists of intensive absorbance only in the ultra-violet region, owing to charge transfer from the valence band (formed mainly by the 2p orbitals of the oxygen anions) to the respective conduction band (formed mainly by the 3d orbitals of the Ti^{4+} cations) [17]. The absorbance edge of the pure TiO_2 is about 390 nm. In contrast to it the absorbance edge in the spectrum of the synthesized samples of CdS/TiO_2-2 is registered at 530 nm. A red shift towards greater wavelengths is observed in the range of visible light (Figure 2). The band gaps E_g of the samples were calculated on the basis of the formula of Tauc: $\alpha h\nu = A\,(h\nu - Eg)^{n/2}$ [18], where α is the absorbance coefficient, A is a constant, $h\nu$ is photon energy and Eg is the band gap. In case of direct band gap the n is ½. The plots of the dependences $(\alpha h\nu)^2$ as a function of photon energy $h\nu$ are presents in Figure 3.

The linear sections of the curves were extrapolated down to crossing the abscise $[\alpha h\nu]^{1/2} = 0$. The evaluated band gap values of the samples are as follows: for TiO_2 P 25 - 3.3 eV; for CdS - 2.46 eV; CdS/TiO_2-1 – 2.2 eV and for CdS/TiO_2-2 – 2.35 eV. The band gap for the mechanochemically synthesized composites CdS/TiO_2 lies between those of P 25 and CdS, giving evidence for their hybrid nature. Serpone supposes that the decrease in the value of the band gap is not due to reduction of the actual band gap but it is rather due to the presence of some localized electron states, associated with the oxygen vacancies [19]. Most of the other authors ascribe the shifting in the band gap to exchange interactions between electrons of the dopant and the electrons of the valence band and the conduction band of TiO_2 [20].

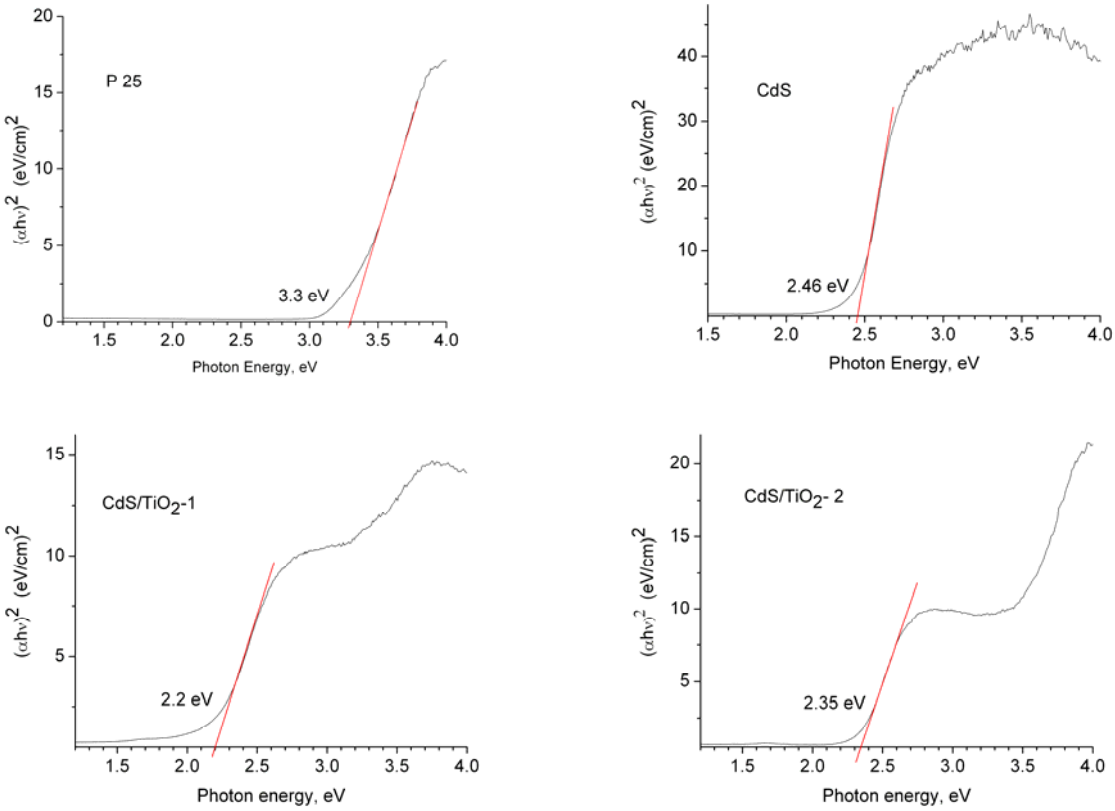

Fig. 3. The band gap energy of: initial TiO_2 P25 Degussa and mechanochemically synthesized samples: CdS, CdS/TiO_2-1 and CdS/TiO_2-2

Photocatalytic activity tests were carried out. Methyl Orange (MO) was used as model contaminant. No activity was registered in the absence of photocatalyst (blank experiment checking the possibility of direct photolysis) in view of the fact that MO is a very stable azodye. The bi-component TiO_2 P25 is known to possess very high photocatalytic activity in the removal of organic contaminants from aqueous solutions under UV-light irradiation. This is owing to the occurrence of various phase transitions between the two polymorphous forms, when they are in close contact [21].

Figure 4 represents the ratio (C_t/C_o) between the concentration at a given moment of time C_t and the initial concentration C_o in the presence of the two mechanochemically synthesized composites as a function of the time interval of illumination. The obtained results show that in the case of irradiation with UV-C light the sample CdS/TiO_2-2 shows higher activity and it leads to almost decolorization of the solution after a period of 120 min of illumination. The increase in the specific surface area of the sample CdS/TiO_2-2 gives as a result a larger number of active sites on the surface. The oxidative photodegradation of MO can be approximated to pseudo-first order reaction.

The time dependence under illumination with visible light is seen in Figure 5 of the photocatalytic oxidative decolorization of the dye in the presence of TiO_2 P 25 and the mechanochemically synthesized powder composites. The P 25 sample shows exceptionally low MO conversion degree with visible light (only 0.5 %), which can be due to the rutile phase (Eg 3.0 eV corresponding to 413 nm).

The energy of the visible light photons is not sufficient for the photoexcitation of the anatase phase TiO_2 (Eg 3.2 eV corresponding to 389 nm). The band gaps of the mechanochemically synthesized samples were narrower: 2.2 and 2.35 eV, which increases considerably their photocatalytic activity under visible light illumination. The sample CdS/TiO_2-2 manifested higher activity, which could be due to the following reasons: a) better utilization of visible light (Figure 2) and both CdS containing samples generate photoexcited electrons and positively charged holes under the effect of visible light photons, b) higher specific surface area, exceeding with some 50 % that of P 25 and c) higher degree of crystallinity.

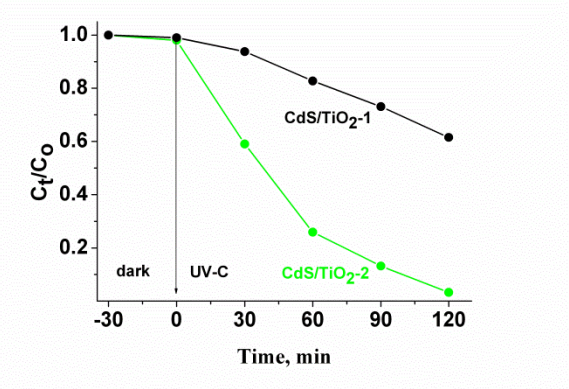

Fig. 4 Decrease in the relative concentration C_t/Co of MO with the course of time in the presence of the mechanochemically synthesized composites CdS/TiO_2 after irradiation with UV-C light.

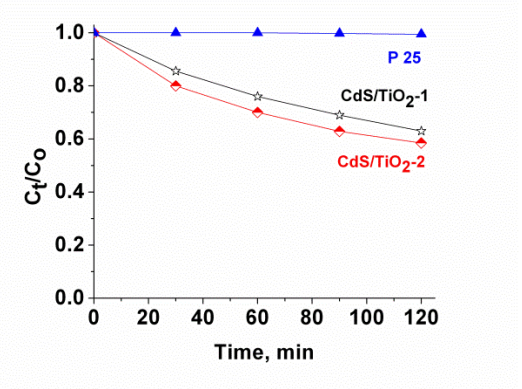

Fig. 5 Decrease in the relative concentration C_t/Co of MO with the course of time in the presence of P 25 and the mechanochemically synthesized composites CdS/TiO_2 after irradiation with visible light.

The photocatalytic destruction of the dye molecules under visible light illuminatione is not so strong as that under UV-light illumination, as the visibile light carries less energy than the ultraviolet light.

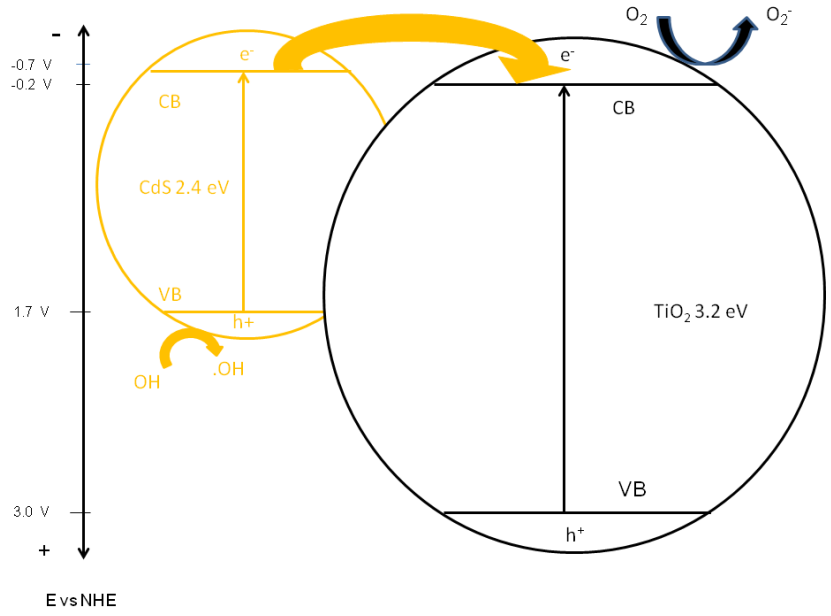

Fig. 6 Scheme of photocatalytic mechanism of the mechanochemically prepared CdS/TiO_2 composites

In view of the fact that the band gap of CdS is much more narrow than that of TiO_2 (see Fig. 3), in this case the visible light is able to generate electron-hole couples and it excites electrons from the valence band to the conduction band of CdS. As the CdS conduction band is more negative (-0.7 V NHE) than that of TiO_2 (-0.2 V negative potential). The photogenerated electrons will pass over from the conduction band of CdSto that of TiO_2, while the holes will remain in the valence band of CdS. This improves the separation of the charge carriers, involved in the reactions. A representative scheme of these transitions is shown in Figure 6. The valence bands of CdS and TiO_2 are separated to a great extent, there is no overlapping, which makes the migration of holes impossible – only the transition from the conduction band of CdS to the CB of TiO_2 is possible thermodynamically.

8. CONCLUSIONS

CdS/TiO_2 composite samples were synthesized mechanochemically. The specific surface area of the CdS/TiO_2-2 sample, obtained by direct mechanochemical synthesis is quite higher than that of TiO_2 P25. This sample shows the highest photocatalytic activity in comparison with the other samples. The diffuse-reflectance spectra give clear indication for a blue shift of the absorbance edge of the composite materials comparing with the initial TiO_2. The use of CdS- modified TiO_2 promotes the photodegradation of the textile azodye Methyl Orange under visible light irradiation. The photocatalytic destruction of the organic contaminants is a promising technology for wastewater decontamination.

ACKNOWLEDGMENTS This research work was supported by bilateral cooperation project between the Bulgarian Academy of Sciences and Slovak Academy of Sciences, VEGA 2/0097/13 and 2/0027/14, project APVV-14-0103 and by Bulgarian Science Fund of the Bulgarian Ministry of Education and science for the financial support under project T02 -17/2014.

REFERENCES

1. NAKATA, K. B., A. FUJISHINA, TiO_2 photocatalysis: Design and applications, Journal of Photochemistry and photobiology reviews, **13**, 2012, 169-189.
2. HOFFMAN, M.R., S.T. MARTIN,, W.Y. CHOI, Environmental application of semiconductor photocatalysis, Chemical Reviews, **95**, 1995, 69-96.
3. HUANG, D., S. LIAO, A. S. QUAN, L.LIU, Z. HE, J. WAN, W. ZHOU, Synthesis and Characterization of visible light responsive mixed crystal by a modified hydtothermal process, Journal of Non-Crystalline Solids, **354**, 2008, 3965-3972.
4. TRESCHEV, S.Y., P-W. CHOU, Y-H. TSENG, J-B. WANG, E.V. PEREVEDENTSEVA, CH-L. CHENG, Photoactivities of the visible-light-activated mixed-phase carbon-containing titanium dioxide: The effect of carbon incorporation, Applied Catalysis B: Environmental, **79**, 2008, 8-16.
5. BALÁŽ, P., M. ACHIMOVIČOVÁ, M. BALÁŽ, P. BILLIK, Z. CHERKEZOVA-ZHELEVA, J.M. CRIADO, F. DELOGU, E. DUTKOVÁ, E. GAFFET, F.J. GOTOR, R. KUMAR, I. MITOV, T. ROJAC, M. SENNA, A. STRELETSKII, K. WIECZOREK-CIUROWA, Chem. Soc. Rev., **42,** 2013, 7571-7637.
6. DUTKOVÁ, E., P. BALÁŽ, P. POURGHAHRAMANI, S. VELUMANI, J.A. ASCENCIO, N.G. KOSTOVA, Journal of Nanoscience and Nanotechnology, **9,** 2009, 6600-6605.
7. FABIAN M., ANTIC B., GIRMAN V., VUCINIC-VASIC M., KREMENOVIC A., SUZUKI S., HAHN H., ŠEPELAK V., Mechanosynthesis and structural characterization of nanocrystalline $Ce_{1-x}Y_xO_{2-\delta}$ (x=0.1-0.35) solid solutions. Journal of Solid State Chemistry, **230**, 2015, 42-48.
8. RALPHS, K., HARDACRE, C., JAMES, S.L., Application of heterogeneous catalysts prepared by mechanochemical synthesis, Chemical Society Reviews, **42** (18), 2013, 7701-7718
9. MOLCHANOV, V.V., R.A. BUYANOV, Scientific grounds for the application of mechanochemistry to catalyst preparation, Kinetics and Catalysis, **42**, (3), 2001, 406-415.
10. KOSTOVA, N.G., M. ACHIMOVIČOVÁ, A. ELIYAS, V. STOYANOVA, M. SHOPSKA, N. VELINOV, P. BALÁŽ, Structural and photocatalytic properties of mechanochemically synthesized nanosized zinc ferrite, Nanoscience and Nanotechnology, **12**, 2012, 52-55.
11. NIU, J.Z. W.W. XU, H.B. SHEN, S. LI, H.Z WAG, L.S. LI, Synthesis of CdS, ZnS and CdS/ZnS Core/shell nanocrystals using dodecanethiol, Bulletin of Korean Chemical Society, **33**, 2012, 393-397.
12. BALAZ P. Mechanochemistry in Nanoscience and Minerals Engineering, Springer, Berlin, Heidelberg, 2008.
13. THOMPSON, T.L, J.T. YATES, Surface science of the photoactivation of TiO_2. New photochemical processes, Chemical Reviews, **106**, 2006, 4428-4453.
14. SEPELAK, V., A. DUVEL, M. WILKENING, K-D. BECKER, P. HEITJANS, Mechanochemical reactions and synthesis of oxides, Chemical Society Reviews, **42**, 2013, 7507-7520.
15. LIN, I.J., S. NADIV, Review of the phase transformation and synthesis of inorganic solids obtained by mechanical treatment, Materials Science and Engineering **39**, 1979, 193-201.
16. CHOUDHURY B., A. CHOUDHURY, Dopant induced changed in structural and optical properties of Cr^{3+} doped TiO_2 nanoparticles, Materials Chemistry and Physics, **132**, 2012, 1112-1118.
17. VENKATACHALAM, N., M. PALANICHAMY, V. MURUGESAN, Sol-gel preparation and characterization of alkaline earth metal doped nano TiO_2: Efficient photocatalytic degradation of 4-chlorphenol, Journal of Molecular Catalysis A, **273** (1-2) 2007, 177-185.
18. BAGHERI-MOHAGHEGHI, M., N. SHAHTAHMASEBI, M. ALINEJAD, The effect of the post-annealing temperature on the nano-structure and energy band gap of SnO_2 semiconducting oxide nanoparticles synthesized by polymerizing-complexing sol-gel methods, Phys. B:Condensed Materials **403**, 2008, 2431-2437.
19. SERPONE, N. Is the band gap of pristine TiO_2 narrowed by cation-doping of titanium dioxide in second generation photocatalysts? Journal of Physical. Chemistry B, **110**, 2006, 24287–24293.
20. BOUAINE, A., N. BRIHI, G. SCHMERBER, C.U. BOUILLET, S. COLIS, A. DINIA, J. Phys. Chem. C 111, 2007, 2924–2928.
21. HENDERSON, M.A., A surface science perspective on TiO_2 photocatalysis, Surface Science Reports **66** (6-7), 2011, 185-297.

CORRESPONDENCE

Nina G. Kostova
Institute of Catalysis, Bulgarian Academy of Sciences,
acad. G. Bonchev Str. Bl. 11, 1113 Sofia, Bulgaria
e-mail: nkostova@ic.bas.bg

Tribological Journal BULTRIB Vol. 5, 2015
Papers from the International Conference **BULTRIB '15**
September 11-13, 2015, Sozopol, Bulgaria
Society of Bulgarian Tribologists
FIT – Technical University of Sofia

TRIBOLOGIC PROBLEMS WITH HEAVY DUTY WHEELED CRANES

Marusia Teofilova

Abstract: *Performance problems with heavy duty wheeled cranes are a predominantly tribologics character. The regime-violations of friction and hermetic, have resulted, leading to pathological or abrasive wearing out of the functionally significant details and manirulatorite systems. In the work is the analysis of the renovation work and analysis of their economic efficiency.*

Key Words: *friction, wearing out, hermetic, cranes*

ТРИБОЛОГИЧНИ ПРОБЛЕМИ НА ТЕЖКОТОВАРНИ МАНИПУЛАТОРИ

Маруся Теофилова

Резюме: *Експлоатационните проблеми при тежкотоварните колесни кранове имат преобладаващо трибологичен характер. Нарушенията в режимите на триене и херметичност водят до патологично или абразивно износване на функционално значими детайли и системи на манипулаторите. В работата са анализирани ремонтните дейности и икономическата ефективност на абонаментното сервизно обслужване.*

Ключови думи: *триене, износване, херметичност, кранове.*

1. ВЪВЕДЕНИЕ

Тежкотоварните манипулатори са специфични трибосистеми, съставени от работещи в екстремни режими подсистеми, чието функционално състояние е предпоставка за невъзвратими патологични трибологични явления. Преодоляването им е свързано с разход на висококвалифициран труд и средства, скъпи елементи и консумативи, ниска експлоатационна продуктивност на машините.

В работата е направен анализ на характера и повтаряемостта на отказите с трибологична предопределеност с цел предотвратяването им чрез изграждане на система за превенция и завишен контрол за изпълнението на предписаните такива норми.

2. СЪСТОЯНИЕ НА ПРОБЛЕМА

Анализът е направен въз основа на възникналите повреди за група от петдесет тежкотоварни кранове и подвижни работни площадки стрелови тип (вишки) от различна марка и клас, товароподемност и работен обхват – таблица 1 [1].

Таблица 1. Марки и характеристики на анализираните манипулатори

марка	***товароподемност***	***и дължина на стрелата***	***марка***
Автокран FABLOK	25 тона	22 тона	Автокран РН
Автокран ТАТРА	20, 28 тона, до 20м	20 тона	Автокран ГОТВАЛД
Автовишка "ШИПКА"	200 – 500 кг, 14, 16, 22м		Самотоварач "МАН"
Автокран ГАЗ	25 тона	16 тона	Автокран BUMAR,
Автокран IFA - ADK 70 Автокран IFA - ADK 125	7 тона 12.5 тона	7-12 тона, 15м	Автокран МАЗ
Автокран LIEBHERR 1030 Автокран LIEBHERR 1070	30 тона 70 тона	16 - 20 тона	Автокран ШКОДА К100
Автокран GROVE	60 тона	200 – 500 кг	Автовишки - ЗИЛ, ГАЗ

Въпреки габаритите им, при тежкотоварните кранове контактът с околната среда е съсредоточен в зони с ограничена геометрия на условно дефинираните “вход” и “изход” на системата – работният орган и стабилизиращите опори. Тази им особеност ги класифицира като трибосистеми от “полуотворен” тип, принципно изобразени на фиг.1. Това са изключително рискови и уязвими трибосистеми, защото всички привидно незначителни отклонения от функционалните характеристики на всеки детайл, съчетани с екстремните и често ударни натоварвания, бързо мултиплицират в патологични трибологични състояния, които се преразпределят и поемат от съставните подсистеми.

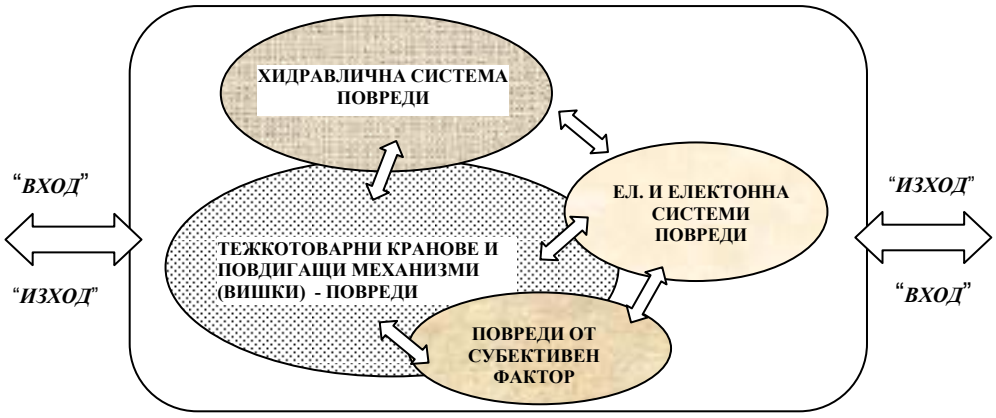

Фиг. 1. Трибосистема от “полуотворен” тип

Обикновено предпоставките за отказ възникват в хидравличната система на манипулаторите. Най-често срещаните са описани в таблица 2.

Таблица 2. Трибологични предпоставки за отказ

проявление	повреда	последствия
наличие на теч	-износени уплътнения -дефектирали елементи на системата	- формиране на режими на “сухо” триене, поява на патологични форми на износване (задиране, наклеп); - проникване на твърди частици в системата, дефектиране на елементи, абразивно износване; - загуба на устойчивост на съоръжението („пропадане“ на опори); - загуба на масло (до 400 l е разходът при почистване на системата); - замърсяване на околната среда; - загуба на експлоатационен ресурс; - скъпи ремонтни дейности
загуба на мощност в хидросистемата	-износени части на елементите; -запушени филтри; -понижени характеристики на елементи системата поради изтекъл експлоатационен ресурс; -загуба на вътрешна херметичност поради износени или с изчерпан ресурс части на елементи на системата	-нарушения в силовите вериги; -неконтролирано поведение във веригите за управление и защита, сработване на релета и клапани; -поява на твърди частици в системата, запушване на филтри, индикации за аварийни състояния при занижени налягания
нехарактерен шум в елементи на системата	-запушени филтри, наличие на твърди частици в системата; -форми на интензивно и абразивно износване на елементи	-формиране на нерегламентирани подбутални обеми или такива в помпата, което изменя експлоатационните им характеристики; -загуба на мощност и блокиране на системата

За илюстрация на фиг.2 са показани снимки на патологично износване с пренос на материал и задиране на бутало на 50 тонен ТАКРАФ, следствие от износено уплътнение.

Фиг. 2. Патологично износване

Формирането на режим на “сухо триене” в съчетание с голямо натоварване и наличие на твърди частици в системата са предпоставка за интензивно механохимично и абразивно износване, показани на фиг.3. Повредените детайли са само част от пораженията в системата, следствие от ненавременна смяна на уплътнения и маслото на КАМАЗ.

Фиг. 3. Абразивно износване

Филтрите са друго рисково звено в системата. Липсата на диагностика и ненавременната им подмяна са в основата на последващи откази – фиг. 4.

Фиг. 4. Запушени филтри

Таблица 3. Разпределение на броя на отказите между системите и елементите им

повреди в хидравлична система						
уплътнения	клапани	разпределители	цилиндри	помпи	филтри	маркучи, тръби и др.
12	19	6	3	3	5	5 + 3
повреди в електрическа и в електронна системи				9		
други повреди на конструкцията				6		

От данните в горната таблица се вижда, че отказите са съсредоточени в хидравличната система на манипулаторите. Парадоксално е, че най-уязвимото й място се оказват клапаните – почти два пъти повече дефектирали клапани от броя на повредените уплътнения. Анализът на тази заблуждаваща разлика доказва тревожната тенденция преобладаващо елементите на системата да бивat ремонтирани и по-рядко подменяни с нови. Превантивните дейности са сведени до подмяна на уплътнения и филтри. Работи се с остарял машинен парк, обикновено – реновиран. Нарушават се предписаните режими на експлоатация, пренебрегват се диагностичните дейности и нормативните документи за сервизно обслужване [2].

За илюстрация на икономическата ефективност от превантивните дейности при сервизна експлоатационна поддръжка и диагностика са съпоставени разходите от функционално-стойностните изчисления за конкретен авариен ремонт с тези при съответното сервизно обслужване – таблица 4.

Таблица 4. Функционално-стойностен анализ на авариен ремонт и сервизно обслужване

извършени дейности при авариен ремонт	дейности при абонаментно сервизно обслужване
смяна на филтри на целулозна основа; смяна на масло и промиване на системата (~400l) почистване на филтър тарелков тип; ремонт на цилиндър; ремонт на клапан; загуби от експлоатационно време; начисления за труд; транспортни разходи	смяна на филтри на целулозна основа; смяна на масло на 2000 часа (~250l); абонамент; начисления за труд; транспортни разходи
Приблизителна стойност: 6000 лв.	Приблизителна стойност: 2000 лв.
Не са начислени потенциалните предстоящи разходи от абразивно износени детайли на непосочени елементи от системата.	Не са описани разходите за диагностика на съоръжението, безвъзмездно съпътстващи абонаментния сервиз.

3. ЗАКЛЮЧЕНИЕ

Експлоатационните проблеми с трибологичен характир при тази техника са неизбежни, но е възможно минимизиране на разходите за решаването им чрез превантивни дейности, стриктно прилагане на нормативните документи, обучение на кадри, нови форми на сътрудничество между клиентите и обслужващите звена. Горните изчисления красноречиво доказват икономическата ефективност на абонаментното сервизно обслужване.

БЛАГОДАРНОСТИ

Авторът изказва благодарност за любезното съдействие и предоставения фактологичен материал на фирма “ВИРА–90”.

ЛИТЕРАТУРА

1. Данни от протоколи на фирма “ВИРА–90”.
2. Наредба за безопасната експлоатация и технически надзор на повдигателни съоръжения, Глава 3, Раздели: Поддържане, ремонт и преустройване, Технически надзор, Технически прегледи и проверки. В сила от 18.10.2010.

КОРЕСПОНДЕНЦИЯ

Доц. д-р Маруся Теофилова
ТУ – София, „Климент Охридски“ 8
e-mail: mat@tu-sofia.bg

Tribological Journal BULTRIB Vol. 5, 2015
Papers from the International Conference **BULTRIB '15**
September 11-13, 2015, Sozopol, Bulgaria
Society of Bulgarian Tribologists
FIT – Technical University of Sofia

SOME ASPECTS OF OPTICIAN BUILDING GLASS RELATED HEATING SYSTEM DESIGN

Lachezar Grigorov

Abstract: Background/importance of research topic: Optical characteristics determine more reflection to less transition and back. Tendency to decrease expense for air-conditions of buildings lead to usage of specific glass with great reflection. So we have two negative results: reflection to around spice with blinding-effect and more thermal influence in around space and less into building. But exactness our choice depends of calculation method.

Purpose/hypothesis (thesis or statement of problem): Now we have dates about effects of reflection only in case of perpendicular direction of sun rays to glass surface. Let take in mind, which at the effect must be different in general case, when the angle is different from 90 degree. Differences are bigger about UV rays. We need of correct optical dates about building-glass systems.

Procedures/Data/Observations: Summary of procedures, emphasizing key points or steps are correct calculations, based on actual cases where the incident angle is other than 90 degrees, and particularly for UW rays.

Conclusions/Applications:

To spend money for air condition must have correct base for calculations. It is necessary to have standard about methods of calculation in glass-transparency and reflection. Up to now methods are not correct. abstract should be in 10pt Arial, Italic, Justified – not more than 6 lines long, summarising the work and placing it in an appropriate context.

Key Words: *Standard, air condition calculations, transparency and reflection in glass.*

INTRODUCTION

Now we have great diversity of difference building-glass with main characterizations:-coefficient of transition of UW-rays; coefficient of thermal transition; reflection; solidity and tempering; color; weigh; sound-isolation; quality of treatment; additional quality, ell-glass; prize. Optical characteristics determine more reflection to less transition and back. Tendency to decrease expense for air-conditions of buildings lead to usage of specific glass with great reflection. So we have two negative results: reflection to around spice with blinding-effect and more thermal influence in around buildings. But exactness our choice depends of calculation method. Now we have dates about effects of reflection only in case of perpendicular direction of sun rays to glass surface. Let take in mind, which at the effect must be much different in general case, when the angle is different from 90 degree.

1. FORMULAS AND PHYSICAL EFFECTS

When passing the light from the atmospheric space in the windows of the building , light is distributed in three directions - and refraction pass , reflection and absorption . This is illustrated as follows:

Io = Ir + It + Ia,
r + t + a = 1.

The intensity of all light = the sum of intensities of reflected , refracted and absorbed light energy . The sum of the coefficients of reflection, refraction and absorption = 1 .

According to the law of Snellius: , where n is the refractive index .
Glass n = 1,515. (Fig.1, Fig.2)
Simple calculations show that in order to obtain total internal reflection of the glass is necessary sinus alpha = 0.999 , or the incident beam to be nearly parallel to the glass. In practice, we can not get this option and do not care associated with construction glass. (Fig.1)

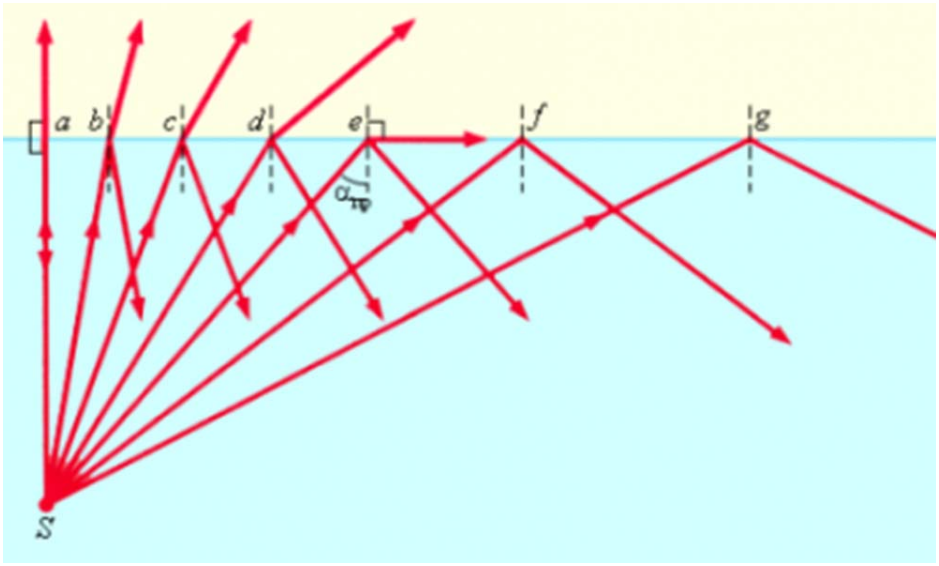

Fig.1

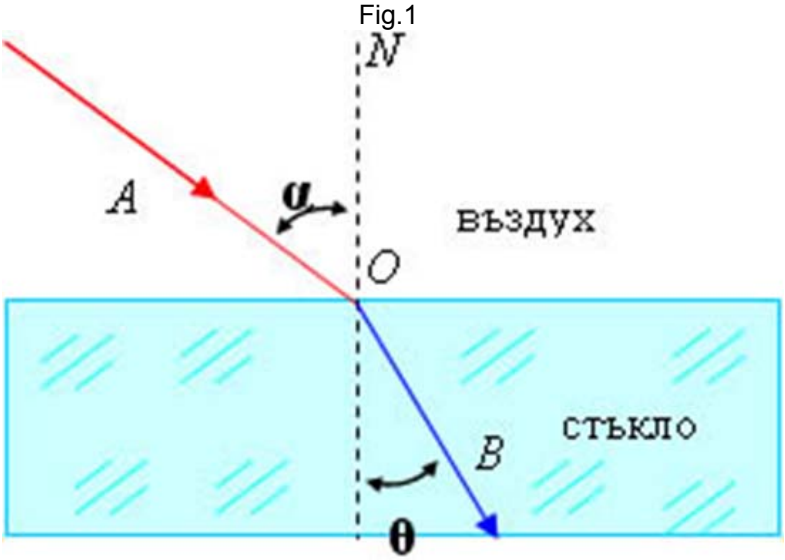

Fig.2

What is interesting is the fact that reflectivity depends on the angle of incidence of light a (it seems particularly well in dielectrics) . Most have little impact in vertically or almost vertically incident light - at Alpha from 0 to 30 °. With increasing angle , reflectivity is growing rapidly and reaches 1 if a = 90 °. Therefore, coefficient of reflection r of a surface is defined at an angle of 0 ° or in the range of 0 to 30 °.

Such is the practice of manufacturers and suppliers of building windows - they give relevant indicators for the case when light falls perpendicular to the glass surface. Only the case 90 degrees. In reality, virtually no such case ! However, all calculations are precisely on this basis.

2. ISSUES

What happens in practice? - HVAC engineers do their calculations for non-existent case. Accordingly, the investor pays for the building installation that is not calibrated correctly , as the basis for calculation is not correct , and later spent years paying for air conditioning in more than the correct case. Moreover, most likely the selection of lenses will only my be appropriate . There is another point. As is known , the coefficient of the switch is dependent on the dielectric constant / The index of refraction is expressed as the square root of the product of magnet and the dielectric permeability of the medium and depends on the properties of the substance and the wavelength of the radiation / . And she in turn determines the different refraction and switch to different frequencies of light. This means that for the various cases will have noticeable deviations in the calculations, for angles greater than 30 degrees.

Perhaps smoothing minor differences , but for large buildings , especially buildings with large glazing percentage this difference represents interest for the one who pays the cost of air conditioning.

There is another point concerning the presentation of glass for construction. The principle of Huygens - Fresnel explains how the swelling of light inside the glass (Fig.3)

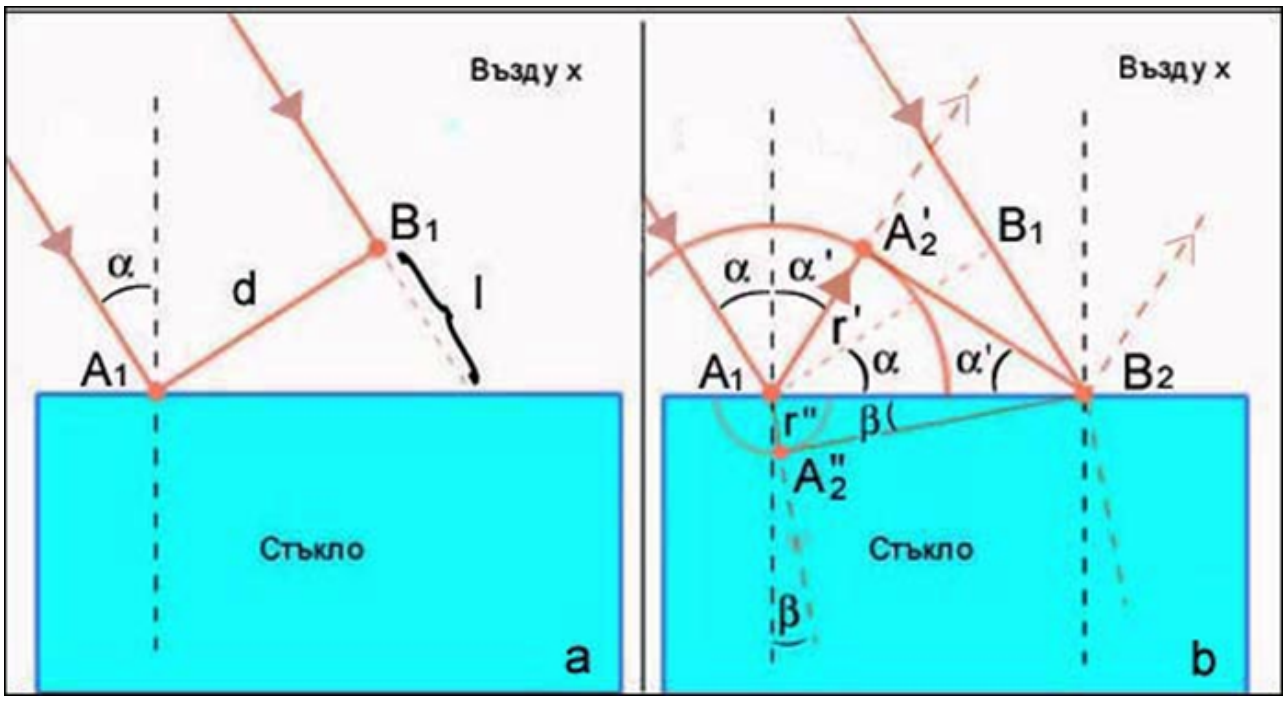

Fig.3

Some samples presentation of construction glass. Curious is the relationship with Formula 1 .
(Fig.4, Fig.5, Fig.6)

Sample applications of different kind of glass (Fig.7, Fig.8, Fig.9, Fig.10)
BBC – building, Sofia, Bulgaria (2008-2010), project:2006-2009 “STEFAN DOBREV– ARCH&DESIGN” (arch. Stefan Dobrev, arch. Lachezar Grigorov, arch. D. Pass),
inv. ” Benchmark” AD. There are roof-glass, north-direction-glass, south-direction glass, double-skin facade, printed glass. (Tall engineering).

Your composition:

10 10.2 Stratobel 2x Planibel Clear

Personal notes:

LIGHT		ENERGY	
Transmission	82	Solar factor	67
Reflection	7	Energy Reflection	6

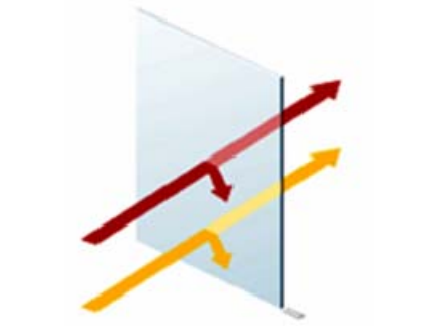

THERMAL PROPERTIES (EN 673)	EN 673
Ug-Value - W/(m².K)	5.2

LIGHT PROPERTIES (EN 410)	EN 410
Light Transmission - τv (%)	82
Light Reflection - ρv (%)	7
Internal light reflection - ρvi (%)	7
Colour Rendering - RD65 - Ra (%)	95

ENERGY PROPERTIES	EN 410	ISO 9050
Solar factor - g (%)	67	66
Energy Reflection - ρe (%)	6	6
Direct Energy Transmission - τe (%)	58	56
Total Energy absorption - αe (%)	36	38
Shading coefficient - SC	0.77	0.76
UV Transmission - UV (%)	0	
Schattenfaktor (DE) - b-Faktor		83.0

OTHER PROPERTIES	
Resistance to fire - EN 13501-2	NPD
Reaction to fire - EN 13501-1	NPD
Bullet Resistance - EN 1063	NPD
Burglar Resistance - EN 356	P1A - P2A
Pendulum body impact resistance - EN 12600	1B1
Direct airborne sound insulation(Rw (C;Ctr) - ESTIMATED) - dB	40 (-1, -3)

Fig.4

Your composition:

6 mm Stopray Vision-60 pos.2 - 16 mm Argon 90% - 44.2 Stratobel 2x Planibel Clear

Personal notes:

LIGHT		ENERGY	
Transmission	59	Solar factor	34
Reflection	15	Energy Reflection	31

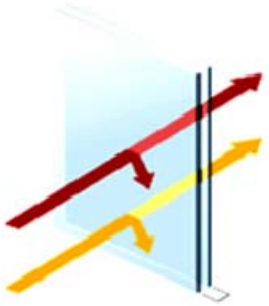

THERMAL PROPERTIES (EN 673)	EN 673
Ug-Value - W/(m².K)	1.0

LIGHT PROPERTIES (EN 410)	EN 410
Light Transmission - τv (%)	59
Light Reflection - ρv (%)	15
Internal light reflection - ρvi (%)	17
Colour Rendering - RD65 - Ra (%)	95

ENERGY PROPERTIES	EN 410	ISO 9050
Solar factor - g (%)	34	32
Energy Reflection - ρe (%)	31	33
Direct Energy Transmission - τe (%)	29	27
Solar abs. Glass 1 - αe (%)	36	37
Solar abs. Glass 2 - αe (%)	4	3
Total Energy absorption - αe (%)	40	40
Shading coefficient - SC	0.39	0.37
UV Transmission - UV (%)	0	
Schattenfaktor (DE) - b-Faktor		40.0

OTHER PROPERTIES	
Resistance to fire - EN 13501-2	NPD
Reaction to fire - EN 13501-1	NPD
Bullet Resistance - EN 1063	NPD
Burglar Resistance - EN 356	P1A - P2A
Pendulum body impact resistance - EN 12600	NPD / 1B1
Direct airborne sound insulation(Rw (C;Ctr) - ESTIMATED) - dB	37 (-1, -3)

Fig.5

ECKELT GLASTECHNIK

AWT/EXCEL/KARL/technical values Litex with 31_19

Licht- und Strahlungstechnische Daten

San Stefano
D G U
8mm SECURIT clear Float with Litex #2,
Colour standard white BF2WS, IPASOL 31_18
16mm Argon (90%)
8mm clear Float / 0,76mm PVB / 8mm clear Float

LT = Light Transmittance
LRE = Outdoor Light reflectance
TE = Energy Transmittance
RE = Outdoor Energy reflectance
g-Wert = Solar factor g
b-Wert = Shading coefficient

Bedeck. in %	LT	LRE	TE	RE	g-WERT	b-Wert
0	29%	25%	13%	29%	18%	0,21
5	28%	26%	13%	29%	18%	0,20
10	27%	28%	12%	30%	17%	0,20
15	26%	29%	12%	30%	17%	0,19
20	26%	30%	11%	31%	16%	0,19
25	25%	31%	11%	31%	16%	0,18
30	24%	33%	11%	32%	15%	0,18
35	23%	34%	10%	32%	15%	0,17
40	22%	35%	10%	33%	14%	0,17
45	21%	36%	9%	33%	14%	0,16
50	21%	38%	9%	34%	14%	0,16
55	20%	39%	9%	34%	13%	0,15
60	19%	40%	8%	34%	13%	0,14
65	18%	41%	8%	35%	12%	0,14
70	17%	43%	7%	35%	12%	0,13
75	16%	44%	7%	36%	11%	0,13
80	15%	45%	7%	36%	11%	0,12
85	15%	46%	6%	37%	10%	0,12
90	14%	48%	6%	37%	10%	0,11
95	13%	49%	5%	38%	9%	0,11
100	12%	50%	5%	38%	9%	0,10

Die Berechnung erfolgte mit der Standard-Farbe BF2WS (Standard weiß)
Die bekanntgegebenen Werte sind Richtwerte und können um absolut größer +- 5% schwanken.

The calculation was done with the standard colour BF2WS (standard white)
The communicated values are appoximate values and can deviate absolutely more than +- 5%

LITEX BLEND- UND SONNENSCHUTZGLAS

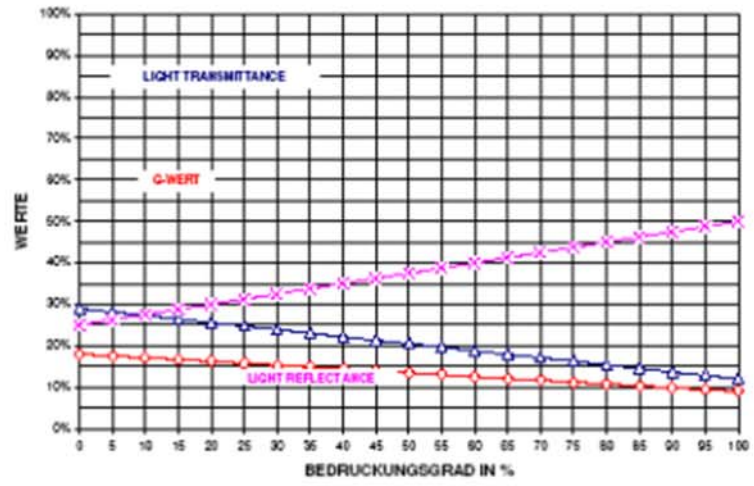

Stand 18.03.2013

NUR INTERN VERWENDEN

Fig.6

3. WHAT IS NEEDED TO CORRECT SELECTION OF CONSTRUCTION GLASS, EXCEPT PRACTICED SO FAR.

3.1. Manufacturers and suppliers to develop a database for cases when the angle of incident light is greater than 30 degrees. Specially attention about UV light.

3.2. To develop tables that help the user to reflect how factors operate at different exposure of the facade. Obviously facade, which does not fall on direct solar radiation , the glass will be quite different compared to oslanchenite surfaces. It should be applied factor diffuse lighting and how the glasses will work in this case.

3.3. The user can not orientate himself , and manufacturers do not do anything in that direction , at least visibly . Therefore, a standard that :

3.3.1. To regulate methods of presentation of the product , taking into account the realities - namely the needs of the buildings - calculations incident beam in the range above 30 degrees.

3.3.2. To develop tables that user understand the case with diffusely illuminated facades.

3.3.3.Tables orienting the applications on different latitudes to be developed

Fig.7
South elevation, main entrance, double skin façade, titanium covering in low levels.

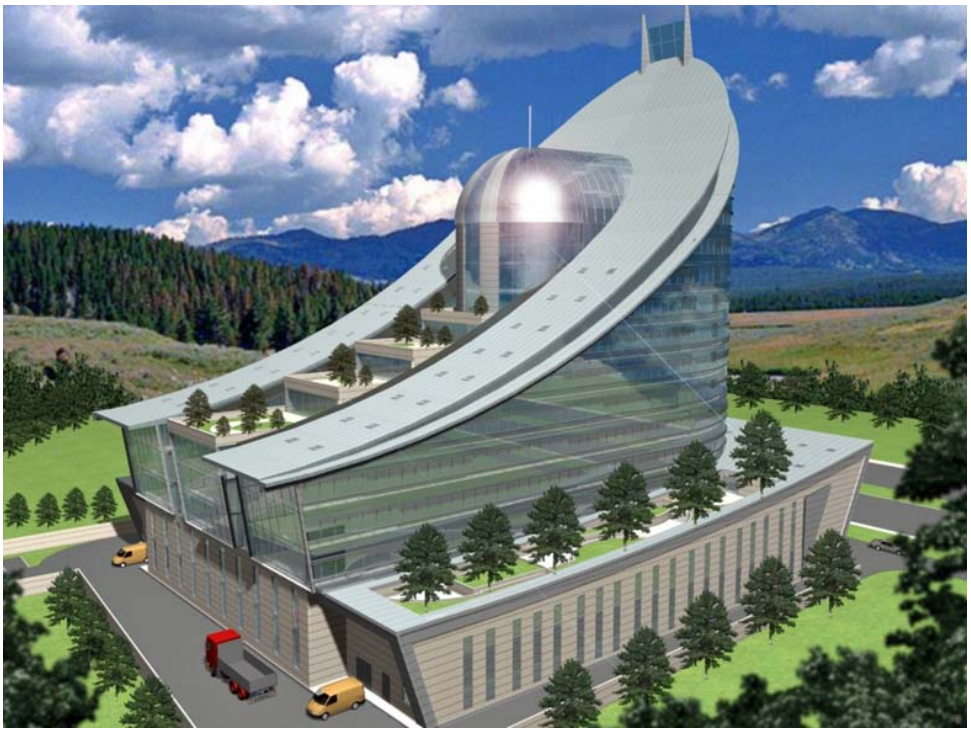

Fig.8
Side elevation, back (north) elevation, roof – glass, atrium, roof-garden

Fig.9. Atrium – look to up

Fig.10 Under glass-roof – 4 months before final building efforts. (Autor is in middle)

*4.*CONCLUSION

Now we have dates about effects of reflection only in case of perpendicular direction of sun rays to glass surface. Let take in mind, which the effect must be to much bigger in general case, when the angle is different from 90 degree, in particular for an angle exceeding 30 degrees.

Another case is indirect sunlight . Nobody take in mind effects of reflection and transition as system, in depending of solar effect into spice inside building and around spice together. All this set necessity new correct method of presentation, helping for correct choice of glass in buildings. The problem must be shown complexly, responsibly and in all aspects. This is in connection with expenses for climatic conditions, comfort of inhabitation and not at last – safety of inhabitation.

If we make calculations, we can see differences is my be not so great to take in mind in generally daylight . If we examine more precisely the things we find that the difference between the real and the represented characteristics increases with the spectral frequency. Otherwise, a high- end offset is larger and especially for ultraviolet - rays .

Below we show some concrete numbers .

Calculations show 16% deviation on 60 to 30 degrees for dayly light and +2% for UV.

REFERENCES

1.www.Your Glass.com YOUR GLASSPOCKET AGC.(2013)
2.Technical specifications EKONTROL – GLASS (2013)
3.Kiril Welkowski Report for results of computer simulation (2012) (BBC – building)
4.Eckelt Glasstechniks (2014)
5.Architect Haine Architectur. Karlstadt Dortmund Germany. Glass guid. Saint-Gobain Glass. (2015)

CORRESPONDENCE

Lachezar Grigorov
Assistant, TU – Sofia/Bulgaria,
madra_horn@abv.bg

Tribological Journal BULTRIB Vol. 5, 2015
Papers from the International Conference **BULTRIB '15**
September 11-13, 2015, Sozopol, Bulgaria
Society of Bulgarian Tribologists
FIT – Technical University of Sofia

ALUMINA BASED PHOTOCATALYSTS FOR DEGRADATION OF REACTIVE BLACK 5 TEXTILE DYE AQUEOUS SOLUTION

Katya MILENOVA[1], Katerina ZAHARIEVA[1], Ivalina AVRAMOVA[2], Alexander ELIYAS[1], Irina STAMBOLOVA[2], Vladimir BLASKOV[2], Ljubomir DIMITROV[3], Zara CHERKEZOVA-ZHELEVA[1], Boris KUNEV[1], Slavcho RAKOVSKY[1]

[1]Institute of Catalysis, Bulgarian Academy of Sciences, "Acad. G. Bonchev" St., Bl.11, 1113 Sofia, Bulgaria
[2]Institute of General and Inorganic Chemistry, Bulgarian Academy of Sciences, "Acad. G. Bonchev" St., Bl.11, 1113 Sofia, Bulgaria
[3]Institute of Mineralogy and Crystallography "Acad. I. Kostov", "Acad. G. Bonchev" St., Bl.109, 1113 Sofia, Bulgaria.

Abstract: *Alumina based samples were synthesized by precipitation method, calcined at two temperatures. The degree of oxidation of Reactive Black 5 textile dye under UV-light was measured spectrophotometrically. The mechanochemical activation (MCA) results in higher photocatalytic activity. The mechanochemical treatment increases the conversion to 40%, compared to 29% of the non-treated sample. The rate constant k (calculated from the slope of -ln(C/C$_0$)=kt) of non treated sample is 2.3x10^{-3} min^{-1}, while MCA-treated sample exhibits higher rate constant (2.9 x10^{-3} min^{-1}).*

Key Words: *alumina, mechanochemical activation, Reactive Black 5 dye, photocatalysis, wastewaters*

1. INTRODUCTION

In the last years, alumina has been regarded as an essential material in view of its high surface area, large pore volume, uniform pore size and low toxicity, finding various applications for environmental purification, as catalyst [1], adsorbent [2÷7], electrochemical sensor [8], photocatalyst and others [2]. Some researchers reported about application of Al_2O_3 for the removal of textile dye from aqueous solutions [9]. The bleaching of wastewaters is necessary not only because of aesthetic considerations but mainly due to environmental concerns about degrading hazardous substances in effluent from textile dyeing industry. The photocatalytic removal of pollutants is effective in the degradation of various organic impurities in wastewaters [9]. Mesoporous alumina was applied to the adsorption of Methyl Orange [2,3], Congo Red [3,4,5], binary systems including Methyl Orange + Bromothymol Blue, Methyl Orange + Reactive Yellow and Methyl Orange + Methyl Violet [5] also mixture of Alizarin Red and Alizarin Yellow [6] from aqueous media. Modified immobilized activated alumina was used for the adsorption of Cibacron Reactive Yellow dye [7].

Al_2O_3 was applied up now as photocatalyst for the degradation of phenolic compounds in presence of UV light [10]. In reference [11] authors have studied photomineralization of phenol on Al_2O_3. Alumina doped calcium oxide with band gap of 3.3 eV was used in photodegradation of 2,4,6-trinitrophenol [12]. Romanias and co-workers have studied the photodegradation of pyrene on Al_2O_3 surfaces [13]. TiO_2–Al_2O_3 binary oxide surfaces were utilized in order to develop an alternative photocatalytic NOx abatement approach [14].

Alumina powders have been obtained by photo cross-linked poly(dimethyl acrylamide) hydrogels [15], template method using dodecylamine [4], sol–gel method [10], combination of sol–gel, electrospinning [2], homogeneous precipitation method [3], hydrothermal reaction [8] etc. It is important to develop a facile and environmentally friendly method for increasing photodegradation efficiency of Al_2O_3 for organic pollutants removal [3].

The aim of the present work was to apply the mechanochemical activation on alumina containing powders and to study their photocatalytic efficiency in the degradation of Reactive Black 5 textile dye under UV-light.

2. EXPERIMENTAL

The three investigated samples were obtained by procedures, described in Bulgarian Patent [16]. Alumina containing powders were synthesized by precipitation method using $Al(OH)_3$, $CaCO_3$ and ammonia at constant pH 8. The suspension of $Al(OH)_3$ and $CaCO_3$ was filtered, washed and calcined at different temperatures. The ratio $Al(OH)_3$ and $CaCO_3$ was preset in view of preparing 90 wt % Al_2O_3 and 10 % wt CaO. One set of samples annealed at 1000°C for 2h was denoted as (AC). The other set was calcined at 500°C for 1h first and afterwards at 1000°C for 1h (ACO).

The alumina based photocatalyst (ACO) was mechanochemically activated on a highenergy planetary ball mill type PM 100, Retsch, Germany using agate milling container with volume 80 ml. The sample was treated for milling time interval of 15 minutes and milling speed 400 rpm. The weight ratio between treated material and balls was 1:9. The treated sample is denoted as ACO-MCA.

The powder X-ray diffraction patterns (PXRD) of AC and ACO powders were recorded on a TUR M62 apparatus, Germany with PC control and data acquisition, using HZG-4 goniometer and CoKα radiation. The identification of the phases registered in PXRD patterns was accomplished based on JCPDS database (Powder Diffraction Files, Joint Committee on Powder Diffraction Standards, Philadelphia PA, USA, 1997).

The X-ray diffraction (XRD) patterns of ACO-MCA sample were recorded on a Bruker D2 Phaser diffractometer varying the 2θ values from 20º to 70º using Cu K_α radiation (λ = 0.154056 nm) at 40 kV.

SEM studies were carried out on a JSM – 5510 JEOL scanning electron microscope. The accelerating voltage 10 kV was used for morphology observations of the samples.

The X-ray photoelectron spectroscopy (XPS) studies were performed in a VG Escalab II electron spectrometer using AlKα radiation with energy of 1486.6 eV under base pressure 10^{-7} Pa and a total instrumental resolution 1eV. The binding energies (BE) were determined utilizing the C 1s line (from an adventitious carbon) as a reference with energy of 285.0 eV. The accuracy of the measured binding energy was 0.2 eV. The C1s, O 1s, Al2p and Ca2p, photoelectron lines were recorded and corrected by subtraction of a Shirley's-type of background and quantified using the peak area and Scofield's photoionization cross-sections.

The photocatalytic oxidative degradation of Reactive Black 5 (RB5) was carried out using 150 ml dye aqueous solution with initial concentration of 20 ppm. Photocatalytic activity measurements were accomplished using polychromatic UV-A lamp illumination (18 W, 320-400nm) with a maximum of the emission at 365 nm. The process of discoloration was monitored by UV-Vis spectrophotometer CamSpec M501, based on the absorbance of the dye solution in the wavelength range from 200 to 800 nm. The samples were stirred in the dark for about 30 min to reach adsorption-desorption equilibrium before switching on the illumination.

3. RESULTS AND DISCUSSIONS

Fig. 1 illustrates the powder X-ray diffraction patterns of the studied powder samples. They show the presence of α-Al_2O_3 (PDF-10-0173), ɵ-Al_2O_3 (PDF-35-0121) and $Ca_3Al_2O_6$ (PDF-38-1429) phases. We can see in the figure the differences between XRD patterns of the AC sample, which was annealed at 1000°C and ACO sample, which was calcinated first at 500°C and afterwards at 1000°C. These differences in intensity and presence of some of the registered phase are probably due to differences in calcination procedure. According to XRD pattern of AC sample the quantity of $Ca_3Al_2O_6$ phase is higher. On the contrary in ACO sample the appearing diffraction peaks of α-Al_2O_3 possess higher intensity, because of longer high temperature calcination. The X-ray diffractogram of the mechanochemically activated ACO-MCA sample is represented in Figure 2. The presence of the same phases - α-Al_2O_3 (PDF-10-0173), ɵ-Al_2O_3 (PDF-35-0121) and $Ca_3Al_2O_6$ (PDF-38-1429) having different peak intensities, being registered after mechanochemical treatment. The X-ray amorphous halo peaks are observed in the spectra of mechanochemically activated ACO-MCA catalyst also.

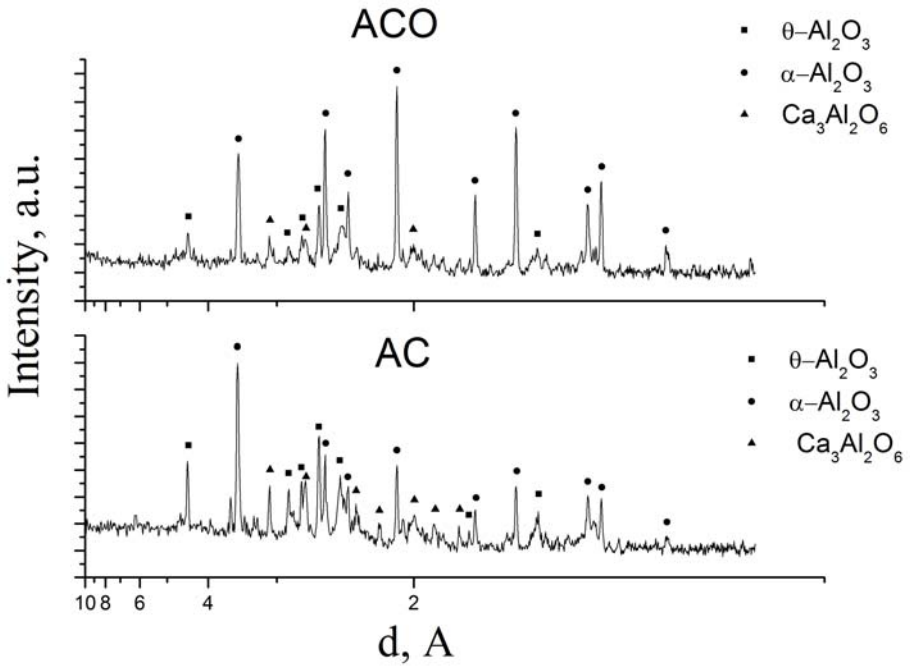

Fig. 1. XRD patterns of alumina based samples

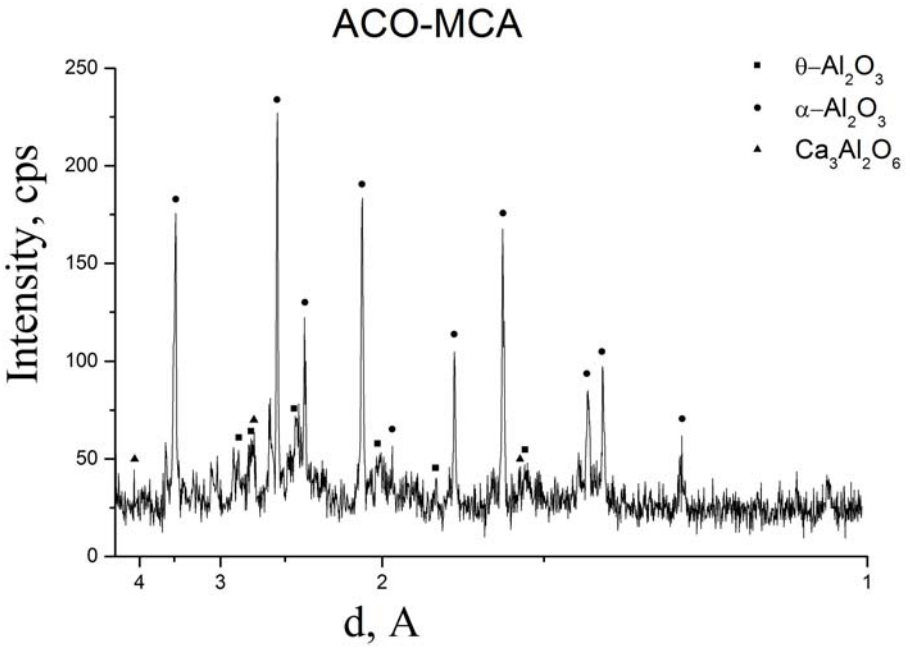

Fig. 2. XRD pattern of mechanochemically activated alumina based sample

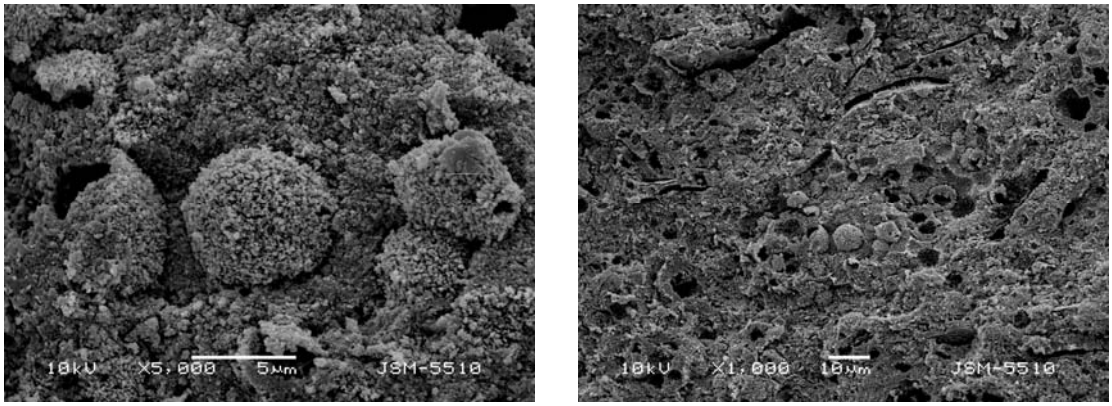

(a) (b)

Fig. 3. SEM pictures of sample AC at (a) magnification 5,000; (b) magnification 1,000

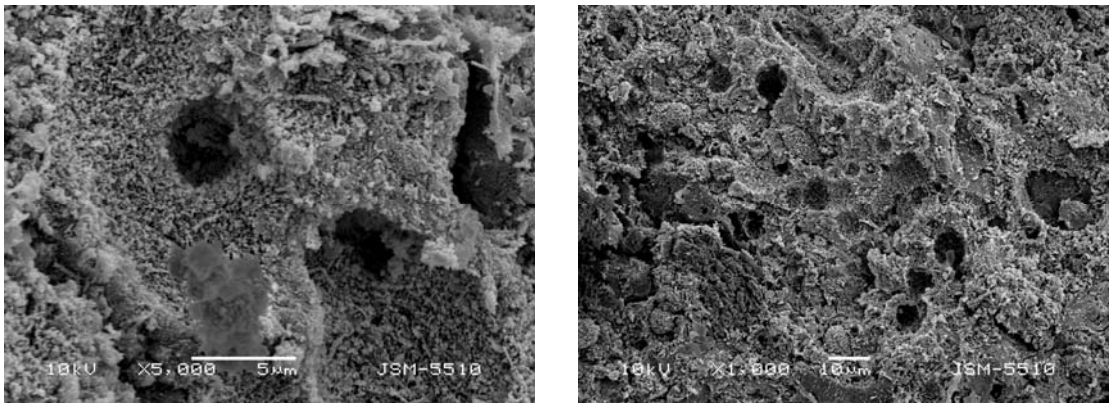

(a) (b)

Fig. 4. SEM pictures of sample ACO (a) magnification 5,000; (b) magnification 1,000

SEM images of both AC and ACO samples are represented in Figures 3 and 4. The SEM micrograph of the AC sample reveals the presence of aggregates, which consist of rods and small balls (spheres). This implies a multiphase composition of the sample (Fig. 3). Some pores are visible, which are appearing as a result of the liberation of gases during the thermal treatment. The sample ACO exhibits slightly different microstructure than that of the AC powders (Fig. 4). The structure is non homogeneous with presence of compact spots and porous areas containing pores with different size. These sintering areas are formed differently due to the different specific thermal treatment of the ACO powder. An active photocatalyst is considered to provide adsorption sites for the organic pollutants, which means that an open porous structure with high specific surface area is needed [9].

The obtained O1s, Al2p and Ca2p X-ray photoelectron spectra (not shown here) of the constituent element on the surface of the CaO/Al_2O_3 catalysts denoted by AC and ACO are typical of the Al_2O_3 and CaO oxides. The surface content and the O/Al ratios for both catalysts have been calculated. The O/Al atomic ratio for the AC catalyst is equal to 1.4, the value is close to that of the stoichiometric Al_2O_3 oxide. The surface content of Ca for the same catalyst is higher in comparison to the same quantity, evaluated for the ACO one and this is related to the facilitated formation of CaO oxide acting as modifier in the Al_2O_3 oxide matrix. This is in agreement with the obtained results for this type of phase formed in the studied catalyst, obtained by X-ray diffraction analysis. The well-formed phases, are obviously leading to higher catalytic activity over AC catalyst in comparison to that of the ACO one, which is showing lower degree of activity.

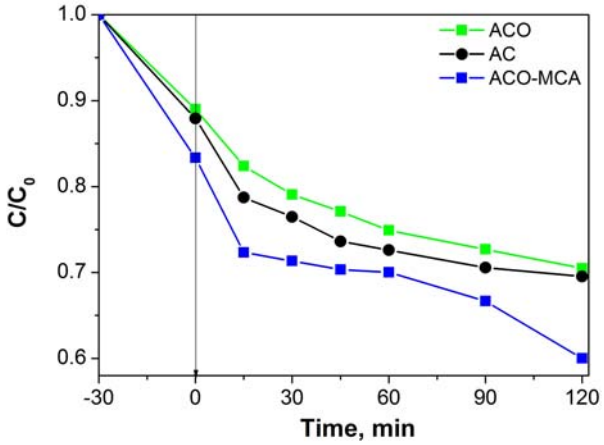

Fig. 5. Reaction course as a function of the time interval of illumination (C/C_0) of the Reactive Black 5 dye on investigated samples

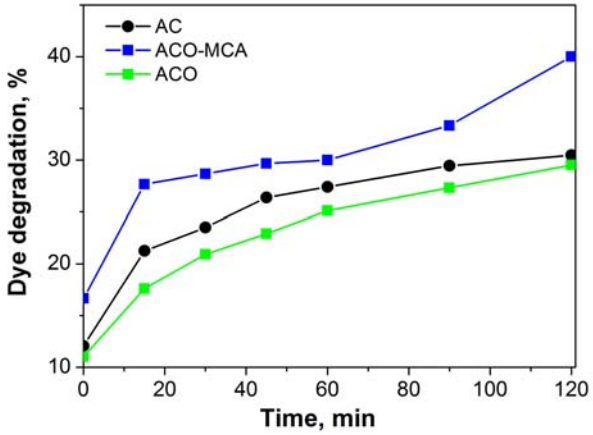

Fig. 6. Dye degradation with time of UV light illumination of the solution of Reactive Black 5 dye on two examined catalysts

Figures 5 and 6 represent the reaction course as a function of the time interval of illumination (C/C_0) and the respective degree of dye degradation of model pollutant Reactive Black 5 on the investigated alumina containing samples. The mechanoactivated powder showed the highest adsorption capacity (Fig. 5). The ACO-MCA sample also exhibits the highest degree of oxidative degradation (40%), in comparison with those of AC (30%) and ACO (29%). Alumina can significantly control the photochemical reactivity of adsorbed molecules due to electronic interaction between the molecules and the surfaces [12]. The degradation of RB5 on alumina based samples exhibits pseudo first-order reaction kinetics. Degradation rate constants were calculated using the logarithmic equation $-\ln(C/C_0) = kt$ on the basis of the slope of linear dependence and they are presented in Table 1. In Figure 7 the rate constants of the investigated catalysts were compared and evaluated base on 7 experimental measurement points in the course of two hours UV light illumination of the solution of Reactive Black 5 dye. The values of the rate constants for all three samples increase in the next order: ACO (2.3×10^{-3} min^{-1}) < AC (2.5×10^{-3} min^{-1}) < ACO-MCA (2.9×10^{-3} min^{-1}). The best photocatalytic activity is exhibited by the mechanochemically activated sample.

Table 1. Rate constants (k) and degree of degradation of investigated photocatalysts

Sample	k ($x10^{-3}$ min^{-1})	Degradation,% 120 min
AC	2.5	30
ACO	2.3	29
ACO-MCA	2.9	40

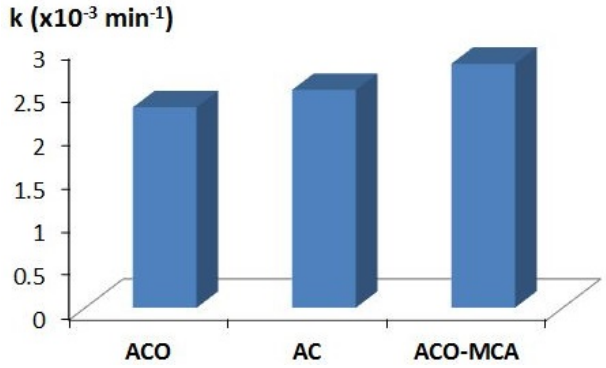

Fig. 7. Rate constants of the investigated catalysts estimated in the course of two hours of UV light illumination of the solution of Reactive Black 5 dye

We can conclude that the different conditions of calcination on AC and ACO influenced not only their structure and morphology, but also the homogeneity and other characteristics. However the photocatalytic efficiency of these two samples (AC and ACO) is similar. In contrast to them, when mechanochemical activation was applied on sample (ACO) the degradation of dye contaminant RB5 increased from 29 to 40%.

4. CONCLUSIONS

Three different alumina samples, prepared by precipitation of 90% aluminum hydroxide and 10 % calcium carbonate were used in our investigation. The first one was annealed at 1000°C (AC), the second one was calcined at 500°C first and afterwards at 1000°C and third mechanochemically activated ACO (ACO-MCA). The photocatalytic properties of the prepared samples were tested in the photocatalytic oxidation of Reactive Black 5 (RB5) dye under UV light illumination. They were characterized by PXRD, SEM and XPS analysis. The PXRD analysis detected the following phases: α-Al_2O_3, ɵ-Al_2O_3 and $Ca_3Al_2O_6$. The SEM micrographs show porous structure. XPS revealed that the surface content of Ca for the AC photocatalyst is higher in comparison with that of the ACO sample, which led to facilitated formation of CaO oxide acting as modifier in the Al_2O_3 oxide matrix. The photocatalytic efficiencies of both ACO and AC photocatalysts are almost similar and reaching about 30% conversion degree, while the mechanochemically treated AC sample reached 40%. In our case the mechanochemical activation leads to increase in photocatalytic activity.

ACKNOWLEDGMENTS

The authors gratefully acknowledge financial support by National Science Fund, Ministry of Education and Sciences of Bulgaria (Contract DFNI – T-02-16).

REFERENCES

1. SINGH, S., SRIVASTAVA, V. C., MANDAL, T. K., MALL, I. D., Synthesis of different crystallographic Al_2O_3 nanomaterials from solid waste for application in dye degradation, RSC Adv.,**4**, 2014, 50801–50810.
2. SHEN, J., LI, Z., WU, Y., ZHANG, B., LI, F., Dendrimer-based preparation of mesoporous alumina nanofibers by electrospinning and their application in dye adsorption, Chemical Engineering Journal, **264**, 2015, 48–55.
3. LAN, S., GUO, N., LIU, L., WU, X., LI, L., GAN, S., Facile preparation of hierarchical hollow structure gamma aluminaand a study of its adsorption capacity, Applied Surface Science, **283**, 2013, 1032–1040.
4. RENUKA, N.K., SHIJINA, A.V., PRAVEEN, A.K., Mesoporous γ-alumina nanoparticles: Synthesis, characterization and dye removal efficiency, Materials Letters, **82**, 2012, 42–44.
5. YAHYAEI, B., AZIZIAN, S., Rapid adsorption of binary dye pollutants onto the nanostructred mesoporous alumina, Journal of Molecular Liquids, **199**, 2014, 88–95.
6. ZOLGHARNEIN, J., ASANJRANI, N., BAGTASH, M., AZIMI, G., Multi-response optimization using Taguchi design and principle component analysis for removing binary mixture of alizarin red and alizarin yellow from aqueous solution by nano γ-alumina, Spectrochimica Acta Part A: Molecular and Biomolecular Spectroscopy, **126**, 2014, 291–300.
7. WASTI, A., ALI AWAN, M., Adsorption of textile dye onto modified immobilized activated alumina, Journal of the Association of Arab Universities for Basic and Applied Sciences, 2014, article in press.
8. CHEN, X., WU, K., SUN, Y., SONG, X., Highly sensitive electrochemical sensor for sunset yellow based on the enhancement effect of alumina microfibers, Sensors and Actuators B, **185**, 2013, 582– 586.

9. MONDAL, K., SHARMA, A., Photocatalytic Oxidation of Pollutan Dyes in Wastewater by TiO_2 and ZnO nano-materials – A Mini-review, Nanoscience & Technology for Mankind, Edited by Ashok Misra, Jayesh R. Bellare, **5**, 2014, 36-72.
10. TZOMPANTZI, F., PINA, Y., MANTILLA, A., AGUILAR-MARTÍNEZ, O., GALINDO-HERNÁNDEZ, F., BOKHIMI, X., BARRERA, A., Hydroxylated sol–gel Al_2O_3 as photocatalyst for the degradation of phenolic compounds in presence of UV light, Catalysis Today, **220–222**, 2014, 49– 55.
11. KARUNAKARAN, C., DHANALAKSHMI, R., GOMATHISANKAR, P., Photomineralization of phenol on Al_2O_3: synergistic photocatalysis by semiconductors, Res. Chem. Intermed., **36**, 2010, 361–371.
12. IMTIAZ, A., FARRUKH, M.A., KHALEEQ-UR-RAHMAN, M., ADNAN, R., Micelle-Assisted Synthesis of Al_2O_3 CaO Nanocatalyst:Optical Properties and Their Applications in Photodegradation of 2,4,6-Trinitrophenol, **ID 641420**, 2013, http://dx.doi.org/10.1155/2013/641420.
13. ROMANIAS, M. N., ANDRADE-EIROA, A., SHAHLA, R., BEDJANIAN, Y., ZOGKA, A., PHILIPPIDIS, A., DAGAUT, P., Photodegradation of Pyrene on Al_2O_3 Surfaces: A Detailed Kinetic and Product Study, J. Phys. Chem., A, **118** (34), 2014, 7007–7016.
14. SOYLU, A. M., POLAT, M., ERDOGAN, D. A., SAY, Z., YILDIRIM, C., BIRER, Ö., OZENSOY, E., TiO_2–Al_2O_3 binary mixed oxide surfaces for photocatalytic NOx abatement, Applied Surface Science, **318**, 2014, 142–149.
15. BIRNBAUM, W., WEINBERGER, C., SCHILL, V., HAFFER, S., TIEMANN, M., KUCKLING, D., Synthesis of Mesoporous Alumina through Photo Cross-linked poly (dimethylacrylamide) hydrogels, Colloid Polym. Sci. **292**, 2014, 3055-3060.
16. SHISHKOV, D., KASSABOVA, N., VELINOVA, C., ANGELOV, L., MARINOVA, J., IORDANOVA, V., ILIEV, I., HRISTOV, G., LUBENOV, S., POPOVA, V., ANDONOV, G., VALOV, N., DOCEVA, A., Method of preparation of α-Al_2O_3 based support as catalysts for reforming of hydrocarbons, in Bulgarian Patent № BG 46635 A, (in Bulgarian), 1994.

CORRESPONDENCE

Chief Assistant Professor Katya MILENOVA
Institute of Catalysis, Bulgarian Academy of Sciences, “Acad. G. Bonchev” St., Block 11, 1113
Sofia, Bulgaria
e-mail:kmilenova@ic.bas.bg

Tribological Journal BULTRIB Vol. 5, 2015
Papers from the International Conference **BULTRIB '15**
September 11-13, 2015, Sozopol, Bulgaria
Society of Bulgarian Tribologists
FIT – Technical University of Sofia

PHOTOCATALYTIC PERFORMANCE OF ACID IMPREGNATED ZnO POWDERS AND MECHANOCHEMICAL TREATMENT FOR DISCOLOURING OF TEXTILE DYE

Katerina ZAHARIEVA[1], Katya MILENOVA[1], Alexander ELIYAS[1], Irina STAMBOLOVA[2], Sasho VASSILEV[3], Vladimir BLASKOV[2], Zara CHERKEZOVA-ZHELEVA[1], Slavcho RAKOVSKY[1], Ivan MITOV[1]

[1]Institute of Catalysis, Bulgarian Academy of Sciences, "Acad. G. Bonchev" St., Bl.11, 1113 Sofia, Bulgaria
[2]Institute of General and Inorganic Chemistry, Bulgarian Academy of Sciences, "Acad. G. Bonchev" St., Bl.11, 1113 Sofia, Bulgaria
[3]Institute of Electrochemistry and Energy Systems, Bulgarian Academy of Sciences, Acad. G.Bonchev bl. 10, 1113, Sofia, Bulgaria

Abstract: *ZnO powders, prepared in advance by precipitation, were impregnated with 0.1 M solutions of H_3PO_4, HCl, H_2SO_4 and HNO_3. The catalysts were mechanochemically treated (MCT). The degree of discoloring of RB5 dye (taken as measure of the activity) under UV light using mechanochemically treated ZnO-HCl-MCT sample is the highest (98%), compared with that of all the other tested samples. The impregnation of ZnO with HNO_3* leads to obtaining of photocatalyst *yielding the highest degree of discoloring of RB5 (89%) than the materials treated with H_3PO_4, HCl and H_2SO_4.*

Key Words: *zinc oxide, mechanochemical treatment, photocatalysis, Reactive Black 5, azo dye pollutant*

1. INTRODUCTION

The industrial progress has led to environmental problems such as pollution of water by organics, for example dyes from the textile industry or agricultural chemicals (such as pesticides or herbicides) [1]. Heterogeneous photocatalysis is a method for water and air purification and remediation because it can effectively decompose and even mineralize contaminant and/or undesirable compounds [2]. ZnO is one of the most promising photocatalysts for degradation and complete mineralization of azo dyes because of its exclusive properties such as non-toxicity, low cost, high chemical stability, high ultraviolet (UV) absorption and absence of any hazardous products of the process [3]. The photocatalytic properties of ZnO were studied for photodegradation of Reactive Black 5 [4,5]. The change of a specific surface area of the nanosized particle and its functionalization with different functional groups is widely investigated. The modification of the surface properties, such as surface free energy, without changing its intrinsic properties is a requirement in most of the cases [6]. The highly crystalline mesoporous TiO_2 was produced by post-treatment in nitric acid-ethanol solution, and shows excellence photocatalytic activity [7]. The TiO_2/allophane mixed samples at various mixing ratios were acid-treated with 1.0 mol/l hydrochloric acid solution to obtain a highly active photocatalyst [8]. Surface modification of titania powder Degussa P25 with phosphate and phosphoric acid was reported in ref. [9]. Nitrogen-doped TiO_2 catalysts were prepared by a precipitation method and acidic treatment of the calcined materials was performed using sulfuric acid activation [10]. The surface of nanosized TiO_2 was fast and easily modified by chemical adsorption in saturated solution of 5-sulfosalicylic acid [11]. Photocatalytic oxidation of phenol was studied over acid pre-treated TiO_2 synthesized by a sol–gel method. The nitric, sulfuric and phosphoric acids were used in the acid pre-treatment [12]. The surface of nanodimensional TiO_2 was fast and easily modified by chemical adsorption in saturated solution of salicylic acid. The surface modification leads to enhancement of the TiO_2 adsorption capacity for 4-nitrophenol [13]. Deposition of Pt and Pd particles onto TiO_2 Degussa P25 by mild chemical reduction allowed obtaining very active photocatalyst. Adding of sulfuric acid increased the activity at low Pt content but decreased it at high Pt content [14]. The nanoparticles of TiO_2 possessing high surface area were produced by mild acidic treatment with HCl or HI and tested in photocatalytic propene oxidation [15]. The influence of surface modification using H_2S and NH_3 on the photocatalytic activity of TiO_2 for degradation of toluene was studied in [16]. The modified TiO_2 using salicylic acid was investigated as a photocatalyst in the degradation of monochlorobenzene via Pickering emulsion approach [17]. Mesoporous anatase TiO_2 modified with tungstosilicic acid possessed higher photocatalytic activity in the 4-chlorophenol degradation than that of the pure TiO_2 [18]. The surface modification of pre-

pared nanosized ZnO was performed using adding drop-wise oleic acid [19]. The photocatalytic activity of non-impregnated and impregnated La doped ZnO materials with solution of hydrochloric acid were compared for degradation of Reactive Black 5 dye in [20]. Mechanochemical processing is well-established for producing nano-sized materials [21]. This method results in a physical size reduction process in a conventional ball mill with chemical reactions mechanically activated on the nanoscale level during the milling process [22].

The goal of the present paper was to study the influence of acidic impregnation using different acids such as H_3PO_4, HCl, H_2SO_4, HNO_3 and mechanochemical treatment on the photocatalytic properties of zinc oxide. The photocatalytic activity of acidically impregnated and mechanochemically treated zinc oxide photocatalysts were tested and compared in photocatalytic reaction of oxidative discoloration of Reactive Black 5 (RB5) dye under UV irradiation.

2. EXPERIMENTAL

2.1. Preparation of the samples

The synthesis method of activated zinc oxide (ZnO) has already been reported in a Bulgarian Patent [23]. The preparation technique includes dissolution of commercial ZnO in NH_4OH solution upon CO_2 bubbling, leading to precipitation of $Zn(OH)CO_3$. Then the samples were calcined for 2h at 400^oC. The impregnation of ZnO samples was performed using 0.1M solutions of H_3PO_4, HCl, H_2SO_4 and HNO_3 acids. The impregnated ZnO samples were then dried at 100^oC for 2 h. The samples were denoted as ZnO-H_3PO_4; ZnO-HCl; ZnO-H_2SO_4; ZnO-HNO_3. The mechanochemical treatment of impregnated ZnO materials with acids was carried out in a high-energy planetary ball mill type PM 100, Retsch, Germany. The samples were treated for 10 minutes milling time interval in an agate milling container of 80 ml volume and milling speed of 380 rpm. The mass ratio between balls and sample was 35:1. The milling atmosphere was air. The materials were labeled as ZnO-H_3PO_4-MCT; ZnO-HCl-MCT; ZnO-H_2SO_4-MCT; ZnO-HNO_3-MCT.

The X-ray diffraction (XRD) investigation of sample was performed using Philips PW 1050 with CuK_α-radiation.

2.2. Photocatalytic tests for discoloring of Reactive Black 5 dye

The photocatalytic activity measurements of the oxidative degradation degree of Reactive Black 5 (RB5) were performed using 150 ml dye aqueous solution with starting concentration of 20 ppm. The polychromatic UV-A lamp illumination (18 W, 320-400nm) with a maximum of the emission at 365 nm was used for irradiation during photocatalytic experiments. The discoloration degree of the dye aqueous solutions was registered by UV-Vis spectrophotometer CamSpec M501, based on the absorbance of the dye solution in the wavelength range from 200 to 800 nm. The adsorption-desorption equilibrium of the investigated samples was achieved in the dark for about 30 min before switching on the irradiation. The photocatalytic activity tests were carried out by taking sample aliquots of the suspension from the reaction vessel at regular time intervals and filtering them. After measuring the absorbance the amount was returned to the reactor to have constant volume operation.

3. RESULTS AND DISCUSSION

Figures 1 and 2 represent the degree of discoloration and reaction course as dependences of (C/Co) on the time interval under UV light irradiation of the RB5 dye using zinc oxide photocatalysts treated with following acids: H_3PO_4, HCl, H_2SO_4 and HNO_3. The photocatalytic measurements established that degree of discoloring of Reactive Black 5 dye after 120 minutes under UV light illumination increases in the following order of activities for the tested acidically treated photocatalysts: ZnO-H_3PO_4(8%)<ZnO-HCl(57%)<ZnO-H_2SO_4(74%)<ZnO-HNO_3(89%). The highest degree of discoloring of Reactive Black 5 dye (89%) was achieved using acid impregnation of ZnO sample with nitric acid. Milenova et al. [24] established by X-ray photoelectron spectroscopy measurements that treatment with nitric acid leads to nitrogen incorporation into the ZnO crystal lattice enhancing the photonic efficiency in oxidative discoloration of Reactive Black 5 dye solutions. The acidic treatment exerts favourable effect on the photocatalytic activity and on the adsorption capacity [24]. The acidic treatment results in formation of hydroxide containing phases. The influence of the acidic treatment is promoting the number of acidic hydroxyl groups on the surface in the form of $Zn(NO_3)(OH).H_2O$ and $4Zn(OH)_2.Zn(NO_3).2H_2O$ [24].

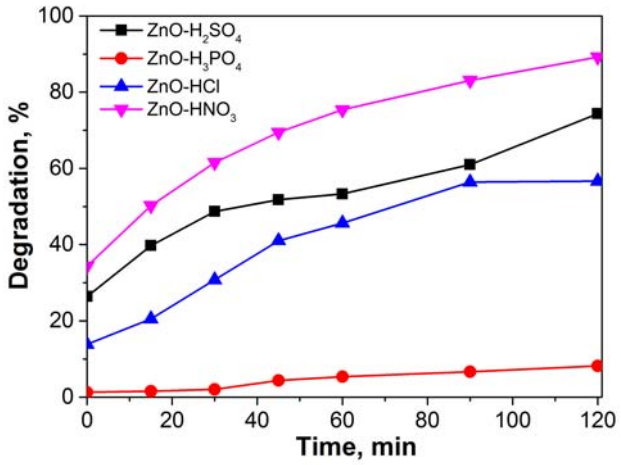

Fig. 1. Degree of discoloration of the RB5 dye after different time intervals of UV-light irradiation using acid treated ZnO samples with H_3PO_4, HCl, H_2SO_4 and HNO_3

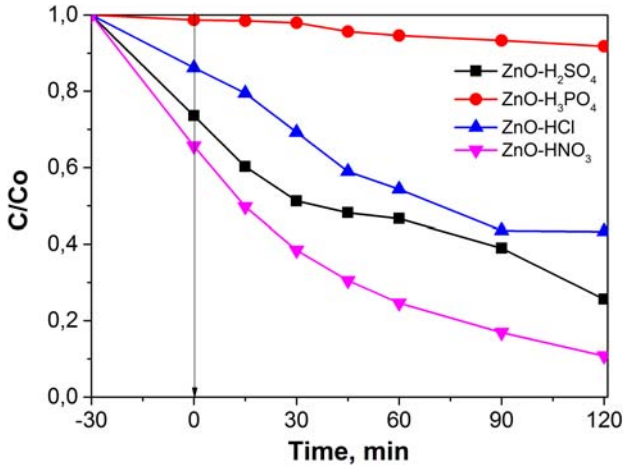

Fig. 2. Concentration changes of RB5 dye during UV-light illumination after different time intervals using acidically treated ZnO photocatalysts

The additional mechanochemical treatment of the acid impregnated zinc oxide materials promotes additionally the photocatalytic activity of the investigated samples. As it can be seen in the Figs. 3 and 4 the photocatalytic activity tests gave the following sequence of activities ZnO-HCl-MCT(98%)>ZnO-HNO_3-MCT(78%)>ZnO-H_2SO_4-MCT(38%)>ZnO-H_3PO_4-MCT(27%). The mechanochemical activation (MCA) of treated ZnO sample with HCl leads to increasing of degree of discoloring of Reactive Black 5 dye solution compared to the ZnO treated with HNO_3 without and with mechanochemical treatment. The effect of mechanochemical treatment on the photocatalytic efficiency could be explained by the formation of the various surface defects and emergence of new interfaces during the milling reactions [25,26]. An additional effect of MCA is the enhancement of the adsorption capacity of the samples. This effect is stronger in the cases of HNO_3 and HCl treated samples. After mechanochemical treatment of impregnated with sulfuric acid sample X-ray amorphous halo peaks are registered and broadened reflexes of single phase $Zn_4SO_4(OH)_6.0.5H_2O$ (PDF-44-0674) or $ZnSO_4.3Zn(OH)_2$ (PDF-44-0675) in the XRD spectrum (Fig. 5).

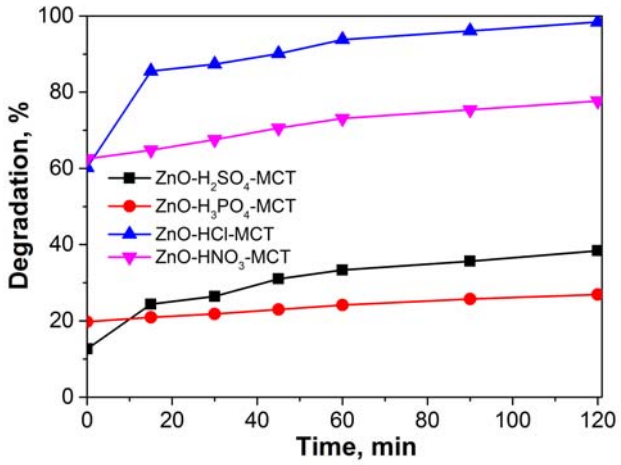

Fig. 3. Degree of discoloration of the RB5 dye after different time intervals of UV-light irradiation using acid and mechanochemical treated photocatalysts

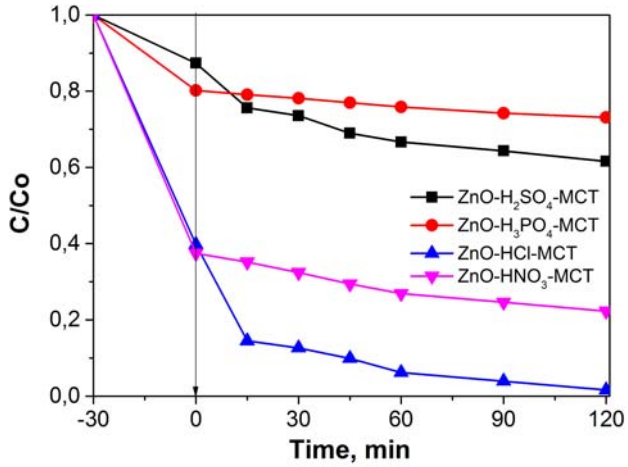

Fig. 4. Concentration changes of RB5 dye during UV illumination after different time intervals using acid and mechanochemical treated photocatalysts

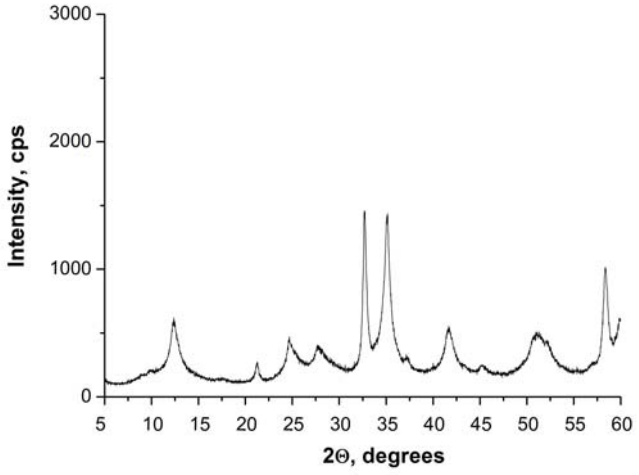

Fig. 5. XRD pattern of sample treated with H_2SO_4 after mechanochemical treatment

The rate constants ***k*** are illustrated in Table 1. The values were estimated by the slope of the linear relation: –ln(C/Co)**=*kt*** (where Co and C are the concentrations of the solution before and after UV-light irradiation for the selected time interval at 599 nm absorbance maximum, attributed to the peak of the diazo bond (-N=N-). The highest photocatalytic activity ($k=27.9x10^{-3}$ min^{-1}) in the reaction of discoloration of RB5 dye is shown by the zinc oxide sample impregnated with HCl acid and afterward mechanochemically treated (ZnO-HCl-MCT), compared to the other tested materials.

Table 1 Rate constants for RB5 dye

Photocatalyst	***k*** **($x10^{-3}$ min^{-1})**
ZnO-HCl-MCT	27.9
ZnO-HNO_3	15.5
ZnO-H_2SO_4	8.3
ZnO-HCl	6.5
ZnO-HNO_3-MCT	4.7
ZnO-H_2SO_4-MCT	3.5
ZnO-H_3PO_4-MCT	0.8
ZnO-H_3PO_4	0.6

4. CONCLUSIONS

The effects of impregnation using *H_3PO_4, HCl, H_2SO_4 and HNO_3* acids and of the mechano-chemical treatment on the photocatalytic activity of ZnO samples were successfully investigated. The photocatalytic discoloring degree of Reactive Black 5 dye as model contaminant under UV irradiation was measured. The order of activities of the tested photocatalysts is: ZnO-HCl-MCT(98%)>ZnO-HNO_3(89%)>ZnO-HNO_3-MCT(78%)>ZnO-H_2SO_4(74%)>ZnO-HCl(57%)>ZnO-H_2SO_4-MCT(38%)>ZnO-H_3PO_4-MCT(27%)>ZnO-H_3PO_4(8%). The photocatalytic results established that HCl impregnation followed by mechanochemical treatment of ZnO powder for 10 minutes leads to obtaining of photocatalyst possessing the highest activity i.e. degree of discoloring (98%) of RB5 azo dye under UV-light illumination. The treatment with HNO_3 enhances the degree of discoloring of RB5 up to 89% compared to those of the samples impregnated with H_2SO_4 (74%), HCl (57%) and H_3PO_4 (8%).

ACKNOWLEDGMENTS

The financial support by the Bulgarian Science Fund at the Ministry of Education and Science under contracts DFNI E02/2/2014 and DFNI – T-02-16 is gratefully acknowledged.

REFERENCES

1. MOURÃO, Henrique A.J.L.., MALAGUTTI, Andréa R., RIBEIRO, Caue., Synthesis of TiO_2-coated $CoFe_2O_4$ photocatalysts applied to the photodegradation of atrazine and rhodamine B in water, Applied Catalysis A: General, **382**, 2010, 284–292.
2. JING, L., QIN, X., LUAN, Y., QU, Y., XIE, M., Synthesis of efficient TiO_2-based photocatalysts by phosphate surface modification and the activity-enhanced mechanisms, Applied Surface Science, **258**, 2012, 3340– 3349.
3. MOHAGHEGH, N., TASVIRI, M., RAHIMI, E., Gholami, Mohammad Reza., Nano sized ZnO composites: Preparation, characterization and application as photocatalysts for degradation of AB92 azo dye, Materials Science in Semiconductor Processing, **21**, 2014, 167–179.
4. LAOHAPRAPANON, S., MATAHUM, J., TAYO, L., YOU, Sheng-Jie., Photodegradation of Reactive Black 5 in a ZnO/UV slurry membrane reactor, Journal of the Taiwan Institute of Chemical Engineers, **49**, 2015, 136–141.
5. AMISHA, S., SELVAM, K., SOBANA, N., SWAMINATHAN, M., Photomineralisation of Reactive Black 5 with ZnO using Solar and UV-A Light, Journal of the Korean Chemical Society, **52** (1), 2008, 66-72.
6. ZHU, F., KONG, Eric Siu-Wai., ZHANG, J., ZHANG, Y., Surface modification of TiO_2 nanoparticles through plasma polymerization of acrylic acid, Chemical Physics Letters, **423**, 2006, 270–275.
7. HAO, H., ZHANG, J., Low temperature synthesis of crystalline mesoporous titania with high photocatalytic activity by post-treatment in nitric acid ethanol solution, Materials Letters, **63**, 2009, 106–108.
8. ONO, Y., KATSUMATA, Ken-ichi., Enhanced photocatalytic activity of titanium dioxide/allophane mixed powder by acid treatment, Applied Clay Science, **90**, 2014, 61–66.

9. DJAFER, L., AYRAL, A., BOURY, B., LAINE, Richard M., Surface modification of titania powder P25 with phosphate and phosphonic acids – Effect on thermal stability and photocatalytic activity, Journal of Colloid and Interface Science, **393**, 2013, 335–339.
10. KUN, R., TARJÁN, S., OSZKÓ, A., SEEMANN, T., ZÖLLMER, V., BUSSE, M., DÉKÁNY, I., Preparation and characterization of mesoporous N-doped and sulfuric acid treated anataseTiO_2 catalysts and their photocatalytic activity under UV and Vis illumination, Journal of Solid State Chemistry, **182**, 2009, 3076–3084.
11. LI, Shun-xing., ZHENG, Feng-ying., LIU, Xian-li., WU, Feng., DENG, Nan-sheng., YANG, Jian-hong., Photocatalytic degradation of p-nitrophenol on nanometer size titanium dioxide surface modified with 5-sulfosalicylic acid, Chemosphere, **61**, 2005, 589–594.
12. COLÓN, G., SÁNCHEZ-ESPAÑA, J.M., Hidalgo, M.C., Navío, J.A., Effect of TiO_2 acidic pre-treatment on the photocatalytic properties for phenol degradation, Journal of Photochemistry and Photobiology A: Chemistry, **179**, 2006, 20–27.
13. SHUN-XING, L., FENG-YING, Z., WEN-LIAN, C., AI-QIN, H., YU-KUN, X., Surface modification of nanometer size TiO_2 with salicylic acid for photocatalytic degradation of 4-nitrophenol, Journal of Hazardous Materials B, **135**, 2006, 431–436.
14. KOZLOVA, Ekaterina A., VORONTSOV, Alexander V., Noble metal and sulfuric acid modified TiO_2 photocatalysts: Mineralization of organophosphorous compounds, Applied Catalysis B: Environmental, **63**, 2006, 114–123.
15. OUZZINE, M., MACIÁ-AGULLÓ, J.A., LILLO-RÓDENAS, M.A., QUIJADA, C., LINARES-SOLANO, A., Synthesis of high surface area TiO_2 nanoparticles by mild acid treatment with HCl or HI for photocatalytic propene oxidation, Applied Catalysis B: Environmental, **154–155**, 2014, 285–293.
16. ZHANG, F., WANG, M., ZHU, X., HONG, B., WANG, W., QI, Z., XIE, W., DING, J., BAO, J., SUN, S., GAO, C., Effect of surface modification with H_2S and NH_3 on TiO_2 for adsorption and photocatalytic degradation of gaseous toluene, Applied Catalysis B: Environmental, **170-171**, 2015, 215–224.
17. NSIB, Mohamed Faouzi, MAAYOUFI, A., MOUSSA, N., TARHOUNI, N., MASSOURI, A., HOUAS, A., CHEVALIER, Y., TiO_2 modified by salicylic acid as a photocatalyst for the degradation of monochlorobenzene via Pickering emulsion way, Journal of Photochemistry and Photobiology A: Chemistry, **251**, 2013, 10–17.
18. RENGIFO-HERRERA, Julián A., FRENZEL, Romina A., BLANCO, Mirta N., PIZZIO, Luis R., Visible-light-absorbing mesoporous TiO_2 modified with tungstosilicicacid as photocatalyst in the photodegradation of 4-chlorophenol, Journal of Photochemistry and Photobiology A: Chemistry, **289**, 2014, 22–30.
19. HONG, R., PAN, T., QIAN, J., LI, H., Synthesis and surface modification of ZnO nanoparticles, Chemical Engineering Journal, **119**, 2006, 71–81.
20. ZAHARIEVA, K., MILENOVA, K., AVRAMOVA, I., ELIYAS, A., BLASKOV, V., STAMBOLOVA, I., CHERKEZOVA-ZHELEVA, Z., KUNEV, B., NIKOLOV, P., KASSABOVA, N., RAKOVSKY, S., Photocatalytic properties of La-doped ZnO non-impregnated and impregnated with HCl solution for oxidative degradation of Reactive Black 5 dye, Scientific conference "Actual problems of security", November 13-14, 2014, Veliko Tarnovo, Bulgaria, in press.
21. AO, W., LI, J., YANG, H., ZENG, X., MA, X., Mechanochemical synthesis of zinc oxide nanocrystalline, Powder Technology, **168**, 2006, 148–151.
22. ESPITIA, P. J. P., SOARES, N. F. F., COIMBRA, J. S. R., ANDRADE, N. J., CRUZ, R. S., MEDEIROS, E. A. A., Zinc Oxide Nanoparticles: Synthesis, Antimicrobial Activity and Food Packaging Applications, Food Bioprocess Technol, **5**, 2012, 1447–1464.
23. SHISHKOV, D., VELINOVA, C., KASSABOVA, N., CANOV, C., IVANOV, D., KLISSURSKI, D., IORDANOVA, V., UZUNOV, I., (1980), Method of preparation of activated zinc oxide. Bulgarian Patent 28915/1980 (Classification Index C 01 G 9/02) (in Bulgarian).
24. MILENOVA, K., ELIYAS, A., BLASKOV, V., STAMBOLOVA, I., VASSILEV, S., RAKOVSKY, S., KASABOVA, N. A., Nitric Acid Activation of La-doped ZnO Photocatalyst for Water Decontamination, Journal of Chemical Technology and Metallurgy, 2015, after review.
25. GOTOR, F.J., ACHIMOVICOVA, M., REAL, C., BALAZ, P., Influence of the milling parameters on the mechanical work intensity in planetary mills, Powder Technology, **233**, 2013, 1–7.
26. BALÁŽ, P., ACHIMOVIČOVÁ, M., BALÁŽ, M., BILLIK, P., CHERKEZOVA-ZHELEVA, Z., CRIADO, J. M., DELOGU, F., DUTKOVÁ, E., GAFFET, E., Gotor, F. J., KUMAR, R., MITOV, I., ROJAC, T., SENNA, M., STRELETSKII, A., WIECZOREK-CIUROWA, K., Hallmarks of mechanochemistry: from nanoparticles to technology, *Chem. Soc. Rev.*, **42**, 2013, 7571-7637.

CORRESPONDENCE

Chief Assistant Professor Dr. Katerina ZAHARIEVA
Institute of Catalysis, Bulgarian Academy of Sciences, “Acad. G. Bonchev” St., Block 11, 1113 Sofia, Bulgaria
e-mail: zaharieva@ic.bas.bg

Tribological Journal BULTRIB Vol. 5, 2015
Papers from the International Conference **BULTRIB '15**
September 11-13, 2015, Sozopol, Bulgaria
Society of Bulgarian Tribologists
FIT – Technical University of Sofia

WEAR RESISTANCE INVESTIGATION OF COMPOSITE LAYERS CLADDED BY SELECTIVE LASER MELTING (SLM) METHOD

Rayna DIMITROVA, Mara KANDEVA, Yavor SOFRONOV, Lukan CHERVENKOV

Abstract: *The present work is concerned with a wear resistance investigation of metal (aluminium) matrix composite layers in the conditions of dry friction surface with abrasive particles. The metalized micro SiC particles layers are cladded on the aluminium alloy matrix by a Selective Laser Melting (SLM) method. A methodology is developed in accordance with the valid standards. Comparative results are obtained for the mass wear rate, the intensity of wear and the wear resistance of the cladded layers. The experimental results are presented in graphs and tables.*

Key Words: *tribology, wear resistant layers, metalized micro SiC particles, Selective Laser Melting (SLM), laser cladding.*

ИЗНОСОУСТОЙЧИВОСТ НА МИКРОНАВАРЕНИ КОМПОЗИТНИ СЛОЕВЕ, ПОЛУЧЕНИ ЧРЕЗ СЕЛЕКТИВНО ЛАЗЕРНО СТОПЯВАНЕ (SLM)

Райна ДИМИТРОВА, Мара КАНДЕВА, Явор СОФРОНОВ, Лукан ЧЕРВЕНКОВ

Резюме: *В настоящата работа се изследват характеристиките на износването и износоустойчивостта на микронаварени слоеве от дисперсно уякчен композитен материал в условията на сухо триене по повърхнина с абразивни частици. Слоевете, съдържащи* метализирани микрочастици силициев карбид, *са наварени върху матрица от алуминиева сплав чрез метода Селективно Лазерно Стопяване (SLM). Разработена е методика в съответствие с действащите стандарти. Получени са сравнителни резултати за масовото износване, скоростта, интензивността на износване и износоустйчивостта на микронаварените слоеве, представени в табличен и графичен вид.*

Ключови думи: *трибология, износоустойчиви слоеве, метализирани микро частици силициев карбид, Селективно Лазерно Стопяване (SLM)*, *микронаваряване.*

1. УВОД

Лазерите осигуряват мощен, високоскоростен източник с прецизен контрол на подаваното количество енергия. На тяхна база е разработена технологията Селективно Лазерно Стопяване (SLM), която се използва за локално стопяване на прахови смеси с цел послойно изграждане на монолитни детайли, както и за наваряване на отделни слоеве [1, 2].

Целта на настоящата работа е да се изследват характеристиките на износването на микро наварени слоеве от дисперсно уякчен композитен материал върху матрица от алуминиева сплав чрез метода Селективно Лазерно Стопяване (SLM).

Използвани са два вида прахови смеси с различно съдържание на метализирани микрочастици силициев карбид. Въвеждането на уякчаващата фаза от метализирани микрочастици SiC се извършва чрез предварително нанасяне и последващо стопяване на прахова смес за получаване на микронаварен слой от композитен материал върху металната матрица.

Микронаваряването на слоевете от композитен материал върху металната матрица е извършено със SLM 125 HL система за селективно лазерно стопяване в Прототипна лаборатория към МТФ, ТУ-София, под ръководството на проф. Г. Тодоров.

Експерименталното изследване на износоустойчивостта е осъществено в условията на сухо триене, по методика, разработена в научно-приложната лаборатория „Трибология” към катедра „МТМ”, МТФ, ТУ-София под ръководството на доц. д-р М. Кандева [3, 4, 5].

2. МАТЕРИАЛИ И АПАРАТУРА

За реализиране на изследването са използвани следните материали и апаратура:

- Никелирани микрочастици силициев карбид, фракция 7 - 10 μм
- Алуминиев прах, фракция, пресят в с размер на отворите от 200 μm и 100 μm
- Основа от алуминиева сплав EN AW-2017A
- Машина за селективно лазерно стопяване: SLM 125HL

Химичното безтоково метализиране на микро/нано частици силициев карбид е извършено в алкален разтвор на основата на две никелови соли (сулфат и хлорид) за химично никелиране при стайна температура, позволяващ и следващо помедняване, в условията на интензивно разбъркване с магнитна бъркалка и/или ултразвукова вана чрез изкуствено предизвикване на локална екзотермична реакция по повърхността на частиците [6].

Механичните показатели на алуминиева сплав EN AW-2017A са, както следва: - граница на провлачане Rp0.2 = 279 MPa; - якост на опън – Rm = 437 MPa.

Химичният състав на сплавта е даден в Таблица 1:

Таблица 1. Химичен състав на алуминиева сплав EN AW-2017A

	Si	Fe	Cu	Mn	Mg	Cr	Zn	Ti+Zr	Други
Min	0.20	0.00	3.50	0.40	0.40	0.00	0.00	0.00	0.00
Max	0.80	0.70	4.50	1.00	1.00	0.10	0.25	0.25	0.15
Действ.	0.654	0.194	4.379	0.786	0.815	0.013	0.136	0.046	0.023

Микронаваряването е извършено със SLM 125 HL система с излъчващ източник YLR-Faser-Laser. Основните параметри на системата са, както следва: максимална мощност на лазера 100/200 W, скорост на сканиране от 400 до 600 мм/сек, размер на фокусното петно 200 μm и разстояние между щриховете 200 μm.

Микронаваряването е извършено върху основа (базов метал) от алуминиева сплав EN AW-2017A, с размери 125 x 125 x 10 mm (Фиг. 1).

Върху двете основи от базовата алуминиева сплав са нанесени два вида прахообразни смеси, съставени от:

- проби 1L – никелирани микро частици силициев карбид и алуминиев прах в съотношение 1:1 (Фиг. 1а);
- проби 2L – само от никелирани микро частици силициев карбид (Фиг. 1б);

а) 1L – никелирани микро частици силициев карбид и алуминиев прах 1:1

б) 2L – никелирани микро частици силициев карбид

Фиг. 1 Микро наваряване върху основа от алуминиева сплав EN AW-2017A

Върху всяка от двете основи са наварени по пет слоя с размери: ширина 16 мм и дължина 80 мм при режими, обхващащи пет различни скорости на селективно лазерно стопяване (SLM)- през 50 mm/s в диапазона от 400 до 600 mm/s. За целите на настоящото изследване са изготвени съответно по пет броя образци (1L и 2L) с еднакви размери, както и еталонен образец от базовия метал, без нанесено покритие.

3. МЕТОДИКА

Методиката за изследване характеристиките на износването се основава на измерване на масовото износване на образците за определен път на триене при постоянно зададени условия – натоварване, скорост на плъзгане, вид на абразива, след което се пресмятат следните характеристики: скорост на износване, интензивност на износване, абсолютна и относителна износоустойчивост.

Експерименталната част на методиката включва следните операции:

- Подготовка на образци с еднакви размери 15.0 x 15.0 mm.
- Измерване масата $\mathbf{m_o}$ на образеца с помощта на електронна везна WPS 180/C/2 с точност до 0.1 mg (преди всяко измерване на везната образецът се почиства от механични и органични частици и се подсушава с етилов алкохол за предотвратяване на електростатичния ефект).
- Прикрепване на образеца към държач от натоварващата глава на триботестера, задаване на определено нормално натоварване **P** и реализиране на определен път на триене.
- Измерване на масата $\mathbf{m_i}$ на образеца след изминаване на определения път на триене.

Изчисляват се следните характеристики (параметри) на масовото износване:

❖ Масово износване *m*, [mg] – разрушената маса m от повърхностния слой на образеца за определен път на триене L, т.е.

$$m = m_o - m_i \tag{1}$$

❖ Скорост на масовото износване **γ** [mg/s] – разрушената маса m за краен интервал от време на триене *t*:

$$\gamma = \frac{m}{t} \tag{2}$$

❖ Относителна интензивност на износването i [mg/ cm^2.m] – колко милиграма маса m се разрушава от номинална контактна площадка A_a =1 [cm^2] за път на триене L =1 метър:

$$i = \frac{m}{A_a L} \tag{3}$$

❖ Относителна износоустойчивост I [m/ cm^2.mg] – показва колко метра път на триене L ще измине образец с номинална контактна площадка A_a =1 [cm^2], за да се разруши от повърхнината му маса m =1 [mg], т.е.

$$I = \frac{L}{A_a . m} \tag{4}$$

Относителна промяна на износоустойчивостта $\Delta\varepsilon_{i,e},\%$ се определя по формулата:

$$\Delta\varepsilon_{i,e} = \frac{I_i - I_e}{I_o}.100,\% = \frac{I_i - I_o}{I_o}.100,\% \tag{5}$$

Относителната износоустойчивост $\Delta\varepsilon_{i,e},\%$ е безразмерно число, което показва с колко процента износоустойчивостта на изследвания образец е по-голяма (+) или по-малка (-) от износоустойчивостта на образеца, приет за еталон.

4. УСТРОЙСТВО

Абразивното износване при сухо триене с плъзгане по кинематичната схема „Палец-диск" е изследвано в лабораторни условия с устройство, чиято функционална схема е представена на Фиг. 2.

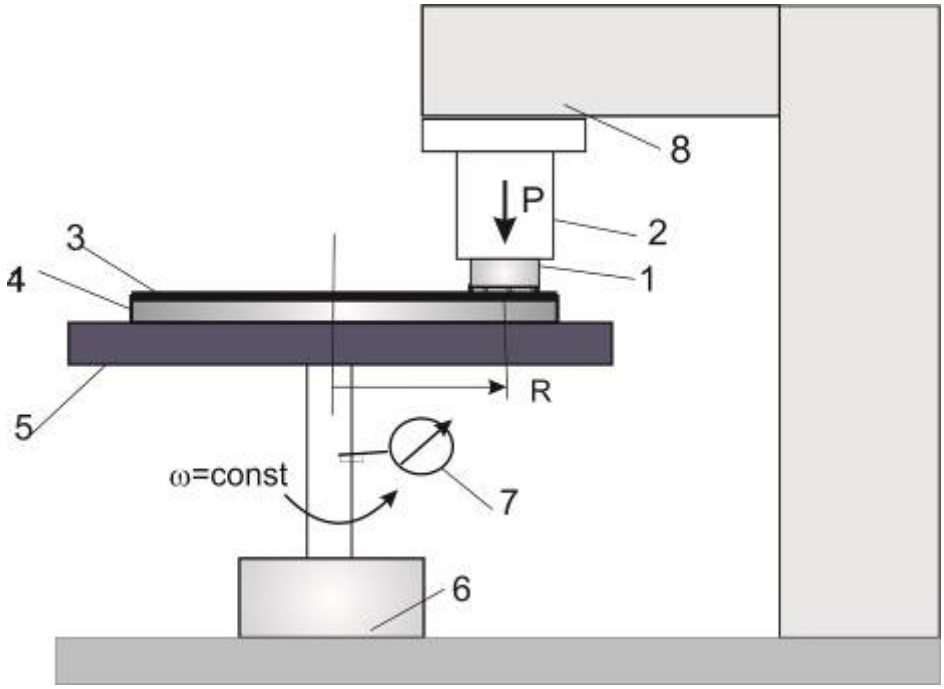

Фиг. 2 Схема на триботестер за изследване на износването при триене по повърхнина със закрепен абразив по схемата «Палец-диск»

Изследваният призматичен образец с покритие 1 (палец) се закрепва неподвижно в леглото на държач 2 в натоварваща глава 8, така че челната повърхнина на образеца (покритието) контактува с абразивната повърхнина 3, захваната неподвижно за хоризонтален диск 4. Дискът 4 се задвижва от електродвигател 6 и се върти около вертикалната си централна ос с ъглова скорост $\omega = const$.

Нормалното натоварване P е приложено в центъра на тежестта на контактната площадка между образеца и абразивната повърхнина и се осигурява с тежести с помощта на лостова система в натоварващата глава. Пътят на триене се задава чрез броя обороти с оборотомера 7. Устройството позволява изменение на скоростта на плъзгане чрез изменение на разстоянието R между оста на въртене на диска 4 и оста на образеца 1.

Абразивната повърхнина 3 се моделира чрез импрегниран корунд (Е) с твърдост 9.0 по скалата на Моос, което гарантира изискването на стандарта за минимум 60% по-висока от твърдостта на повърхностния слой на изпитваните материали [4, 5].

В Таблица 2 са представени данни за условията на експеримента.

Таблица 2. Параметри на изпитването на износоустойчивост

Нормално натоварване	P = 4,53 [N]
Номинална контактна площ	$A_a = 225.10^{-6}$ [m^2]
Номинално контактно налягане	$P_a = 2,01$ [N/cm^2]
Средна скорост на плъзгане	V = 13,1 [cm/s]
Абразивна повърхнина	Корунд Р 320

5. ЕКСПЕРИМЕНТАЛНИ РЕЗУЛТАТИ И АНАЛИЗ

Получените резултати от опитните образци (15.0 x 15.0 mm) след абразивното износване при сухо триене с плъзгане, заедно с абразивната повърхнина, след изпитването на износоустойчивост с триботестера са дадени на фиг. 2.

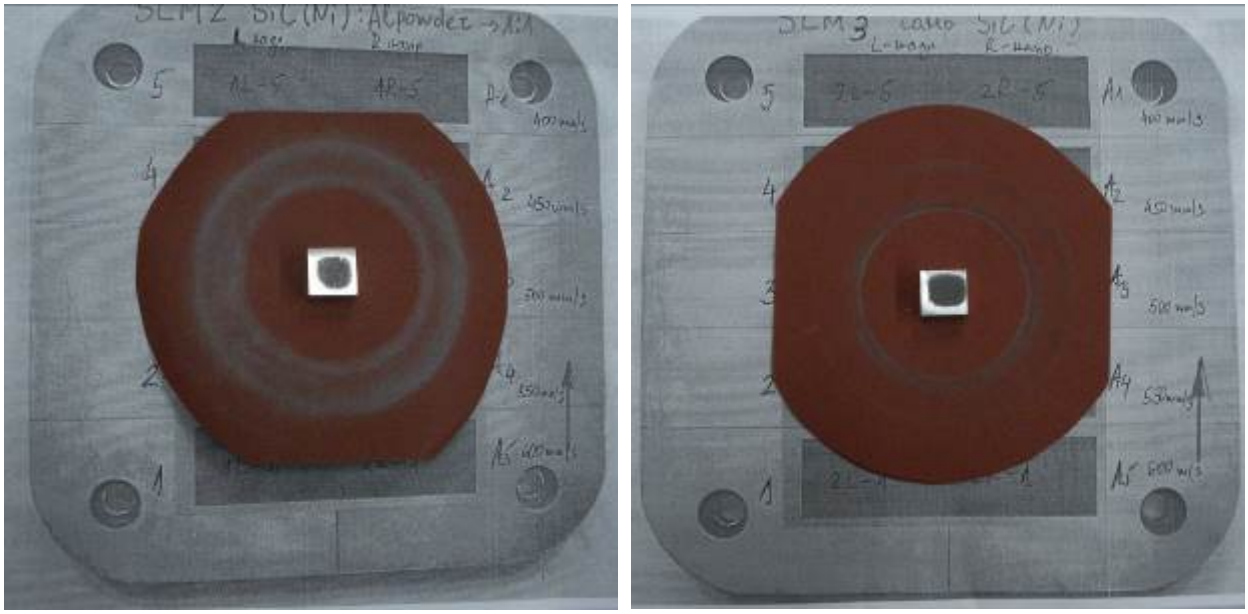

а) 1L – никелирани микро частици силициев карбид и алуминиев прах 1:1

б) 2L – никелирани микро частици силициев карбид

Фиг. 2 Резултати след изпитване на износоустойчивост

С описаната методика и устройство са получени експериментални резултати за характеристиките на износването при условията на изпитване (Таблица 2), представени за всеки образец в таблиците по долу.

5.1. Експериментални резултати за еталонен образец

Трибологичните параметри на еталонния образец (базовия метал – основата от алуминиева сплав EN AW-2017A) при изпитването на износване са дадени в Таблица 3.

Таблица 3. Параметри на износването на еталонния образец

Брой цикли *N*	25	50	75	100
Време на триене *t*, [s]	7,05	14,1	21,15	28,2
Път на триене *L*, m	5,75	11,5	17,25	23
Еталонен образец				
Износване m, [mg]	5,9	10,3	14,6	18,4
γ [mg/s]	0,84	0,73	0,69	0,65
$i = m / A_a.L$, [mg/cm^2.m]	$0{,}46.10^{-3}$	$0{,}40.10^{-3}$	$0{,}38.10^{-3}$	$0{,}36.10^{-3}$
$I = L / A_a.m$, [m/cm^2.mg]	$0{,}43.10^{3}$	$0{,}49.10^{3}$	$0{,}52.10^{3}$	$0{,}56.10^{3}$

Характеристиките на износването при дадените условия на изпитване, за образците от базов метал показват наличие на деформационно уякчаване и почти линейно нарастване на относителната интензивност на износването при увеличаване броя на циклите.

5.2. Експериментални резултати за образци 1L

Получените експериментални резултати за характеристиките на износването при дадените условия на изпитване за образци 1L (никелирани микро частици силициев карбид и алуминиев прах) са дадени в Таблица 4:

Таблица 4. Параметри на износването на образци 1L

Брой цикли *N*	25	50	75	100
Време на триене *t*, [s]	7,05	14,1	21,15	28,2
Път на триене *L*, m	5,75	11,5	17,25	23
Образец 1L-1 - 600 mm/s				
Износване m, [mg]	5	9,2	13,7	14,3
γ [mg/s]	0,71	0,65	0,65	0,5
$i = m / A_a.L$, [mg/cm^2.m]	$0{,}39.10^{-3}$	$0{,}35.10^{-3}$	$0{,}35.10^{-3}$	$0{,}27.10^{-3}$
$I = L / A_a.m$, [m/cm^2.mg]	$0{,}51.10^{3}$	$0{,}55.10^{3}$	$0{,}35.10^{3}$	$0{,}71.10^{3}$
Образец 1L-2 - 550 mm/s				
Износване m, [mg]	5	9	12	16,4
γ [mg/s]	0,71	0,64	0,57	0,58
$i = m / A_a.L$, [mg/cm^2.m]	$0{,}39.10^{-3}$	$0{,}34.10^{-3}$	$0{,}31.10^{-3}$	$0{,}31.10^{-3}$
$I = L / A_a.m$, [m/cm^2.mg]	$0{,}51.10^{3}$	$0{,}56.10^{3}$	$0{,}63.10^{3}$	$0{,}62.10^{3}$
Образец 1L-3 - 500 mm/s				
Износване m, [mg]	4,3	7,9	9,9	12,8
γ [mg/s]	0,61	0,56	0,47	0,45
$i = m / A_a.L$, [mg/cm^2.m]	$0{,}33.10^{-3}$	$0{,}3.10^{-3}$	$0{,}25.10^{-3}$	$0{,}24.10^{-3}$
$I = L / A_a.m$, [m/cm^2.mg]	$0{,}59.10^{3}$	$0{,}64.10^{3}$	$0{,}77.10^{3}$	$0{,}79.10^{3}$
Образец 1L-4 - 450 mm/s				
Износване m, [mg]	4,2	7,2	10,2	11,6
γ [mg/s]	0,6	0,51	0,48	0,41
$i = m / A_a.L$, [mg/cm^2.m]	$0{,}32.10^{-3}$	$0{,}275.10^{-3}$	$0{,}26.10^{-3}$	$0{,}22.10^{-3}$
$I = L / A_a.m$, [m/cm^2.mg]	$0{,}60.10^{3}$	$0{,}70.10^{3}$	$0{,}74.10^{3}$	$0{,}87.10^{3}$
Образец 1L-5 - 400 mm/s				
Износване m, [mg]	4,2	8	10,4	15,4
γ [mg/s]	0,6	0,57	0,49	0,55
$i = m / A_a.L$, [mg/cm^2.m]	$0{,}32.10^{-3}$	$0{,}31.10^{-3}$	$0{,}26.10^{-3}$	$0{,}29.10^{-3}$
$I = L / A_a.m$, [m/cm^2.mg]	$0{,}60.10^{3}$	$0{,}63.10^{3}$	$0{,}73.10^{3}$	$0{,}66.10^{3}$

Резултатите от проведените изпитвания за скоростта на масово износване и за относителна интензивност на износването на образци 1L са дадени на фигури 3 и 4.

Характеристиките на базовия метал (нулев образец) са дадени с пунктирана линия.

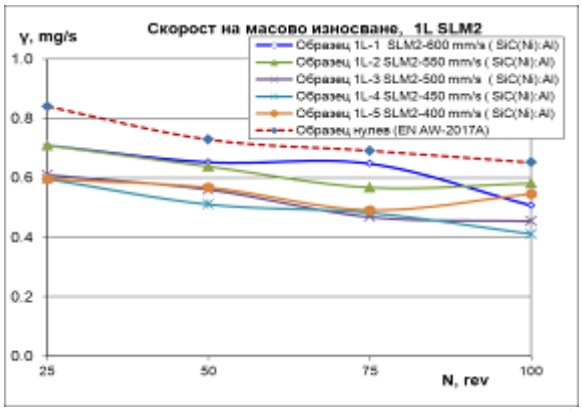

Фиг. 3 Скорост на масово износване на образци 1L при различни скорости на микронаваряване

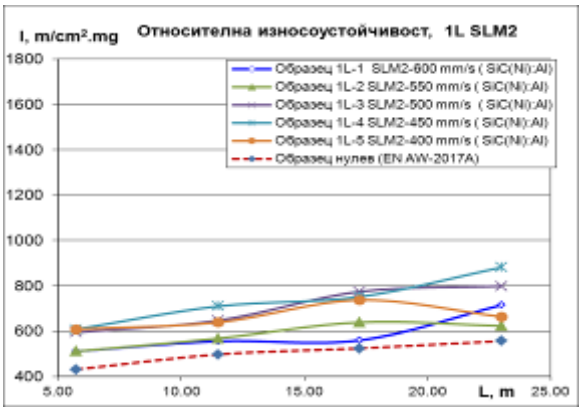

Фиг. 4 Относителна износоустойчивост на образци 1L при различни скорости на микронаваряване

Образците 1L (никелирани микро частици силициев карбид и алуминиев прах), получени при по-ниска скорост на наваряване (в диапазона 400 – 500 mm/s) показват най-ниска скорост на масово

износване и най-висока относителна износоустойчивост. Това се дължи на сравнително по-високата линейна енергия и реализирането на по-добро локално (селективно) лазерно разтопяване на алуминиевата матрица.

Резултатите от проведените изпитвания за относителна промяна на износоустойчивостта при различни скорости на микронаваряване на образци 1L са представени на Фигура 5.

Средната относителна промяна на износоустойчивостта при образци 1L (никелирани микро частици силициев карбид и алуминиев прах) е сравнително ниска – от 14% до 34%. Това показва сравнително ниско увеличаване на износоустойчивостта в сравнение с базовия метал, поради получаване на слоеве с нисък процент сплавена и усвоена уякчаваща фаза от никелирани микро частици силициев карбид в тях.

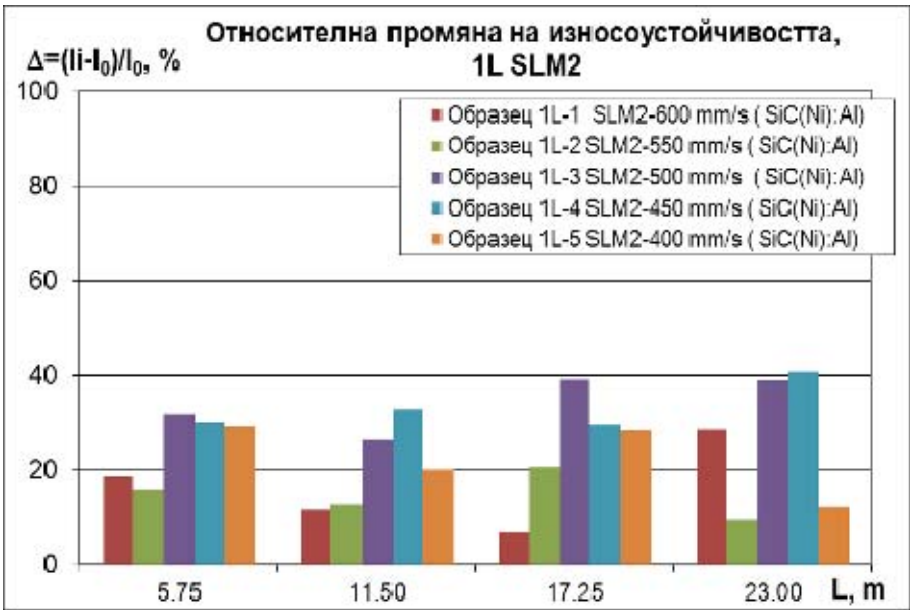

Фиг. 5 Относителна промяна на износоустойчивостта на образци 1L при различни скорости на микронаваряване

5.3. Експериментални резултати за образци 2L

Получените експериментални резултати за характеристиките на износването при дадените условия на изпитване за образци 2L (само от никелирани микрочастици силициев карбид) са дадени в Таблица 5:

Таблица 5. Параметри на износването на образци 2L

Брой цикли *N*	25	50	75	100
Време на триене *t*, [s]	7,05	14,1	21,15	28,2
Път на триене *L*, m	5,75	11,5	17,25	23
Образец 2L-1 - 600 mm/s				
Износване m, [mg]	1,5	4,1	6,9	8
γ [mg/s]	0,21	0,36	0,33	0,28
$i = m / A_a.L$, [mg/cm^2.m]	$0{,}11.10^{-3}$	$0{,}16.10^{-3}$	$0{,}18.10^{-3}$	$0{,}15.10^{-3}$
$I = L / A_a.m$, [m/cm^2.mg]	$1{,}69.10^{3}$	$1{,}23.10^{3}$	$1{,}1.10^{3}$	$1{,}27.10^{3}$
Образец 2L-2- 550 mm/s				
Износване m, [mg]	2,4	5,9	7	8
γ [mg/s]	0,34	0,42	0,33	0,28
$i = m / A_a.L$, [mg/cm^2.m]	$0{,}18.10^{-3}$	$0{,}22.10^{-3}$	$0{,}18.10^{-3}$	$0{,}15.10^{-3}$
$I = L / A_a.m$, [m/cm^2.mg]	$1{,}05.10^{3}$	$0{,}86.10^{3}$	$1{,}08.10^{3}$	$1{,}27.10^{3}$
Образец 2L-3 - 500 mm/s				
Износване m, [mg]	3,4	5,2	6,8	8,3
γ [mg/s]	0,48	0,37	0,32	0,29
$i = m / A_a.L$, [mg/cm^2.m]	$0{,}26.10^{-3}$	$0{,}2.10^{-3}$	$0{,}17.10^{-3}$	$0{,}16.10^{-3}$
$I = L / A_a.m$, [m/cm^2.mg]	$0{,}74.10^{3}$	$0{,}97.10^{3}$	$1{,}12.10^{3}$	$1{,}22.10^{3}$
Образец 2L-4 - 450 mm/s				
Износване m, [mg]	2,1	3,7	4,9	5,7
γ [mg/s]	0,3	0,26	0,23	0,2
$i = m / A_a.L$, [mg/cm^2.m]	$0{,}16.10^{-3}$	$0{,}14.10^{-3}$	$0{,}12.10^{-3}$	$0{,}11.10^{-3}$
$I = L / A_a.m$, [m/cm^2.mg]	$1{,}2.10^{3}$	$1{,}4.10^{3}$	$1{,}55.10^{3}$	$1{,}78.10^{3}$
Образец 2L-5 - 400 mm/s				
Износване m, [mg]	2,3	5,9	7,6	9
γ [mg/s]	0,33	0,42	0,36	0,32
$i = m / A_a.L$, [mg/cm^2.m]	$0{,}18.10^{-3}$	$0{,}22.10^{-3}$	$0{,}19.10^{-3}$	$0{,}17.10^{-3}$
$I = L / A_a.m$, [m/cm^2.mg]	$1{,}1.10^{3}$	$0{,}86.10^{3}$	1.10^{3}	$1{,}12.10^{3}$

Резултатите от проведените изпитвания за скоростта на масово износване и за относителна интензивност на износването на образци 2L (само от никелирани микро частици силициев карбид) са дадени на следващите фигури 6 и 7.

Характеристиките на базовия метал са представени с пунктирана линия.

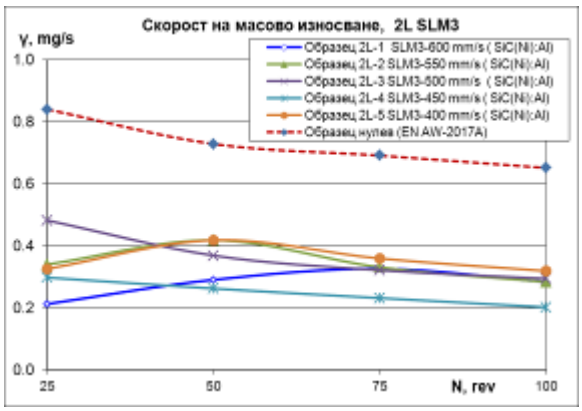

Фиг. 6 Скорост на масово износване на образци 2L при различни скорости на микро-наваряване

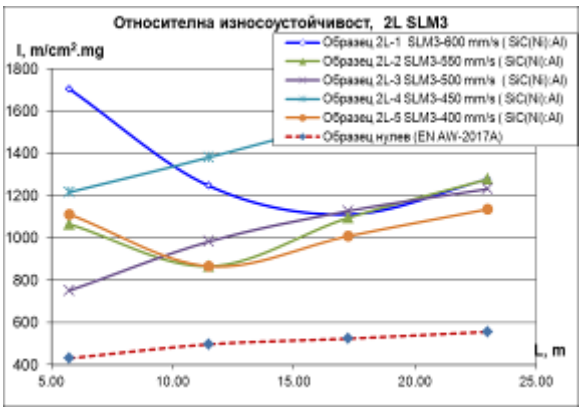

Фиг. 7 Относителна износоустойчивост на образци 2L при различни скорости при раз-лични скорости на микронаваряване

Образците 2L (само от никелирани микрочастици силициев карбид) при по-висока скорост на наваряване (в диапазона 600 – 550 mm/s) показват най-ниска скорост на масово износване и съответно най-висока относителна износоустойчивост.

Резултатите от проведените изпитвания за относителна промяна на износоустойчивостта при различни скорости на микронаваряване на образци 2L са представени на следващата фигура.

Средната относителната промяна на износоустойчивостта при образци 2L (само от никелирани микрочастици силициев карбид) е висока – от 37% до 172%. Това показва чувствително увеличаване на износоустойчивостта в сравнение с базовия метал и получаване на покритие с висок процент сплавена и усвоена уякчаваща фаза от никелирани микро частици силициев карбид.

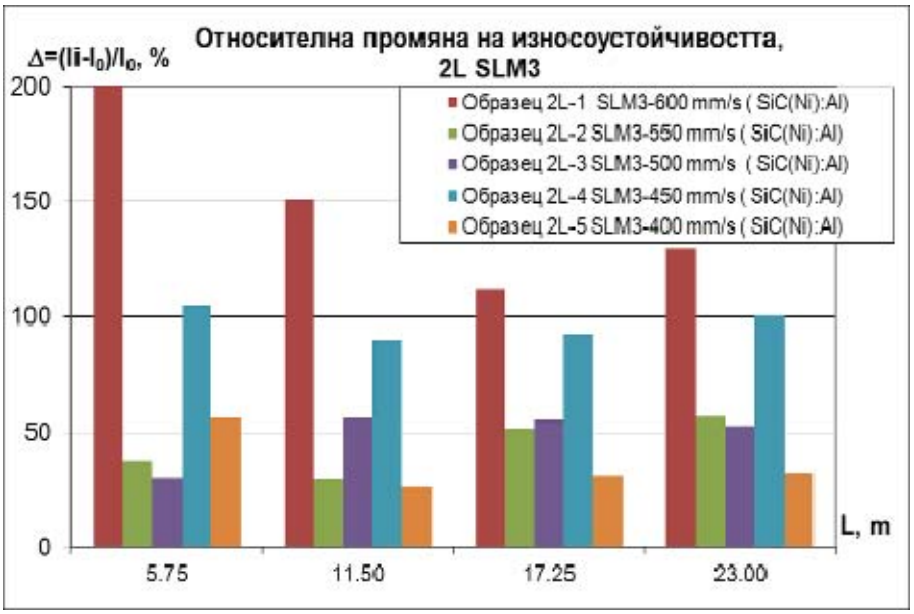

Фиг. 9 Относителна промяна на износоустойчивостта на образци 2L при различни скорости на микронаваряване

5.4. Анализ и сравнение на получените резултати

Сравняването на различните покрития е извършено по отношение на относителната износоустойчивост при различни скорости на микронаваряване в диапазона 400 – 600 mm/s, получени при сравнително устойчивите данни от изпитването за 75 и 100 цикъла. Обобщените данни от изпитването са дадени на Фиг. 10. Характеристиките на базовия метал са представени с пунктирана с две точки права.

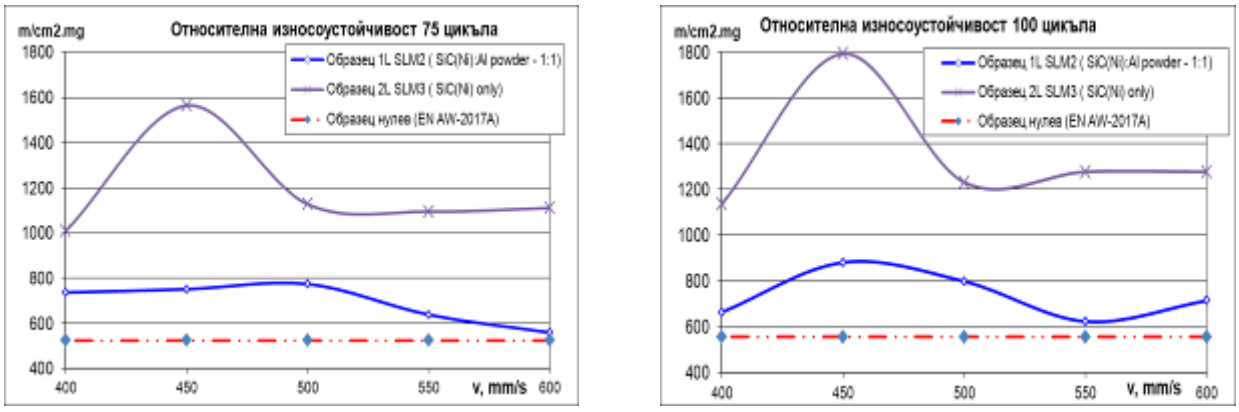

Фиг. 10 Относителна износоустойчивост при 75 и 100 цикъла за различните покрития в диапазона 400 – 600 mm/s скорост на микронаваряване

При наварени с метализирани микрочастици силициев карбид и алуминиев прах в съотношение 1:1 слоеве (*образци 1L*), се наблюдава сравнително слабо увеличаване на износоустойчивостта при

400 – 500 mm/s (увеличена с 1.2 до 1.5 пъти средна относителна износоустойчивост), но при по-високите скорости тя става почти равна на базовия метал. Това сравнително ниско увеличаване на износоустойчивостта вероятно се дължи на реализираното покритие с нисък процент сплавена и усвоена уякчаваща фаза от никелирани микро частици силициев карбид.

При наварени с метализирани микрочастици силициев карбид слоеве (*образци 2L*), в целия диапазон от скорости се наблюдава увеличена от 1.9 до 3.0 пъти средна относителна износоустойчивост, като максимумът на износоустойчивостта е при скорост на микронаваряване от 450 mm/s. Увеличаването на износоустойчивостта на слоя до 3.0 пъти в сравнение с базовия метал се дължи на реализирането на слой с висок процент сплавена и усвоена уякчаваща фаза.

6. ИЗВОДИ

В работата е представено изследване на износването на микронаварени слоеве от метализирани микрочастици SiC върху матрица от алуминиева сплав, получени чрез метода селективно лазерно стопяване (SLM).

Основните резултати и констатации се свеждат до, както следва:

1. Микронаваряването на дисперсно уякчен композитен материал от метализирани микрочастици SiC върху матрица от алуминиева сплав EN AW-2017A чрез метода селективно лазерно стопяване (SLM) осигурява износоустойчиви слоеве при скорости в диапазона от 400 mm/s до 600 mm/s.

2. Микронаваряването на уякчаващата фаза от метализирани микрочастици SiC осигурява 3 пъти по-висока относителна износоустойчивост в сравнение с базовия метал, а смесването им с алуминиев прах намалява относителната износоустойчивост до стойности, съизмерими с тази на алуминиевата матрица.

3. Установените максимални стойности на относителната износоустойчивост, отговарящи на висок процент сплавена и усвоена уякчаваща фаза в повърхностния слой, получен чрез метода селективно лазерно стопяване, са получени при скорост на наваряване от 450 mm/s.

БЛАГОДАРНОСТИ

Получаването на микронаварени слоеве по метода на селективното лазерно стопяване е реализирано със SLM 125 HL система, закупена по договор Договор № ДУНК-01/3 „Създаване на Университетски научно-изследователски комплекс (УНИК) за иновации и трансфер на знания в областта на микро/нано технологии и материали, енергийната ефективност и виртуалното инженерство”. Тематиката, свързана с изследване на износоустойчивостта на микронаварени композитни слоеве, получени чрез селективно лазерно стопяване, е част от актуализираната работна програма на договора.

ЛИТЕРАТУРА

1. YADROITSEV, I., GUSAROV, A., YADROITSAVA, I., SMUROV, I., Single track formation in selective laser melting of metal powders, Journal of Materials Processing Technology, Volume 210, Issue12, 1 September 2010, Pages 1624-1631, ISSN 0924-0136;
2. YADROITSEV, I., SMUROV, I., Selective laser melting technology: From the single laser melted track stability to 3D parts of complex shape, Physics Procedia, Volume5, Part B, 2010, Pages 551-560, ISSN 1875-3892;
3. TASHEVA, P., KANDEVA, M., PETROV, P., An Investigation on The Wear Properties of Carbon Steel Coated With Nanoparticles Using Electron Beam Technique, Journal of the Balkan Tribological Association, № 2, Vol.20, pp 227-333, 2014;
4. ASTM G 99 - 95a. Standard test method for wear testing with a pin-on-disk apparatus;
5. БДС 14289-77. Метод за изпитване на абразивно износване при триене върху закрепени абразивни частици;
6. DIMITROVA, R., Electroless nickel coatings on silicon carbide particles using two nickel salts in alkaline solution, International Working Conference “Total Quality Management – Advanced and Intelligent Approaches”, 1st – 5th June, 2015, Belgrade, Serbia, pp 387-393.

КОРЕСПОНДЕНЦИЯ

Маг. инж. Райна Димитрова
Технически Университет – София, бул. “Климент Охридски” № 8
e-mail: r_dimitrova@tu-sofia.bg

Tribological Journal BULTRIB Vol. 5, 2015
Papers from the International Conference **BULTRIB '15**
September 11-13, 2015, Sozopol, Bulgaria
Society of Bulgarian Tribologists
FIT – Technical University of Sofia

COMPARISON OF THE PHOTOCATALYTIC ACTIVITIES OF Ag/ZnO AND MECHANOCHEMICALLY ACTIVATED Ag/ZnO IN THE DECOMPOSITION OF REACTIVE BLACK 5 AND MALACHITE GREEN DYES

Katya MILENOVA[1], Katerina ZAHARIEVA[1], Alexander ELIYAS[1], Irina STAMBOLOVA[2], Vladimir BLASKOV[2], Ognjan DIMITROV[3], Ljubomir DIMITROV[4], Zara CHERKEZOVA-ZHELEVA[1], Slavcho RAKOVSKY[1]

[1]Institute of Catalysis, Bulgarian Academy of Sciences, "Acad. G. Bonchev" St., Bl.11, 1113 Sofia, Bulgaria
[2]Institute of General and Inorganic Chemistry, Bulgarian Academy of Sciences, "Acad. G. Bonchev" St., Bl.11, 1113 Sofia, Bulgaria
[3]Institute of Electrochemistry and Energy Systems, Bulgarian Academy of Sciences, Acad. G.Bonchev bl. 10, 1113, Sofia, Bulgaria
[4]Institute of Mineralogy and Crystallography "Acad. I. Kostov", Bulgarian Academy of Sciences, "Acad. G. Bonchev" Str, Bl.109, 1113 Sofia, Bulgaria.

Abstract: *The precipitation method was used to synthesize zinc oxide powders. The powders were impregnated with $AgNO_3$ obtaining 0.5wt% Ag/ZnO. The Ag/ZnO sample was mechanochemically activated (Ag/ZnO-MCA). The photocatalytic activity of samples was investigated in oxidative degradation of two textile dyes under UV-light illumination. Degradation degree of Reactive Black 5 dye after 2 hours of illumination was 25% on Ag/ZnO, while for Ag/ZnO-MCA it was higher - 93%. Degradation degree of Malachite Green dye on both samples was similar 98-99%.*

Key Words: *zinc oxide nanopowder, silver doping, mechanochemical activation, photocatalysis, azo dyes*

1. INTRODUCTION

Toxic organic compounds, including some azo dyes, appear in wastewater as pollutants, are known to be harmful to human and animal health. Among the wide variety of green chemistry projects under way, semiconductor photocatalysis has emerged as one of the most promising technologies for wastewaters purification because it represents a cheap and easy way to utilize the energy of either natural sunlight or artificial indoor illumination, which is available everywhere in the world [1].

ZnO has been known to be an effective photocatalyst for wastewater detoxification, air decontamination from organic pollutants and other self-cleaning applications. It has high mineralization and reaction rates and also provides large number of active sites available on high specific surface area [2]. To improve further photocatalytic efficiency, ZnO photocatalysts can be modified by the addition of various dopants or activators which are functioning as electron traps by suppressing electron–hole recombination. As far as ZnO is concerned, various methods have been reported to synthesize heterostructures by loading noble metals like Ag, Pd and Au on ZnO surface [3]. Noble metal deposition seems to be the most promising method due to enhancement of the photocatalytic properties of semiconductors [4]. Since silver is a well-known but rather expensive antibacterial material, it is of interest to study the extent to which a small amount of silver increases the photocatalytic activity [5]. Ag deposits acted not only as electron traps to enhance the separation of photoexcited electrons from holes, but also as charge carrier recombination sites [6]. Silver doping on ZnO enhanced its photocatalytic activity [7, 4] and photostability of the photocatalyst [8] to achieve mineralization of azo dyes [9] for water purification. Ag/ZnO was investigated for photocatalytic degradation of Methylene Blue in aqueous solutions [1,10], Methyl Orange [4,7], Acid Orange 7 [9] and others.

Mechanical treatment is a well known method for augmentation of chemical activity of the materials. Milling induces mechanical activation of fine powders - a variety of crystalline defects such as increased number of grain inter-phase boundaries, dislocations, vacancies and interstitial atoms, stacking faults, and deformed and ruptured chemical bonds [10]. The mechanochemical activation exhibits some specific characteristics, compared to other traditional methods such as heating and wet chemical methods, making engineering applications possible. The structural changes in silver iodide under mechanochemical impact have been investigated in [11]. It is well known that ball milling of silver results in the reduction of silver oxide to silver metal [12].

The aim of this paper was to study the effect of mechanochemical activation (MCA) on the structure, phase composition and photocatalytic activity for degradation of two model pollutants over Ag/ZnO samples.

2. EXPERIMENTAL

Zinc oxide photocatalyst was obtained by the method described in ref. [13]. The synthesis procedure includes dissolution of commercial ZnO in HNO_3, then adding NH_4OH and bubbling CO_2 through the solution leading to precipitation of precursor $Zn(OH)CO_3$, which was then calcined at 400°C. So the activated ZnO powder was impregnated with such a quantity of the aqueous solutions of $AgNO_3$ as to prepare ZnO doped with 0.5 wt.% Ag loading.

The mechanochemical activation of the so prepared Ag-doped ZnO sample was performed in a high-energy planetary ball mill type PM 100, Retsch, Germany. The mechanochemical treatment of Ag/ZnO catalyst was carried out in agate milling container of volume 80 ml at milling speed 400 rpm for 10 minutes milling time. The Ag/ZnO sample to balls mass ratio was 1:21.

The X-ray diffraction (XRD) patterns were recorded on a Bruker D2 Phaser diffractometer within the range of 2θ values between 20º and 70º using Cu K_α radiation (λ = 0.154056 nm) at 40 kV. The crystallites sizes were estimated by Scherrer's formula.

A scanning electron microscope (SEM) JEOL, model JEM-200CX, equipped with scanning adaptor EM-ASID3D, was used for morphology observations of the sample.

The photocatalytic oxidative degradation of Reactive Black 5 (RB5) was carried out using 150 ml dye aqueous solution with initial concentration of 20 ppm at 599 nm wavelength of maximal absorbance, specific for RB5.

Malachite Green (MG) experiments were carried out using 150 ml of the dye aqueous solution with initial concentration of 5 ppm, having maximal absorbance at 615 nm. Photocatalytic activity measurements were accomplished using polychromatic UV-A lamp illumination (18 W, 320-400nm) with a maximum of the emission at 365 nm. The process of discoloration was monitored by UV-Vis spectrophotometer CamSpec M501, based on the absorbance of the dye solution in the wavelength range from 200 to 800 nm. The samples were equilibrated in the dark for about 30 min before switching on the illumination.

3. RESULTS AND DISCUSSIONS

XRD analysis of both samples proved the existence of hexagonal wurtzite type structure of ZnO (JCPDS 36-1451) (Fig.1). The silver phase has not been registered due to its small quantity (0,5 wt%) below the sensitivity threshold. The mechanochemical activation influenced intensity from around 1100 to 650, which revealed that MCA exerts effect on the degree of crystallization. Another effect of MCA is the decreasing of the mean crystallites size. As it can be seen in Fig. 2 after MCA the size of the crystallites is decreased significantly with 6.4 nm.

SEM images of Ag–ZnO nanostructures show some plate-like shape with some particles present on the surface (Fig 3–a). At higher magnification agglomerates of particles become visible (Fig 3-b). Similar aggregation of particles has been observed by Kuriakose et al. [14] for ZnO powders, prepared by wet chemical method.

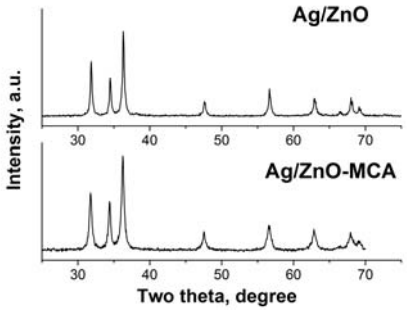

Fig. 1. XRD patterns of Ag/ZnO samples

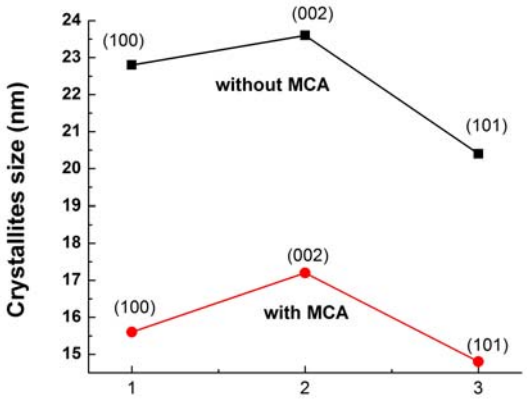

Fig. 2. Crystallites size of Ag/ZnO samples estimated by the three main crystallographic peaks of wurtzite phase

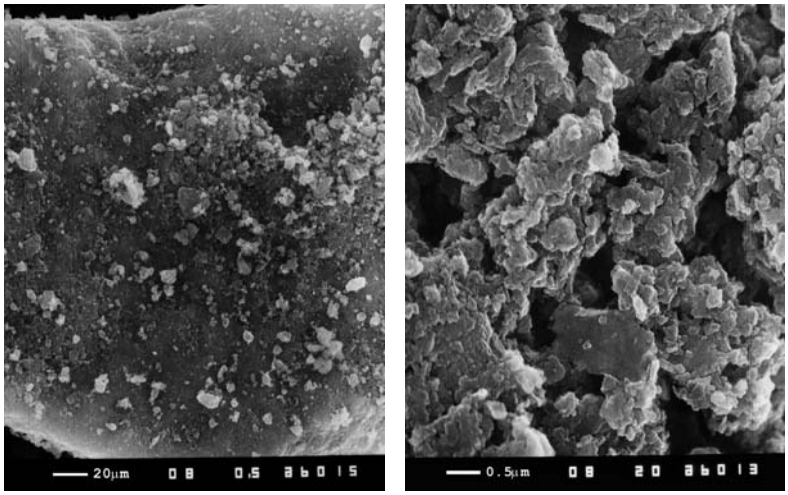

a) **b)**

Fig. 3. SEM photographs of Ag/ZnO sample at different magnifications

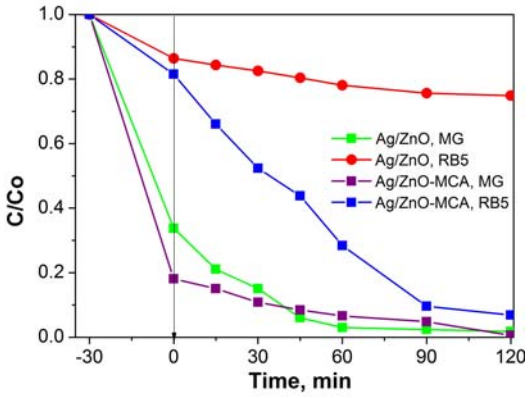

Fig. 4. Reaction course of MG and RB5 dyes discoloration using samples without and with MCA treatment with the time of illumination

Table 1. Rate constants for MG and RB5 dyes

Sample	*Dye*	*k (x10^{-3} min^{-1})*
0.5wt% Ag/ZnO	MG	28.8
0.5wt% Ag/ZnO-MCA	MG	21.9
0.5wt% Ag/ZnO	RB 5	1.4
0.5wt% Ag/ZnO-MCA	RB 5	20.4

Fig. 4 shows the reaction course as dependences of (C/Co) on the time interval under UV light illumination. The rate constants were calculated using the logarithmic straight line equation –ln(C/Co) = *k*t on the basis of the slope ***k*** of the plotted dependence (Table 1). Fig. 5 represents the degradation rates of both kinds of dyes on the non-treated and mechanochemically treated Ag/ZnO powders suspended in the dye solution. Explanation of the enhanced activity of Ag doped ZnO was proposed by Zhang et al [1] based on the prolonged effective lifetime of photogenerated holes by electron-trapping by the metallic silver clusters on the surface of the ZnO nanoparticles. The metal deposits serve as electron reservoirs, which lead to an enhanced rate of superoxide anion-radical generation, facilitating the generation of hydroxyl radicals, and thereby increasing the photocatalytic activity [1] by the addition of radical-chain mechanism in the bulk phase (indirect oxidation mechanism in addition to the direct oxidation mechanism on the surface of ZnO).

The higher values of degradation rates were observed with both types of Ag/ZnO photocatalysts in regard to photocatalytic degradation of MG dye. The samples activated by mechanochemistry possess high photoactivity with respect to both MG and RB5 dyes. As it can be seen in Fig. 2 the crystallites sizes of the powders after MCA treatment are smaller than those in the freshly prepared samples, which could be the reason for high photocatalytic activity. This effect is even stronger in the case of RB5 dye. Similar effect of mechanochemical activation on the antimicrobial efficiency of Ag doped ZnO has been proved in [15]. It has to be noted that regardless of the weaker degree of crystallization of the MCA treated samples, they exhibit higher photoactivity than that of the non-treated samples.

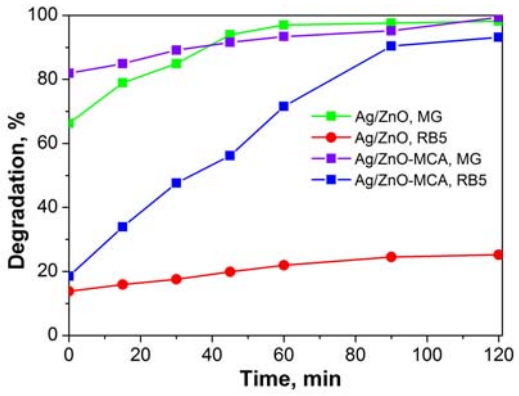

Fig. 5. Effect of mechanochemical activation on the degradation rate of MG and RB5 dyes on silver doped ZnO powders

4. CONCLUSION

Precipitation and impregnation methods were used for the synthesis of silver doped (0,5wt%) zinc oxide nanopowders. One set of the samples was mechanochemically activated for 10 minutes (Ag/ZnO-MCA). The XRD analyses estimated formation of wurtzite phase. The Ag/ZnO and Ag/ZnO-MCA samples were investigated in the reactions of oxidative degradation of two textile dyes: Malachite Green (MG) and Reactive Black 5 (RB5) under Ultraviolet light illumination. The Ag/ZnO and Ag/ZnO-MCA photocatalysts degrade MG dye completely for 2 hours. The mechanochemically activated Ag/ZnO shows considerably higher value of RB5 degradation-93% than that of the non-activated sample. The rate constants of photocatalysts are decreasing in the following order Ag/ZnO, MG (28.8×10^{-3} min^{-1}) > Ag/ZnO-MCA, MG (21.9×10^{-3} min^{-1}) > Ag/ZnO-MCA, RB5 (20.4×10^{-3} min^{-1}) > Ag/ZnO, RB5 (1.4×10^{-3} min^{-1}). The post-synthesis mechanochemical activation of ZnO powders is a very promising method to obtain highly effective photocatalysts for dyes solutions discoloration, which could find application in practice.

ACKNOWLEDGMENTS

The authors gratefully acknowledge financial support by National Science Fund, Ministry of Education and Sciences of Bulgaria (Contract DFNI – T-02-16).

REFERENCES

1. ZHANG, D., Effects of Deposited Metallic Silver on Nano-ZnO for the Environmental Purification of Dye Pollutants, S. Afr. J. Chem., **65**, 2012, 98–103.

2. MONDAL, K., SHARMA, A., Photocatalytic Oxidation of Pollutan Dyes in Wastewater by TiO_2 and ZnO nano-materials – A Mini-review, Nanoscience & Technology for Mankind, Edited by Ashok Misra, Jayesh R. Bellare, **5**, 2014, 36-72.

3. TAN, T., LI, Y., LIU, Y., WANG, B., SONG, X., LI, E., WANG, H., YAN, H., Two-step preparation of Ag/tetrapod-like ZnO with photocatalytic activity by thermal evaporation and sputtering, Materials Chemistry and Physics, **111**, 2008, 305–308.

4. YILDIRIM, O. A., UNALAN, H. E., DURUCAN, C., Highly Efficient Room Temperature Synthesis of Silver-Doped Zinc Oxide (ZnO:Ag) Nanoparticles: Structural, Optical, and Photocatalytic Properties, J. Am. Ceram. Soc., **96** (3), 2013, 766–773.

5. IBANESCU (BUSILA), M., MUSAT, V., TEXTOR, T., BADILITA, V., MAHLTIG, B., Photocatalytic and antimicrobial Ag/ZnO nanocomposites for functionalization of textile fabrics, Journal of Alloys and Compounds, **610**, 2014, 244–249.

6. REN, C., YANG, B., WU, M., XU, J., FU, Z., LV, Y., GUO, T., ZHAO, Y., ZHU, C., Synthesis of Ag/ZnO nanorods array with enhanced photocatalytic performance, Journal of Hazardous Materials, **182**, 2010, 123–129.

7. UDOM, I., ZHANG, Y., RAM, M., STEFANAKOS, E., HEPP, A., ELZEIN, R., SCHLAF, R., YOGI GOSWAMI, D., A simple photolytic reactor employing Ag-doped ZnO nanowires for water purification, Thin Solid Films, **564**, 2014, 258–263.

8. XIE, W., LI, Y., SUN, W., HUANG, J., XIE, H., ZHAO, X., Journal of Photochemistry and Photobiology A: Chemistry, **216** , 2010, 149–155.

9. SHINDE, S.S., BHOSALE, C.H., RAJPURE, K.Y., Oxidative degradation of acid orange 7 using Ag-doped zinc oxide thin films, Journal of Photochemistry and Photobiology B: Biology, **117**, 2012, 262–268.

10. ZHANG, Q., SAITO, F., A review on mechanochemical syntheses of functional materials, Advanced Powder Technology, **23**, 2012, 523–531.

11. TOMAEV, V. V., TVERYANOVICH YU. S., BALMAKOV, M. D., Structural Changes in Silver Iodide upon Mechanochemical Treatment, Glass Physics and Chemistry, **38** (1), 2012, 155–161.

12. RALPHS, K., HARDACRE, C., JAMES, S. L., Application of heterogeneous catalysts prepared by mechanochemical synthesis, Chem. Soc. Rev., **42**, 2013, 7701-7718.

13. MILENOVA, K., ELIYAS, A., BLASKOV, V., STAMBOLOVA, I., RAKOVSKY, S., Doping silver to activated ZnO to promote the photocatalytic efficiency for azo dye degradation, Journal of International Scientific Publications: Materials, Methods &Technologies, **8**, 2014, 259-264.

14. KURIAKOSE, S., CHOUDHARY, V., SATPATI, B., MOHAPATRA, S., Enhanced photocatalytic activity of Ag–ZnO hybridplasmonic nanostructures prepared by a facile wet chemical method, Beilstein J. Nanotechnol. **5**, 2014, 639–650.

15. TALARI, M. K., MAJEED, A. B. A., TRIPATHI, D. K., TRIPATHY, M., Synthesis, Characterization and Antimicrobial Investigation of Mechanochemically Processed Silver Doped ZnO Nanoparticles, Chem. Pharm. Bull., **60** (7), 2012, 818–824.

CORRESPONDENCE

Chief Assistant Professor Dr.Katya MILENOVA
Institute of Catalysis, Bulgarian Academy of Sciences, “Acad. G. Bonchev” St., Block 11, 1113
Sofia, Bulgaria
e-mail:kmilenova@ic.bas.bg

Tribological Journal BULTRIB Vol. 5, 2015
Papers from the International Conference **BULTRIB '15**
September 11-13, 2015, Sozopol, Bulgaria
Society of Bulgarian Tribologists
FIT – Technical University of Sofia

FRICTION IN CONTACT SYSTEM "SLCAM "IPM"- 304 – STEEL" IN VACCUUM AND IN AIR

Tinka GROZDANOVA

Abstract: *This article presents a study on the Coefficient of friction dependency of "self-lubricating composite antifrictional material – steel" contact system from distance in vacuum and in air. A comparison between the values in two cases, when the studied material is A) in position "body" and B) in position "contra-body", has been made. The type and the spectral analysis of the frictional surface have been examined.*

Key words: *Tribology, Coefficient of friction, Antifrictional materials*

ТРИЕНЕ В КОНТАКТНА СИСТЕМА „СКАМ „ИПМ"- 304 – СТОМАНА" В УСЛОВИЯ НА ВАКУУМ И ВЪЗДУШНА СРЕДА

Тинка ГРОЗДАНОВА

Резюме: *В статията е представено изследване на зависимостта на динамичния коефициент на триене от пътя на триене в трибосистема „самосмазващ се композитен антифрикционен материал – стомана" във вакуум и във въздушна среда. Направено е сравнение на стойностите в два случая: А - когато изследваният материал е в кинематична позиция „неподвижно тяло" и Б - когато изследваният материал е в кинематична позиция „въртящо се контратяло". Разгледани са вида и спектралния състав на триещата се повърхност на изследвания материал.*

Ключови думи: *Трибология, коефициент на триене, антифрикционни материали.*

1. ВЪВЕДЕНИЕ

Процесите триене и износване протичат при взаимодействие между повърхностите на телата, затова състоянието и структурата на повърхността оказва решаващо влияние върху формирането на силите на триене и механизмите на износване.

При триене на въздух повърхностните окиси се явяват като защитен слой, който се разрушава под действие на силата на триене, на температурата и на деформационните процеси в микроконтактите. Но поради наличието на кислород, този слой се възстановява и запазва защитните си свойства [1].

Във вакуум газовата среда рязко се променя, нарушава се динамичното равновесие между нея и адсорбционните слоеве, протича тяхната десорбция, а образуването на окисни слоеве силно се възпрепятства. Износването на защитните повърхностни слоеве при триене във вакуум води до тяхното необратимо премахване и до нарастване силата на адхезия. Получава се сухо триене и в контакт влизат атомно-чисти (ювенилни) повърхности. При тези обстоятелства трибологичните процеси засягат не само микрогеометрията на повърхността, но и нейното физико-химично състояние [2].

В условия на дълбок вакуум (10^{-4} - 10^{-12} Pa), при отсъствие на конвекционно топлоотдаване, се получава интензивно нагряване на материалите в контактната зона и на контактуващите тела. Високата температура предизвиква деструкция на смазващите слоеве, на адсорбционните покрития, намалява якостта на материала и подпомага развитието на пластична деформация в него. Всичко това води до силно увеличение на коефициента на триене, възникване на задиране и поява на студена заварка [1].

Един от съвременните начини за преодоляване на този проблем представлява използването на самосмазващи се композитни антифрикционни материали (СКАМ) на основата на медта. Такъв тип материали бяха разработени и изследвани по съвместна научна програма между Института за космически изследвания и технологии към БАН и Института по проблеми на материалознанието към НАН – Украйна.

Тези материали носят общото название „ИПМ” и за тях е характерно, че притежават високохетерогенна структура, като съставните компоненти имат строго определени функции. Разработени са на медна основа, легирана с фосфор, и един от елементите манган, никел и калай. Съдържат изолирани глобуларни образувания на олово, което практически не взаимодейства с медта. Основен технологичен принцип при създаването им е постигането на оптимизирани параметри: нисък коефициент на триене, висока износоустойчивост, голяма товароносимост, защита срещу образуване на центрове на зацепване и задиране в контакта, при работа в условия на сухо триене във вакуум. Медта и нейните сплави изграждат носеща матрица, оловото изпълнява антифрикционни функции [3,4,5].

Целта на настоящата работата е да се проведе сравнително изследване на динамиката на процеса на триене във вакуум и във въздушна среда в контактни системи, съдържащи два от материалите: „ИПМ”- 304 и „ИПМ”- 305.

2. ИЗПОЛЗВАНА АПАРАТУРА И МЕТОДИКА

За изследване на коефициента на триене на материалите във вакуумна среда е използван високовакуумен трибометър “BALZERS” и компютризирана система за управление, регистриране, обработка и получаване на опитните резултати в графичен вид. Приложен е методът “Ball-on-Disc” („Сфера върху диск”), при който дискът се движи с равномерна скорост 1m/s, силата на натоварване е 2N, степента на вакуума е 1.10^{-3} Pa. Изследването на въздух е извършено при температура на околната среда t = 25°C. Като партньор в трибосистемата е използван материал стомана AISI 52100 (100Cr6) с твърдост 740 HV [6,7]. На фиг. 1 е показана снимка на вътрешността на вакуумната камера и разположения в нея трибометър.

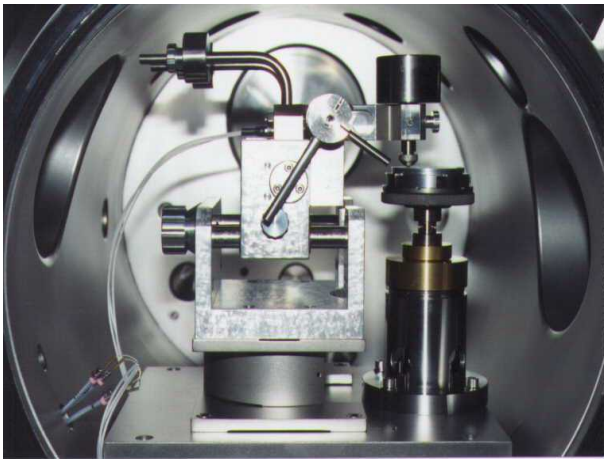

Фиг. 1. Вакуумна камера и трибометър

Структурата и морфологията на триещата се повърхност са изследвани със сканиращ електронен микроскоп (SEM).

Анализ на елементния състав на триещата се повърхност е извършен с рентгенова микросонда (SEM/EDX).

Изследването на коефициента на триене, снимките и спектралния анализ на триещата се повърхност на материалите са направени в два случая [7]:

Случай А**,** при който образецът от изследвания материал е в кинематична позиция „неподвижно тяло”, с форма на сфера с диаметър d = 6 mm.

Случай Б**,** при който образецът от изследвания материал е в кинематична позиция „въртящо се контратяло”, с форма на хоризонтален диск с размери: d = 65 mm и дебелина 5 mm.

3. МАТЕРИАЛ СКАМ „ИПМ”- 304

Материалът СКАМ „ИПМ”- 304 е получен чрез прахова металургия. Съдържа мед, фосфор, калай и олово (Cu + P + Sn + Pb) и притежава твърдост 150 HB. Микроструктурата е изградена от твърди разтвори на калая и частично на фосфора в медта. Съставните компоненти имат диференцирани функции. Медта и нейните сплави изграждат носеща част (матрица). Оловото изпълнява ролята на твърда смазка.

Останалата част фосфор образува фазата меден фосфид, която, във вид на разкъсана мрежа, е разположена около зърната на твърдите разтвори и повишава износоустойчивостта на материала. Легирането с калай подобрява механичните и антифрикционни свойства. Фазата меден фосфид уякчава и намалява пластичната деформация на композита в условия на сухо триене във вакуум [8,9,10].

На фиг. 2 е показана микроструктурата на материала, където светлите участъци представляват мрежата от меден фосфид, сивите – твърд рзтвор Cu-Sn, тъмните – олово.

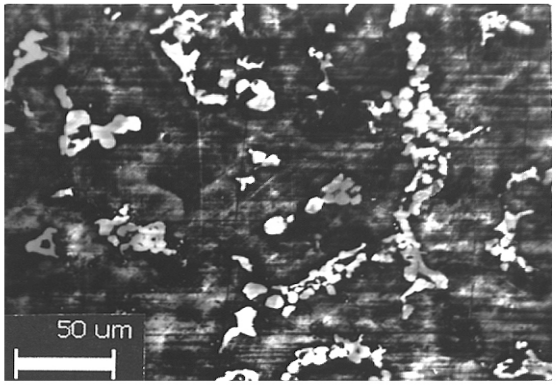

Фиг. 2. Микроструктура на СКАМ „ИПМ”- 304

4. ЕКСПЕРИМЕНТАЛНИ РЕЗУЛТАТИ

4.1. Изследване на динамичния коефициент на триене на СКАМ „ИПМ”- 304

На фиг. 3 и фиг. 4 са показани графиките на зависимостта на динамичния коефициент на триене на материал „ИПМ”- 304 от пътя на триене, във вакуум и на въздух, за двата описани случая.

Случай А

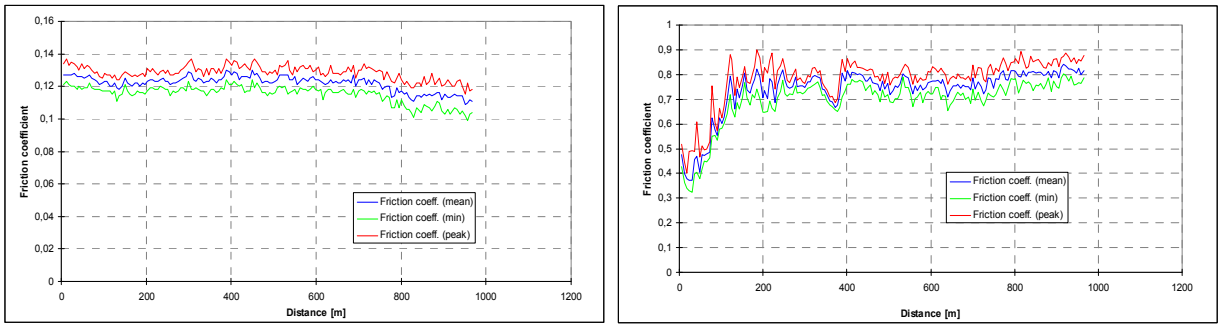

а) ***б)***

Фиг. 3. Зависимост на коефициента на триене на „ИПМ”- 304 от пътя на триене: а) във вакуум; б) на въздух

Коефициентът на триене във вакуум се изменя от 0,13 до 0,11 като с удължаване на разстоянието намалява. На въздух стойността му варира от 0,4 до 0,8 с тенденция към увеличаване.

Случай Б

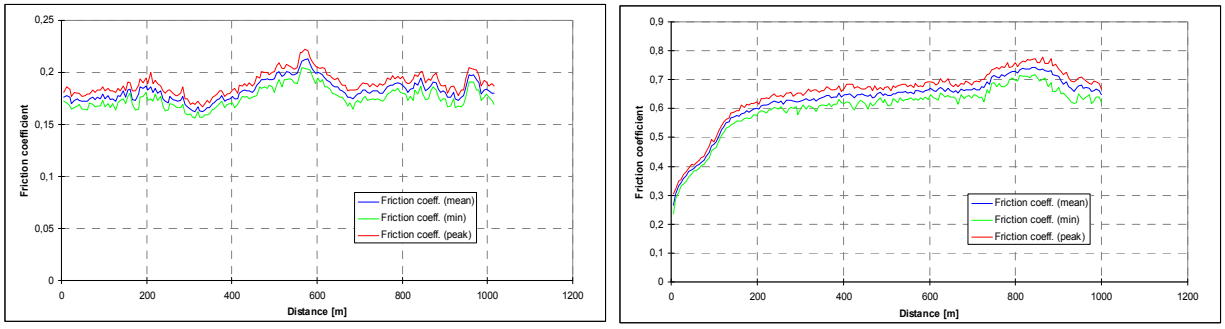

а) ***б)***

Фиг. 4. Зависимост на коефициента на триене на „ИПМ”- 304 от пътя на триене: а) във вакуум; б) на въздух

В този случай коефициентът на триене във вакуум се изменя от 0,18 до 0,21 като с удължаване на разстоянието запазва почти постоянна стойност и графиката има равномерен ход. На въздух стойността му нараства от 0,3 до 0,7.

В таблица 1 са показани усреднените стойности на коефициента на триене на материал „ИПМ”- 304 във вакуум и на въздух за двата описани случая.

Таблица 1. Средни стойности на коефициента на триене на „ИПМ”- 304

Кинематична позиция	Товар	Скорост	Коефициент на триене	
			Във вакуум	На въздух
„Неподвижно тяло” (сфера)	2N	1 m/s	0,12	0,61
„Въртящо се контратяло” (диск)	2N	1 m/s	0,18	0,48

4.2. Изследване на триещата се повърхност на СКАМ „ИПМ”- 304

Случай А

На фиг. 5 са показани снимки на повърхността на СКАМ „ИПМ”- 304 след един и същи път на сухо триене, във вакуум и на въздух.

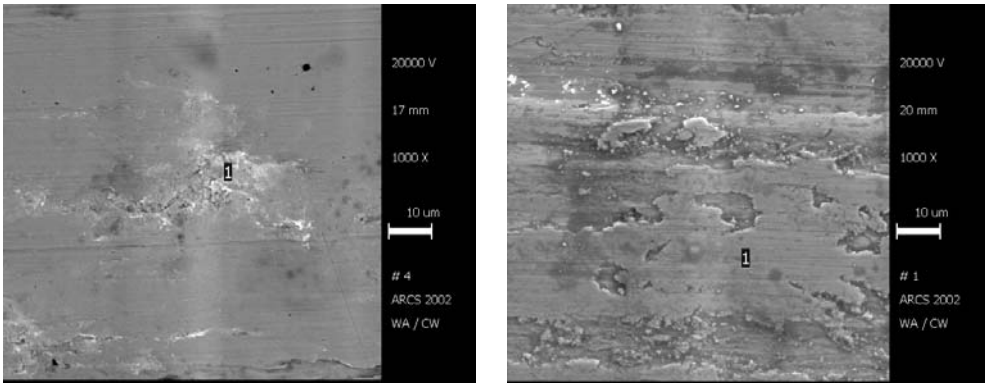

а) б)

Фиг. 5. Морфология на повърхността на „ИПМ”- 304: а) във вакуум; б) на въздух

При триене във вакуум в точка 1 се наблюдава разнасяне на оловна глобула по повърхността. При триене на въздух върху повърхността се образува смесен слой.

На фиг. 6 са представени емисионните спектри на повърхността на СКАМ „ИПМ”- 304 след сухо триене във вакуум и на въздух.

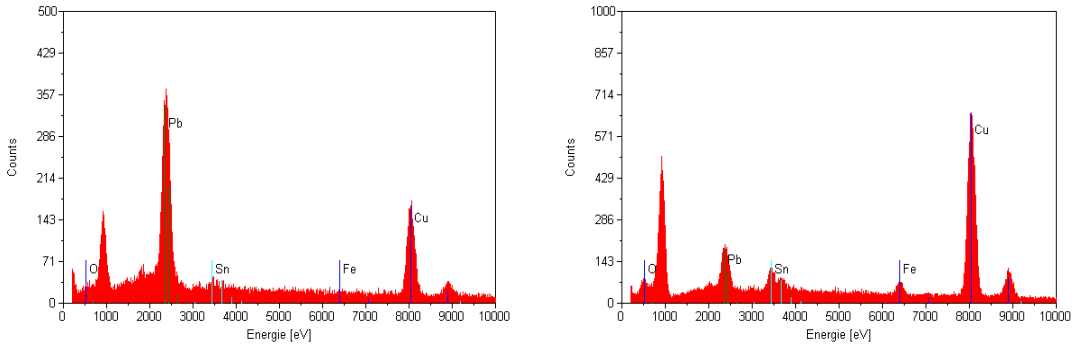

а) б)

Фиг. 6. Спектри на елементния състав на повърхността на „ИПМ”- 304: а) във вакуум; б) на въздух

Във вакуум повърхностният слой съдържа елементи от матрицата, но оловото преобладава (фиг. 6а). На въздух се наблюдава значително количество мед, вижда се наличие на кислород от образу-

валия се оловен окис и елементите от основния състав на композита са с по-високи стойности. Регистрира се присъствие на желязо от стоманата на партньора в трибосистемата (фиг. 6б).

Случай Б

На фиг. 7 са показани снимки на повърхността на СКАМ „ИПМ”- 304 след сухо триене във вакуум и на въздух.

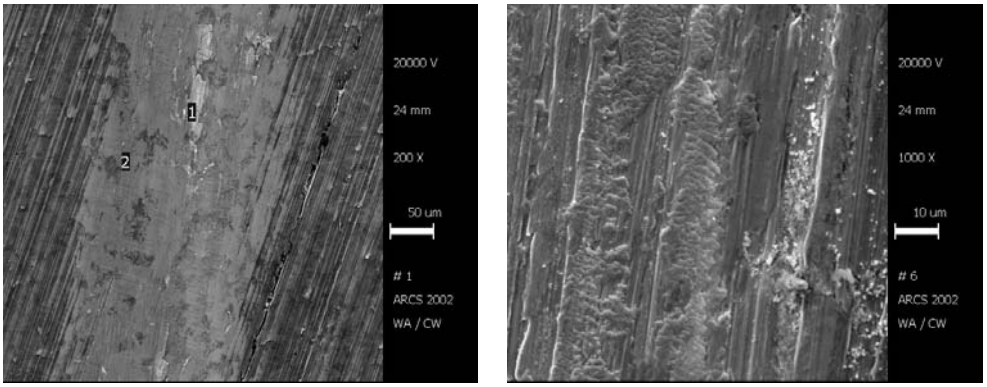

а) ***б)***

Фиг. 7. Морфология на повърхността на „ИПМ”- 304: а) във вакуум; б) на въздух

След триене във вакуум върху повърхността се образува плътен слой, обогатен с олово (фиг. 7а). След триене на въздух повърхността е набраздена и върху нея е образуван неравномерен слой с различна плътност (фиг. 7б).

На фиг. 8 са показани емисионните спектри на повърхността на СКАМ „ИПМ”- 304.

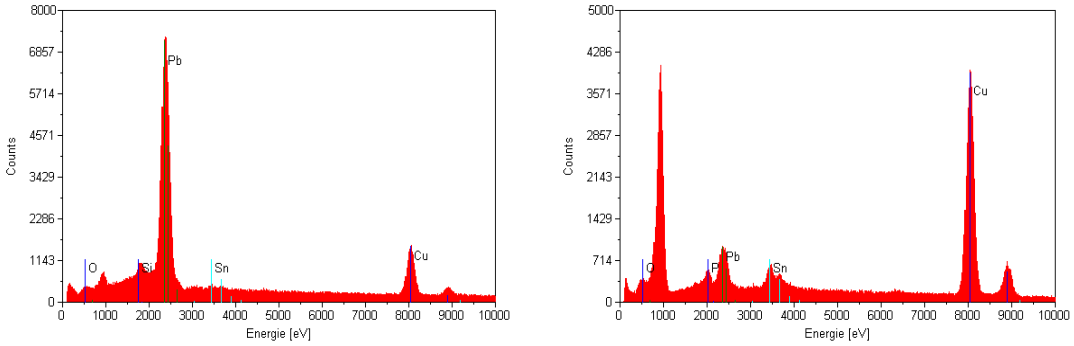

а) ***б)***

Фиг. 8. Спектри на елементния състав на повърхността на „ИПМ”- 304: а) във вакуум; б) на въздух

Елементният състав на повърхността във вакуум показва, че количеството олово многократно надвишава останалите елементи (фиг. 8а). На въздух се отчита значително присъствие на мед и кислород от образувалия се оловен окис (фиг.8б).

5. ЗАКЛЮЧЕНИЕ

В работата е проведено сравнително изследване на динамичния коефициент на триене в контактната система „СКАМ „ИПМ”- 304 – стомана AISI 52100” (100Cr6) в условия на сухо триене във вакуумна и въздушна среда при две кинематични позиции на материала: – като „неподвижно тяло” (сфера) и като „въртящо се контратяло” (хоризонтален диск), при еднакви динамични условия – скорост на плъзгане и нормално натоварване.

Основният извод от получените експериментални резултати е, че стойността на коефициента на триене в трибосистемата „СКАМ „ИПМ”- 304 – стомана AISI 52100” (100Cr6) в условия на вакуум 1.10^{-3} Ра е значително по-малка в сравнение с тази на въздух и се изменя в диапазона от 0,12 до 0,18.

По-конкретните изводи се свеждат до:

I. При сухо триене във вакуумна среда:

- в случай А, когато материалът е в позиция „сферично неподвижно тяло” коефициентът на триене има постоянна стойност 0,12, като се наблюдава тенденция към намаляване при увеличаване на пътя на плъзгане.

- в случай Б, когато материалът е в позиция „хоризонтално въртящо се контратяло” (диск) зависимостта на коефициента на триене от пътя на триене има неравномерен и нелинеен характер. Средната стойност на коефициента на триене е 0,18 – по-висока от тази на случай А.

От металографските снимки се вижда, че повърхността на изследвания материал се покрива със смазващ слой. Спектралният състав на този слой показва присъствие на елементи от изграждащата матрица, но количеството на олово е значително по-голямо. Слоят е равномерен и плътен.

II. При сухо триене във въздушна среда:

- в двата случая (случай А и случай Б) зависимостта на коефициента на триене от пътя на триене има слабо изразен нелинеен характер с тенденция към нарастване при увеличаване на пътя на плъзгане.

- наблюдава се разлика в стойността на коефициента на триене в случаите на различна позиция на материала. В случай Б, когато тялото е в позиция на „хоризонтално въртящо се контратяло”, коефициентът на триене има по-малка стойност в сравнение със стойността му в случай А, когато тялото е в позиция на „сферично неподвижно тяло”.

От металографските снимки се вижда, че повърхността е неравна и полученият слой е неравномерен. Спектралният състав на този слой показва, че в него има високо съдържание на мед и кислород от образувания оловен окис; стойностите на калай са по-високи в сравнение с тези във вакуум. Отчита се наличие на желязо и фосфор. От това следва, че самосмазването е по-слабо ефективно.

БЛАГОДАРНОСТИ

Изказваме нашата благодарност на акад. А. Г. Косторнов, д-р О. И. Фущич и н. с. Т. М. Чевичелова за плодотворното сътрудничество и активното участие в провежданите научни изследвания.

Изказваме нашата благодарност на Европейския съюз и на Европейската Комисия за оказаното съдействие при изследването на СКАМ „ИПМ”, извършено в отдел „Аерокосмически материали и технологии” на изследователски център в гр. Зайберсдорф - Австрия, което беше финансирано от програма „Подобряване на изследователския потенциал” (Contract № HPRI-CT-1999-00024-User II-49-2002).

ЛИТЕРАТУРА

1. Дроздов, Ю.Н., В.Г. Павлов, В.Н. Пучков, Трение и износ в экстремальных условиях, Москва, „Машиностроение”, 1986.

2. Крагельский, И.В., И.М Ломбарский, А. А. Гусляков, Г.И. Трояновская, В.Ф. Удовенко, Трение и износ в вакууме, Москва, „Машиностроение”, 1973.

3. Kostornov, A. G., O. I. Fushchich, T. M. Chevichelova, Y. M. Simeonova, A. D. Kostenko, Relationships at friction, wear and synthesis of the friction surface of composite self-lubricating materials, ISSN 0032-4795, “Powder Metallurgy”, No 3/4, pp. 11-19, 2007 (In Russian).

4. Фущич, О.И., А. Д. Панасюк, Л. Ф. Колесниченко, А. И. Юга, Л. Д. Игнатенко, П. А. Верховодов, Влияние олова на формирование межфазной границы в антифрикционной композиции медь-свинцово-оловянистие сплавы, „Адгезия расплавов и пайка материалов”, 8, 1987, Киев, 41-45.

5. Колесниченко, Л. Ф., О.И. Фущич, А. Д. Панасюк, А. А. Сотник, В. И. Решетняк, Г. Э. Брайнин, Л. Д. Игнатенко, Влияние фосфористой меди на формирование межфазной границы в антифрикционной композиции медные сплавы-фосфористая медь, „Порошковая металлургия”, 1992, №7, Киев, 87-93.

6. Friction and Wear under vacuum, UHV-Tribometer, Austrian Research Centers, Seibersdorf, Austria.

7. Simeonova, Y., G. Sotirov, Study of the Parameters of New Antifrictional Materials under Dry Friction Vacuum Conditions, BAS, ARC - Seibersdorf, Austria, ARC-W-0136, pp. 2-30, 2002 (Data Bank of the AMTT), http: //www.2.arcs.ac.at/amtt.

8. Колесниченко, Л.Ф., О.И.Фущич, А.Д. Панасюк, И. Я. Дзыкович, Л. Д. Игнатенко, Контактное взаимодействие структурных составляющих композиционных антифрикционных материалов на основе меди, „Порошковая металлургия”, №4, 1984, 82-86.

9. Фущич, О.И., А.Д. Панасюк, Л. Ф. Колесниченко, Л. Д. Игнатенко, Г. Н. Гордань, Межфазное взаимодействие структурных составляющих антифрикционных композиционных материалов на основе меди, „Адгезия расплавов и пайка материалов”, 13, 1984, 61-66.

10. Симеонова, Ю., М. Аструкова, Т. Грозданова, Изследване на нови антифрикционни материали за работа във висок вакуум за космически приложения, Международен научен проект на ИКИТ-БАН и ИПМ-НАНУ, 2009.

11. Симеонова, Ю., Г. Сотиров, М. Аструкова, Т. Грозданова, Нови самосмазващи се антифрикционни материали за работа в екстремни условия, SENS 2009, Fifth Scientific Conference with International Participation, 2-4 Nov., 2009, Sofia, Bulgaria, Proceedings, 293.

12. Грозданова, Т., Развитие на триботехническите материали за работа във вакуум, 26-th International Scientific Conference, Sozopol, Bulgaria, 13-16 Sept., 2010, Proceedings, 612.

13. Грозданова, Т., Физико-химически изменения в структурата на самосмазващи се композитни материали при работа във вакуум, SES 2010, Sixth Scientific Conference with International Participation “SPACE, ECOLOGY, SAFETY”, November 2-4, 2010, Sofia, Bulgaria. Proceedings, 148-151.

14. Грозданова, Т., Трибологично състояние на антифрикционен материал във вакуум и атмосферна среда, SES 2012, Eight Scientific Conference with International Participation, “SPACE, ECOLOGY, SAFETY”, 4-6 November, 2012, Sofia, Bulgaria, Proceedings, 275-279.

КОРЕСПОНДЕНЦИЯ:
Тинка ГРОЗДАНОВА
Гл. Асистент, Институт за космически изследвания и технологии – БАН,
София, ул.”Акад. Г. Бончев” бл. 1.
e-mail: tinka_gr@abv.bg

Tribological Journal BULTRIB Vol. 5, 2015
Papers from the International Conference **BULTRIB '15**
September 11-13, 2015, Sozopol, Bulgaria
Society of Bulgarian Tribologists
FIT – Technical University of Sofia

FRICTION IN CONTACT SYSTEM ”SLCAM ”IPM”- 305 – STEEL” IN VACCUUM AND IN AIR

Tinka GROZDANOVA

Abstract: *This article presents a study on the Coefficient of friction dependency of “self-lubricating composite antifrictional material – steel” contact system from distance in vacuum and in air. A comparison between the values in two cases, when the studied material is A) in position “body” and B) in position “contra-body”, has been made. The type and the spectral analysis of the frictional surface have been examined.*

Key words: *Tribology, Coefficient of friction, Antifrictional materials*

ТРИЕНЕ В КОНТАКТНА СИСТЕМА „СКАМ „ИПМ”- 305 – СТОМАНА” В УСЛОВИЯ НА ВАКУУМ И ВЪЗДУШНА СРЕДА

Тинка ГРОЗДАНОВА

Резюме: *В статията е представено изследване на зависимостта на динамичния коефициент на триене от пътя на триене в трибосистема „самосмазващ се композитен антифрикционен материал – стомана” във вакуум и във въздушна среда. Направено е сравнение на стойностите в два случая: А - когато изследваният материал е в кинематична позиция „неподвижно тяло” (сфера) и Б - когато изследваният материал е в кинематична позиция „въртящо се контратяло” (диск). Разгледани са вида и спектралния състав на триещата се повърхност на изследвания материал.*

Ключови думи: *Трибология, коефициент на триене, антифрикционни материали.*

1. МАТЕРИАЛ СКАМ „ИПМ”- 305

Този материал е получен чрез прахова металургия и има твърдост 100 HB. Той съдържа мед, фосфор, никел и олово (Cu + P + Ni + Pb). Микроструктурата е изградена от твърди разтвори на никел и частично на фосфор. Останалата част фосфор образува твърди фази меден фосфид и никелов фосфид, разпределени във вид на разкъсана мрежа по границите на зърната на твърдите разтвори. По този начин се повишава якостта на материала, без да се намалява пластичността [1,2]. Легирането с никел и фосфор повишава неговите механични свойства. Никелът допринася за увеличаване на якостта и корозионноустойчивостта, фосфорът образува с медта твърда фаза, която повишава износоустойчивостта [1,2,3,4]. На фиг. 1 е представено изображение на микроструктурата на материала, на което светлите участъци представляват мрежата от меден фосфид, сивите – твърд рзтвор Cu-Ni, тъмните – олово [5,6].

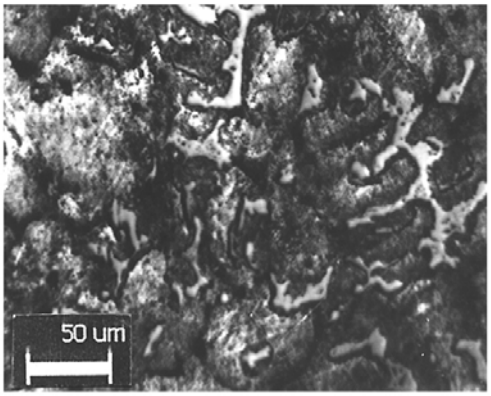

Фиг. 1. Микроструктура на СКАМ „ИПМ”- 305

2. ЕКСПЕРИМЕНТАЛНИ РЕЗУЛТАТИ

Изследването на коефициента на триене, снимките и спектралния анализ на триещата се повърхност на материала са направени в два случая [7]:

СЛУЧАЙ А, при който образецът от изследвания материал е в кинематична позиция „неподвижно тяло", с форма на сфера с диаметър d = 6 mm.

СЛУЧАЙ Б, при който образецът от изследвания материал е в кинематична позиция „въртящо се контратяло", с форма на диск с размери: d = 65 mm и дебелина 5 mm.

2.1. Изследване на динамичния коефициент на триене на СКАМ „ИПМ"- 305

Случай А

На фиг. 2 и фиг. 3 са показани графиките на зависимостта на коефициента на триене на материал „ИПМ"- 305 от пътя на триене във вакуум и на въздух за двата описани случая.

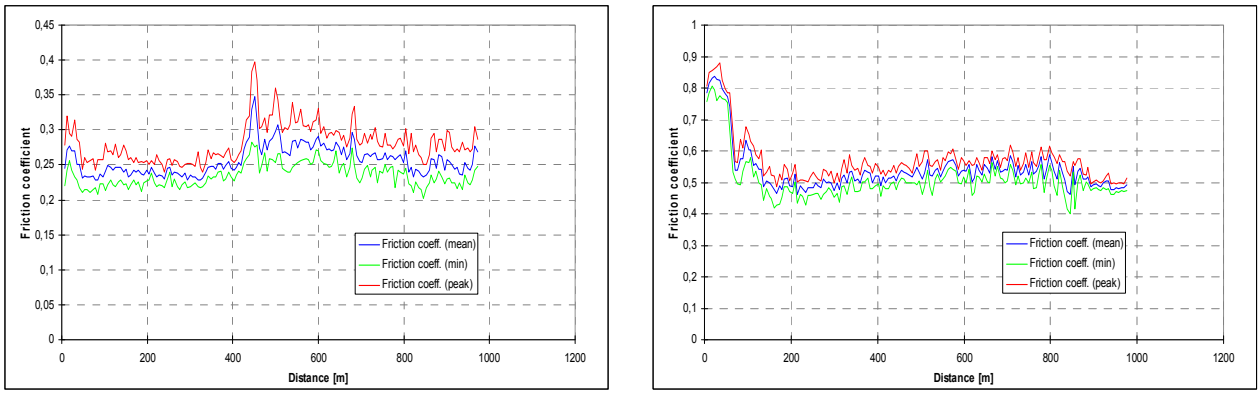

а) *б)*

Фиг. 2. Зависимост на коефициента на триене на „ИПМ"- 305 от пътя на триене: а) във вакуум; б) на въздух

Във вакуум стойността на коефициента на триене се изменя от 0,25 до 0,35 (фиг. 2а). На въздух линията е плавна със стйности от 0,5 до 0,6 (фиг. 2б).

Случай Б

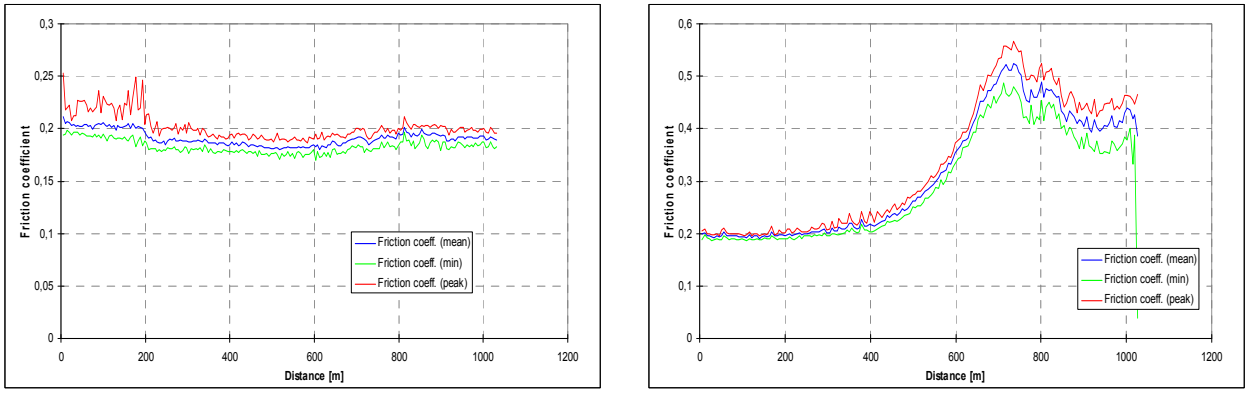

а) *б)*

Фиг. 3. Зависимост на коефициента на триене на „ИПМ"- 305 от пътя на триене: а) във вакуум; б) на въздух

Стойността на коефициента на триене във вакуум е приблизително 0,2 със слабо изменение (фиг. 3а). На въздух тя се променя рязко от 0,2 до 0,54 (фиг. 3б).

В табл.1. са показани усреднените стойности на коефициента на триене на материал СКАМ ИПМ-305 за описаните по-горе случаи.

Таблица 1. Средни стойности на коефициента на триене на „ИПМ”- 305

Кинематична позиция	Товар	Скорост	Коефициент на триене	
			Във вакуум	На въздух
„Неподвижно тяло” (сфера)	2N	1 m/s	0,24	0,61
„Въртящо се контратяло” (диск)	2N	1 m/s	0,2	0,38

2.2. Изследване на триещата се повърхност на СКАМ „ИПМ”- 305

На фиг. 4 са показани снимки на повърхността на СКАМ „ИПМ”- 305 след един и същи път на сухо триене, във вакуум и на въздух.

Случай А

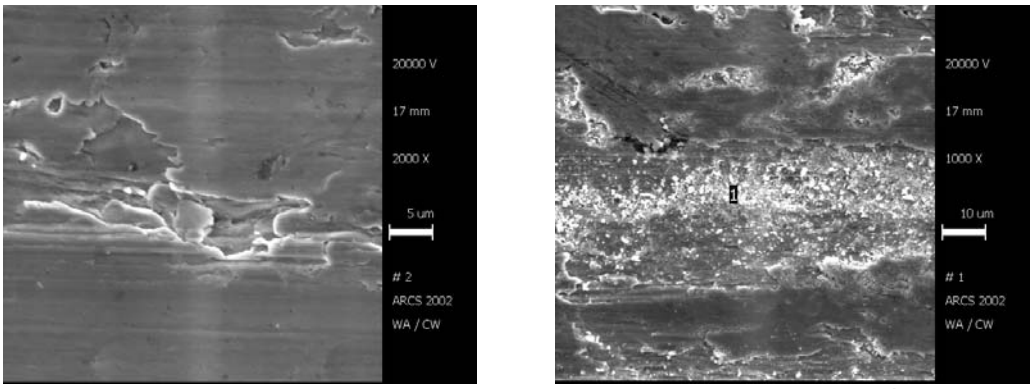

а) ***б)***

Фиг. 4. Морфология на повърхността на „ИПМ”- 305: а) във вакуум; б) на въздух

При сухо триене във вакуум върху повърхността на материала се образува следа от олово по посока на движението (фиг. 4а). При триене на въздух върху повърхността се виждат също така и примеси (фиг. 4б).

На фиг. 5 са представени емисионните спектри на повърхността на материал „ИПМ”- 305 след сухо триене във вакуум и на въздух.

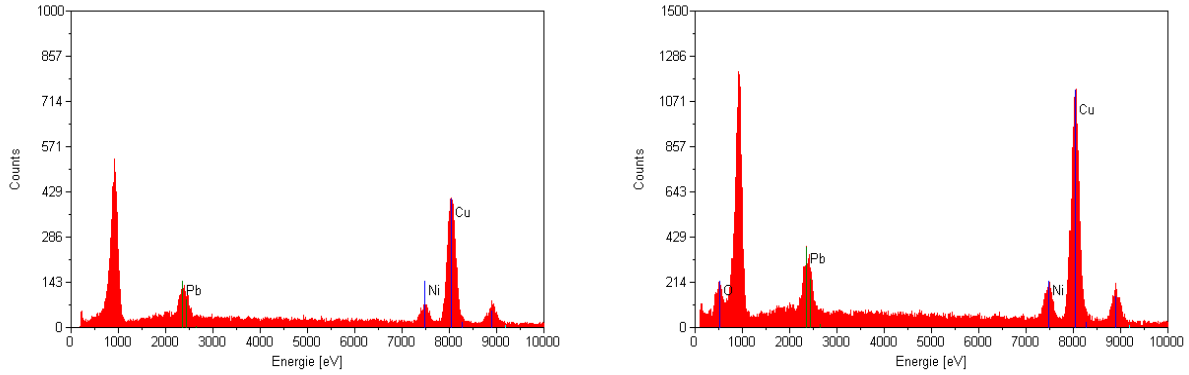

а) ***б)***

Фиг. 5. Елементен състав на повърхността на „ИПМ”- 305: а) във вакуум; б) на въздух

Във вакуум в повърхностния слой се отчита наличие на олово, никел и мед (фиг. 5а). На въздух стойностите на никел и мед са значително по-високи, отчита се наличие на кислород от образувалия се оловен окис (фиг. 5б).

Случай Б

На фиг. 6 са показани снимки на повърхността на СКАМ „ИПМ”- 305 след сухо триене във вакуум и на въздух.

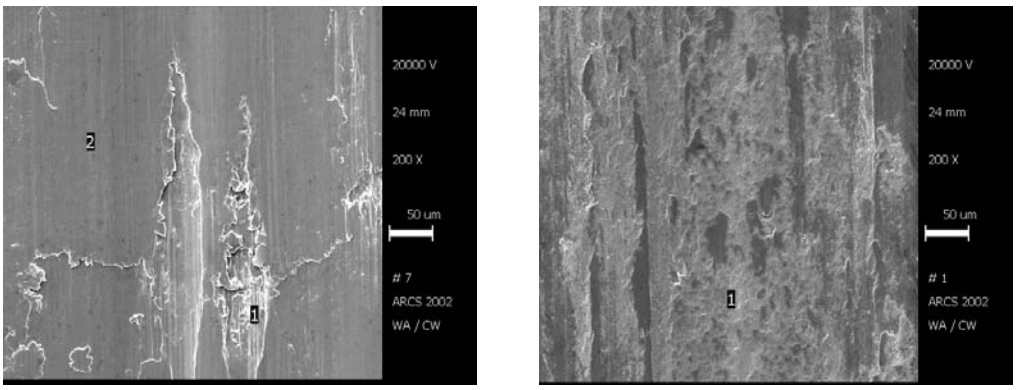

а) ***б)***

Фиг. 6. Морфология на повърхността на „ИПМ”- 305: а) във вакуум; б) на въздух

При триене във вакуум се вижда разнасянето на оловните глобули върху повърхността на материала (фиг. 6а). На въздух образуваният повърхностен слой е нравномерен със слоиста структура (фиг. 6б).

На фиг.7 са показани емисионните спектри на повърхността на материал „ИПМ”- 305 след сухо триене във вакуум и на въздух.

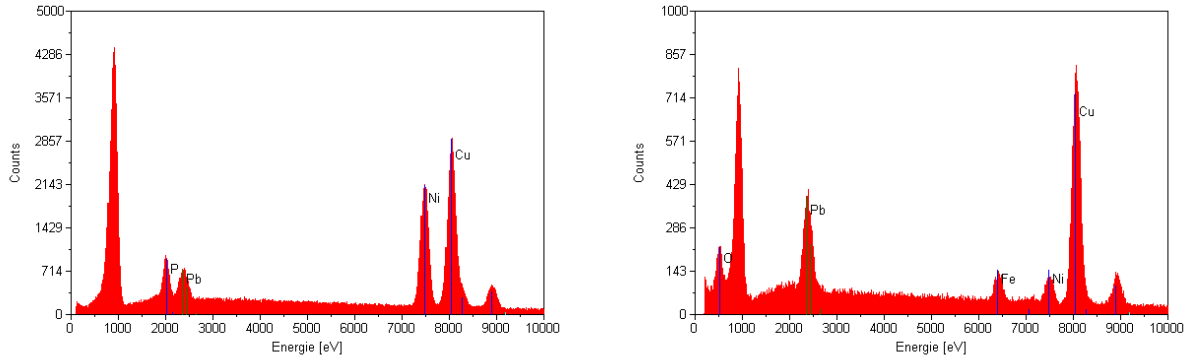

а) ***б)***

Фиг. 7. Елементен състав на повърхността на „ИПМ”- 305: а) във вакуум; б) на въздух

Елементният състав на повърхностния слой във вакуум показва наличие на мед, никел фосфор и олово (фиг. 7а). На въздух се отчитат мед, никел, малки количества олово, кислород от образувания оловен окис, и желязо (фиг. 7б).

3. ЗАКЛЮЧЕНИЕ

В работата е проведено сравнително изследване на динамичния коефициент на триене в контактна система „СКАМ „ИПМ”- 305 – стомана AISI 52100” (100Cr6) в условия на сухо триене във вакуумна и въздушна среда при две кинематични позиции на материала – като „неподвижно тяло” (сфера) и като „въртящо се контратяло” (хоризонтален диск) при еднакви динамични условия – скорост на плъзгане и нормално натоварване.

Основният извод от получените експериментални резултати е, че стойността на коефициента на триене в трибосистемата „СКАМ „ИПМ”- 305 – стомана AISI 52100” (100Cr6), в условия на вакуум със стойност 1.10^{-3} Pa, е значително по-малка, в сравнение с тази на въздух и се изменя в диапазона от 0,24 до 0,2.

По-конкретните изводи се свеждат до:

I. При сухо триене във вакуумна среда:

- в случай А, когато материалът е в позиция „сферично неподвижно тяло” коефициентът на триене се изменя от 0,25 до 0,35, като се наблюдава тенденция към установяване около 0,24, при увеличаване на пътя на триене.
- в случай Б, когато материалът е в позиция „хоризонтално въртящо се контратяло” (диск) зависимостта на коефициента на триене от пътя на плъзгане има равномерен характер. Средната стойност на коефициента на триене е 0,2.

От металографските снимки се вижда образуването на следа от олово по посока на движението. Спектралният състав на повърхностния слой показва, че количеството на олово е по-малко в сравнение с това на мед и никел; в случай Б се отчита и наличие на фосфор. При този материал никелът взима участие в смазващите функции [3].

II. При сухо триене във въздушна среда:

- в случай А зависимостта на коефициента на триене има линеен характер с тенденция за установяване около стойност 0,5 при увеличаване на пътя на плъзгане.
- в случай Б зависимостта на коефициента на триене има нелинеен характер със стръмен скок след разстояние 400 m.
- наблюдава се разлика в стойността на коефициента на триене в случаите на различна позиция на материала. В случай Б, когато тялото е в позиция на „хоризонтално въртящо се контратяло”, коефициентът на триене има по-малка стойност в сравнение със стойността му в случай А, когато тялото е в позиция на „сферично неподвижно тяло”.

От металографските снимки се вижда, че повърхността е неравна и полученият слой е неравномерен. Спектралният състав на този слой показва, че в него има високо съдържание на мед, известно количество никел, кислород (от образувания оловен окис), а в случай Б и желязо. От това следва, че самосмазването е по-слабо ефективно.

БЛАГОДАРНОСТИ

Изказваме нашата благодарност на акад. А. Г. Косторнов, д-р О. И. Фущчич и н. с. Т. М. Чевичелова за плодотворното сътрудничество и активното участие в провежданите научни изследвания.

Изказваме нашата благодарност на Европейския съюз и на Европейската Комисия за оказаното съдействие при изследването на СКАМ „ИПМ”, извършено в отдел „Аерокосмически материали и технологии” на изследователски център в гр. Зайберсдорф - Австрия, което беше финансирано от програма „Подобряване на изследователския потенциал” (Contract № HPRI-CT-1999-00024-User II-49-2002).

ЛИТЕРАТУРА

1. Колесниченко, Л. Ф, О.И. Фущич, В. К. Юлюгин, Ю. Г. Ткаченко, И. Г. Донец, Триботехнические характеристики порошковых самосмазывающихся материалов на основе меди при повышенных температурах, „Порошковая металлургия”, 1986, №2, Киев, 69-74.

2. Kostornov, A. G., O. I. Fushchich, T. M. Chevichelova, Y. M. Simeonova, A. D. Kostenko, Relationships at friction, wear and synthesis of the friction surface of composite self-lubricating materials, ISSN 0032-4795, “Powder Metallurgy”, No 3/4, pp. 11-19, 2007 (In Russian).

3. Колесниченко, Л.Ф., О.И.Фущич, А.Д. Панасюк, И. Я. Дзыкович, Л. Д. Игнатенко, Контактное взаимодействие структурных составляющих композиционных антифрикционных материалов на основе меди, „Порошковая металлургия”, №4, 1984, 82-86.

4. Фущич, О.И., А. Д. Панасюк, Л. Ф. Колесниченко, Л. Д. Игнатенко, Г. Н. Гордань, Межфазное взаимодействие структурных составляющих антифрикционных композиционных материалов на основе меди, „Адгезия расплавов и пайка материалов”, вып. 13, 1984, Киев, 61-66.

5. Симеонова, Ю., Г. Сотиров, М. Аструкова, Т. Грозданова, Нови самосмазващи се антифрикционни материали за работа в екстремни условия, SENS 2009, Fifth Scientific Conference with International Participation, 2-4 Nov., 2009, Sofia, Bulgaria, Proceedings, 293.

6. Грозданова, Т., Физико-химически изменения в структурата на самосмазващи се композитни материали при работа във вакуум, SES 2010, Sixth Scientific Conference with International Participation “SPACE, ECOLOGY, SAFETY”, November 2-4, 2010, Sofia, Bulgaria, Proceedings, 148-151.

7. Simeonova, Y., G. Sotirov, Study of the Parameters of New Antifrictional Materials under Dry Friction Vacuum Conditions, BAS, ARC - Seibersdorf, Austria, ARC-W-0136, pp. 2-30, 2002 (Data Bank of the AMTT), http: //www.2.arcs.ac.at/amtt.

8. Симеонова, Ю., М. Аструкова, Т. Грозданова, Изследване на нови антифрикционни материали за работа във висок вакуум за космически приложения, Международен научен проект на ИКИТ-БАН и ИПМ-НАНУ, 2009.

9. Грозданова, Т., Трибологично състояние на антифрикционен материал във вакуум и атмосферна среда, SES 2012, Eight Scientific Conference with International Participation, “SPACE, ECOLOGY, SAFETY”, 4-6 November, 2012, Sofia, Bulgaria, Proceedings, 275-279.

КОРЕСПОНДЕНЦИЯ

Тинка ГРОЗДАНОВА

Гл. Асистент, Институт за космически изследвания и технологии – БАН
София, ул.”Академик Г. Бончев” бл. 1
e-mail: tinka_gr@abv.bg

Tribological Journal BULTRIB Vol. 5, 2015
Papers from the International Conference **BULTRIB '15**
September 11-13, 2015, Sozopol, Bulgaria
Society of Bulgarian Tribologists
FIT – Technical University of Sofia

THE PROJECT-ORIENTATED INTERDISCIPLINARY TEACHING AND THE REQUIREMENTS OF LABOR MARKET

Emil MANOLOV, Georgi TODOROV, Yordanka PETROVA, Ivajlo PANDIEV, Mara KANDEVA

Abstract: *The paper analyzes the relationship between the preparation of engineering specialists and the assessment of the enterprise managers about their knowledge подготовката на ин and skills according to the requirements of labor market. The used approaches, procedures and teaching models are considered, which provide education quality improvement in the age new spirit. Evaluation of the effectiveness of application the new approach of project-oriented interdisciplinary teaching based on the new MSc program and syllabus for the discipline "Microtechnologies and nanoengineering" with the participation of three faculties of the Technical University - Sofia.*

It has been established that real conditions are created for modern and high-quality teaching of learned and skillful engineers which match the development of the globalizing Bulgarian economics and can obtain realization in High Technologies area.

Keywords*: interdisciplinary approach, method of projects, project-based teaching, labor market*

ПРОЕКТНО ОРИЕНТИРАНОТО ИНТЕРДИСЦИПЛИНАРНО ОБУЧЕНИЕ И ИЗИСКВАНИЯТА НА ПАЗАРА НА ТРУДА

Емил МАНОЛОВ, Георги ТОДОРОВ, Йорданка ПЕТРОВА, Ивайло ПАНДИЕВ, Мара КАНДЕВА

Резюме: *В доклада е анализирана връзката между подготовката на инженерни кадри и оценката на работодателите за техните знания и умения в съответствие с изискванията на пазара на труда. Разгледани са използваните методи, подходи и модели на обучение, осигуряващи повишаване качеството на образованието в духа на изискванията на новото време. Извършена е оценка на ефективността от прилагане на нов подход на проектно базирано интердисциплинарно обучение в новосъздадената с участието на три факултета съвместна магистърска специалност по „Микротехнологии и наноинженеринг". Установено е, че са създадени реални условия за съвременно и висококачествено обучение на адекватни по знания и умения инженери, отговарящи на икономическото развитие и глобализиращата се българска икономика, които с успех ще могат да се реализират в областта на "високите технологии".*

Ключови думи*: интердисциплинарен подход, метод на проектите, проектно-базирано обучение, пазар на труда*

1. ВЪВЕДЕНИЕ

Свидетели сме на коренни промени, които разстърсиха света и оставиха своя отпечатък върху социално-икономическите и духовни основи на обществото, като се отразиха много осезаемо и върху образованието. Според редица автори новото време е век на "глобалното информационно общество", а според други – основната характеристика на 21 век е, че това е век на "знанието", което се превръща в материална сила и в богатство, променящо изцяло социално икономическите парадигми, господствали векове наред.

Независимо от различните определения, в света, в който живеем познанието все повече доминира като фактор на устойчивото развитие и оказва влияние върху образованието, което означава, че значението на ВУЗ като генератор на знания и занапред значително ще нараства.

Естествено възниква въпросът, възможно ли е висшите училища да се справят с назряващото фундаментално противоречие между засилващата се тенденция към нарастване на проблемните ситуации в световен мащаб и трайните тенденциите на инертност в образованието, науката и културата, което се определя от проф. Н. Манолов по следния начин: „Проблемите се глобализират, а подходите за тяхното преодоляване се диференцират и локализират" [1]. Решение на проблема авторът

намира единствено в развитието на интердисциплинния подход на обучение и появата на нови интердисциплинарни направления, заемащи водещи позиции в развитието на цялата наука.

Според проф. Хр. Христов, в доклада си „Някои мисли за висшето образование в началото на 21 век" [1] „като значим фактор за социално икономическия живот, образованието е призвано да помогне за адаптацията на хората към новото общество и затова трябва да се изгражда на нови образователни парадигми", най-съществените от които са:

- нова мисия на образованието, базирана на 4 основни принципа (да се научим да бъдем; да знаем; да правим и да живеем с другите)
- нов тип подготовка за професионалната адаптация на младите хора, съобразена с изискванията на пазара на труда и
- култивиране у младите хора на трайни умения за учене (учене през целия живот), а не само предоставяне на знания.

Анализирайки казаното и сравнявайки го с мисълта, изказана през миналия век от акад. Ангел Балевски: „Ние трябва да учим студентите така, че да могат да правят и това, на което не сме ги научили", не може да не отбележим колко актуално звучи и днес тази мисъл, станала мото на МТФ към ТУ–София.

Общото, около което се обединяват всички автори, заинтересовани от проблема е, че глобализацията като понятие и дух е призвана да предизвика появата на подходящи за ситуацията идеи и доктрини или казано с други думи – необходима е появата на нов подход, който да бъде адекватен и то най-вече при кризисни ситуациии.

Целта на настоящия доклад е да се анализира и оцени ефекта от прилагането на съвременен модел на проектно базирано (Project Based Learning – PjBL) интердисциплинарно обучението за повишаване качеството на образованието в съответствие с изискванията на пазара на труда в новосъздадената съвместна магистърска специалност „Микротехнологии и наноинженеринг".

2. ПОДХОДИ, МЕТОДИ И МОДЕЛИ НА ОБУЧЕНИЕ, ВОДЕЩИ ДО ПОВИШАВАНЕ КАЧЕСТВОТО НА ОБРАЗОВАНИЕТО

Известно е [1], че в световен мащаб години наред са „господствали" 2 подхода:

- ***теоретичен подход***, обединяващ ценостите и постиженията на традиционните парадигмални дисциплини, при които изложението се изгражда с аксиоматичност и строгост, а в образованието усилията са насочени към изучаване и прилагане на различни методи за решаване на конкретни задачи на основата на детерминирани алгоритми и т.нар.
- ***„практологичен" подход***, използващ постиженията на съвременните технологии с акцент върху многообразието и стихията на пазара, като в сферата на образованито възможностите на либералния пазар и стремежът към материално богатство се абсолютизират и приоритетни се оказват висшите технологии за производство на пазарни продукти, гарантиращи големи печалби.

Анализът на предимствата и недостатъците на тези подходи на обучение пораждат идеята за създаване на нов подход и в края на 20 век като хибрид между двата се налага интегралният подход. Според привържениците на контактния подход инженерите трябва да бъдат обучавани в един широк профил, а в следващи научни степени да се специализират и усъвършенстват, за да могат да оценят, че „реалните ефективни решения винаги са в контактните области".

С появата, или по-скоро с утвърждаването на интердисциплинарните направления в науката възниква нов подход на обучение, който в края на 20 век „запълва вакуума" и от дисциплинната парадигма се преминава към индтердисциплинарно мислене, култура и поведение на информационното общество [1]. Новият подход обединява и хармонизира в единство първите 2 подхода и гарантира функционалност по целия спектър на проблемните ситуации в общочовешката дейност.

В основата на моделите за интердисциплинарно обучение е залегнало проектно-базираното обучение (Project Based Learning – PjBL), състоящо се в работа на един екип по даден проект, с който се цели създаване на краен продукт, а формата на обучение се определя като интердисциплинарна поради факта, че във всеки учебен проект се обединяват знания от различни предметни области.

Методът на проектите, застъпен в интердисциплинарното обучение е възникнал като идея на Дж. Дюи и У. Килпатрик за нова организация и подход за обучение [2,3], базиран върху разработването на проекти и "учене чрез правене" (learning by doing) още през далечната 1918 г. Основната характеристика на метода е възможността за овладяване на комбинация от знания, умения, нагласи, желание, личностни качества, способности и опит, които са необходими за решаване на проблемни ситуации от реалния живот.

Редица автори доразвиват този метод и го определят като „хуманен по своята същност метод, който успешно се интегрира в реалния учебен процес и способства за постигане на образователните цели" [4], а според други – това е „модел на обучение, базиран на предварително добре планирано интердисциплинарно обучение на младите специалисти".

Съществуват редица изследвания върху възможностите за прилагане на Метода на проектите в обучението в различни области на познанието. Резултатите дават основание да се твърди, че разработването и представянето на съвместни или самостоятелни проекти от студентите спомага за придобиване на нови знания и компетентности, за формиране на умения за откриване и решаване на проблеми, за практическо прилагане на изследваната информация и не на последно място - за работа в екипи и засилване на вътрешната мотивация към ученето.

Етапите на проектно-базираното обучение са известни и се прилагат с успех не само в редица дисциплини по различни специалностите в ТУ-София, но и при разработване на научно-изследователски проекти с участие на студенти и докторанти. Опитът показва, че едни от най-трудните задачи за студентите са идентифицирането на социално значимите проблеми, откриването на подходящи информационни източници и допълнителната самоподготовка, а за преподавателите – усилията за мотивиране у студентите на навици за разработване и успешен завършек на проектите.

Много успешни и широко приложими се оказват и ***интерактивните методи*** на обучение (проблемното обучение, методът на учебните проекти, методите на изследователска работа с прилагане на информационните и комуникационните технологии, комбинираните методи на обучение и др.), тъй като студентите участват активно в съвместна или самостоятелна дейност за създаване или откриване на факти и зависимости. Основните предимства на интерактивните методи на обучение пред традиционните методи се изразяват в практическо прилагане на знания, умения и компетенции за постигане на определени цели и известна атрактивност на обучението, което допада на младите хора.

Проучването, свързано с гореспоменатите методи показа, че разработването и прилагането на съвременни образователни модели, които включват и интерактивни методи на обучение и учене, отговарят на актуалните нужди от повишаване качеството на обучението във ВУЗ.

В стремежа си за непрекъснато усъвършенстване на работата по обучение на студентите, преподавателските екипи на Факултета по електронна техника и технологии, Факултета по комуникационна техника и Машинно технологичния факултет към ТУ-София, в сътрудничество с външните партньорски организации Вистеон Електроникс България ЕООД, Фондация „Клъстер Информационни и Комуникационни технологии” (ИКТ Клъстер) и Българска стопанска камара - Съюз на българския бизнес (БСК) участваха в разработването на Проект BG051PO 001.3.1.07-0048 „Актуализиране на учебни планове и програми на специалностите на ФЕТТ, ФТК и МТФ на ТУ-София и създаване на нова съвместна магистърска специалност в съответствие с потребностите на пазара на труда“, финансиран със средства от Оперативна програма "Развитие на човешките ресурси“. С изпълнението на всяка една от дейностите, предвидени в Проекта се целеше постигане на общо повишаване на качеството на обучение, с оглед успешна реализация на завършващите инженерни кадри.

3. ИЗСЛЕДВАНЕ НА ПОТРЕБНОСТИТЕ НА ПАЗАРА НА ТРУДА

До неотдавна активната страна във взамоотношенията между образованието и бизнеса бяха университетите, но през последните години фирмите от индустрията и то фирми с производствен профил станаха много по-активни, по-инициативни и разкриват неподозиран потенциал за сътрудничество, свидетелство за което е Изложението на работодатели “Стажове” в ТУ-София. Разбира се, не са изключения и критиките по отношение на учебната документация във ВУЗ, за липсата на добре подготвени инженерни кадри и за необходимостта от закриването на някои специалности и разкриване на нови.

Във връзка с проучване по Дейност 1 от Проекта беше извършено допитване чрез анкетни карти, „адресирано” до трите страни, участници в пазара на труда: инженерни кадри–ВУЗ–работодатели. И ако в едно изречение трябва да се представи мнението на една част от работодателите на инженерните кадри, обучавани в ТУ- София то е, че „младите специалисти имат много добра теоретична подготовка, но им липсва практически опит”. Подобно проучване, извършено от БСК показва [5], че “чуждестранни фирми, в сферата на машиностроителната, електротехническата и др. пормишлености обмислят да напуснат страната поради липса на кадри”. От друга страна, според същото проучване, завършилите технически университети у нас се реализират по-успешно в сравнение с останалите специалности и реализацията на инженерите, работещи по специалността е около 20%. Изводът, който се прави в доклада на БСК е, че “държавата отново финансира образование, което не е нужно на обществото и на икономиката”.

Отговорите на част от въпросите от независима анкета, провеждана ежегодно сред абсолвенти, обучавани в МТФ, дадени на фиг.1, потвърждават данните от проучването на БСК по отношение на подготовката и реализацията на инженерните кадри.

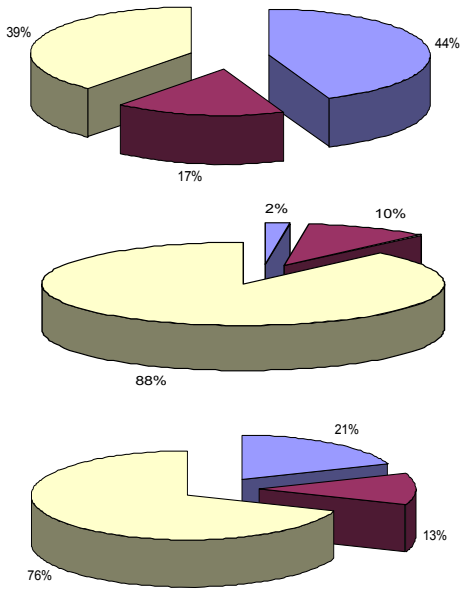

Фиг.1. Частични резултати от анкета, провеждана сред абсолвенти на МТФ

На въпроса «Професионалната Ви реализация свързана ли е със завършената от Вас специалност?”, отговорът на 44% от анкетираните е ”ДА”, на 17% - “Не мога да си намеря работа по специалността”, и 39% “Не работят по специалността, а в друга сфера”.

Отговарите на въпроса ”Смятате ли, че придобитите практически умения и компетенции по време на следването Ви са полезни за настоящата или бъдещата Ви работа?”, са: 88% -”Да, полезни са”, 2% - ”Не, тъй като не работя по специалността” и 10% - „Не мога да преценя, тъй като не работя и не мога да си намеря работа”.

На въпроса «Какво е становището Ви за връзката между придобитите общи познания по време на следването и настоящата Ви работа?”, 76% дават отговора „Познанията са задълбочени и полезни за работа ми”, 13% -„Придобитите познания не са ми достатъчни”, а 21% оценяват, че „Познанията не отговарят на изискванията на фирмите и на моментната ситуация на пазара на труда в страната”.

Данните от изследванията на БСК в над 405 машиностроителни фирми от страната са анализирани и от гледна точка на релацията “абсолвенти - машинни инженери и изискванията на индустрията” в [6,7]. Установено е, че всеки четвърти нает специалист има по-висока квалификация от изискваната от фирмата, 12% от анкетираните са с по-ниска квалификация от необходимата и при около 40% придобитата квалификация от следването не отговаря на изискванията. По-интересното е, че всеки втори от анкетираните е трябвало да премине въвеждащо обучение в бизнеса на фирмата, а 90% от отговорите са, че се е наложило да усвояват допълнителни знания и умения за работното място, на което са назначени. Причините за това състояние на пазара на труда са лесно обясними, тъй като е известно, че жизненият цикъл на компетенциите е най кратък за информационните технологии - 4 години, за производствените инженери е 7 години, а при икономистите – 9 години, или казано с други думи, новите технологии, нормативната уредба и добрите практики са области, в които най-често се налага обновяване на знанието.

От анализа на изнесените по-горе данни, от срещи, проведени с представители на бизнес средите, от отговорите и изказаните мнения на работодателите по всички въпроси от анкетните карти, могат да се формулират основните изисквания към обучението на младите специалисти и условията при наемането им на работа, които се свеждат до следното:

1). Всички приоритетни области и тяхното бъдещо развитие, и всички разностранни приложения на новите технологии не биха имали своята реализация, ако при подготовката на висококвалифицирани млади специалисти не се вземат адекватни мерки за своевременно и висококомпетентно разработване на учебни планове и пакет учебни програми, които да отразяват съвременното ниво на разглежданите проблеми.

2). За професионалната адаптация на младите хора е необходима нов тип подготовка – гъвкава и хармонизирана с изискванията на пазара на труда.

Сега условията за наемане на работна сила с ново качество и нови професонални умения налагат решаването на други задачи от висшите училища, адекватни на новото време, в което живеем. В тази връзка, инженерната образователна система трябва да възпитава студентите не само в компютърна грамотност, а главно в следните много важно неща: да бъдат иноватори като дефинират нови идеи, да могат да ги превръщат в работни проекти, да организират реализацията им, да имат добра езикова подготовка и комуникативни способности за работа в екип и не на последно място остава личностната мотивация да се обогатяват непрестанно с нови познания. Всичко това е възможно и е свързано с огромен кръг от научни, технически, икономически и др. познания, които да осигурят една задълбочена и многостранна интердисциплинарна теоретична подготовка на младите инженери, обвързана с високоспециализирана научно-изследователска практика.

Актуалността на проблема с поготовката и реализацията на младите специалисти заема място и в редица официални правителствени документи, в които се заявява необходимостта за българската икономика от преструктуриране в сферите на науката, висшето образование и технологичните дейности. В Актуализираната стратегия по заетостта на Република България [8] се заявява необходимостта от подобряване на връзката между образованието и обучението от една страна и от друга - с потребностите на пазара на труда и изискванията на работните места. В същия

документ се анализират „Перспективи за развитие на европейските икономики“, сред които и българската за периода до 2020 г., като се дефинира необходимостта от осъществяване на продължителни структурни промени, които (според стратегията) ще се отразят на развитието и създаването на нови работни места в почти всички икономически сектори.

В изпълнението на утвърдената от Европейския съюз Оперативната програма „Наука и образование за интелигентен растеж” (ОПНОИР) [9], насочена към развитие на науката и образованието в България до 2020 година се предвижда да продължи модернизирането на системата за висшето образование в съответствие с принципите на Болонския процес и основните тенденции в Европейското пространство за висше образование. Основният акцент се поставя върху осигуряване на качество на образованието и обвързаността с потребностите и изискванията на работните места, а средствата се предвижда да се разпределят по три основни оси: „Научни изследвания и технологично развитие“ и създаване на т. нар. „Центрове за върхови постижения и центрове за компетентност“; „Образование и учене през целия живот“- свързано с достигане на дял от 36% на завършилите висше образование между 30÷34-годишна възраст и третата ос е свързана със средното образование.

ОПНОИР, съгласно [7,9] трябва да изиграе решаваща роля за активизиране на българския иновационен потенциал. Навременното осигуряване на точните знания и умения, в съответствие с новите потребности и изисквания на пазара ще има съществено значение за постигане на адекватно на търсенето предлагане на работна сила, намаляване на неравновесието на пазара на труда, постигане на по-висока производителност на труда и конкурентоспособност на пазарните продукти.

В същото време е необходимо задължително обвързване на все по-голяма част от държавното финансиране на университетите с техния рейтинг, като по този начин се увеличат стимулите за предлаганото качество на обучението в специалности, които се реализират успешно на пазара на труда.

Сега вече може твърдо да се заяви, че във връзка с широко дискутираният през последните години проблем на образованието и реализацията на завършващите инженерни кадри, оживлението в производството и пазара на труда “обърна посоката” на търсене, и фирмите имат много атрактивни предложения за съвместна дейност, за инвестиции в подготовката на младите специалисти във ВУЗ, осъзнавайки, че привличането им трябва да става на по-ранен етап от следването им.

4. АКТУАЛИЗИРАНЕ НА УЧЕБНИ ПЛАНОВЕ И ПРОГРАМИ НА СПЕЦИАЛНОСТИТЕ ВЪВ ФЕТТ, ФТК И МТФ НА ТУ-СОФИЯ

След изпълнение на първите стъпки от дейностите по Проекта беше извършен задълбочен сравнителен анализ на учебната документация на сродни специалности във водещи университети в света. Преподавателите от Факултета по Електронна техника и технологии (ФЕТТ), съвместно с партньорите, извършиха проучване на основните тенденции в обучението по електроника, в резултат на което бяха актуализирани учебните планове за ОКС „бакалавър“ и ОКС „магистър“ за специалност „Електроника” и всички учебни програми за специализиращите модули: „Електронни уреди и системи“, „Биомедицинско инженерство”, „Силова електроника” и „Микроелектроника”.

Основно внимание беше отделено на проектирането и приложението на съвременните програмируеми електронни устройства и системи. В резултат на това бяха въведени нови практикуми по програмиране на микроконтролери, програмиране на системи с отворен код, по приложение на графични програмни среди и конструиране на електронна апаратура.

С изпълнение на основните дейности по Проекта, преподавателите към Машинно-технологичния факултет (МТФ), съобразявайки се с най-новите постижения в областта на технологиите и с образователните програми на водещите университети осъществиха актуализиране на учебните планове и учебни програми за ОКС „Бакалавър“ в специалностите ”Индустриални технологии” и ”Компютърно проектиране и технологии в машиностроенето” (КПТМ) като създадоха реални условия за осигуряване на съвременно и висококачествено обучение на адекватни по квалификация, знания и умения инженери, отговарящи на изискванията на икономическото развитие, на променящите се обществени очаквания и глобализиращата се българска икономика.

Основните области от стратегията за развитие на МТФ (фиг. 2), застъпени в дисциплини от актуализираните учебни планове предполагат солидна базова инженерна подготовка, съчетана с владеене на най-модерните технологии. Освен специализирана техническа е предвидена и практически насочена подготовка в областта на индустриалните технологии, както и задълбочена компютърна подготовка и използване на съвременни CAD/CAM/CAE технологии, и методи за обработване на информационни потоци.

Обучението по атуализирания учебен план и програми в магистърската специалност по “КПТМ” ще даде солидна подготовка по компютърните средства и технологии на тримерното моделиране, виртуалното инженерство, инженерните анализи, симулации и управление на инженерна информация и бази данни.

Фиг.2. Основни области от стратегията за развитие на МТФ

Актуализираните учебни планове и на всички профилиращи и специализиращи учебни програми по дисциплините от специалност „Телекомуникации" за ОКС „бакалавър" и за ОКС „магистър" на ФТК са с акцент върху увеличаване на часовете за учебни и специализиращи практики, както и за осигуряване на по-профилирано обучение, посредством актуализиране на списъците с избираеми дисциплини.

Обновените учебни планове и програми ще дадат знания, умения, навици, нагласи, ценности и компетенции, релевантни на съвременните бързо развиващи се комуникационни и информационни технологии, на информационното общество и на икономиката, основана на знания, а абсолвентите ще са готови за успешна професионална реализация в пазарната среда на променящия се свят.

5. НОВА СПЕЦИАЛНОСТ ПО „МИКРОТЕХНОЛОГИИ И НАНОИНЖЕНЕРИНГ" В ТУ-СОФИЯ

Безспорно, най-съществен момент от успешно приключилият Проект е създаването на нова магистърска специалност. Екипът по проекта от три факултета, вземайки предвид всички предизвикателства на новото времето, в което живеем и на всички съвременни методи, подходи и модели на обучение, използвани за повишаване качеството на образованието, както и препоръките и изискванията на работодателите на инженерни кадри ги „облече" в един съвместен учебен план за проектно ориентирано интердисциплинарно обучение по "Микротехнологии и наноинженеринг".

По структура, учебният план включва общо 3 семестъра, 27 учебни дисциплини, от които 12 избираеми и възможност за избор на една от предлаганите три магистърски програми (фиг.3).

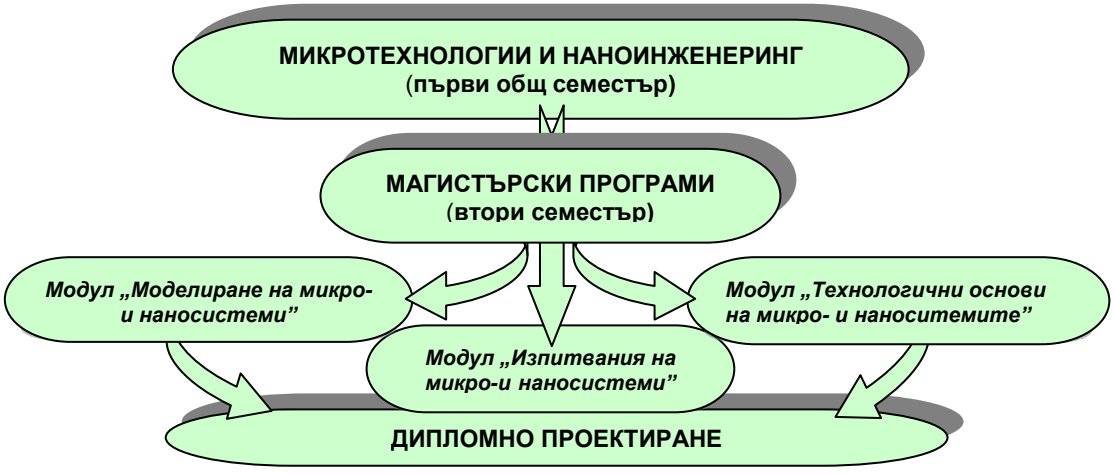

Фиг.3. Обща структура на проектно базирания учебен план за магистърската специалност "Микротехнологии и наноинженеринг"

Това е първият приет от АС на ТУ-София проектно базиран учебен план, който беше създаден, за да отговори на изискванията на бизнеса и да запълни вакуума от висококвалифицирани кадри с инженера подготовка и с познания за спецификата на микро- и нанотехниката.

Формата на обучение в новата магистърска специалност, разработена и обслужвана педагогически и научно от трите факултета – ФЕТТ, ФТК и МТФ по своята същност е интердисциплинарна, тъй като в нея са заложени теоретични и практически знания, основаващи се на значително количество научни постижения с висок иновативен потенциал.

Предложените учебните дисциплини са със съдържание, съобразено с препоръките на работодателите и с нуждите на пазара на труда и в основната си част са поети от преподаватели от катедра "Микроелектроника" на ФЕТТ (18 на брой), 5 дисциплини от МТФ и 2 дисциплини от ФТК [10].

Освен добра теоретична подготовка (в първия семетър от следването) се дава и много по-добра, в сравнение с класическите форми на обучение практическа подготовка на студентите, благодарение на увеличения хорариум на практическите занятия, които са организирани в съответствие със заложения в специалността принцип на проектно базираното обучение [10].

Анализът и оценката на ефективността от прилагането на съвременния модел на проектно ориентираното интердисциплинарно обучение в новосъздадената съвместна магистърска специалност „Микротехнологии и наноинженеринг" са извършени въз основа на съответствието между нововъведенията и изискванията на пазара на труда, и очакваното повишаване на качеството на образованието.

Извършеното проучване по Проекта показа, че в практиката на редица престижни университети работата по изпълнение на определени практически задачи (индивидуални и групови проекти) намира все по-голямо приложение като образователна технология, която има важно значение за повишаване на качеството на образованието.

По новия учебен план, чрез работата си по индивидуални задания, студентите задълбочават познанията си в принципите на действие и придобиват практически умения за проектиране на различни микроелементи, микроелектромеханични устройства и микро- и наносистеми. Нововъведенията в дисциплините от втори семетър по учебния план за специалността, когато на практика студентите се ориентират към една от трите магистърски програми (фиг.3) са съчетаването на групови и индивидуални задачи и гъвкавостта при избор на дисциплини и на тематика за курсови проекти, с което се цели насърчаване на екипната работа (без да се подценява индивидуализма), каквото е и едно от изискванията на бизнеса.

При обучение на студентите е апробиран и нов, модерен подход за обучение, чрез електронна система, намираща се на уеб адрес: http://ecad.tu-sofia.bg/nanomat/. Системата дава възможност за отчитане на рейтинг на всеки студент и за оценка на най-високи постигнати резултати и най-оригинални решения на поставените проблеми.

Изразената от фирмите потребност за засилване и създаване на по-тесни връзки между бизнеса и образованието в новия учебен план е застъпена много сериозно в две направления:

- изнасяне на лекции от гост-лектори и експерти от фирми за запознаване на студентите с актуалните разработки в областта на микроелектромеханичните системи (MEMC), комуникационните мрежи и свръхвисокочестотните филтри – области, които са заложени като материал за изучаване от студентите в новия учебен план "Микротехнологии и наноинженеринг" и
- посещение на студентите в производствени лаборатории на фирмите, като Централна лаборатория по слънчева енергия и нови енергийни източници, Институт по обща и неорганична химия към БАН и др.

Още едно достойнство на новия учебен план е специализираният технически английски език, който студентите практикуват, което също е дефинирано като изискане от работодателите на младите кадри.

6. ЗАКЛЮЧЕНИЕ

По мнение на участниците в проекта, както и на оценителите му (независимо, че оценките трябва да се направят след завършване на първия випуск по новата специалност), с помощта на приложения модел на обучение в новата магистърска програма „Микротехнологии и наноинженеринг“ ще се постигнат множество положителни резултати, като един от съществените, очертаващ се като тенденция още на този момент резултат е, че ще се запълни „нишата” от инженери-технолози, обслужващи високотехнологичната и вече налична скъпа техника в ТУ-София.

Другият съществен ефект е очакването, че бизнесът ще получава абсолвенти с добра теоретична и в достатъчна степен практическа подготовка, способни да решават сложни задачи с оптимизационен характер, включително и извън техните компетенции.

Най-оптимистичните очаквания на този етап се коренят в предимствата на модела на проекто базираното интердисциплинарно обучение, които най-общо се заключават в развиването на способности у студентите на мислещи и творчески личности, които решават конкретни проблеми, работейки по даден проект и не са в позицията на пасивни слушатели. Това е модел на обучение, формиращ комуникационни умения, способност за самооценка и социални умения в младите инженери, което ги прави годни за сътрудничество, за работа в екип и по-стойностни членове на обществото – едно от огромните му предимства в сравнение с класическите форми на обучение.

Постигнатите към момента резултати показват, че са създадени реални условия за съвременно и висококачествено обучение на адекватни по знания и умения инженери, отговарящи на икономическото развитие и глобализиращата се българска икономика, които с успех ще могат да се реализират в областта на “високите технологии”.

БЛАГОДАРНОСТИ

Докладът е изготвен с финансовата подкрепа на Оперативна програма “Развитие на човешките ресурси”, съфинансирана от Европейския социален фонд на Европейския съюз в изпълнение на проект BG051PO 001.3.1.07-0048 „Актуализиране на учебни планове и програми на специалностите на ФЕТТ, ФТК и МТФ на ТУ-София и създаване на нова съвместна магистърска специалност в съответствие с потребностите на пазара на труда“,

ЛИТЕРАТУРА

1. Проект №33/11.06.2003 г. „Подобряване на висшето техническо образование на основата на интердисциплинен подход”, ОУБО-МОН, Сборник доклади, Издателска къща „Св.Иван Рилски”, София, 2004,
2. Dewey, J., Democracy and education, *The middle works of John Dewey*, 1916, Vol. 9, Carbondale: Southern Illinois University Press
3. Kilpatrick, W. H., The project method, Teachers College Record*,*1918, 319-335++++++++
4. Полат, Е., М. Букаркина, М. Моисеева, А. Петров, Новые педагогические и информационные технологии в системе образования, Учебно пособие для студ. пед. Вузов и системы повыш квалиф. пед. кадров, Изд. център ”Академия”, 2002, 272 с.
5. БСК, “Университетите бълват ненужни кадри”, в-к Дневник, 15.08.2011 г.
www.dnewnik.bg
6. Йорданова В., Всеки четвърти зает с по-висока квалификация , в-к Днес, 02.12.2012
WWW.dnes.bg/business/2013/12/02/
7. Ангелов Н., Квалификацията на абсолвентите машинни инженери и изискванията на пазара на труда, в-к Технически авангард”, бр.3, май 2014г.
8. Актуализирана стратегия по заетостта на Република България, 2013-2020г., Министерство на труда и социалната политика, 09.10.2013.

9. Оперативна програма „Наука и образование за интелигентен растеж“
http://www.programme_Snapshot_2014BG05M2OP001_1_3_bg.pdf
10. Александрова М., В.Видеков, Кр. Денишев, Т.Тодоров, Г. Маринова, Ем. Манолов, Създаване и апробиране на нова магистърска специалност “Микротехнологии и наноинженеринг“ във ФЕТТ на ТУ-София, Национален форум “ЕЛЕКТРОНИКА 2015”, 14-15 май 2015, Национален дом на науката и техниката, София, стр.8-13,

КОРЕСПОНДЕНЦИЯ

Доц. д-р инж. Емил МАНОЛОВ
София 1000, бул. „Кл. Охридски” № 8, ТУ-София
E mail: edm@tu-sofia.bg,

Проф. д-р инж. Георги ТОДОРОВ
София 1000, бул. „Кл. Охридски” № 8, ТУ-София
E mail: gdt@tu-sofia.bg

Доц. д-р инж. Йорданка ПЕТРОВА
София 1000, бул. „Кл. Охридски” № 8, ТУ-София
E mail: jtp@tu-sofia.bg

Доц. д-р инж. Ивайло ПАНДИЕВ
София 1000, бул. „Кл. Охридски” № 8, ТУ-София
E mail: ipandiev@tu-sofia.bg

Доц. д-р инж. Мара КАНДЕВА
София 1000, бул. „Кл. Охридски” № 8, ТУ-София
E mail: kandevam@gmail.com

Tribological Journal BULTRIB Vol. 5, 2015
Papers from the International Conference **BULTRIB '15**
September 11-13, 2015, Sozopol, Bulgaria
Society of Bulgarian Tribologists
FIT – Technical University of Sofia

STRUCTURE AND PROPERTIES OF WELDED COATINGS AFTER THERMAL IMPACT

Sergei Kirov - *TU-Varna, Faculty of Machine Technology, Depart. MTM, E-mail: s_kirov@abv.bg.*
Radostina Yankova- *TU-Varna, Faculty of Machine Technology, Depart.MTM, E-mail: radyankova@abv.bg.*

Abstract: *Research has been carried out with the aim of selecting a suitable material for manual electric arc welding of local worn off surfaces, with subsequent mechanical and thermal processing of the welded surfaces, keeping the starting properties, roughness and dimensions of the not welded zones. Sample specimens have been used, welded with different materials on which thermal impact has been applied. By researching the microstructure and hardness HV5, an optimal mode has been selected, ensuring improved processability and high hardness after the final thermal processing.*
Keywords: *welding, thermal impact, worn off surfaces*

СТРУКТУРА И СВОЙСТВА НА НАВАРЕНИ СЛОЕВЕ СЛЕД ТЕРМИЧНО ВЪЗДЕЙСТВИЕ

Доц. д-р Сергей Киров - *ТУ- Варна, МТФ, кат. МТМ, E-mail: s_kirov@abv.bg.*
Радостина Янкова- *ТУ-Варна, МТФ, кат.МТМ, E-mail: radyankova@abv.bg.*

Резюме: *Проведено е изследване с цел подбор на подходящ материал за ръчно електродъгово наваряване на локално износени повърхнини, с последваща механична и термична обработка на наварените зони, като се запазват изходните свойства, грапавост и размери на ненаварените зони. Използвани са пробни образци, наварени с различни материали, на които е приложено термично въздействие. Чрез изследване на микроструктурата и твърдостта HV5 е подбран оптимален режим, осигуряващ подобрена обработваемост и висока твърдост след окончателната термична обработка.*
Ключови думи: *наваряване, термично въздействие, износени повърхнини*

1. УВОД

Наваряването с цел възстановяване, в голяма част от случаите се явява окончателен процес за формиране на експлоатационните структура и свойства на детайлите. За някой от машинните елементи задължително се прилага термична обработка, с цел понижаване на напреженията, хомогенизиране на структурата, повишаване на износоустойчивостта и др. [3].

В практиката често се налага да се възстановяват локално износени, относително сложни повърхнини на детайли с неголеми размери. За запазване на техните изходни свойства е необходимо температурата на нагряване на детайла като цяло да не надвишава тази на окончателната термична обработка при изработането му.

За целта трябва да се използат подходящи за наваряване материали, които не изискват високи температури при предварително подгряване, както и при следващи термични обработки за подобряване на обработваемостта. За получаване на окончателната структура и свойства на възстановената повърхност се използват локални методи за нагряване като: газопламъчно или ток с висока честота.

Примери за такива детайли са изходящи или валове от вариаторни шайби от транспортната и земеделска техника с нарушени лагерни шийки, шлицеви и шпонкови съединения (фиг. 1). Подходящ метод за възстановяването им се явява ръчното електродъгово наваряване със следващи механична и термична обработки до определна конфигурация.



а) ***б)*** ***в)***

Фиг. 1. Реални детайли от земеделска техника
а) и б) - износени след употреба
в) - наварен

2. ЦЕЛ И ЗАДАЧА

Целта на настоящата разработка е да се извършат сравнителни изследвания за избор на подходящ материал за ръчно елекртодъгово наваряване на локално износени повърхнини на детайли с относително малки размери.

Поставени са изисквания чрез термично въздействие по време и след наваряването да се подобри обработваемостта на слоя без да се променят структурата , свойствата и геометричните параметри на останалата част от детайла.

3. ЕКСПЕРИМЕНТАЛНА ЧАСТ

Използвани са два метода за наваряване:

- *ръчно електродъгово наваряване с обмазани електроди*
- *ръчно наваряване с електродна тел в защитна среда от инертен газ аргон (ВИГ)*

Химичният състав на добавъчните материали е посочен в табл. 1.

Наварените слоеве са нанесени върху образци от средновъглеродна, нисколегирана стомана 40Х с размери 20х20х100 mm.

Таблица 1. Химичен състав на материалите за наваряване

Марка	***Химичен състав***			
	C, %	***Si, %***	***Mn, %***	***Cr, %***
ЕН 550	0.50	2.40	0.40	9.0
65 Г	0.6 - 0.7	0.2 - 0.3	0.9 – 1.2	0.25

Извършено е еднослойно, едношевно наваряване с цел предотвратяване възникването на зони на отвръщане от термичното въздействие на следващите наварени слоеве. Подборът на режими на наваряване е съобразен с предписаните от завода производител параметри, а така също за да се получат добре формирани изпъкнали слоеве с тънка зона на сплавяване между основния и добавъчния метал. Непосредствено преди наваряването образците се подгряват до 200°С. След него се охлаждат на спокоен въздух.

За провеждане на сравнителния анализ образците са предварително термично обработени по два режима; отгряване за първия и закаляване за втория – табл. 2.

Таблица 2. Предварителна термична обработка на образците от ст.40Х

Пробни образци	
Образец 1 предварително отгрят	твърдост 180-200 НВ
Образцец 2 предварително закален	твърдост 48-50 HRC

За решаване на поставената задача наварените слоеве са подложени на следващо термично въздействие, като образците се нагряват обемно при температури 400°C, 500°C, 600°C и 700°C със задържане 20 min след достигане на съответната температура.

Влиянието на термичната обработка върху структурата и твърдостта на наварения и основния метал е изследвано чрез напречен микрошлиф. Измерената твърдост HV5 по дълбочина на слоя е показател за изменението на обработваемостта на наварения метал.

2. РЕЗУЛТАТИ

Формираните при наваряване слоеве са с ясно изразена изпъкнала повърхност с височина 5 mm, малка зона на сплавяване с основния метал и зона на термично влияние, като в най-голяма степен това се отнася при наваряването чрез ВИГ с електродна тел марка 65Г.

От микроструктурен аспект слоевете от двата вида добавъчен материал имат различна морфология. Докато тези получени при ръчно електродъгово наваряване с обмазани електроди ЕН 550 имат типично лята дендритна структура (фиг. 2.б) , то слоя наварен с нисколегирана средновъглеродна тел марка 65Г има характерната дребно иглеста структура за тази стомана в закалено състояние (фиг.2.а).

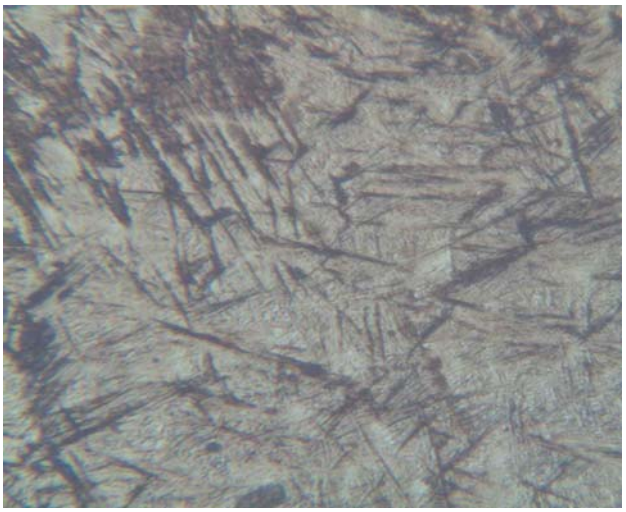

а) иглест мартензит

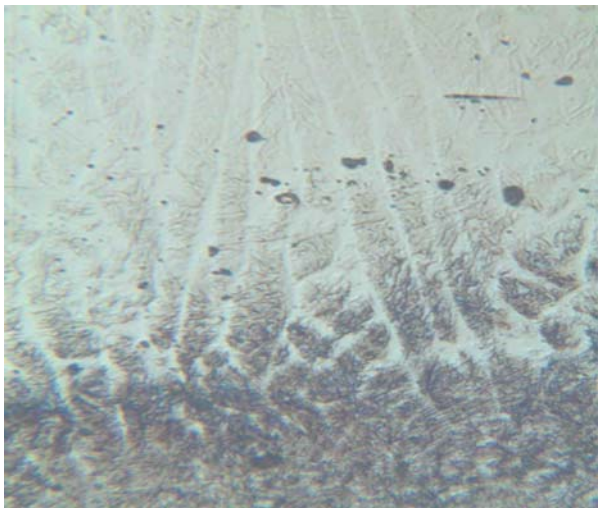

б) дендритна структура

Фиг.2. Микроструктура на наварени зони с :
а) марка 65Г;
б) базичен електрод ЕН 550

Наличието на големи количества хром в електродите за наваряване ЕН 550 води до получаването на труднопроявима, бяла дендритна зона с висока твърдост 700 HV5. Структурата е типично лята с фини дендрити в първичната зона , нарастващи в посока обратна на топлоотвеждането.

Високият процент хром – 9% води до формирането на известните за системата Fe– Cr –C карбиди, като $Cr_{23}C_6$; Cr_7C_3; Cr_2C_2. Високата твърдост се дължи както на тях , така и на получения при високите скорости на охлаждане дисперсен мартензит.

Въпреки относително крехката структура не е открито наличието на пукнатини. Подложените на следващо термично въздействие наварени слоеве запазват относително висока твърдост като при нагряване до 700°C тя е над 500 HV5 (фиг. 3.а,б). Това основно се дължи на повишената стабилност на легираната с хром многофазна структура. От гледна точка на износоустойчивостта на такива слоеве това е добре, но при необходимост от следващи механични обработки след наваряване високата твърдост силно намалява обработваемостта, особено на по-сложни повърхнини.

При използването на електродна тел марка 65Г наварения слой има значително по-висока твърдост достигаща до 850 HV5 на повърхността (фиг. 3.в,г), дължаща се на формирания дисперсен мартензит.

Липсата на следващи наварени слоеве не предизвиква зони на отвръщане и понижаване на твърдостта. Тази стомана не е особено устойчива при повишаването на температурата на отвръщане и както се вижда от (фиг.3. в) между 400°C и 700°C, твърдостта се понижава плавно от 600 до 300 HV5.

Този процес благоприятства възможността за следваща механична обработка, извършена след локално отвръщане до не високи температури на наварените слоеве. Подобряване на обработваемостта настъпва още при 500- 600°C. Отвръщането при тези температури трябва да се

извърши краткотрайно с локални методи за нагряване само на наварените слоеве при екраниране на останалия обем от детайла.

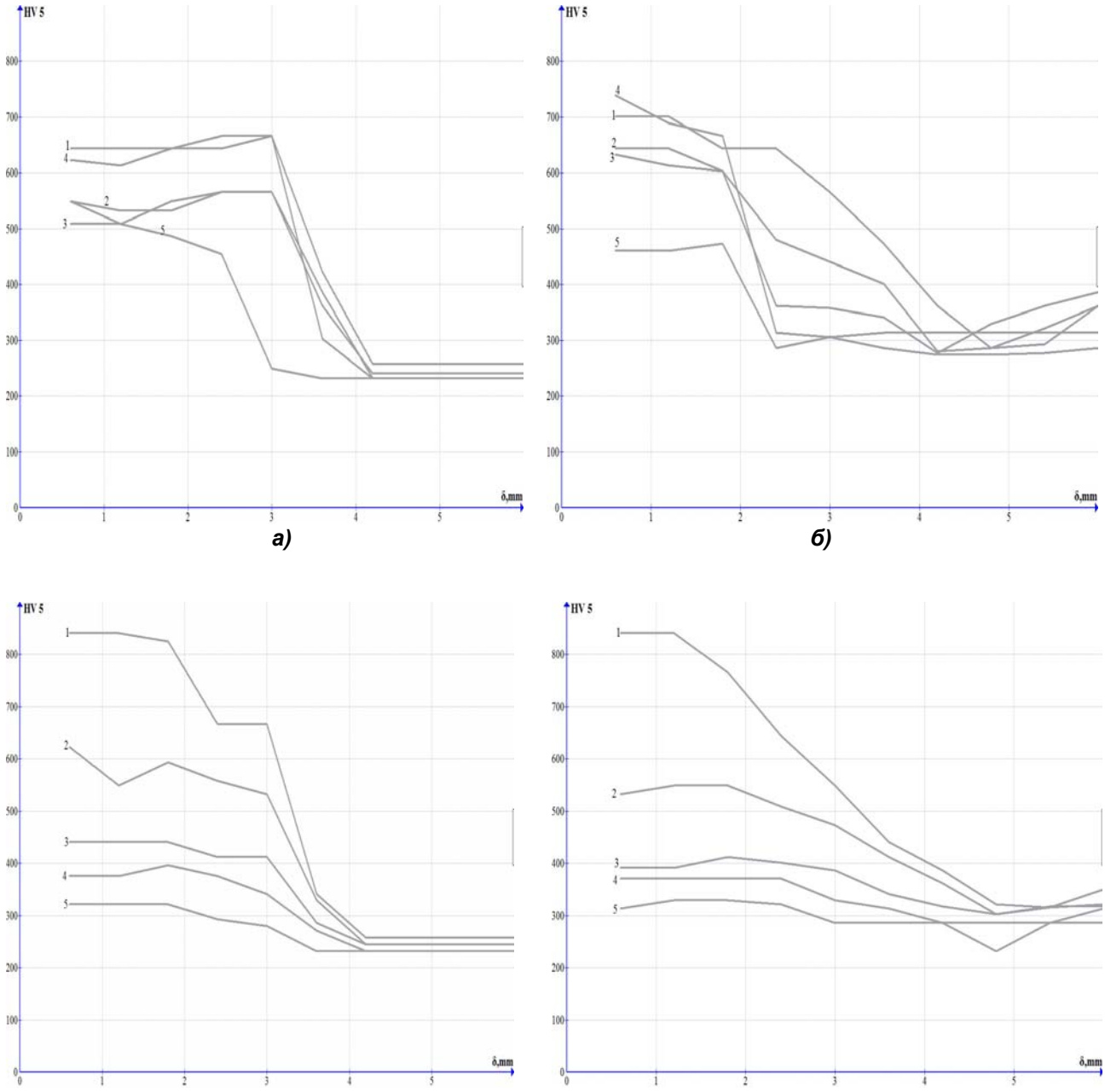

Фиг. 3. Изменение на твърдостта по дълбочина на наварения слой върху:
а) отгрят образец, наварен с електрод ЕН 550;
б) закален образец, наварен с електрод ЕН 550;
в) отгрят образец, наварен с тел марка 65 Г;
г) закален образец, наварен с тел марка 65Г;

1 – след наваряване;
2 – при нагряване от 400°С ;
3 – при нагряване от 500°С;
4 - при нагряване от 600°С;
5 - при нагряване от 700°С

След извършване на механичната обработка се прилага локално закаляване на възстановените участъци, за повишаване на износоустойчивостта и контактната им якост. За целите на експеримента окончателната термична обработка е обемна и нагряването се извършва в пещи при температури 830-850°С, отговарящи за съответната стомана (65Г) или по предписание на завода производител за ЕН 550. Охлаждането при закаляване е извършено в минерално масло.

Измерената по дълбочина твърдост (фиг. 4) показва високи стойности (850 HV5) за слоя от стомана 65Г, която плавно се снижава до твърдостта на основния метал (600 HV5). Значително по-

ниски са стойностите при закаляване на образеца наварен с електроди ЕН 550. Твърдостта достига едва 350-400 HV5, което не съответства на стойността от 500 НВ, посочена от завода производител.

Това най-вероятно се дължи на ниската температура на нагряване (850°С), която не е достатъчна за разтваряне на хромовите карбиди и получаване на мартензитна структура в наварения слой. Сравняване на твърдостите непосредствено след наваряване (650-700 HV5) и след закаляване (350-400 HV5) , показва че разликата е значителна, и най-вероятния фактор влияещ върху това е температурата. И при двата образеца твърдостта на основния материал е със стойностите , съответващи на справочните данни 550-600 HV5.

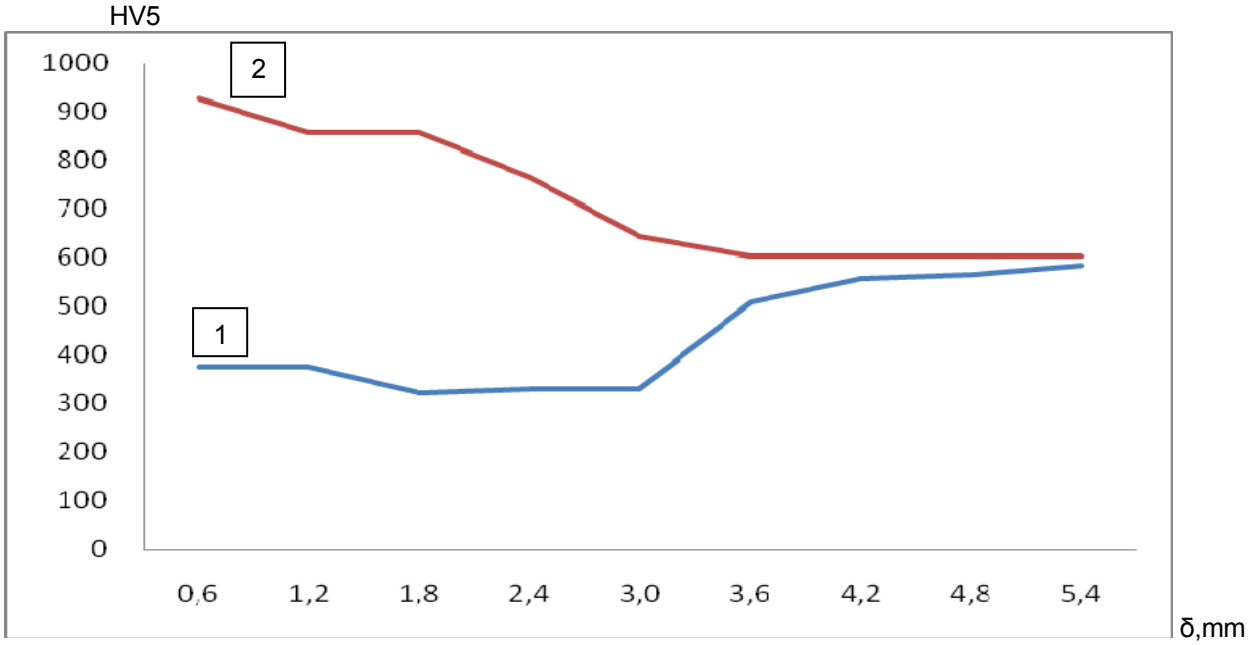

Фиг. 4. Изменение на търдостта по дълбочина на наварените слоеве след окончателната ТО - закаляване :

1. след наваряване с базичен електрод ЕН 550

2. след наваряване с марка 65Г

4. ЗАКЛЮЧЕНИЕ

- Слоя наварен с ЕН 550 запазва повишена твърдост и влошена обработваемост при отвръщане-то след наваряване и е с относително ниска твърдост след окончателното закаляване.
- Подходящ материал за поставената цел – локално наваряване с последваща механична и термична обработка на наварените зони, се явява средновъглеродната нисколегирана тел с марка 65Г, тъй като е с подобрена обработваемост при по-ниски температути на отвръщане и с висока твърдост след окончателно закаляване.

ЛИТЕРАТУРА

[1]. ESAB, Наръчник по заваряване при ремонт и възстановяване ,

[2]. Лейначук, Е. И., Электродуговая наплавка деталей при абразивном и гидроабразивном износе, Киев Наукова думка, 1985

[3]. Ливщиц, Л. С., Хакимов, А. Н. , Металловедение сварки и термическая обработка сварных соединений, Москва Машиностроение, 1989.

[4]. Блюменауера Х., Испытание материалов, Москва, 1979.

[5]. Золоторевский В., Механические испытания и свойства металлов, Москва, 1974.

Научните изследвания, резултатите от които са представени в настоящата публикация, са извършени по ***проект НП19/2015 с р-л доц. д-р Сергей Киров*** *в рамките на присъщата на ТУ-Варна научноизследователска дейност, финансирана целево от държавния бюджет.*

Tribological Journal BULTRIB Vol. 5, 2015
Papers from the International Conference **BULTRIB '15**
September 11-13, 2015, Sozopol, Bulgaria
Society of Bulgarian Tribologists
FIT – Technical University of Sofia

SHAPE OF THE TEETH OF GEARS TRANSFERRING GREAT TORQUE FOR MADE FROM PLASTICS

Stanislav ALEKSIEV, Miroslav ALEKSIEV, Angel POPAROV

Abstract: *The destruction of the gears made of plastic material occurs most often with notch wear of the tooth at the root. This means that the bending strength of the tooth is small. The article offers a shape of gears with increased resistance to bending.*

Key Words: *gears, gear tools, curves pitching, speed gliding and gliding specific polymer materials.*

ФОРМА НА ЗЪБИТЕ НА ЗЪБНИ КОЛЕЛА ПРЕНАСЯЩИ ГОЛЯМ ВЪРТЯЩ МОМЕНТ ПРЕДНАЗНАЧЕНИ ЗА ИЗРАБОТВАНЕ ОТ ПЛАСТМАСИ

Станислав АЛЕКСИЕВ, Мирослав АЛЕКСИЕВ, Ангел ПОПАРОВ

Резюме: *Разрушаването на зъбните колела изработени от пластмаса настъпва най-често с изкъртване на зъба в основата. Това означава, че якостта на огъване на зъба е малка. В статията се предлагат форми на зъбни колела с повишена устойчивост на огъване.*

Ключови думи: *зъбни колела, якост на огъване, полимерни материали.*

1. ВЪВЕДЕНИЕ

Производството на зъбни колела от пластмаса навлиза все повече в уредите използвани от човека. Пластмаси са по-добри от металите с характеристики, като: цена, тегло, шум, вибрации, самосмазване, химична усойчивост, употреба в хранителната промишленост и не на последно място висока производителност, ако се шприцват итн. Но са с по-слаби якостни характеристики. Промяната на формата на зъбите може да доведе до значително увеличаване на устойчивостта на огъване, което обуславя актуалността на разработката.

2. *ВИДОВЕ КРИВИ ЗА ЗЪБООФОРМЯНЕ НА ПРОФИЛА НА ЗЪБА С ЦЕЛ УВЕЛИЧАВАНЕ НА УСТОЙЧИВОСТТА НА ЗЪБА НА ОГЪВАНЕ НА ЗЪБНИ КОЛЕЛА ПРОИЗВЕЖДАНИ ОТ ПОЛИМЕРНИ МАТЕРИАЛИ.*

Обикновенно, зъбите на пластмасовите зъбни колела се изкъртват в основата. Да си поставим за цел да увеличим дебелината на зъба там. Съвсем очевидно е, че ползвайки стандартното еволвентно зацепване (изходен инструментален контур с трапецовидна форма и наклон на бедрото му 20^0), това е невъзможно, защото формата е предопределена. Нека задачата да е да намерим такъв профил на зъб в напречно сечение, който да изпитва едни и същи напрежения на огъване във всяко едно сечение. Или казано по друг начин да е еднакво здрав навсякъде, а не най-слаб в основата.

Ако се приеме, че единия профил от зъба е прав и радиално насочен, да се намери, другия профил така, че зъба да е с еднакво напрежение на огъване ($\sigma_{ог}$) по цялото си сечение (фиг.1). Нека във върха на зъба действа периферна сила F. При така подбрана координатна с-ма, силата F ще създава огъващ момент Мог = F*y, а съпротивителния момент на зъба е -

$Mc = W\sigma_{ог} = \frac{l x^2}{6} \sigma_{ог} \geq Mог = F*y$, където l е дължина на зъба.

След решаване на горното у-ние спрямо у се получава - $y = (l * \sigma_{ог} / 6F)\ x^2 = a * x^2$.

При определени условия $a = (l\ \sigma_{ог}/6F) = const$, откъдето се вижда, че оптималния профил на зъба от якостна гледна точка е параболичен. Понеже, параболата не е взаимообвиваща се крива, за зъбни профили тя се заменя с еволвента, която е изобразена заедно с основната си окръжност. Еволвентата е така подбрана, че да е възможно най-близка до параболата, което се вижда след завъртането на параболата до еволвентата.

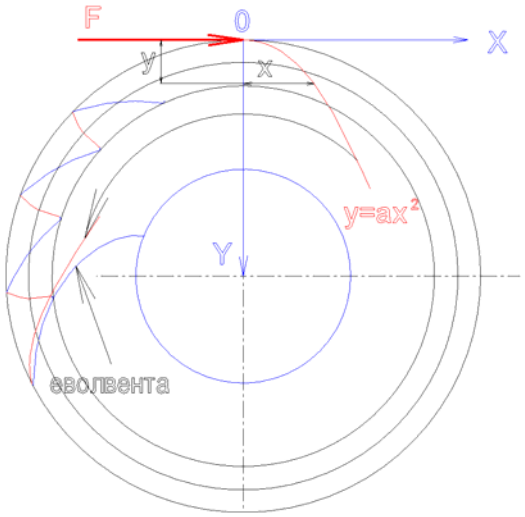

Фиг. 1. Зъбно колело с несиметричен профил изграден от еволвентни и циклоидни криви

Зъбно колело на фиг.1 е с несиметричен профил изграден от еволвентни и циклоидни криви с уравнения:

- еволвента е с уравнение:

$x = r_b * (t* sin(t) + cos(t))$

$y = r_b * (- t*cos(t) + sin(t)).$ (1)

където *(t)*- ъглов параметър $0\text{-}360^0$

- епи и хипоциклоиди с у-ние:

$x = (r_b \mp r_c)*cos(t) \pm r_c * cos(((r_b / r_c) \mp 1)*t)$

$y = (r_b \mp r_c)* sin(t) - r_c * sin(((r_b / r_c) \mp 1)*t),$ (2)

- където горните знаци се отнасят за хипоциклоида, а долните за епициклоида.

На фиг. 2. е изобразена зъбна двойка със зъбни колела с несиметричен профил.

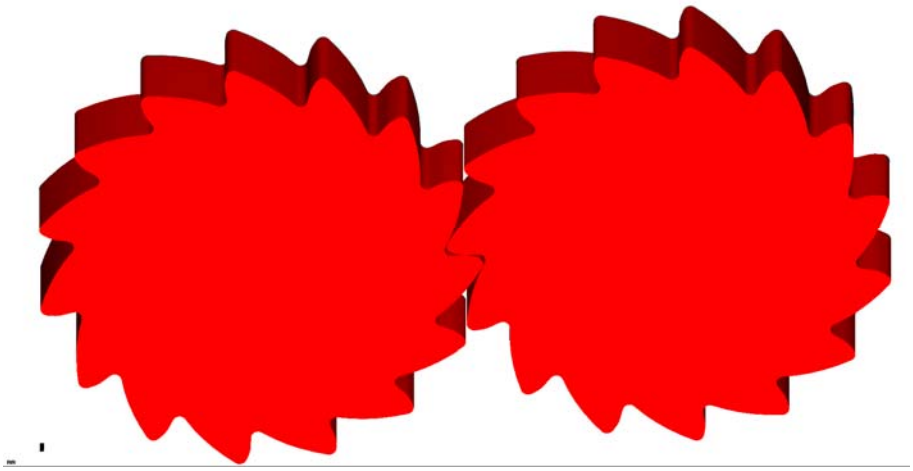

Фиг. 2. Зъбна двойка с колела с несиметричен профил

Зъбната двойка ще работи при различни условия в зависимост от това, кое от зъбните колела е водещо. От гледна точка на по-добро пренасяне на въртящия момент (по-малък ъгъл на предаване на силата) зъбната двойка ще работи по-добре, ако дясното колело е водещо и се върти обратно на часовниковата стрелка. Или зъбната двойка с несиметричен профил е подходяща за вграждане в еднопосочни механизми.

Ако условно зъба се раздели по делителната окръжност, то се получават четири, възможни за синтез криви - две за глава и две за основа на зъба. Освен това, ако се ползва еволвента тя може да формообразува едновременно основата и главата на зъба така както е на фиг.1.

Това дава възможност за изграждане на **32 случая** различни само по вида на кривите профили. Не бива да се забравя възможноста, за промяна и на самите криви.

За предаване на въртящия момент в двете посоки при еднакви условия се предлага симетрична зъбна двойка изобразена на фиг.3.

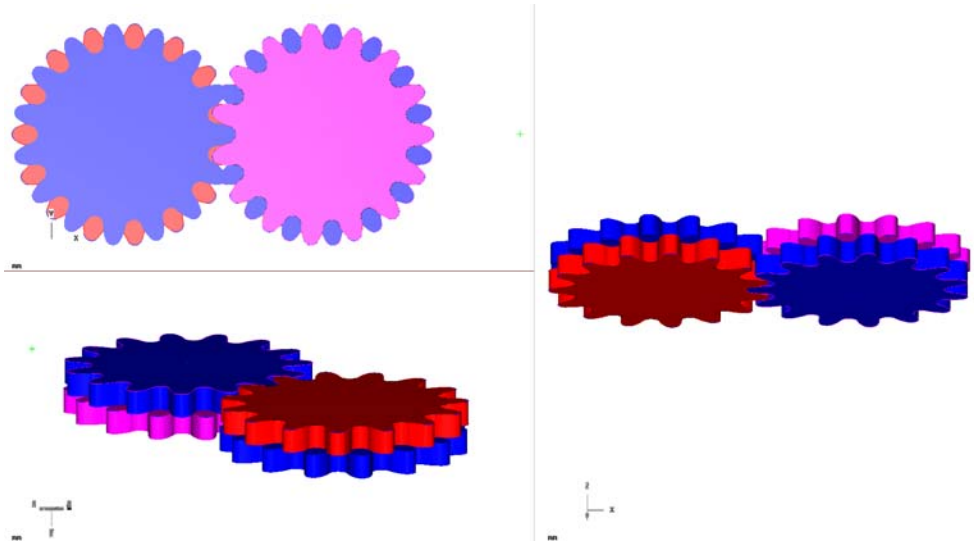

Фиг. 2. Зъбна двойка с колела със симетричен профил

Всяко от зъбните колела е монолитно и се състои условно от две зъбни колела завъртяни едно спрямо друго на половин окръжна стъпка. На фигурата са изобразени с два цвята само за по-голяма яснота. Фрезоването на едно такова колело става, като се направи половината на една установка, след това се завърта заготовката на 180^0 и прави другата половина. Това прави зъба много по-дебел и як в основата, отколкото нормалното извесно зъбно колело с прави зъби. Осен това се увеличава и плавността на работа и коефициента на препокриване, подобно на тези с наклонени зъби, но без осова съставка на предаваната сила. Изглежда трудоемко защото се фрезова два пъти но, ако зъбното колело се шприцва от полимерни материали това няма значение за производителността, а колелото е с възможност за пренасяне приблизително на два пъти по-голям въртящ момент.

3. ЗАКЛЮЧЕНИЕ

1. Зъбите с циклоиден профил са по-подходящи за зъбни колела изработвани от полимерни материали и за предаване на еднопосочен въртящ мометнт трябва да се ползват такива с несиметричен профил
2. За предаване на въртящия момент в двете посоки при еднакви условия се предлага симетрична зъбна двойка, като всяко едно от колелата е монолитно и се състои условно от две зъбни колела завъртяни едно спрямо друго на половин окръжна стъпка.

БЛАГОДАРНОСТИ

Авторите изказват благодарности за финансиране на участието в научната конференция по научноизследователски проект в помощ на докторанти-152ПД0057-24

ЛИТЕРАТУРА

1. Mastercam MC9

КОРЕСПОНДЕНЦИЯ

Доц. д-р Станислав АЛЕКСИЕВ
ТУ-София филиал Пловдив
e-mail: stanislav_al@abv.bg

маг. Инж. Мирослав АЛЕКСИЕВ
ТУ-София филиал Пловдив
e-mail: miro.0328@gmail.com

гл.ас. д-р Ангел Попаров
ТУ-София филиал Пловдив
e-mail: poparan@tu-plovdiv.bg

Tribological Journal BULTRIB Vol. 5, 2015
Papers from the International Conference **BULTRIB '15**
September 11-13, 2015, Sozopol, Bulgaria
Society of Bulgarian Tribologists
FIT – Technical University of Sofia

THEORETICAL JUSTIFICATION FOR THE SELECTION OF CURVES ENGAGE MANUFACTURING OF GEARS FROM POLYMER MATERIAL

Stanislav ALEKSIEV, Miroslav ALEKSIEV

Abstract: Development of gears of polymeric materials can be made of conventional gear-cutting equipment, CNC machines or by injection. Produced with standard tools, which determines the use of involute profile. He is not the most appropriate for gears, as evidenced in the article.

Key Words: *gears, gear tools, curves pitching, speed gliding and gliding specific polymer materials.*

ТЕОРЕТИЧНА ОБОСНОВКА ЗА ИЗБОР НА КРИВИ НА ЗАЦЕПВАНЕ ЗА ИЗРАБОТВАНЕ НА ЗЪБНИ КОЛЕЛА ОТ ПОЛИМЕРНИ МАТЕРИАЛИ

Станислав АЛЕКСИЕВ, Мирослав АЛЕКСИЕВ

Резюме: *Изработването на зъбни колела (ЗК) от полимерни материали може да се извърши на конвенционално зъбообработващо оборудване (с инструменти червячна фреза (ЧФ) или със зъбодълбачно колело (ЗДК)), на машини с ЦПУ или чрез шприцване. Произведените ЗК с ЧФ, ЗДК или гребен се извършва със стандартни инструменти, което предопределя използването на еволвентен профил. Той не е най-подходящия за ЗК от полимерни материали, което се доказва в статията.*

Ключови думи: *зъбни колела, зъбообработващи инструменти, криви на зацепване, скорост на плъзгане и специфично плъзгане, полимерни материали.*

1. ВЪВЕДЕНИЕ

Полимерните материали изместват металите в зъбните колела, ако зъбната двойка не е толкова силово натоварена. Във всички други случаи ЗК от пластмаси са с по-добри характеристики, като: тегло, шум, вибрации, самосмазване, химична усойчивост, употреба в хранителната промишленост и не на последно място висока производителност, ако се шприцват итн. Повишаването на якостните характеристики, намалаването на триенето в мястото на контакт в голяма степен зависят от вида на кривите на зацепване. Еволвентното зацепване е предизвикано от технологичната немощ на миналия век - изходния инструментален контур е трапец с ъгъл на наклона на бедрото - 20^0 *(стандарт)* те. права линия, защото лесно се прави и контролира. Съвременните машини с ЦПУ могат да изработват с висока точност всякакви криви стига, инженерния състав теоретично да е запознат с тях и предимствата им. Всичко това, обуславя актуалността на разработката.

2. *СРАВНЯВАНЕ НА ЕВОЛВЕНТНО С ЦИКЛОИДНО ЗАЦЕПВАНЕ ПО ГОЛЕМИНА НА СПЕЦИФИЧНОТО ПЛЪЗГАНЕ*

За да се направи сравняването възможно най- коректно е необходимо да се сравнят зацепени зъбни двойки с еднакви геометрични параметри. Нека това стане със зъбна двойка с еволвентно зацепепване между две еднакви зъбни колела със 17-зъба, с m = 1mm, които са изработени с инструмент червячна фреза без закрагление на върха на зъбите. Не случайно е подбран такъв инструмент и обработка, защото това е най-разпространения и производителен начин за формообразуване на зъбите. Профилирането на зъбите на фиг. 1 се извършва използвойки следните криви:

- Еволвентната крива е с уравнение:

$x = r_b *(t* sin(t) + cos(t))$

$y = r_b *(- t*cos(t) + sin(t)).$ (1)

където *(t)*- ъглов параметър 0-360^0
Преходната крива се получава удължена еволвента с у-ние:

$x = r_w *(t* sin(t) + (r_a / r_w) *cos(t))$

$y = r_w *(- t*cos(t) + (r_a / r_w)* sin(t)).$ (2)

При циклоидното зацепване основната окръжност (окр. по която се търкаля образуващата окръжност r_c и се получава епи и хипоциклоидна крива) съвпада с делителната. Т.е. $r_w = r_b$.

- Епи и хипоциклоидата се получават с у-ние (2):

$x = (r_b \mp r_c)*cos(t) \pm r_c *cos(((r_b / r_c) \mp 1)*t)$

$y = (r_b \mp r_c)* sin(t) - r_c * sin(((r_b / r_c) \mp 1)*t),$ (3)

- където горните знаци се отнасят за хипоциклоида, а долните за епициклоида.

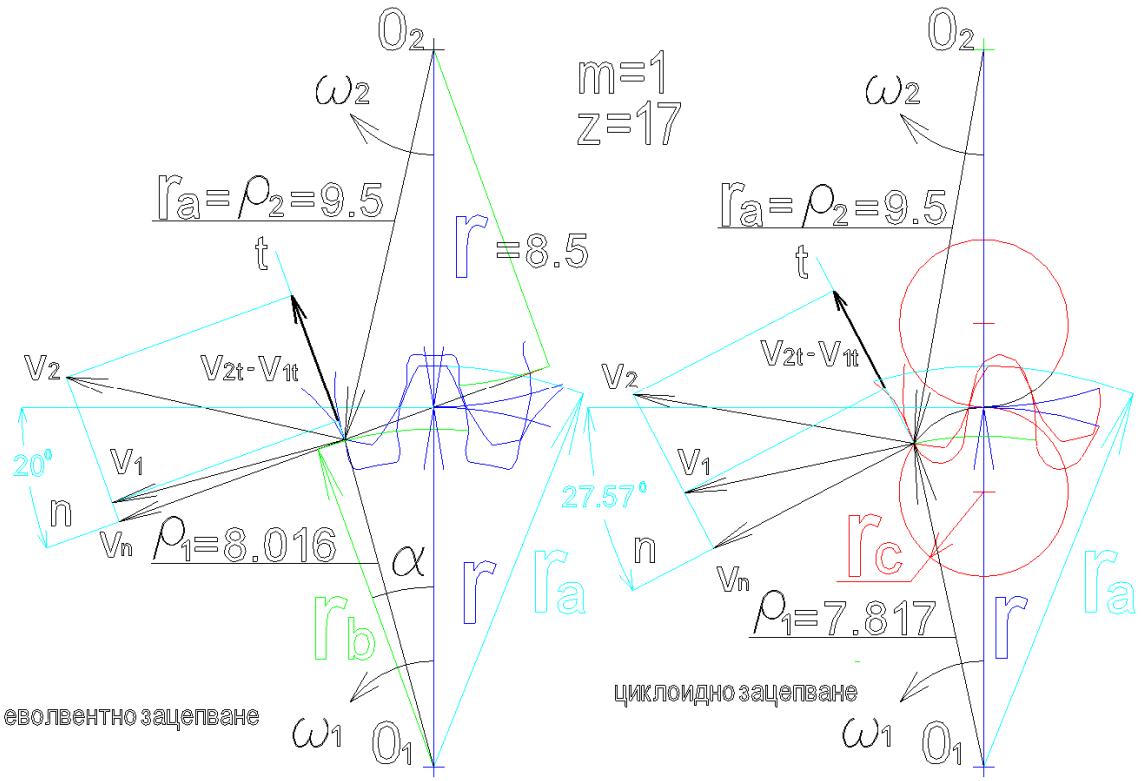

Фиг. 1. Еволвентно и циклоидно зацепване на ЗК z = 17, m = 1mm

Нека задвижващото колело да е второто т.е. с център O_2. Скоростта $v_2 = \rho_2 \omega_2$ е перпендикулярна на ρ_2 и е еднаква за двете двойки ЗК. Избрана е крайната точка на зацепване и за

двата разглеждани случая. В тази точка са построени нормалите и тангентите към контактуващите зъбни профили. Построява се и вектора на скоростта в т.1 и за ЗК1. Скоростта v_1 е перпендикулярна на ρ_1. Проекциите на v_2 и v_1 върху нормалата към профилите съвпадат защото е изпълнен закона на зъбозацепването и в двата случая. Проекциите на v_2 и v_1 върху тангентата към профилите са съответно v_{2t} и v_{1t}. Разликата (v_{2t} - v_{1t}) представлява скоростта на плъзгане.

Отношението на скоростта на плъзгане към скоростта на съответното колело, се нарича специфично плъзгане и се отбелязва с Q. Очевидно:

$$Q_1 = (v_{2t} - v_{1t})/v_1 \; > \; Q_2 = (v_{2t} - v_{1t})/v_2 \qquad (3)$$

Графиките на Q_1 и Q_2 за двете зацепвания са построени върху увеличените профили на зъбите в произволен но еднакъв и за двете зацепвания мащаб и са показани на фиг. 2.

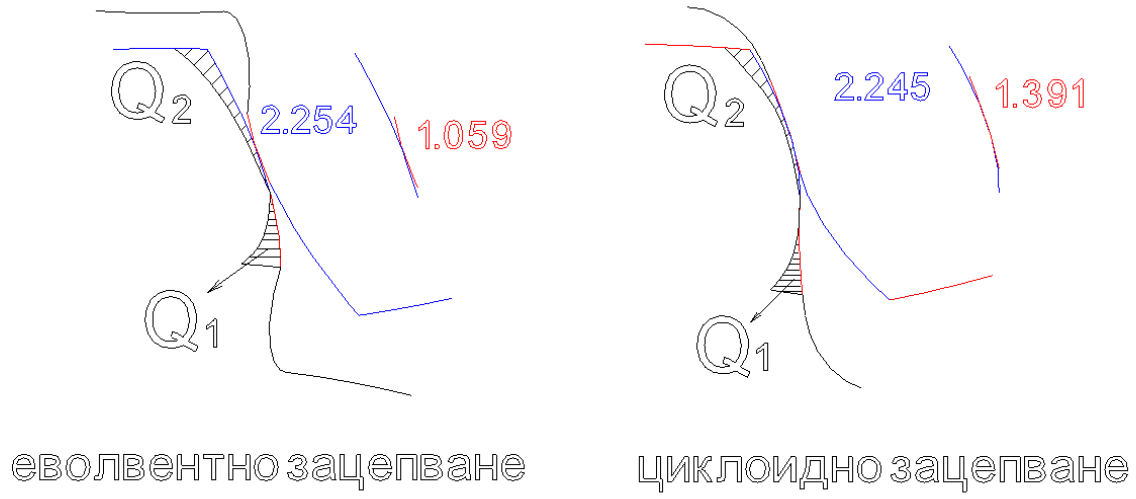

Фиг. 1. Графики на Специфично плъзгане Q_1 и Q_2

Над увеличените профили на зъбите е показано, с каква част от основата на зъба на едното ЗК работи главата на другото ЗК.
От графиките на Q_1 се вижда, че специфично плъзгане е най-голямо за най-ниската част от активния профил на зъба в основата му. Там се наблюдава и най-голямото износване на зъбите.
От графиките на Q_1 и Q_2 се вижда, че стойностите на специфично плъзгане за еволвентното зацепване са $Q_{1\text{еволв}}/Q_{1\text{циклоидно}}$ = 1,22 и $Q_{2\text{еволв}}/Q_{2\text{циклоидно}}$ = 1,19 пъти по-големи от тези на циклоидното зацепване. Отношението на $Q_{1\text{еволв}}$ / $Q_{2\text{еволв.}}$ = 1,18, а $Q_{1\text{ циклоидно}}$ / $Q_{2\text{ циклоидно.}}$ = 1,20.

Може да се направят следните изводи:
- Главата на зъба условно ще се износва 20% по-малко от тази на основата на зъба.
- Специфичното плъзгане при еволвентното зацепване е 22% - 19% по-голямо от това на циклоидното зацепване.
- Като не се забравя и това, че циклоидното зацепване се извършва по вблъбнат с изпъкнал профил, което увеличава изчислителния приведен радиус на кривина, при изчисляване на контактна якост, става ясно защо износването в циклоидното зацепване е по-малко.

3. *СРАВНЯВАНЕ НА ЕВОЛВЕНТНО С ЦИКЛОИДНО ЗАЦЕПВАНЕ ПО НАПРЕЖЕНИЕ НА ОГЪВАНЕ*

Да се направи сравняването се използва фиг. 3. Фигурата е получена от фиг. 1, като е разгледан случая на излизане на водещия зъб от контакт с водимия те. в края на активната част от линията на зацепване. Активната част от линията на зацепване при еволвентното такова е част от образуващата права (наклонена под 20^0 спрямо отсечката свързваща двата центъра) ограничена от върховите окръжности на двете ЗК. Активната част от линията на зацепване при циклоидното такова е по дъгите на образуващите окръжности (с радиус r_c) на циклоидните криви, също ограничена от върховите окръжности на двете ЗК. Предаването на въртящия момент поражда тангенциална сила F перпендикулярна на радиуса в тази точка. Нека и двете зъбни двойки да предават еднакъв въртящ момент те. и силата и рамото са еднакви за двете. Най-слабото сечение за еволвентния зъб е на разтояние 1,94 mm от върха на зъба и то е с дебелина на зъба в основата 1,551 mm. На същото разтояние циклоидния зъб е дебел 1,763 mm. В такъв случай огъващия момент за двата зъба на двата вида зацепвания е еднакъв M_{or}= F*1,94.

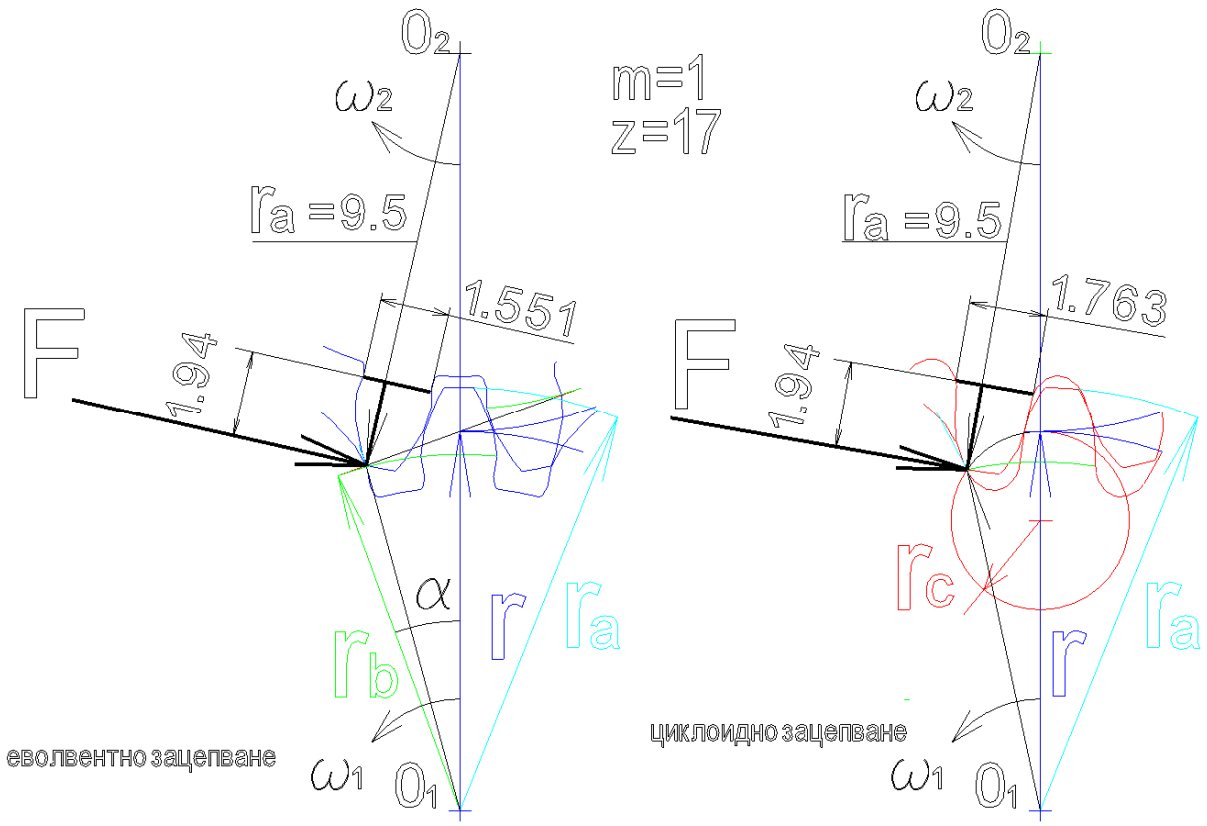

Фиг. 3. Схема за определяне натоварването на зъб с еволвентно и циклоидно сечение

От известна формула от „Съпротивление на материалите" G_{or}= M_{or}/ W_{or}. Ако се приеме, че и двете зъбни двойки се изработват от един и същи материал то тогава и G_{or} е еднакъво за двете зъбни двойки. За срявняване е необходимо да се приеме, че и дебелината (в) на зъбните колела също е еднаква. Но съпротивителния момент на правоъгълно сечение е $W_{or\ на\ зъба\ с\ еволвентно\ сечение}$ = в*$1{,}551^2$ /6 и $W_{or\ на\ зъба\ с\ циклоидно\ сечение}$ = в*$1{,}763^2$ /6. Отношението на $W_{or\ циклоидно}$ / $W_{or\ еволвентно}$= $1{,}763^2$ / $1{,}551^2$ = 1,29 показва, че зъбната двойка с циклоиден профил на зъба е 29% по-яка на огъване от тази с еволвентен.

4. ЗАКЛЮЧЕНИЕ

3. Зъбна двойка, която се изработва с циклоиден профил на зъба в напречно сечение допуска пренасяне на 29% по-голям въртящ момент от тази с еволвентен профил.
4. Зъбите с циклоиден профил са по-подходящи за зъбни колела изработвани от полимерни материали без смазване защото специфичното плъзгане 20% по-малко тези с еволвентен.

БЛАГОДАРНОСТИ

Авторите изказват благодарности за финансиране на участието в научната конференция по научноизследователски проект в помощ на докторанти-152ПД0057-24

ЛИТЕРАТУРА

1. Mastercam MC9

КОРЕСПОНДЕНЦИЯ

Доц. д-р Станислав АЛЕКСИЕВ
ТУ-София филиал Пловдив
e-mail: stanislav_al@abv.bg

маг. Инж. Мирослав АЛЕКСИЕВ
ТУ-София филиал Пловдив
e-mail: miro.0328@gmail.com

Tribological Journal BULTRIB Vol. 5, 2015
Papers from the International Conference **BULTRIB '15**
September 11-13, 2015, Sozopol, Bulgaria
Society of Bulgarian Tribologists
FIT – Technical University of Sofia

HYDRO-ABRASIVE WEAR OF SHPEROIDAL GRAPHITE CAST IRON MICROALLOYED by Sn

Mara KANDEVA[1], Boryana IVANOVA[2], Plamen IVANOV[1], Emilia ASSENOVA[3]
[1]Laboratory for Tribology, Faculty of Industrial Technology, Technical University - Sofia, Bulgaria
[2] Dept. Material Science and Technology, Faculty of Industrial Technology, Technical University – Sofia, Bulgaria
[3]Society of Bulgarian Tribologists, Sofia, Bulgaria

Abstract: The paper considers the study of wear parameters of spheroidal graphite cast iron unalloyed and microalloyed by various percent content of tin (Sn) under conditions of contact interaction between specimen and water jet with abrasive (abrasivejet). Experimental results are obtained about mass wear, wear rate, wear intensity and wear resistance at equal interaction conditions. It is established that the presence of tin results in wear reduction. Cast iron specimens microalloyed by 0,032% Sn show highest wear resistance, e.g. 150% higher than that of cast iron without Sn microalloyage. The increase of Sn content to more than 0,032% results in wear resistance decrease.

Key Words: tribology***,*** hydroabrasive wear, spheroidal graphite cast iron

ХИДРОАБРАЗИВНО ИЗНОСВАНЕ НА СФЕРОГРАФИТЕН ЧУГУН, МИКРОЛЕГИРАН С КАЛАЙ

Мара КАНДЕВА[1], Боряна ИВАНОВА[2], Пламен ИВАНОВ[1], Емилия АСЕНОВА[3]
[1]Лаборатория по трибология, Машинно-технологичен факултет, ТУ-София, България
[2]Департ. по материалознание, Машинно-технологичен факултет, ТУ-София, България
[3]Общество на триболозите в България - София

Abstract: Настоящата работа е свързана с изследване параметрите на износване на сферографитен чугун без калай и с различна концентрация на калай в условия на контактно взаимодействие с водна струя, носеща абразивни частици. Получени са експериментални резултати за масовото износване, скоростта, интензивността на износване и износоустойчивостта при еднакви условия на взаимодействие. Установено е, че наличието на калай в сферографитен чугун намалява износването. Най-висока износоустойчивост имат образци от чугун, микролегиран с 0,032% калай, която е 150% по-висока от тази на чугун без калай. С повишаване съдържанието на калай над 0,032% износоустойчивостта намалява.

Key Words: трибология**,** хидроабразивно износване, сферографитен чугун

1. ВЪВЕДЕНИЕ

Обект на настоящото изследване са сферографитни чугуни с подобрени механични и трибологични свойства, получени чрез микролегиране с различно процентно съдържание на калай.

Сферографитните чугуни се използват като триботехнически материали, работещи в различни експлоатационни условия в различни области на машиностроенето, индустрията и транспорта. По-конкретно, от тях се изработват детайли на редуктори, плъгащи лагери, направляващи, открити зъбни предавки и други, които работят в условия на триене при плъзгане, при търкаляне и триене при търкаляне с приплъзване в режими на течно, гранично, смесено мазане и в много случаи на сухо триене. Чугуните се използват за детайли от строително оборудване, земеделски машини, минни машини, смилащи системи, помпи, флотационно оборудване и други, работещи в режим на абразивно, газо- и/или хидроабразивно износване, ерозия, ударно-абразивно износване в присъствие на агресивни среди и др. [1-10].

Целта на работата е да се проведе сравнително изследване на характеристиките на износването на сферографитен чугун без калай и микролегиран с различна концентрация на калай при контактно взаимодействие с хидроабразивни частици.

Решават се следните основни задачи:

- Разработване на устройство и усвояване на методика за хидроабразивно износване на твърди повърхнини;
- Получаване на експериментални резултати за масовото износване, скоростта, интензивността на износване и износоустойчивостта на образци от сферографитен чугун без калай и микроле-

гиран с различно съдържание на калай при еднакви условия на взаимодействие с водно-абразивна струя.

2. МАТЕРИАЛИ

Изследваните образци са 5 проби от сферографитен чугун: един образец без съдържание на калай и четири броя образци, микролегирани със съдържание на калай съответно 0,018%, 01020%, 0,0325 и 0,051% Sn.

Образците са изработени от пробни тела, отляти в Завод за сферографитен чугун «Осъм» АД - гр. Ловеч, България по метода «Капак-кофа». Топенето на метала включва две основни операции – топене и шихтоване, съпроводени с непрекъснат контрол по изпълнението им. Микролегирането с калай е направено с цел да се получат чугуни с марки GJS 400-15, GJS 500-2, GJS 600-3, GJS 700-2. В таблица 1 е представен химичният състав на образците.

Таблица 1: *Химичен състав на образци от сферографитен чугун без и със съдържание на калай*

№ химичен елемент	Химичен елемент, %	Номер на образеца				
		0	**1**	**2**	**3**	**4**
1	C	3,87	3,87	3,87	3,87	3,87
2	**Sn**	**-**	**0,018**	**0,020**	**0,032**	**0,051**
3	Si	1,55	1,55	1,55	1,55	1,55
4	Mn	0,34	0,34	0,34	0,34	0,34
5	P	0,029	0,068	0,063	0,075	0,077
6	S	0,012	0,051	0,059	0,047	0,060
7	Cr	0,030	0,030	0,030	0,030	0,030
8	Mo	0,018	0,019	0,020	0,017	0,018
9	Ni	0,024	0,024	0,024	0,024	0,024
10	Co	0,013	0,017	0,014	0,013	0,013
11	Cu	0,051	0,058	0,077	0,059	0,070
12	Ti	0,0013	0,0013	0,0018	0,0015	0,0013
13	W	0,126	0,126	0,135	0,123	0,126
14	Pb	0,039	0,039	0,043	0,040	0,039
15	As	0,036	0,036	0,037	0,038	0,040
16	Zr	0,003	0,003	0,003	0,003	0,003
17	B	0,0083	0,0083	0,0074	0,0091	0,0088

Металографски анализ на микроструктурата е направен с оптичен микроскоп Neophot 32 - фиг. 1 а), б), с), d) и е) [15,16].

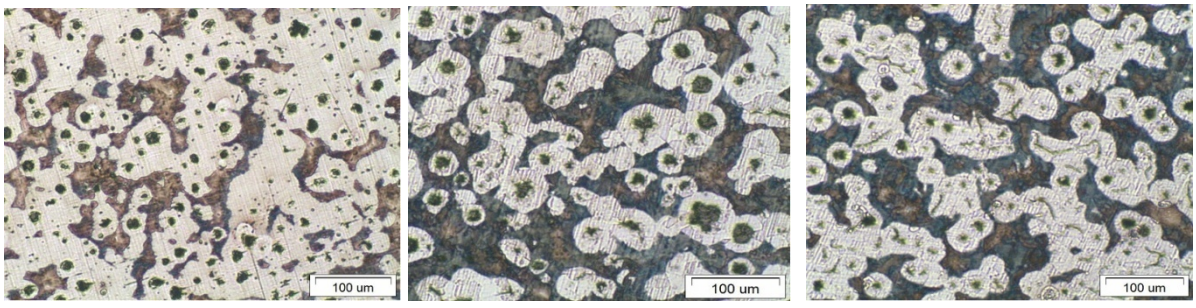

a) – 0 % Sn *b)* – 0,018 % Sn *c)* – 0,02 % Sn

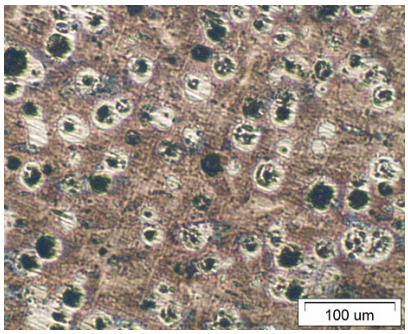

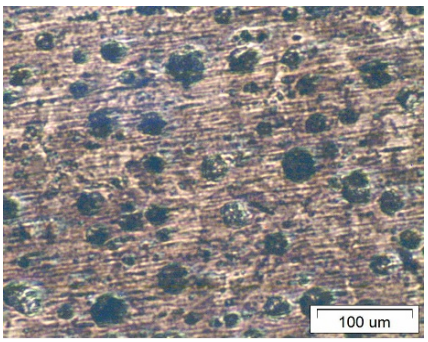

d) – 0,032 % Sn *e)* – 0,051 % Sn

Фиг. 1. *Микроструктура на проявени образци от сферографитен чугун: a) без калай и микролегиран с различно съдържание на калай – b), c), d), e)*

Резултатите за твърдостта на изследваните образци, измерена по метода на Бринел, са представени в таблица 2 [11-14].

Таблица 2. *Твърдост на сферографитен чугун без и със съдържание на калай*

№ образец	**0**	**1**	**2**	**3**	**4**
Sn, %	-	0,018	0,020	0,032	0,051
Твърдост, HB	179	197	203	262	277

Получени са резултати за следните механични характеристики на образците: якост на опън *Rm*, граница на провлачване *Rp0,2* и относително удължение ε.

Средните стойности на измерените величини са представени в таблица 3. [15,16]

Таблица 3. *Усреднени стойности на Rm, Rp0,2, ε, и E*

№ на образеца	**Съдържание на калай [%]**	**Якост на опън, Rm [MPa]**	**Граница на провлачване Rp0,2 [MPa]**	**Относително удължение ε , [%]**	**Модул на еластичност *E*, [Pa]**
0	-	500	360	16	$0{,}33.10^{10}$
1	0,018	460	330	8,6	$0{,}53.10^{10}$
2	0,020	492	330	7,8	$0{,}63.10^{10}$
3	0,032	691	435	2,4	$2{,}9.10^{10}$
4	0,051	569	369	0,5	$11{,}4.10^{10}$

3. УСТРОЙСТВО И МЕТОДИКА

Изследването на хидроабразивното износване на сферографитен чугун без и със съдържание на калай се осъществява с устройство, чиято функционална схема е представена на фиг.2.

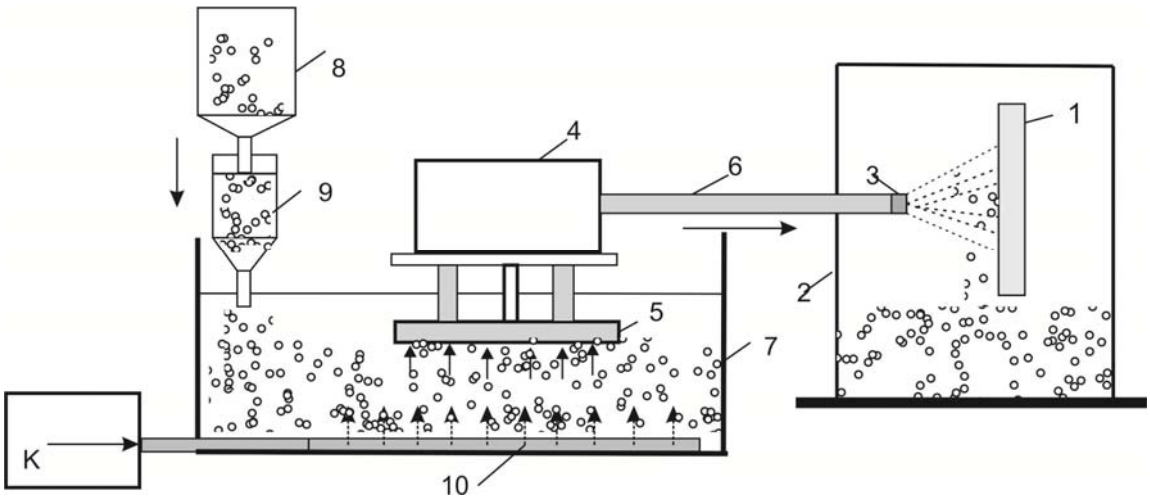

Фиг. 2. *Функционална схема на устройство за изследване на хидроабразивно износване*

Образецът 1 от изпитвания материал е закрепен неподвижно в камера 2 и се обтича от двуфазна водна струя, съдържаща абразивни частици, изтичащи от изходна дюза 3. Повърхнината на образеца 1 се позиционира в държач перпендикулярно на оста на дюзата 3 и на разстояние от изходящата дюза $\ell = 15$ mm.

Двуфазната струя постъпва в тръбопровода 6 от смукателя 5 на водната смукателна помпа 4. Формирането на двуфазната смес „вода-абразивни частици" се осъществява в смесителната камера 7, запълнена с вода до определено ниво. Абразивният материал – кварцов пясък, корунд и т.н., преминава от бункера 8 през дозатора 9 и изтича гравитационно в камера 7. Дебитът на абразива се регулира чрез подходящ диаметър на изходящата дюза на дозатора 9, с предварително тариране. Дозаторът поддържа постоянно ниво на абразивния материал, което гарантира постоянния му дебит (скорост на изтичане).

Хомогенизирането на двуфазната смес „вода-абразив" се осъществява с помощта на пневматичен струен барбуратор 10, разположен на дъното на камерата. Барбураторът 10 представлява тръба с малки отвори, през които изтичат вертикални въздушни струи с висока скорост. Струите турбулизират водната среда, като предотвратяват седиментацията на абразивните частици. Барбураторът 10 се захранва с въздух от компресора К с налягане, което се регулира от пневмо-подготвяща група, разположена на изхода на компресора.

Работата с устройството протича в следната последователност:

- Образецът 1 се закрепва в камера 2, като се позиционира така, че повърхнината му да е разположена перпендикулярно на оста на дюзата - $\alpha = 0°$. Закрепващото приспособление позволява изменение на ъгъла на взаимодействие между струята и образеца α;
- Камера 7 се пълни с вода до определено ниво, съобразено с дебита на смукателната помпа 4 и времето на експеримента;
- Бункерът 8 се зарежда с определено количество абразивен материал, който предварително се пресява със ситова машина и се подсушава при температура 120°С в сушилен шкаф;
- От компресора К се подава въздух с постоянно налягане към барбуратора 10;
- Включва се помпата 4 и чрез хронометър се отчита времето на хидроабразивно взаимодействие между водно-абразивната струя и образеца;
- След приключване на облъчването образецът се сваля от държача, изсушава се в сушилен шкаф 30 минути при температура 120°С, оставя се на стайна температура до изстиване и се измерва масата му с електронна везна.

Устройството е изработено и влязло в употреба в Лабораторията по трибология на ТУ-София.

Методиката за изследване на хидроабразивна ерозия се състои в следното:

- Определяне на масовото износване m на образеца като разлика на неговата маса преди и след определено време на ерозиране t. Измерването на масата се осъществява с електронна везна с точност 0,1 mg. Преди всяко измерване с везната образецът се почиства с обезмаслителна течност и се подсушава 5 минути с гореща въздушна струя.

- Определяне на скоростта на хидроабразивна ерозия по формулата:

$$\dot{m}_w = \frac{m}{t}$$

където t е времето на облъчване.

- Определяне на интензивността на хидроабразивно износване, която представлява отношение на скоростта на хидроабразивното износване $\dot{m}_w$ и масовия дебит на абразива $\dot{m}_a$:

$$i_w = \frac{\dot{m}_w}{\dot{m}_a}$$

Параметърът i_w е безразмерно число, което показва каква маса от повърхнината на образеца се разрушава за даден интервал от време под действието на маса от абразивния материал, попадащ върху нея за същия интервал от време.

- Определяне на хидро-абразивната износоустойчивост по формулата:

$$I_w = \frac{1}{i_w} = \frac{\dot{m}_a}{\dot{m}_w}$$

Физическият смисъл на износоустойчивостта е следният: износоустойчивостта е безразмерно число, което показва какво количество абразив от даден материал е необходимо, за да се разруши определена маса от повърхнината на образеца при единица време на облъчване.

4. ЕКСПЕРИМЕНТАЛНИ РЕЗУЛТАТИ И АНАЛИЗ

С описаната методика и устройство е проведено сравнително изследване на хидроабразивното износване на петте вида образци от сферографитен чугун.

Всички образци са изследвани при едни и същи условия на експеримента, които са представени в таблица 4.

Таблица 4. *Условия на експеримента при хидроабразивно износване*

№	Параметър	Стойност
1	Налягане преди дюзата	5,5 kPa
2	Размер на абразивните частици	d_a = 180 μm
3	Масов дебит на абразива	1000g/min
4	Вид на абразива	SiO_2 min 99,5%;H_2O max 0,2% Глинести примеси 0,4%
5	Воден дебит	6 *l* /min
6	Помпа смукателна ПСМ-25	W=0,18 kW; n=3000 tr/min; Q=25 ℓ / min
7	Диаметър на дюзата	*ф* = 4 mm
8	Време на облъчване	t = 4 min
9	Ъгъл на взаимодействие	$\alpha = 0^o$
10	Разстояние между дюзата и образеца	$\ell = 15$ mm
11	Размери на образците	20x20x10 mm

В таблица 5 се представени експерименталните резултати за масовото износване, скоростта на износването, интензивността и износоустойчивостта на всички изследвани образци.

Таблица 5. *Данни за параметрите на хидроабразивно износване*

№ обр.	маса преди износване,g	маса след износване,g	масово износване,g	скорост на износване,mg/min	интензивност на износване	износоустойчивост
0	23,9909	23,9859	0,005	1,25	$1,25.10^{-6}$	$0,8.10^{6}$
1	26,8941	26,8895	0,0046	1,15	$1,15.10^{-6}$	$0,9.10^{6}$
2	32,7429	32,7408	0,0021	0,53	$0,53.10^{-6}$	$1,9.10^{6}$
3	32,0485	32,0465	0,002	0,5	$0,5.10^{-6}$	$2,0.10^{6}$
4	30,6294	30,6269	0,0025	0,62	$0,62.10^{-6}$	$1,6.10^{6}$

На фиг. 3 е представена графично зависимостта на интензивността на хидроабразивното износване от процентното съдържание на калай в сферографитен чугун, а на фиг.4 – диаграмата на износоустойчивостта на различните изпитвани образци.

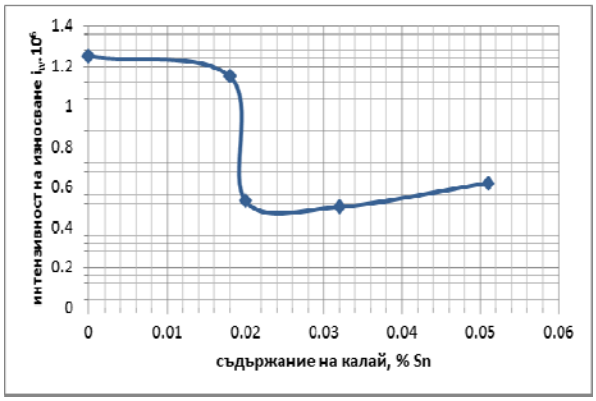

Фиг. 3. *Интензивност на хидроабразивно износване от % Sn*

Фиг. 4.*Износоустойчивост на хидроабразивно при различно % Sn*

Анализът на резултатите показва следното:

- наличието на калай в сферографитния чугун влияе на износването му при контактно взаимодействие с водноабразивна струя;
- интензивността на износване намалява с увеличаване процентното съдържание на калай и остава винаги по-ниска от тази на чугун без калай;
- зависимостта на интензивността на износване, съответно на масовото износване, има силно нелинеен характер. При малко съдържание на калай – до 0,018% интензивността на износване много малко намалява, но при Sn = 0,02% интензивността рязко намалява със скок и достига минимална стойност $i_w = 0,5.10^{-6}$ при Sn = 0,032%.
- повишаването на процентното съдържание на калай над 0,032% води до бавно нарастване на интензивността на износване и при Sn = 0,051% достига стойност $i_w = 1,6.10^{-6}$, която е 2 пъти (100%) по-малка от интензивността при чугун без съдържание на калай.

5. ЗАКЛЮЧЕНИЕ

В настоящата работа е представено сравнително изследване на характеристиките на износването на сферографитни чугуни без легиране и микролегирани с различно съдържание на калай в условия на хидроабразивно износване.

Получени са експериментални резултати за масовото износване, скоростта, интензивносста на износване и износоустойчивостта на образци от сферографитен чугун без калай и микролегиран с различно съдържание на калай при еднакви условия на взаимодействие с водно-абразивна струя.

Установено е, че наличието на калай в сферографитен чугун води до намаляване на хидроабразивното износване в сравнение с чугун без калай. Най-висока износоустойчивост имат образци от чугун, микролегиран с 0,032% калай – Iw = 2.10^6, която е 150% по-висока от тази на чугун без калай. С повишаване съдържанието на калай над 0,032% износоустойчивостта намалява.

БЛАГОДАРНОСТИ

Изследването е направено във връзка с разработването на докторска дисертация в ТУ-София и във връзка с изпълнението на задачи по Договор ***ДУНК-01/3*** *"Създаване на Университетски научно-изследователски комплекс (УНИК) за иновации и трансфер на знания в областта на микро/нанотехнологии и материали, енергийната ефективност и виртуалното инженерство".*

This study is connected with the completion of a PhD dissertation and of the tasks under the Project ***ДУНК-01/3*** *"University R&D Complex for innovation and transfer of knowledge in micro/nano-technologies and materials, energy efficiency and virtual engineering" funded by the Bulgarian Ministry of Education and Science.*

ЛИТЕРАТУРА

1. Бондаренко С.И., И.П.Гладкий, *Гидроабразивная износостойкость чугунов с разной формой графита, легированных Cu, Cr, Ni, Mo*. в. ХНАДУ, вып. 46, Харьков, 2009, с. 131-133.
2. Бондаренко С.И., *Влияние структуры и механических свойст на гидроабразивную износостойкость чугунов*, в. ХНАДУ, Харьков, вып.52, 2010, с. 53-60.
3. Беркун М.Н., Топал В.И., Гудеревич Н.А., *Влияние титана на свойства высокохромистого чугуна* // Технология и организация производства. 1970. - № 6. с. 61-62.
4. Бондаренко С.И., И.П.Гладкий, *Повышение эксплуатационных свойств чугунов, работающих в условия гидроабразивного износа*, вісник Харківськ державн. Техніч. Університету , вып. 14, Харьков, 2007, с. 388-391
5. Федоров Г.Е., М.М.Ямшинский, Е.О.Платонов, А.Ю.Кузьменко, К.С.Радченко, *Повышение гидроабразивной износостойкости высоколегированного белого чугуна*, НауковіНГУУ „КПТ" 2009/1
6. Иванова Б., *Структури, свойства и контактни взаимодействия на високояк чугун, микролегиран с калай*, Автореферат на докт. дисертация, С., 2015
7. Иванова Б., М. Кандева, *Структура и свойства на сферографитен чугун микролегиран с калай*, сп. Инженерни науки, кн. 4, 2013, pp. 64-71.
8. Kandeva M., B. Ivanova, D. Karastoyanov, E. Assenova, *Static and dynamic friction of spherographite cast iron with Sn microalloy*, in: Proceedings of the 2nd Austrian-Indian Symposium on Materials Science and Tribology – MaTri'14, 26-29.05.2014, Wiener Neustadt, Austria.
9. Kandeva M., B. Ivanova, *Abrasive wear and wear resistance of high strength cast iron containing Sn microalloy*, Journal of the Balkan Tribological Association, Vol. 19, No. 4, 539-546, 2013.
10. Kandeva M., B. Ivanova, E. Assenova, A. Vencl, *Influence of additives and selective transfer on wear reduction in the lubricated contact*, in: Proceedings of the International Conference on Materials, Tribology, Recycling – MATRIB 2014, 26-28.06.2014, Vela Luka, Croatia, pp. 197-206.
11. БДС EN ISO 1563:2012 - *Леярство.Сферографитен чугун*.
12. БДС EN ISO 945-1:2009 - *Микроструктура на чугуни.Част I.*
13. БДС EN ISO 6892-1:2009 - *Метални материали,изпитване на опън.Част I*
14. БДС EN ISO 6506-1:2006 - *Метали, изпитване на твърдост по Бринел. Част I: Метод на изпитване.*

CORRESPONDENCE

Mara KANDEVA
Laboratory for Tribology,
Faculty of Industrial Technology,
Technical University - Sofia, Bulgaria
kandevam@gmail.com

Tribological Journal BULTRIB Vol. 5, 2015
Papers from the International Conference **BULTRIB '15**
September 11-13, 2015, Sozopol, Bulgaria
Society of Bulgarian Tribologists
FIT – Technical University of Sofia

MODELING OF SURFACE FINISH IN TURNING OF A BRASS ALLOY BASED UPON STATISTICAL MULTI-PARAMETER ANALYSIS

N.M. Vaxevanidis[1], N.A. Fountas[1], C. Koraidis[1], A. Koutsomichalis[2], P. Psyllaki[3]

[1]School of Pedagogical and Technological Education, Department of Mechanical Engineering Educators, GR 14121 N. Heraklion Attikis, Greece. e-mail: vaxev@aspete.gr
[2]Hellenic Air-Force Academy, Faculty of Aerospace Studies, Dekelia Air Force Base, GR 19005, Greece, e-mail: a.koutsomichalis@gmail.com
[3]Piraeus University of Applied Sciences, Department of Mechanical Engineering, Egaleo, Greece
e-mail: psyllaki@teipir.gr

Abstract: *A multi-parameter analysis of surface finish imparted to an industrial brass alloy, namely CuZn39Pb3 (CW614N - brass 583) by turning is presented. The interrelationship between surface texture parameters is emphasized. An increased number of parameters was studied including amplitude, hybrid, as well as random process and fractal parameters. The correlation of these parameters with the machining conditions was investigated. By applying analysis of variance and response surface analysis to the experimental data close correlation is revealed between certain surface finish parameters (R_a and R_t) and the machining conditions; single and multiple regression models were also developed.*

Key Words: *surface finish, multi-parameter analysis, turning, brass alloy*

2. INTRODUCTION

Metal cutting operations are widespread in manufacturing industry and the prediction and/or the control of relevant machinability parameters always attracts interest. One basic machinability parameter is the surface texture, as it is closely associated with the quality, reliability and functional performance of components [1, 2]. Turning is the primary operation in metalworking industry for producing axisymmetric components. These components, typically, possesses critical features that require specific surface finish and the best possible functional behaviour. Due to inadequate knowledge of the complexity of the process and factors affecting the surface integrity in turning operation [3], an improper decision may cause high production costs and low machining quality. The proper selection of cutting tools and process parameters for achieving high cutting performance in a turning operation is a critical task [2-4]. An arc chain surface pattern is typical for turning but significant deviations appear due to irregular chip formation phenomena, namely built-up edge, discontinuous chip, very low feed rates, chatter and intense tool flank wear. These phenomena occur many times, especially when limitations in productivity or in material selection exist [1].

The various manufacturing processes applied in industry produce the desired shapes of the components within prescribed dimensional tolerances and surface quality requirements. Therefore, any proposed description of a technological surface should take into account the features of the profile imparted by the machining process performed. This is a crucial point because the process can be controlled through surface texture recognition, and also be used to generate suitable profiles for tribological functioning [5].

In the common industrial practice surface roughness is evaluated by profile amplitude parameters such as R_a, R_t etc., which, however, do not provide information on the shape of the profile. Characteristics like inclination and curvature of the surface roughness asperities, “emptiness” or “fullness” of the profile, distribution of the profile material at various heights are registered in the profile shape. The essential tribological aspects (e.g. friction, wear, state of lubrication) are highly dependent on profile shape [5, 6]. In this regard, the characterization of machined surface shapes is necessary, and this can be achieved through multi- parameter statistical analysis [6-10].

The present work is related to research outlined above [1, 3-5, 9, 10] with additional emphasis directed towards the multi-parameter statistical analysis of the surface finish of turned copper alloy (CW614N - brass 583) rods in relation to process parameters. Based on industrial demand, as well as on ISO 4287 (1997) standard mostly [4, 5], an increased number of parameters was studied including amplitude, hybrid as well as random process and fractal parameters. Statistical regression models were developed, when possible, to express the correlation of the machining conditions with the imparted surface finish characteristics.

It should be noted that for the study of the influence of cutting speed, feed rate and depth of cut on machining performance during turning, besides statistical methods, soft computing techniques such as artificial neural networks and genetic algorithms can be applied see for example Refs [3, 11, 12] and [13] respectively.

3. SURFACE ROUGHNESS PARAMETERS

Surface roughness evaluation is very important for many fundamental problems such as friction, contact deformation, heat and electric current conduction, tightness of contact joints and positional accuracy. For this reason surface roughness has been the subject of experimental and theoretical investigations for many decades. The real surface geometry is so complicated that a finite number of parameters cannot provide a full description. If the number of parameters used is increased, a more accurate description can be obtained. This is the main reason for introducing new parameters for surface evaluation [7]. More than one hundred parameters have been proposed in the literature, owing to the fact that a real profile shape is usually very complicated, and the functional requirements for the components are very high in today's industry [5].

Since the estimation of the roughness performed with one parameter is ambiguous, the multi-parameter estimation of roughness is recommended [8, 10, 14]. Surface roughness parameters are normally categorized into three groups according to its functionality. These groups are defined as amplitude parameters, spacing parameters, and hybrid parameters [7]. The surface roughness parameters under study were:

- the arithmetic average, R_a;
- the maximum height of the profile; R_t or R_{max};
- the skewness of the amplitude distribution, R_{sk};
- the kurtosis of the amplitude distribution, R_{ku};
- the fractal dimension, *D*.

4. EXPERIMENTAL

4.1. Design of cutting experiments

An L_{27} full factorial experimental design was selected in order to study the effect of machining conditions, i.e., cutting speed (v), feed rate (s) and depth of cut (a) on surface roughness when turning *CuZn39Pb3 (CW614 – brass 583)* alloy and generate possible prediction models for surface roughness parameters. The order of the experiment's runs is depicted via the representation cube shown in Fig. 1 whilst in Table 1 the levels set for the three cutting conditions investigated are tabulated.

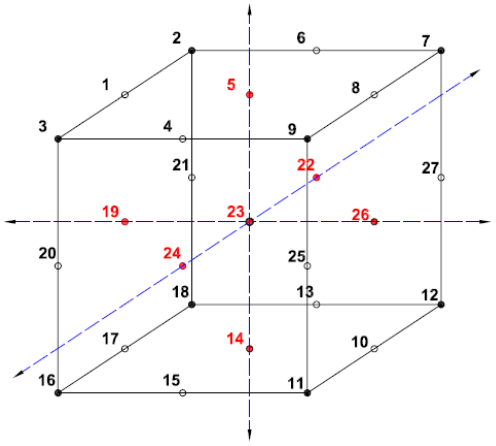

Fig. 1. Representation of full 3^3 factorial design

Table 1. Investigated machining conditions and levels

Parameter	Units	Level 1	Level 2	Level 3
Spindle speed (n)	rpm	420	600	850
Feed rate (s)	mm/rev	0.06	0.10	0.15
Depth of cut (α)	mm	0.5	1.0	1.5

4.2. Experimental procedure and test material

Turning experiments were conducted using a Kern Modell D18L conventional lathe. A SECO® coated tool insert, coded as TNMG 160404 – MF2 with TP 2000 coated grade, was selected as a cutting tool for the series of experiments performed. The tool had a triangular geometry with cutting edge angle, $K_r = 55^o$.

The test material was an industrial brass alloy, namely CuZn39Pb3 (CW614N - brass 583) typically used for machining applications. Its hardness is 130 HB). Studies concerning the microstructure and machinability of CuZn39Pb3 alloy have already reported in [15, 16].

The surface roughness analysis was performed using a Rank Taylor-Hobson® Surtronic 3 profilometer equipped with the Talyprof® software. The cut-off length was selected at 0.8 mm whilst 5 measurements were conducted on every pass at the longitudinal direction. A typical filtered profile of a turned surface is presented in Fig. 2. Measured average values for all surface roughness parameters under study are tabulated in Table 2 together with the corresponding cutting variables.

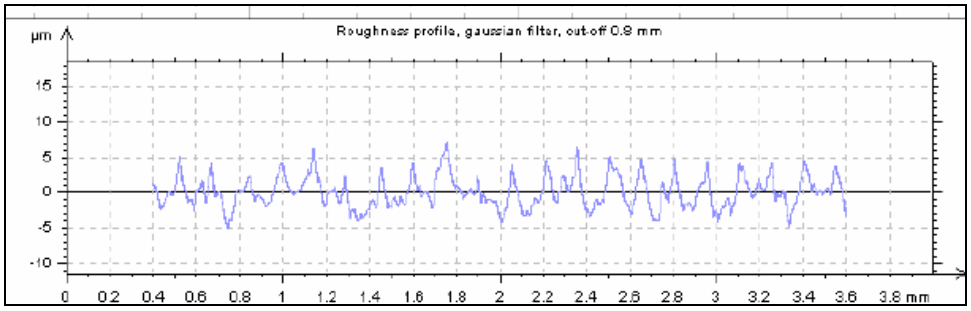

Fig. 2. Typical filtered profile of a turned surface (n=420 rpm, s=0.15 mm/rev and a=0.5 mm)

Table 2. Measured values for surface roughness parameters

No. Exp.	n (rpm)	s (mm/rev)	α (mm)	R_a (μm)	R_t (μm)	R_{ku}	R_{sk}	Fractal dimension D
1	420	0.06	0.5	4.26	12.90	3.13	0.421	1.31
2	420	0.06	1.0	4.36	13.20	3.48	0.711	1.31
3	420	0.06	1.5	4.36	13.10	3.46	0.704	1.31
4	420	0.10	0.5	1.38	9.63	2.85	-0.079	1.35
5	420	0.10	1.0	1.41	9.01	2.71	0.022	1.34
6	420	0.10	1.5	1.44	10.10	2.85	-0.029	1.34
7	420	0.15	0.5	1.84	13.00	3.46	0.704	1.31
8	420	0.15	1.0	1.62	10.70	3.37	0.812	1.31
9	420	0.15	1.5	1.78	11.40	2.59	0.129	1.31
10	600	0.06	0.5	1.52	10.80	3.00	0.213	1.33
11	600	0.06	1.0	1.86	12.80	2.43	0.066	1.28
12	600	0.06	1.5	1.98	13.90	3.05	0.421	1.31
13	600	0.10	0.5	1.42	9.34	2.61	-0.072	1.34
14	600	0.10	1.0	1.68	12.20	3.12	-0.169	1.32
15	600	0.10	1.5	1.7	13.10	3.04	0.078	1.31
16	600	0.15	0.5	1.81	12.50	2.77	0.032	1.29
17	600	0.15	1.0	1.76	12.80	3.05	0.421	1.31
18	600	0.15	1.5	2.14	14.40	2.89	0.017	1.28
19	850	0.06	0.5	1.52	10.80	3.00	0.213	1.31
20	850	0.06	1.0	1.63	14.60	4.72	0.560	1.24
21	850	0.06	1.5	1.68	14.80	4.72	0.560	1.24
22	850	0.10	0.5	1.53	10.60	2.74	0.008	1.33
23	850	0.10	1.0	1.67	13.40	3.61	-0.105	1.31
24	850	0.10	1.5	1.7	11.90	2.99	-0.065	1.33
25	850	0.15	0.5	2.01	13.90	3.02	0.119	1.3
26	850	0.15	1.0	1.84	13.90	3.09	0.381	1.31
27	850	0.15	1.5	1.8	12.30	2.77	0.389	1.3

RESULTS AND DISCUSSION

4.3. Experimental observations

The variation of measured values of R_a and R_t in correspondence to experimental runs is presented in Fig.3. Note that, whilst in general for turning of steels it has been reported that the surface roughness decreases with the increase of cutting speed and the decrease of depth of cut and feed rate [4, 17], such a behavior was not verified in the case of brass 583. During presented series of experiments it is observed that low-to-medium cutting speed and medium feed rate are necessary to minimize surface roughness; see similar remarks in Ref. [13]. Moreover, the combination of low value for both cutting speed and feed rate resulted in the highest values or R_a and R_t; see Fig.3 and Table 2.

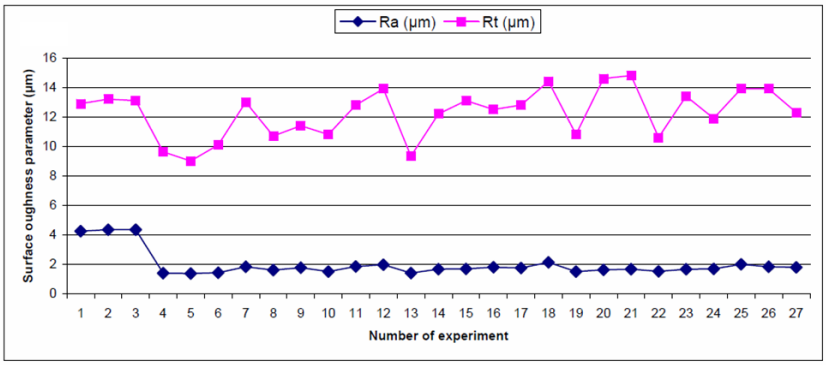

Fig. 3. Roughness parameters R_a and R_t values corresponded to experimental runs

The variation of measured values of R_{sk}, R_{ku} and D in correspondence to experimental runs is presented in Fig.4. As far as the variation of R_{sk}, R_{ku} is concerned, it was revealed that these parameters can not be related neither with cutting conditions in a higher or lesser degree, nor to be correlated with typical amplitude parameters such as R_a or R_t; i.e., they belong to the so-called "unrelated surface roughness parameters"; see Ref. [10].

Kurtosis (R_{ku}) typically describes the sharpness of the probability density of the surface profile [2]. Measured values of this parameter are in most cases in the range of around 3 indicating normally distributed high peaks and low valleys. Note that if R_{ku}>3 the distribution curve of the surface profile is said to be leptokurtoic and has relatively many high peaks and low valleys [7]; see tests no 20 and 21 in Fig. 4.

Skewness parameter (R_{sk}) is typically used to measure the symmetry of the profile about the mean line and is sensitive to deep valleys or high peaks [2, 7]. The variation of skewness of turned surfaces for all tests is illustrated in Fig 4, see also Table 2; in general, it appears uncorrelated to machining parameters; see Fig. 4. Judging from the measured skewness values, the turned profiles are revealed to be "empty" of material as indicated from the positive values in the majority of tests.

Fractal-based methods for describing surface texture have attracted great interest since they can provide information that conventional surface roughness parameters cannot [9]. The fractal dimension *D* was calculated via the power spectrum method and it appears, in general insensitive to cutting parameters. Measured values of this parameter are in most cases in the range of around 1.3. These observations are consistent, in general, with corresponding ones reported in Ref. [18].

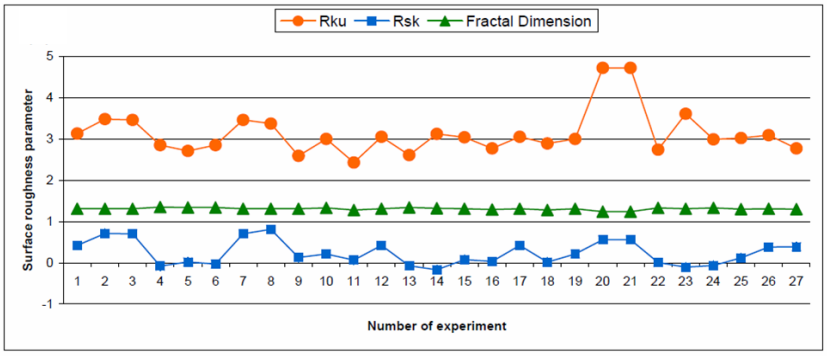

Fig. 4. Roughness parameters R_{ku}, R_{sk} and D values corresponded to experimental runs

4.4. Statistical analysis

Statistical analysis was performed in order to examine the variation of cutting conditions upon roughness average, R_a and maximum roughness height, R_t parameters. MINITAB® 17 software was employed to perform the analysis and to obtain the necessary outputs for results interpretation.

The main effects plot and the plot presenting the interactions among parameters indicate the influence of each parameter and their combination respectively on the response. From Fig. 5a it is evident that as far as average roughness (R_a) is concerned, feed rate and spindle speed (and consecutively cutting speed) dominates against depth of cut which does not seem to affect significantly the surface roughness. The product of spindle speed and feed rate yields noticeable influence in terms of the response whilst interactions between spindle speed and depth of cut and feed rate with depth of cut are also existed; see Fig. 5b.

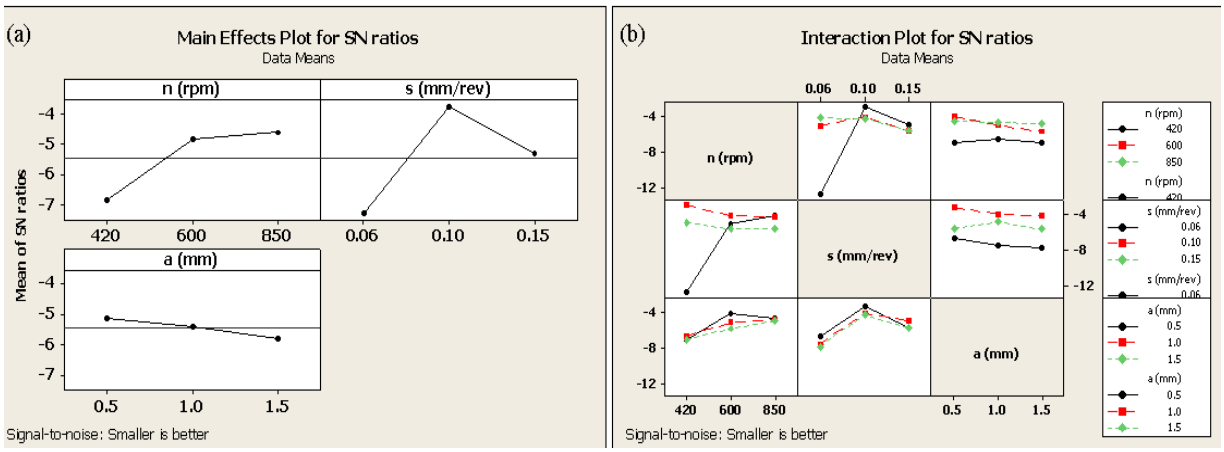

Fig. 5. (a) Main effects plot and (b) interaction plot for R_a

Similar analysis was followed to interpret the effect of cutting conditions on maximum roughness height, (R_t). Figures 6a and 6b illustrate the main effects of independent variables and their interactions. According to these outputs, R_t is strongly affected by all three machining conditions with feed rate to exert the largest influence considering the preset levels.

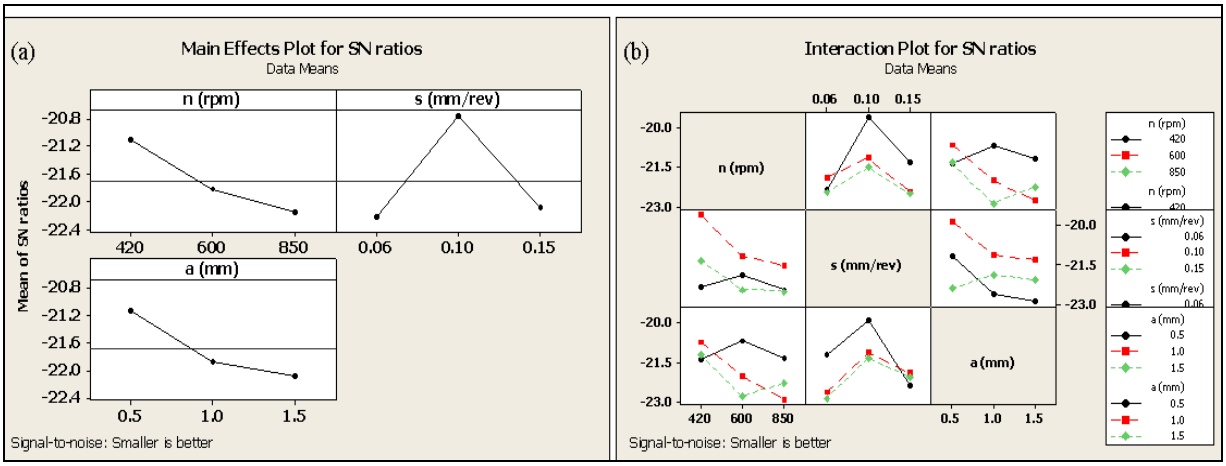

Fig. 6. (a) Main effects plot and (b) interaction plot for R_t

More accurate results concerning the effects of machining parameters on the responses of R_a and R_t can be obtained by conducting ANOVA analysis. Through the outputs of *ANOVA* analysis significance of the prediction models to be created is obtained and regression according the original outputs is facilitated. Table 3 summarizes the ANOVA attributes for both R_a and R_t.

Table 3. Analysis of variance for R_a and R_t.

ANOVA for R_a									
Source	*Sum of squares*	*DF*	*Mean square*	*F*	*Prob>F*	*R-sq.*	*R-sq. (adj)*	*Pred. R-sq.*	*Ad.Precision*
Model	19.32	18	1.07	221.14	<0.0001	0.9640	0.9935	0.9772	51.223
n	3.46	2	1.73	356.88	<0.0001				
s	5.02	2	2.51	517.73	<0.0001				
a	0.090	2	0.045	9.26	0.0083				
n x s	10.53	4	2.63	542.48	<0.0001				
n x a	0.11	4	0.028	5.77	0.0175				
s x a	0.096	4	0.024	4.97	0.0262				
Residual	0.039	8	4.853E-003						
Cor.Total	19.36	26	-						
Std.Dev.	0.070								
Mean	1.99								
C.V.	3.50								
PRESS	0.44								
ANOVA for R_t									
Source	*Sum of squares*	*DF*	*Mean square*	*F*	*Prob>F*	*R-sq.*	*R-sq. (adj)*	*Pred. R-sq.*	*Ad.Precision*
Model	39.58	18	2.20	0.56	0.8509	0.5593	-0.4322	-4.0197	3.141
n	3.10	2	1.55	0.40	0.6848				
s	7.74	2	3.87	0.99	0.4120				
a	2.14	2	1.07	0.27	0.7670				
n x s	2.73	4	0.68	0.18	0.9450				
n x a	7.98	4	1.99	0.51	0.7297				
s x a	15.90	4	3.97	1.02	0.4524				
Residual	31.19	8	3.90						
Cor.Total	70.77	26	-						
Std.Dev.	1.97								
Mean	12.26								
C.V.	16.10								
PRESS	355.22								

Based on ANOVA analysis and specifically "*F*" values corresponded to roughness average - *Ra*, the product of spindle speed and feed rate is the dominant attribute for Ra. Feed rate parameter comes second in terms of influence followed by spindle speed, depth of cut, the product of spindle and depth of cut and finally the product of feed rate and depth of cut. The model *F*-value of 221.14 implies that the model is significant and there is only a 0.01% chance that a "model F-value" that large could occur owing to noise. Values of "*Prob > F*" less than 0.0500 indicate that model terms are significant. The "*Pred-R.sq.*" of 0.9772 is in reasonable agreement with the "*R-sq. (adj*)" of 0.9935. "*Adeq. Precision*" measures the signal-to-noise ratio. A ratio greater than 4 is generally desirable. The ratio of 51.223 suggests an adequate signal; hence, the model can be used to navigate the design space.

In the case of maximum roughness height (R_t), the product of feed rate and depth of cut comes first in terms of influence on the response. R_t is also affected by feed rate (second influential parameter), the product of spindle speed and depth of cut, the spindle speed as an independent parameter, the depth of cut and the product of spindle speed and feed rate. Yet again, "*F*"-values reveal the order of influence of all studied parameters concerning R_t as the response. The model *F*-value of 0.56 implies that the model is not significant relative to the noise and there is a 85.09% chance that a "model F-value" that large could occur owing to noise. Even though R_t is generally affected by machining conditions as it is well-known from machining theory regardless of the material, the terms of the model seem to hold no significance. This could be justified using the evidence assembled concerning the tool wear and system vibration during the experiments since it is expected for R_t to follow a quite similar trend to that of R_a. A solution to such case is to reduce the model's terms in order to reduce the parameters only to those deemed necessary. Another alternative involves the implementation of a higher-order polynomial regression or exponential (power) functions to correlate the data. The problem of developing models for predicting R_t was addressed following both suggestions.

4.5. Variations of R_a and R_t through Response Surface Analysis

Besides the experimental curves plotted in Figures 3 and 4, 3D surface plots were produced in order to study the effects yielded when response variables (R_a and R_t) are subjected to different variations in terms of the value levels of cutting parameters (spindle speed *n*, feed rate *s* and depth of cut *α*). Response surface contours were produced by taking into account the range of values for two of the three independent variables whilst keeping in *Z* axis the response to see its variance. Note, that the response surfaces are just as many as the independent variables. In this paper three response surfaces (for each roughness parameter) were produced by considering spindle speed - *n* as the constant parameter while varying feed rate (s) and depth of cut (a). The exponential (convex or concave) trend of the surfaces reveals the strong interactions existed in this variation. In Figure 7 the response surface R_a (s, a) is presented whilst Figure 8 depicts the R_t (s, a) response surface. *Wolfram Research MATHEMATICA® 8.0* software was employed to produce these plots.

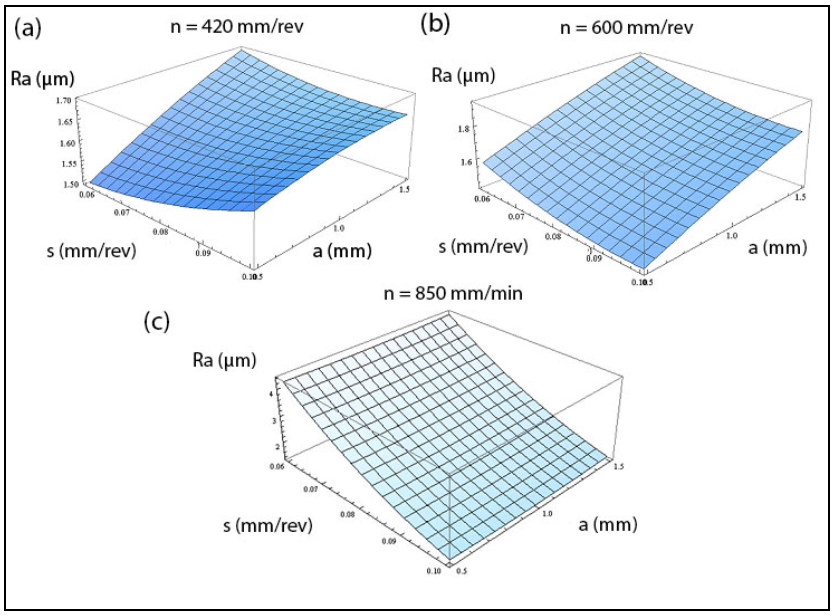

Fig. 7. Response surfaces for R_a (s, a) for n: (a) 420 mm/min; (b) 600 mm/min; (c) 850 mm/min

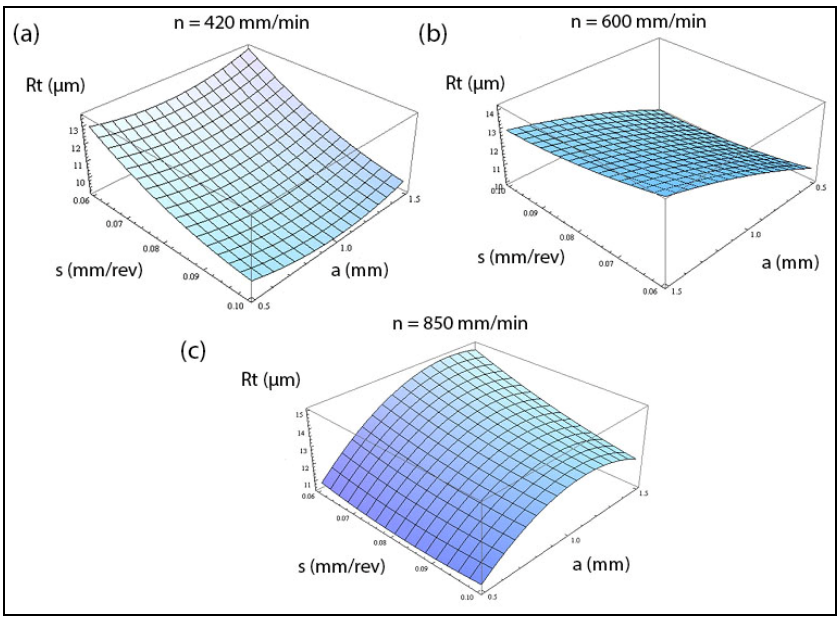

Fig. 8. Response surfaces for R_t (s, a) for n: (a) 420 mm/min; (b) 600 mm/min; (c) 850 mm/min

4.6. Prediction models for roughness parameters

Based on *ANOVA* outputs several prediction models of different types were formulated. These models include: a) the general linear model for first-order; b) the least squares approach – second order model; – and c) the “Gauss-Newton” algorithm for non-linear regression; see Fig. 9.

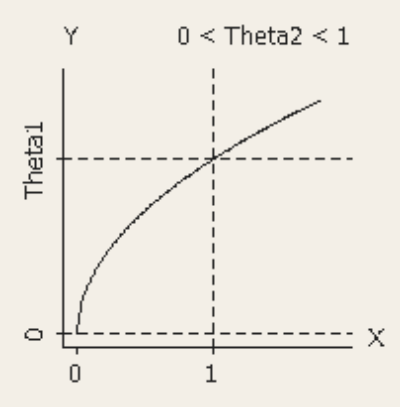

Fig. 9. The "Gauss-Newton” algorithm for non-linear regression (power function model fitting)

The case of the first-order model generation is trivial; thus, it is not further discussed. Besides, it is a straight-forward output of *ANOVA* and via this simple model further transformations may be employed to end-up with higher-order regression polynomials. Second-order mathematical expressions and power functions are generally preferred against first-order relations when it comes to two-way interactions of independent variables [6]. A second-order model may be obtained as follows:

$$\widehat{y} = b_0 x_0 + b_1 x_1 + b_2 x_2 + b_3 x_3 + b_{11} x_1^{\,2} + b_{22} x_2^{\,2} + b_{33} x_3^{\,2} + b_{12} x_1 x_2 + b_{23} x_2 x_3 + b_{13} x_1 x_2 \qquad (1)$$

where *b* values are to be estimated via the implementation of the "*Least Squares*" approach. Note that $\widehat{y}$ is the estimated response on logarithmic scale.

First-order prediction models were developed according to *ANOVA*. In the case of R_t the terms of the first-order linear model were reduced to the main cutting conditions by neglecting the interactions. Specifically for the first-order model of R_a, R^2 (or *R.-sq.*) is 0.9640 indicating that 96.4% of the total variation can be explained. For the first-order linear model of R_t, an R^2 (*R.-sq.*) equal to 0.7497 was achieved suggesting that good correlation may be obtained to some extend. The new ratio (*Adeq.Precision*) obtained was equal to 7.314 > 4 thus indicating a good signal to navigate the design space. *DESIGN-EXPERT® 6.0.8* was employed to produce the new model for R_t along with *MINITAB® 17.* The mathematical models of first-order for R_a and R_t are given in Eq. 2 and Eq. 3 respectively; see below and involve the first and the second levels of the three parameters according to the regression plots in Fig. 10. The normal plots of residuals in this figure indicate that the residuals are normally distributed. The straight line in the two histograms represents the actual values; whilst the dots illustrate the predicted ones. Thereby, the closer the dots to the center line the better the correlation (efficient prediction) is.

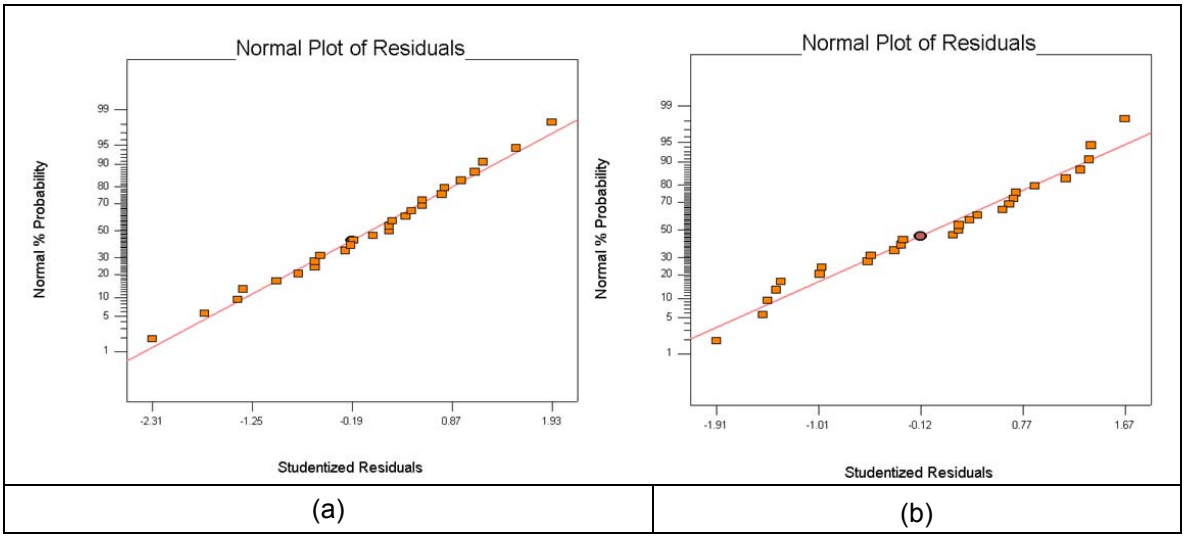

Fig. 10. Normal plots of residuals for: (a) R_a and (b) R_t prediction

The first and second order as well as the exponential prediction models for R_a and R_t surface roughness parameters examined, along with the relevant coefficients of determination (R^2) are listed in Tables 4, 5 and 6 respectively.

Table 4. First-order prediction models for R_a and R_t using the ANOVA "general linear model" approximation

R_a = 1.99 + 0.51 *n* + 0.59 *s* - 0.064 *a* + 1.25 *n s* + 0.073 *n a* - 0.077 *s a*.	R^2 = 0.964	(2)
R_t = 12.26 - 0.81 *n* + 0.73 *s* - 0.77 *a*.	R^2 = 0.750	(3)

The "*least squares"* approach for each constant parameter while varying the rest, was implemented to develop the second-order prediction models at it was mentioned. Table 5 gives the respective models for R_a and R_t.

Table 5. Second-order prediction models for R_a and R_t using "least-squares" approximation

R_a		R^2	
n=const=420 mm/min	R_a = 3.45 - 27.37*s* + 135 s^2 - 1.53 a + 0.35 *s a* + 0.73 a^2	*0.968*	(4)
n=const=600 mm/min	R_a = 2.23 - 21.53 *s* + 112.778 s^2+0.53 *a* - 0.60 *s a* - 0.067 a^2	*0.975*	(5)
n=const=850 mm/min	R_a = 1.35 - 2.64 *s* + 46.29 s^2 +0.53 *a* - 3.9 *s a* - 0.047 a^2	*0.994*	(6)
R_t			
n=const=420 mm/min	R_t = 27.48 - 296.63 *s* + 1439.6 s^2 - 3.9 *a* - 20.87 *s a* + 2.87 a^2	*0.788*	(7)
n=const=600 mm/min	R_t = 12.50 - 111.86 *s* + 639.6 s^2 + 6.48 *a* - 14.31 *s a* - 1.04 a^2	*0.796*	(8)
n=const=850 mm/min	R_t = 6.88 - 87.26 *s* + 709.26 s^2 + 20.312 *a* - 62.05 *s α* - 6.33 a^2	*0.812*	(9)

The exponential models (power functions) for roughness parameters considering spindle *n (rpm)*, feed rate *s (mm/rev)* and depth of cut, *a (mm)* were developed according to Eq. 10.

$$R_a = c \times n^k \times s^l \times a^m \times \varepsilon \qquad (10)$$

In Eq. 10 *c, k, l* and *m* are constants ("theta" parameters – see Fig. 9) whilst *ε* represent the random error. Based on Eq.10 a logarithmic representation may be extracted in order to calculate the constants involved. Hence, Eq.11 can be alternatively represented as a linear combination of the logarithmic expression of the independent variables as follows:

$$\ln R_a = \ln c + k \ln n + l \ln s + m \ln a + \ln \varepsilon \quad (11)$$

The power functions finally developed to predict R_a and R_t are given in Eq. 12 and Eq. 13 respectively; see Table 6.

Table 6. Exponential prediction models for R_a and R_t using "Gauss-Newton" power function

$R_a = 4.00052\ n^{-0.387491}\ s^{-0.408521}\ a^{-0.504174}$	$R^2 = 0.998$	(12)
$R_t = 12.097\ n^{0.108481}\ s^{-0.0418982}\ a^{-0.0464876}$	$R^2 = 0.983$	(13)

It is evident that in all three types of models examined better correlation is exhibited by R_a than by R_t. Moreover, for both surface roughness parameters examined, closer correlation is provided by the exponential model as compared to the first and second order ones.

5. CONCLUSIONS

By applying analysis of variance and statistical multi-regression analysis to the experimental data close correlation is revealed between certain surface finish parameters (R_a and R_t) and the machining conditions (spindle speed, *n*; feed rate, *s* and depth of cut, *α*) when turning CuZn39Pb3 brass alloy. For both R_a and R_t roughness parameters examined, closer correlation is provided by the exponential model as compared to the first and second order ones

On the contrary, as far as the variation of R_{sk}, (skewness) and R_{ku} (kurtosis) is concerned, it was revealed that these parameters can not be related neither with cutting conditions in a higher or lesser degree, nor to be correlated with typical amplitude parameters such as R_a or R_t; i.e., they belong to the so-called "unrelated surface roughness parameters".

The fractal dimension *D* is an intrinsic property of the surface, which is scale-independent and reflects the 'complexity' of the profile structure. The fractal dimension D appears, in general insensitive to cutting parameters. Measured values of this parameter are in most cases in the range of around 1.3.

The mutually independent parameters such as R_a, R_t and R_{sk}, R_{ku}, D are considered to make-up a minimum set for surface texture description regarding both industrial quality control and applied scientific research.

ACKNOWLEDGMENTS

The authors are grateful to Dr.-Ing. G.A. Pantazopoulos of ELKEME Hellenic Research Centre for Metals s.a for the supply of CuZn39Pb3 brass specimens and to Prof. D.E. Manolakos, Director of Manufacturing Processes Division at National Technical University of Athens (NTUA) for providing the machining facilities. They also wish to thank Mr. N. Melissas, technician at NTUA for performing the cutting experiments.

REFERENCES

1. PETROPOULOS, G.P., VAXEVANIDIS, N.M., PANDAZARAS, C.N., ANTONIADIS, A.T., Control of representative turned surface textures, Wear, **257** (12), 2004, 1270-1274.

2. PETROPOULOS, P., PANDAZARAS, C.N., DAVIM, J.P., Surface Texture Characterization and Evaluation Related to Machining, in Surface Integrity in Machining, Springer, Ed. J.P. Davim, 2010, pp. 37-66.

3. VAXEVANIDIS, N.M., KECHAGIAS, J.D., FOUNTAS, N.A., MANOLAKOS, D.E., Evaluation of Machinability in Turning of Engineering Alloys by applying Artificial Neural Networks, Open Constr. & Building Technol. J., **8**, 2014, 389-399.

4. VAXEVANIDIS, N.M., GALANIS, N., PETROPOULOS, G.P., KARALIS, N., VASILAKAKOS, P., SIDERIS, J., Surface Roughness Analysis in High Speed-Dry Turning of Tool Steel, in Proceedings of ESDA 2010: 10th Biennial ASME Conference on Engineering Systems Design and Analysis, July 12-14, 2010, Istanbul, Turkey, (paper ESDA 2010-24811).

5. PETROPOULOS, G.P., PANDAZARAS, C.N., VAXEVANIDIS, N.M., ANTONIADIS, A., Multi-parameter identification and control of turned surface textures, Int. J. Adv. Manuf. Technol., **29** (1-2), 2006, 118-128.
6. PETROPOULOS, G., VAXEVANIDIS, N., IAKOVOU, A., DAVID, K., Multi-parameter modeling of surface texture in EDMachining using the design of experiments methodology, Mat. Sci. Forum, **526**, 2006, 157-162.
7. GADELMAWLA, E.S., KOURA, M.M., MAKSOUD, T.M.A., ELEWA, I.M., SOLIMAN, H.H., Roughness parameters, J. Mat. Proces. Techn., **123** (1), 2002, 133-145.
8. GRZESIK, W., BROL, S., Hybrid approach to surface roughness evaluation in multistage machining processes, J. Mat. Proces. Techn., **134** (2), 2003, 265-272.
9. PETROPOULOS, G., VAXEVANIDIS, N., PANDAZARAS, C., KOUTSOMICHALIS, A., Postulated Models for fhe Fractal Dimension of Turned Metal Surfaces, J. Balk. Tribol. Assoc., **15** (1), 2009, 1-9.
10. PETROPOULOS, G., PANDAZARAS, C., VAXEVANIDIS, N.M., NTZIANTZIAS, I., KORLOS, A., Selecting subsets of mutually unrelated ISO 13565-2: 1997 surface roughness parameters in turning operations, Int. J. Comput. Mater. Sci. Surf. Eng., **1** (1), 2007, 114-128.
11. ÖZEL, T., KARPAT, Y., Predictive modelling of surface roughness and tool wear in hard turning using regression and neural networks, Int. J. Mach. Tools Manuf., **45**, 2005, 467-479.
12. VAXEVANIDIS, N.M., FOUNTAS, N.A., KECHAGIAS, J., MANOLAKOS, D.E., Estimation of main Cutting Force and Surface Roughness in turning of Ti-6Al-4V titanium alloy using Design of Experiments and Artificial Neural Networks, in Proceedings of the International Conference on Engineering and Applied Sciences Optimization (OPT-i), June 4-6, 2014, Kos, Greece, pp. 2889-2906, 2014.
13. GAITONDE, V.N., KARNIK, S.R., DAVIM, J.P., Optimal MQL and Cutting Conditions determination for desired Surface Roughness in Turning of Brass using Genetic Algorithms, Mach. Sci. Technol., **16** (2), 2012, 304-320.
14. NOWICKI, B., Multiparameter representation of surface roughness, Wear, **102** (3), 1985, 161-176.
15. PANTAZOPOULOS, G., Leaded brass rods C 38500 for automatic machining operations: a technical report, J. Mater. Eng. Perform., **11**, 2002, 402-407.
16. TOULFATZIS, A.I., PANTAZOPOULOS, G.A., PAIPETIS, A.S., Fracture behavior and characterization of lead-free brass alloys for machining applications, J. Mat. Eng. Perform., **23** (9), 2014, 3193-3206.
17. GALANIS, N.I., MANOLAKOS, D.E., Surface roughness prediction in turning of femoral head, Int. J. Adv. Manuf. Technol., **51** (1-4), 2010, 79-86.
18. HASEGAWA, M., LIU, J., OKUDA, K., NUNOBIKI, M., Calculation of the fractal dimensions of machined surface profiles, Wear, **192** (1), 1996, 40-45.

.

CORRESPONDENCE

Nikolaos VAXEVANIDIS:
Professor, School of Pedagogical and Technological Education (ASPETE), Department of Mechanical Engineering Educators, ASPETE Campus, GR 14121, N. Heraklion Attikis, Greece.
e-mail: vaxev@aspete.gr

Tribological Journal BULTRIB Vol. 5, 2015
Papers from the International Conference **BULTRIB '15**
September 11-13, 2015, Sozopol, Bulgaria
Society of Bulgarian Tribologists
FIT – Technical University of Sofia

SLIDING WEAR BEHAVIOUR OF NICKEL ELECTRODEPOSITED COATINGS

A. Koutsomichalis[1], N. Vidalis[1], N. Vaxevanidis[2]

[1]Hellenic Air-Force Academy, Faculty of Aerospace Studies, Dekelia Air Force Base, GR 19005, Greece, e-mail: a.koutsomichalis@gmail.com
[2]School of Pedagogical & Technological Education, Department of Mechanical Engineering Educators, GR 14121 N. Heraklion Attikis, Greece, e-mail: vaxev@aspete.gr

Abstract: *Ni coating was deposited on carbon steel by electrolysis. The tribological behaviour of the coating was measured on a standard ball-on-disk tribometer at four different loads 1 N, 2 N, 5N and 10 N. Friction coefficient was found to quickly stabilize; the higher the applied load the faster the friction coefficient reached stabilization. Wear volume was found to increase in proportion to the applied load and the sliding distance. The wear behaviour is strongly related to the tribofilm formed which was found to consist of plastically deformed splats and wear debris.*

Key Words: *electroplating; nickel (Ni) coating; sliding wear*

6. INTRODUCTION

Electrodeposited coatings are widely used as protective surface coatings of engineering components to improve their wear resistance and service life [1-5]. This process is very attractive for large scale industrial applications, offering an inexpensive method to produce large area samples. Electrodeposited nickel coatings, particularly using sulfamate electrolytes, are widely popular in the electroplating industry due to their high deposition rates, greater film thickness, good mechanical and corrosion resistant properties and low residual stress [6-9]. Nickel electrodeposited coatings are reported to exhibit anisotropy and high sensitivity to electroplating conditions e.g. current density [10]. The enhanced mechanical properties of Nickel (Ni) electrodeposits (for example, high hardness and strength) are expected to lead to improved tribological properties, i.e., increased resistance to wear.

A higher current density can be detrimental for the mechanical properties of the thick Ni deposits due to both structural changes in growing film and to residual stresses [11]. On the other hand, lower deposition rates (current density) are expected to produce deposits with improved mechanical properties along with lower tensile stresses for films thicker than 1 μm [12]. Polycrystalline (10-100 μm grain size) electrodeposited Ni coatings exhibited lower wear resistance and higher friction coefficient than nanocrystalline nickel (10-20 μm grain) size in the standard pin-on-disk test [13].

Studies on the nickel plating have been performed by other workers [14-16] and they have reported on mechanism and characteristics of nickel plating. However, there are a few problems to be solved such as increase of toxic wastewater amount from the plating industry and decrease of plating productivity due to limited technical enhancement and high production cost [17].

Some researchers using DC electrodeposited specimens, found that nickel increase in hardness following the Hall-Petch relationship ($H=Ho+k/d^{1/2}$), where d is the layer thickness, Ho is the rule of mixture hardness and k is a constant. This Hall-Petch strengthening was manifested in abrasive wear measurements [18,19].

The present research focuses on the study of the structure, composition, and wear behaviour of an electrodeposited Ni coating on a steel substrate.

7. EXPERIMENTAL

Nickel electrodeposits were produced by direct current (DC) plating in a nickel sulfamate electrolyte with 240 g/l $NiSO_46H_2O$, 45 g/l $NiCl_26H_2O$, 30g/l boric acid. Electroplating was performed in a electrolyte which was filtered with circulating pump during plating to remove the impurity debris. The electrodeposition was conducted at 50±1 °C (with temperature control module), without stirring and at a pH of 3.5. Nickel balls in a plastic basket were used as anode.

The current density was 5 A dm^{-2} following the literature [10,13, 20]. The deposition time was varied to keep the total charge constant according to Faraday's law, thus enabling different nominal thickness for each set of measurements.

The substrate was steel specimens with dimensions of 5 cm x 1 cm x 0.1 cm. The steel substrates were mechanically polished by wet grinding down to 1200 mesh-grit using standard metallographic techniques. This process was followed by polishing with 6, 1 and 0.25 µm diamond pastes, The average roughness of the polished surface was about 0,04 µm. Subsequently these samples were cleaned ultrasonically in acetone for 5 min to remove diamond particles followed by alkali cleaning to degrease the surface and then rinsed in water followed by acid dip (10% H_2SO4) for 10 s to remove the residual alkali prior to deposition, and finally prepared by a nickel electrolytic deposition mechanism. The average deposit thicknesses, as measured by profilometry after electrodeposition, were found to be 25, 30 and 40 µm. The surface morphology and the composition of the Ni-electrodeposits were characterized by a scanning electron microscope (JEOL 6300) with energy dispersive analyzer system (EDAX) operated at 20 kV accelerating voltage.

The friction and wear tests were performed at room temperature in a ball-on-disc type tribometer with a constant rotation speed of 200 r/min at a constant radius of 2.5 mm and *with* four different loads 1 N, 2 N,5 N and 10 N under non-lubricated conditions. Si_3N_4 ceramic balls with 2 mm in diameter were used as the counter body. Each wear test lasted for 1 h for a total distance of 188.4 m. The friction coefficients vs cycling number were recorded automatically during the test. All the friction pairs were cleaned by ultrasonically washing in acetone before and after each test. The volume loss of the samples was detected to evaluate the wear resistance of the coatings. Three replicating tests were carried out so as to minimize data scattering, and every value reported was an average of three measurements. After the wear test, the worn surfaces of the coatings were investigated using SEM.

8. RESULTS AND DISCUSSION

Figure 1 shows the SEM micrographs of the Ni surface electrodeposited at a current density of 50 mA cm^{-2} for 90 min using nickel sulfamate bath. A uniform layer growth of nickel deposit has been observed. The surface, though macroscopically smooth (figs 1a & 1b), contains several irregular domains with microscale roughness. The surface exhibits small scale roughness and presence of point defects which can be characterized macroscopically as uniform and smooth. Higher magnification of the surface view (fig 1c) reveals the development of grains sized 2-5 µm which are easily distinguished and the grain boundaries which may act as initiation start of the corrosion phenomenon.

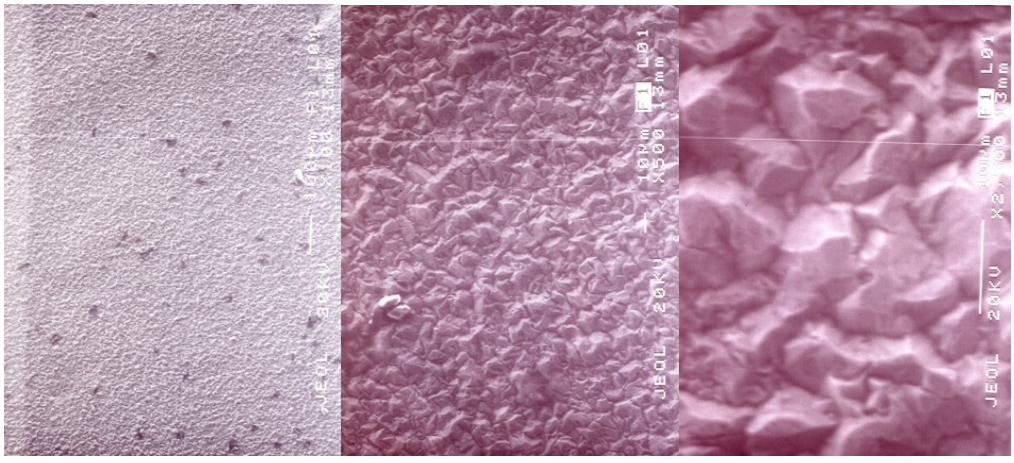

(a) (b) (c)

Fig. 1. SEM micrograph of the nickel electrodeposit top view

The microstructure of deposits consists of columnar grains, with size becoming larger with thickness. Ni deposited appears to have a “cauliflower” structure, with deep crevices outlining groups of smaller substructures [21]. Thick Ni electrodeposits plated at lower current densities (3-15 mA cm^{-2}) have been reported to have a characteristic columnar microstructure where the grains often extend through the thickness of the

deposit, with the grain size increasing with increasing current densities [13, 22]. The surface morphologies of the deposits have also been shown to change from a 'cauliflower' to a 'truncated pyramidal' structure with increase in current densities [21].

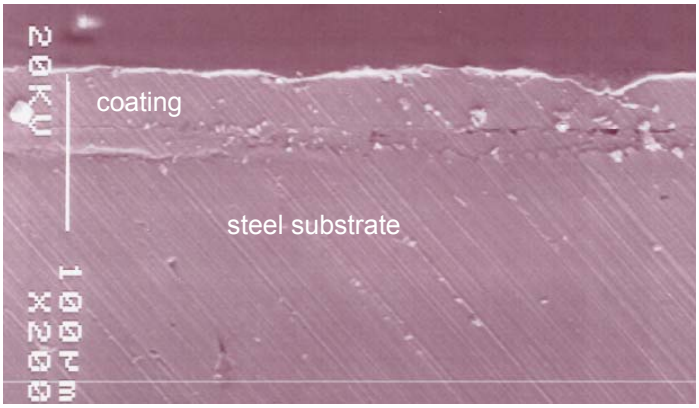

Fig. 2. SEM micrograph of the nickel electrodeposit cross section

Fig 2 shows the cross section of the Ni electrodeposits which exhibits a good interface with the steel substrate. It should be mentioned that during electrodeposition metal thin films typically grow under non-equilibrium conditions, which often result in internal (or residual) stresses even in the absence of any external force or temperature gradient [23].

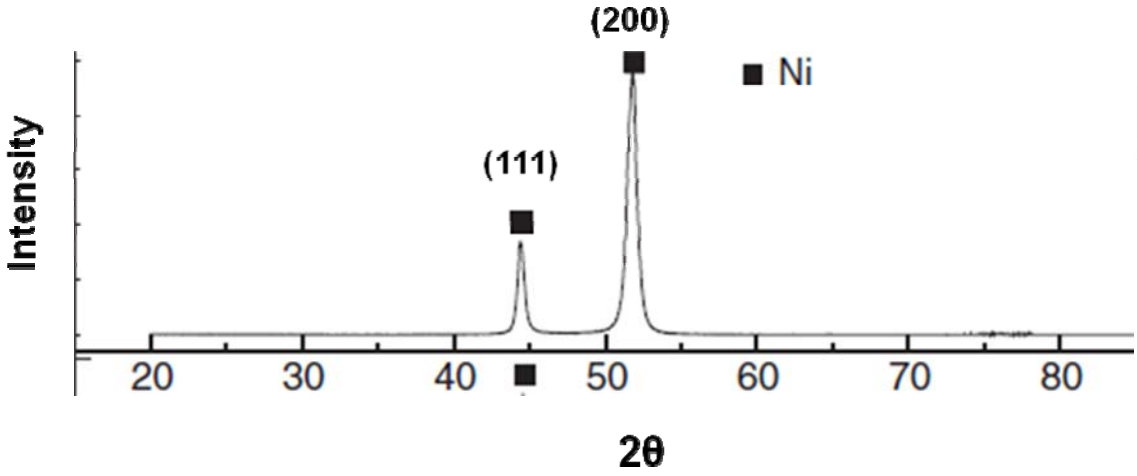

Fig. 3. X-ray diffraction spectra of the electrodeposited nickel

The crystal structure of the electrodeposited nickel was studied by X-ray diffraction analysis. Fig. 3 shows respectively the XRD of electrodeposited nickel at 10 mA cm^{-2} for 1 h. The X-ray diffraction patterns clearly show the characteristic reflections expected for nickel with face centered cubic (fcc) structure [24]. It is thus clearly visible that the nickel crystals in the pure nickel deposits have a preferential [100] orientation. The grain size d of Ni can be determined from the (200) peak via the Scherrer equation [25]:

$$d = \frac{k\lambda}{\beta(\theta)\cos\theta} \tag{1}$$

where k is the X-ray wavelength, β the full width of half maximum of the (200) diffraction peak, θ the diffraction angle and the constant k≈1. From Eq. (1) the average grain size of this Ni deposit was about 40 nm. In addition, the XRD results also showed that the Ni coating had an evident {200} preferred texture, which may be attributed to the electrodeposition conditions given that the Ni electrodeposits are usually known for showing numerous, well-defined preferred orientations depending on the deposition conditions (temperature, pH, current density, electrolyte composition, etc) [26,27].

The Ni electrodeposited coating is characterized by residual stresses that results from particular plating conditions and bath composition [28]. Residual stress has been measured in polycrystalline nickel by X-ray diffraction ($\sin^2\psi$ method) and found to be 130MPa (compression) [29].

The crystallographic texture for thick (~microns) Ni electrodeposits is rather independent of the substrate material but is dependent strongly on the current density, pH, and the presence of organic additives in the electroplating solution [8, 30]. Two general textures have been reported for electrodeposited Ni: a strong <100> texture caused by a regime of 'free growth' at higher current densities ($\geq$ 10 mA cm^{-2}), and a <110> texture at lower current densities ($\leq$ 5 mA cm^{-2}) where Ni growth is inhibited due to impurities and/or hydrogen adsorption on the plating surface [13,31].

Fig.4 shows the friction coefficient of the as-electrodeposited pure Ni film at loads ranging from 1N to 10N. A running-in period with an increase in the friction coefficient can be observed for all loads. Three successive stages can be clearly distinguished and correlated to micro-phenomena taking place at the coating / counterbody interface: (a) In the first sliding stage, the friction coefficient tends to a value around 0.25, which is related to the initial wear of the Ni electrodeposits, via their plastic deformation at the micro-contact areas (b) In the second sliding stage, the friction coefficient increases to a value of around 0.3-0.5 in dependence of the applied load. This transition can be attributed to the increase of the real contact area that induces higher drag forces during sliding and (c) in the last sliding stage, the friction coefficient remains practically constant, around an average value of 0.40. Such a behaviour can be explained by the intervention of the metallic debris remaining at the contact interface, where they are adherent after having been plastically deformed.

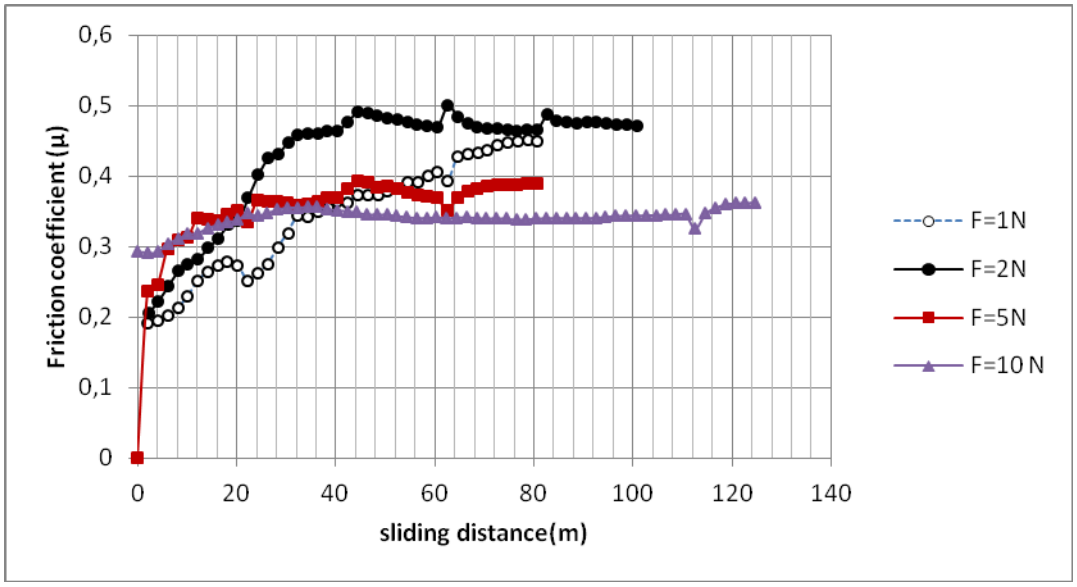

Fig. 4 Friction coefficient of Ni electrodeposits vs. sliding distance at 1, 2, 5 and 10 N load

The variation of wear volume with sliding distance, for all test performed, is presented in Fig.5. For a certain sliding distance wear volume increases with the increase of normal load except for the test under the load of 2 N where a higher non-analogous variation is observed. Note that for this test the highest friction coefficient was identified; see fig.3 in relation to fig.4

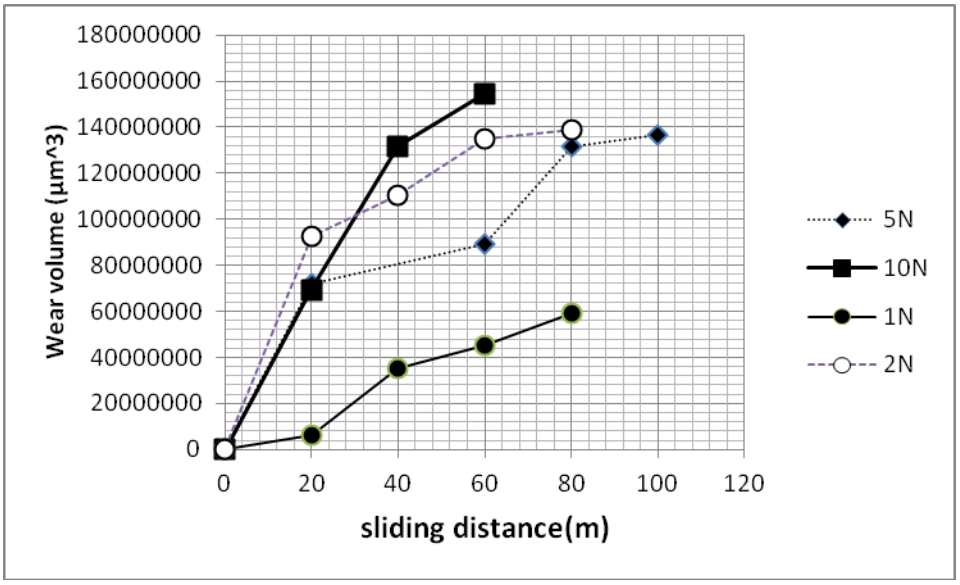

Fig. 5 Wear volume of Ni electrodeposits vs. sliding distance at 1, 2, 5 and 10 N load

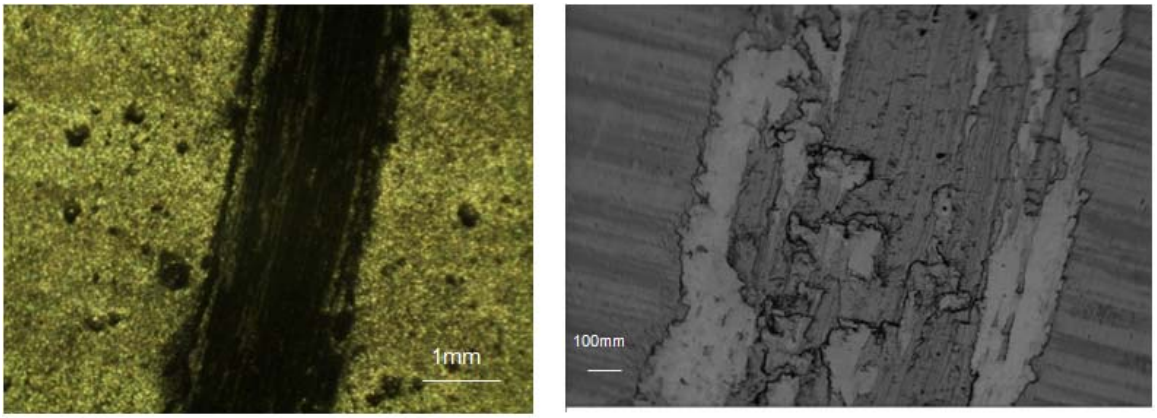

(a) (b)

Fig. 6 (a) *Micrograph of the sliding ditch on the Ni electrodeposit (b) SEM micrograph of the wear track*

On the nickel electrodeposits surface (Fig. 6) cracking and spalling can be seen which causes lots of wear loss. Furthermore, a larger tendency for plastic deformation of asperity junctions results in a higher and unstable friction coefficient. Extensive plastic deformation occurs by the plowing action with extensive side-ridges due to its high ductility. It can be assumed that, in the early stages of the wear test, a considerable amount of nickel is redistributed over the surface in form of these side-ridges and smeared by the repeated sliding action [32] rather than being removed by micro-cutting (or chipping). With increasing sliding distance the Ni coating seems to experience work-hardening as a result of this localized material flow, resulting in microcutting and material removal which is indicated by the increase in the wear volume [33]. Steady state wear rates are obtained towards the end of the test at which point the wear rate of the surface work-hardened polycrystalline nickel is measured.

9. CONCLUSIONS

Nickel electrodeposits were produced by direct current (DC) plating in a nickel sulfamate electrolyte. The microstructure of deposits consisted of columnar grains with a “cauliflower” structure, with deep crevices outlining groups of smaller substructures. The surface, though macroscopically smooth, contained several irregular domains with microscale roughness.

The X-ray diffraction patterns of the Ni electrodeposits showed the characteristic reflections expected for nickel with face centered cubic (fcc) structure.

During wear tests a running-in stage was identified during which the friction coefficient was increasing. Three stages could be recognized during sliding wear: In the first sliding stage (running-in period), the friction coefficient tends to a value around 0.25, which is related to the initial wear of the Ni electrodeposits, via their plastic deformation at the micro-contact areas; (b) in the second sliding stage, the friction coefficient increases to a value of around 0.3-0.5 in dependence of the applied load and (c) in the last sliding stage, the friction coefficient remains practically constant around an average value of 0.40.

REFERENCES

1. GOMES A., PEREIRA I., FERNANDEZ B., PEREIRO R., Electro-deposition of metal matrix nanocomposites: improvement of the chemical characterization techniques, in: Boreddy Reddy (Ed.), Advances in Nanocomposites–Synthesis, Characterization and Industrial Applications, In Tech., 2011, 503.
2. HOVESTAD A.,JANSSEN L.J.J, Electroplating of metal matrix composites by co deposition of suspended particles, in :B.E. Conway (Ed.), Modern Aspects of Electrochemistry, Kluwer Academic/Plenum Publishers, New York, 2005.
3. LOW C.J., WILLS R.A., WALSH F.C., Electrodeposition of composite coatings containing nanoparticles in a metal deposit, Surf. and Coat.Technol. **201,** 2006, 371-383.
4. HOVESTAD R., JANSSEN L.J., Electrochemical codeposition of inert particles in a metallic matrix, J. Applied Electroch., **25**, 1995, 519-527.
5. STOJAK J.L., FRANSAER J., TALBOT J.B., Review of electro-codeposition, in: R.C. Alkire, D.M.Kolb(Eds.), Advances in Electrochemical Science and Engineering, **7**, Wiley VCH Verlag-GmbH, 2001,193.
6. MANDICH N.V., BAUDRAND D.W., Trouble Shooting Decorative Nickel Plating Installations- Part III, Metal Finish. **100**, 2002, 38-46.
7. LI G.Y., LIAN J.S., NIU L.Y., JIANG Z.H., Investigation of nanocrystalline zinc–nickel alloy coatings in an alkaline zincate bath, Surf. Coat. Technol, **191**(1), 2005, 59-67.
8. PATHAK S., GUINARD M., VERNOOIJ M., COUSIN B., WANG Z.,MICHLER J., PHILIPPE L., Influence of lower current densities on the residual stress and structure of thick nickel electrodeposits, Surf. & Coat. Technol., **205**, 2011, 3651-3657.
9. EL-SHERIK A. M., ERB U., in Proceedings of Nickel-Cobalt 97, Ed. F. N. Smith et al., vol. IV, p. 257, Canadian Institute for Minerals, Metals, and Petroleum, Montreal (1997).
10. BUCHHEIT T., MICHAEL J., CHRISTENSON T., LAVAN D., LEITH S., Microstructural and Mechanical properties Investigation of Electrodeposited and annealed LIGA Nickel Structures, Metall. Mater. Trans. **A 33**, 2002, 539-554.
11. KNAPP B.B., Notes on Nickel Plating From Sulfamate Solutions, Plating, **58**, 1971, 1187-1193.
12. RASMUSSEN, A.A., MØLLER P., SOMERS M.J. Process-microstructure-hardness relations of electrodeposited nickel layers, Surf. Coat. Technol. **200**, 2006, 6037-6046
13. MARQUIS E.A., TALIN A.A, KELLY J.J., GOODS S.H., MICHAEL J.R., Effects of Current density on the structure of Ni and N i-Mn electrodeposits, J. Appl. Electrochem. **36**, 2006, 669-676.
14. ABDEL-HAMID Z., Improving the throwing power of nickel electroplating baths, Materials Chemistry and Physics **53**, 1998, 235-238
15. MIN B.S.,. CHUNG W.S, KIM I.G., Effect of frequency on properties of film in Cu electroplating using square pulse plating, J. Kor. Inst. Met. & Mater., **40**, 2002, 1281-1286.
16. QU N.S., ZHU D., CHAN K.C., LEI W.N., Pulse electrodeposition of nanocrystalline nickel using ultra narrow pulse width and high peak current density, Surf. Coat. Technol., **168**, 2003, 123-128.
17. HONG K.M., KIM M.S., CHUNG J.G. Study on effect of electrolyte/surfactant composition on nickel nano-electroplating in supercritical nano-plating system, Appl. Chem., **7**, 2003, 145-148.
18. FARHAT Z.N., DING Y., NORTHWOOD D.O., ALPAS A.T., Effect of grain size on friction and wear of nanocrystalline aluminum, Mater Sci Eng., **A206**, 1996, 302-313.
19. PALUMBO G., GONZALEZ F., BRENNENSTUHL A.M., ERB U., SHMAYDA W., LICHTENBERGER P.C., In-situ nuclear steam generator repair using electrodeposited nanocrystalline nickel, Nanostructured Materials, **9** (1-8), 1997, 737-746.
20. SAFRANEK W.H., The Properties of Electrodeposited Metals and Alloys: A Handbook, Elsevier Science Ltd, 1974.
21. BANOVIC S.W., BARMAK K., MARDER A.R., Microstructural characterization and hardness of electrodeposited nickel coatings from a sulfamate bath, J. Mater. Sci., **33**, 1998, 639-646.
22. DINI J.W., Electrodeposition: The Materials Science of Coatings and Substrates, 1rst ed. William Andrew, 1994.
23. OHRING M., Materials Science of Thin Films, Second edition, Academic Press, San Diego, 2002, p. 711
24. HAMMOND C., The Basics of Crystallography and Diffraction, Oxford University Press, Oxford, 1997.
25. BIRKS L.S., FRIEDMAN H., Particle Size Determination from X-Ray Line Broadening J. Appl. Phys. 17, 1946, 687-692.

26. CZERWINSKI F., SZPUNAR J.A., Controlling the Surface Texture of Nickel for High Temperature Oxidation Inhibition, Corros. Sci. **41**, 1999 729-740.
27. EL-SHERIK A.M, ERB U., PAGE J., Microstructural evolution in pulse plated nickel electrodeposits Surf. Coat. Technol. **88**, 1997, 70-78.
28. EL-SHERIK A.M, SHIROKOFF J., ERBC U. Stress measurements in nanocrystalline Ni electrodeposits, J. Alloys and Compounds **389**, 2005, 140-143.
29. RUDD C.O., MCDOWELL R.J., SNOHA D.J., An XRD investigation of a Face-Centered Cubic Metallic Plating, Powder Diffr. **1**, 1986, 22-27.
30. LEE E.C., CHOI J.W., A study on the mechanism of formation of electrocodeposited Ni–diamond coatings, Surf. Coat. Technol. 148**, (2001 234-240.**
31. SAFRANEK W.H., The Properties of Electrodeposited Metals and Alloys: A Handbook, Elsevier Science Ltd, 1974.
32. AKAGAKI T., KATO K., Plastic flow process of surface layers in flow wear under boundary lubricated conditions, Wear, **117**(2), 1987, 179-196.
33. GARBAR I. I., SKORININ J. V., Metal Surface Layer Structure Formation Under Sliding Friction, Wear. **51**, 1978, 327-336.

CORRESPONDENCE

Nikolaos VAXEVANIDIS:
Professor, School of Pedagogical & Technological Education (ASPETE), Department of Mechanical Engineering Educators, ASPETE Campus, GR 14121, N. Heraklion Attikis, Greece
e-mail: vaxev@aspete.gr